An Investigation into Shock Events on Martian Analogue Minerals using Raman Spectroscopy

By

Ricky John Colin Hibbert

A thesis presented for the degree of

Doctor of Philosophy

School of Physical Sciences

University of Kent

Canterbury, UK

July 2019

Declaration

The content of this thesis has been composed by the author, and has not been submitted for a further degree at any other higher educational institute.

The content comprising Chapter 3, Sections 3.2 and 3.4 was adapted and extended from work which has been published in Hibbert *et al.* (2017).

The content comprising Chapter 3, Sections 3.3 and 3.4 was carried out in conjunction with Mike Cole, the experimental officer of the University of Kent's Centre for Astrophysics and Planetary Science research group. Sections 3.3.1, 3.4.1, 3.4.2, and 3.4.6 describe work that was completed before the author's research began, while Sections 3.3.2, 3.3.3, 3.4.3, 3.4.4, 3.4.5, 3.4.7, and 3.4.7.7 describe how that work continued once the author joined the project.

The fitting scripts used in Chapter 4 and Chapter 5, as well as the map plotting script used in Chapter 5, were written by T. M. Kinnear of the University of Kent's Centre for Astrophysics and Planetary Science research group.

All data used in this thesis is the author's own, unless stated otherwise.

Acknowledgements

I would like to thank my supervisor Dr Mark Price for his patience, guidance and advice. I have learnt a great deal throughout the course of the PhD and I wouldn't have had this opportunity without you.

Thank you to the other members of the impact research group Professor Mark Burchell, Dr Penny Wozniakiewicz and Dr Kathryn Harris. Thank you for all of your input during the Friday morning meetings and for your advice and support whenever I asked for it. A huge special thank you to Mike Cole, without whom this thesis (and those of many past impact group students) would not exist. Thank you for teaching me how to use the LGG and being patient with all of my stupid questions about the gun. You invested a great deal of time and energy into helping make the low-speed gun (mostly) work, for which I am eternally grateful.

I would also like to thank Dr Timothy Kinnear for writing the original data processing script and also for always being willing to help with my coding problems as well as just generally being a good friend.

To Justin, we had quite a few late night chat/rants about our work. Thank you for always being a good friend and living with me for three years. I could not have asked for a better housemate.

A big thank you to the other PhD students in the impact group who let me talk ideas and concepts through (/at) them: Nisha, Jamie, Luke, James, and also to all the other postgraduates who are too numerous to name that I have been fortunate to call friends over the course of my PhD.

Thank you to Martin Beard who has always taken an interest in my research and whose company MJ's supplied the punches for the low-speed gun. Progress would have halted (and did) without you.

To my parents, my mum Julie, my dad Keith and my step-dad Tony; thank you for all of your support both emotional and financial. Without you, I would not be the person I am today and would not have been able to achieve half of what I have.

And finally to Lorelei, who has been with me throughout my entire PhD and as a consequence, has had to deal with all of the frustrations that that entails. Thank you from the bottom of my heart for everything. For listening to my rants when I got home; for letting me talk at you about my work as I try to get something straight in my head; for always helping in any way that you can; and especially for always being there when I need you. What we have truly is a partnership and I hope to be able to return the favour and help you pursue your goals in the future.

Abstract

In early 2021 both *NASA*'s *Mars 2020* and *ESA*'s *Rosalind Franklin* rovers will land on Mars carrying Raman spectrometers. This will be the first time that a Raman spectrometer has been deployed on another planetary body and both rovers will conduct their mission in regions that contain impact craters and, therefore, it is likely that both missions will encounter samples that have been subjected to shock.

This thesis examines how the Martian environment can potentially influence the Raman spectrum of minerals, which was achieved by examining the effects of temperature and shock.

The first series of experiments investigated the influence of temperature on the Raman spectrum of the three minerals: olivine, quartz, and labradorite. These experiments showed that the Raman peak positions vary based on the temperature of the sample. As the sample temperature was increased, the Raman peak position decreased (at varying rates) for all three minerals, which could lead to the misinterpretation of the exact composition of the minerals samples if not properly corrected for. Further temperature investigations were also conducted into the degree of 'laser heating' generated in samples by the Raman spectrometer during acquisition.

Mineral samples with a range of grain sizes were tested to determine if there is a relationship between the size of the sample and the amount of 'laser heating'. This experiment was not able to detect the presence of any 'laser heating' in any of the samples, however, an experimental procedure has now been developed and can be repeated with smaller, more appropriately sized grains in the future.

The second series of experiments explored the effects of shock on the Raman spectrum of the same three minerals. For this experiment, each of the minerals was impacted using the light gas gun at the University of Kent at a range of velocities (and therefore shock pressures) before being examined using a Raman spectrometer. An attempt was made to determine if the induced changes in the Raman spectrum of the samples could be used as a shock barometer to infer the magnitude of shock experienced by the sample. Results showed that this was generally not possible as much of the shocked material had been excavated during the crater formation process.

It was found that lower speed shots, which merely produced an indentation on the surface of the samples without the loss of material, were better suited to such an investigation. As such, methods of firing the light gas gun at a lower velocity were used. This was done to preserve the experimental procedure across all velocities in order to reduce the chance of introducing systematic errors to the dataset. This required the development of an entirely new firing system known as the electronic burst disk which is presented here in full for the first time.

Table of Contents

Declaration i
Acknowledgements ii
Abstract iii
Table of Contents iv
List of Figures vii
List of Tables xvii
Chapter 1 - Introduction 1
1.1 Outline of Thesis 4
Chapter 2 - Background 6
2.1 Impacts 6
2.1.1 Importance of Impact Studies 6
2.1.2 Meteorites 7
2.1.3 Crater Formation 8
2.1.4 High-Pressure Polymorphs 10
2.1.5 Complications 10
2.2 Raman Spectroscopy 11
2.2.1 History of Raman Spectroscopy 11
2.2.2 Theory of Raman Spectroscopy 12
2.2.3 Problems with Raman Spectroscopy - Fluorescence 16
2.2.4 Problems with Raman Spectroscopy - Destructive 18
2.2.5 Applications of Raman Spectroscopy 19
2.3 Summary 22
2.3.1 Possible Application to the *ExoMars* Rover 22
Chapter 3 - Instrumentation 23
3.1 The Raman Spectrometer at the University of Kent 23
3.1.1 Operating Principles 23
3.1.2 Other Features 26
3.2 The Light Gas Gun 26
3.2.1 Upgrades 27
3.2.2 Firing Procedure 31
3.3 Low Speed Gun 32
3.3.1 Development Process 34
3.3.2 Secondary Problem 36
3.3.3 Single Stage 36
3.4 Electronic Burst Disk 39
3.4.1 Fusing Bench Testing 39

3.4.2 Design Phase 39
3.4.3 Electronic Central Breech Bench Test 43
3.4.4 Gun Tests 43
3.4.5 Punches 46
3.4.6 Firing Control System 47
3.4.7 Firing Procedure 48
3.4.8 Current Status 61
3.5 Shot ID Numbers 61
3.6 Summary 62
Chapter 4 - Raman Thermometry 63
4.1 Introduction 63
4.2 Mineral Sample Selection 64
4.2.1 Olivine 65
4.2.2 Quartz 66
4.2.3 Labradorite 68
4.2.4 Chosen Samples 70
4.3 Methodology 70
4.4 Results 74
4.4.1 Peak Position Versus Sample Temperature 74
4.4.2 Stokes Temperature versus Sample Temperature 77
4.4.3 Calibration Test 79
4.4.4 Corrected Data 83
4.5 Sample Temperature as a Function of Sample Size 88
4.5.1 Methodology 89
4.5.2 Results 91
4.6 Summary 94
Chapter 5 - Raman Spectrometry as a Shock Barometer I 96
5.1 Introduction 96
5.2 Methodology 96
5.2.1 Accuracy of the Data 99
5.2.2 Intensity Maps 100
5.2.3 Calculating the Peak Shock Pressure 101
5.3 Results 102
5.3.1 Quartz 105
5.3.2 Olivine 121
5.3.3 Labradorite 143
5.4 Summary 167
Chapter 6 - Raman Spectrometry as a Shock Barometer II 169

6.1 Introduction 169
6.2 Peak Intensity 169
6.3 Peak Width 170
6.3.1 Annealing Test 171
6.3.2 Quartz 173
6.3.3 Olivine 173
6.3.4 Labradorite 180
6.4 Peak Position 190
6.4.1 Elemental Composition 190
6.4.2 Structural Changes 191
6.4.3 Quartz 193
6.4.4 Olivine 199
6.4.5 Labradorite 204
6.5 Summary 210
Chapter 7 - Conclusions and Future Work 213
7.1 Conclusions 213
7.2 Future work 218
Bibliography 220
Appendix A – Stokes Temperature Tables 233

List of Figures

Figure 2.1: Topographical map of Mars showing Hellas Planitia and Utopia Planitia [25]. 6

Figure 2.2: The phases of crater formation. Image courtesy of the Lunar and Planetary Institute, credit: Bevan M. French and David A. Kring of the Lunar and Planetary Institute. 9

Figure 2.3: Schematic of the set-up of the Raman experiment carried out in 1928... 11

Figure 2.4: Schematic diagram of the Rayleigh and Raman scattering process..... 12

Figure 2.5: An example Raman spectrum of silicon with the peak at 520.6 cm^{-1} highlighted in red..... 14

Figure 2.6: The symmetrical vibrations of an O_2 molecule. The outer ellipse is a visual representation of the change in the polarisability of the electron cloud. 15

Figure 2.7: The symmetric and asymmetric vibrations of a CO_2 molecule. The outer ellipse around each molecule is a visual representation of the change in the polarisability of the electron cloud. In the case of the symmetric vibration, there is a change in the polarisability of the electron cloud. In the case of the asymmetric vibration, there is no change in the polarisability of the electron cloud..... 16

Figure 2.8: Example of a fluorescent spectrum (blue) using a blue (473 nm) laser and how this can be overcome by changing the excitation wavelength to a NIR (784.15 nm) laser (black). 17

Figure 2.9: Diagram showing the process of fluorescence emission in comparison to Rayleigh and Raman scattering [67]..... 17

Figure 2.10: Melting of a bismuth-ferrite sample (melting point 800°C) due to exposure to a Raman spectrometer's laser (20.10 mW) for 10 seconds..... 18

Figure 2.11: The fusion crust surrounding the interior of the NWA 7496 meteorite (image credit: Dr. Randy Korotev of Washington University in Saint Louis). 21

Figure 3.1: A simple diagram to show a 90° collection system. 23

Figure 3.2: The University of Kent's Horiba LabRam HR Raman spectrometer. 24

Figure 3.3: A diagram showing the optical path inside the Horiba LabRam HR Raman spectrometer including the 180° collection system. 24

Figure 3.4: Diagram demonstrating how a diffraction grating separates the different wavelengths of light and spreads them across a CCD detector. 26

Figure 3.5: The LGG facility at the University of Kent as of November 2017 27

Figure 3.6: A split sabot illustrating the four interlocking segments and the central hole which houses the projectile(s). 27

Figure 3.7: (A) The hot target holder with a 60 mm diameter cylinder of sandstone housed in the centre ready for heating. (B) A water ice layer over a solid basalt target impacted at an impact angle of 45° (target diameter 40 cm).. 29

Figure 3.8: (left) A spherical target in the rotating target holder at the moment of impact and (Right) during complete disruption of the target (approximately 5 milliseconds later)..... 30

Figure 3.9: The ocean target holder showing the frame holding two bags of water. The arrow indicates the path of the incoming projectile. 31

Figure 3.10: Schematic diagram of the LGG [166]. 33

Figure 3.11: Projectile speed versus initial pressure for krypton gas. 35

Figure 3.12: A central breech that has been split in two after being impacted by a piston at too great a velocity. 36

Figure 3.13: 100 micron aluminium foil fusing bench test. (A) Before the test. (B) After the test. (C) After the test – magnified. 40

Figure 3.14: Technical drawing for the modified central breach known as the electronic central breach (ECB) to be used with the electronic burst disk (EBD) system. 41

Figure 3.15: Technical drawing for a standard LGG central breach 42

Figure 3.16: Technical drawings of the electrodes inside the electronic central breach (ECB). 42

Figure 3.17: Technical drawings of the burst disk support that the electronic burst disk (EBD) is mounted to inside the electronic central breach (ECB). 42

Figure 3.18: A fused 100 micron aluminium foil after a bench test inside the electronic central breach. 43

Figure 3.19: The electronic central breach (ECB) mounted in the light gas gun (LGG) being held in place with ECB bolts. 44

Figure 3.20: Melted burst disk support with the central hole obstructed by the molten material. 44

Figure 3.21: CAD drawing showing the layers involved in the electronic burst disk. From left to right: (a) Steel electrodes, (b) 100 micron thick aluminium foil, (c) adhesive tape, (d) acetate backing, (e) adhesive tape, (f) nylon holder and (g) adhesive tape. 45

Figure 3.22: The prototype foil punch made from brass and constructed using a CNC milling machine. 46

Figure 3.23: The prototype punch being used to punch a 100 micron thick aluminium foil electronic burst disk on a "Sizzex Big Shot" die cutting machine. 47

Figure 3.24: Technical drawings for the punches used to manufacture the electronic burst disk (EBD) layers. (A) Foil punch. (B) Tape/acetate punch. (C) Small tape punch. 47

Figure 3.25: The powder chamber and firing pin mechanism in place on the LGG. ... 49

Figure 3.26: Two of the three electronic central breach (ECB) bolts in place on the LGG for an electronic burst disk (EBD) shot. 49

Figure 3.27: The launch tube in the single stage position. The single stage marking is aligned with the front face of the launch tube clamp. 49

Figure 3.28: The firing control system of the electronic burst disk system. 50

Figure 3.29: A foil being pressed in the tensometer is held in place with the tensometer support while the brass guide aligns the position of the 8.0 mm impression rod. 51

Figure 3.30: Examples of a rejected (left) and a correctly (right) impressed foil..... 51

Figure 3.31: (A) The foil punch in the platen correctly aligned with the large pins. (B) An impressed foil placed onto the punch with the impression aligned across the large pins. (C) A correctly aligned foil secured in place using tape. 52

Figure 3.32: A stack of three 0.75 mm thick polystyrene sheets being held above a punch ready of pressing..... 52

Figure 3.33: The stack of packing material being held in place while the punch being run through the Big Shot press. 52

Figure 3.34: An electronic burst disk foil layer with the notches cut (scale divisions are 0.5 mm). 53

Figure 3.35: The completed layers of the electronic burst disk (EBD) system. (A) 100 micron thick Al foil. (B) Large double-sided adhesive tape. (C) 0.25 mm thick acetate backing. (D) Large double-sided adhesive tape. (E) Small double-sided adhesive tape..... 54

Figure 3.36: The electronic burst disk at various stages of assembly. (A) The assembly guide. (B) The burst disk support on the assembly guide. (C) A tape layer on the bust disk support. (D) The foil mounted to the burst disk support. (E) The small tape mounted to the rear of the burst disk support. 55

Figure 3.37: The foil layer of the electronic burst disk folded 90° along the impression. 55

Figure 3.38: The smoothing tool being used on the surface of the foil attached to the burst disk support. 56

Figure 3.39: The rubber insulator protruding above the electrode inside the electronic central breach (ECB). 56

Figure 3.40: (A) The rubber spacer (left) and the nylon spacer. (B) The spacers mounted in the ECB. The nylon spacer is visible between the electrodes. 57

Figure 3.41: The fully assembled burst disk support inside the ECB with the orientation markers aligned. 57

Figure 3.42: The electronic central breach (ECB) mounted on the Light Gas Gun and connected up ready for firing. 58

Figure 3.43: The gas filling system of the Light Gas Gun..... 59

Figure 3.44: Example of a burst disk having been successfully fused to expose the aperture on the support. 60

Figure 4.1: Olivine powder after having been burnt by the laser of a Raman spectrometer. 63

Figure 4.2: The crystal structure of olivine. Each tetrahedron consists of four oxygen atoms (red) and one silicon atom (blue). Between the tetrahedra are the metal ion sites (orange) which contain either magnesium or iron. Image courtesy of *Crystallography365* using the VESTA software. 65

Figure 4.3: Raman spectra of Mg-rich olivine, forsterite, with the doublet peaks at 823 cm^{-1} and 855 cm^{-1} labelled as P1 and P2 respectively; and Fe-rich olivine, fayalite, with the doublet peaks at 815 cm^{-1} and 839 cm^{-1} labelled as P1 and P2 respectively. 66

Figure 4.4: The crystal structure of quartz made up of silica tetrahedra containing oxygen (red) and silicon (blue). Image courtesy of *Crystallography365* using the VESTA software. 67

Figure 4.5: Raman spectrum of quartz with the peak at 483 cm^{-1} labelled as P1. 67

Figure 4.6: The ternary phase diagram for feldspars [176]. 68

Figure 4.7: Raman spectrum of labradorite, with the doublet peaks at 483 cm^{-1} and 510 cm^{-1} labelled as P1 and P2 respectively. 69

Figure 4.8: The crystal structure of feldspar. Tetrahedra consisting of oxygen atoms (red) and a silicon or an aluminium atom (blue and grey respectively). Between the tetrahedra are the metal ion sites which contain either calcium, sodium, or potassium (white, grey and yellow respectively). Image courtesy of *Crystallography365* using the VESTA software. 69

Figure 4.9: An example gemstone with its faces and positions labelled [179]. 70

Figure 4.10: Examples of the quartz (A), olivine (B), and labradorite (C) gemstones. 71

Figure 4.11: The Linkam temperature stage for the Raman spectrometer. 71

Figure 4.12: The Raman spectrometer configured for a low temperature experiment. 72

Figure 4.13: The Linkam stage inside the Raman spectrometer configured for a low temperature experiment. 72

Figure 4.14: Temperature versus peak position (including linear equations of best fit) for the main peaks in each of the mineral samples for the uncorrected data. 75

Figure 4.15: An example picture of the Linkam stage controller showing the stage temperature and the multimeter showing the resistance of the PT100 sensor. 81

Figure 4.16: A graph showing the sample temperature calculated using the pt100 sensor versus the stage controller temperature as determined by the Linkam stage. 81

Figure 4.17: Corrected temperature versus peak position (including linear equations of best fit) for the main peaks in each of the mineral samples. 86

Figure 4.18: Measured Stokes/anti-Stokes ratio versus Stokes/anti-Stokes ratio (including linear equations of best fit) for the main peaks in each of the mineral samples. If no correction were necessary, the slope would be equal to "1.0". 87

Figure 4.19: The spectrum of olivine as the sample is undergoing thermal decomposition as a result of laser heating. 88

Figure 4.20: An example optical image of an isolated particle from the grain size experiment taken using the microscope on the Raman spectrometer. 90

Figure 4.21: An example of how the cross sectional area of this particle was determined by dividing the grain's area into triangles before summing the areas of those triangles. 90

Figure 4.22: Cross sectional area versus P1 Stokes temperature for quartz grains. .. 92

Figure 4.23: Cross sectional area versus P1 Stokes temperature for olivine grains. .. 92

Figure 4.24: Cross sectional area versus P2 Stokes temperature for olivine grains. .. 93

Figure 4.25: Cross sectional area versus P1 Stokes temperature for labradorite grains. 93

Figure 4.26: Cross sectional area versus P2 Stokes temperature for labradorite grains. 94

Figure 5.1: Optical microscope image (x63 magnification) of a labradorite gemstone with a crack running through the surface. The black flecks within the gemstone are inclusions of black magnetite. This gemstone was rejected as a potential target..... 96

Figure 5.2 A quartz gemstone mounted to an aluminium target plate using Leit C-plast..... 97

Figure 5.3: Baseline peak shift maps for P1 and P2 of olivine. 97

Figure 5.4: A 8000 x 8000 micron montage image of the quartz gemstone target from shot G151014#1 (V = 1.35 km s^{-1})..... 98

Figure 5.5: G271114#2 where V = 5.27 km s^{-1} (A) Intensity map, (B) Optical microscope image. 100

Figure 5.6: The phase diagrams for quartz (A) and olivine (B) [183, 184].....103

Figure 5.7: Optical montage images (x50 magnification) of the quartz targets (A) S030615#2 where V = 0.373 km s^{-1} and (B) S241117#1 where V = 0.525 km s^{-1}.....106

Figure 5.8: Optical montage images (x50 magnification) of the quartz targets (A) S091014#1 where V= 0.910 km s^{-1} and (B) G151014#1 where V = 1.35 km s^{-1}.....107

Figure 5.9: Optical montage images (x50 magnification) of the quartz targets (A) G051114#3 where V = 2.02 km s^{-1} and (B) G241014#1 where V = 3.32 km s^{-1}. 108

Figure 5.10: Optical montage images (x50 magnification) of the quartz targets (A) G270515#3 where V = 4.48 km s^{-1} and (B) G271114#2 where V = 5.27 km s^{-1}. 109

Figure 5.11: Optical montage images (x50 magnification) of the quartz target G100615#1 where V = 6.40 km s^{-1}.....110

Figure 5.12: Raman map images for the quartz target S030615#2 where V = 0.373 km s^{-1}. (A) Intensity map. (B) Peak shift map. (C) FWHM map. (D) σ_{resid} map. 111

Figure 5.13: Raman map images for the quartz target S241117#1 where V = 0.515 km s^{-1}. (A) Intensity map. (B) Peak shift map. (C) FWHM map. (D) σ_{resid} map. 112

Figure 5.14: Raman map images for the quartz target S091014#1 where V = 0.910 km s^{-1}. (A) Intensity map. (B) Peak shift map. (C) FWHM map. (D) σ_{resid} map. 113

Figure 5.15: Raman map images for the quartz target G151014#1 where V = 1.35 km s^{-1}. (A) Intensity map. (B) Peak shift map. (C) FWHM map. (D) σ_{resid} map..114

Figure 5.16: Raman map images for the quartz target G051114#3 where V = 2.02 km s^{-1}. (A) Intensity map. (B) Peak shift map. (C) FWHM map. (D) σ_{resid} map..115

Figure 5.17: Raman map images for the quartz target G241014#1 where V = 3.32 km s^{-1}. (A) Intensity map. (B) Peak shift map. (C) FWHM map. (D) σ_{resid} map..116

Figure 5.18: Raman map images for the quartz target G270515#3 where V = 4.48 km s^{-1}. (A) Intensity map. (B) Peak shift map. (C) FWHM map. (D) σ_{resid} map..117

Figure 5.19: Raman map images for the quartz target G271114#2 where V = 5.27 km s^{-1}. (A) Intensity map. (B) Peak shift map. (C) FWHM map. (D) σ_{resid} map..118

Figure 5.20: Raman map images for the quartz target G100615#1 where V = 6.40 km s^{-1}. (A) Intensity map. (B) Peak shift map. (C) FWHM map. (D) σ_{resid} map..119

Figure 5.21: Optical montage images (x50 magnification) of the olivine targets (A) E240614#1 where V = 0.576 km s^{-1} and (B) E130614#1 where V = 0.602 km s^{-1}.....122

Figure 5.22: Optical montage images (x50 magnification) of the olivine targets (A) S260614#1 where V = 0.638 km s^{-1} and (B) G151014#1 where V = 1.35 km s^{-1}.....123

Figure 5.23: Optical montage images (x50 magnification) of the olivine targets (A) G150114#1 where V = 1.57 km s^{-1} and (B) G051114#3 where V = 2.02 km s^{-1}. 124

Figure 5.24: Optical montage images (x50 magnification) of the olivine targets (A) G150114#2 where V = 3.03 km s^{-1} and (B) G241014#1 where V = 3.32 km s^{-1}. 125

Figure 5.25: Raman map images for the olivine target E240614#1 where V = 0.576 km s^{-1}. (A) P1 Intensity map. (B) P2 intensity map. (C) P1 FWHM map. (D) P2 FWHM map. 126

Figure 5.26: Raman map images for the olivine target E240614#1 where V = 0.576 km s^{-1}. (E) P1 shift map. (F) P2 shift map. (G) Peak separation map. (H) σ_{resid} map. 127

Figure 5.27: Raman map images for the olivine target E130614#1 where V = 0.602 km s^{-1}. (A) P1 Intensity map. (B) P2 intensity map. (C) P1 FWHM map. (D) P2 FWHM map. 128

Figure 5.28: Raman map images for the olivine target E130614#1 where V = 0.602 km s^{-1}. (E) P1 shift map. (F) P2 shift map. (G) Peak separation map. (H) σ_{resid} map. 129

Figure 5.29: Raman map images for the olivine target S260614#1 where V = 0.638 km s^{-1}. (A) P1 Intensity map. (B) P2 intensity map. (C) P1 FWHM map. (D) P2 FWHM map. 130

Figure 5.30: Raman map images for the olivine target S260914#1 where V = 0.638 km s^{-1}. (E) P1 shift map. (F) P2 shift map. (G) Peak separation map. (H) σ_{resid} map. 131

Figure 5.31: Raman map images for the olivine target G151014#1 where V = 1.35 km s^{-1}. (A) P1 Intensity map. (B) P2 intensity map. (C) P1 FWHM map. (D) P2 FWHM map. 132

Figure 5.32: Raman map images for the olivine target G151014#1 where V = 1.35 km s^{-1}. (E) P1 shift map. (F) P2 shift map. (G) Peak separation map. (H) σ_{resid} map. 133

Figure 5.33: Raman map images for the olivine target G150114#1 where V = 1.57 km s^{-1}. (A) P1 Intensity map. (B) P2 intensity map. (C) P1 FWHM map. (D) P2 FWHM map. 134

Figure 5.34: Raman map images for the olivine target G150114#1 where V = 1.57 km s^{-1}. (E) P1 shift map. (F) P2 shift map. (G) Peak separation map. (H) σ_{resid} map. 135

Figure 5.35: Raman map images for the olivine target G051114#3 where V = 2.02 km s^{-1}. (A) P1 Intensity map. (B) P2 intensity map. (C) P1 FWHM map. (D) P2 FWHM map. 136

Figure 5.36: Raman map images for the olivine target G051114#3 where V = 2.02 km s^{-1}. (E) P1 shift map. (F) P2 shift map. (G) Peak separation map. (H) σ_{resid} map. 137

Figure 5.37: Raman map images for the olivine target G150114#2 where V = 3.03 km s^{-1}. (A) P1 Intensity map. (B) P2 intensity map. (C) P1 FWHM map. (D) P2 FWHM map. 138

Figure 5.38: Raman map images for the olivine target G150114#2 where V = 3.03 km s^{-1}. (E) P1 shift map. (F) P2 shift map. (G) Peak separation map. (H) σ_{resid} map. 139

Figure 5.39: Raman map images for the olivine target G241014#1 where V = 3.32 km s^{-1}. (A) P1 Intensity map. (B) P2 intensity map. (C) P1 FWHM map. (D) P2 FWHM map. 140

Figure 5.40: Raman map images for the olivine target G241014#1 where V = 3.32 km s^{-1}. (E) P1 shift map. (F) P2 shift map. (G) Peak separation map. (H) σ_{resid} map. 141

Figure 5.41: Optical montage images of the labradorite targets (A) S250915#1 where V = 0.291 km s^{-1} (x100) and (B) S160915#1 where V = 0.646 km s^{-1} (x50). 144

Figure 5.42: Optical montage images (x50 magnification) of the labradorite targets (A) S300715#1 where V = 0.997 km s^{-1} and (B) G181217#1 where V = 1.36 km s^{-1}. 145

Figure 5.43: Optical montage images (x50 magnification) of the labradorite targets (A) G170615#2 where V = 1.81 km s^{-1} and (B) G050815#1 where V = 1.99 km s^{-1}. 146

Figure 5.44: Optical montage images (x50 magnification) of the labradorite targets (A) G120815#1 where V = 2.72 km s^{-1} and (B) G100715#2 where V = 3.39 km s^{-1}. 147

Figure 5.45: Optical montage images (x50 magnification) of the labradorite target G160915#2 where V = 5.06 km s^{-1}. 148

Figure 5.46: Raman map images for the labradorite target S250915#1 where V = 0.291 km s^{-1}. (A) P1 Intensity map. (B) P2 intensity map. (C) P1 FWHM map. (D) P2 FWHM. 149

Figure 5.47: Raman map images for the labradorite target S250915#1 where V = 0.291 km s^{-1}. (E) P1 shift map. (F) P2 shift map. (G) Peak separation map. (H) σ_{resid} map. 150

Figure 5.48: Raman map images for the labradorite target S160915#1 where V = 0.646 km s^{-1}. (A) P1 Intensity map. (B) P2 intensity map. (C) P1 FWHM map. (D) P2 FWHM map. 151

Figure 5.49: Raman map images for the labradorite target S160915#1 where V = 0.646 km s^{-1}. (E) P1 shift map. (F) P2 shift map. (G) Peak separation map. (H) σ_{resid} map. 152

Figure 5.50: Raman map images for the labradorite target S300715#1 where V = 0.997 km s^{-1}. (A) P1 Intensity map. (B) P2 intensity map. (C) P1 FWHM map. (D) P2 FWHM map. 153

Figure 5.51: Raman map images for the labradorite target S300715#1 where V = 0.997 km s^{-1}. (E) P1 shift map. (F) P2 shift map. (G) Peak separation map. (H) σ_{resid} map. 154

Figure 5.52: Raman map images for the labradorite target G181217#1 where V = 1.36 km s^{-1}. (A) P1 Intensity map. (B) P2 intensity map. (C) P1 FWHM map. (D) P2 FWHM 155

Figure 5.53: Raman map images for the labradorite target G181217#1 where V = 1.36 km s^{-1}. (E) P1 shift map. (F) P2 shift map. (G) Peak separation map. (H) σ_{resid} map. 156

Figure 5.54: Raman map images for the labradorite target G170615#2 where V = 1.81 km s^{-1}. (A) P1 Intensity map. (B) P2 intensity map. (C) P1 FWHM map. (D) P2 FWHM map. 157

Figure 5.55: Raman map images for the labradorite target G170615#2 where V = 1.81 km s^{-1}. (E) P1 shift map. (F) P2 shift map. (G) Peak separation map. (H) σ_{resid} map. 158

Figure 5.56: Raman map images for the labradorite target G050815#1 where V = 1.99 km s^{-1}. (A) P1 Intensity map. (B) P2 intensity map. (C) P1 FWHM map. (D) P2 FWHM map. 159

Figure 5.57: Raman map images for the labradorite target G050815#1 where V = 1.99 km s^{-1}. (E) P1 shift map. (F) P2 shift map. (G) Peak separation map. (H) σ_{resid} map. 160

Figure 5.58: Raman map images for the labradorite target G120815#1 where V = 2.72 km s^{-1}. (A) P1 Intensity map. (B) P2 intensity map. (C) P1 FWHM map. (D) P2 FWHM map. 161

Figure 5.59: Raman map images for the labradorite target G120815#1 where V = 2.72 km s^{-1}. (E) P1 shift map. (F) P2 shift map. (G) Peak separation map. (H) σ_{resid} map. 162

Figure 5.60: Raman map images for the labradorite target G100715#2 where V = 3.39 km s^{-1}. (A) P1 Intensity map. (B) P2 intensity map. (C) P1 FWHM map. (D) P2 FWHM map. 163

Figure 5.61: Raman map images for the labradorite target G100715#2 where V = 3.39 km s^{-1}. (E) P1 shift map. (F) P2 shift map. (G) Peak separation map. (H) σ_{resid} map. 164

Figure 5.62: Raman map images for the labradorite target G160915#2 where V = 5.06 km s^{-1}. (A) P1 Intensity map. (B) P2 intensity map. (C) P1 FWHM map. (D) P2 FWHM map. 165

Figure 5.63: Raman map images for the labradorite target G160915#2 where V = 5.06 km s^{-1}. (E) P1 shift map. (F) P2 shift map. (G) Peak separation map. (H) σ_{resid} map. 166

Figure 6.1: The FWHM map generated from the Raman map of the quartz gemstone before the annealing test. 172

Figure 6.2: The FWHM map generated from the Raman map of the quartz gemstone after the annealing test. 172

Figure 6.3: The P1 FWHM map from the olivine shot G151014#1 (1.35 km s^{-1}) re-displayed with an upper limit of 8.0 cm^{-1} and a lower limit of 5.3 cm^{-1}. 174

Figure 6.4: The P1 FWHM map from the olivine shot G150114#1 (1.57 km s^{-1}) re-displayed with an upper limit of 7.0 cm^{-1} and a lower limit of 5.0 cm^{-1}. 175

Figure 6.5: The P1 FWHM map from the olivine shot G051114#3 (2.02 km s^{-1}) re-displayed with an upper limit of 7.0 cm^{-1} and a lower limit of 5.0 cm^{-1}. 176

Figure 6.6: The P1 FWHM map from the olivine shot G150114#2 (3.03 km s^{-1}) re-displayed with an upper limit of 7.0 cm^{-1} and a lower limit of 5.0 cm^{-1}.....177

Figure 6.7: The P2 FWHM map from the olivine shot G150114#1 (1.57 km s^{-1}) re-displayed with an upper limit of 7.5 cm^{-1} and a lower limit of 6.0 cm^{-1}.....179

Figure 6.8: The P2 FWHM map from the olivine shot G150114#2 (3.03 km s^{-1}) re-displayed with an upper limit of 7.5 cm^{-1} and a lower limit of 5.5 cm^{-1}.....179

Figure 6.9: The P1 FWHM map from the labradorite shot G170615#2 (1.81 km s^{-1}) re-displayed with an upper limit of 8.0 cm^{-1} and a lower limit of 6.0 cm^{-1}.....182

Figure 6.10: The P1 FWHM map from the labradorite shot G050815#1 (1.99 km s^{-1}) re-displayed with an upper limit of 8.0 cm^{-1} and a lower limit of 5.0 cm^{-1}...182

Figure 6.11: The P1 FWHM map from the labradorite shot G120815#1 (2.72 km s^{-1}) re-displayed with an upper limit of 7.5 cm^{-1} and a lower limit of 3.5 cm^{-1}...183

Figure 6.12: The P1 FWHM map from the labradorite shot G100715#2 (3.39 km s^{-1}) re-displayed with an upper limit of 8.5 cm^{-1} and a lower limit of 6.5 cm^{-1}...183

Figure 6.13: The P2 FWHM map from the labradorite shot S300715#1 (0.997 km s^{-1}) re-displayed with an upper limit of 10.0 cm^{-1} and a lower limit of 8.0 cm^{-1}. 185

Figure 6.14: The P2 FWHM map from the labradorite shot G170615#2 (1.81 km s^{-1}) re-displayed with an upper limit of 10.0 cm^{-1} and a lower limit of 7.0 cm^{-1}. 185

Figure 6.15: The P2 FWHM map from the labradorite shot G050815#1 (1.99 km s^{-1}) re-displayed with an upper limit of 9.0 cm^{-1} and a lower limit of 7.5 cm^{-1}...186

Figure 6.16: The P2 FWHM map from the labradorite shot G120815#1 (2.72 km s^{-1}) re-displayed with an upper limit of 9.0 cm^{-1} and a lower limit of 7.0 cm^{-1}...187

Figure 6.17: The P2 FWHM map from the labradorite shot G100715#1 (3.39 km s^{-1}) re-displayed with an upper limit of 10.0 cm^{-1} and a lower limit of 7.5 cm^{-1}. 188

Figure 6.18: The P2 FWHM map from the labradorite shot G160915#1 (5.06 km s^{-1}) re-displayed with an upper limit of 9.5 cm^{-1} and a lower limit of 6.5 cm^{-1}...189

Figure 6.19: Quartz P1 peak position vs static pressure. Data recreated from Dean *et al* [129] and Jean *et al* [130].....192

Figure 6.20: Olivine P1 and P2 peak position vs static pressure. Data recreated from Besson *et al* [132] and Chopelas [133].....192

Figure 6.21: The shift map from the quartz shot G151014#1 (1.35 km s^{-1}) re-displayed with an upper limit of 0.7 cm^{-1} and a lower limit of -0.5 cm^{-1}.....195

Figure 6.22: The shift map from the quartz shot G051114#3 (2.02 km s^{-1}) re-displayed with an upper limit of 0.75 cm^{-1} and a lower limit of -0.5 cm^{-1}....196

Figure 6.23: The shift map from the quartz shot G270515#3 (4.48 km s^{-1}) re-displayed with an upper limit of 0.60 cm^{-1} and a lower limit of 0.0 cm^{-1}. 196

Figure 6.24: The shift map from the quartz shot G271114#2 (5.27 km s^{-1}) re-displayed with an upper limit of 0.50 cm^{-1} and a lower limit of -0.1 cm^{-1}. The poorly fit pixels have been replaced with white pixels. 197

Figure 6.25: The shift map from the quartz shot G100615#1 (6.40 km s^{-1}) re-displayed with an upper limit of 0.75 cm^{-1} and a lower limit of -0.25 cm^{-1}. .197

Figure 6.26: The P2 shift map from the olivine shot S260914#1 (0.638 km s^{-1}) re-displayed with an upper limit of 1.0 cm^{-1} and a lower limit of -1.0 cm^{-1}.....199

Figure 6.27: The P2 shift map from the olivine shot G150114#2 (3.03 km s^{-1}) re-displayed with an upper limit of 1.0 cm^{-1} and a lower limit of -0.5 cm^{-1}.....202

Figure 6.28: The P2 shift map from the olivine shot G241014#1 (3.32 km s^{-1}) re-displayed with an upper limit of 1.0 cm^{-1} and a lower limit of -0.3 cm^{-1}.....202

Figure 6.29: The P1 shift map from the labradorite shot G120815#1 (2.72 km s^{-1}) re-displayed with an upper limit of 1.0 cm^{-1} and a lower limit of -0.5 cm^{-1}.....207

Figure 6.30: The P2 shift map from the labradorite shot G120815#1 (2.72 km s^{-1}) re-displayed with an upper limit of 0.5 cm^{-1} and a lower limit of -1.0 cm^{-1}.....207

Figure 6.31: The P1 shift map from the labradorite shot G160915#2 (km s^{-1}) re-displayed with an upper limit of 2.0 cm^{-1} and a lower limit of 0.0 cm^{-1}.....208

Figure 6.32: The P1 shift map from the labradorite shot G160915#2 (km s^{-1}) re-displayed with an upper limit of 0.0 cm^{-1} and a lower limit of -5.0 cm^{-1}.....208

List of Tables

Table 3.1: Lowest projectile speed attainable for each of the standard light gas gun gases at their maximum initial pressures. 34

Table 3.2: The speed attainable using each of the standard gases in with the 50 micron burst disk single stage set up..... 38

Table 3.3: The test shots for the Electronic Burst Disk (EBD) system with the addition of the 0.25 mm thick acetate backing. The 'E' in the shot numbers denotes that the shots were performed using the EBD system. The burst disk support had a central hole with a diameter of 2.0 mm for all of these shots. 45

Table 4.1: The Mohs hardness, density and melting points of the three minerals chosen for this investigation: olivine, quartz, and labradorite [180]..... 70

Table 4.2: The forsterite number calculated for the olivine sample based on the measured peak positons at each sampling temperature. 77

Table 4.3: Resistance and Time for the hold points of the calibration experiment. 82

Table 5.1: Shot numbers, impact velocities, and peak shock pressures (calculated using the planar impact approximation) for the shots for each mineral. 104

Table 5.2: A summary of the data for each shot, including: velocity, peak shock pressure, peak shift, and changes in the FWHM of the peaks. 168

Table 6.1: The annealing temperatures of the minerals examined in this study.....171

Table 6.2: The elemental ratios for each of the mineral targets before and after being shocked due to impact.....191

Chapter 1 - Introduction

From near the very beginning of spaceflight, Mars has been at the forefront of planetary science and exploration. In 1960, just three years after the launch of Sputnik, the USSR launched the first mission to Mars, Marsnik 1. The mission was intended to be a flyby of the red planet but was destroyed in a launch failure. This sparked the beginning of dozens of missions from both the USA's National Aeronautics and Space Administration (NASA) and USSR's[1] Soviet Space Program, later being joined by the European Space Agency (ESA) and the Indian Space Research Organisation (ISRO).

The first spacecraft to successfully reach Mars was NASA's *Mariner 4* in 1964, which performed a flyby of the planet and returned the first pictures of its surface. This was followed up by further flyby missions in the form of *Mariner 6* and *Mariner 7* in 1969. Both spacecraft flew over heavily cratered regions of Mars that gave scientists the impression that its surface looked much like that of the Moon.

This misconception was not corrected until the arrival of *Mariner 9*, the first spacecraft to orbit another planet, and the last spacecraft in the *Mariner Program* to be bound for Mars. *Mariner 9* arrived at Mars on the 14th of November 1971 just thirteen days before *Mars 2* and eighteen days before *Mars 3*, its Russian counterparts, achieved orbit. All three spacecraft arrived during a planet-wide dust storm which initially obscured the surface from observation. All that could be seen was the peaks of mountains poking above the storm. *Mariner 9* remained in orbit and operational for nearly a year and in that time it transmitted images of 85% of the Martian surface. *Valles Marineris*, one of the largest canyon systems in the solar system, is named after *Mariner 9*.

Mars 2 and Mars 3 however, were not simply orbital missions. Each spacecraft carried a lander module that was to descend to the Martian surface to study atmospheric conditions. The *Mars 2* lander failed during descent, but the *Mars 3* lander became the first successful soft landing on another planet. Unfortunately, the lander lost communication with the orbiter a few minutes after landing, before even the first image could finish being transmitted.

The next spacecraft to reach Mars were the NASA landers *Viking 1* and *Viking 2* in 1974. *Viking 1* returned the first 'clear' image and the first colour image from the surface of Mars. The *Viking* spacecraft performed the first direct analysis of the Martian surface which yielded evidence to suggest that some meteorites found on Earth were actually of Martian origin [1]. Both landers also contained experiments designed to search for evidence of life, the results of which remain controversial to this day [2].

Mars exploration then takes a break until the arrival of NASA's *Mars Pathfinder* in 1997, from this point onwards there has always been an active mission at Mars. *Pathfinder* carried an imaging system as well as a suite of atmospheric and meteorological sensors. However, most importantly, it also carried the *Sojourner* rover, the first rover to operate on another planet. *Sojourner* carried a variety of instruments designed to analyse the geology and composition of the rocks on the Martian surface. It was determined that two of the rocks investigated by the rover,

[1] Known as the Russian Federation since the dissolution of the USSR in 1991.

'Barnacle Bill' and 'Yogi', were primarily made up of the minerals orthopyroxene, feldspars, and quartz [3].

On the 27th of September 1997, fifteen days before contact with *Pathfinder* was lost, the global mapping mission *Mars Global Surveyor* (*MGS*) arrived at Mars. During its nine year operational lifetime, *MGS* mapped the entire Martian surface showing evidence of weathering of the surface and the formation of sand dunes in a similar fashion to some terrestrial deserts [4]. These images also showed evidence for the presence of flowing water in Mars's recent past in the form of gullies and channels [5].

The search for water on Mars intensified with the arrival of *Mars Odyssey* in 2001. *Odyssey*'s primary mission was to look for evidence of past or present water on Mars and did so by using its gamma ray spectrometer to map the distribution of hydrogen in the surface Martian soil [6].

The European Space Agency (ESA) officially joined the realms of planetary exploration in 2003 with *Mars Express*. The spacecraft consisted of the *Mars Express Orbiter* (*MRO*) and the, UK-built *Beagle 2* lander. *MEO* has been used to map the mineralogy of the Martian surface and has recently discovered a subglacial lake 1.5 km below Mars's southern ice cap which is thought to be the first known stable body of water on Mars [7]. Communications were lost with *Beagle 2* during decent, resulting in the astrobiology experiments designed to search for evidence of past or present life on the Martian surface never being carried out [8]. Recently, *Beagle 2* has been re-discovered with images appearing to show the solar array having failed to fully deploy, thereby blocking the communications antenna [9].

Building upon the success of the *Sojourner* rover, NASA sent two rovers to Mars as part of its *Mars Exploration Rover* mission program. Named *Spirit* and *Opportunity*, both rovers arrived in January 2004 and performed many geological experiments designed to characterise the composition of minerals and rocks on the Martian surface, as well as to look for more evidence of and the effects of water on Mars [10]. Each mission was designed to last 90 sols (Martian days), but both rovers exceeded this, with *Spirit* maintaining mobile operations for 1,892 sols before becoming permanently embedded in soft sand and *Opportunity* operating for 5,332 sols before loss of contact due to a planetary dust storm.

In 2006 the *Mars Reconnaissance Orbiter* (*MRO*) arrived at Mars and began its primary mission of using its high-resolution imaging system to map the Martian landscape. These images have been used in selecting the landing sites for lander and rover missions that have since made the journey to Mars [11, 12]. Following the completion of its primary mission *MRO* has had its mission extended in order to serve as a communication and navigation relay for current and future lander and rover missions [13].

The *Phoenix* lander was the next successful mission to reach Mars, touching down in the northern polar region in 2008. *Phoenix* used its robotic arm to dig trenches in the Martian surface which revealed the presence of water ice confirming the prediction made by gamma ray spectrometer data from *Mars Odyssey* [14]. *Phoenix* eventually succumbed to the cold of the harsh Martian winters 157 days after landing.

In 2012 NASA's *Mars Science Laboratory* Rover *Curiosity* landed inside Gale Crater. The sheer complexity and size of this rover meant that a new approach to landing was needed. NASA developed, and used, a "Sky Crane" landing system to achieve this,

allowing them to successfully deploy the 899 kg rover on the Martian surface [15]. *Curiosity* contains a broad array of scientific instruments, which are used to investigate: Martian climate and geology, the conditions required for microbial life, and the habitability of the planet in preparation for manned missions. *Curiosity* has had such great success that NASA's future *Mars 2020* mission is based on its design and its mission has been extended indefinitely beyond its planned mission duration.

With past missions having shown evidence for flowing water on Mars in the past, NASA's *Mars Atmosphere and Volatile EvolutioN* (*MAVEN*) was designed to determine how and why Mars's atmosphere can no longer support liquid water on the surface. Since arriving in 2014, *MAVEN* has determined that the Martian atmosphere was stripped away by solar wind after the loss of the Martian global magnetic field due to the cooling of the planet's core [16, 17].

India has recently become the latest nation to join the exploration of Mars with the arrival of the *Mars Orbiter Mission* (*MOM*) in 2014, becoming the first nation to do so on its first attempt. The mission's primary purpose was a technological demonstration of the systems required to perform planetary missions.

The most recent surface mission to Mars is the NASA *Interior Exploration using Seismic Investigations, Geodesy and Heat Transport* (*InSight*) lander. *Insight* is designed to explore the deep interior of Mars in order to better understand the processes that formed the rocky planets, including Earth. Having successfully touched down in November 2018, the lander is currently in the process of deploying all of its instruments, but on 23rd of April 2019 NASA reported that *InSight* had detected its first "Marsquake" [18] .

The *ExoMars* program is a joint Mars exploration program currently underway between ESA and Roscosmos. It includes two parts, an orbiter (known as the *Trace Gas Orbiter*, or *TGO*) and a Rover (known as *Rosalind Franklin*). The *TGO* arrived at Mars in 2016 and has since reached the orbit required for scientific observation. In April 2018 the spacecraft took its first photos of the Martian surface and in April 2019 it was announced that *TGO* had not yet detected any methane [19].

The *NASA* mission *Mars 2020* rover is expected to land within Jezero crater and, therefore, be surrounded by impacted material. The rover will carry a wide range of instruments which will allow it to complete one of its mission objectives, which is to cache samples for a future sample return mission.

Rosalind Franklin will carry a Raman Laser Spectrometer (RLS) which will be used to examine samples from up to 2.0 m below the surface by means of its core drill. The rover is scheduled to land in March 2021 on *Oxia Planum, a* region of Mars that contains impact craters. As such, the surface material is likely to have previously undergone shock.

The pressures and temperature changes created by impacts have been shown to alter minerals [20, 21] and their respective Raman signatures. Therefore, it is important to characterise these changes due to shock so as to better understand the history of the Martian surface.

This study aims to address this by determining if Raman spectroscopy can be used to ascertain the degree of shock a mineral sample on the Martian surface has been subjected to. This was done by accomplishing the following goals:

1 Creating and utilising a controlled method for producing shock events in mineral samples at a wide range of shock pressures, which will have a minimum effect on the quality of the Raman spectra produced by the sample.

2 Determining if the environment in which the Raman spectra will be gathered (i.e. the Martian surface) has a significant effect on the Raman spectra produced by the samples.

3 Determining if Raman spectroscopy can be used to detect changes in shocked mineral samples, and if the extent of those changes can be used to determine the degree of shock experienced by the sample as a shock barometer.

In order to meet these goals, the light gas gun at the University of Kent [22] was used to create shock events in minerals via impacts before analysing the mineral samples using a Raman spectrometer. Various additions and improvements were developed by the author for both pieces of equipment to better facilitate the attainment of these goals.

1.1 Outline of Thesis

The following is a list, and brief description of, the chapters contained within this thesis:

"Chapter 2- Background" provides background information on impacts and Raman spectroscopy. The use of impact studies as a tool for understanding the history of our planet and the Solar System is discussed. The cratering formation process is explained, using examples of high-pressure polymorphs generated by impacts given, in an effort to highlight the mineralogical changes that can occur due to the impact process. A basic overview of the theory and history of Raman spectroscopy is discussed, including applications of Raman spectroscopy to various fields of research. Disadvantages of the technique, including methods used to overcome these disadvantages, are also described.

"Chapter 3- Instrumentation" describes the working principles of the specific instrumentation used in this study, including the Horiba "LabRam HR" micro-Raman spectrometer, the light gas gun (LGG), and the low speed gun. The development of the low speed gun, as well as instructions on the operation of the new system, are fully described here.

"Chapter 4- Raman Thermometry" explores the use of Raman spectroscopy to remotely measure the temperature of a sample. This chapter describes two techniques for Raman thermometry and presents the results of experimentation testing the validity of both of these techniques. Also included in this chapter are details of an experiment designed to determine the influence of sample grain size on Raman thermometry.

"Chapter 5- Raman Spectrometry as a Shock Barometer I" is the first of the two chapters which present the results of the impact investigation. This chapter describes the experimental procedure used for this investigation, presents the dataset produced, and provides a cursory interpretation of those data.

"Chapter 6- Raman Spectrometry as a Shock Barometer II" is the second of the two chapters which presents the results of the impact investigation. This chapter examines

the dataset more closely and describes trends discovered in the data, as well as possible explanations for the occurrence of those trends.

"Chapter 7- Conclusions and Future Work" summarises the findings and conclusions of this study, and suggests future experimentation that could be undertaken to further our understanding of this research area.

Chapter 2 - Background

2.1 Impacts

2.1.1 Importance of Impact Studies

Impacts have been ubiquitous throughout the Solar System and their effects are observed on a variety of different types of bodies. Probably the most well-known impact on the Earth is the Chicxulub crater, which has a diameter of 182 km and a depth of 20 km making it the third largest confirmed crater on Earth (with the 250 km diameter Sunbury Basin and the 300 km diameter Vredefort crater being larger). The Chicxulub impactor was a large asteroid, or comet, estimated to be between 11 and 81 km in size [23], and is the impact event that is thought to be responsible for the mass extinction which killed the dinosaurs [24]. The date of the impact coincides precisely with the end of the Cretaceous period and the beginning of the Paleogene period, leading to the widely accepted theory that the impact caused a worldwide disruption in climate conditions that triggered the mass extinction event.

The largest visible impact crater in the Solar System is Hellas Planitia on Mars with a width of 2,300 km and a basin floor that is 7.1 km deep. The Utopia Planitia, also on Mars, is the largest known impact basin in the Solar System with an estimated width of 3,300 km (Figure 2.1).

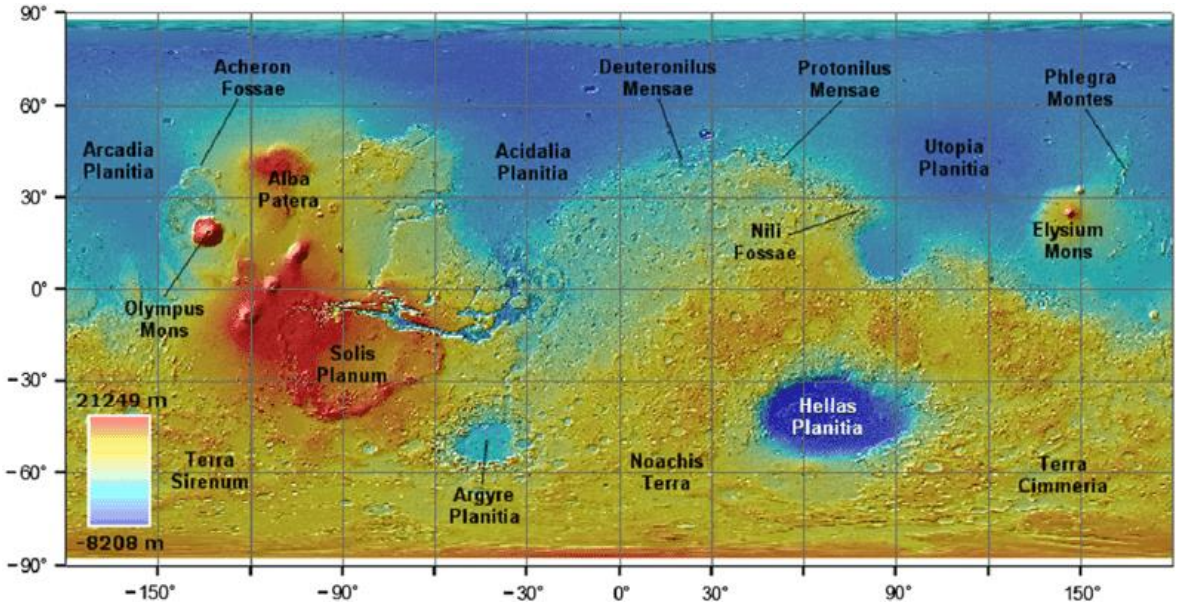


Figure 2.1: Topographical map of Mars showing Hellas Planitia and Utopia Planitia [25].

However, there have been even larger impacts in the history of our Solar System. The giant-impact hypothesis suggests that Earth's Moon was formed from a massive collision 4.5 billion years ago between the Earth and another body, approximately the size of Mars, called Theia [26]. The debris left over from this impact coalesced to form the Moon. One major piece of evidence that supports this theory is that the stable-isotope ratios of lunar and terrestrial rocks are identical which suggests that they have a common origin [27-29].

The examples outlined above demonstrate that impact events have played an important part in shaping the Solar System as we know it today. The giant-impact hypothesis is an example of how a single large impact event can significantly alter a planetary system [26]; while the Chicxulub impact permanently changed the course of the evolution of life on Earth [24].

Impact events are still a common occurrence. On the small (sub-millimetre) scale, this is evident by the abundance of impact craters that can be observed on spacecraft such as the International Space Station (ISS) [30, 31]. While on a larger scale, the 20 m Chelyabinsk meteor exploded in an air burst over Russia on 15th February 2013 [32]. The meteor exploded at a height of approximately 29.7 km, but fortunately most of the released energy was absorbed by the atmosphere as it is estimated that just prior to atmospheric impact the meteor had a kinetic energy equivalent to the blast yield of a nuclear weapon in the 400 - 500 kiloton range (1.4 – 1.8 PJ) – approximately 30 times more powerful than the atomic bomb detonated at Hiroshima [33].

As they are so prevalent, interpreting impact events is key to understanding the history of our Solar System.

2.1.2 Meteorites

One important area of impact research is the study of meteorites. A meteorite is a piece of rock, or metal-rich body, which has fallen to Earth from space. Their origin has been a subject of speculation for millennia, with the ancient Egyptians believing meteorites to be gifts from the gods that would allow the owner priority passage into the afterlife [34]. The Egyptian pharaoh Tutankhamun was mummified more than 3,300 years ago and entombed alongside him was an iron dagger, which was shown to be constructed from an iron-nickel meteorite of extra-terrestrial origin [35].

Today we conduct active searches for meteorites: ranging from amateurs who search in their spare time, to planned professional expeditions to remote regions, as well as the occasional 'meteorite scramble'. A meteorite scramble occurs in the aftermath of an air burst, when local residents and professional meteorite hunters swarm the area in an effort to locate fragments of the parent body. This is due to the potential value of such fragments, either monetary or scientific, depending on a person's motives.

Professional expeditions are often done in remote regions, typically deserts (hot or cold). This is because meteorites are easier to spot in locations with fewer terrestrial rocks and because the dry conditions mean they are less likely to have been altered by water. A group of scientists will travel to an isolated area and conduct a methodical search for meteorites; carefully documenting their location and size when one is found [36-38]. These searches are conducted because we know that meteorites are comprised of materials that have come from other rocky bodies in the Solar System. Usually, they have arrived on Earth because an impact elsewhere in the Solar System has created ejecta that has managed to escape the gravitational pull of its parent body. These ejecta have then travelled until captured by Earth's gravity well and fallen onto the Earth's surface.

As previously mentioned, impacts occur throughout the Solar System; as such meteorites can have a range of parent bodies. There are over 50,000 meteorites that have been discovered on Earth, 99.8% of these originate from asteroids, with 0.1% being Lunar meteorites and 0.1% being Martian meteorites [39]. It is also possible for meteorites to be terrestrial in origin, which occurs when a body impacts the Earth and

creates ejecta that is thrown up beyond the atmosphere and into space. Unless the impact was extremely energetic, most of the ejecta will not have been travelling fast enough to have escaped Earth's gravity, and will eventually fall back down onto the surface. Such rocks would be difficult to identify as meteorites, as their lithology and geochemistry will show them to be terrestrial in origin, meaning a fusion crust on their exterior would be the only way of identifying them as meteorites [40]. The fusion crust is formed as meteoroids travel through Earth's atmosphere at speeds ranging from 11 km s^{-1} to 72 km s^{-1} [41]. These high speeds generate heat due to the friction of the meteoroid traveling through the air. This heat is sufficient to cause the exterior of the meteoroid to become molten, and smaller meteoroids are often completely vaporised by this process. The molten surfaces of those meteorites large enough to survive complete vaporisation are then allowed to cool, which then solidifies into a thin fusion crust. As about 70% of the Earth's surface is water, most of these impacts occur in in the ocean and the meteorite is lost. Those meteorites that do impact land, have usually slowed sufficiently (about 200 m s^{-1}) due to atmospheric drag that the meteorite survives the impact relatively intact.

This is not so for larger impacts: asteroids below 100 m in diameter that impact the Earth generate an air blast (such as the previously mentioned Chelyabinsk meteor) that showers the region with smaller fragments. Asteroids above 100 m in diameter typically survive atmospheric entry intact and fall to the surface with sufficient energy to form a crater.

2.1.3 Crater Formation

(The following discussion is based on references [42-45])

Crater formation is generally broken down into three stages: 'contact', 'excavation and growth', and 'modification'. During the contact phase, the impactor makes contact with the target surface, which generates a shock wave inside the impactor and the target. When an impactor is travelling faster than the speed-of-sound of its constituent material, the time it takes the impact shock wave to travel to the rear of the impactor is longer than the time it takes the rear of the impactor to reach the position of the origin of the shock wave. Due to this delay, the rear of the impactor continues travelling at its original impact velocity for longer than the front of the impactor, this results in the flattening (or 'pancaking') of the impactor, and the generation of high pressures and temperatures within the impactor. The timescale for this phase of the cratering process is dependent on the impact speed, and the size of the impactor (Equation 2.1). Dividing the diameter of the impactor (m) by the impact velocity (m s^{-1}), we obtain the characteristic time τ. The contact phase is often taken to last for approximately 5τ.

$$\tau = \frac{d}{v} \tag{2.1}$$

During the contact phase there is some penetration into the target, as shown in Figure 2.2. Although the shock wave typically reaches the rear of the projectile after $\sim 1\tau$, the shocked state of the projectile is not unloaded until after a few τ, when the shock wave at the front of the projectile has been released. After this point the impactor plays only a small role in the formation of the crater. Intact fragments of the impactor may be deposited in the crater, or thrown out as ejecta. If any of the impactor has melted, due to the high temperatures caused by the shock and release, the melted material may mix with melted target material. If part of the impactor has been heated

to high enough temperatures to cause vaporisation of material, this material forms an expanding vapour plume above the impact crater.

The next stage is the excavation phase. Initially the shock waves radiate out from the impact point in a hemispherical fashion. These shock waves set material in motion as they propagate through the target. Near the surface, material is able to travel upwards above the original surface height. This generates a build-up of material that behaves in a similar way to the crest of a wave in a fluid, causing a 'rim' to form around the crater that is above the original height of the target surface.

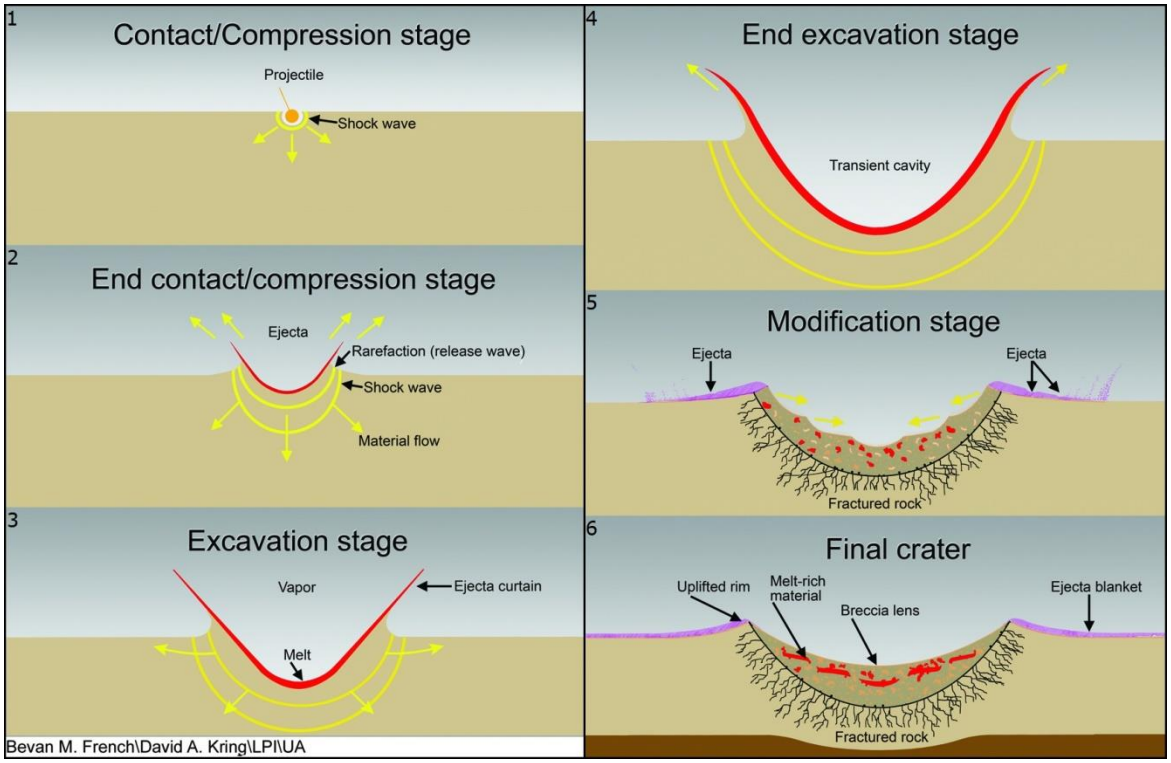


Figure 2.2: The phases of crater formation. Image courtesy of the Lunar and Planetary Institute, credit: Bevan M. French and David A. Kring of the Lunar and Planetary Institute.

Unlike the surface, material directly below the crater is more difficult for the propagating shock wave to set into motion, as there is no empty space into which it can freely move, therefore it must compress the material. Due to the material's natural resistance to compression, the maximum depth of the crater is reached before the maximum diameter. This causes the original hemispherical propagation to become more bowl-shaped, resulting in the excavation of a bowl-shaped crater (Figure 2.2).

The final stage of crater formation is 'modification'. During this phase, rim walls collapse under gravity causing some material to fall back into the crater, reducing the crater depth and steepness of the walls. Some rim material falls outwards resulting in a lowering and widening of the rim wall, thereby having the effect of increasing the diameter of the crater. Some of the material which was ejected upwards also falls back down and lands within the crater, covering the floor of the crater and further reducing its depth: this layer of material is known as the breccia lens.

For very large craters, the bowl shape is distorted by lithostatic rebound in the centre of the crater causing a central peak to rise up. On Earth, this occurs for craters greater than 2 km in diameter in sedimentary rocks, or greater than 4 km in denser crystalline

rocks. However, these thresholds are inversely dependent on local gravity. For example, craters of 15 km or more are needed for central peaks to appear on the Moon. It is possible for these central peaks to become so large that they themselves undergo collapse under gravity. In these instances, the central peak becomes a peak ring structure at the centre of the crater.

The modification phase can continue for thousands/millions of years, as natural erosion and infill processes occur. Wind and water can also deposit dust and sediment into the crater floor, as well as life (flora and fauna) recolonising the site and causing further alteration.

2.1.4 High-Pressure Polymorphs

The impact process means that all of the materials involved (including the original impactor, the crater and any ejecta) have been subjected to shocks resulting in extreme pressure and temperature. These extreme conditions can alter the structure of the minerals in the material involved. An example of such changes occurs in quartz (SiO_2). In 1953, Coes *et al* [46] showed that it is possible to transform quartz into coesite under static pressure. Later, coesite was discovered at Meteor Crater in Arizona [47] (now known as Barringer Crater), leading to the suggestion that its presence was evidence of extreme shock pressures at the site. Coesite is thought to form from quartz at shock pressures of ~35 GPa in dense non-porous crystalline rocks, but it is possible for it to form at lower pressures (as low as 5.5 GPa) in porous sandstone [48]. This discrepancy in pressure values is likely due to pressure concentration effects at pore/crystal interfaces, thereby allowing more porous rocks to form the same high-pressure forms of minerals from lower initial shock pressures.

Stishovite is another high-pressure form of quartz that was discovered through static pressure experiments [49]. It was subsequently synthesised by explosive shock experiments [50] proving that it too can be formed due to shock pressures. This discovery, coupled with its presence in Barringer Crater, added support to the claim that that structure was the result of a large shock event.

Impact diamonds are diamonds formed from graphite in rocks that have been shocked at impact sites. Diamonds of millimetre size have been discovered at a few impact sites [51] and in some cases diamonds of micrometre sizes have been found [52]. It has been argued that those of micrometre size formed from vapour deposition from material in the vapour plume generated by the impact [53]. Static pressure experiments have shown carbon to convert to diamond at ~80 GPa, whilst, in contrast, shock experiments have found that 20 GPa is sufficient. Such experiments demonstrate the need to conduct appropriate shock experiments in order to fully understand the pressures required for certain minerals to form in craters. However, it is important not to become reliant on using the presence of high-pressure polymorphs as the sole method of identifying terrestrial impact structures, as many such polymorphs can be formed in terrestrial settings unassociated with impact events: both coesite and diamond have been found without the need for shock induced impact pressures[46]. Until recently, stishovite had only ever been associated with shocks, but traces of it have now been found in other rocks [45].

2.1.5 Complications

The problem with analysing samples (meteorites) from other planetary bodies is that we are only looking at the end result of a complex process of shocks and heating. This

means it is difficult to say exactly what has happened to a sample, such as a meteorite, between leaving the parent body and it being analysed.

It is possible to use laboratory experiments to attempt to trace the shock history of mineral samples by using analogues samples and subjecting them to the approximate conditions that the original sample is believed to have experienced. Unfortunately, such experimental data are very scarce due to the time and resource intensive nature of the experiments required.

2.2 Raman Spectroscopy

Raman Spectroscopy has been used to study meteoritic material since the 1980's [20, 54, 55]. It has also been used in the analysis of other material of non-terrestrial origin such as: *Apollo* samples [56], *Stardust* grains [57, 58], and Hayabusa grains [59]. It is possible that some (or all) of this material would have been subjected to shocks in its lifetime.

2.2.1 History of Raman Spectroscopy

Although the phenomenon of inelastic scattering of light was originally predicted in 1923 by A. Smekal [60], it was not experimentally observed until 1928 by C. V. Raman, who published the results of the experiments conducted by himself and K. S. Krishnan [61]. This experiment involved directing a powerful beam of sunlight towards a liquid sample by means of a telescope objective combined with a short focus lens. Before reaching the sample, the light was first passed through a blue-violet filter and when a complementary green filter was placed in conjunction with the blue-violet filter, all illumination disappeared, causing no sunlight to reach the sample (Figure 2.3). If, however, the green filter was placed after the sample, light could be observed, though less brightly. This led to the conclusion that the sample must be scattering (at least some of) the incident blue-violet light to green light. This phenomenon has come to be known as Raman scattering.

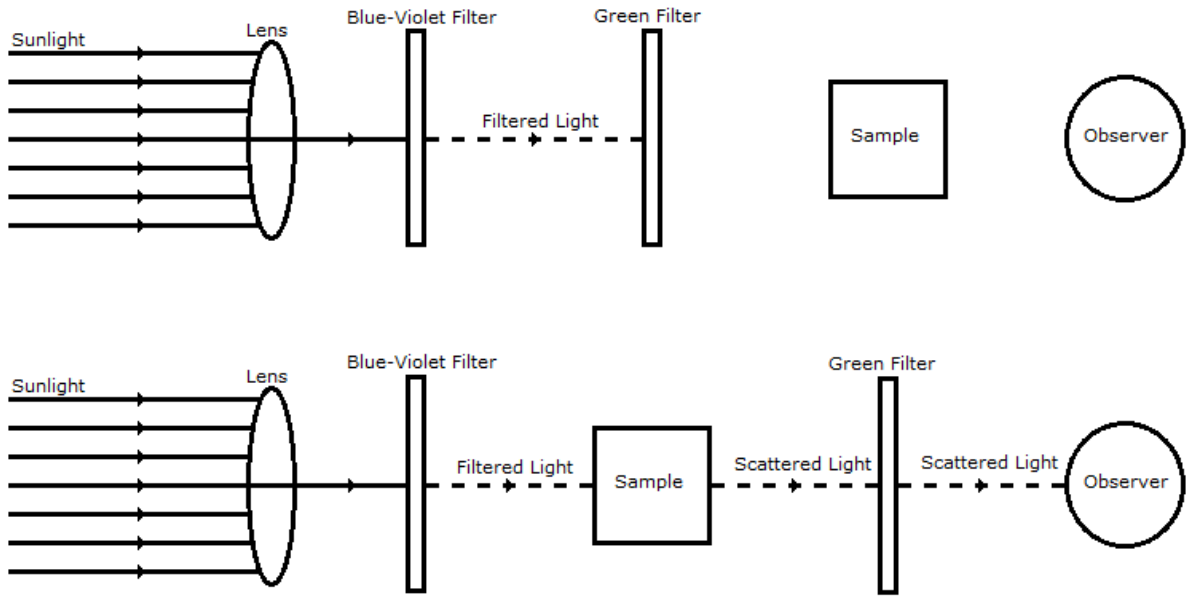


Figure 2.3: Schematic of the set-up of the Raman experiment carried out in 1928.

2.2.2 Theory of Raman Spectroscopy

When light is directed through gaseous matter, the photons may pass through the material and not interact with it in any way, but it is also possible for the photons to be absorbed or scattered by the material. If the energy of an incident photon is equal to the energy gap between the ground state of a molecule and an excited state, the photon may be absorbed, and that molecule elevated to a higher energy excited state. This interaction forms the basis of absorption spectroscopy.

Incident photons can also be scattered, causing a change in the direction of travel of the photons. During the scattering process, when photons interact with a molecule, they polarise the electron cloud around the nuclei and form 'complex' states. These 'complex' states are very short-lived and, as such, the nuclei do not have sufficient time to move in order to reach a new equilibrium in this state. This results in an unstable, high energy form of the molecule that has experienced a significant rearrangement of electron geometry, but no nuclear movement. This unstable 'complex' then releases the gained energy as scattered light radiation. In most instances, this interaction is elastic and the photon loses no energy; this is known as Rayleigh scattering. In rare instances nuclear motion does occur: a 'complex' state is formed, but the movement of the much heavier nuclei (compared to the electrons) causes a transfer of energy. This energy can be transferred either from the incident photon to the molecule, or from the molecule to the scattered photon. The energy transfer causes the process to become inelastic, meaning that the energy of the scattered photon will be different to that of the incident photon. This process is called Raman scattering, and occurs for approximately one in every 10^6 – 10^8 photons.

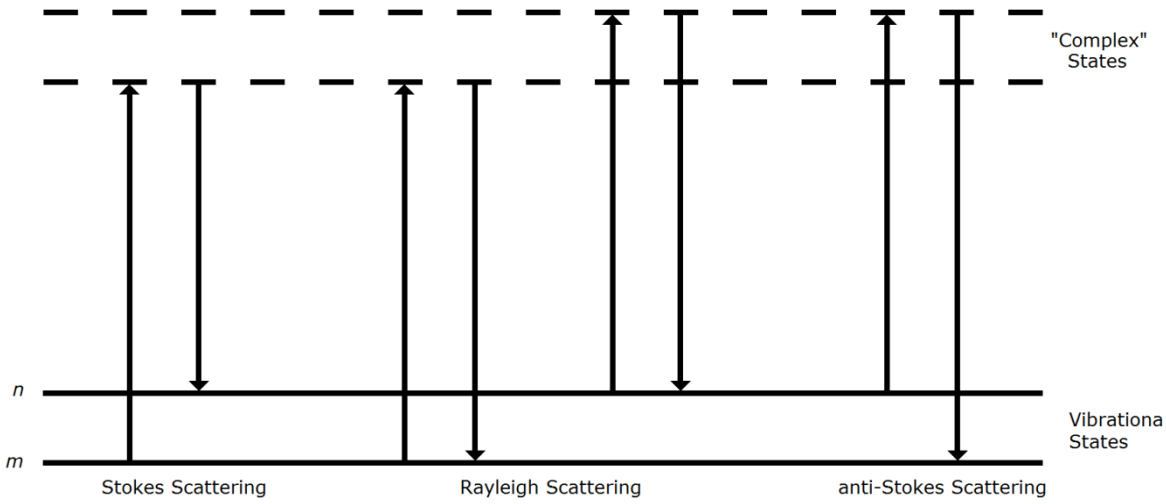


Figure 2.4: Schematic diagram of the Rayleigh and Raman scattering process.

As the energy transfer in Raman scattering can happen in one of two ways; from the incident photon to the molecule, or from the molecule to the scattered photon, we can characterise two types of Raman scattering: Stokes scattering and anti-Stokes scattering (Figure 2.4). At room temperature most of the molecules are in their lowest energy vibrational state (*m*). If Raman scattering occurs to these molecules, energy is transferred from the incident photon to the molecule, promoting the molecule to a higher energy vibrational state (*n*). Thus, the photon is scattered with a lower energy than the incident photon; this is known as Stokes scattering. If, however, Raman scattering occurs on a molecule that is already in a higher energy vibrational state (*n*), due to thermal energy in the surroundings, then it is possible for energy to be

transferred from the molecule to the scattered photon as the molecule drops down to a lower energy vibrational state (*m*). Thus, the photon is scattered with a higher energy than the incident photon: this is known as anti-Stokes scattering.

The majority of molecules in a sample at room temperature will be in the ground vibrational state, making Stokes scattering the dominant form of Raman scattering. The ratio between the intensities of Stokes and anti-Stokes scattering is dependent on the ratio of the number of molecules in the ground and excited vibrational states. The latter ratio is dependent on the amount of thermal energy in the surroundings, meaning that the Boltzmann equation can be used to link them:

$$\frac{N_n}{N_m} = exp\left[\frac{-(E_n - E_m)}{kT}\right] \tag{2.2}$$

Where; N_n is the number of molecules in the excited vibrational state (*n*), N_m is the number of molecules in the ground vibrational state (*m*), (E_n – E_m) is the difference in energy between the vibrational energy levels in Joules, *k* is the Boltzmann constant (1.3807 x 10^{-23} J K^{-1}) and T is the temperature in Kelvin. Interestingly, if the intensities of a particular peak are known in both the Stokes and anti-Stokes, Equation 2.2 provides a way to determine the temperature of the sample during acquisition.

Tuschel 2016 [62] considers the idea of Raman thermometry in detail and describes two methods of using the Raman spectrum of a sample to determine its temperature at the time of acquisition. The first method involves observing the peak position of a narrow Raman band. Peak positions have been observed to shift due to changes in sample temperature, which is due to the increase in temperature causing an increase in the bond length, thereby resulting in a reduction in the energy of the vibrational mode. However, this method is only useful for samples where it has been possible to perform a calibration beforehand to determine what extent the vibrational mode is influenced by changes in temperature and cannot be used if only a single (or very few, spectra) are available. The second method has already been described and relates to Equation 2.2. Both of these methods are further explored in Chapter 4.

In Raman spectroscopy, a monochromatic light source, such as a laser, is used to irradiate a sample. The scattered light is detected and the change in energy of the photons is calculated, recorded, and presented as a Raman spectrum. An example Raman spectrum of silicon can be seen in Figure 2.5.

The y-axis of a Raman spectrum is labelled as intensity. In the example spectrum of silicon in Figure 2.5, the peak at 0.0 cm^{-1} goes off the scale showing that it is much larger than the intensity of the peak at 520.6 cm^{-1}. This is to be expected in all Raman spectra. as the majority of scattering is Rayleigh scattering, and thus the 0.0 cm^{-1} peak should be the dominant feature in any Raman spectrum (unless it is otherwise filtered out or removed in post-processing), as this represents the excitation source.

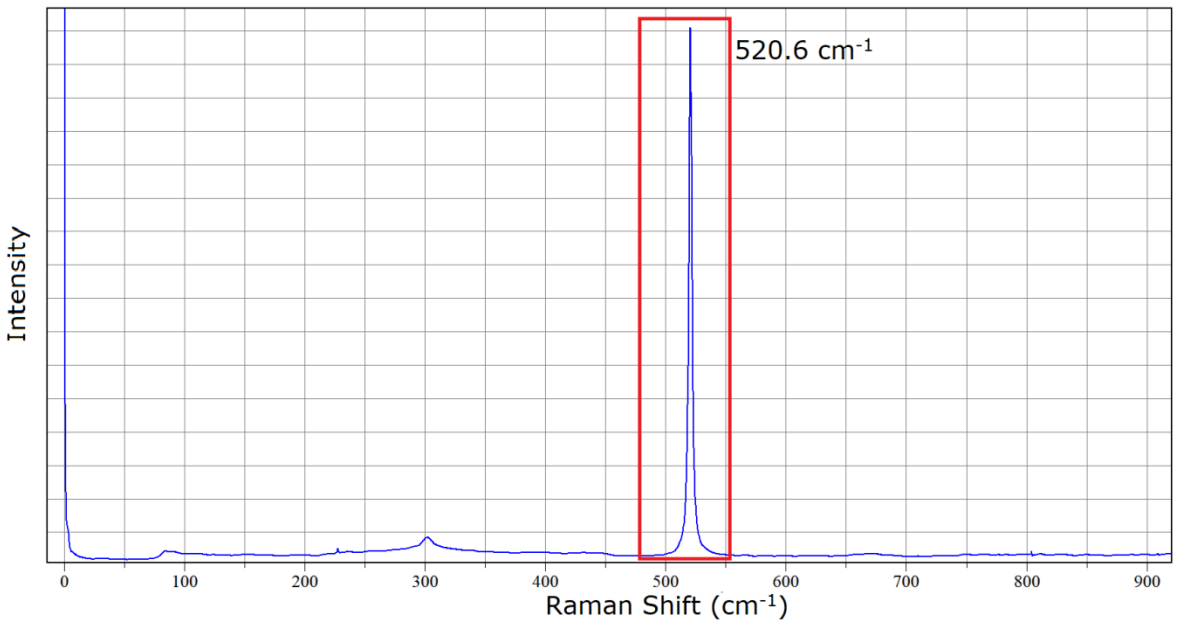


Figure 2.5: An example Raman spectrum of silicon with the peak at 520.6 cm^{-1} highlighted in red.

The intensity of a Raman peak is governed by the change in polarisability (α) of the molecule. The polarisability of a molecule is a measure of the distortion of the electron cloud around that molecule due to an external electric field, such as that of incident light waves. Raman scattering is a result of the dipole moment induced in the molecule by the oscillating electric field of the incident light. This induced dipole (or polarisation) can be represented by:

$$\mu = \alpha E \tag{2.3}$$

Where μ is the dipole moment (C m) created in the molecule by the electric field E (N C^{-1}), from the incident photon and α is the polarisability of the molecule.

Of the two peaks present in Figure 2.5, the peak at 0.0 cm^{-1} represents photons that have undergone Rayleigh scattering and have not changed their energy, while the peak at 520.6 cm^{-1} is a Raman band and represents a change in energy of the incident photons. The position of the peak along the x-axis is dependent on the magnitude of the change in energy that occurs during the Raman scattering process. Although Stokes scattering represents a decrease in energy of the scattered photon, by convention, Stokes shifts are presented on the positive side of the x-axis. This is likely because most Raman spectroscopy work is conducted at room temperature where Stokes scattering will be dominant over anti-Stokes scattering. These shifts are represented in wavenumbers (cm^{-1}), although strictly speaking, as Raman spectra are constructed from recording a series of shifts in energy, the units should be Δcm^{-1}, however, this is almost never observed and convention has dictated that the units be represented as simply cm^{-1}.

The magnitude of this change in energy is dependent on the molecular system that the incident photon interacted with. Different molecular bonds have different vibrational frequencies (or different vibrational energies) and because an individual peak position represents a particular value for the change in energy, it follows that a particular Raman peak position can be used as a way to identify the type of bond that

formed said peak. From an extremely simplified point of view, molecular bonds can be thought of as a system of masses connected by springs floating in free space. The frequency of the vibration between the individual atoms in a bond will be dependent on the mass in the system and the strength of the spring (or bond). This type of arrangement can be mathematically described using Hooke's law:

$$v = \frac{1}{2\pi c}\sqrt{\frac{K}{\mu}} \tag{2.4}$$

Where; v is the vibrational frequency (Hz), c is the speed of light (m s^{-1}), K is the force constant (N m^{-1}) of the bond (classically known as the spring constant), and μ is the effective mass of the system (kg) [63]. This shows us that vibrations between lighter atoms will generate peaks at a higher frequency than vibrations between heavier atoms. The strength of the bond also contributes to the vibrational frequency in that the stronger bond is, the higher the frequency will be.

A vibration is 'Raman active' if the polarisability of the molecule changes during said vibration: this is known as the Basic Selection Rule. Consider a basic diatomic molecule such as O_2 (Figure 2.6) that we know is not infrared active. This molecule has a symmetric vibration where the bond is stretched and we expect a change in polarisability to occur. As such, we would expect to detect a single peak in the Raman spectrum of O_2, but no band in the infrared spectrum.

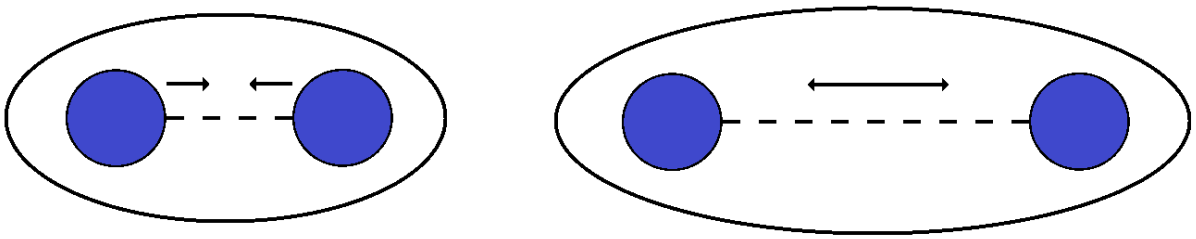


Figure 2.6: The symmetrical vibrations of an O_2 molecule. The outer ellipse is a visual representation of the change in the polarisability of the electron cloud.

For molecules with a centre of symmetry, another selection rule applies called the Mutual Exclusion Rule. This rule states that a particular vibration can either be Raman or IR active, but not both.

Now consider CO_2 (Figure 2.7). If the molecule vibrates in the asymmetric form, there is no change in the polarisability of the electron cloud making the vibration Raman inactive. However, there is a change in the dipole of the molecule making it IR active. In the case of the symmetrically vibrating CO_2, there is a change in the polarisability of the electron cloud making the vibration Raman active but IR inactive due to the lack of change in the dipole. This makes Raman spectroscopy and IR spectroscopy complementary to one another and, by using them in conjunction, it is easier to identify a sample than it would be using a single technique.

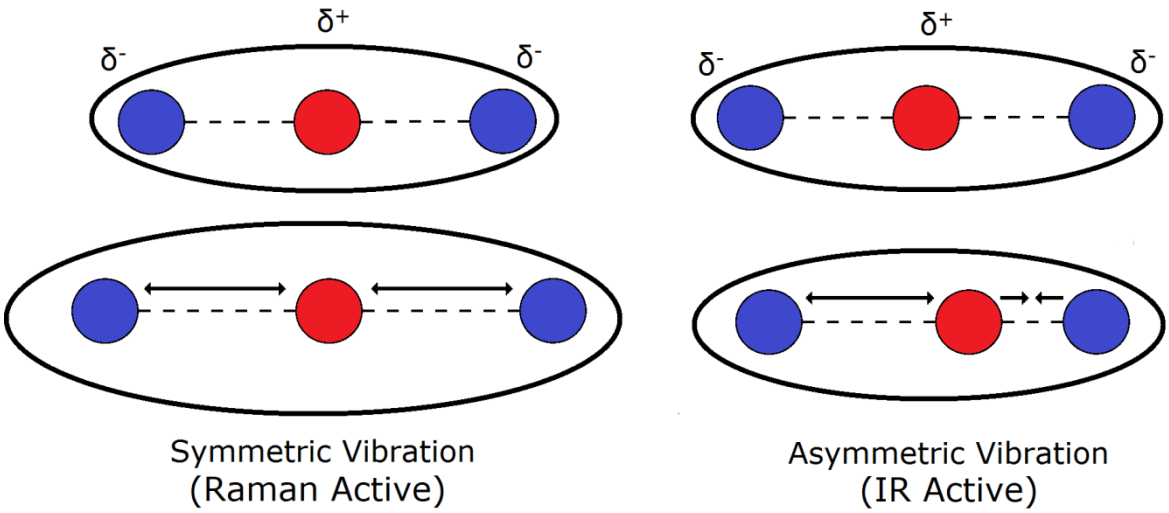


Figure 2.7: The symmetric and asymmetric vibrations of a CO_2 molecule. The outer ellipse around each molecule is a visual representation of the change in the polarisability of the electron cloud. In the case of the symmetric vibration, there is a change in the polarisability of the electron cloud. In the case of the asymmetric vibration, there is no change in the polarisability of the electron cloud.

2.2.3 Problems with Raman Spectroscopy - Fluorescence

Fluorescence, also known as luminescence emission, is a familiar problem to any Raman spectroscopist. It can generally be identified by a very intense, broad band (Figure 2.8). The 'complex' states used to describe the Raman effect are so short-lived that the interaction between an incident photon with a molecule, and the re-emission of the scattered photon, can be considered to occur almost simultaneously [64]. It is because these 'complex' states are virtual in nature that the Raman effect is not dependent on the wavelength of the excitation. Nevertheless, when the energy of an incident photon is close in magnitude to the transition energy between two electronic states of a molecule, that molecule is excited to that higher electronic energy state before relaxing again to a lower electronic energy state. During the relaxation process a photon with less energy than the incident photon is emitted (Figure 2.9).

Fluorescence is generally far more intense than Raman scattering. Even fluorescence generated by a trace impurity of a sample can be strong enough to obscure Raman signals from a sample.

Fortunately, the samples discussed in this body of work were not prone to fluorescence; however, there are many techniques available to help combat fluorescence should it arise.

2.2.3.1 Changing the Excitation Wavelength

As previously explained, fluorescence is generated when the energy of an incident photon is close in magnitude to the transition energy between two electronic states of a molecule. This presents a simple, but effective, option for tackling fluorescence: changing the energy of the incident photons so that they do not have enough energy to cause any electronic transitions. This is done by changing the wavelength of the excitation source to a laser with a longer wavelength (and therefore lower energy), such as a near-infrared laser [65, 66] as seen in Figure 2.8.

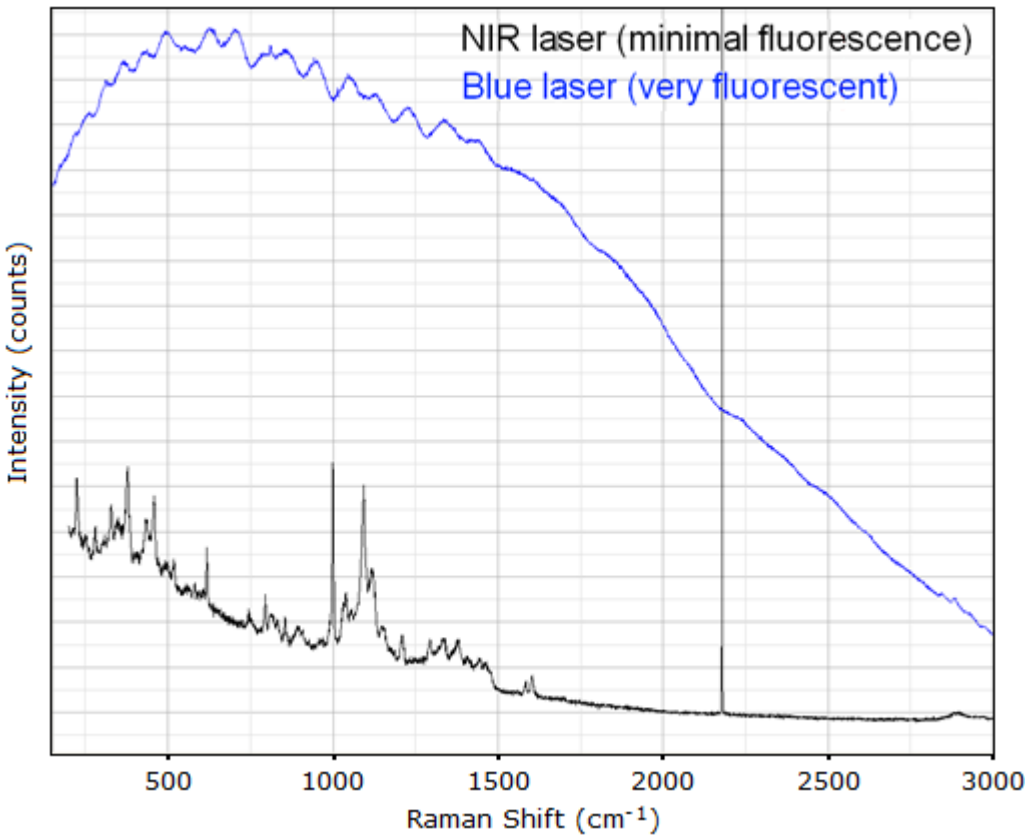


Figure 2.8: Example of a fluorescent spectrum (blue) using a blue (473 nm) laser and how this can be overcome by changing the excitation wavelength to a NIR (784.15 nm) laser (black).

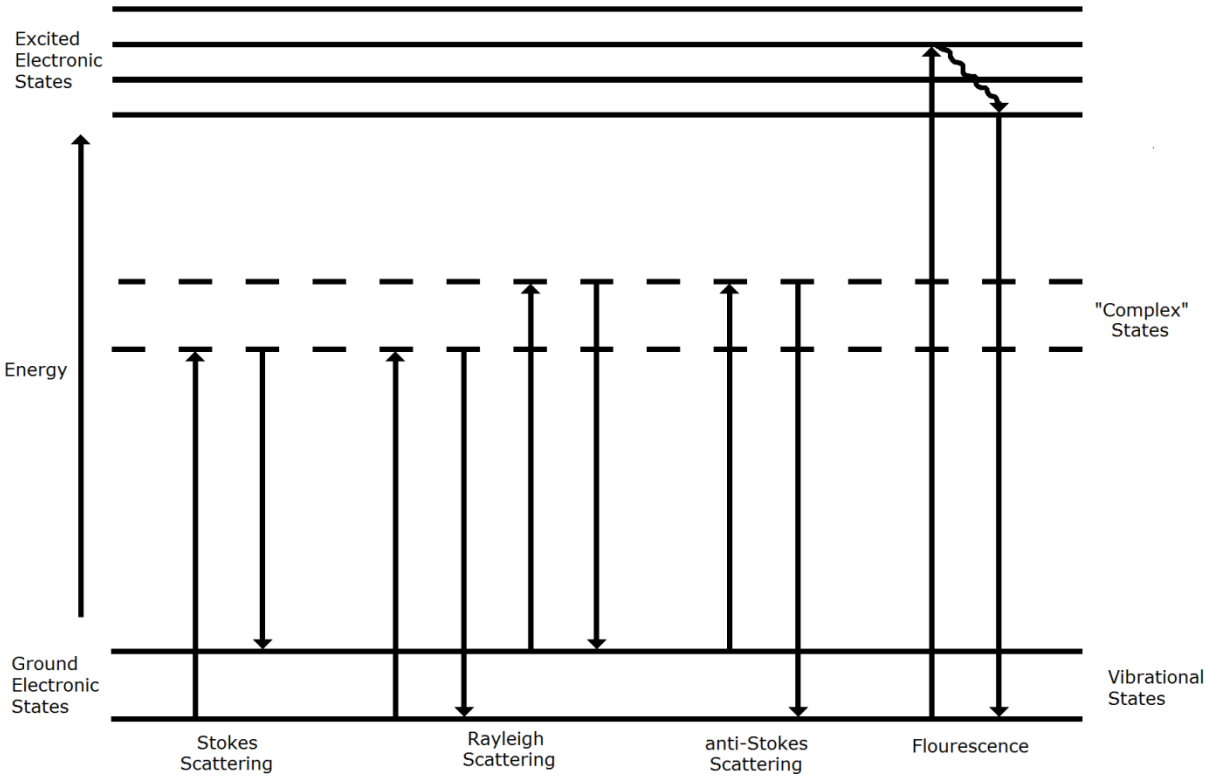


Figure 2.9: Diagram showing the process of fluorescence emission in comparison to Rayleigh and Raman scattering [67].

There is, however, a trade-off in implementing this solution. Raman signal intensity (I) is proportional on the fourth power of the frequency (v) (Equation 2.5) [63], so by lowering the frequency the intensity also decreases. This can make changing the excitation wavelength an unsuitable solution for samples that already generate a weak Raman signal under normal conditions. This can be overcome by using a more powerful laser but this solution can generate problems of its own, namely damage to the sample. This is further discussed in Section 2.2.4.

$$I \propto v^4 \tag{2.5}$$

2.2.3.2 Photobleaching

Photobleaching is another simple method of reducing fluorescence. It involves irradiating the sample for an extended period (from a few minutes up to several hours) in order to cause photodecomposition/degrading of the fluorescent molecules. However, long exposure has been found to cause physical and chemical changes in compounds making the method unsuitable for use on samples that are irreplaceable, such as, for example, forensic evidence, or artwork [68-70].

For the experiments contained in this body of work, photobleaching is the preferred method of removing fluorescence, as the samples did not degrade though long exposure to the laser radiation. In fact, when fluorescence was detected it was found to be contaminates on the surface of the samples generating the fluorescence making photobleaching, and therefore photodecomposition, an ideal method.

2.2.4 Problems with Raman Spectroscopy - Destructive

Raman spectroscopy is widely considered to be a non-destructive technique, however, it is possible to damage a sample using Raman spectroscopy. At the most basic level, Raman spectroscopy involves directing a high powered laser onto a small area (~ 1 micron diameter spot size) of a sample. This can result in 'burning' the sample (Figure 2.10). Care must always be taken to ensure that there is not too much power being directed at the sample. In the work here, typical powers of 6.29 mW were used.

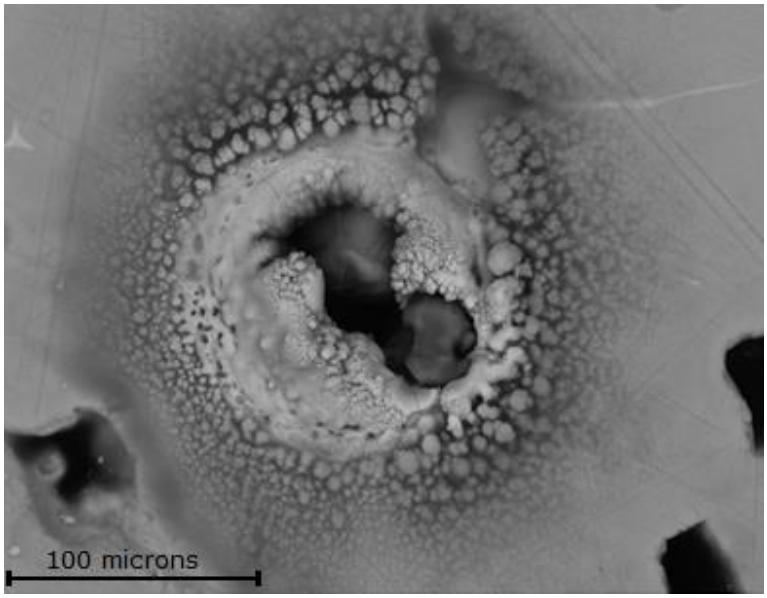


Figure 2.10: Melting of a bismuth-ferrite sample (melting point 800°C) due to exposure to a Raman spectrometer's laser (20.10 mW) for 10 seconds.

2.2.5 Applications of Raman Spectroscopy

Raman spectroscopy is an extremely versatile technique; as such, it can be used for a wide variety of applications. These include: biology, pharmaceutical science, nanotechnology, forensic science, art and archaeology, materials science and mineralogy.

2.2.5.1 Biology

A huge advantage of using Raman spectroscopy for biological applications is that it is a non-invasive technique that is able to take *in situ* measurements. Also, water has a weak Raman signal which is of great benefit when looking at biological material containing water. One major problem with using Raman spectroscopy for biological applications is that it can easily cause damage to sensitive tissue due to the highly focused laser beam.

Examples of studies using Raman spectroscopy for biological applications include: the transition of amino acid crystals [71], single cell bacteria [72], bacterial spores [73], carotenoids in organisms [74, 75], fungi [75], benign and malignant tissue in thyroid [76], and human breast tissues [77].

2.2.5.2 Pharmaceutical science

Raman spectroscopy has become a successful tool in pharmaceutical science largely due to its ease of use and minimal sample handling and preparation. There are also definitive differences in the scattering strengths of packaging materials, non-medicinal tablet casings and the active medical agents.

Examples of studies using Raman spectroscopy for pharmaceutical applications include: the detection of counterfeit drugs [78, 79], the interaction between drug molecules and their target cells [80] and the binding of anti-cancer drugs [81, 82].

2.2.5.3 Art and Archaeology

The *in situ* nature of Raman spectroscopy makes it a preferred method for the analysis of artwork and archaeological artefacts. Raman spectroscopy requires no sample preparation, meaning valuable, often irreplaceable, samples need not be altered in any way; which is a key requirement. It is also possible to gain significant amounts of chemical information without destroying any portion of the sample.

Extensive work has been carried out regarding the composition of pigments and dyes used throughout history [83-90]. Raman spectroscopy can be used to characterise these pigments and dyes chronologically [91] and, therefore, the age of the work can be determined [92]. By being able to extensively analyse the constituents of the pigments present on an artefact, it is also possible to determine whether or not the artefact is authentic [93].

2.2.5.4 Forensic science

As with the use of Raman spectroscopy in art and architecture, the non-destructive, non-invasive nature of Raman spectroscopy is also important when analysing samples in forensic science. This allows for repeated measurements of samples without introducing any contaminates that may influence results. Raman spectroscopy can also be conducted without the sample needing to be removed from its original

evidence bag [94-96], further reducing any risk of contamination. It also allows for samples to be preserved, should they need to be further analysed at a later date.

The use of Raman spectroscopy can lead to a more in-depth understanding of the evidence than would otherwise be obtainable. For example, the compounds in unidentified aqueous solutions can be identified [63] and distinctions can be made between different gunpowders [97] and explosives [98, 99], giving investigators more accurate information to work from. Investigators can also use Raman spectroscopy to identify potentially illicit drugs on a suspect's clothing [100] or fingerprints [101] to quickly know whether or not the suspect has been using illegal drugs, and, if so, exactly which drug. Raman spectroscopy can also help investors establish links between what may otherwise be seen as separate incidences, such as the same car paint [102-104] being found at multiple scenes or a specific ink dye being used for forging documents [105, 106] in different locations.

2.2.5.5 Nanotechnology

Due to its ability to analyse samples that are microscopic in size, Raman spectroscopy is an effective tool for the investigation and characterisation of materials used in nanotechnology. Examples include the characterisation of carbon nano-structures [107] and the quantitative analysis of nanomaterials [108].

2.2.5.6 Materials science

Being such a versatile technique, Raman spectroscopy, can be readily applied to any material system. Previous uses range from the analysis of environmental contaminants; such as searching for perchlorate in water [109], nitrate and nitrite during the wastewater treatment process [110] and uranium in environmental samples [111]; to electrical applications, such as studying the effectiveness of various semiconductors [112] and superconductors [113, 114]. Further uses for Raman spectroscopy in materials science include characterising ceramics [115] and cement [116], investigating the structure of glasses and crystals, and investigating the composition and crystalline behaviour of polymers [117-120].

2.2.5.7 Mineralogy

The non-destructive nature of Raman spectroscopy, coupled with the fact that no sample alteration/preparation is needed before analysis, makes it a powerful tool when investigating mineral samples. Mineral samples typically have strong and distinctive Raman signatures that allows for quick and accurate identification of the sample.

Natural rock samples are comprised of multiple minerals, with each mineral having its own chemical composition and crystalline structure. Raman spectroscopy is highly sensitive to even slight differences in chemical structures [121] and is able to provide substantial information that can be used to discriminate between different structural groups, or phases of minerals, even when they are in the same mineral class.

One example of this is olivine, $(Mg^{2+}_{x}\ Fe^{2+}_{1-x})_2SiO_4$, which has a structure that allows Fe or Mg to take up position in the crystal lattice. This leads to a mineral having a range of ratios of the elements that can be in that position. The magnesium end member (Mg_2SiO_4) is known as forsterite, while the iron end member (Fe_2SiO_4) is known as fayalite. The Raman spectrum of olivine changes depending on the ratio of Mg and Fe present in the sample [122].

By its very nature, a great deal of important geology is done during field work and Raman spectroscopy has the advantage of being able to be carried out on-site during fieldwork due to the availability of mobile units [123, 124]. This is a significant advantage over many other analytical techniques, especially those that require a vacuum chamber, such as electron microscopy, which would be impractical to do in the field.

Mineralogy is an important aspect of planetary science as all the rocky bodies in the Solar System (such as planets, satellites, asteroids, etc.) contain minerals. Samples from these bodies, such as meteorites, are rare mineralogical samples and therefore precious, and any damage or alteration should be avoided. This makes Raman spectroscopy an ideal tool for the analysis of these samples. However, these samples are extremely likely to have been shocked: firstly when they were ejected from their parent body and, secondly, when they impacted the Earth. They were also heated as they entered Earth's atmosphere, forming a fusion crust of melted and heavily modified material (Figure 2.11).

Due to its non-destructive nature, Raman spectroscopy is often used to examine meteorite samples [125-128]. These studies often attempt to identify the mineralogical composition of the meteorites in order to identify their parent body. Raman spectroscopy can also be used to investigate the processes involved in the formation of the minerals present. However, a drawback of analysing meteorite samples is that (as described in Section 2.1.5) they have been subjected to an unknown amount of pressure and heating during the impact event which caused them to be separated from their parent body and again when they impacted the Earth. Therefore, while extremely valuable resources for examining the processes that resulted in the formation of the solar system, meteorites have been subjected to a number of unknown conditions that will have had an effect on their composition. This can potentially cause complications in the interpretation of any information gained from their analysis.

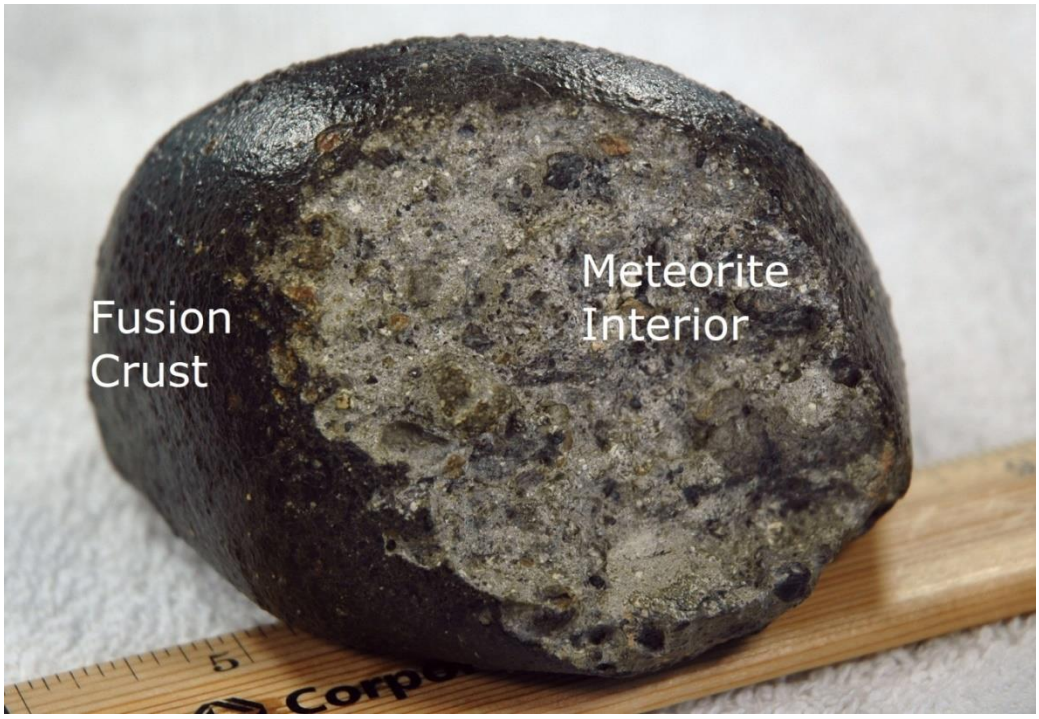


Figure 2.11: The fusion crust surrounding the interior of the NWA 7496 meteorite (image credit: Dr. Randy Korotev of Washington University in Saint Louis).

2.3 Summary

This thesis aims to determine if Raman spectroscopy can be used to infer the shock history of a mineral grain similar to those found in a meteorite sample, or on a planetary surface. The first question that needs to be addressed is how these shock events alter the Raman spectrum of the minerals.

Previous studies have been undertaken to determine the effects of pressure on the Raman spectrum of minerals [129-135], but these are almost entirely quasi-static pressure tests (and therefore do not accurately simulate the processes that occur during an impact) or only focus on peak positions and not the Raman spectrum as a whole. This leaves a real lack of data for mineral samples that can be compared before, and after, they have been subjected to dynamic shocks. It is this gap in the available data that the work within this thesis aims to fill.

2.3.1 Possible Application to the *ExoMars* Rover

The European Space Agency (ESA) *ExoMars* rover, *Rosalind Franklin,* will have a Raman spectrometer as part of its instrumentation payload [136, 137]. When *Rosalind Franklin* arrives on the surface of Mars in 2021 it will land in Oxia Planum and be near to (or possibly even within) an impact crater. This will allow for *in situ* analysis of rock strata that has been exposed by an impact event (similar to what has been done with the curiosity rover). Such impact shock events can alter the Raman spectrum of those minerals, thereby leading to possible misinterpretation of what minerals are present and creating an inaccurate view as to what the surface consists of.

In preparation for *ExoMars*, minerals that can be found on the Martian surface have been chosen for the experiments conducted in this Thesis. Details on these minerals can be found in Section 4.2.

This investigation may also be relevant for the *Mars 2020* rover which will also carry a Raman spectrometer. However, as explained in Section 4.1, the laser used in this study matches the laser on-board *Rosalind Franklin* and as such this is the main focus of comparison for this thesis.

Chapter 3 - Instrumentation

3.1 The Raman Spectrometer at the University of Kent

3.1.1 Operating Principles

As detailed in Chapter 2, Raman scattering produces a change in energy (or frequency) of an incident photon. In order to record these shifts in energy, the initial energy (or frequency) needs to be accurately known and it is for this reason that a monochromatic light source is the best choice for the excitation source and why lasers are now used almost exclusively in Raman spectrometers.

The laser in a micro-Raman spectrometer is directed onto the sample via a microscope. In the majority of modern systems, this microscope is integrated into the spectrometer which has the advantage of allowing very small amounts of material (or specific microscopic areas of a larger sample) to be analysed. The light that has been scattered is then collected at either 90° or 180° to the incident light. In the case of the 90° collection system (Figure 3.1) a lens is placed at 90° to the incident light beam which then passes the light into the spectrometer.

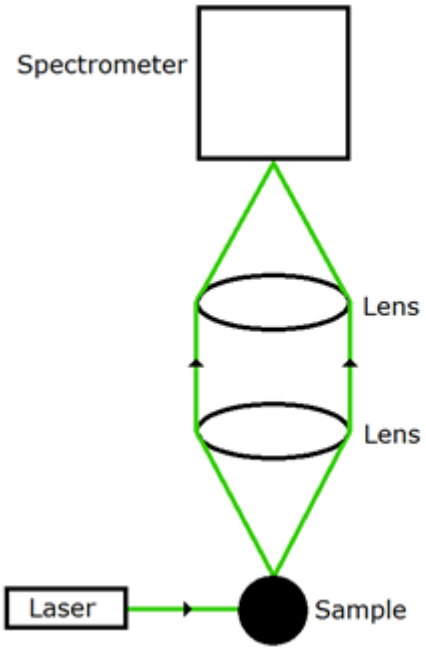


Figure 3.1: A simple diagram to show a 90° collection system.

The University of Kent's Raman spectrometer is a Horiba "LabRam HR" and uses a 180° collection system (Figure 3.2 and Figure 3.3). There are four different lasers available in the University of Kent's Raman system: a 472.98 nm blue laser (4.87 mW); a 532.00 nm green laser (6.29 mW); a 632.81 nm red laser (1.65 mW); and a 784.15 nm infrared laser (20.10 mW)[1]. This range of choice allows a user to select an excitation wavelength that works best for their particular sample, and means that fluorescence can often be overcome by changing the excitation source.

[1] Power values quoted here correspond to the amount of power exiting the objective lens of the Raman system when optimally aligned.

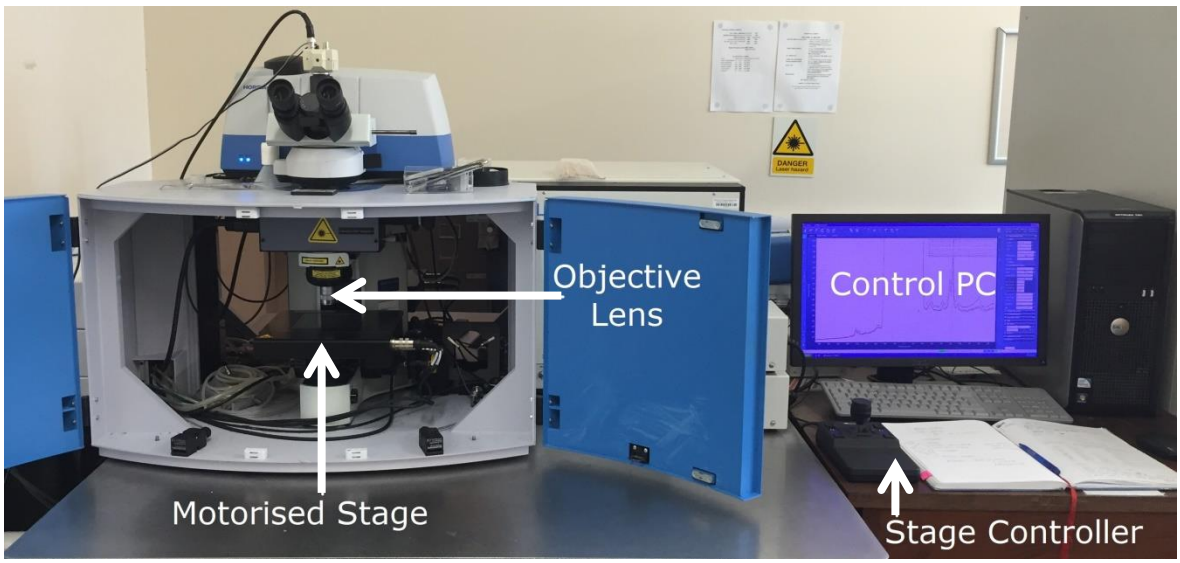


Figure 3.2: The University of Kent's Horiba LabRam HR Raman spectrometer.

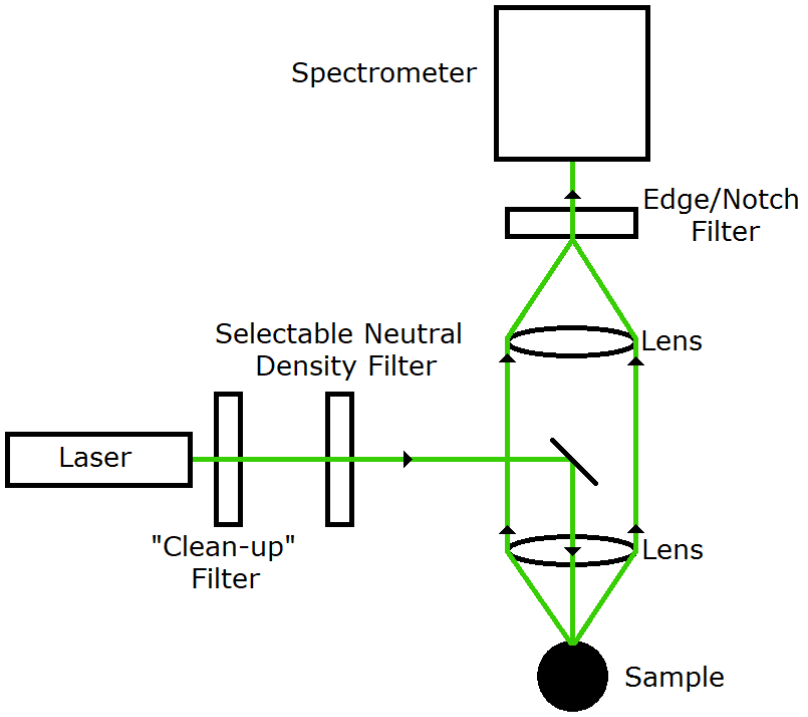


Figure 3.3: A diagram showing the optical path inside the Horiba LabRam HR Raman spectrometer including the 180° collection system.

Figure 3.3 shows a diagram of the optics involved in the Horiba LabRam HR. Once an incident photon has been emitted by the laser, it is first passed through a "clean-up" filter to ensure the monochromaticity of the light. The light then passes through a neutral density filter so that the amount of power being supplied to the sample can be controlled, helping to avoid problems such as overheating of the sample or saturation of the detector. There are seven neutral density filters available: 0.01%, 0.1%, 1%, 10%, 25%, 50%, and 100%, where the percentage values indicate the amount of laser radiation that passes through the filter.

The incident beam then passes through a beam splitter which allows half of the incident light to pass through, and reflects the other half of the incident light towards the objective lens of the Raman spectrometer's microscope.

The initial light is then focussed onto the sample through a x50 objective (to give a spot size of ~2 μm in diameter). It is here that Raman scattering takes place (Chapter 2). Any of the light that is scattered by 180° is collected by the microscope's objective lens and now travels in the opposite direction to the incident light beam. The scattered light then reaches the beam splitter, where half of it is reflected towards the laser source and the other half is allowed to pass through on its way to the spectrometer. Before reaching the spectrometer, it first passes through an edge (Stokes) or notch (anti-Stokes) filter. At this point, the majority of photons will have undergone Rayleigh scattering, not Raman scattering, and as such will have a Raman shift of 0 cm^{-1}. Laser rejection filters are used to absorb the photons that have a shift of within approximately ± 100 cm^{-1} of the incident light. Higher quality (and more expensive) filters can reduce this number in order to make measurements closer to the excitation frequency.

There are two types of laser rejection filters available for each of the laser wavelengths: edge filters and notch filters. An edge filter is a long pass filter designed to absorb all wavelengths up to a certain value, typically slightly higher than the wavelength of the excitation source (i.e. an edge filter designed for a 532 nm laser would absorb all light up to approximately 534 nm). This results in only allowing photons with a longer wavelength (lower frequency and energy) than the excitation source to pass through, meaning only Stokes-shifted photons are analysed. In contrast, a notch filter has a sharp, discrete absorption band, the centre of which is designed to match the excitation wavelength. Typically, these bands are only a few nanometres in width, meaning that both Stokes and anti-Stokes shifted photons outside of this band are allowed to pass [138].

There are two main reasons why the Rayleigh scattered photons must be filtered out of the light that enters the spectrometer. The first reason is that these photons do not contain any information and are therefore uninteresting. The second reason is that if these photons were to pass into the spectrometer there would be a huge amount of light falling onto a small area of the CCD which would lead to saturation of the CCD and loss of detection of Raman scattered photons.

After passing through the laser rejection filter, the scattered light then enters the spectrometer where it is focused onto a diffraction grating (Figure 3.4). There are two gratings available: a 600 grooves per mm grating, and a higher resolution 1800 grooves per mm grating. The diffraction grating separates the light into its component wavelengths and directs them onto a CCD detector that records the data.

To ensure that the spectrometer is working correctly, it is calibrated (at least) once a day before any analyses are carried out. This is done by checking the position of a known Raman peak from a calibration standard. A variety of standards with different peak positions are available, common standards include: silicon (520 cm^{-1}), barium sulphate (988 cm^{-1}), and diamond (1364 cm^{-1}). A test spectrum is taken of the calibration sample and the position of the peak can be corrected for (this is usually done automatically by the software).

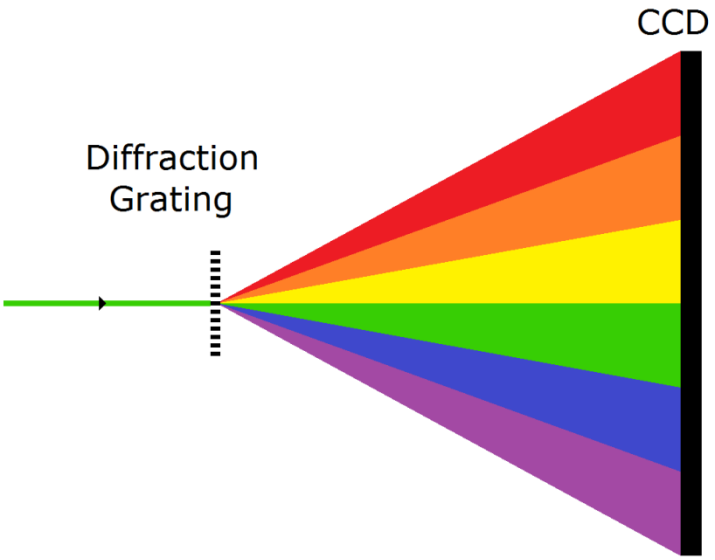


Figure 3.4: Diagram demonstrating how a diffraction grating separates the different wavelengths of light and spreads them across a CCD detector.

3.1.2 Other Features

One of the useful features of a modern micro-Raman system is sample mapping. The University of Kent's Raman spectrometer is fitted with a motorised microscope stage capable of moving in the XYZ axes to a stated accuracy of 0.1 microns. This allows for a series of points to be preselected so that Raman spectra can be gathered at each of them in one experimental run. Raman mapping is extremely useful for characterising changes across a large area of a sample, and was used extensively for the work in Chapter 5 and Chapter 6.

Kent's Raman system is also equipped with a "Linkam" temperature stage [139]. The Linkam stage is capable of achieving sample temperatures of between -193 °C and 600 °C (80 K and 873 K). It uses liquid nitrogen and a liquid nitrogen pump to obtain temperatures lower than room temperature and is also capable of analysing samples under different atmospheres. The Linkam stage was used extensively for the work in Chapter 4.

3.2 The Light Gas Gun

The University of Kent's two stage Light Gas Gun (LGG) has been in operation for over 25 years [22]. It was purchased from Physics Applications Inc [140], and the first shot occurred in August of 1989. Since the facility first came online, the LGG has undergone a number of upgrades and modifications which has diversified the shock physics research that researchers at the University of Kent can perform.

The LGG facility was used extensively in this body of work to generate shock pressures on mineral samples similar to the pressures present in a planetary impact. The results of these experiments are described in Chapter 5 and Chapter 6.

There have been a number of enhancements and upgrades made to the Kent LGG facility over its lifetime and below is a brief summary of these upgrades and the research associated with them. In addition, Section 3.3.2 explains the working principle behind the LGG and describes the firing procedure.

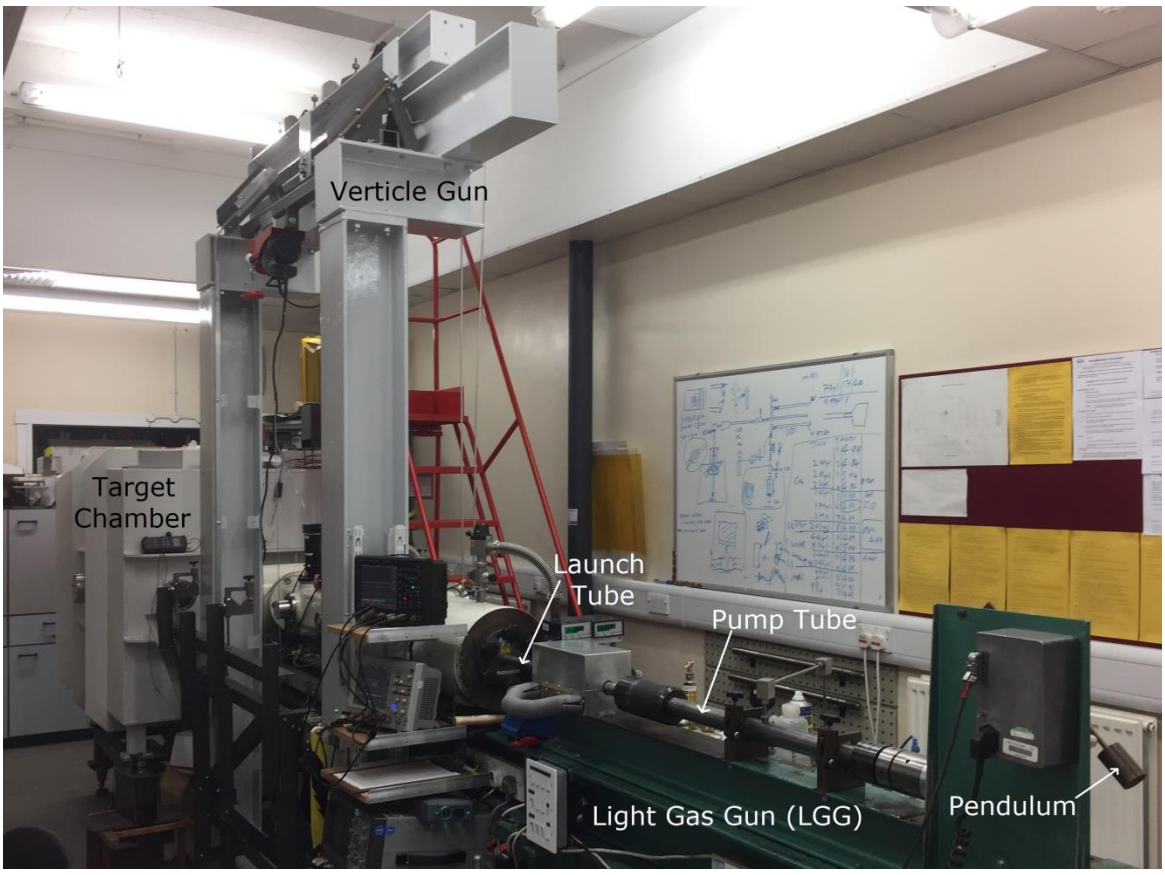


Figure 3.5: The LGG facility at the University of Kent as of November 2017

3.2.1 Upgrades

3.2.1.1 Projectiles

Originally, the Kent light gas gun (Figure 3.5) was only capable of firing 0.170" diameter nylon cylinders with a length of approximately 4 mm and diameter of 4.5 mm[1]. The simplest modification made to the projectile set-up was the addition of rifled launch tubes. The rifling of the launch tubes produces one full rotation of the projectile for every 0.7 m the projectile travels, thus giving the projectile a rotational speed.

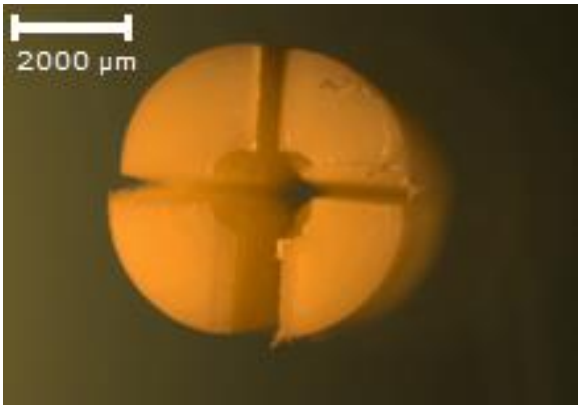


Figure 3.6: A split sabot illustrating the four interlocking segments and the central hole which houses the projectile(s).

[1]Units converted to metric from the imperial units used by the LGG's manufacturer.

The addition of rifled launch tubes has added the ability to use split-sabots (Figure 3.6), which are comprised of four interlocking segments that are capable of housing a projectile within them. The rifled launch tube imparts a rotational component to the velocity of the sabot during acceleration; once the sabot is no longer confined by the launch tube, the four segments begin to spin away from the gun axis while leaving the projectile to continue down the gun range. The split sabot system is described in greater detail in [22].

The encased projectile can take a variety of forms. Single projectiles ranging in size from 0.1 to 3.0 mm can be used, provided that the material is capable of withstanding the extreme acceleration and "jerk" (acceleration/time) of $\sim 10^9 - 10^{10}$ m s^{-3} they experience during launch. Using rifled launch tubes and split-sabot technology it is also possible to fire a buckshot of material consisting of many small particles (buckshot as small as 100 nm silica spheres has been successfully fired). These small particles can be used as analogues for dust particles found throughout the Solar System, such as cometary or interplanetary dust [141-143].

Since their introduction in 1993, split sabots have been used extensively in the impact research undertaken at Kent. One example of work that relied heavily on the use of split sabots is the experimental simulations of dust particle impacts onto aluminium foils carried out by Kearsley et al (2006) [141]. These experiments were used to support the NASA Stardust mission to comet 81P/Wild-2 [142, 143]. These works enabled a better understanding of the impact craters found on the *Stardust* aluminium foils (used to secure the aerogel captures cells within the sample return capsule), and aided in the creation of a calibration for the size of the dust particles that had impacted the foils [141, 144] and also provided a calibration for the pre-impact size of the particles capture in the aerogel itself [145]. These results helped provide insight into the structure of comet Wild-2, as well as a serendipitous discovery that led to a much greater understanding of the cratering mechanisms of very small particles at high speeds when strain rate dependent strengths become significant [146].

Another example to demonstrate the flexibility of using split-sabots is the firing of live bacteria onto a variety of target materials in order to test their survivability in the context of the theory of Panspermia [147]. This shot program impacted bacteria infused into porous ceramic projectiles directly onto plates of nutrient material at speeds of 5.0 – 5.3 km s^{-1}. The target plates were then incubated and examined for colony growth. Growth was discovered on several target plates demonstrating that it is possible for bacteria to survive hypervelocity impacts and was one of the first demonstrations that living organisms could survive such extreme shock pressures.

In addition, the Kent light gas gun has the capability to fire frozen projectiles in the form of solid ice (plus any constituents) frozen into a hollowed-out cylinder. This is then fired as a single projectile as there is (currently) no way to strip the encasing cylinder from its frozen contents. These ice filled cylinders are often used for research related to the field of astrobiology, such as investigating the survivability of yeast spores and fossils in hypervelocity impact events. Yeast spores were shown to be able to survive impacts up to 7.4 km s^{-1}; the survival probabilities were calculated to be ~50% for 1 km s^{-1} impacts, but fell to $\sim 10^{-3}$% for 7.4 km s^{-1} impacts [148].

These hollowed out sabots were also used to fire fossilized diatoms either frozen in ice or suspended in liquid water (when a cap was placed to seal the hollowed out sabot) which permits the firing of liquid samples. The diatom fossils were found to be capable of surviving intact when subjected to impacts up to 5 km s^{-1} (19 GPa). While the larger

fossils broke up during the impact events, intact fossils up to 30 μm in size were found at 5 km s^{-1}, implying that larger structures are broken first at lower shock pressures [147, 149].

3.2.1.2 Targets

As well as being able to fire onto standard bulk material targets, we have also developed a variety of target holders that allow the investigation of targets at a range of temperatures (from 100 K to 1000 K). These target holders are used to simulate impacts on different bodies throughout the Solar System, where there is a large temperature variation, ranging from Pluto at 33 K to Venus at 735 K. For example, a hot target holder capable of heating cylindrical targets up to 1000 K using a heating coil, and maintaining the desired temperature until just prior to impact, (Figure 3.7.A) has been used to study the cratering efficiency of metal targets as a function of temperature and the mixing of molten target and projectile material. For example, craters in metal targets were shown to increase in size as the target material approaches its melting point, due to the thermal softening of the material and therefore a loss in yield strength [150]. While the mixing of molten target and projectile material has been difficult to achieve in the laboratory [151], other studies that have relied extensively on the hot target holder include investigations into the cratering formation process on rocky bodies [152, 153].

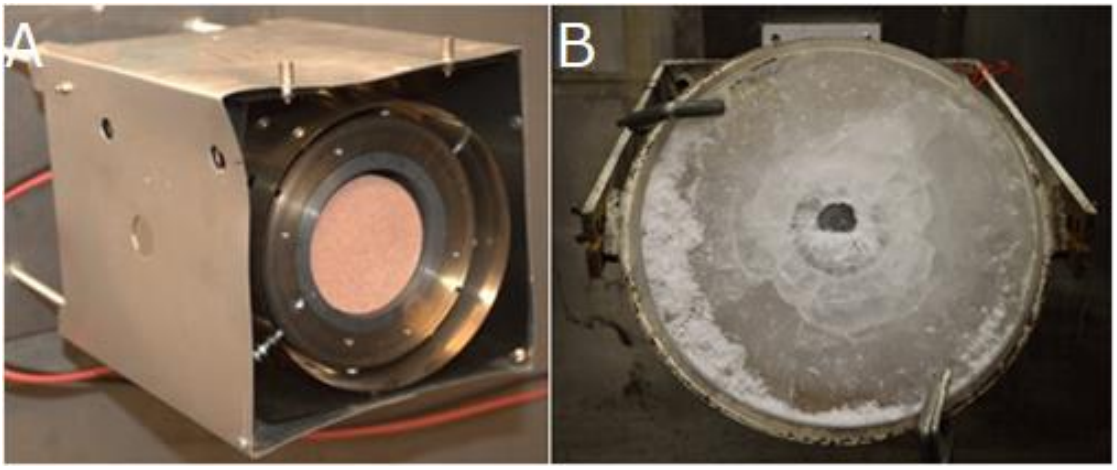


Figure 3.7: (A) The hot target holder with a 60 mm diameter cylinder of sandstone housed in the centre ready for heating. (B) A water ice layer over a solid basalt target impacted at an impact angle of 45° (target diameter 40 cm).

To complement the hot target holder, it is also possible to impact onto frozen targets. This method utilises standard freezers in the lab to cool a target before a shot, which is then transferred to the target chamber whilst the gun is prepared for firing (Figure 3.7.B). This allows us to construct large targets made of ices that can be used to simulate icy bodies in the outer Solar System. This facility has been used to determine how changes in velocity [154], impact angle [155] and ice temperature [156] influence crater morphology in water ice targets. Investigations have also been conducted to determine the effect of ice layers over other target materials such as (liquid) water, sand and basalt. This study indicated that the density of the subsurface material does result in differing crater morphology [157].

Additionally, a rotating target holder capable of rotating spherical targets up to 150 mm diameter at speeds of up to 3.5 Hz has been constructed (Figure 3.8). This allows investigations into whether a rotating target has a lower catastrophic disruption

energy than a stationary target and, if so, how this energy changes as a function of target rotational velocity. This is particularly important for understanding the dynamics of asteroid fragmentation [158].

As the Kent light gas gun is a horizontal gun it can be problematic to simulate impacts onto bodies of water and therefore the "water-target holder" was developed to address this problem. It consists of an aluminium container with a 30 mm circular opening on one side to allow the passage of a projectile. Inside the container is a frame holding a very thin (approx. 10 microns thick) plastic bag filled with liquid to simulate a body of water (Figure 3.9). After the impact, this water can be collected and filtered to examine the remnants of the projectile. This target holder has been successfully used to investigate the theory of Panspermia by simulating oceanic impacts by measuring the survival rates of simple organisms after impact events [148, 159], such as the experiment involving the survivability of yeast spores mentioned earlier, and by testing if sufficient volumes of material (with the potential to house such organisms) survive the impact process. It has been used to show that large fragments (~10% of the original mass) from millimetre sized projectiles are capable of surviving a 5 km s^{-1} impact into water, demonstrating that large asteroids may deliver significant volumes of solid material to Earth; thus providing a possible mechanism for Panspermia [160].

The ocean target holder has also been used to determine the influence on crater formation for a solid rock target with a layer of water above the target. It was found that an overlying water layer resulted in a reduction of crater dimensions when compared to a corresponding impact without a water layer. The study showed that a layer of water approximately 12 times the projectile diameter was required to stop crater formation in the rock target [161].

Finally, it is also possible to pressurise the target chamber up to 100 mbar with any inert gas (or air) and can be used to determine if the presence of certain atmospheric constituents alters the physical or chemical interactions between the projectile and the target during impact. The method was used to investigate the possible sources of methane in the Martian atmosphere. The results from these impact experiments showed that the atmospheric methane on Mars is likely not due to release from impacts onto methane bearing basalt and they also demonstrated that the impact pressures achievable with the light gas gun were not sufficient to induce rapid serpentinisation, which is another suggested theory for the presence of methane on Mars [162].



Figure 3.8: (left) A spherical target in the rotating target holder at the moment of impact and (Right) during complete disruption of the target (approximately 5 milliseconds later).

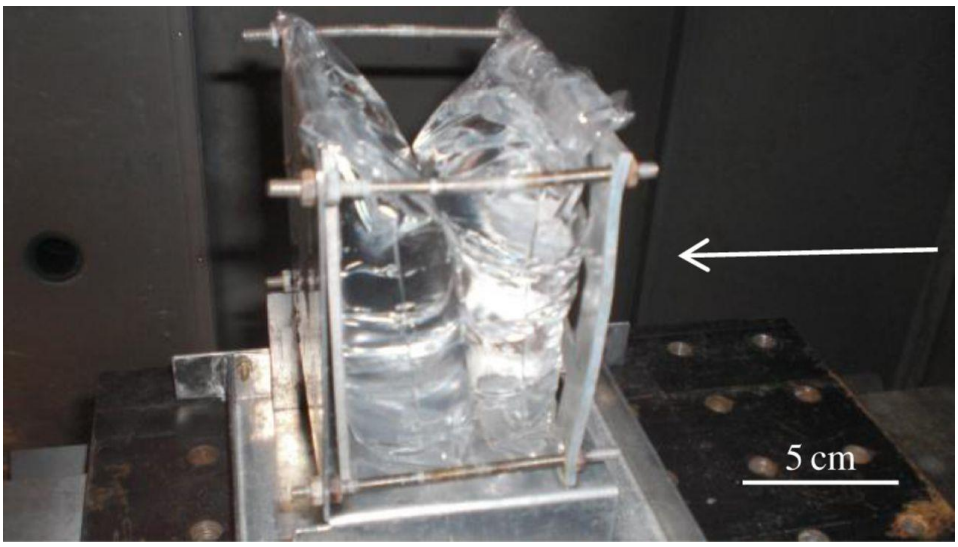


Figure 3.9: The ocean target holder showing the frame holding two bags of water. The arrow indicates the path of the incoming projectile.

There is also a host of instrumentation that can be used to monitor the target during/after the impact, these include:

- Video cameras (e.g. Panasonic HX WA30, Nikon D3400, Nikon V1, and an FPS4000)
- Ejecta capture systems [163].
- An impact flash detector which can be used to trigger other instrumentation such as a spectrometer.
- A range of electrical feedthroughs are also available in order to add instrumentation to the inside of the target chamber or directly to the target (illumination, PVDF sensors, temperature sensors, etc.).

3.2.2 Firing Procedure

To fire the LGG, a pendulum is released which then strikes a firing pin. This firing pin detonates a primer (CCI 209M Magnum) in a 12-gauge shotgun cartridge filled with rifle powder. Various rifle powders with different burn rates are used depending on the speed required for the shot. The burning of the rifle powder releases hot, rapidly expanding gases that then propel the piston along the pump tube.

The pump tube is filled with gas and the piston compresses this gas until it reaches approximately 2 kBar. Once this pressure has been attained, the aluminium alloy burst disk ruptures, allowing the gas to expand into the vacuum maintained beyond this point (labelled as "burst disk" in Figure 3.10). As the gas expands, it exerts a force on the sabot placed in the launch tube. The sabot is accelerated by the expanding gas and begins to travel down the launch tube; the projectile is housed within this sabot.

The gases typically used in the pump tube are hydrogen, helium, or nitrogen. The reason these 'light gases' are used is because the maximum speed of a projectile is dependent on the speed-of-sound in the expanding gas (Equation 3.1): this expansion speed is higher for lighter gases than it is for heavier gases (Equation 3.2) and allows for a higher rate of acceleration in the launch tube, and therefore an overall higher maximum velocity for the projectile.

$$U_{p\,max} = \frac{2}{\gamma - 1} c \tag{3.1}$$

$$c = \sqrt{\frac{\gamma R T}{m}} \tag{3.2}$$

Where, $U_{p\ max}$ is the maximum projectile speed (m s^{-1}), c is the speed-of-sound in the gas (m s^{-1}), γ is the specific heat ratio of the gas, R is the ideal gas constant (J kg^{-1} K^{-1}), T is the gas temperature (K), and m is the molecular weight of the gas (g) [164, 165].

As mentioned in Section 3.2.1.1, the launch tube itself is rifled, causing the sabot to rotate. Once the sabot has entered the blast tank, and is no longer confined by the launch tube, the segments of the sabot begin to separate from each other due to the angular momentum imparted to them by the rifling, while the projectile continues down the gun's firing axis. Segments from the split sabot impact into a 0.5 inch (12.7 mm) thick steel plate known as the "blast tank exit aperture" preventing them from proceeding further, while the projectile passes through a hole in the plate's centre and continues on towards the target chamber. The projectile then passes through the time-of-flight system which is comprised of two laser curtains separated by a distance of 499 mm. It is the passage through these two laser curtains that is used to calculate the projectile's speed. Finally, the projectile enters the target chamber and impacts the target.

3.3 Low Speed Gun

By definition cratering means the excavation of material from the target. This presents a complication when the aim of the experiment is to analyse the target material that has sustained the greatest shock pressure, as this is the material that is excavated in the cratering process and is ejected. The solution to this problem was to impact the target at speeds less than 1 km s^{-1}, thereby shocking the target but (hopefully) not removing any target material. Other members of the Centre for Astrophysics and Planetary Science research group have also encountered similar problems in the past, the most notable of which being ice projectiles. Ice projectiles in the light gas gun have demonstrated a tendency to break-up due to the rapid acceleration in the launch tube, even at the lowest possible speed. This usually results in a spray of fine ice particles impacting the target rather than the intended solid ice projectile [148].

Unfortunately, the minimum velocity of the LGG is 1.2 km s^{-1}. Velocities below this threshold are possible with the use of gases much heavier (such as krypton) than those typically used (hydrogen, helium, and nitrogen), but this has proven to be an expensive solution, and only lowers the minimum speed to 1.0 km s^{-1}. The simplest solution would be to use a facility that is specifically designed for velocities of less than 1.0 km s^{-1}. However, this is undesirable for shot programmes that require shots with velocities both above and below 1.0 km s^{-1}, as the targets for these shots would have been subjected to different environments potentially introducing contaminants, or some other form of systematic error.

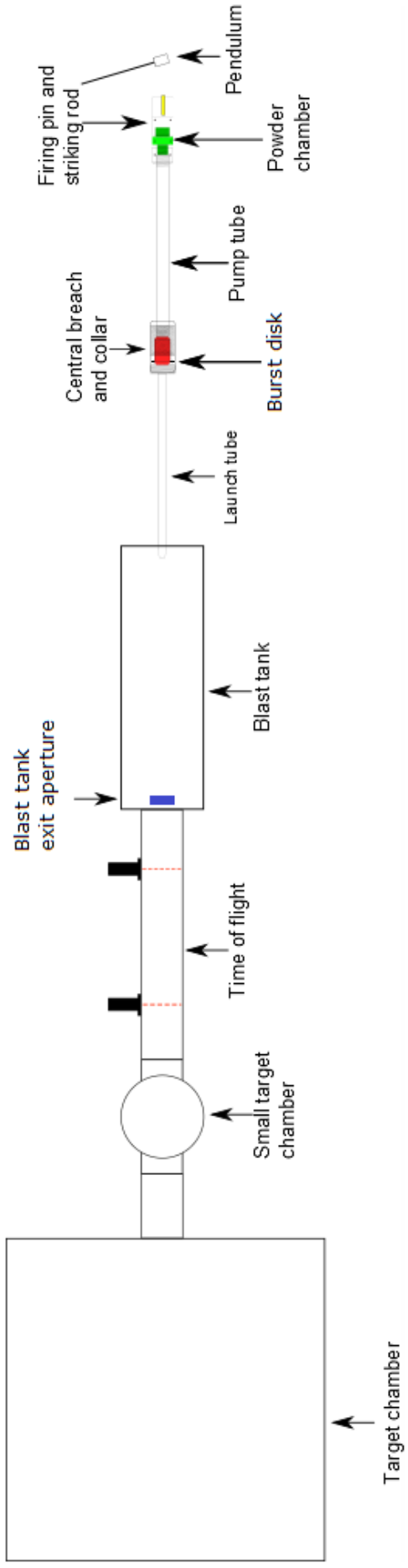


Figure 3.10: Schematic diagram of the LGG [166].

The decision was made to develop a modification to the existing two-stage light gas gun that would allow the user to attain reproducible speeds of less than 1.0 km s^{-1}. The aim would be to achieve as low a velocity as possible; defined by the minimum horizontal velocity needed in order for the projectile to enter the target chamber before gravity could pull the projectile off-axis enough to cause it to impact one of the apertures along the range of the gun; this speed is approximately 0.028 km s^{-1}.

3.3.1 Development Process

In order to develop a method for lowering the minimum speed of the LGG, we first have to identify what causes this limitation. When the LGG fires, the gas in the pump tube is compressed by the piston; when this compression reaches a critical pressure (2.0 kbar) the burst disk ruptures and the gas expands down the launch tube accelerating the sabot. Our aim is to reduce the magnitude of this acceleration, thereby lowering the velocity of the projectile.

The variables that can be controlled are as follows:

1. The initial pressure of the gas.
2. The type of gas used.
3. The strength of the burst disk.

The burst disk ruptures at approximately 2.0 kbar, this pressure is achieved by having the piston compress the gas in the pump tube. Decreasing the initial pressure of the gas in the pump tube decreases the resistive force on the piston as it attempts to compress the gas. This results in the required 2.0 kbar of pressure being achieved with a smaller volume of gas. This smaller volume has a higher temperature than a larger volume of the same gas at the same pressure and Equation 3.2 shows that the speed-of-sound of a gas increases with the temperature of that gas. Thus a hotter gas allows for more rapid expansion into the vacuum when the burst disk ruptures and results in a larger velocity of the projectile (Equation 3.1). Therefore, in order to achieve the slowest possible speed, the highest initial pressure possible must be used. For the LGG the maximum possible initial pressure is dependent on the pressure of the gas cylinder used for the chosen gas. For the three standard gases used those pressures are 137 bar, 170 bar, and 170 bar for hydrogen, helium, and nitrogen respectively. This provides a practical limit on the maximum possible initial pressure in the pump tube. The speeds attained for shots using each of these three gases at their maximum initial pressures can be seen in Table 3.1; this constrains the minimum speed to 1.2 km s^{-1}.

Table 3.1: Lowest projectile speed attainable for each of the standard light gas gun gases at their maximum initial pressures.

Gas	**Speed (km s^{-1})**
Nitrogen	1.2
Helium	2.2
Hydrogen	3.0

There is also a theoretical maximum initial pressure, which is defined by the resistive force generated on the piston during compression of the gas. It is possible for the initial pressure to be so high that the piston is incapable of compressing the gas to the 2.0 kbar required to rupture the burst disk. Therefore, increasing the initial pressure

beyond this limit will not lower the minimum speed of the gun but instead cause the gun to misfire. This theoretical limit on the initial pressure is unknown.

As discussed earlier, a heavier gas with a slower sound speed can be used, as this will lower the rate of expansion of the gas down the launch tube. This solution, however, presents two problems. First, using a heavier gas does not reduce the speed of the LGG by a significant amount; this can be seen from Figure 3.11, which presents speed versus initial pressure for krypton. These data show a 0.041 km s^{-1} change in velocity for a 10 bar increase in initial pressure. Therefore, in order to reach a velocity of 0.5 km s^{-1}, the initial pressure of krypton would have to be in the region of 190 bar. This exceeds the practical limit of the initial pressure possible in the launch tube, thereby limiting the utility of a two-stage LGG.

The standard aluminium 7075-T6 burst disks used in the LGG are 0.5 mm thick and are designed to rupture at a pressure of 2.0 kbar. Altering these burst disks to rupture at a lower pressure for the two-stage light gas gun would present safety issues. The piston relies on the resistive force generated by the compression on the gas in order to slow it as it approaches the central breech. Lowering the pressure at which the burst disk ruptures means lowering this resistive force and allowing the piston to impact the central breech at a higher velocity: Figure 3.12 shows how destructive this can be. The central breech being shattered in this way would allow for the gas to escape and, in the worst possible scenario, potentially send shrapnel flying from the gun, posing an unacceptable risk. However, reducing the rupture pressure of the burst disk is only an issue when using the gun in the two-stage configuration. If no piston were needed to compress the gas, than it could not impact the central breech. Therefore, the decision was made to convert the LGG to a single stage configuration for speeds less than 1 km s^{-1}.

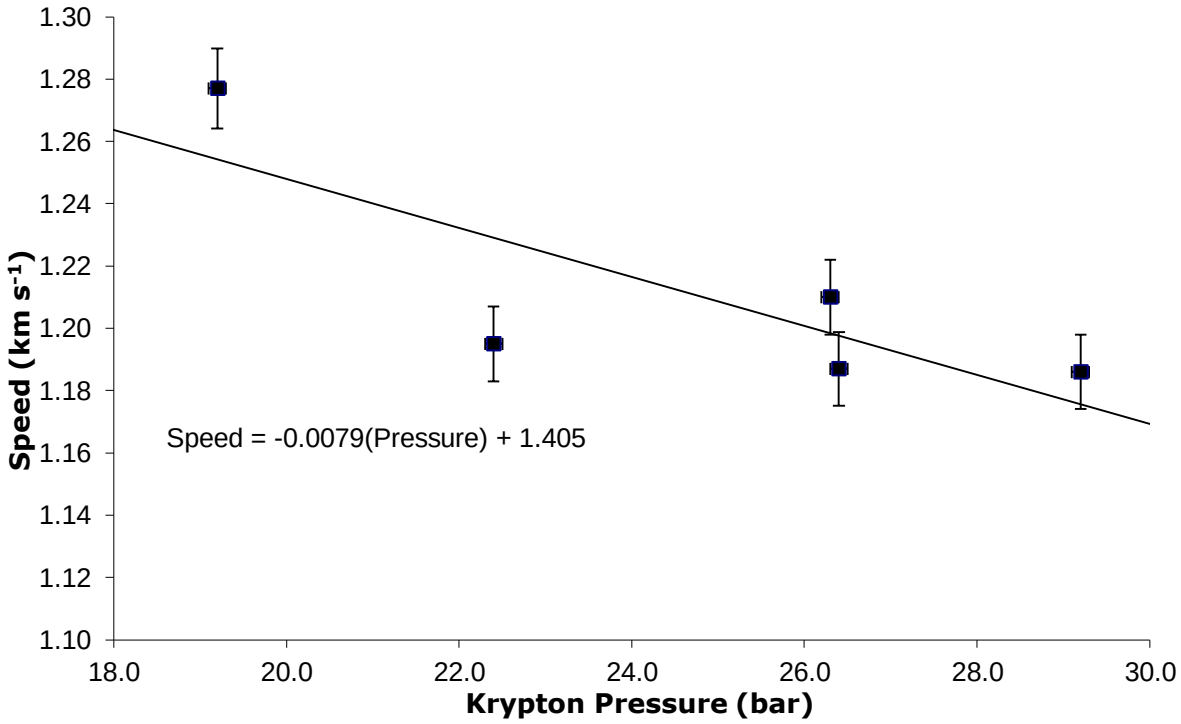


Figure 3.11: Projectile speed versus initial pressure for krypton gas.



Figure 3.12: A central breech that has been split in two after being impacted by a piston at too great a velocity.

A single stage gas gun only uses the second stage of the two stages and eliminates the need for the first stage. The first stage uses a shotgun cartridge filled with rifle powder to accelerate the piston which compresses the gas in the pump tube, thereby rupturing the burst disk. For a single stage gun, the pump tube holds the gas at the desired pressure before simply releasing it into the evacuated launch tube. This is typically accomplished with some form of fast-acting valve in place of the burst disk. The result is a much lower pressure being used to accelerate the projectile and therefore a much lower final velocity for the projectile [167, 168].

3.3.2 Secondary Problem

During the development process outlined here, other researchers at the University of Kent were investigating the possibility of having simultaneously firing light gas guns that would be capable of firing onto the same target. Achieving this requires very fine control over the timing of the firing mechanism, which precludes the use of a cartridge and rifle powder, as such a system relies on the highly variable process of burning rifle powder. A fast acting valve typically takes 0.5 seconds to open or close and is extremely reliable and is sufficient for a single stage gun; however, when trying to operate two such guns simultaneously with the aim of both projectiles striking the target within micro-seconds of each other, these valves do not act fast enough.

While the main aim of this development process continued to be the alteration of the two-stage light gas gun into a single stage configuration, a secondary goal was now present; to investigate alternatives to valve-based gas release that would be suitable for simultaneous gun firing.

3.3.3 Single Stage

Having decided that the use of a valve for the gas release mechanism was not ideal, alternative release methods were considered. The tried and tested method of gas release for the LGG is a 0.5 mm thick aluminium burst disk, which will not rupture at single stage pressures (approximately 100 bar). However, using a weaker burst disk for the two-stage gun provides a significant safety risk due to the lack of resistive

force on the piston; in a single stage configuration there is no moving piston to pose a safety risk. When using the LGG in a single stage configuration with a weaker burst disk, there are three possibilities:

1) The disk is too weak and will rupture during the filling of the pump tube. This causes the gun to fire before the intended pressure is reached and results in the projectile having a lower velocity than originally planned.

2) The burst disk is too strong and does not rupture once the desired pump tube pressure has been attained. This forces the user to either abandon the shot or increase the pressure until the disk does rupture, resulting in a higher than intended velocity.

3) The burst disk ruptures as soon as the desired pressure is reached and the projectile accelerates to the expected velocity. This scenario is obviously the preferred outcome; however, each time the gun is fired it has a low probability of occurring due to mechanical variation introduced to the burst disk during manufacture.

The first two scenarios, while undesirable, are not dangerous and therefore the decision was made to test weaker burst disks, in conjunction with a single stage configuration, in order to determine the reliability and repeatability of such a system.

3.3.3.1 Testing

For these tests the 0.5 mm thick aluminium burst disk was replaced with a 50 micron thick aluminium foil. However, a burst disk must have a minimum thickness to sit correctly on the launch tube in order to create a good seal against the central breech. This minimum thickness was attained by fixing an acetate backing to the foil which was 0.25 mm in thickness and had a 2.0 mm central hole, allowing the gas to flow when the foil was ruptured.

Ideally such a burst disk should have a fixed pressure at which it will fail. In most cases this was found to be 86 bar ± 2 bar, effectively giving three new speeds for the light gas gun, one for each of the gases commonly used (Table 3.2). After a short series of shots to test this method, it was discovered that on some occasions the burst disk would rupture at a much lower pressure than expected, causing the gun to fire at a lower speed than planned. After investigating this problem further it was determined that the handmade nature of the burst disks was to blame. To make a single stage burst disk, a 12.5 mm punch was used on sheet material to produce both the foil and acetate disks. A central 2 mm hole was then drilled (by hand) into the acetate backing disk before fixing the two disks together using double-sided tape. The punching out of the foil commonly resulted in the foil being bent slightly as it was removed from the punch. This bending of an already much weaker burst disk is believed to be the cause of these unreliable shots as it likely introduced imperfections onto the surface of the disk that further weakened it.

A 100 micron thick aluminium foil was then tested to try and eliminate the unreliability of the 50 micron foil. The reasoning behind this decision was that the 100 micron foil would still be weaker than the 0.5 mm burst disk, but would hopefully prove to be more resistant to bending during the manufacturing process. The 100 micron burst disks were manufactured in the same way as the 50 micron burst disks.

Table 3.2: The speed attainable using each of the standard gases in with the 50 micron burst disk single stage set up.

Gas	Velocity (km s^{-1})	Standard Deviation
Nitrogen	0.372	0.0147
Helium	0.606	0.0167
Hydrogen	0.703	N/A

The 100 micron foil also ruptured at a fixed pressure, found to be 190 bar ±5 bar. This is beyond the maximum fillable pressure of the pump tube and as such cannot be used to fire the single stage gun. However, the 100 micron burst disks have proven to be much more reliable than the 50 micron burst disks with regards to gas leaking past the burst disk during preparation of the gun. This meant that the 100 micron burst disks were ideal for retaining the gas in the pump tube, but could not be used to fire the gun.

During the test firing process, if the gas pressure reaches the expected failure value and the burst disk remained intact, the pressure is maintained for a short while to allow time for the burst disk to weaken under the constant pressure. If the burst disk still does not rupture, a decision was then made as to whether to abandon the shot or continue to increase the pressure knowing that the projectile speed would be higher than intended. This was preferred to having the burst disk fail at a lower pressure (as is commonly encountered with the 50 micron system) as here the experimenter still has some limited control over the outcome of the shot.

While these tests have shown that the 50 micron single stage system can be used to produce speeds of less than 1 km s^{-1}, the choice of speeds is limited. Table 3.2 shows that using the 50 micron burst disk in combination with each of the standard gases generates an average speed of; 0.372 (with a standard deviation of 14.7) for nitrogen, 0.606 (with a standard deviation of 16.7) for helium, and 0.703 for hydrogen[1]. This system provides no fine control over the speed of the projectile; both in terms of the final velocity or the timing of the shot. This makes it challenging to use the observation systems mentioned in Section 3.2.1.2 that are not triggered by the gun itself but are reliant on activation by the user just before firing (such video recording systems). Also, it is possible that this system could fire of its own accord when the user is not present (i.e. when more gas is being retrieved to fill the pump tube).

[1] There is only one data point for hydrogen as the speed achieved was deemed to be easier to obtain by using burst disks constructed of other materials, which was deemed to be outside the scope of this investigation.

3.4 Electronic Burst Disk

Having concluded that using a weakened burst disk does not provide the level of reliability and control desired, the problem was re-analysed and a fresh approach was taken.

For the gun to propel a projectile in a single stage configuration, part of the gun needs to be under vacuum while the rest of the gun needs to be pressurised with a (light) gas. These two parts of the gun need to be separated by some barrier, which at some point (of the user's choosing) can be removed to allow the pressurised gas to expand into the vacuum and propel the projectile.

The part of this scenario that is of most concern is the barrier: essentially, material needs to be "present" and then, once a particular condition is met, "not present". A common device that uses such a principle is an electrical fuse. Fuses consist of a piece of material that is capable of carrying an electrical charge that melts if the electrical current exceeds a pre-determined value, thereby breaking the circuit. If we were to treat the burst disk of the LGG like a fuse, then when the circuit is broken due to the melting of the fuse material this would also release the pressurised gas and begin the firing process.

As discussed in Section 3.3.3.1, the 100 micron aluminium foil burst disk is capable of withstanding pressures of up to 190 bar ± 5 bar without bursting, providing a stable barrier at pressures below this limit. Aluminium is also capable of carrying an electrical current. Therefore, provided it is possible to fuse the 100 micron foil, it is an ideal candidate for use as an electronic burst disk (EBD).

3.4.1 Fusing Bench Testing

The first step in determining if the 100 micron aluminium foil would be suitable to use as an EBD was to test if it was possible to fuse it. A bench test was performed whereby a piece of 100 micron aluminium foil mounted on a nylon insulator (using double-sided adhesive tape) was connected to a 12.0 V car battery (Figure 3.13 shows the foil before and after this test). The nylon insulator that the foil was mounted to had a 2.0 mm hole drilled though it underneath where the foil was mounted. This, combined with removing material to make a thinner area over the hole, was done in an effort to determine if the foil could be fused over the aperture of the pump tube allowing the pressurised gas to expand.

Figure 3.13.C clearly shows the foil has been fused. It also shows that the hole in the nylon insulator has been exposed. This result indicated that using the 100 micron aluminium foil as an EBD was potentially a viable option and was worthy of further investigation.

3.4.2 Design Phase

The next step for the EBD was to determine how it could be used on the existing LGG. As the LGG is comprised of metal parts, a new system needed to be developed in order to mount the EBD so that it was electrically insulated from the rest of the gun. The burst disk is typically mounted in the front of the launch-tube (Figure 3.10 shows its location on the LGG); however, manufacturing a modified launch tube would be an expensive undertaking as each launch-tube is rifled, requiring specialist outside companies to perform the work. Instead the decision was taken to modify a central

breech using already available retired components and doing the modifications in-house.

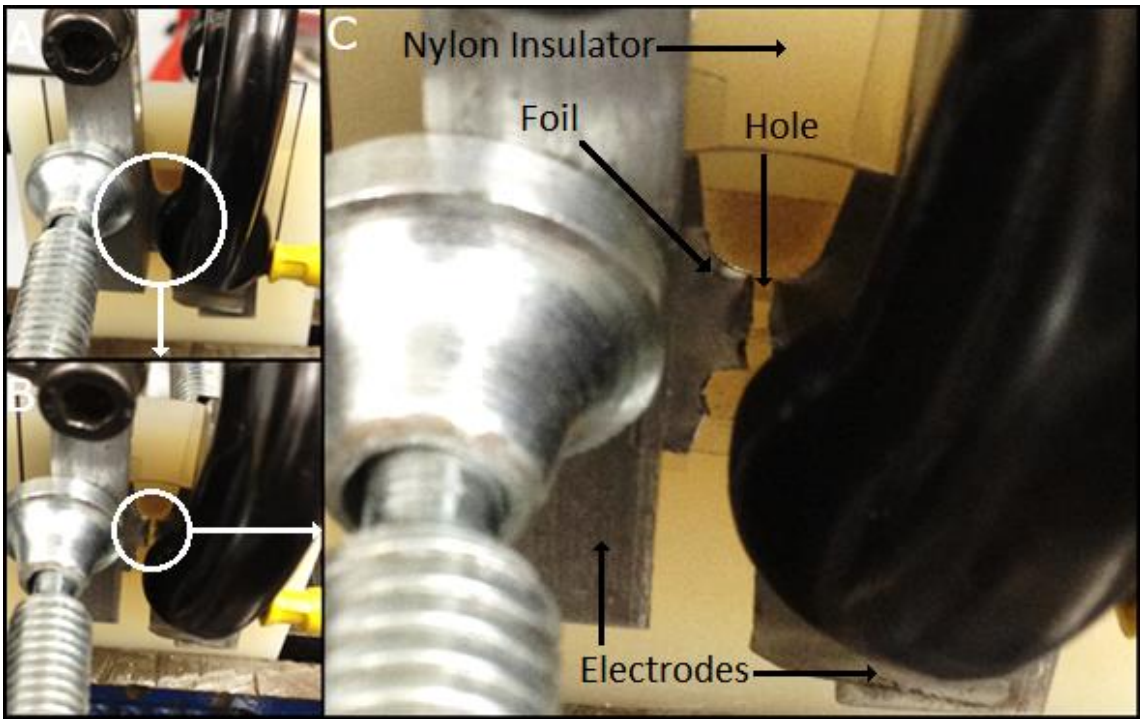


Figure 3.13: 100 micron aluminium foil fusing bench test. (A) Before the test. (B) After the test. (C) After the test – magnified.

Figure 3.14 shows the drawing for the modified Electronic Central Breech (ECB) and Figure 3.15 the drawing for a standard central breech. The launch-tube end of the central breech has been extended to allow for the accommodation of electrodes (Figure 3.16) that the EBD will be in contact with. One of these electrodes (the negative) is in direct contact with the rest of the central breech (and therefore the LGG) while the other is insulated from the gun and is held in place with an insulated bolt from the outside of the central breech that is used as the electrical contact for that electrode (the positive electrode).

The burst disk is usually in direct contact with the launch tube, therefore an insulator needs to be added between the EBD and the launch tube to prevent an electrical contact that would result in a short circuit. The bore of the ECB is also larger than the diameter of the sealing surface on the front of the launch tube and as such the insulator needs to be able to accommodate this. Figure 3.17 shows the drawing for this insulator, known as the burst disk support. There are four holes around the edge of the burst disk support that will allow bolts to clamp it down to the electrodes, ensuring a good electrical contact between the foil and the electrodes. The burst disk support also has a 2.0 mm central hole as standard to allow the gas to flow once the EBD has fused, (although this size could be altered to provide another means of controlling the final speed).

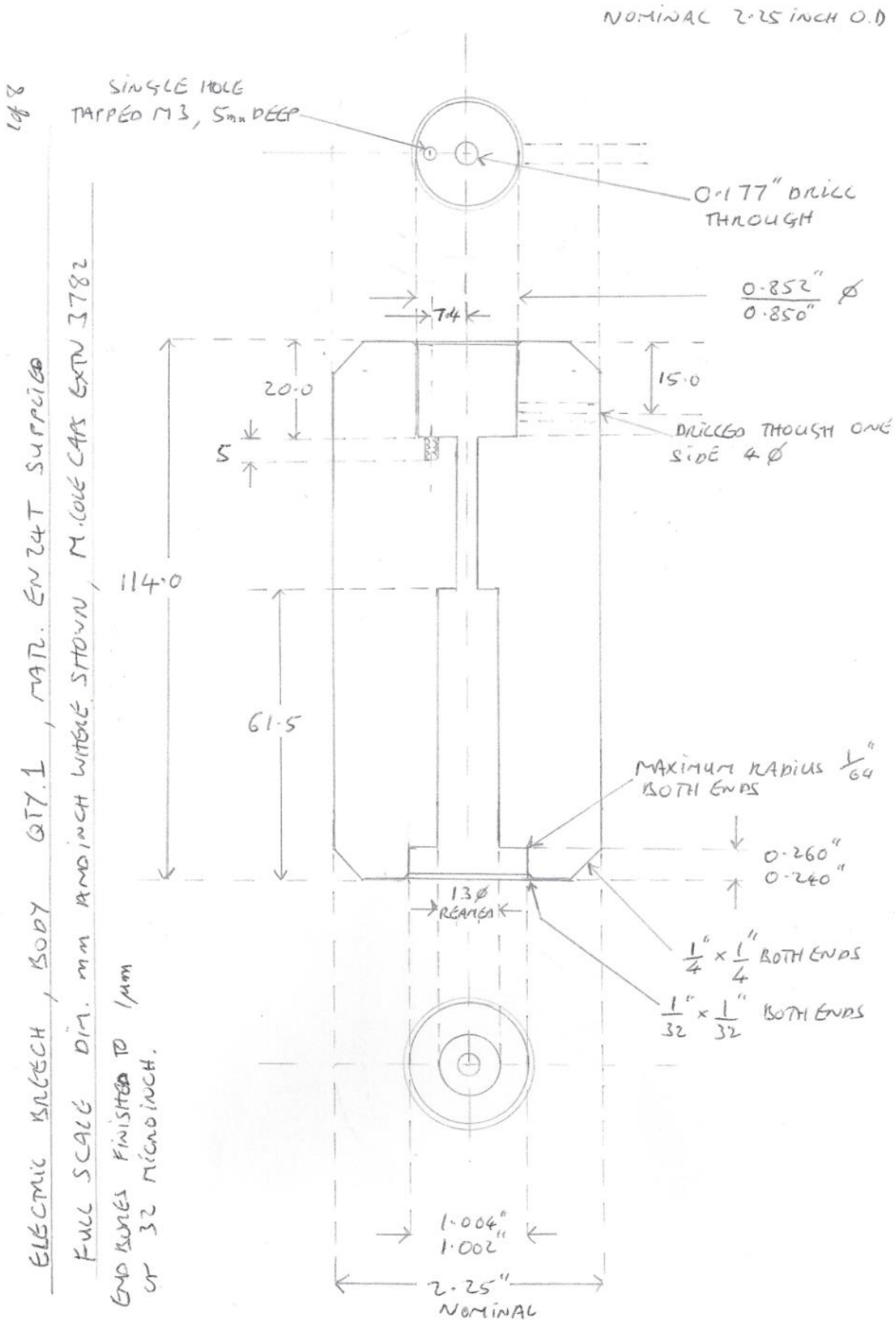


Figure 3.14: Technical drawing for the modified central breach known as the electronic central breach (ECB) to be used with the electronic burst disk (EBD) system.

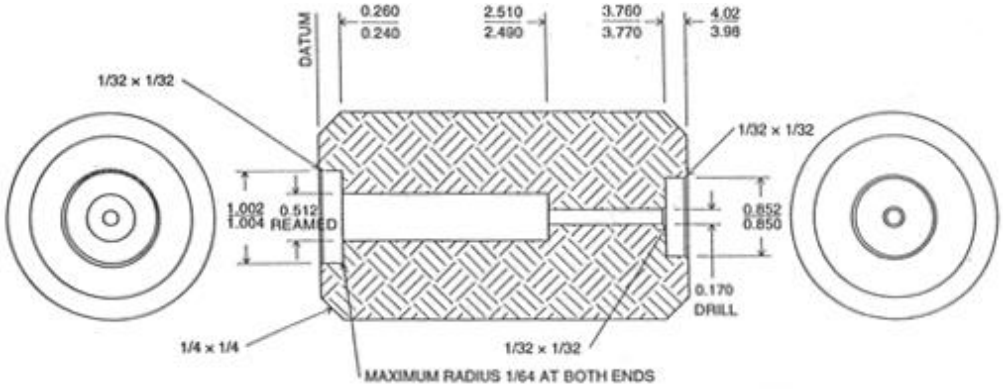


Figure 3.15: Technical drawing for a standard LGG central breach

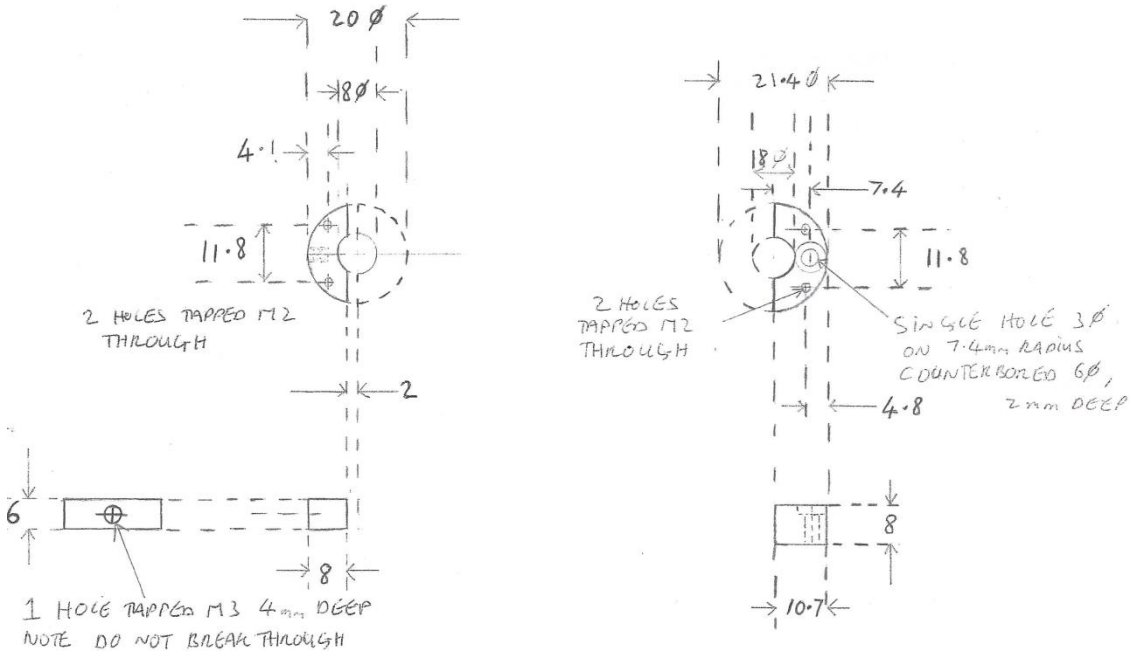


Figure 3.16: Technical drawings of the electrodes inside the electronic central breach (ECB).

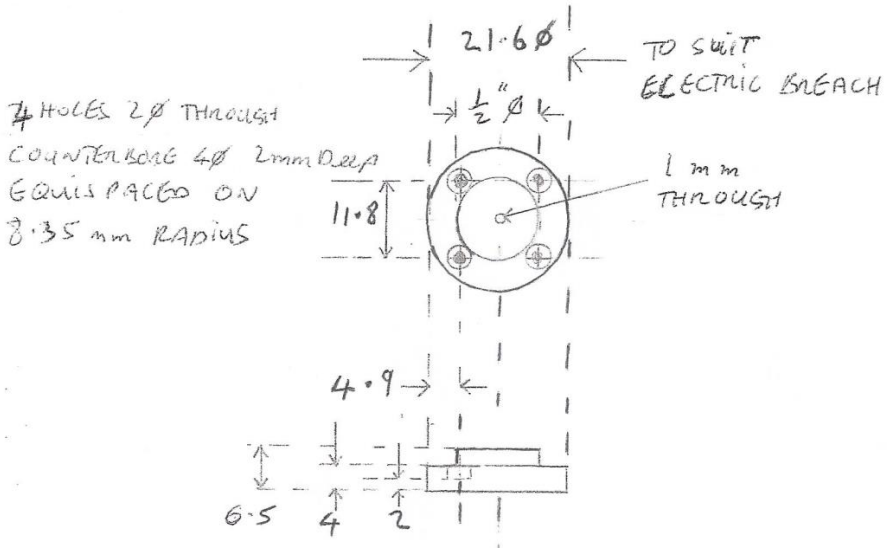


Figure 3.17: Technical drawings of the burst disk support that the electronic burst disk (EBD) is mounted to inside the electronic central breach (ECB).

3.4.3 Electronic Central Breech Bench Test

With the required components manufactured, the system could undergo a bench test. After the success of the fusing bench test, the narrowing of the central part of the 100 micron aluminium foil over the aperture was continued. As this involves making two notches in the foil to create the narrow section in the centre, the process became known as 'notching' the foil.

Figure 3.18 shows the foil after the ECB bench test. A break down the centre of the foil between the notches can clearly be seen. This result indicated that the ECB design is a viable mount for an EBD system and could move onto testing on the LGG.

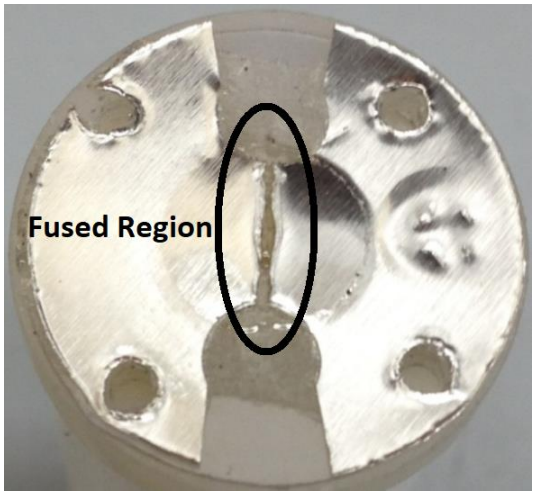


Figure 3.18: A fused 100 micron aluminium foil after a bench test inside the electronic central breach.

3.4.4 Gun Tests

Due to the need to connect the central breech to an electrical circuit, the standard collar over the central breech was no longer fit for purpose. To that end it was replaced with a set of three bolts seen in Figure 3.19.

Two test shots were conducted using this system. For these shots a solid nylon cylinder was used as the projectile and the pump tube was pressurised with 50 bar of N_2. This allowed for the speeds attained to be compared to the speeds for the same shot using the single stage method. 271 m s^{-1} was the expected speed for these test shots based on those data; however the speeds generated in these tests were slightly lower than predicted at 245 and 215 m s^{-1}. A possible explanation for this is that the fusing process takes longer than the rupturing method used in the standard single stage set up. This means it would take longer to achieve the full size of the aperture that the gas will flow through, thereby producing a reduced rate of gas expansion (and therefore reduced acceleration of the projectile) for the electronic burst disk shots. The reason for the discrepancy in speed is that the heating of the EBD during the fusing process was also sufficient to cause melting of the nylon burst disk support, which resulted in material obstructing the aperture in the burst disk support thereby reducing the gas flow and therefore the speed of the shot. Figure 3.20 shows the melting of the surface of the burst disk support after these shots.

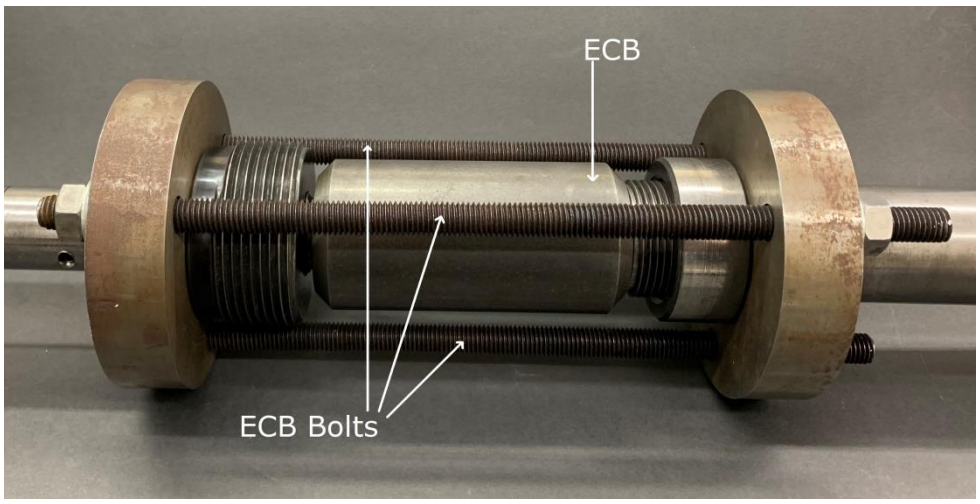


Figure 3.19: The electronic central breach (ECB) mounted in the light gas gun (LGG) being held in place with ECB bolts.

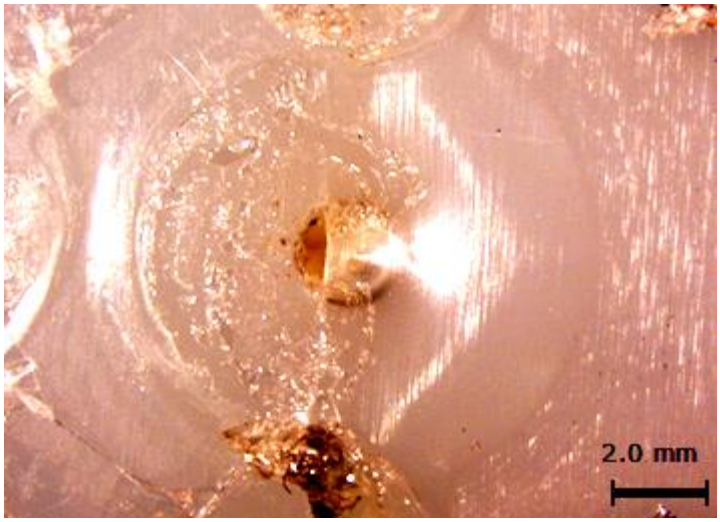


Figure 3.20: Melted burst disk support with the central hole obstructed by the molten material.

In an attempt to combat this problem, a layer of 0.25 mm thick acetate was added between the burst disk foil and the support. The addition of this layer also required a second layer of adhesive tape in order to affix it to the support (Figure 3.21 shows the layers of this new configuration).

Several test shots were conducted using this new configuration (Table 3.3). None of the shots showed melting of the burst disk support, however, only two of the shots performed as expected by fusing the burst disk and accelerating the projectile; resulting in speeds of 131 and 161 m s^{-1}. Three of the shots suffered from severely reduced speeds (49, 54 and 75 m s^{-1}) due to the burst disk failing to fuse properly. Instead the heat generated during the firing process was enough to soften the aluminium burst disk allowing the gas pressure to rupture the disk, resulting in a smaller aperture for the gas to expand through thereby reducing the speed. Another test shot fused correctly, but the aperture became clogged, restricting the gas flow and reducing the speed to 67 m s^{-1}. A seventh test shot failed entirely to fuse the burst disk. A number of other test shots were abandoned before the point of firing due to gas leaks at the point of the burst disk.

Table 3.3: The test shots for the Electronic Burst Disk (EBD) system with the addition of the 0.25 mm thick acetate backing. The 'E' in the shot numbers denotes that the shots were performed using the EBD system. The burst disk support had a central hole with a diameter of 2.0 mm for all of these shots.

Shot Number	Speed (m s^{-1})	Notes
E250317#1	131	Fused Cleanly
E140617#1	161	Fused Cleanly
E260917#1	49	Softened and Burst
E220617#2	54	Softened and Burst
E090617#1	75	Softened and Burst
E220617#1	67	Fused but Aperture Blocked
E010617#1	N/A	Failed to Fuse

For the shot that failed to fuse, the foil was inspected after the test and it was determined that the distance between the notches was too great. At 6.3 mm it was 0.8 mm larger than that of the foils used in the bench tests. It is likely that this increase in distance causes too great a reduction in electrical resistance and therefore did not allow for enough heating to fuse the burst disk.

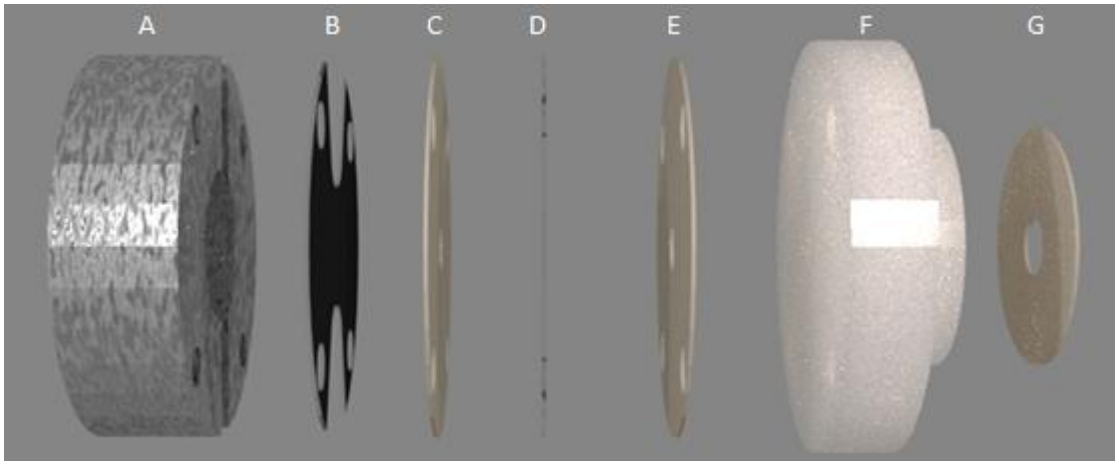


Figure 3.21: CAD drawing showing the layers involved in the electronic burst disk. From left to right: (a) Steel electrodes, (b) 100 micron thick aluminium foil, (c) adhesive tape, (d) acetate backing, (e) adhesive tape, (f) nylon holder and (g) adhesive tape.

Upon inspection of the shot that produced a reduced speed due to a blockage, it was determined that the material that was obstructing the aperture mostly consisted of glue from the adhesive tape that holds the layers together. It appears that due to the hand-made nature of the construction, and assembly of the layers, that the central holes in the layers leading to the aperture in the burst disk support were misaligned.

The shots that did fuse correctly generated speeds slower than those predicted from the single stage data (271 m s^{-1}) as well as those seen in the test shots performed without the backing layer (215 and 245 m s^{-1}). This reduction in speed may also be attributed to a misalignment of the EBD layers, albeit one less serious than that of the failed shot.

The foil, acetate and tape layers were all constructed by hand using a wadding punch for the outer diameter, and a leather punch for the smaller holes. Although the positions of these holes were carefully marked out, the final cut was still done by

lining the punch up by eye. These layers were then placed atop one another, again by hand. The errors that this process introduced appear to be the cause of some of the reliability issues faced by the EBD system.

The solution to this problem was to remove as much of the human element of the construction as possible by creating a "mass production" process. This method aimed to accurately punch the positions of the holes in all the layers, thereby ensuring a consistent distance between the notches, and improving the alignment of the layers. As such, it was decided that a set of punches were to be constructed that could be used in a press to punch out a single layer needed for the EBD system.

3.4.5 Punches

A prototype punch was constructed by CNC (computer numerical control) milling a piece of brass (Figure 3.22) to include pillars for punching the four mounting screw holes and two pillars that would ensure the correct position of the notching of the foil. The holes around the perimeter of the cutting disk allow for the foil to be more easily removed from the punch after pressing. This punch was used in conjunction with a "Sizzix Big Shot" die cutting machine (Figure 3.23) to successfully manufacture EBD foils with accurate positioning of the holes.

The brass punch was also used to test the possibility of punching adhesive tape and acetate backing layers: it was discovered that this prototype punch was capable of punching all of the necessary materials: aluminium foil, adhesive tape, and the acetate backing.

Following the success of the prototype punch, a set of punches were designed for each of the required layers: foil, adhesive tape and acetate backing. These new punches were more rigid than the prototype punch as they are manufactured from stainless steel instead of brass (Figure 3.24). These punches were also not CNC milled but were constructed from turned stainless steel with removable pillars that can be replaced.

With the completion of the punches, the mass manufacture of components could be undertaken. The punching of each layer was tested with varying thicknesses of packing material before deciding on a set thickness for each layer.



Figure 3.22: The prototype foil punch made from brass and constructed using a CNC milling machine.



Figure 3.23: The prototype punch being used to punch a 100 micron thick aluminium foil electronic burst disk on a "Sizzex Big Shot" die cutting machine.

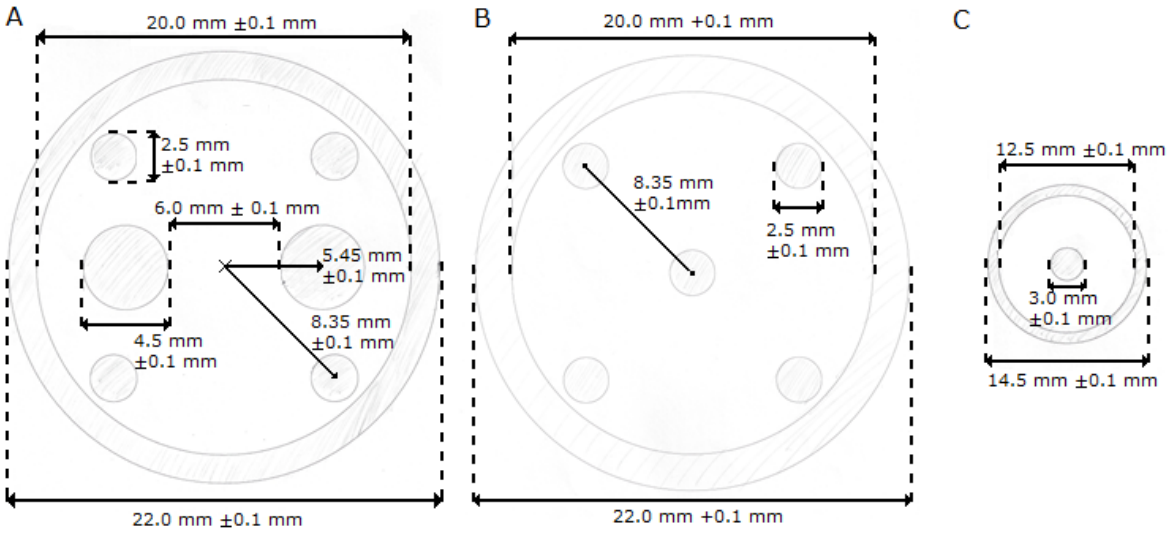


Figure 3.24: Technical drawings for the punches used to manufacture the electronic burst disk (EBD) layers. (A) Foil punch. (B) Tape/acetate punch. (C) Small tape punch.

3.4.6 Firing Control System

The firing control system is used to fire the LGG when using the Electronic Burst Disk system (Figure 3.28). As its primary function, the firing control system uses a relay switch to close the circuit that allows current to flow through the burst disk from a 12.0 V car battery, before opening the circuit again after five seconds. As secondary functions, the system provides the facility to allow monitoring of various parts of the system (the battery voltage, foil voltage and trigger output) via BNC outputs. It also incorporates a variety of audio/visual indicators to allow users to clearly see what state the system is in, and if it is safe to proceed with the current task.

3.4.7 Firing Procedure

NOTE: Sections 3.4.7 and 3.4.7.7 detail a step-by-step procedure on how to prepare for and fire an Electronic Burst Disk shot as written by the author. It is included here to act as an archived reference for future developers/users of the EBD system.

The addition of the EBD system resulted in alteration to the firing and preparation procedures of the LGG. As such what follows is a guide of how to set up and fire the electronic burst disk system. A number of the steps involved in firing the EBD system are the same as for a standard LGG shot. Only the steps relating specifically to the EBD system will be fully explained here with the overlapping tasks only being mentioned. Full details of these steps can be found in Hibbert 2017, an internal document of the University of Kent's CAPS group [169] which is available on request[1].

3.4.7.1 Initial Preparation

In addition to the standard LGG facility apparatus (Hibbert 2017) the following items are also needed to perform a EBD shot:

- The electronic central breech
- A bust disk support
- The central breech bolts
- The Sizzex Big Shot press
- The stainless steel punches (the foil cutter, the large tape/acetate cutter and the small tape seal cutter)
- The EBD assembly guide
- The foil impression rod and guide
- A 12.0 V car battery
- The EBD firing control box
- A power supply capable of outputting 17.0 V at a current of 0.5 A
- Various materials for the manufacture of the EBD layers:
    - 1x 32x80 mm rectangle of double-sided adhesive sheet ("large tape")
    - 1x 20x80 mm rectangle of double-sided adhesive sheet ("small tape")
    - 1x 30x30 mm squares of 100 micron thick Al foil
    - 3x 20x80 mm rectangles of 0.25mm acetate
    - 1x 30x30x1 mm 6082 Al alloy backing plate
    - 5x 20x80 mm rectangles of 0.75mm thick polystyrene

Begin by performing the standard safety checks performed before any LGG shot and by making ready the detection systems used for determining the speed of the shot. The projectile, piston, and target should also be prepared at this time. The piston should be placed in the pump tube and sealed in place using the powder chamber and firing pin mechanism (Figure 3.25). The target should be placed in the target chamber and the chamber sealed [169].

Once this is complete, remove the central breech collar from the gun and replace it with the CB bolts (Figure 3.26) ensuring that the launch tube is in the single stage position with the correct marking aligned with the front face of the launch tube clamp (Figure 3.27). The projectile can now be placed in the launch tube.

[1]To request access to this document please email mcp2@star.kent.ac.uk.

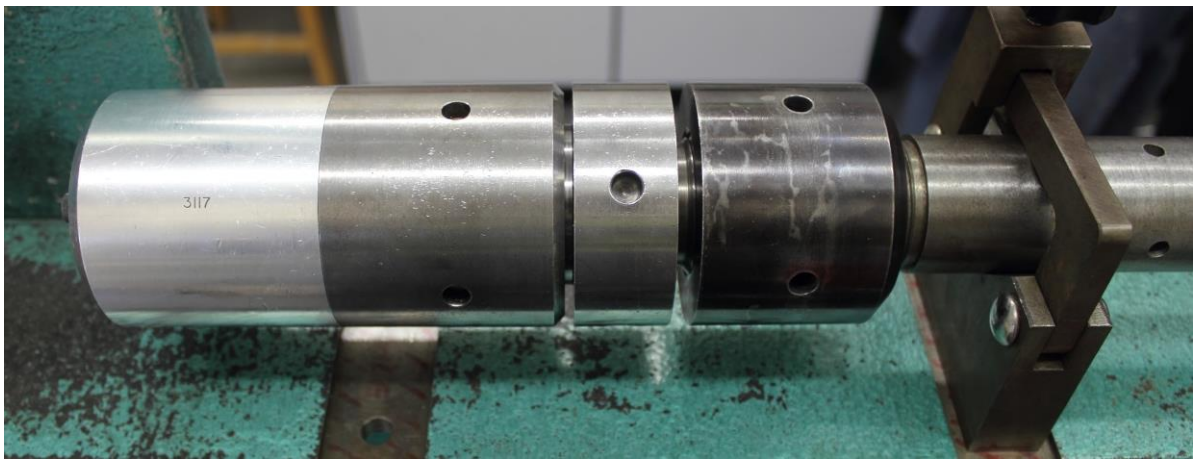


Figure 3.25: The powder chamber and firing pin mechanism in place on the LGG.

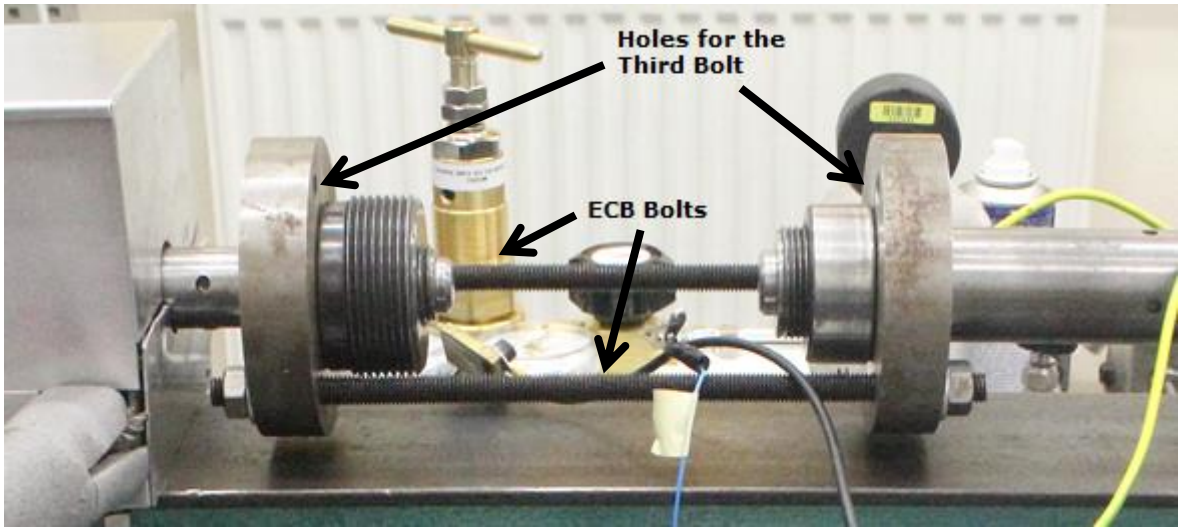


Figure 3.26: Two of the three electronic central breach (ECB) bolts in place on the LGG for an electronic burst disk (EBD) shot.

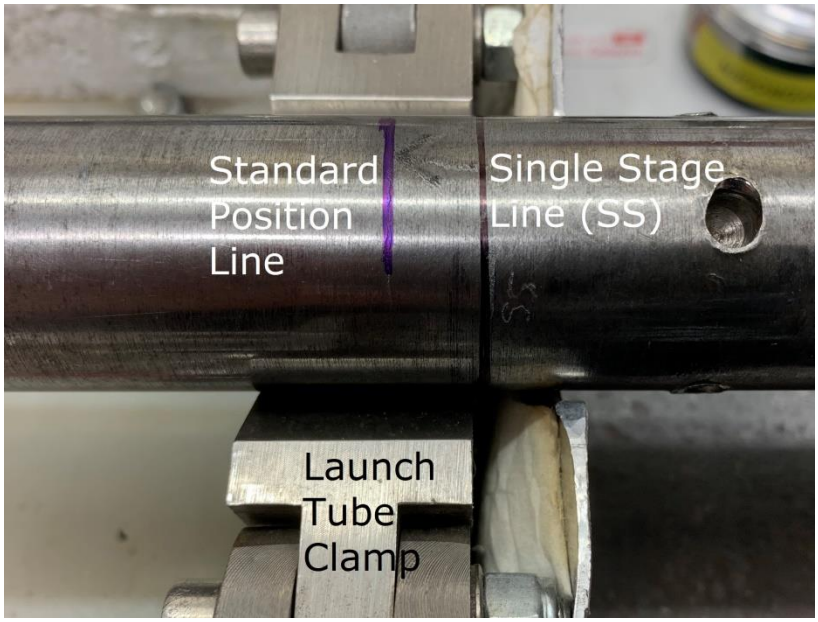


Figure 3.27: The launch tube in the single stage position. The single stage marking is aligned with the front face of the launch tube clamp.

The 12.0 V battery, the EBD firing control box and the 17.0 V power supply should be positioned near the LGG. The power supply and the positive terminal of the battery should be connected to the firing control box (Figure 3.28). The firing control box also has three fused probes that are used to measure the voltage of the system during operation. These are clearly labelled, and those to measure the battery voltage should be connected now (red for the positive terminal, black for the negative terminal). The third probe (blue) is intended for the ECB once it is prepared and in position. The three BNC outputs (battery voltage, foil voltage and trigger output) should also be connected to an oscilloscope. Before continuing, check that the battery is charged by measuring its voltage (12.7 V nominal), and also ensure that the safety fuse is intact.

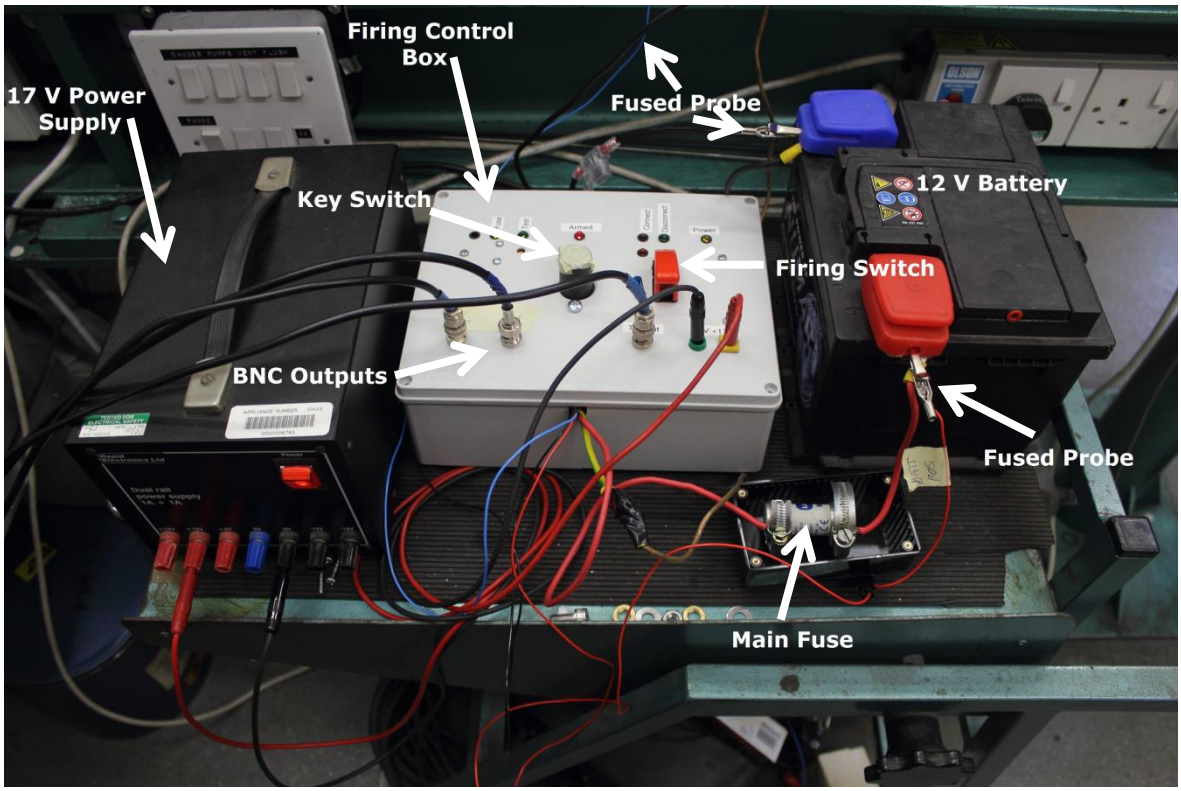


Figure 3.28: The firing control system of the electronic burst disk system.

3.4.7.2 EBD Manufacture

The layers of the EBD can now be manufactured. As shown in Figure 3.21, there are five layers mounted onto the burst disk support that make up the EBD: the foil burst disk, two large tape seals, an acetate backing and a small tape seal.

3.4.7.2a Foil Burst Disk

Place the 30x30 mm square of 1 mm thick 60852 aluminium alloy plate on the tensometer support and rest the 30x30 mm square of 100 micron thick aluminium foil on top of the plate. Place the 8.0 mm diameter steel impression rod on top of the foil using the brass guide to position it correctly (Figure 3.29).

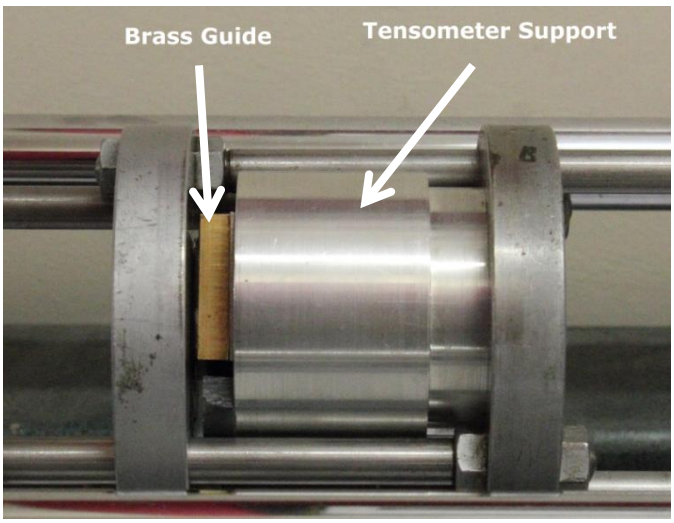


Figure 3.29: A foil being pressed in the tensometer is held in place with the tensometer support while the brass guide aligns the position of the 8.0 mm impression rod.

Place this arrangement into the tensometer and apply 7.00 -7.05 kN of pressure before removing the foil. Check the foil for an even impression that is central on the foil, if the impression is un-even or not central, discard the foil and repeat the process. Figure 3.30 shows examples of a correctly impressed foil and a reject foil. The impression on the rejected foil is not central, and it also wider at one end while the correct foil has an even line down the centre.

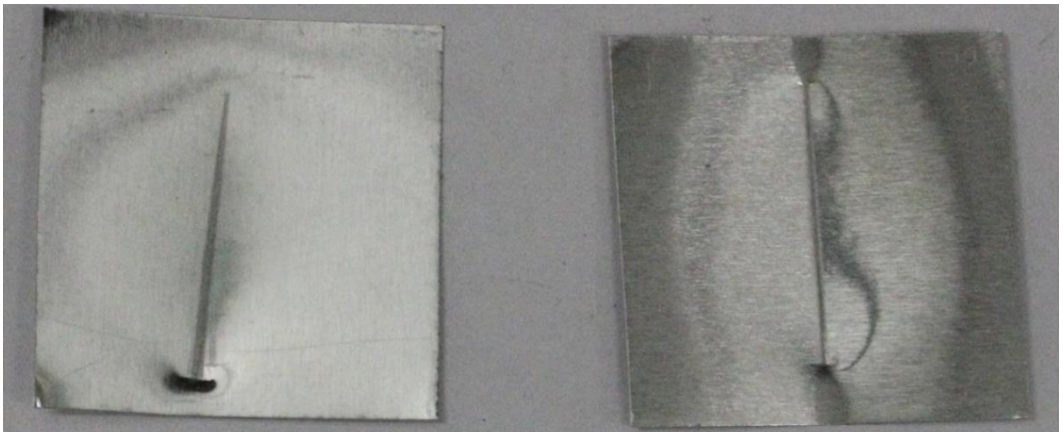


Figure 3.30: Examples of a rejected (left) and a correctly (right) impressed foil.

Set the foil cutter into the punch mount and place two 30x30 mm pieces of paper on top of the cutter. Take the foil and place it on top of the paper with the impression facing downwards, taking care to align the impression across the two large pins on the cutter. Tape the foil into place using masking tape (Figure 3.31).

Create a stack of three 32x80 mm 0.75 mm thick polystyrene sheets. Place this stack on top of the foil, as demonstrated in Figure 3.32, and run the cutter through the "Sizzex Big Shot" press by turning the handle with one hand and supporting the polystyrene stack with the other (Figure 3.33).

Having pressed the foil, remove it from the cutter and use a scalpel blade to complete the notches by cutting from the perimeter of the foil to the edges of the larger holes punched in the foil (Figure 3.34). Occasionally, the foil will not be completely punched

out by this process. If this is the case, use the impressions made by the cutter to align a leather belt punch (for the smaller holes) or a wadding punch (for the outer diameter) in order to finish the foil off by hand.

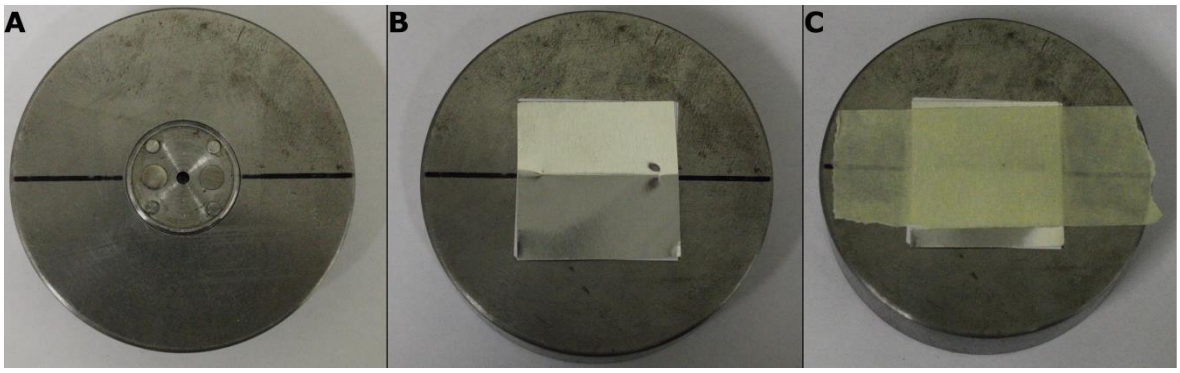


Figure 3.31: (A) The foil punch in the platen correctly aligned with the large pins. (B) An impressed foil placed onto the punch with the impression aligned across the large pins. (C) A correctly aligned foil secured in place using tape.

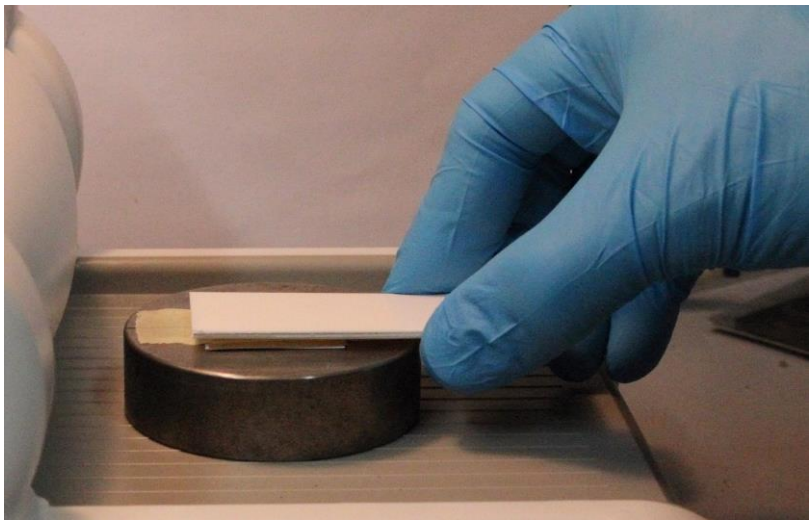


Figure 3.32: A stack of three 0.75 mm thick polystyrene sheets being held above a punch ready of pressing.

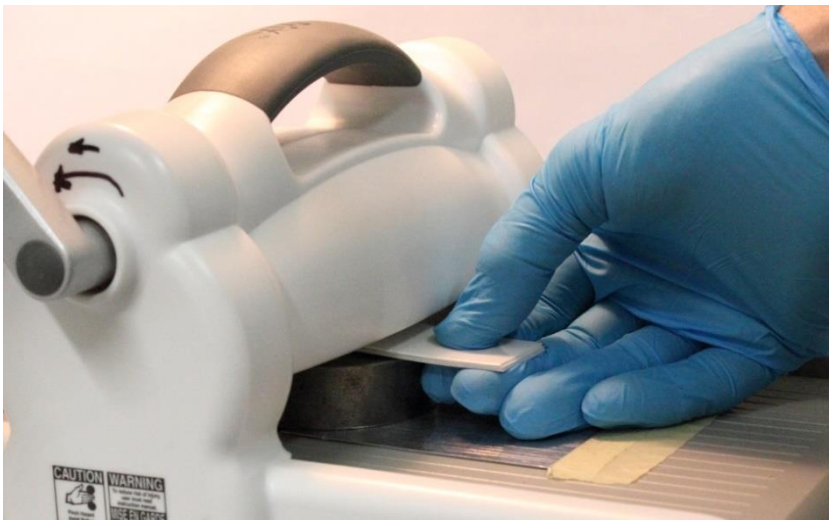


Figure 3.33: The stack of packing material being held in place while the punch being run through the Big Shot press.



Figure 3.34: An electronic burst disk foil layer with the notches cut (scale divisions are 0.5 mm).

3.4.7.2b Large Tape Seal and Acetate Backing

The large tape seals and the acetate backing are the same shape and use the same cutter. For a complete EBD set, two large tape seals and one acetate backing needs to be manufactured.

After placing the large tape/acetate cutter into the punch mount, create a stack of material consisting of three 32x80 mm 0.75 mm thick polystyrene sheets and either a 32x80 mm sheet of double-sided adhesive tape or 0.25 mm thick acetate. Place this stack on top of the cutter, as demonstrated in Figure 3.32 above, and run the punch through the "Sizzex Big Shot" press by turning the handle with one hand and supporting the stack with the other (Figure 3.33).

Remove the tape/acetate layer from the cutter and finish any incomplete holes by hand using a leather belt punch. If the outer diameter needs completing, use a wadding punch.

For the second large tape seal, simply rotate the stack of material and run it through the press again in order to use the other end of the sheet of tape.

3.4.7.2c Small Tape Seal

Set the small tape cutter into the punch mount and create a stack of material consisting of two 20x80 mm 0.75 mm thick polystyrene sheets, two 20x80 mm 0.25 mm thick acetate sheets and 20x80 mm sheet of double-sided adhesive tape. Place this stack on top of the cutter, as demonstrated in Figure 3.32 above, and run the punch through the "Sizzex Big Shot" press by turning the handle with one hand and supporting the stack with the other (Figure 3.33).

Remove the tape layer from the cutter and finish any incomplete holes by hand using a leather belt punch. If the outer diameter needs completing use a wadding punch.

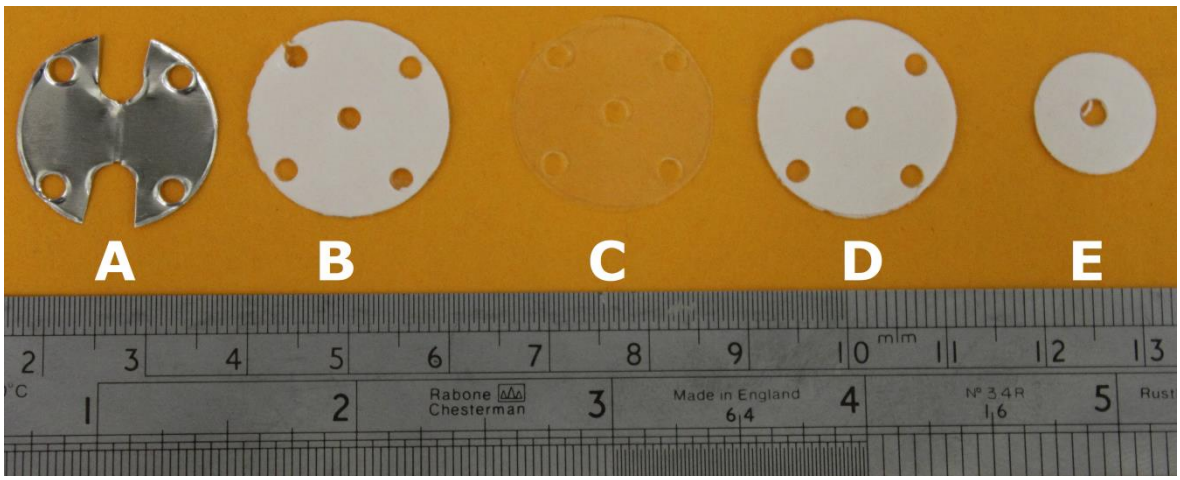


Figure 3.35: The completed layers of the electronic burst disk (EBD) system. (A) 100 micron thick Al foil. (B) Large double-sided adhesive tape. (C) 0.25 mm thick acetate backing. (D) Large double-sided adhesive tape. (E) Small double-sided adhesive tape.

3.4.7.3 ECB Assembly

With the individual layers manufactured, the EBD can now be assembled. Place the nylon burst disk support onto the assembly guide (Figure 3.36.B). Place a large double-sided tape onto the burst disk support ensuring that the tape does not cover any of the central hole (Figure 3.36.C). Next, place the acetate backing onto the burst disk support using the previously placed tape to fasten it in place, again ensuring that the central hole of the support is not obstructed. Place a second large double-sided tape onto the burst disk support sealing it to the acetate backing.

The final layer is the foil burst disk itself. The distance along the impression between the notches needs to be measured to ensure that it is between 5.5 and 6.0 mm. If the distance is larger than 6.0 mm, a scalpel can be used to trim the material until the distance is within the limits. If the distance is smaller than 5.5 mm then the foil should be rejected and disposed of.

Before mounting the foil on the rest of the system it should first be folded along the impression by 90° (Figure 3.37). This is done to further weaken that part of the burst disk and further increase the likelihood of fusing over the aperture of the burst disk support. With the foil now fully prepared, it can be placed onto the burst disk support taking care to ensure that the weakened section is directly over the aperture of the burst disk support (Figure 3.36.D).

Use the smoothing tool (Figure 3.38) to smooth the foil down on the support to make certain a good seal has been achieved. After this has been done, check that no foil is protruding beyond the edge of the burst disk support, as this may cause an electrical short in the system preventing fusing of the burst disk. Trim any excess foil with a scalpel. Finally, place the small double-sided tape on the reverse side of the burst disk support, checking that the central hole is aligned with the aperture.

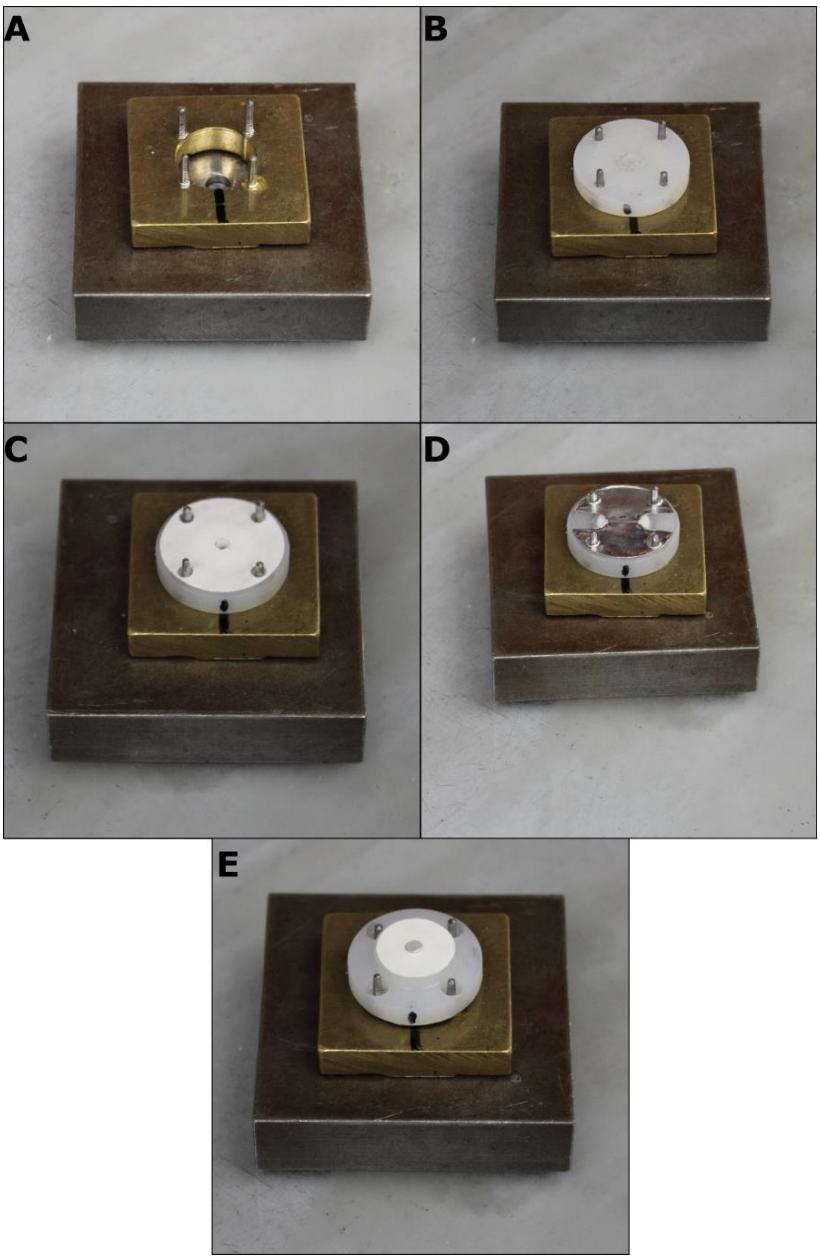


Figure 3.36: The electronic burst disk at various stages of assembly. (A) The assembly guide. (B) The burst disk support on the assembly guide. (C) A tape layer on the bust disk support. (D) The foil mounted to the burst disk support. (E) The small tape mounted to the rear of the burst disk support.

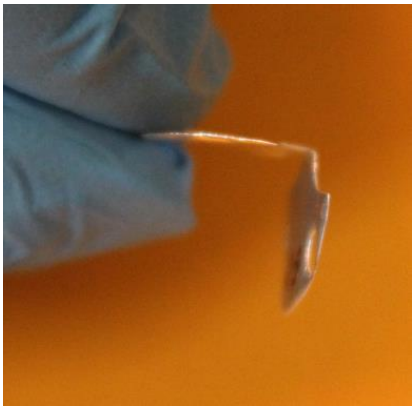


Figure 3.37: The foil layer of the electronic burst disk folded 90° along the impression.

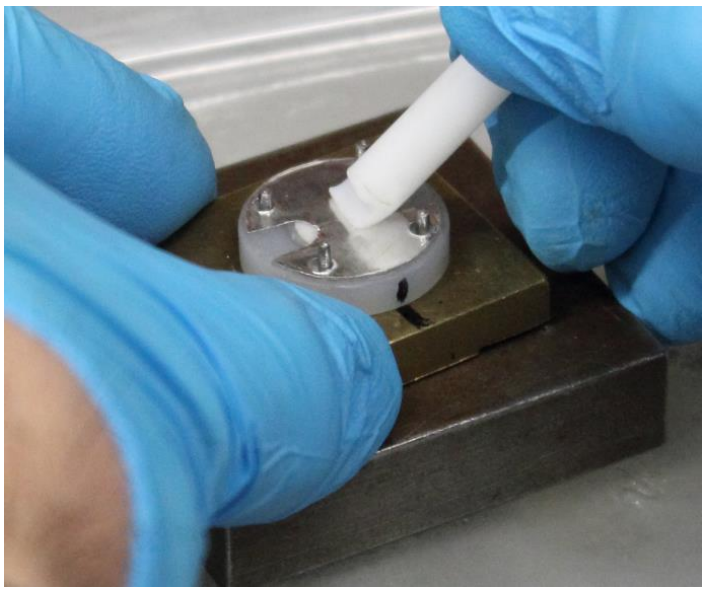


Figure 3.38: The smoothing tool being used on the surface of the foil attached to the burst disk support.

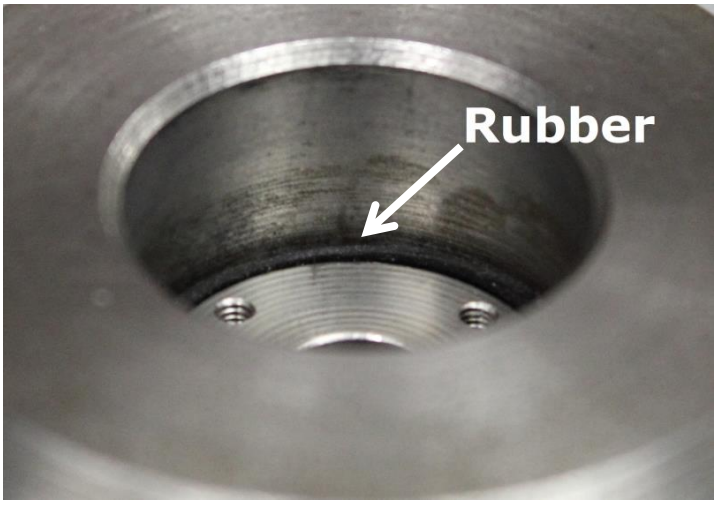


Figure 3.39: The rubber insulator protruding above the electrode inside the electronic central breach (ECB).

Before placing the EBD into the ECB, perform a continuity test on the ECB. The negative electrode inside the ECB should show an electrical connection to the exterior of the ECB while the positive electrode should be insulated from the rest of the ECB and should only show an electrical connection to the bolt protruding from the ECB. If this is not the case, then the electrodes should be removed and cleaned before being replaced, ensuring that the insulation is correctly seated around the positive electrode. The rubber behind the positive electrode needs to be trimmed to the height of the electrode if it is protruding above it (Figure 3.39).

The 1.0 mm thick, torus shaped rubber spacer (Figure 3.40.A) with an outer diameter of 8.0 mm and an inner diameter of 4.0 mm should be placed in the ECB between the electrodes. The nylon spacer (with an outer diameter of 7.9 mm, an inner diameter of 2.5 mm, and a height of 7.1 mm) should be placed on top of that (Figure 3.40.B).

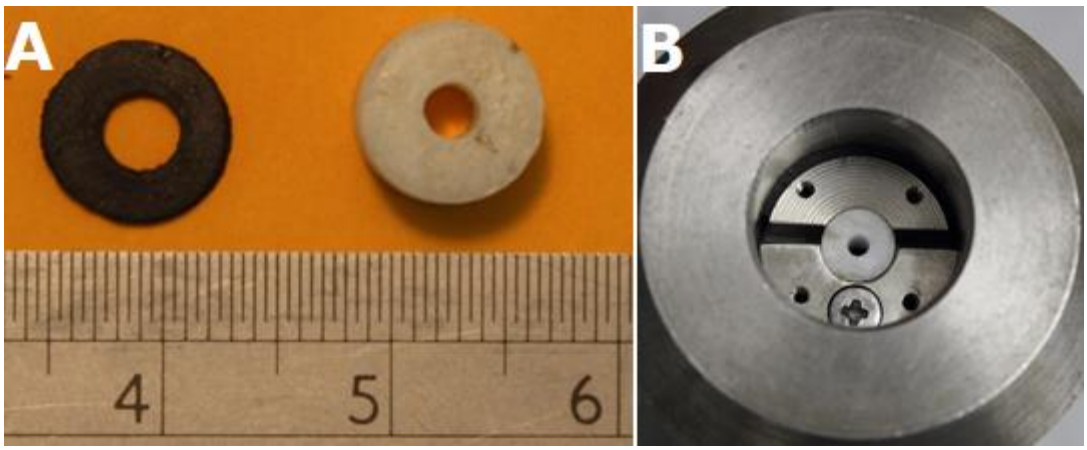


Figure 3.40: (A) The rubber spacer (left) and the nylon spacer. (B) The spacers mounted in the ECB. The nylon spacer is visible between the electrodes.

Place the EBD into the ECB with the foil face down. Ensure that the foil is in the correct orientation across the electrodes by aligning the markers on the ECB and the burst disk support (Figure 3.41). Use the four small bolts to secure the EBD into the ECB taking care not to overtighten them. Place the nylon ring on the back side of the burst disk support to cover the heads of the bolts.

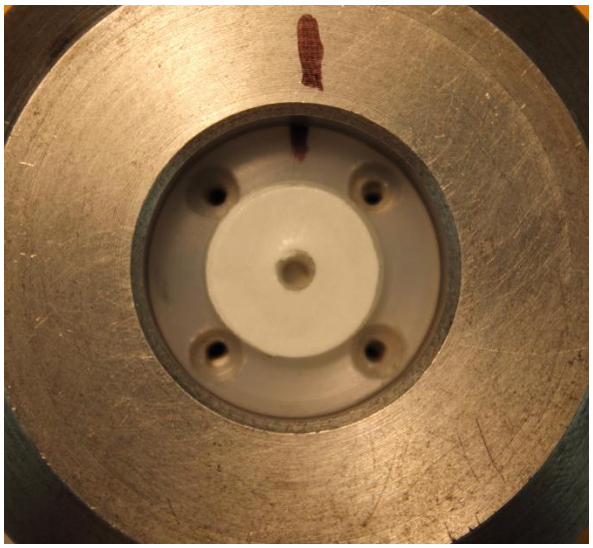


Figure 3.41: The fully assembled burst disk support inside the ECB with the orientation markers aligned.

With the ECB fully assembled, perform another continuity check to ensure that the foil is making good contact across the electrodes. The protruding bolt should now show an electrical connection to the exterior of the ECB.

Place the ECB on the LGG and secure it in place using the central breach bolts. The ECB can now be connected to the firing control box with the connection to the negative terminal of the battery clamped to the exterior of the ECB, and the rod that protrudes from the ECB (which is connected to the positive electrode) attached to the labelled wire coming from the firing control box. The third probe cable (blue) can also be connected to this rod (Figure 3.42). With the firing circuit now fully assembled, perform a continuity check throughout the system to ensure that the foil is still intact and the safety fuse is still operational.

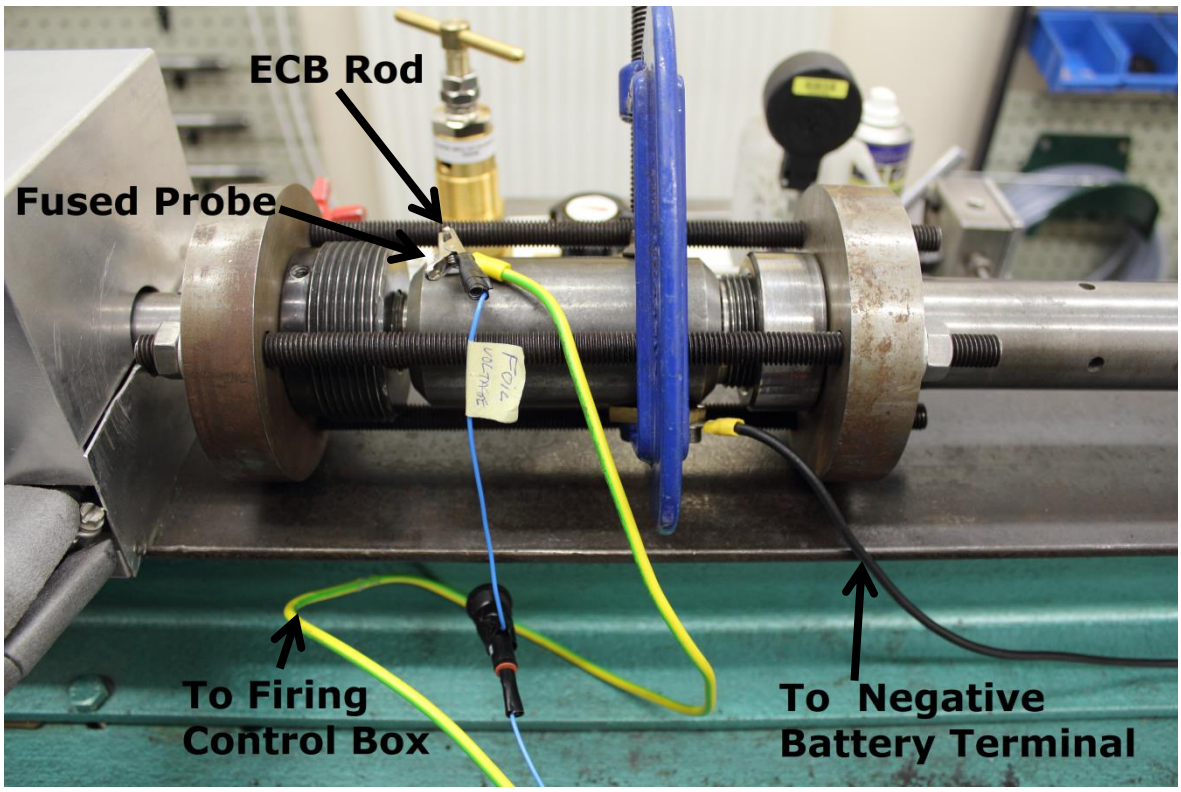


Figure 3.42: The electronic central breach (ECB) mounted on the Light Gas Gun and connected up ready for firing.

3.4.7.4 EBD Monitoring Systems

The firing control box has three BNC outputs: battery voltage, foil voltage and trigger output. During the shot, these outputs should be monitored using an oscilloscope (as well as the other standard outputs that are monitored during all shots)

Depending on the individual shot, specific settings for each output will vary, but as a general guideline the following settings are recommended for each output:

- Blast Tank Exit Aperture: 5 ms per division, 100 mV per division, vertical offset of 0 divisions
- Laser 1: 5 ms per division, 100 mV per division, vertical offset of -1 division
- Laser 2: 5 ms per division, 100 mV per division, vertical offset of -1 division
- Muzzle Detector: 5 ms per division, 500 mV per division, vertical offset of -3 divisions
- Battery Voltage: 500 ms per division, 2 V per division, vertical offset of -3 divisions
- Foil Voltage: 500 ms per division, 2 V per division, vertical offset of -3 divisions
- Trigger Out: 500 ms per division, 5 V per division, vertical offset of -3 divisions

As stated, these values are initial guidelines only and should be refined based on the specific requirements of the shot being conducted.

3.4.7.5 Pressurising the Gun

With the gun fully assembled, the range can now be evacuated. To do this, check that the target chamber is sealed and ensure that the power supply for the electronic valves and the gauges themselves are switched on. Turn on the pumps at the wall and close the air intake valve on the pump under the gun. Now turn on the switches

labelled ‘gauges’ and ‘pump’ on the control panel. Open the manual vacuum valve above the muzzle detector and close the air intake just below that valve. While the range is being evacuated, gas for the pump tube should be retrieved from the correct cylinder in the gas store.

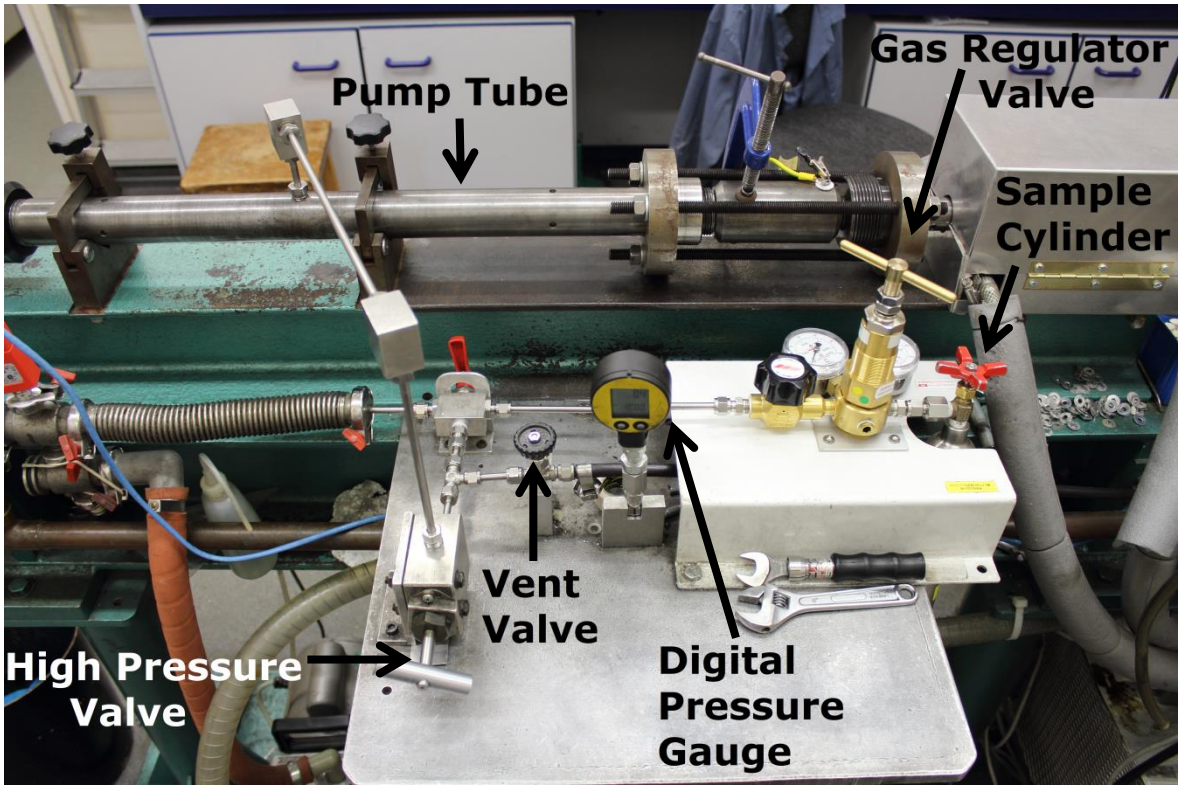


Figure 3.43: The gas filling system of the Light Gas Gun.

Once the chamber vacuum reaches 0.5 mbar the pump tube can be pressurised. Begin by sealing the vent valve and turning on the digital pressure gauge (Figure 3.43). Confirm the desired pressure by referring to the firing sheet. Slowly increase the pressure in the pump tube with the gas regulator valve until the digital gauge reads ~2.0 bar below the desired pressure. Quickly close the high pressure valve before opening it again by one half turn to allow the pressure to slowly increase to the desired pressure. At this point, the regulator should only be used if the pressure ceases to rise. Once the desired pressure has been attained, close the high pressure and sample cylinder valves. Also ensure that the left pressure gauge is on channel 2. The digital gauge should be monitored throughout this process in case the burst disk fails prematurely so that the shot pressure can be recorded.

3.4.7.6 Final Checks and Firing

It is at this stage that final checks should be performed before firing. The test button on the firing control panel should be used to check that the firing circuit correctly cycles. When the button is pressed, the “disconnect” LED indicator should go out and the “connect” LED indicator should illuminate; after five seconds the “connect” LED should go out and the “disconnect” LED should illuminate once again.

With the checks complete, personnel in the room should don goggles. The pressure in the target chamber should be recorded on the firing sheet and the evacuation valves sealed. Next, the pressure in the pump tube should be checked and topped up as needed before the value is recorded on the firing sheet.

The system should be energised by turning the key in the key-switch and anyone present should be alerted that the system is now live by announcing the word 'energised'. Check that the oscilloscopes are in "single mode" before loudly counting down from three. When zero is reached, press the firing button. The "connect" LED should light for five seconds before switching back to the "disconnect" LED. Once the "disconnect" LED has re-lit, the key should be removed from the key-switch in order to make the system safe.

3.4.7.7 After the Shot

At this point the burst disk should have fused successfully firing the gun with the oscilloscopes showing traces to confirm this. The gun can now be made safe and the ECB disassembled to allow inspection of the burst disk.

In order to make the gun safe, begin by opening the vent valve followed by the high pressure valve to release any gas still in the pump tube. Activate the 'vent' switch on the control panel and open the air intake valve above the muzzle detector. It is now safe to remove goggles.

To remove the ECB from the gun, disconnect it from the firing circuit and undo the central breach bolts. The gun can now be disassembled and cleaned according to the standard procedure.

Disassemble the ECB by removing the nylon ring and undoing the bolts that hold the burst disk support in place. Extract the support from the ECB and inspect the foil. If the shot was successful, there should be a fused section down the centre of the foil that exposes the aperture of the support (see Figure 3.44 for an example). Use the digital microscope to measure the size of the gap in the foil across the aperture and record this value on the firing sheet.

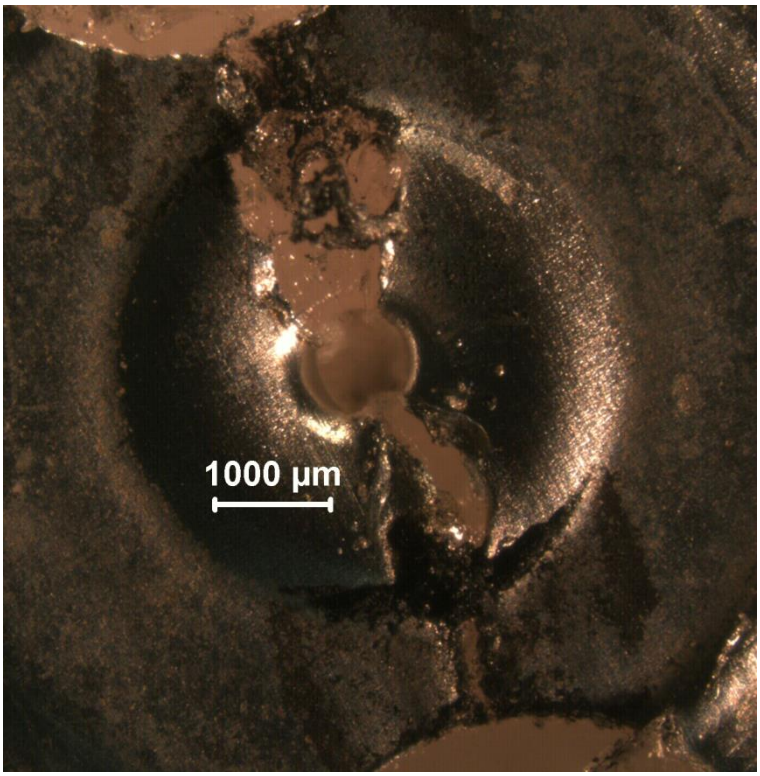


Figure 3.44: Example of a burst disk having been successfully fused to expose the aperture on the support.

If the shot was unsuccessful, the foil may have failed to fuse, or the aperture may have become obstructed with debris. Identify the cause of the failure and record this on the firing sheet.

In some cases the gun fires but the speed of the projectile is much lower than anticipated. Usually this is the result of the foil fusing, but the gas not being able to expand as expected, again due to obstruction of the aperture (albeit less extreme then in the case of a misfire). If this is the case record it on the firing sheet.

In all electronic burst disk shots, the burst disk should be photographed after the shot and the photo's location added to the firing sheet.

3.4.8 Current Status

With the addition of the punches and the development of a standardised construction and firing procedure, the manufacture of the EBD layers has become much more consistent. Gas leaks past the burst disk have become less common, making the set-up process faster and more reliable, and the fusing reliability of the aluminium burst disk is now consistent. However, the success rate of shots remains very low (one partial success in five subsequent test shots). Upon disassembly of the ECB, it was determined that the failure mode for these shots remains the blocking of the aperture in the EBD support structure. However, the material blocking the aperture is no longer the adhesive tape, but instead is made up of molten material from the support structure itself.

It appears that now that the fusing is reliable, the heat required to fuse the 100 micron aluminium foil is also great enough to cause melting of the support structure, even with the addition of the acetate layer to protect it. It has now been seen that the 50 micron thick foil is too weak/fragile to be used as the burst disk, but the 100 micron thick foil is too thick for use as a fusible material. As such, the next step would be to strike a compromise between the two and use 80 micron thick aluminium foil.

Testing of the 80 micron thick foil has shown that, unlike the 50 micron thick foil, it can withstand the pressures used within the pump tube as it has been found to have a failure point of 120 bar ± 5 bar. It is hoped that the reduction in thickness will be sufficient to reduce to amount of heat generated when fusing to prevent the melting of the burst disk support but further, extensive, testing is now required to complete this system.

3.5 Shot ID Numbers

Shots on the light gas gun have traditionally always been identified using a shot ID number. An example Shot ID number could be G150316#2; where the 'G' identifies the shot was performed using the two-stage light gas gun, the next six digits correspond to the date of the shot (in this case the 15th of March 2016), and the final number represents the shot number of that day (in this case the second shot of the day).

With the addition of the single stage and electronic burst disk techniques, alterations needed to be made to the way that shots on the light gas gun are identified. As such, shot numbers beginning with 'S' (for single stage shots) and 'E' (for electronic burst disk shots) were incorporated into the identification method.

Shots using all three of these light gas gun techniques were performed in the experiments discussed in Chapter 5 and Chapter 6, therefore, shot numbers beginning with 'G', 'S', and 'E' will be presented.

3.6 Summary

This chapter has described the capabilities and operating principles of both the Raman spectrometer and the light gas gun at the University of Kent. In addition, the desire to reduce the minimum speed of the light gas gun and the attempts to do so has been explored.

Achieving slower speeds using a two-stage gun method have been shown to be infeasible, while utilising the single stage method has been shown to be successful but with limited speed selection.

The concept of an electronic burst disk has been described and its development process explained. It has also been shown to be a useful technique with the ability to attain a range of speeds; however the systems reliability still requires some attention.

Chapter 4 - Raman Thermometry

4.1 Introduction

Section 2.2.4 discussed how Raman spectroscopy can be a destructive technique as a Raman spectrometer's high powered laser, directed onto a small area, can cause 'burning' of a sample. With this in mind, it is safe to assume that there is some degree of laser heating that occurs while acquiring a Raman spectrum. What is unknown, however, is how much this laser heating alters the Raman spectrum that is produced. The most extreme alteration is that of the previously mentioned 'burning' and Figure 2.10 shows a vivid image of a sample having been burnt by the laser. Another obvious case can be seen in Figure 4.1 where we can see that the sample of olivine powder has been burnt. This is a result of the olivine undergoing thermal decomposition. The change in the spectra of this sample due to the burning is discussed later in this chapter (Figure 4.19).

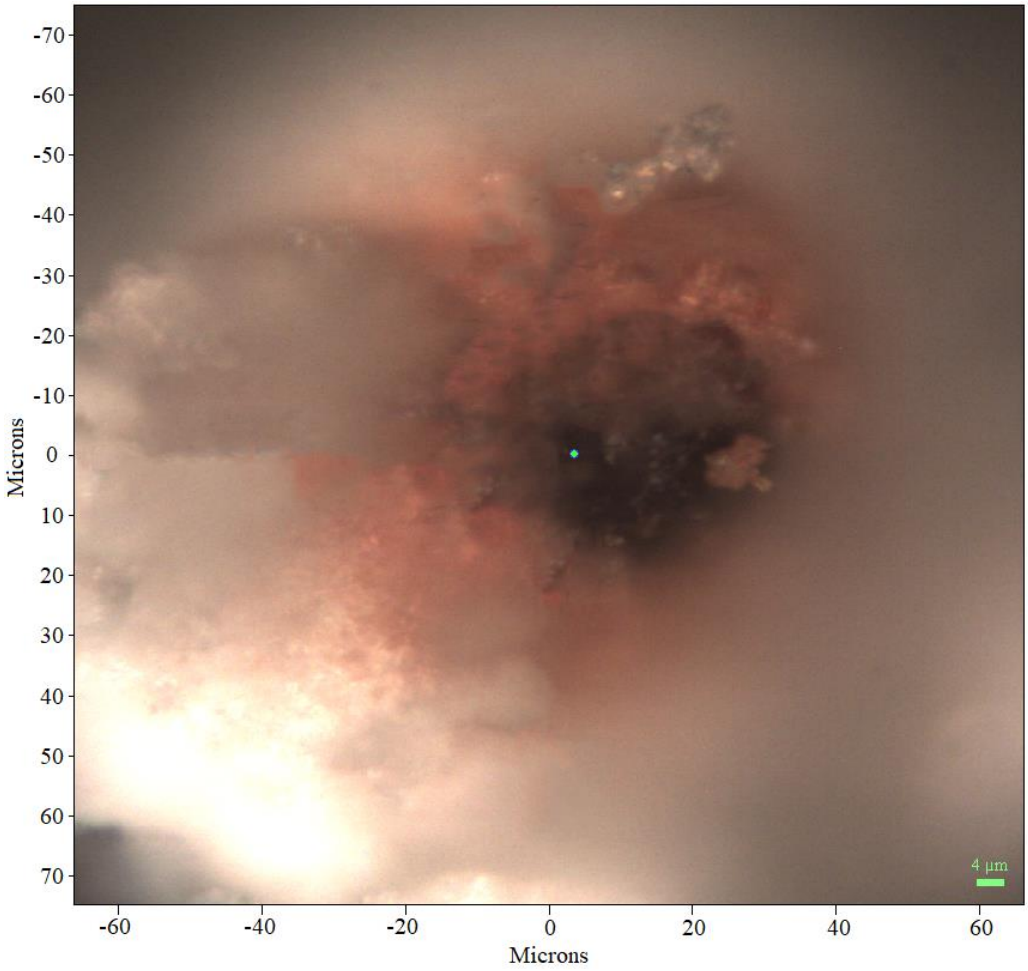


Figure 4.1: Olivine powder after having been burnt by the laser of a Raman spectrometer.

A problem arises when a sample shows no obvious changes after both visual inspection and spectral analysis. If our assumption that some degree of laser heating occurs in all Raman spectra is correct, then how do we determine if this laser heating is altering a sample? If the laser is heating a sample but the spectrum still appears 'normal', has the spectrum been altered at all or is it merely so subtle that it goes undetected?

This is of special concern for the Raman laser spectrometer on the *ExoMars* rover [136, 137]. *Rosalind Franklin* will have to conduct its work on the Martian surface, meaning data acquisition will be limited to the instrumentation payload it has on-board. The data gathered will be transmitted back to Earth for analysis, but if this analysis proves inconclusive in identifying a sample there is little further investigation that can be done due to the limited instrumentation onboard the rover; the only option would be to retrieve the sample at some point in the distant future. Therefore, it is important to characterise this laser heating effect in the laboratory in order to reduce the chances of misinterpretation of Raman data, especially that gathered by the *ExoMars* rover.

In order to characterise this effect, a series of thermal experiments were conducted on mineral samples. Three minerals were selected for this investigation: olivine, quartz, and labradorite; the justification for selecting these minerals can be found in Section 4.2 below.

As discussed in Section 3.1, the University of Kent's Raman spectrometer has a 532 nm laser, which is the same wavelength laser used for the Raman Laser Spectrometer (RLS) on the *ExoMars Rosalind Franklin* Rover [136, 137]. As such, this laser was used for this investigation in order to be able to directly link the results to the data that will eventually be returned by the *ExoMars* mission. Using the 532 nm laser it is possible to burn samples consisting of small grains (10's of microns in size) of the selected minerals, but larger millimetre sized samples of these same materials, subjected to the same powers, survive. As such, larger samples, which were not in danger of undergoing 'burning', were used for the first part of the investigation, which involved determining how the spectrum of these minerals changes when the sample is subjected to a range of temperatures.

Irrespective of any possible effects due to laser heating, this experiment by itself is useful to *ExoMars* as it will be operating on the Martian surface where the temperature varies quite substantially. At the Martian equator the temperature can get up to 20 °C during the day (at the height of summer), but at night it can fall to as low as -73 °C [170]. As such, it is important to know how the Raman spectrum of these Martian analogue minerals is altered by the changes in temperature which occur over the course of a Martian day (known as a Sol).

Section 1.1.1 discussed two techniques for using the Raman spectrum of a sample to determine the temperature of that sample. One of those techniques involves using the observation of how the peak position of narrow Raman peaks shifts due to changes in temperature. However, when very few spectra are gathered, this method is reliant on being able to compare those spectra to a previously obtained dataset from which calibration of peak position versus sample temperature has already been determined.

The experiments detailed in this chapter describe how the peak position versus sample temperature calibration for each of the selected minerals was obtained. These calibrations were then used to investigate the accuracy of the second technique discussed in Section 2.2.2; the use of the Stokes/anti-Stokes ratio to calculate the sample temperature under the laser spot.

4.2 Mineral Sample Selection

The minerals chosen to act as Martian analogues were olivine, quartz, and labradorite. A key reason for these selections is that each of these minerals has been shown to be

present on the Martian surface [171-173]. Other criteria considered were: availability, sample quality, and strength of Raman signal.

4.2.1 Olivine

Olivine is a common mineral, mainly found in the Earth's subsurface, and, as such, is widely available. The molecular structure of olivine (Figure 4.2) consists of silica tetrahedra separated by two distinct metal ion sites. These ion sites are occupied by either Fe or Mg, resulting in a chemical formula of $(Mg_x, Fe_{1-x})_2SiO_4$. The endmembers of this system are known as forsterite (Mg_2SiO_4) and fayalite (Fe_2SiO_4), with the intervening ratios typically denoted by their forsterite number ($Fo_{\#}$), where # represents how much Mg is present.

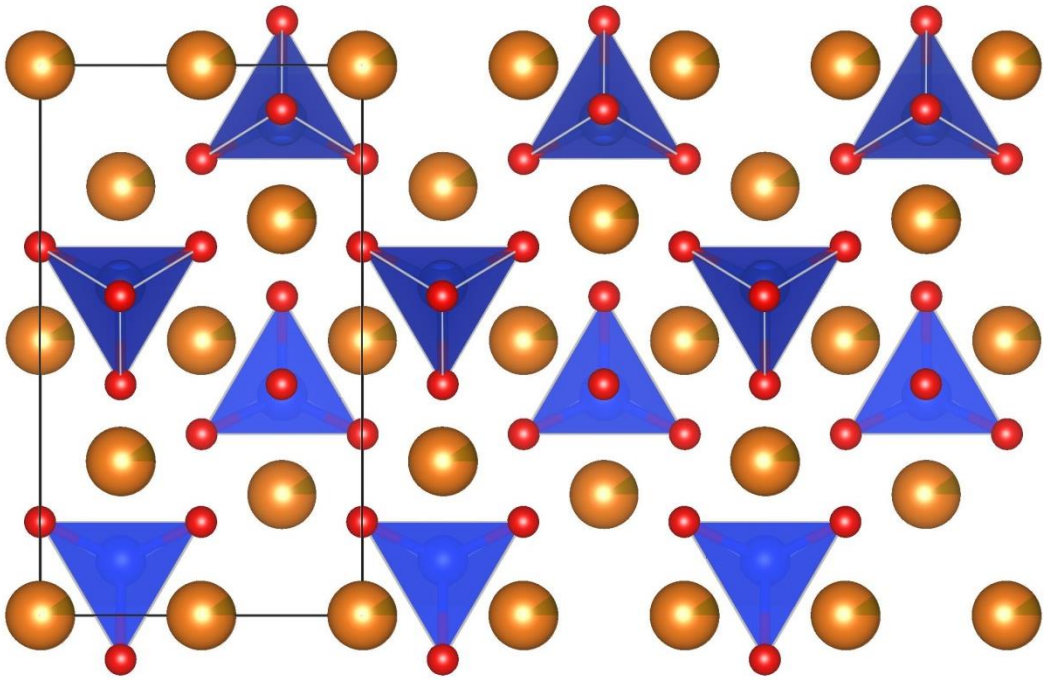


Figure 4.2: The crystal structure of olivine. Each tetrahedron consists of four oxygen atoms (red) and one silicon atom (blue). Between the tetrahedra are the metal ion sites (orange) which contain either magnesium or iron. Image courtesy of *Crystallography365* using the VESTA software.

Olivine has a strong, well-defined Raman spectrum (Figure 4.3). The dominant feature is the doublet of peaks located at ~823 cm^{-1} and ~855 cm^{-1} (labelled P1 and P2 respectively). These peaks are attributed to the internal stretching vibrational modes of the SiO_4 ionic group [122]. The exact positions of these peaks vary depending on the forsterite number of the sample. The position of P1 ranges from 815 cm^{-1} in fayalite (Fo_{00}) to 824.8 cm^{-1} in forsterite (Fo_{100}), while the position of P2 ranges from 837.8 cm^{-1} in fayalite (Fo_{00}) to 856.7 cm^{-1} in forsterite (Fo_{100}). These variations in position result in the doublet for Fe-rich olivine being less well resolved than Mg-rich olivine, with P2 often appearing as a shoulder of P1 (Figure 4.3). For that reason Mg-rich olivine was chosen for the experiments. Gem-quality Mg-rich olivine (peridot) is readily available in large quantities allowing for consistent samples to be used throughout the entire experimental programme.

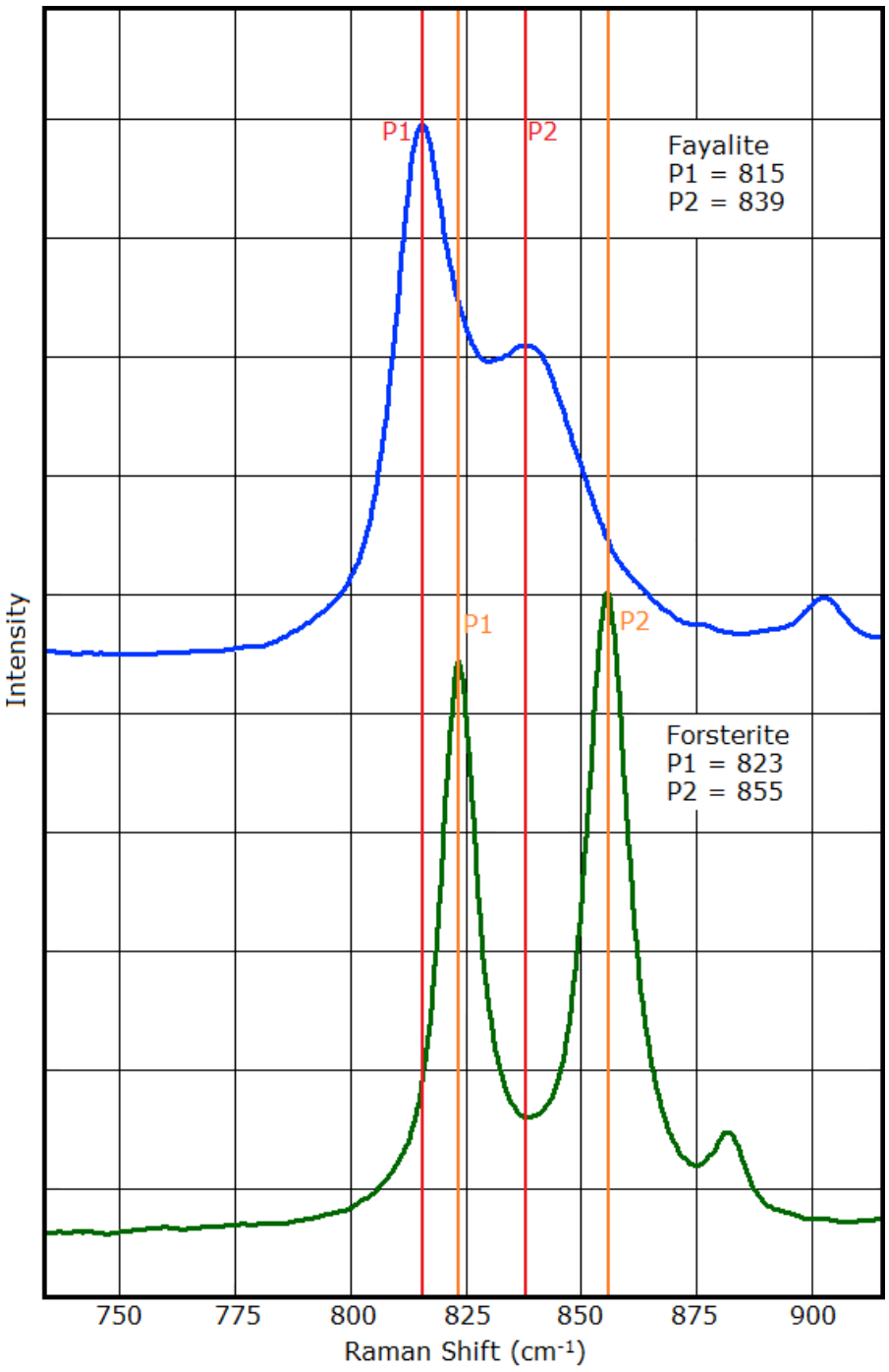


Figure 4.3: Raman spectra of Mg-rich olivine, forsterite, with the doublet peaks at 823 cm^{-1} and 855 cm^{-1} labelled as P1 and P2 respectively; and Fe-rich olivine, fayalite, with the doublet peaks at 815 cm^{-1} and 839 cm^{-1} labelled as P1 and P2 respectively.

4.2.2 Quartz

Quartz is arguably the most well-known mineral and is used in a multitude of applications, from glass manufacture to timepieces, making it readily available as high-purity gemstones. The molecular formula of quartz is SiO_2 and its structure shares the same silica tetrahedra that are found in olivine but with a distinct difference: in olivine these tetrahedra are not in contact with one another as they are separated by metal ions, whereas in quartz, the tetrahedra share oxygen atoms to form the crystal lattice (Figure 4.4).

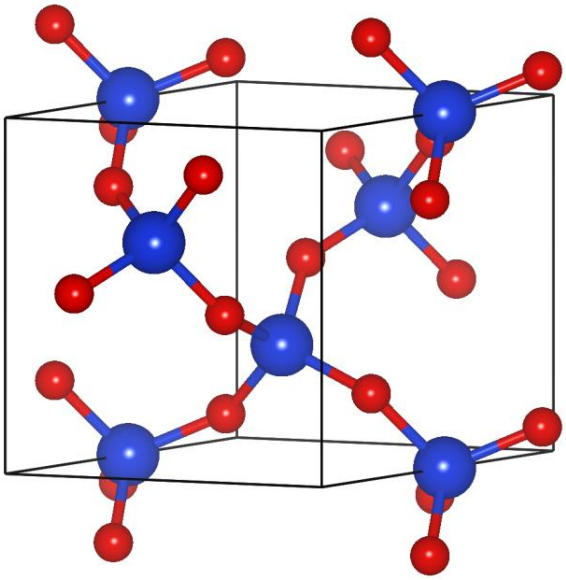


Figure 4.4: The crystal structure of quartz made up of silica tetrahedra containing oxygen (red) and silicon (blue). Image courtesy of *Crystallography365* using the VESTA software.

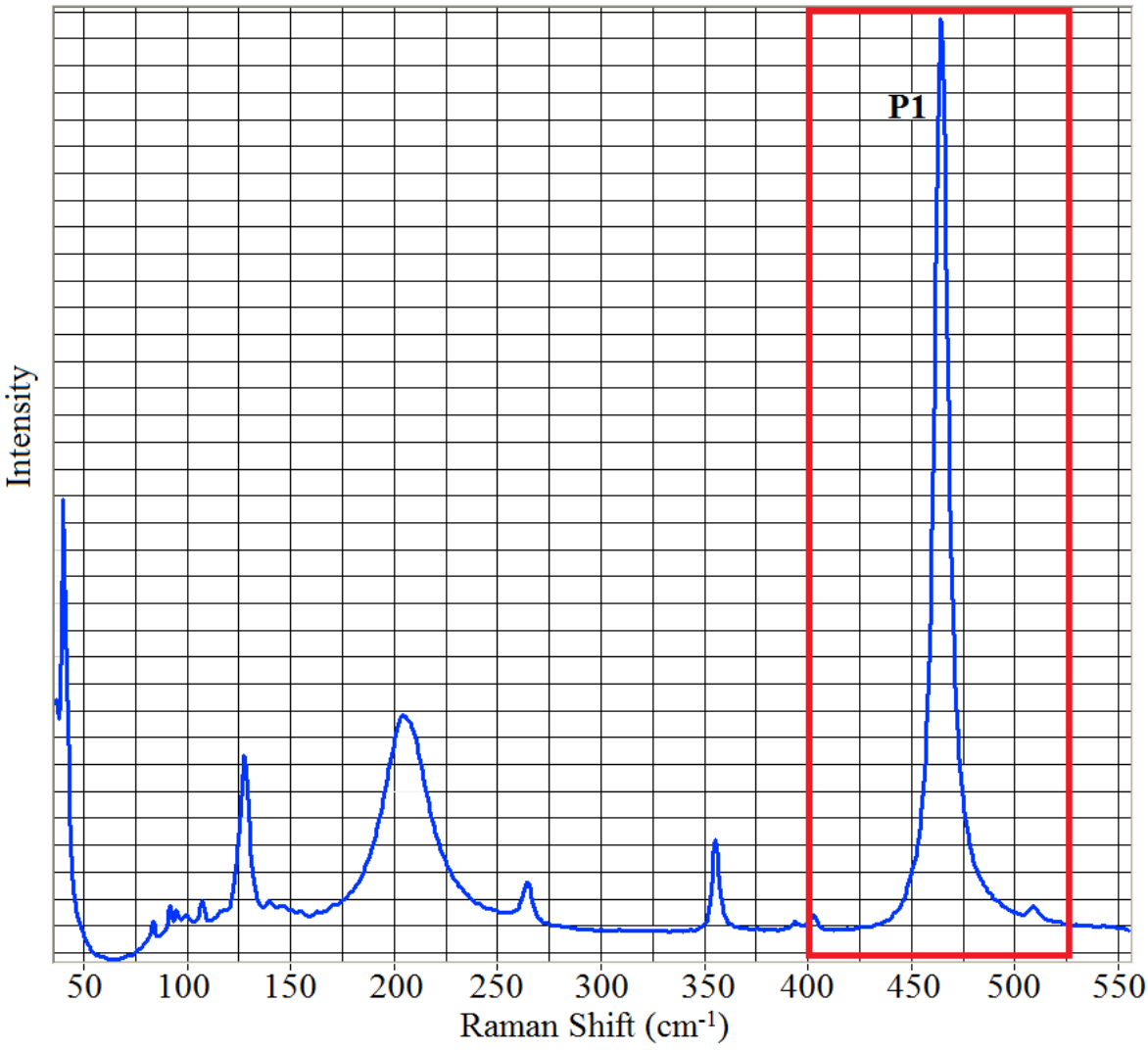


Figure 4.5: Raman spectrum of quartz with the peak at 464 cm^{-1} labelled as P1.

Quartz has a well-known Raman spectrum (Figure 4.5) with a strong peak located at approximately 464 cm^{-1}. This peak represents the O-Si-O bending modes in the quartz [174] and is labelled P1 in Figure 4.5.

4.2.3 Labradorite

Labradorite is a feldspar mineral in the plagioclase series. The feldspar group is made up of a number of different minerals and therefore contains a range of different molecular structures. Figure 4.6 is the feldspar ternary diagram and illustrates the molecular formula for each mineral in the feldspar group. Labradorite has a formula of $(Ca,Na)(Al,Si)_4O_8$ where Ca/(Ca+Na) is between 0.5 and 0.7 (50% – 70%). Feldspar minerals are common constituents of the volcanic rock basalt, which has been identified in many locations across the Solar System including Earth, the Moon, Mars, Venus, Io (moon of Jupiter), and the asteroid Vesta[175].

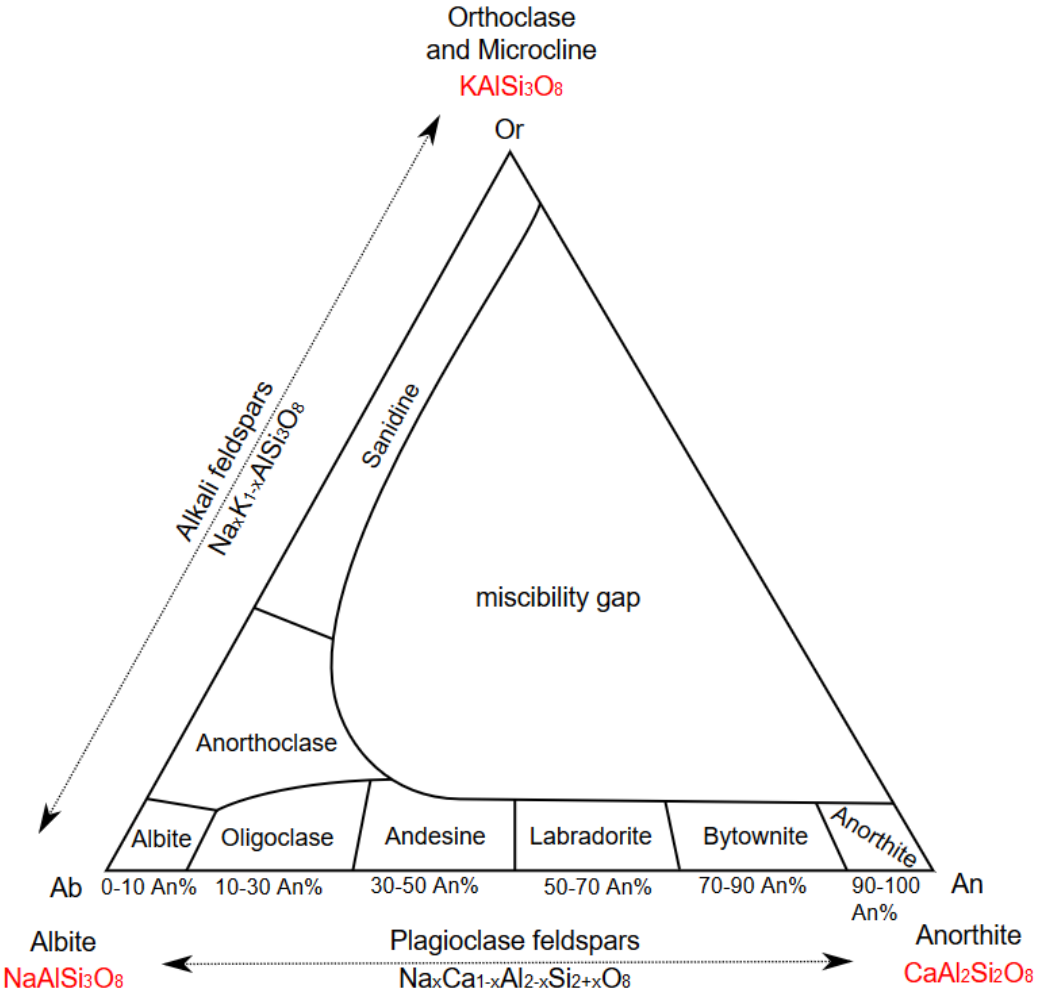


Figure 4.6: The ternary phase diagram for feldspars [176].

The Raman spectrum of labradorite is shown in Figure 4.7. The strongest feature is a doublet of peaks located at ~483 cm^{-1} and ~510 cm^{-1} (labelled P1 and P2 respectively). These peaks are associated with the symmetric stretching mode of the T-O-T linkage [177], where O is oxygen and T can be Si or Al (though Al-O-Al is forbidden [178]), which can be seen in Figure 4.8.

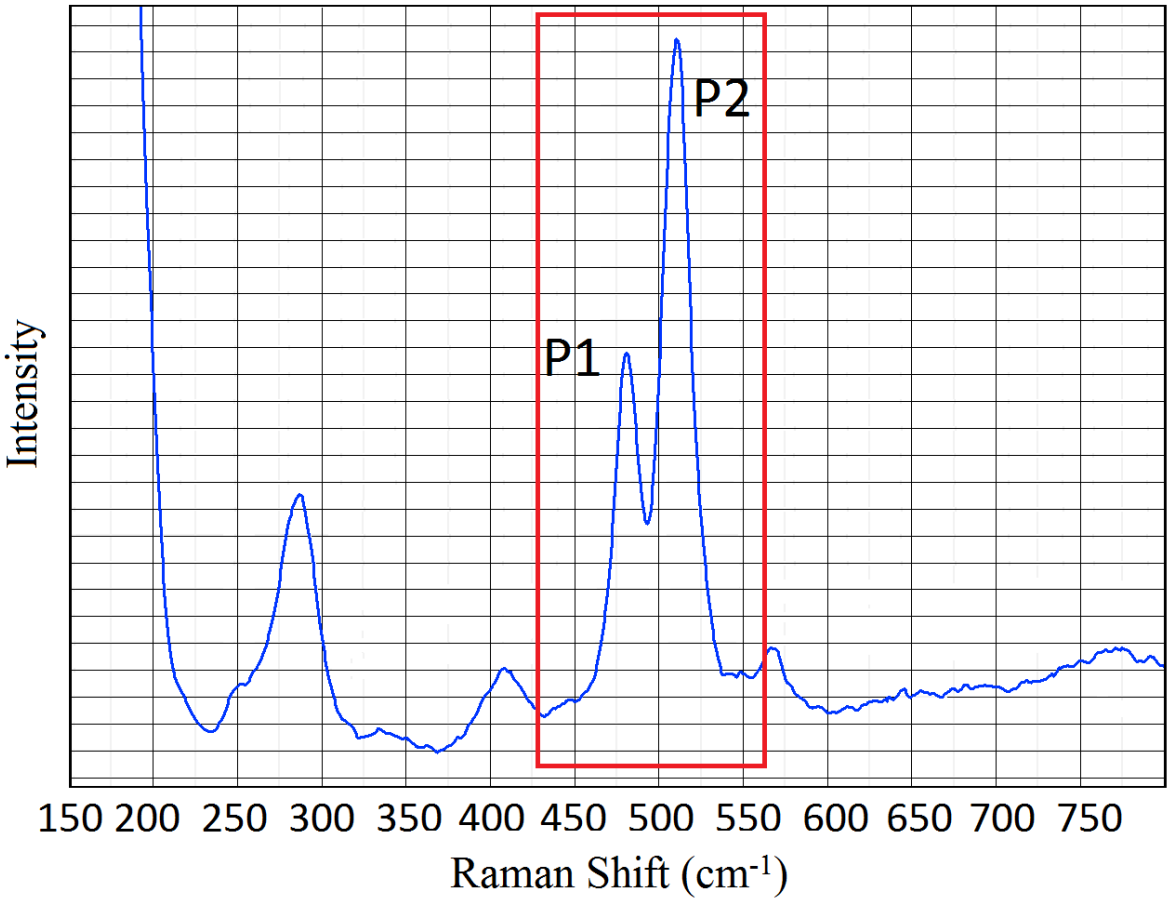


Figure 4.7: Raman spectrum of labradorite, with the doublet peaks at 483 cm^{-1} and 510 cm^{-1} labelled as P1 and P2 respectively.

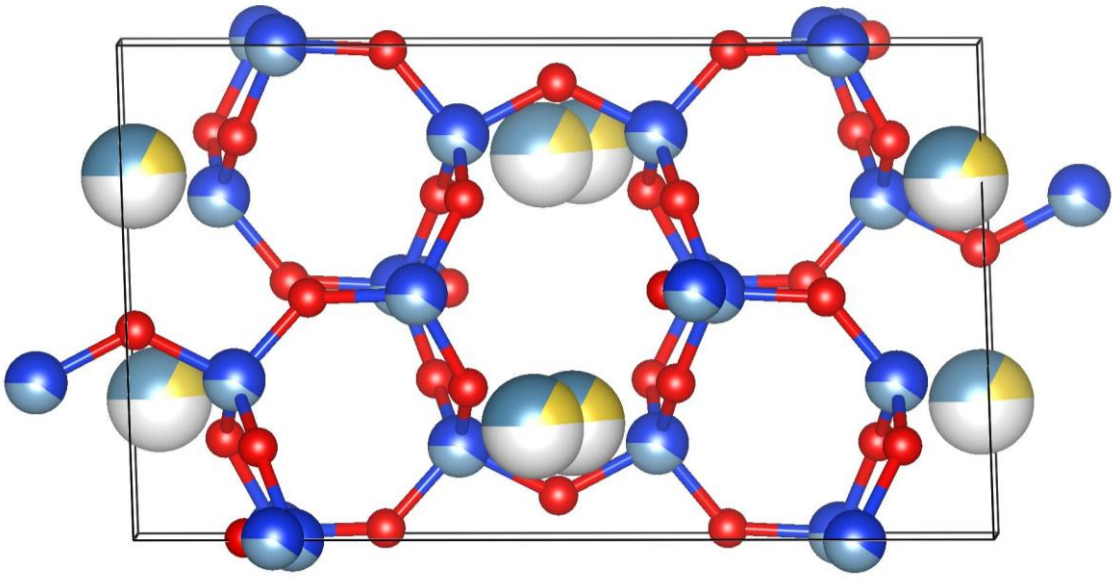


Figure 4.8: The crystal structure of feldspar. Tetrahedra consisting of oxygen atoms (red) and a silicon or an aluminium atom (blue and grey respectively). Between the tetrahedra are the metal ion sites which contain either calcium, sodium, or potassium (white, grey and yellow respectively). Image courtesy of *Crystallography365* using the VESTA software.

4.2.4 Chosen Samples

Each of the minerals detailed above was sourced in the form of a jeweller's stone. This means they have the shape of a typical faceted gemstone. Figure 4.9 is a diagram showing the various terms associated with the different faces and positions on a gemstone. For the work in this thesis, Raman spectroscopy was performed on the table of the gemstone as it provides a large flat surface to investigate. The crown of the gemstone is also mentioned in Chapter 5 and Chapter 6 when impact features are located on the edge of the table.

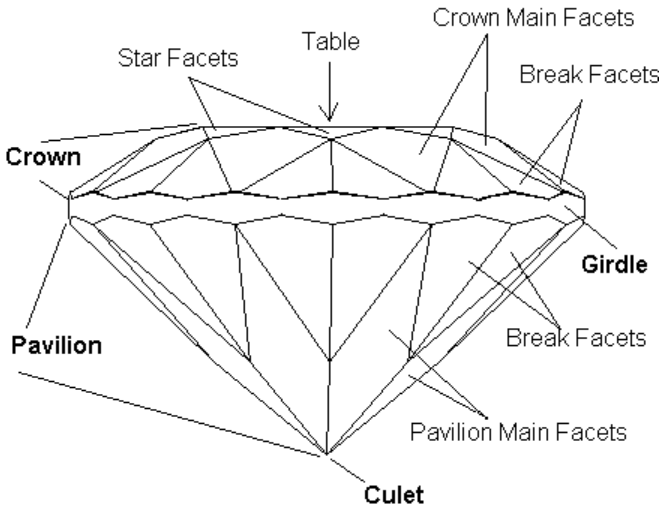


Figure 4.9: An example gemstone with its faces and positions labelled [179].

Figure 4.10 shows examples of each of the gemstones sourced for the work conducted in this thesis. The olivine gemstones (peridots) are Mg-rich olivine (forsterite number of Fo_{91}) with a table size of 5 mm x 5mm. The quartz gemstones are 12 x 16 mm 9.03 cts white quartz. The labradorite samples are 4.67 mm diameter round gemstones. No inclusions can be seen in any of the olivine or quartz samples up to a magnification of x500. However, magnetite inclusions were seen in the labradorite gemstones, and those found to have inclusions on their surface on the table of the gemstone were removed from the batch of viable test candidates.

Table 4.1: The Mohs hardness, density and melting points of the three minerals chosen for this investigation: olivine, quartz, and labradorite [180].

Mineral	Mohs Hardness	Density (kg m^{-3})	Melting Point (°C)
Olivine	6.5 – 7.0	3270 – 3370	1200 – 1900
Quartz	7.0	2600 – 2650	1670
Labradorite	7.0	2680 – 2710	~1300

4.3 Methodology

In order to carry out the experiment for determining the relationship between peak position and sample temperature, an accurate and reproducible technique for changing the temperature of the samples in the Raman spectrometer was needed; a "Linkam" Raman temperature stage (Section 3.1.2) was used to do this, which allows for the acquisition of spectra of samples at various temperatures. The Linkam stage (Figure 4.11) is capable of achieving temperatures of between -193 °C and 600 °C (80 K and 873 K) to an accuracy of ± 1 K. This maximum temperature is below the

melting points of all three of the selected minerals (Table 4.1) and therefore there is no danger of melting the sample inside the temperature stage. Liquid nitrogen is used to obtain temperatures lower than room temperature and the evaporated nitrogen from this process is directed into the stage to expel moisture preventing the build-up of condensation.

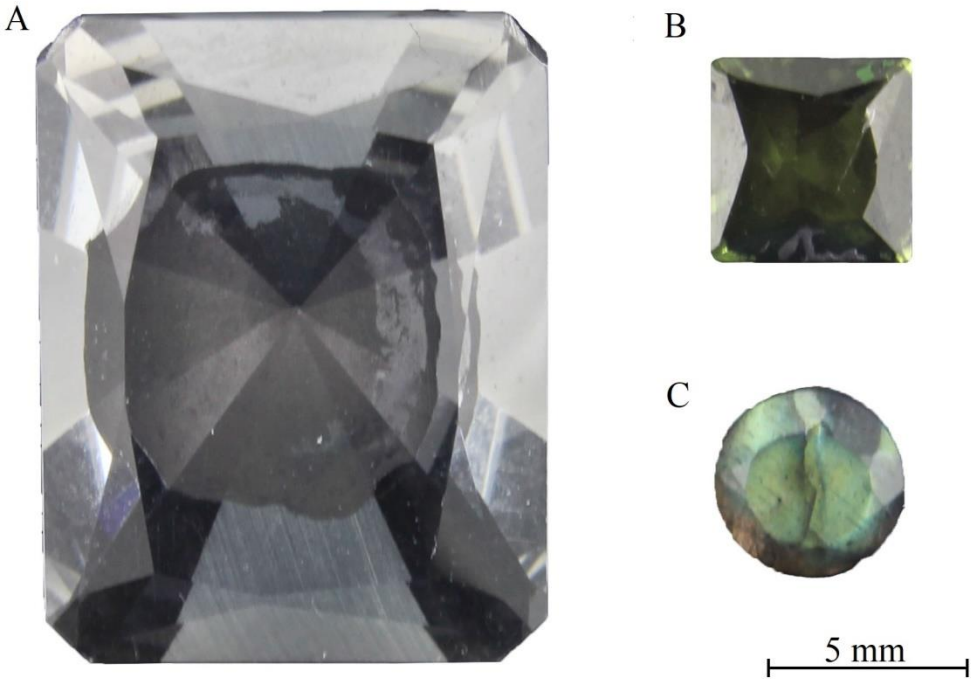


Figure 4.10: Examples of the quartz (A), olivine (B), and labradorite (C) gemstones.

The liquid nitrogen dewar supplied with the Linkam stage is only capable of holding 1 litre, which was not sufficient to maintain low temperatures for an extended period of time. Therefore a new LN_2 feed-system was developed that allowed the connection of a 10 litre dewar directly to the stage (Figure 4.12 and Figure 4.13). The new design also allowed the 10 litre dewar to be refilled without disconnecting it from the rest of the system (which would potentially disturb the experiment), thus low temperatures could be maintained for approximately 24 hours.

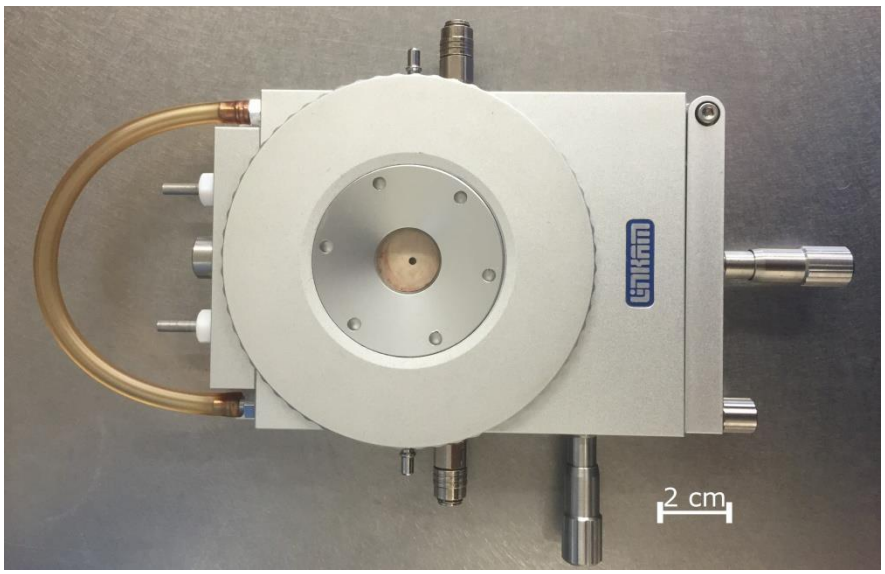


Figure 4.11: The Linkam temperature stage for the Raman spectrometer.

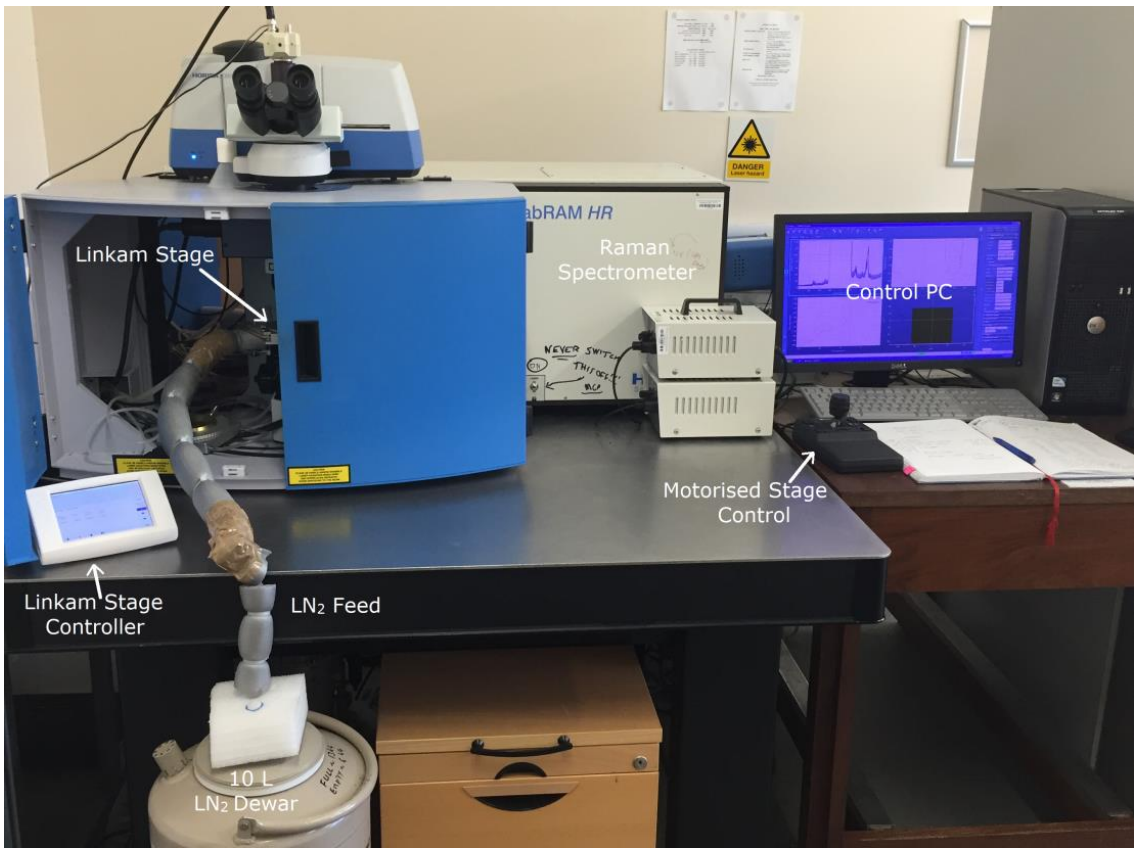


Figure 4.12: The Raman spectrometer configured for a low temperature experiment.

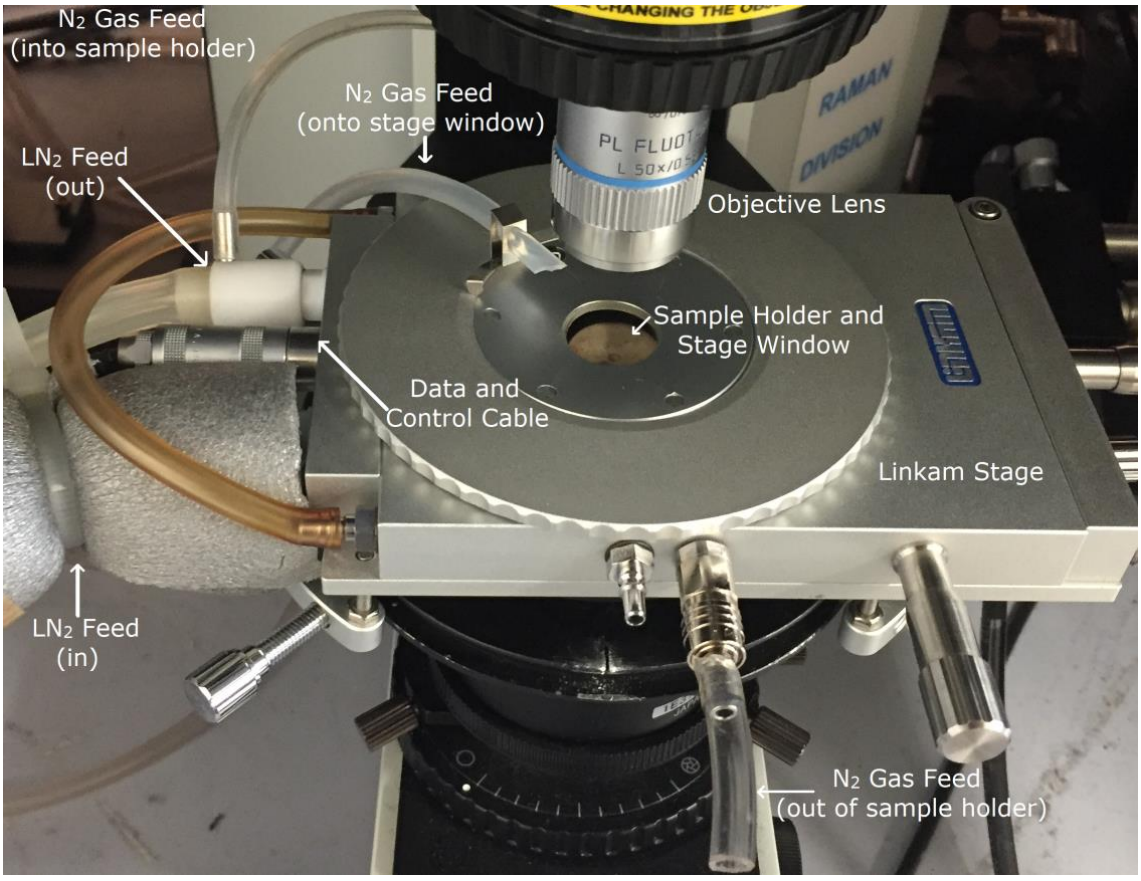


Figure 4.13: The Linkam stage inside the Raman spectrometer configured for a low temperature experiment.

The Linkam stage uses a computer controlled pump to draw the liquid nitrogen through the sample holder of the stage, actively cooling the sample. Once this liquid nitrogen reaches the pump it is normally boiled off and released into the atmosphere, but there is an exhaust tube on the pump that allows the gas to instead be recycled. In these experiments it was discovered to be beneficial to pass the nitrogen gas through the sample chamber to expel any water vapour that would form ice crystals on the inside of the stage window during low temperature experiments. A portion of the nitrogen gas was also directed over the outside of the stage window to prevent external ice from building up.

A test was performed to determine if the introduction of a purely nitrogen atmosphere in the sample chamber, instead of a normal air atmosphere, altered the Raman spectrum of the sample. This change in atmosphere introduced no detectable change in the Raman spectra of the olivine, quartz or labradorite samples.

Once the stage was set up, a control spectrum was taken at 30 °C over a spectral range of -1000 cm^{-1} to 1000 cm^{-1} to encompass the Stokes and anti-Stokes regions. These control spectra were used to ensure that the sample had not been altered between experimental runs, and provided a reference point from which to determine spectral changes due to temperature.

Each sample was measured over a temperature range of -150 °C to 550 °C. This was achieved in two parts: the first was a 'hot' temperature sequence from 30 °C to 500 °C and the second was a 'cold' sequence from 40 °C down to -150 °C. A point spectrum was taken every 10 °C, while the heating/cooling rate was 1 °C per minute. Once each temperature was achieved the sample was held at this temperature for 1 hour before data were taken to allow sufficient time for the sample to reach thermal equilibrium.

This experiment set-up means that for a 'hot' temperature sequence there were 52 data points, while a 'cold' temperature sequence had 20 data points. Each datum requires approximately 75 minutes to be obtained, after considering the heating/cooling rate and the hold-time, on top of the actual data acquisition time. This means that a 'hot' sequence needed approximately 65 hours to complete, while a 'cold' sequence needed 25 hours. Performing these tasks manually in a single experimental run would be impractical as the system would require human input at least once every 75 minutes, therefore, this process was automated.

The software used to control the University of Kent's Raman spectrometer, LabSpec 6, was capable of interfacing directly with the Linkam stage, thereby bypassing the manual controller. Initial test runs performed to assess the functionality of this feature revealed some bugs in the software. The most notable of which was that LabSpec 6 would lose communication with the stage unexpectedly and cause the data acquisition routine to halt on its current operation without any means of recovery. After liaising with Horiba, it was revealed that this was a fault with the software itself and a solution had been implemented in a minor software update issued by Horiba. After updating the software the system was tested again and was found to be reliable for unattended use.

Once the spectral data were obtained for each of the minerals it was then processed using a Python programming script[1]. The script implemented a least-square fitting method to apply a Gaussian curve to selected peaks of each Raman spectrum in the input data. This allows for the determination of the peak positions, intensities, and full-width-at-half-maximum (FWHM) for each of the selected peaks.

To obtain the results of the peak position versus sample temperature experiments, the fitted data were run through another script that plots the temperature against the positions of the main peaks in the minerals.

To obtain the Stokes temperatures for each of the peaks at each of the temperature steps, the baselined intensities of the fitted Stokes and anti-Stokes peaks were used to calculate the Stokes/anti-Stokes ratio. This ratio was then used in Equation 4.2, described in Section 4.4.2.

4.4 Results

4.4.1 Peak Position Versus Sample Temperature

The experimental procedure above was carried out for the three mineral samples: olivine, quartz, and labradorite. Figure 4.14 shows plots of temperature versus peak position for the main peaks in each of the samples.

Each of the peaks presented in Figure 4.14 shows a similar correlation between the peak position and the temperature of the sample. The rate of change is different for each of the peaks, and is even different for different peaks in the same sample, but the direction of the trend remains the same; as the temperature increases the peak position decreases. Likewise, as the temperature is increased, the Raman shift of the peak decreases. These results follow the expected behaviour described in Section 2.2.2 and are due to the increase in temperature causing the length of the bonds associated with each of the peaks to increase. These increased bond lengths result in a decrease in energy of the vibrational mode of the bonds thereby reducing the size of their Raman shifts.

Inspection of the samples showed that none of the samples had undergone 'burning', or any other visible alteration to the surface. Also, initial analyses of any of the individual spectra did not immediately show any obvious changes to the spectrum of a sample. It was only when analysing all the spectra for a particular sample together that it became clear that alteration had occurred with temperature. Therefore, it is reasonable to assume that if Raman spectra were gathered over a period of time in an environment that does not have a constant temperature, it is possible to overlook the fact that peak shifts (or at least part of the shift) could be due to changes in the temperature of that environment.

These data show that it is important to create a calibration dataset for Raman data gathered in environments with fluctuating temperatures, before making any conclusions as to the cause of spectral changes, particularly before assuming that a change in chemical composition has occurred. Figure 4.14 demonstrates that it is relatively simple to create such a calibration dataset that can be used as a

[1] This script was originally written by Dr T. M. Kinnear and further edited by the author R. Hibbert.

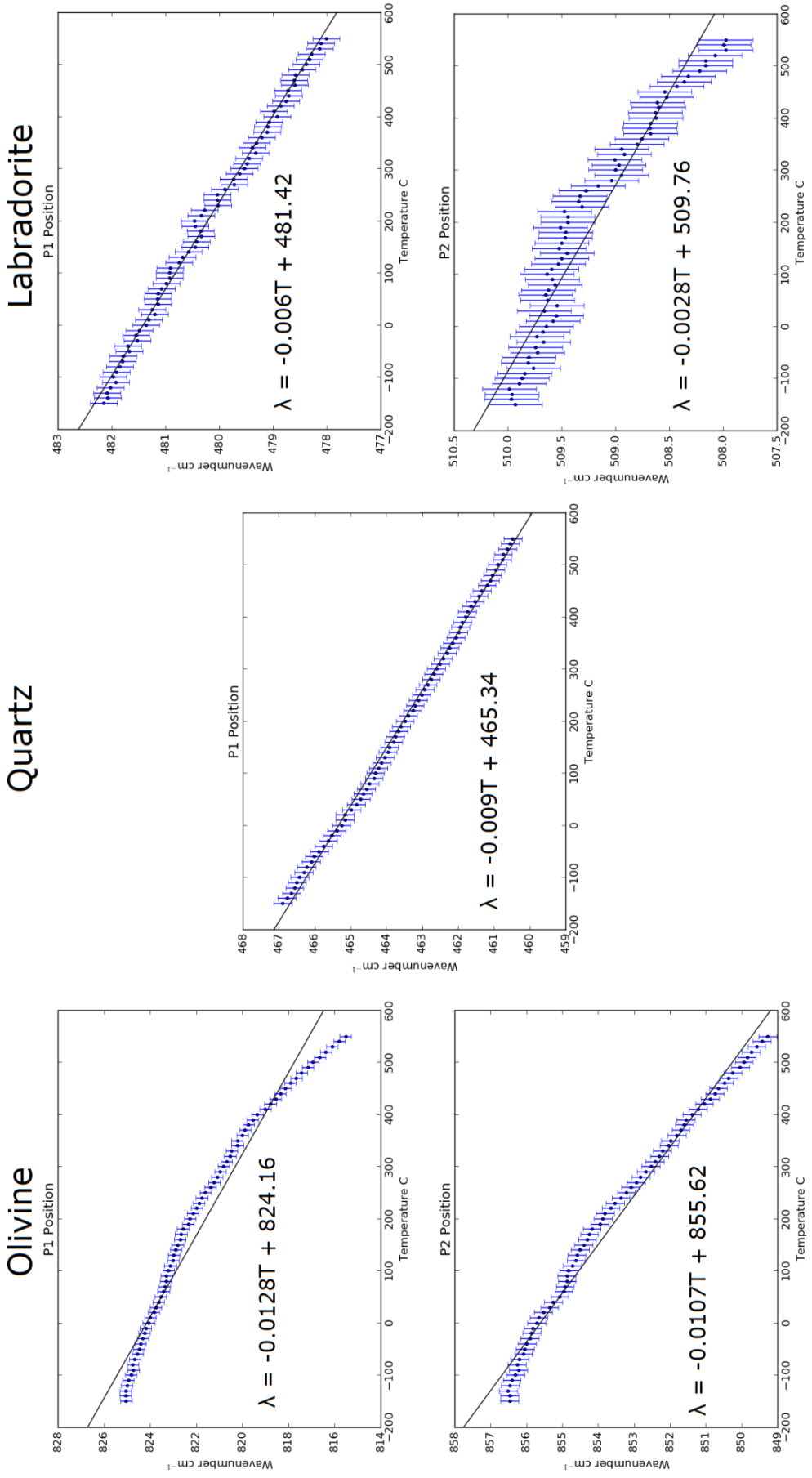


Figure 4.14: Temperature versus peak position (including linear equations of best fit) for the main peaks in each of the mineral samples for the uncorrected data.

'Raman thermometer' to understand these changes in peak shift and determine what the peak position of a particular Raman band should be across a range of temperatures.

A final point of note is that the Raman peak positions of all of the samples used in these temperature experiments returned to their original values after the experiment was concluded, showing that no permanent alteration had occurred.

4.4.1.1 Misinterpretation of Spectra due to Changes in Temperature

As stated in Section 4.2.1, the identification of the composition of olivine through interpretation of Raman spectra is particularly susceptible to changes in the peak positions of P1 and P2. Kuebler *et al* (2006) [122] goes into detail on this subject and has produced a variety of calibration equations that calculate the forsterite number of an olivine sample based on the P1 and P2 positions. One of these equations uses both peaks in its calculation and is stated to be able to determine the forsterite number to within ±10 Fo units (Equation 4.1).

$$\mathrm{Fo}_{\#} = \mathrm{y} + ax_{P1} + bx_{P2} + cx_{P1}^2 + dx_{P2}^2 \tag{4.1}$$

Where x_{p1} is the peak position of P1, x_{p2} is the peak position of P2, and *a*, *b*, *c*, *d*, *y* are constants valued at:

a= 80.190397775029
b= 399.350231139156
c= -0.0424363912074934
d= 0.2357973451030880
y= -206232.988995287

Using Equation 4.1 with data taken of the olivine sample at room temperature yields a forsterite number of $Fo_{97.}$ SEM EDX analysis of the sample shows the forsterite number to be Fo_{91} (Section 6.4.1), which is within the stated error of ±10 Fo units.

Therefore, due to the variation in the peak positions of both P1 and P2 with changes in temperature (as seen in Figure 4.14), variation in the calculated forsterite numbers was seen (Table 4.2). Using the peak positions recorded at either end of the temperature range, -150 °C and 550 °C, yielded forsterite numbers of Fo_{106}[1] at -150 °C and Fo_{26} at 550 °C. This is despite knowing that the sample had not changed composition and remained at Fo_{91} after the experiment.

To put this into context for the Raman laser spectrometer (RSL) on board the *ExoMars* rover, *Rosalind Franklin,* as stated in Section 4.1, the temperature on the Martian surface at the equator the can get up to 20 °C during the day (and at the height of summer), but at night it can fall to as low as -73 °C [170]. Taking the average Martian surface temperature of -60 °C [170], Table 4.2 shows that Equation 4.1 would give a forsterite number of Fo_{102}[1], thereby misinterpreting the composition of the olivine sample.

These results re-enforce the importance of taking the ambient temperature into consideration when gathering Raman spectral data so as to avoid possible misinterpretation of the data with respect to sample composition.

---

[1] Obviously a forsterite number above 100 is not possible. This value is the result of the recorded peak positions at -150 °C being outside of the normal range of peak positions.

Table 4.2: The forsterite number calculated for the olivine sample based on the measured peak positons at each sampling temperature.

Temp °C	P1	P2	Fo#		Temp °C	P1	P2	Fo#
-150	825.05	856.47	106		210	822.14	853.81	86
-140	825.06	856.47	106		220	821.99	853.65	85
-130	825.07	856.51	106		230	821.89	853.53	85
-120	825.00	856.45	105		240	821.76	853.37	84
-110	824.94	856.40	105		250	821.60	853.22	83
-100	824.83	856.31	104		260	821.39	853.09	81
-90	824.73	856.23	104		270	821.22	852.94	79
-80	824.75	856.26	104		280	821.10	852.82	79
-70	824.67	856.19	103		290	820.96	852.67	77
-60	824.54	856.09	102		300	820.82	852.53	76
-50	824.48	856.04	102		310	820.69	852.42	75
-40	824.42	855.99	102		320	820.54	852.30	74
-30	824.31	855.90	101		330	820.46	852.21	73
-20	824.25	855.86	100		340	820.21	852.03	71
-10	824.18	855.82	100		350	820.22	851.99	71
0	824.06	855.72	99		360	820.00	851.81	70
10	823.99	855.66	99		370	819.88	851.70	69
20	823.83	855.53	97		380	819.74	851.60	67
30	823.76	855.35	97		390	819.55	851.56	65
40	823.63	855.26	96		400	819.36	851.39	64
50	823.55	855.07	96		410	819.01	851.22	60
60	823.42	854.96	95		420	818.78	851.05	58
70	823.38	854.92	95		430	818.56	850.88	56
80	823.31	854.87	95		440	818.35	850.75	54
90	823.30	854.88	95		450	818.14	850.65	52
100	823.21	854.82	94		460	817.91	850.48	50
110	823.13	854.73	93		470	817.67	850.36	48
120	823.00	854.62	92		480	817.43	850.25	45
130	822.97	854.59	92		490	817.16	850.04	43
140	822.89	854.50	92		500	816.93	849.94	40
150	822.81	854.41	91		510	816.65	849.85	37
160	822.70	854.30	90		520	816.38	849.74	35
170	822.66	854.25	90		530	816.11	849.58	32
180	822.57	854.17	90		540	815.80	849.44	28
190	822.35	853.96	88		550	815.52	849.28	26
200	822.28	853.87	88					

4.4.2 Stokes Temperature versus Sample Temperature

As described in Section 1.1.1, the ratio between the Stokes and anti-Stokes intensities of the same peak can be used to determine the temperature of the sample during acquisition. Having held the sample at the desired temperature for one hour before each acquisition, it was assumed that the sample had reached thermal equilibrium.

Therefore, performing Stokes/anti-Stokes temperature analysis would provide a measure as to how much the sample temperature increased during acquisition as a result of laser heating.

Stokes/anti-Stokes temperature calculations are based on the Boltzmann distribution (Equation 2.3). As described in Section 3.1.1, the Raman spectrometer used for these experiments employs a CCD as its detection method. As such the following is frequently given to describe the Stokes ratio and the temperature when using a photon counting device such as a CCD [62]:

$$\frac{N_{AS}}{N_S} = \frac{(f_l - f_v)^3}{(f_l + f_v)^3} e^{\frac{-hf_v}{k}} \tag{4.2}$$

Rearranging for T, this equation becomes:

$$T = \frac{-hf_v}{k} \cdot \frac{1}{\ln\left[\frac{N_{AS}}{N_S} \cdot \frac{(f_l - f_v)^3}{(f_l + f_v)^3}\right]} \tag{4.3}$$

Where T is the temperature (in K), k is Boltzmann's constant (in J K^{-1}), h is Planck's constant (in J s), f_l is the frequency of the laser (in Hz), f_v is the frequency of the vibrational mode (the Raman peak position) (in Hz), and N_S and N_{AS} are the number of counts for the intensity of the Stokes and anti-Stokes peaks respectively.

Table A.1 in Appendix A shows the results of the Stokes/anti-Stokes analysis for each of the peaks. The most obvious observation to be made from this table is that data are missing for some of the lower temperatures for the olivine peaks. This is because as the temperature decreases the intensity of the Raman spectrum as a whole decreases. The anti-Stokes peaks suffer from a further complication due to the lower temperature; as a larger proportion of the molecules are in the ground vibrational state further decreasing the intensity of the anti-Stokes peak. This decrease in intensity made it impossible to detect the anti-Stokes peak below a certain temperature (which was specific to each sample).

Upon analysis of the Stokes/anti-Stokes data, several inconsistencies were discovered for each of the minerals. For quartz the Stokes temperatures are higher than the stage temperatures for stage temperatures between -150.0 °C and 80.0 °C implying that the laser is heating the sample. However, when the stage temperature reaches 90.0 °C the Stokes temperatures are calculated to be below the stage temperature for the remainder of the dataset implying that the laser is cooling the sample which is clearly non-physical.

The two peaks for olivine show similar Stokes temperatures across the entire dataset, with the smallest discrepancy between the two Stokes temperatures being 0.2 °C when the stage temperature is at 50.0 °C, while for the rest of the data the difference between the Stokes temperatures of the two peaks are less than 14.0 °C. The calculated Stokes temperatures for olivine are above the stage temperature at all points. This could reasonably be explained as the sample undergoing laser heating while the spectrum was being acquired.

For labradorite the two peaks are in much less agreement with one another. The smallest difference between the peaks is 4.9 °C (at a stage temperature of 150.0 °C), while the largest difference is 70.3 °C (at a stage temperature of 550.0 °C). For P1,

stage temperatures between -150.0 °C and 40.0 °C (cold sequence) show the calculated Stokes temperatures higher than the stage temperatures, again implying laser heating. However, for stage temperatures between 30.0 °C (from the hot sequence) and 140.0°C, the data changes to show Stokes temperatures lower than the stage temperatures. This change is then reversed at a stage temperature of 150.0 °C when the Stokes temperature for both P1 increases significantly to give a value of 271.4 °C (91.4 °C above the stage temperature). The Stokes temperatures quickly decrease from this sudden spike and fall below the stage temperature once again at a stage temperature of 170.0 °C.

For P2, at stage temperatures between -150.0 °C and 140.0 °C the Stokes temperature is above the stage temperature implying laser heating. Like P1, P2 also undergoes a large jump in the calculated Stokes temperatures at 150.0 °C increasing to a value of 266.5 °C (86.5 °C above the stage temperature). Again the Stokes temperatures quickly decrease from this sudden spike, falling below the stage temperature at a value of 190.0 °C and remaining below for the remainder of the dataset. Upon further investigation of the labradorite data, it was discovered that for stage temperatures between 150.0 °C and 190.0 °C both the P1 and P2 anti-Stokes peaks were extremely weak and difficult to interpret. This made the values for their intensities unreliable and therefore the calculated Stokes temperatures) that are reliant on those values) unreliable. As such, the labradorite data between stage temperatures of 150.0 °C and 190.0 °C should be ignored.

The calculated Stokes temperatures from these experiments show conflicting results. The most confusing aspect of these results is the data points showing a decrease in temperature between the stage temperatures and the Stokes temperatures that would imply 'laser cooling'. If there was some anomaly reducing the intensity of the spectrum, it would likely have acted across the entire spectrum reducing its intensity at all points, thereby maintaining the intensity ratio between the Stokes and anti-Stokes peaks. Instead it seems that something is altering either the Stokes or anti-Stokes intensity, not both, and therefore altering the ratio. It is difficult to comprehend how something could have preferentially reduced the intensity of the Stokes or anti-Stokes peak without affecting the other.

This difference in temperature between the measured stage temperatures to the calculated Stokes temperatures has three possible explanations:

1. The laser is cooling the sample during acquisition.
2. One hour is not enough time for the sample to be in thermal equilibrium with the stage.
3. One set of values must be wrong. i.e. the stage is not at the expected temperature or the Stoke/anti-Stokes ratio temperature calculations are incorrect.

The first scenario is physically impossible; but the second and third scenarios are possible and were tested.

4.4.3 Calibration Test

In order to test the second and third scenarios the Linkam stage was removed from the Raman system and placed inside a thermally insulated container. The Linkam stage was connected in the same way as when *in situ* on the spectrometer; however the sample was replaced with a resistance temperature detector (RTD). A PT100

platinum resistance thermometer (PRT) was chosen, which has a resistance of 100 ohms at 0 °C and 138.4 ohms at 100 °C. The sensor used for this calibration experiment was sensitive between -50 °C and 500 °C.

The resistance of a PT100 sensor is governed by the following linearization equation:

$$R_T = R_0 \times [1 + XT + YT^2 + (Z \times (T - 100) \times T^3)] \quad (4.4)$$

Where:

T is the temperature (°C), R_t is the resistance at temperature t (Ohms), R_0 = 100 ohms (the resistance at 0 °C),

X = 3.39083 x 10^{-3}

Y = -5.775 x 10^{-7}

Z = -4.183 x 10^{-12} (below 0 °C) or Z = 0 (above 0 °C)

Above 0 °C the constant Z is equal to 0. Rearranging Equation 4.4 yields:

$$0 = (R_0 - R_t) + R_0Xt + R_0Yt^2 \quad (4.5)$$

Equation 4.5 can be solved for T:

$$T = \frac{-R_0X \pm \sqrt{(R_0X)^2 - \left(4R_0Y(R_0 - R_t)\right)}}{2R_0Y} \quad (4.6)$$

When R_T = 100 ohms, the negative solution to this equation produces a temperature value of 6735.7 °C, while the positive solution produces a temperature value of 0.0 °C. The negative solution is obviously not correct as, by definition, a PT100 sensor has a resistance of 100 ohms at 0 °C. Therefore the positive solution to Equation 4.6 produces the correct value for resistances above 100 ohms.

Below 0 °C (or below R_T = 100 ohms) the constant Z no longer has a value of 0, making the equation a cubic function making an analytical solution more difficult. Therefore an alternative method was devised to convert the resistance value into a temperature value. A Fortran-90 program used Equation 4.4 to generate a lookup table for resistances in the temperature range between 0 °C and -50 °C at a resolution of 0.256 °C, which is equivalent to a resistance change of 0.1 ohms.

The resistance of the system, excluding the PT100 sensor, was measured before the test so that it could be subtracted from the experiment readings in order to give the resistance of just the PT100 sensor. Following a similar experimental procedure to that described in Section 4.3, two experiment runs were performed, one hot and one cold. For the hot run, the Linkam stage was programmed to go from 25 °C up to 450 °C at a rate of 0.1 °C per minute. Once the stage reached 450 °C it was held at temperature for 30 minutes. For the cold run the Linkam stage was programmed to first heat the sample to 50 °C and hold for 30 minutes. It was then programmed to cool the sensor from 50 °C down to -50 °C at a rate of 0.1 °C per minute. Once at -50 °C the stage was held at that temperature for another 30 minutes.

Both the hot and cold runs gathered data at temperatures between 25 °C and 50 °C. This was done to ensure that both sets of data agreed with each other over this range and so that any offset between the runs could be removed. During both runs, the

resistance of the PT100 sensor (measured using a digital multimeter) and the temperature of the stage (as reported by the Linkam controller) were both recorded at 5 minutes intervals by use of a digital camera on an automatic timer. An example of one of these images can be seen in Figure 4.15.



Figure 4.15: An example picture of the Linkam stage controller showing the stage temperature and the multimeter showing the resistance of the PT100 sensor.

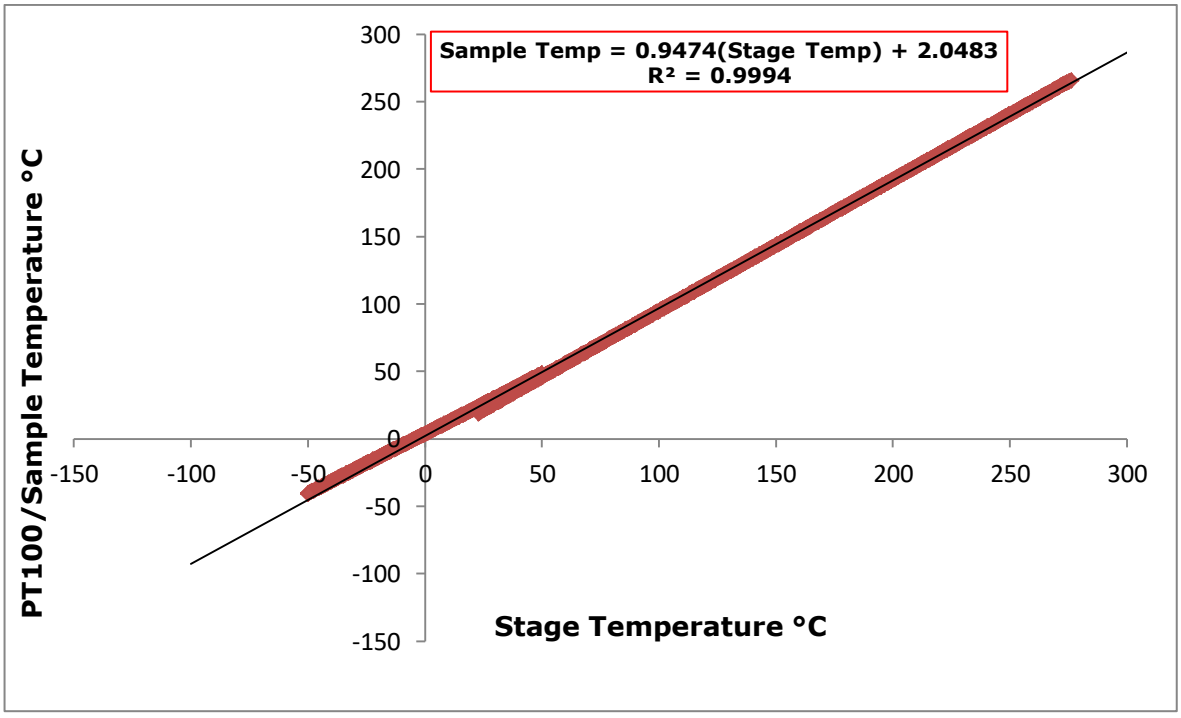


Figure 4.16: A graph showing the sample temperature calculated using the pt100 sensor versus the stage controller temperature as determined by the Linkam stage.

As explained above, at different times during this experiment the stage was held at -50 °C, 50 °C and 450 °C for 30 minutes. This provided data with which to test the second scenario outlined in Section 4.4.2.

Table 4.3: Resistance and Time for the hold points of the calibration experiment.

Temperature (°C)	Time (min:sec)	Resistance (ohms)
-50 °C	02:32	84.1
	07:36	84.1
	12:40	84.1
	17:43	84.1
	22:47	84.1
	27:51	84.1
50 °C	00:32	118.8
	05:36	118.8
	10:40	118.8
	15:45	118.8
	20:49	118.8
	25:43	118.8
450 °C	03:33	289.0
	08:37	289.0
	13:41	289.0
	18:45	289.0
	23:49	289.0
	28:43	289.0

Table 4.3 shows the resistance of the PT100 sensor after having been held at these temperatures for various lengths of time and clearly shows that the resistance of the sensor quickly levels off and does not vary for the remainder of the hold time. This demonstrates that it quickly came into thermal equilibrium with the stage, therefore discounting the second scenario as an explanation as to why the calculated Stokes/anti-Stokes temperature is lower than the measured stage temperature.

After converting the resistance readings into temperature values using Equation 4.6 (for values of R_t above 100 ohms) and the lookup table (for values of R_t below 100 ohms), sensor temperature was plotted against the stage controller temperature (Figure 4.16). The graph clearly shows that the PT100 sensor gives a different value for the temperature reported by the stage controller. This proves that the third scenario outlined in Section 4.4.2 was at least partly true; the stage temperature values (as given by the Linkam stage) were incorrect. Using these data a correction formula for the stage temperature was devised:

$$Sample\ Temp = (0.9474 \times Stage\ Controller\ Temp) + 2.0483 \quad (4.7)$$

4.4.4 Corrected Data

4.4.4.1 Stage Temperature

Alteration to the values for the stage temperature affects the results in both Section 4.4.1 and Section 4.4.2. Using the correction formula (Equation 4.7), the graphs in Figure 4.14 in Section 4.4.1 were replotted with revised values for the temperature of the sample. Figure 4.17 shows that the previously identified trends were still present, but the equations of the lines of best fit have been altered to reflect the update to the axis values.

Table A.2 in Appendix A presents the same calculated Stokes temperature data as Table A.1 in Appendix A discussed in Section 4.4.2, but with the stage temperature values having been corrected using Equation 4.7. Analysis of these corrected data demonstrates the same conclusions as those determined for the uncorrected stage temperature values in Section 4.4.2. This is to be expected as the correction to the stage temperature is minor compared to discrepancies between the stage temperatures and the Stokes temperatures.

This leads to the conclusion that the calculation used to generate the Stokes temperatures is flawed in some way as the other possibilities outlined in Section 4.4.2 had been tested and corrected for.

4.4.4.2 Calculated Stokes Temperatures Correction

Having determined that the calculated Stokes temperatures were incorrect, investigations were undertaken to ascertain why this was the case. The formula used to calculate the Stokes temperatures (Equation 4.6) uses the intensity ratio between the Stokes and anti-Stokes peaks. In order to calculate this ratio, the intensities of the peaks, as reported by the Raman spectrometer, are used. However, this assumes that the Raman spectrometer is accurately reporting these intensities. As previously explained, the Raman system utilises a CCD as a means of counting the scattered photons, but a CCD has varying levels of sensitivity to different wavelengths of light. A problem arises when considering that Stokes scattered photons and anti-Stokes scattered photons from the same molecular bond have different wavelengths due to the nature of the Raman scattering process. As such, the CCD may have different levels of sensitivity for the two wavelengths in question, even though they represent the same degree of Raman shift.

Therefore, in order to use the Stokes/anti-Stokes ratio to be able to accurately determine the temperature of a sample, the CCD's sensitivity to different wavelengths must be known to allow it to be corrected for. This is known as the wavelength dependent instrument response function (IRF). The IRF is not known for the Raman system used; and without accurately correcting for the IRF, it is not possible to accurately determine the temperature of a sample using the Stokes/anti-Stokes ratio alone.

Fortunately, however, it has already been shown that the samples used for this experiment were heated to the stage temperature before the data acquisition took place (Section 4.4.3). This means that if it is assumed that the laser heating effect on these large gemstone samples is negligible, and the Stokes temperatures were calculated correctly, those values should be the same as the stage temperature

values. As such, a correction factor can be calculated for each of the peaks investigated that should correct for the lack of an IRF.

To generate these correction factors, Equation 4.4 was used to calculate the expected Stokes/anti-Stokes ratio for each of the peaks being investigated at each of the stage temperatures. The ratios calculated from the measurements in Section 4.4.2 were plotted against these expected ratios for each peak (Figure 4.18). A line of best fit was determined for each series of data, with the equation of these lines being the correction that should be applied to Stokes/anti-Stokes ratios obtained for their respective peaks.

The corrections for the Stokes/anti-Stokes ratios of each of the peaks are:

$$Quartz\ P1 : Corrected\ Ratio = (1.2426 \times Measured\ Ratio) - 0.0455 \quad (4.8)$$

$$Olivine\ P1 : Corrected\ Ratio = (0.8153 \times Measured\ Ratio) - 0.0031 \quad (4.9)$$

$$Olivine\ P2 : Corrected\ Ratio = (0.7978 \times Measured\ Ratio) - 0.0024 \quad (4.10)$$

$$Labradorite\ P1 : Corrected\ Ratio = (1.2154 \times Measured\ Ratio) - 0.0256 \quad (4.11)$$

$$Labradorite\ P2 : Corrected\ Ratio = (1.1291 \times Measured\ Ratio) - 0.0388 \quad (4.12)$$

Table A.3 in Appendix A shows the corrected stage temperatures (calculated using Equation 4.7) and the corrected Stokes temperatures (calculated using Equation 4.6 and corrected using Equations 4.8 – 4.12). While these corrected Stokes temperatures are not a perfect match to the stage temperature, which is believed to be the temperature of the sample, they are much more closely aligned than their uncorrected counterparts.

For quartz the average difference between the stage temperature and the corrected Stokes temperature is 7.4 °C, with the smallest difference being 0.1 °C and the largest being 28.9 °C. This is greatly improved from the uncorrected Stokes temperatures presented in Table A.2 in Appendix A which showed an average difference of 43.1 °C for quartz.

The corrected Stokes temperatures calculated from the two olivine peaks show good agreement with one another, with an average discrepancy between them of 3.2 °C (the minimum discrepancy is 0.1 °C while the maximum is 10.5 °C). Comparing the calculated Stokes temperatures to the stage temperatures, P1 has an average difference of 4.7 °C (minimum of 0.2 °C, maximum of 11.4 °C) and P2 has an average difference of 4.2 °C (minimum of 0.0 °C, maximum of 9.4 °C). Again, this is greatly improved from the uncorrected Stokes temperatures which showed an average difference of 62.4 °C for P1 and 65.3 for P2.

The two labradorite peaks show much less agreement in their calculated Stokes temperatures with an average discrepancy of 16.7 °C (the minimum discrepancy is 0.3 °C while the maximum is 48.8 °C). Comparing the calculated Stokes temperatures to the stage temperatures, P1 has an average difference of 20.7 °C (minimum of 1.1 °C, maximum of 58.8 °C) and P2 has an average difference of 6.5 °C (minimum of 0.0 °C, maximum of 23.4 °C). The correction has also improved labradorite Stokes temperatures, which previously showed average differences of 51.6 °C for P1 and 23.7 °C for P2. The labradorite P1 peak has proven to have the most inconsistency between

the stage temperatures and the Stokes temperatures and this is likely due to the data having the lowest signal-to-noise ratio of all the peaks discussed in this chapter.

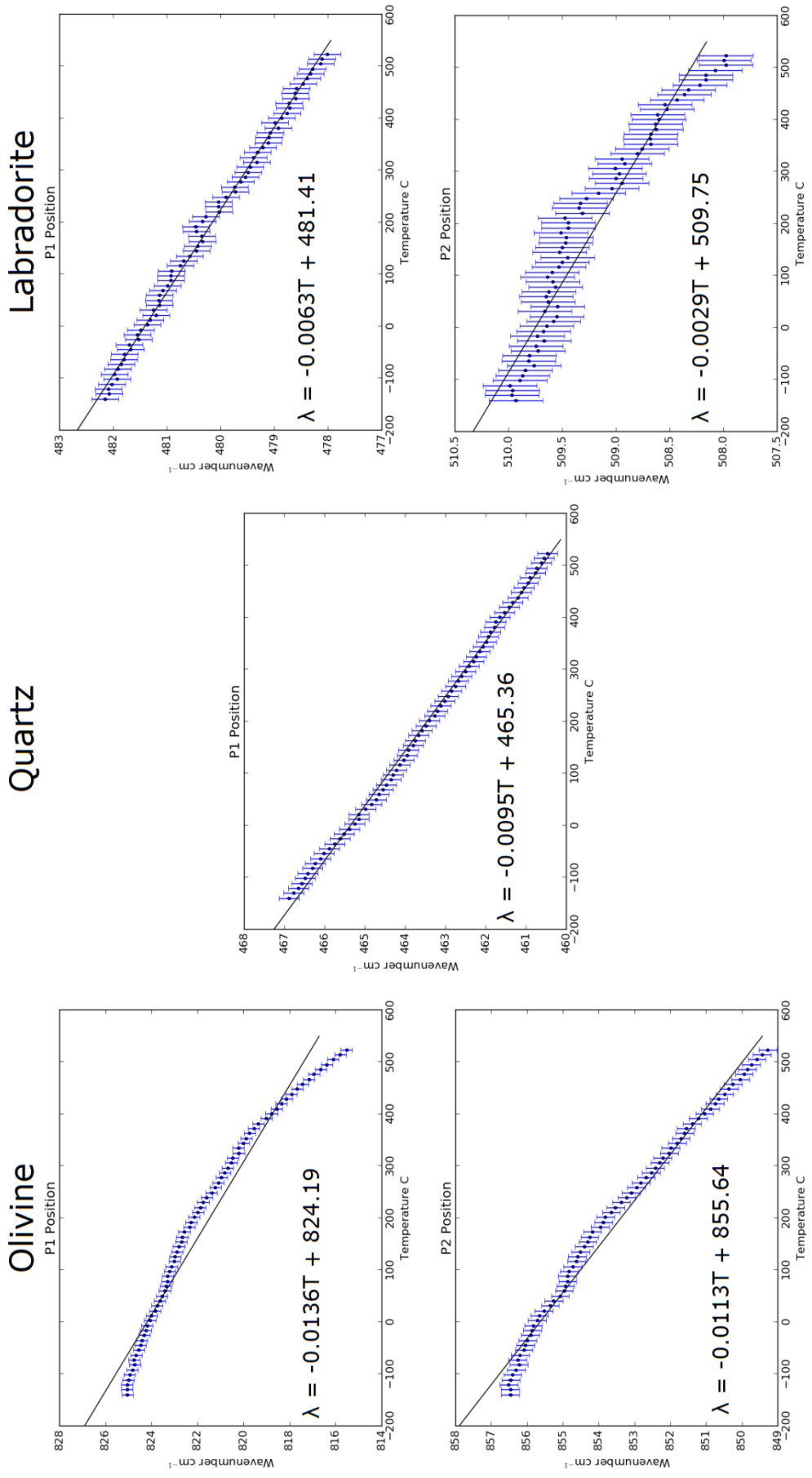


Figure 4.17: Corrected temperature versus peak position (including linear equations of best fit) for the main peaks in each of the mineral samples.

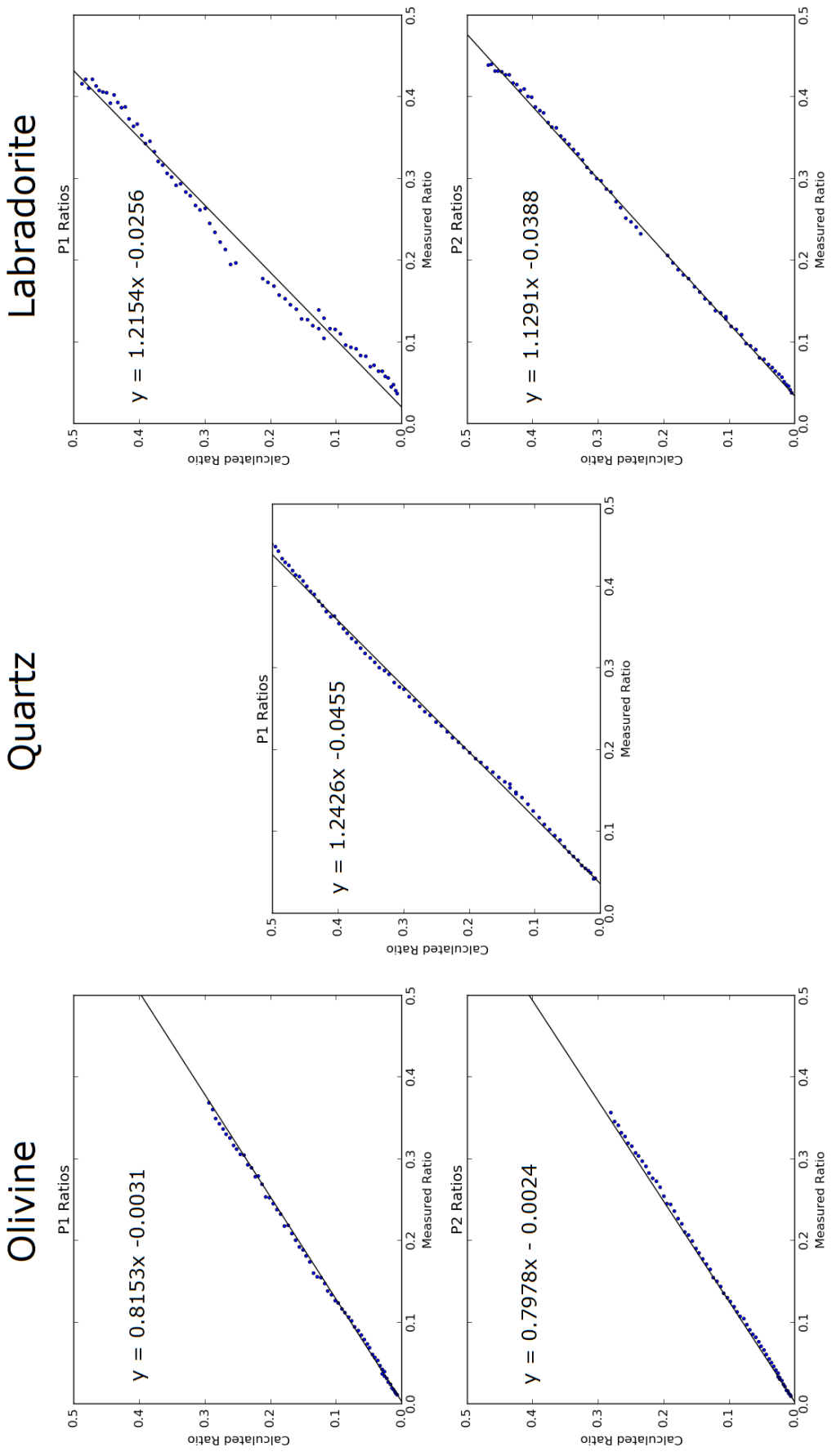


Figure 4.18: Measured Stokes/anti-Stokes ratio versus Stokes/anti-Stokes ratio (including linear equations of best fit) for the main peaks in each of the mineral samples. If no correction were necessary, the slope would be equal to "1.0".

Although the correction method performed here has done a great deal to correct the problem, it has clearly not been able to fully correct the errors in the Stokes temperatures. However, despite the considerable improvement, it would appear that without a good knowledge of the Raman spectrometer's IRF it is not possible to fully compensate for errors in the intensity measurements that lead to miscalculation of the Stokes/anti-Stokes ratio. Despite its shortcomings, without the IRF, this is the best correction that can be attained for this work and as such will be used to determine the temperature of the samples investigated for the remainder of this chapter.

4.5 Sample Temperature as a Function of Sample Size

The temperature experiments detailed so far in this chapter have focused on understanding how the Raman spectrum of the selected mineral samples is altered by the sample temperature. However, as mentioned in Section 4.1, Raman spectroscopy can be destructive if too much laser power is directed at a sample. This destruction can often be seen as burning, resulting in thermal decomposition of the sample and its Raman spectrum (Figure 4.1 and Figure 4.19).

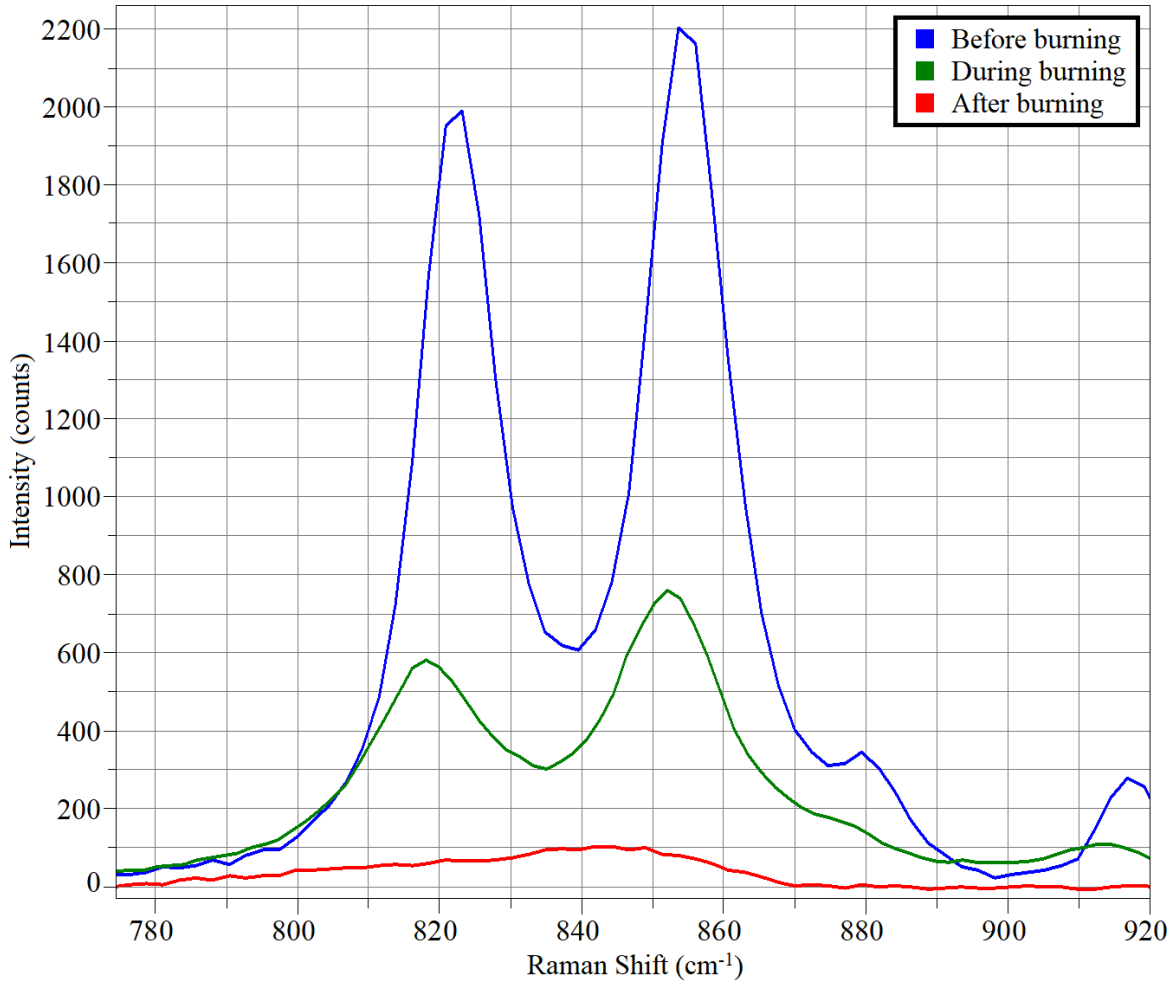


Figure 4.19: The spectrum of olivine as the sample is undergoing thermal decomposition as a result of laser heating.

Figure 4.19 shows the Raman spectra for powdered olivine before, during, and after having been burnt by the laser (6.29 mW of power at the objective lens). However, none of the (bulk) samples in the experiments presented in this chapter have suffered from burning despite being subjected to the same amount of laser power as the

sample in Figure 4.19, and being at temperatures in excess of 500 °C. This inconsistency could be attributed to the sample in Figure 4.19 being a powder with a grain size of approximately 10 microns, while the samples used in the temperature experiments were millimetre sized gemstones. Therefore, grain size may be a factor in determining the amount of laser heating that occurs in a given sample.

4.5.1 Methodology

In order to test this hypothesis, multiple individual particles of each of the minerals were subjected to the same amount of laser power and their temperatures determined using the Stokes/anti-Stokes ratios of their spectra (using the correction formula determined above).

Each particle was placed on a Formvar™ film suspended by a support structure. Formvar™ is the commonly referred to tradename of several polyvinyl formal resins that are used as support films for electron microscopy. The reasoning for such a selection was that Formvar™ films can be made with thicknesses of tens of nanometres. This minimises the amount of heat lost from the sample through conduction, compared to placing the sample on a standard glass microscope slide, or the Raman stage itself. Formvar™ also has the added benefit of not being Raman active and therefore does not interfere with the Raman spectrum of the sample. Testing of the Formvar™ films in the Raman spectrometer also showed that it was not possible to burn the film at full power with any of the lasers.

After a particle was placed onto a Formvar™ film, it was optically imaged in order to measure its size and to determine that it was in the correct position on the film (i.e. only in contact with the film and not the support structure). Figure 4.20 is an example of these optical images and shows that the particle is isolated.

Determining the size of the particles can be difficult as they are often irregular in shape, and the quality of the optical images on the Raman spectrometer is poor due to a small depth-of-focus. This meant that it was not possible to determine an accurate value for the volume of each particle; therefore, the cross-sectional area was used to compare the size of the grains. The cross-sectional area of each grain was determined by dividing a grain into multiple triangles and summing the area of those triangles (Figure 4.21).

Raman spectra (including Stokes and anti-Stokes) were then gathered from each of the particles. Three spectra were obtained at each of three points across the particles, giving a total of nine spectra per particle. These spectra were then averaged before being fit using the same method as that detailed in Section 4.3. This determined the intensities of each of the main peaks for the minerals in both the Stokes and anti-Stokes regions. These intensities could then be used to calculate the Stokes/anti-Stokes ratios for use in Equation 4.6. However, before using the ratios to calculate the Stokes temperatures they were first corrected using the relevant equation from Section 4.4.4.1 (Equations 4.8 – 4.12).

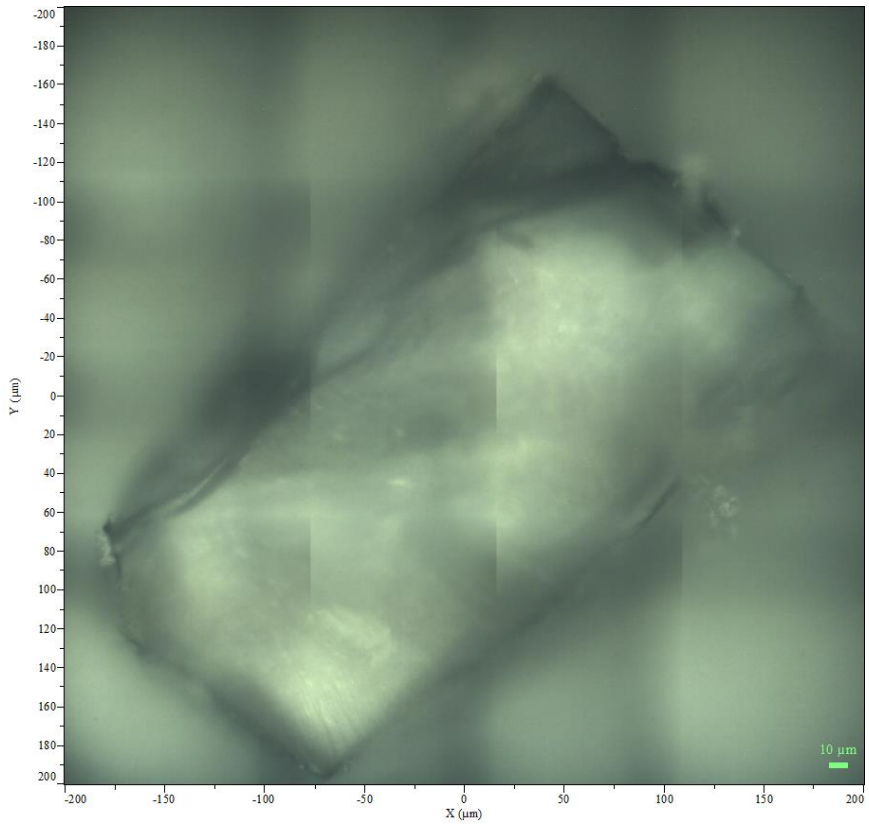


Figure 4.20: An example optical image of an isolated particle from the grain size experiment taken using the microscope on the Raman spectrometer.

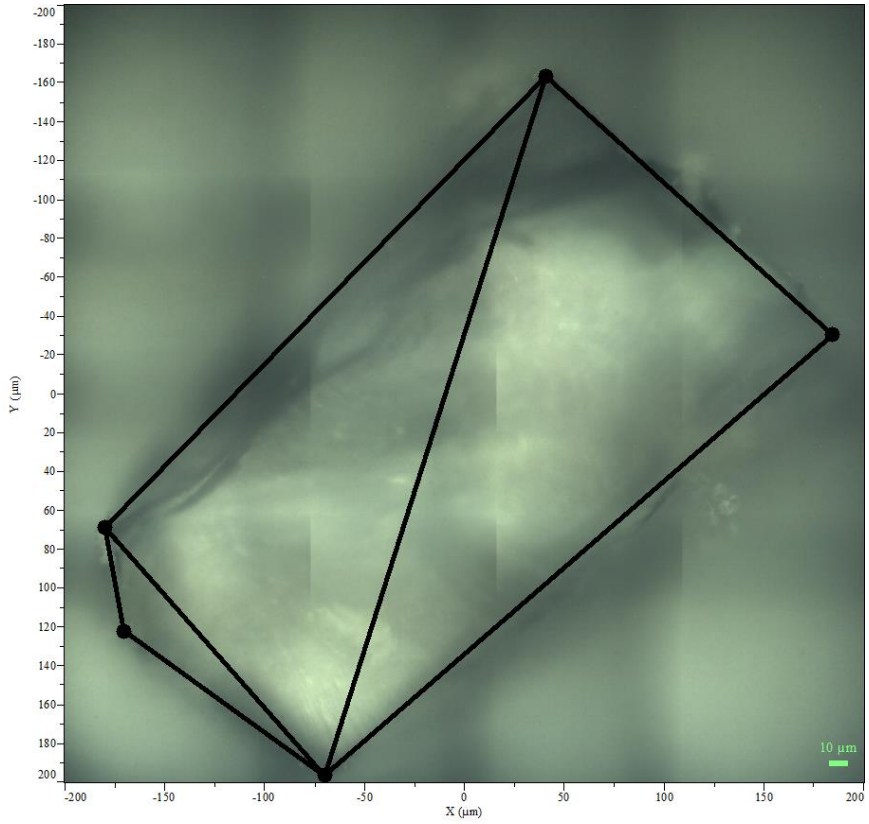


Figure 4.21: An example of how the cross sectional area of this particle was determined by dividing the grain's area into triangles before summing the areas of those triangles.

4.5.2 Results

Figure 4.22 – Figure 4.26 show the plots of the cross-sectional area against the Stokes temperatures of each of the main peaks in particles of quartz, olivine, and labradorite. None of these plots show any trend between the grain size and the Stokes temperature implying that laser heating is not dependent on the size of the particle. While this may be true, there are several reasons to doubt the validity of these data.

One reason is that the variations in the temperature for these particles may be so small that the correction performed to the Stokes calculation is not sufficient to allow the detection of these changes. In order to determine if this is the case, the IRF (discussed in Section 4.4.4.1) would be needed and the data re-analysed.

Another reason is that the particles used here are too large. The Stokes temperatures presented here are all less than 110 °C, far below the temperatures needed to thermally decompose these minerals, which has been shown to be possible in Section 4.1. The spot size of the laser used in this experiment was 1.0 microns in diameter making it three orders of magnitude smaller than the smallest particle in this experiment, in comparison to one order of magnitude smaller for the 'burnt' grains shown in Section 4.1. It may be that the size of the particles used here is sufficient to allow the dissipation of any laser heating that would result in 'burning' of the sample.

Possibly the most obvious problem with this dataset is the size measurement. As explained in Section 4.5.1, determining the size of these particles can be difficult as they are irregular in shape and no three-dimensional information is known about them. Therefore, only the very crude measurement of cross-sectional area has been determined, which is not sufficient to gain any meaningful concept of their sizes in terms of surface area or volume. This essentially invalidates the Y-axis on Figure 4.22 – Figure 4.26 as a measure of the size of the particles.

Overall, the sample size experiment has failed to produce any meaningful results. It has, however, provided the opportunity to test the practicalities of performing the experiment. In that regard, a surface upon which to mount the grains for analysis that does not interfere with the Raman spectra has been determined. The processes used to analyse the data have also been put into place and can be readily used to interpret new data from other grains or indeed, re-analyse these data should the IRF become known.

Ideally, smaller grains, which are of the nanometre to micron scale, would be used in any repeat of this experiment. This would also provide the added benefit of being able to approximate their shape as spherical in order to gain values for the grain's volume and surface area which would be more meaningful for comparison than the cross sectional area. This size of grain could be achieved through the use of ball-milling of the mineral samples to obtain a range of sizes. However, a complication to grains of this size would be the picking of an individual grain for placement on the Formvar™ support film.

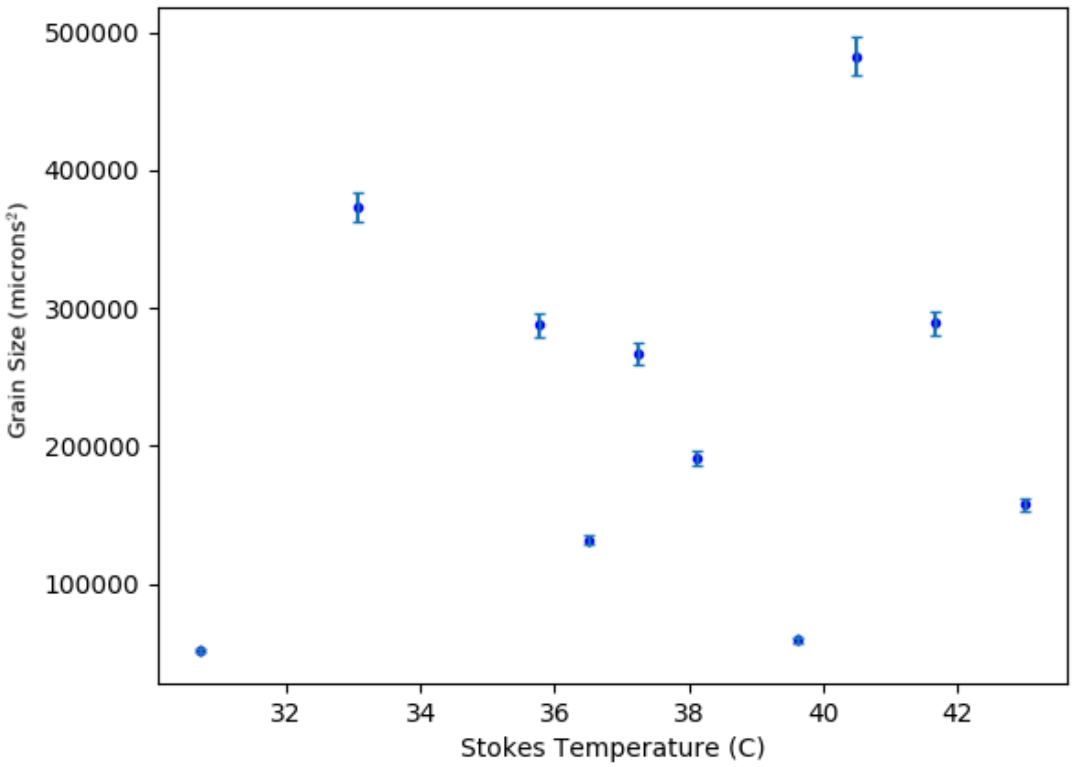


Figure 4.22: Cross sectional area versus P1 Stokes temperature for quartz grains.

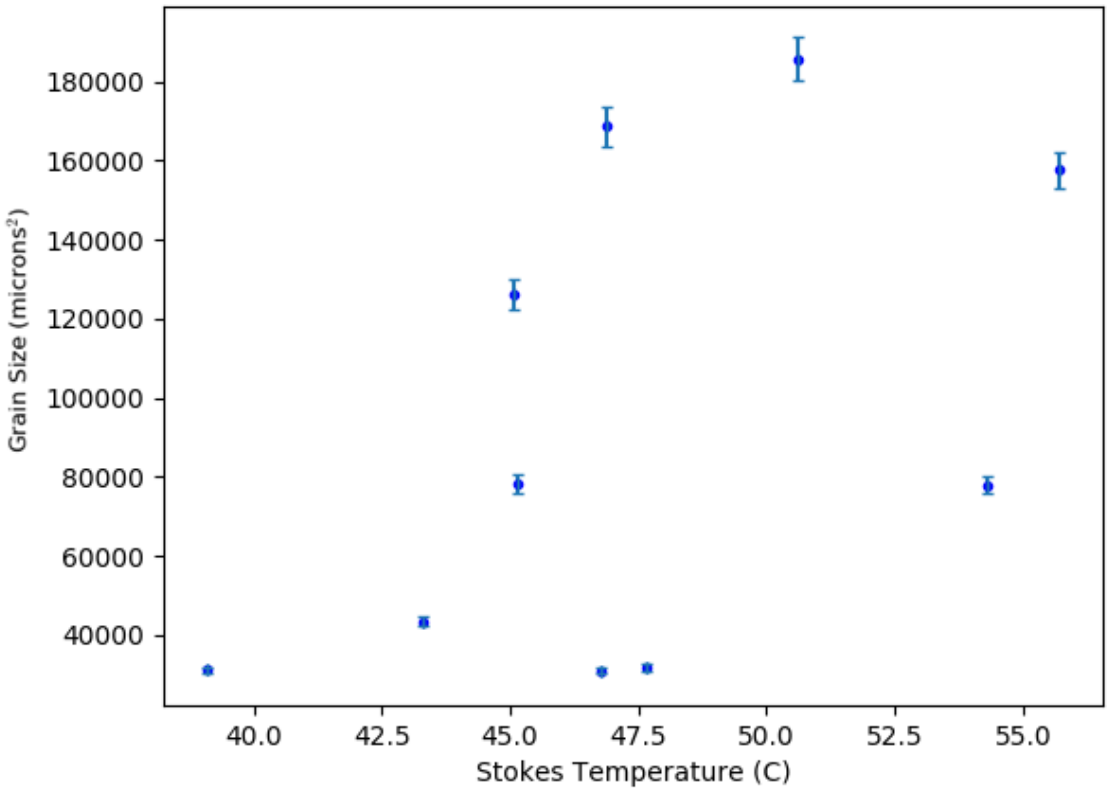


Figure 4.23: Cross sectional area versus P1 Stokes temperature for olivine grains.

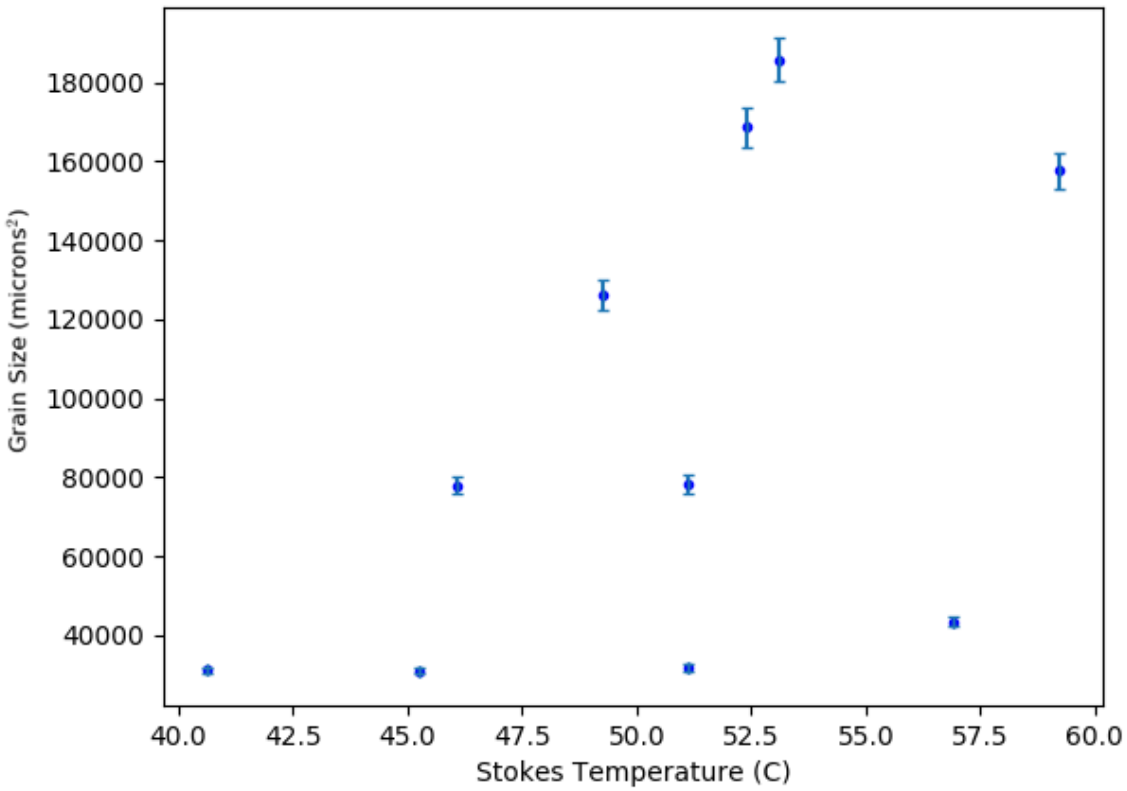


Figure 4.24: Cross sectional area versus P2 Stokes temperature for olivine grains.

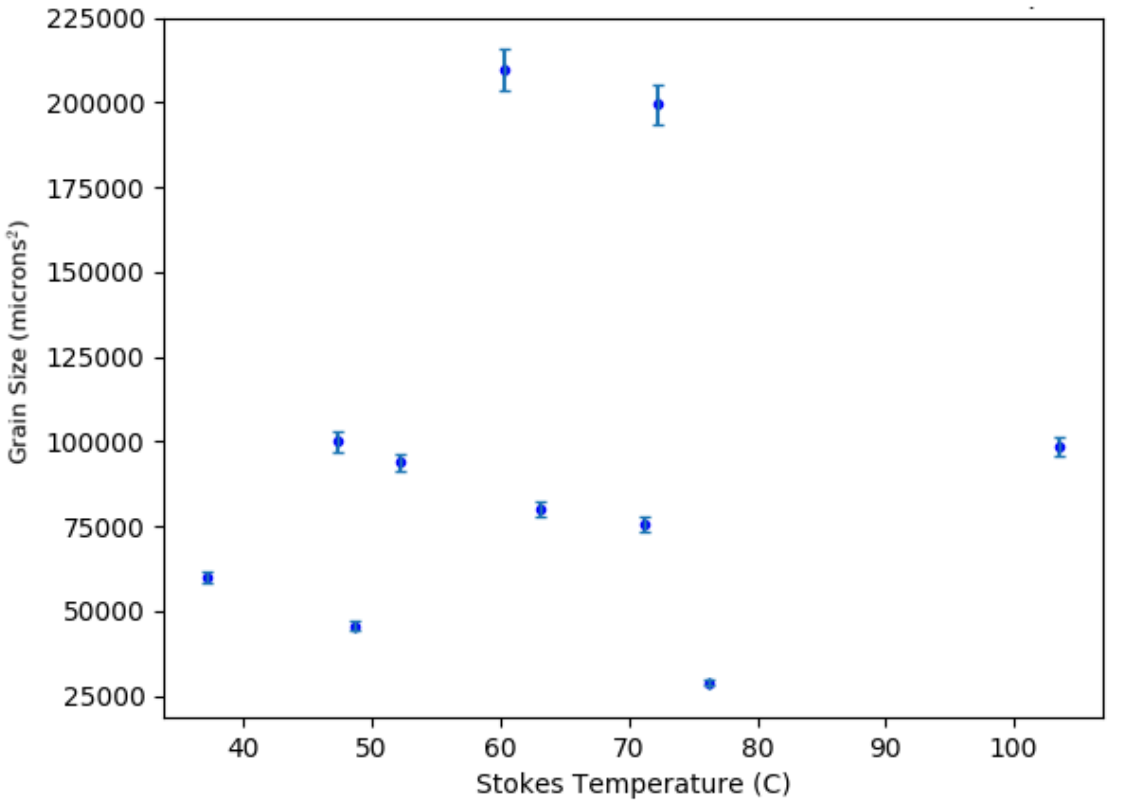


Figure 4.25: Cross sectional area versus P1 Stokes temperature for labradorite grains.

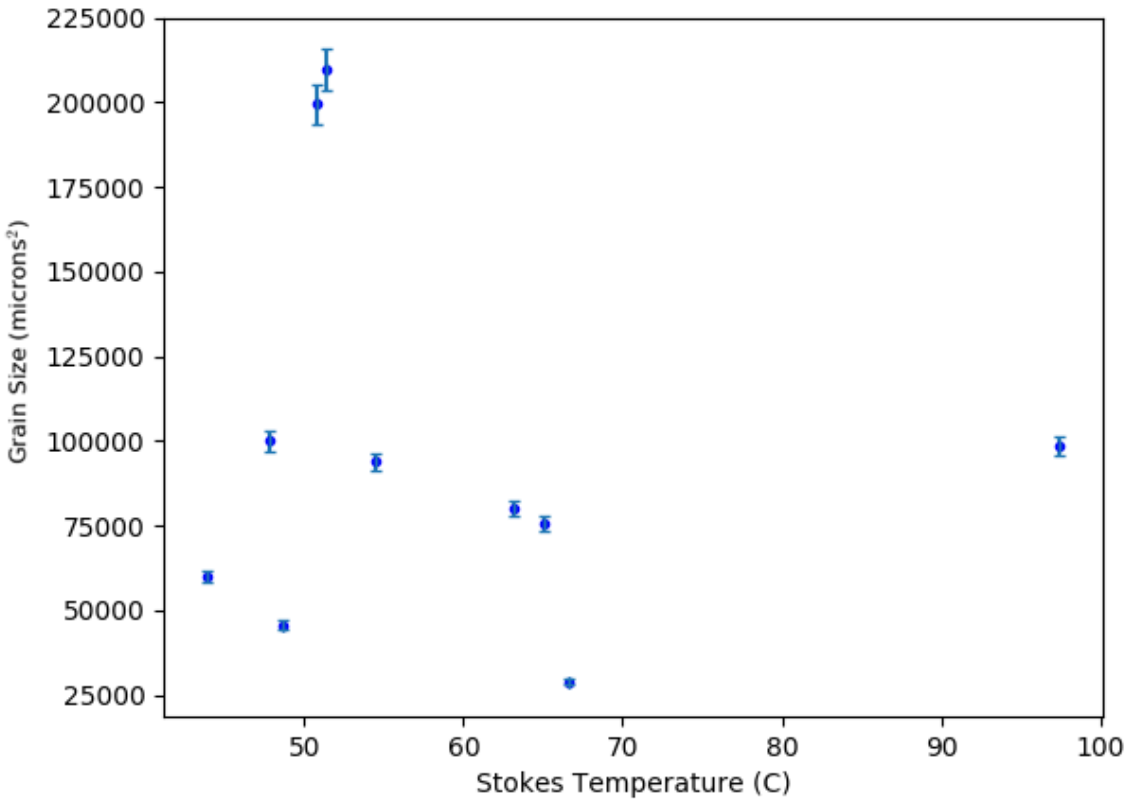


Figure 4.26: Cross sectional area versus P2 Stokes temperature for labradorite grains.

4.6 Summary

The experiments detailed in Section 4.4.1 have shown that it is definitely possible to use the peak position of a Raman band as a thermometer. However, in order to determine the temperature of a sample from a single spectrum, an extensive calibration of peak position as a function of sample temperature must first be performed for that peak.

This can prove difficult for samples where the positions of the peaks vary depending on composition (such as the P1 and P2 peaks of olivine varying positions based on the ratio of Mg/Fe in the sample). In these cases, care must be taken to calibrate the peak position using a calibration specimen with the same composition as the sample under investigation. As shown in Section 4.4.1.1, Raman spectra taken from the same sample of olivine at a variety of temperatures generates incorrect compositional data. Therefore, not using the correct calibration specimen would result in the alterations in peak position due to temperature and the alterations due to compositions becoming intertwined with no way of disentangling them.

These experiments have yielded temperature values for the samples using the Stokes/anti-Stokes method, but these values should only be regarded as approximate. Due to a lack of knowledge of the Raman spectrometer's wavelength-dependent instrument response function, an alternative calibration was devised. While this calibration certainly improved the accuracy of the data, it is not sufficient to fully correct for the lack of an instrument response function and is only valid for the specific peaks that were investigated.

The procedures for conducting an experiment to determine how the size of a mineral grain affects the amount of laser heating generated in a sample have been established. However, the data showed no trend between the size of the grain and the laser heating of the sample for the grains investigated. Several reasons for this have been discussed but in essence, it is likely that the proper calibration function and smaller grains are needed to produce any meaningful results.

Chapter 5 - Raman Spectrometry as a Shock Barometer I

5.1 Introduction

As discussed in Chapter 2, impact events are ubiquitous throughout the Solar System, frequently occurring on the surfaces of rocky bodies such as Mars. The European Space Agency (ESA) *ExoMars* rover *Rosalind Franklin* will land on the surface of Mars in 2021 and will be carrying a Raman spectrometer [136, 137] as a part of its scientific instrumentation payload.

Mars' surface, including the selected landing site within Oxia Planum, has been bombarded with impacts [181], making it likely that the material being analysed by *Rosalind Franklin* will have been previously impacted and therefore been subjected to extreme shock pressures.

This chapter, as well as Chapter 6, investigates if Raman spectroscopy can be used to infer details of the shock history of a mineral sample. This was done by taking mineral samples of a known composition and subjecting them to differing shock pressures using the light gas gun (LGG) before analysing them with a Raman spectrometer. This chapter will focus on presenting the dataset, while Chapter 6 will discuss the analysis of these data and the trends that were found.

5.2 Methodology

The three minerals chosen for this study were quartz, olivine, and labradorite (Section 4.2 describes the reasoning behind this selection), all of which can be obtained in the form of gem quality stones in large numbers. All gemstones were inspected using a Leica MZ16 optical microscope to determine if there were any cracks on the surface that would indicate that a particular gemstone is more likely to fracture during the impact experiment (Figure 5.1). If an imperfection was discovered, the gemstone was removed from the batch of potential targets.

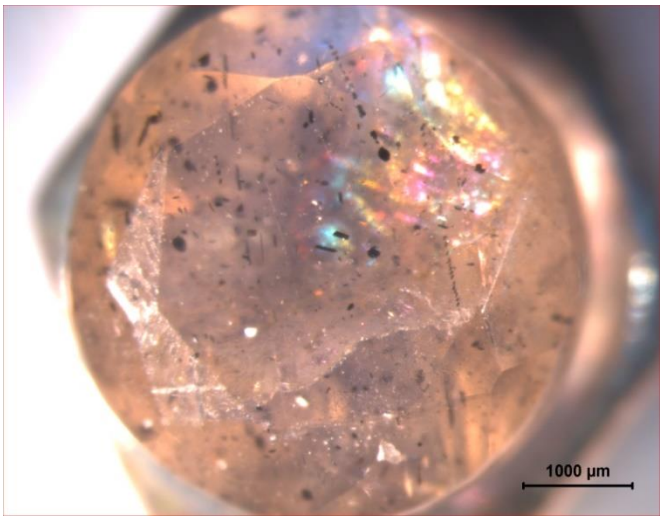


Figure 5.1: Optical microscope image (x63 magnification) of a labradorite gemstone with a crack running through the surface. The black flecks within the gemstone are inclusions of black magnetite. This gemstone was rejected as a potential target.

After the selection process, the target gemstone is mounted onto an aluminium target plate using Leit C-plast carbon putty (Figure 5.2). Leit C-plast is a conductive paste and is primarily used for mounting SEM samples due to its low outgassing properties which makes it ideal for mounting awkwardly shaped targets in the vacuum chamber of the light gas gun. Care is taken to leave the front surface of the gemstone as parallel to the target plate as possible, ensuring that the projectile will strike the target perpendicular to the surface.



Figure 5.2 A quartz gemstone mounted to an aluminium target plate using Leit C-plast.

Before firing onto the target, the target is first analysed in the Raman spectrometer (Section 3.1). A map is taken across the surface of the gemstone in order to obtain baseline values for the peak positions and full-width half-maximum of the relevant peaks of the sample (Figure 5.3). This is done over a wide area to ensure that the sample is uniform across its surface. These baseline spectra are used to determine if any alteration to the Raman spectrum of the sample has taken place after impact.

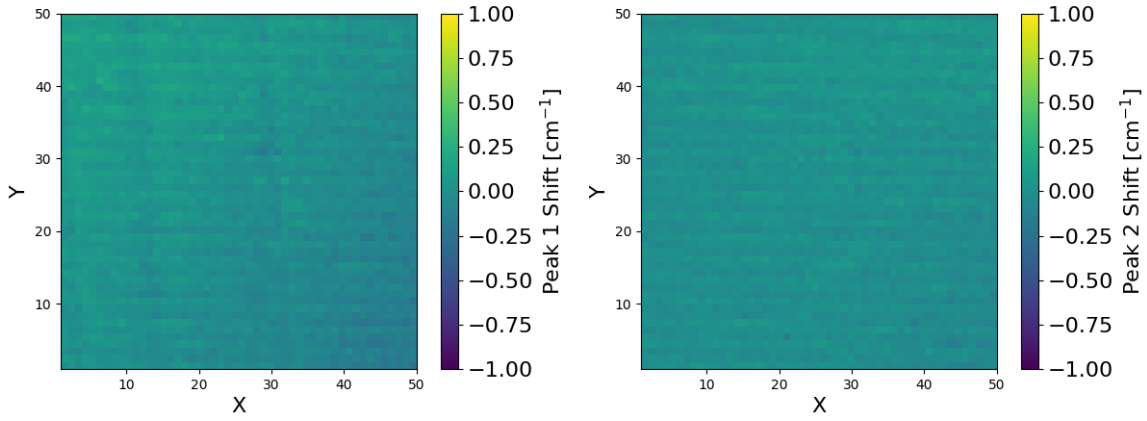


Figure 5.3: Baseline peak shift maps for P1 and P2 of olivine.

With the baseline measurement taken, the target was placed in the target chamber of the LGG and impacted with a buckshot of 50 micron diameter molybdenum spheres at the desired speed (an in-depth explanation of the firing procedure of the LGG can be found in Section 3.2). A buckshot of small particles is used in order to produce a number of small impacts on the surface of the target, thereby increasing the likelihood of finding a suitable crater for analysis. Molybdenum was chosen as the projectile material because it is obtainable as well-formed spheres of high purity, has a high melting point and does not have a Raman signature.

After the shot, the target is retrieved from the target chamber of the LGG and placed back into the Raman spectrometer. Multiple optical images are taken using the Raman's motorised stage to vary the position of the sample before stitching these images together into a montage of the surface of the target (Figure 5.4). This montage is then examined in order to identify isolated craters on the target. This was desirable, as two craters overlapping means that two separate shock waves have propagated through the material in that area, which complicates the analysis. One of the isolated craters was then selected for Raman mapping.

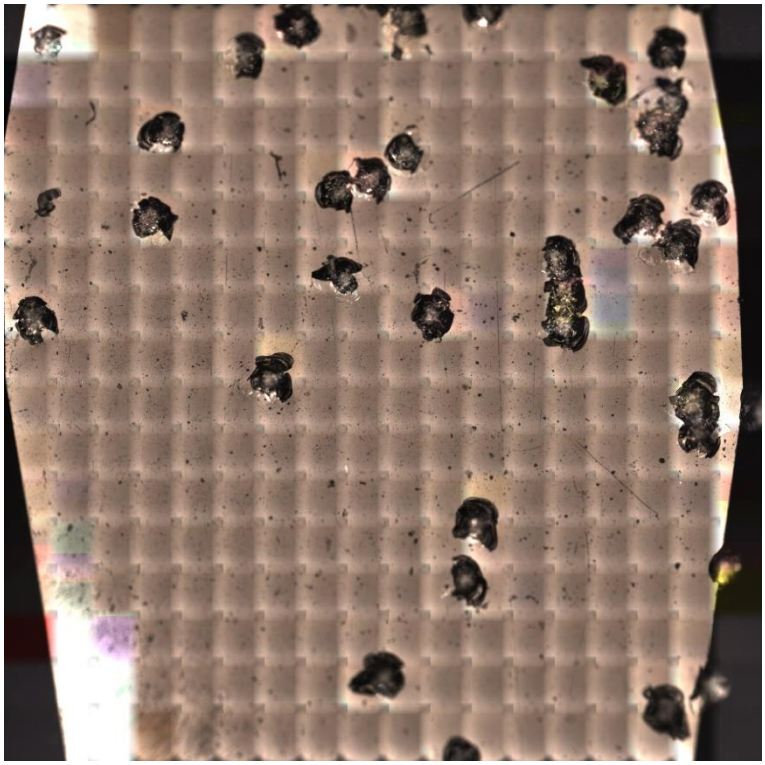


Figure 5.4: A 8000 x 8000 micron montage image of the quartz gemstone target from shot G151014#1 (V = 1.35 km s^{-1})

The Raman spectrometer is then used to produce a 50 x 50 pixel spectral map of the crater taking care to ensure that the map covers an equal physical distance in the X and Y direction; though this distance varied between samples, as the craters range in size considerably. From here on, each individual spectrum in the Raman map will be referred to as a pixel, as each spectrum is later used to create a single pixel on the maps that are presented later in this chapter.

After mapping, the data were analysed to determine the maximum intensity value and an estimate for the maximum shift of the main peaks of the sample. These values

were input into the automatic fitting script[1] and used as upper limits to ensure a good fit. The maximum intensity value is used to filter out cosmic ray peaks from being interpreted as Raman peaks, as these typically saturate the CCD and present a very large intensity value. The maximum peak shift value is used to prevent the script from fitting to any noisy data that are near the peak, instead of to the peak itself. This is done in conjunction with a user input initial un-shocked peak position that is extracted from the pre-shot map. This allows the magnitude of the shift to be calculated for each pixel.

Once the data were fitted, they were then plotted using another script. This second script plots a variety of parameters onto colour maps. The script generates a colour map for the intensity, shift in peak-position, and full-width half-maximum (FWHM) of each fitted peak. If there were two peaks being analysed for a sample (which is the case for the olivine and labradorite samples), then the script also plotted the separation of these peaks. Finally, it produced a plot of a signal-to-noise metric that is used to determine the reliability of the data for each pixel of the maps.

5.2.1 Accuracy of the Data

In order to keep track of the quality of the fit for each pixel a signal-to-noise metric was devised. The process of calculating this metric begins with finding the residual for each data point in a spectrum. The residual of a data point is the difference between the real data point (from our Raman map) and the predicted data point (from our fitted line). This means the residual of a data point is essentially the noise at that point (if the assumption is made that the fit is perfect). The standard deviation of these residuals was then calculated and this process repeated for each spectrum in the map.

The standard deviations of the residuals were then normalised by dividing them by the intensity of the peak being analysed (or the average of the peak intensities if two peaks were analysed). Again, this was repeated for every spectrum in the map. The intensity of the peaks was chosen as the normalisation factor as that was the point of interest for this experiment. This creates a signal-to-noise value, σ_{resid} which is then plotted onto a colour map in the same manner as the other plotted parameters. These signal-to-noise maps have been given display limits of 0.0 to 5.0 σ_{resid} and any pixel with a signal-to-noise value of 5.0 or higher will be displayed as the maximum limit. If all data in the map had a high signal-to-noise value then the map will appear flat and not identify any particular pixels of interest. If, however, a pixel has a signal-to-noise value of less than 5.0 it will be evident on the colour map and can then be analysed to determine if it has a signal-to-noise ratio of less than 3.0. If the value is less than 3.0 then the data contained in that pixel position should be disregarded as it is not statistically reliable.

Occasionally the fitting script fails to fit to a spectrum in the Raman map. This can be due to a number of reasons, such as contaminant material on the target, or a poor signal-to-noise ratio. If the script fails to fit, that pixel of the map has its values for peak intensity, FWHM and peak shift set to the mean of the rest of that map. This is done to prevent the plotting script from assigning an exceptionally large scale to the colour map images due to extreme values in the dataset. The signal-to-noise value for

[1] These two scripts were originally written by Dr T. M. Kinnear and further edited by the author.

these pixels is set to 0 meaning that those pixels are effectively noise and should be disregarded.

5.2.2 Intensity Maps

For each mineral a set of images of the impact craters are presented (Figure 5.7 - Figure 5.11, Figure 5.21 - Figure 5.24, and Figure 5.41 - Figure 5.45). These images were taken using the montage function on the Raman spectrometer. Unfortunately, they are of a low quality due to the small depth of focus of the Raman's optical imaging system. It is for that reason that an alternative method of inspecting the 'shape' of the craters was devised. A Raman spectrometer relies on photons being reflected/emitted back towards the objective lens so that they can be directed towards the spectrometer itself. As such, if a sample is out of focus, or its surface is not perpendicular to the incident light, the number of photons that travel back through the objective lens will be reduced compared to a perfectly focused and aligned sample.

When investigating a crater, this can be used to our advantage by using the intensity of the Raman spectra at multiple points as a "depth gauge". As the depth of the crater changes, the focus of the Raman system also changes, thereby altering the intensity of the spectra obtained. For a perfect sample, one would expect that all of the spectra taken from points of the same height relative to the microscope objective would have the same intensity values (to some degree of error) while points of differing height would have differing intensity values as the sample becomes more in/out of focus.

As an example, Figure 5.5.A shows the intensity map for the 5.27 km s^{-1} impact onto quartz compared to its optical montage image (Figure 5.5.B). In the Raman intensity map, the shape of the crater can clearly be seen. The unaltered area around the crater has a high intensity; however, the intensity drops off towards the centre of the crater due to the increased depth and, therefore, a decrease in focus.

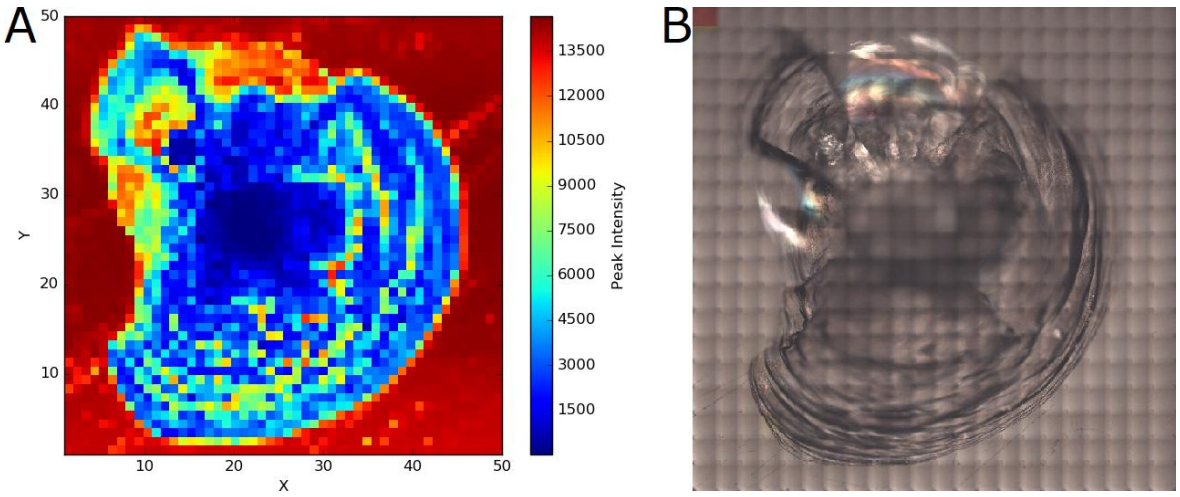


Figure 5.5: G271114#2 where V = 5.27 km s^{-1} (A) Intensity map, (B) Optical microscope image.

5.2.3 Calculating the Peak Shock Pressure

Section 2.1.4 quotes various pressure values as limits for when the structure of minerals can be altered into high-pressure polymorphs. Therefore it is important to be able to calculate the shock pressures involved in impact events in order to determine what processes may occur as a result of that impact. Methods for calculating peak shock pressures can be divided into two categories: numerical modelling and analytical solutions. In this thesis, the analytical method known as the planar impact approximation (PIA) [182] was used to calculate the peak shock pressures attained during the impact experiments.

During the contact and compression phases of an impact, the projectile penetrates the target causing shock waves as the material from both the projectile and target are compressed. The magnitude of these shock waves can be determined by using the Hugoniot equations which are equivalent to the conservation of mass (Equation 5.1), the conservation of momentum (Equation 5.3), and the conservation of energy (Equation 5.3) between the shocked and unshocked material.

$$\rho\left(U - u_p\right) = \rho_0 U \tag{5.1}$$

$$P - P_0 = \rho_0 u_p U \tag{5.2}$$

$$E - E_0 = \frac{1}{2}(P + P_0)\left(\frac{1}{\rho_o} - \frac{1}{\rho}\right) \tag{5.3}$$

Where P is the pressure (Pa), ρ is the density (kg m^{-3}), u_p is the particle velocity behind the shock (m s^{-1}) (unshocked material is assumed to be at rest), U is the shock velocity (m s^{-1}) and E is the internal energy per unit mass (J kg^{-1}). Values for quantities in front of the shock front are denoted by a subscript *0* while values behind the shock front have no subscript.

When these equations are used in conjunction with the equation-of-state, they can be used to determine the pressures involved in an impact. When the equation-of-state is represented as a relation between the shock velocity and the particle velocity (Equation 5.4), it is often a linear relation. This provides a convenient equation-of-state for a material with which to calculate the shock pressures in impact processes, but cannot be used to calculate quantities such as temperature or entropy as it is not a full equation-of-state. This is known as the planar impact approximation.

$$U = c + Su_p \tag{5.4}$$

Where c (m s^{-1}) and S are empirical constants.

When using the planar impact approximation to calculate the peak shock pressure of an impact, the projectile and target are represented as two infinitely wide plates that impact one another at a speed equal to the impact velocity. This arrangement ignores edge effects and therefore provides a one dimensional approximation of the impact. It is possible to use the PIA for oblique impacts by altering the impact velocity U to only represent the vertical component of the impact velocity, $U \sin\theta$, where θ is the angle between the impact direction and the plane of the target.

After first contact, two shock waves propagate away from the projectile-target interface, one traveling into the projectile and one travelling into the target. Both the projectile and target material in the region between these shock waves is raised to the same high pressure. Furthermore, because neither separation nor interpenetration can occur (due to the geometry of the approximation) they must travel at the same particle velocity.

The Hugoniot equations (Equations 5.1 – 5.3), along with the equations-of-state of the projectile and target materials, can then be applied to the individual projectile and target reference frames. As each of the Hugoniot equations in the projectile and target reference frames are linked by the pressure being equal in both materials, the equations allow for a unique solution to be achieved numerically.

When the relation between the shock velocity and the particle velocity is linear for both the projectile and target materials, the algebraic solution for the particle velocity in the target, $u_{t,}$ (Equation 5.5) can be used in conjunction with Equation 5.9 (a combination of Equations 5.2 and 5.4) to obtain a value for the peak shock pressure of the impact.

$$u_t = \frac{-b + \sqrt{b^2 - 4ac}}{2a} \tag{5.5}$$

Where:

$$a = \rho_{0t} S_t - \rho_{op} S_p \tag{5.6}$$

$$b = \rho_{ot} c_t + \rho_{op} c_p + 2\rho_{op} S_p U \tag{5.7}$$

$$c = -\rho_{op} U\left(c_p + S_p U\right) \tag{5.8}$$

$$P = \rho_{0t} u_t (c_t + S_t u_t) \tag{5.9}$$

Where u_t is the particle velocity in the target (m s^{-1}), ρ is the density (kg m^{-3}), U is the shock velocity (m s^{-1}), and c (m s^{-1}) and S are empirical constants. A subscript of p refers to the projectile, while a subscript of t refers to the target.

5.3 Results

The remainder of this chapter will present the data from the impact experiments onto each mineral, while the analysis of these results can be found in Chapter 6.

Several shots were conducted for each mineral. Table 5.1 lists the shot numbers, impact speeds and peak shock pressures (from the planar impact approximation) for each shot.

As discussed in Section 2.1.4, impacts can cause the formation of high pressure polymorphs. Figure 5.6 presents the phase diagrams for quartz and olivine showing the pressures/temperature conditions required for the formation of their respective polymorphs.

For quartz, β-quartz is not found as the pressure increase due to even the slowest impact (2.01 GPa for the 0.373 km s^{-1} shot) is enough to increase the required temperature to above the temperatures that would have been generated during the impact (Figure 5.6). Similarly, β-tridymite and β-cristobalite cannot be formed as the increase in pressure prevents their formation. The conditions required to form coesite (Figure 5.6) are present in all shots up to the 0.910 km s^{-1} shot and perhaps even the

1.35 km s^{-1} shot if the temperature increase was great enough. If the increase in temperature was not sufficient to form coesite in the 1.35 km s^{-1} shot then the conditions were instead sufficient to form stishovite (Figure 5.6), as is the case for the remainder of the quartz shots. However, neither coesite nor stishovite were detected in any of the impact craters.

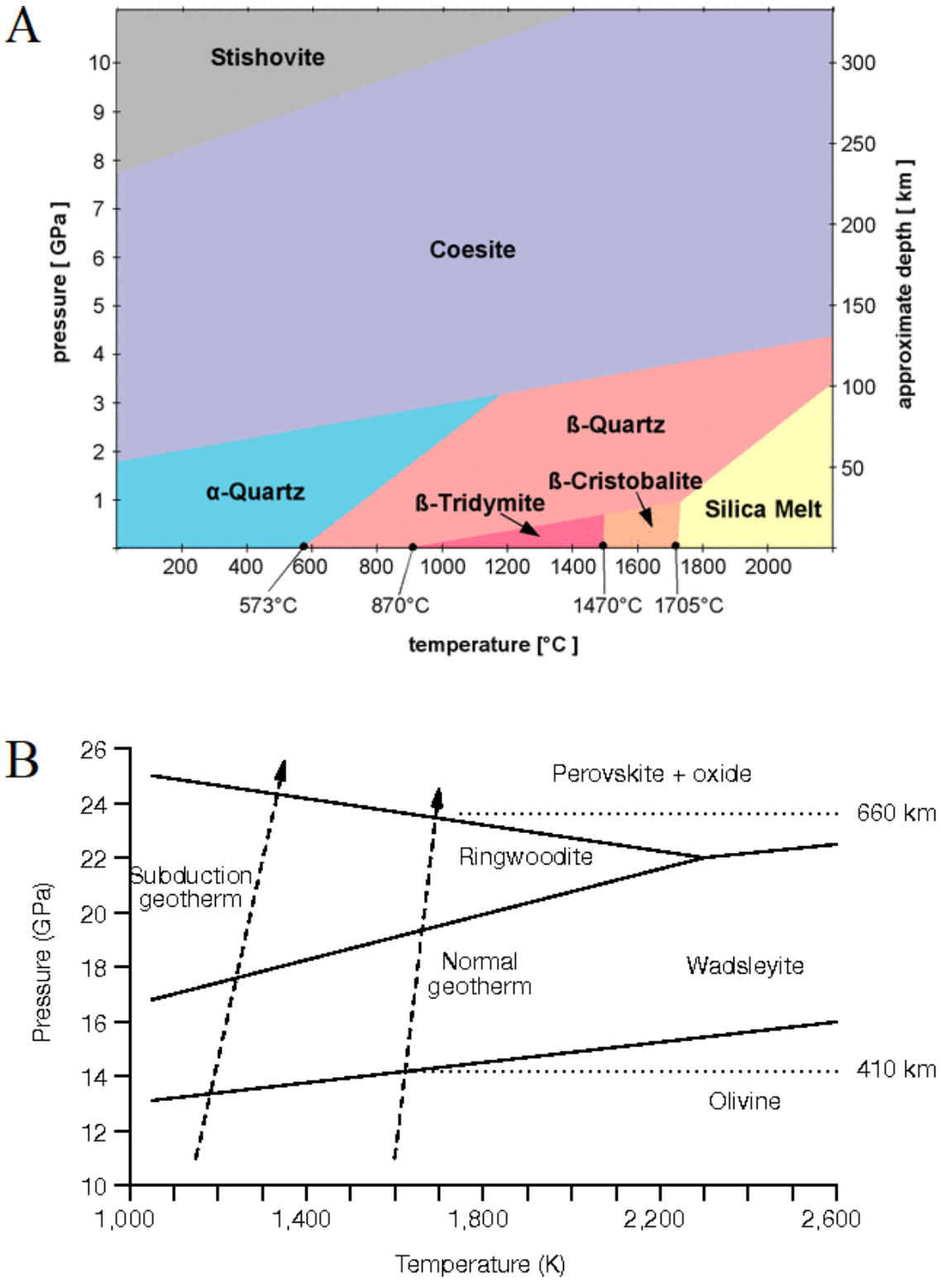


Figure 5.6: The phase diagrams for quartz (A) and olivine (B) [183, 184].

For olivine, depending on the temperature increase during impact, the conditions required to form wadsleyite or ringwoodite (Figure 5.6) were present in the 1.35 km s^{-1} and 1.57 km s^{-1} shots. As of the 2.02 km s^{-1} shot the pressures required to form perovskite were attained (and possibly during the 1.57 km s^{-1} shot if the temperature increase was great enough).

For labradorite, at approximately 28 – 34 GPa plagioclase feldspars, such as labradorite, transform into a diaplectic glass commonly referred to as maskelynite [185]. These pressures are achieved starting with the 2.72 km s^{-1} shot.

While the pressures required to form many of the above polymorphs were attained during some of the shots, none of these minerals were found to be present in the craters for any of the shots presented here. Equation 2.1 tells us that for the impacts described here, the timescale for the formation of the crater is in the order of nanoseconds. Therefore, it is likely that the correct conditions did not persist for a long enough period of time to allow for these polymorphs to form.

Table 5.1: Shot numbers, impact velocities, and peak shock pressures (calculated using the planar impact approximation) for the shots for each mineral.

Quartz Shot Number	**Velocity (km s^{-1})**	**Peak Shock Pressure (GPa)**
S030615#2	0.373	2.01
S241117#1	0.515	2.95
S091014#1	0.910	6.04
G151014#1	1.35	10.23
G051114#3	2.02	18.03
G241014#1	3.32	37.60
G270515#3	4.48	59.67
G271114#2	5.27	77.09
G100615#1	6.40	105.28
Olivine Shot Number	**Velocity (km s^{-1})**	**Peak Shock Pressure (GPa)**
E240614#1	0.576	8.76
E130614#1	0.602	9.18
S260914#1	0.638	9.75
G151014#1	1.35	21.85
G150114#1	1.57	25.85
G051114#3	2.02	34.41
G150114#2	3.03	55.46
G241014#1	3.32	61.98
Labradorite Shot Number	**Velocity (km s^{-1})**	**Peak Shock Pressure (GPa)**
S250915#1	0.291	2.84
S160915#1	0.646	6.70
S300715#1	0.997	10.92
G181217#1	1.36	15.71
G170615#2	1.81	22.22
G050815#1	1.99	25.00
G120815#1	2.72	37.25
G100715#2	3.39	49.88
G160915#1	5.06	86.98

NOTE: quartz is presented first as it only has a single peak of interest and thus the data are simpler to present.

5.3.1 Quartz

As discussed in Section 4.2.2, quartz has a strong, distinctive Raman peak at 465.0 cm^{-1} which represents the O-Si-O bending modes [174]. Four maps are presented for each shot: the peak intensity, the peak shift, the FWHM and $\sigma_{resid.}$

Figure 5.7, Figure 5.8, Figure 5.9, Figure 5.10, and Figure 5.11 show the optical images of the craters analysed for the quartz shot programme. In each Figure the X and Y axes are in micrometres. Note that for the slowest shot of 0.373 km s^{-1}, a "bruise" is formed on the surface rather than a crater. This is because the impact did not have sufficient energy to excavate any target material from the surface and has instead only deformed it.

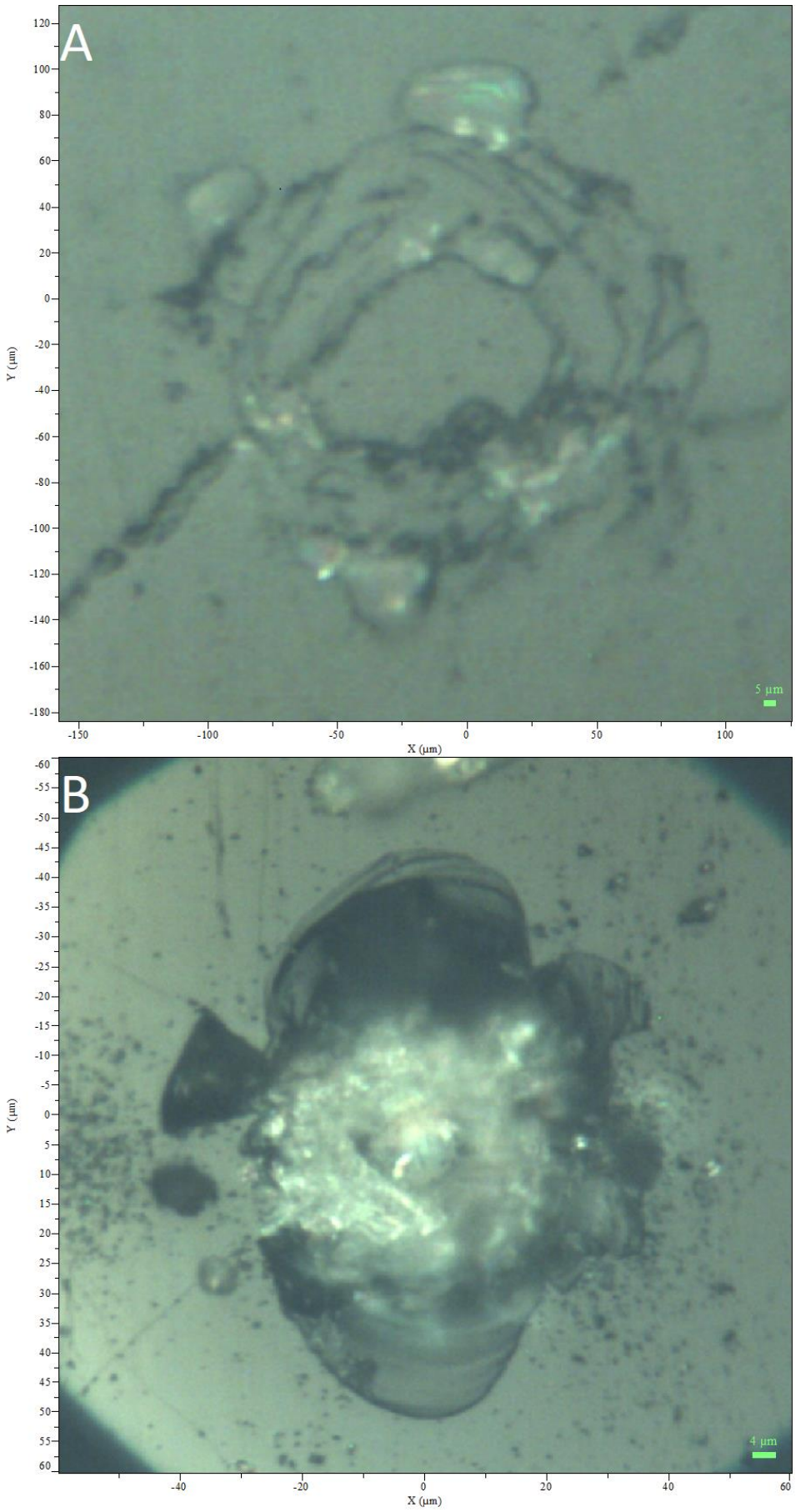


Figure 5.7: Optical montage images (x50 magnification) of the quartz targets (A) S030615#2 where V = 0.373 km s^{-1} and (B) S241117#1 where V = 0.525 km s^{-1}.

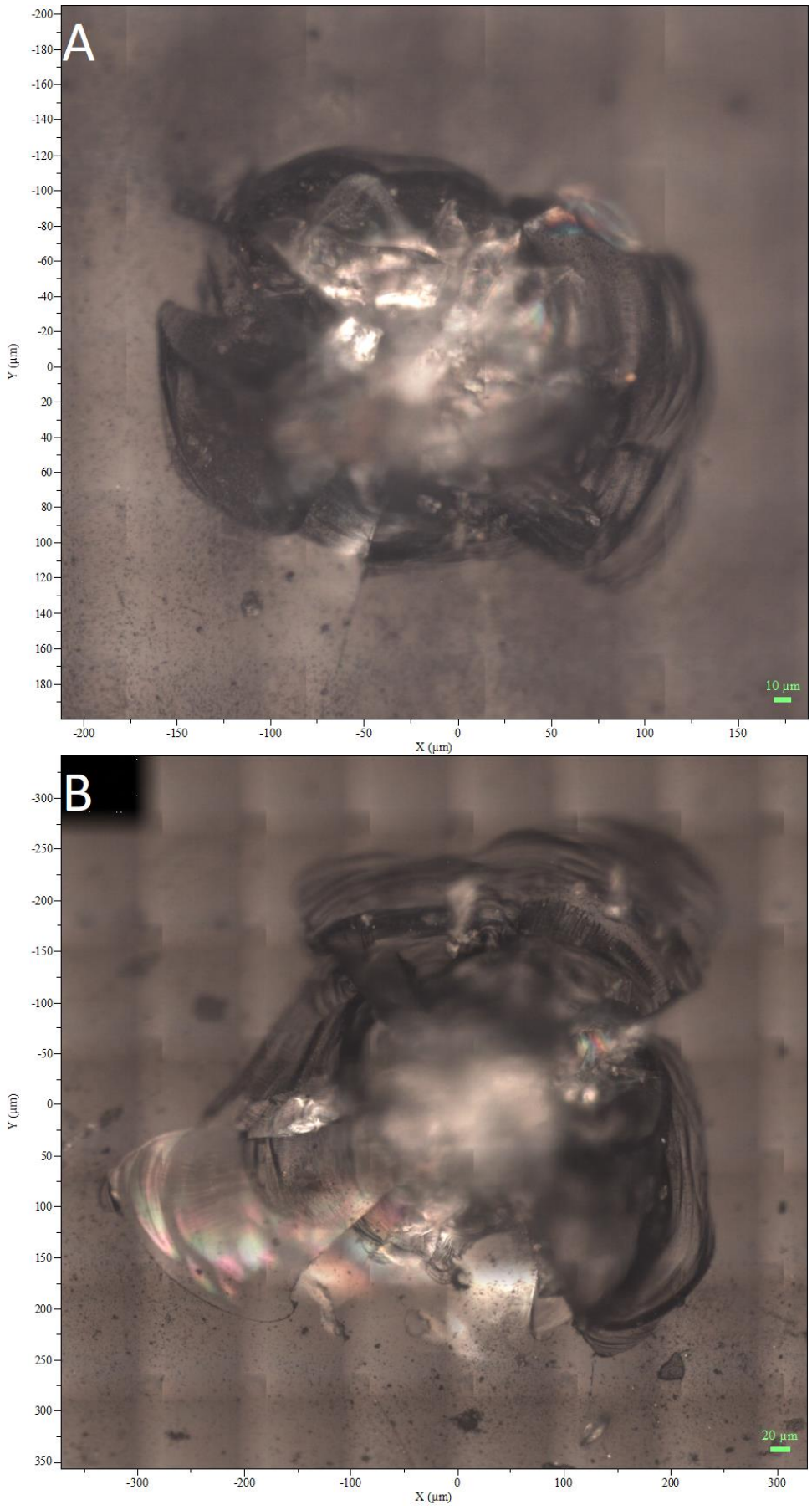


Figure 5.8: Optical montage images (x50 magnification) of the quartz targets (A) S091014#1 where V= 0.910 km s^{-1} and (B) G151014#1 where V = 1.35 km s^{-1}.

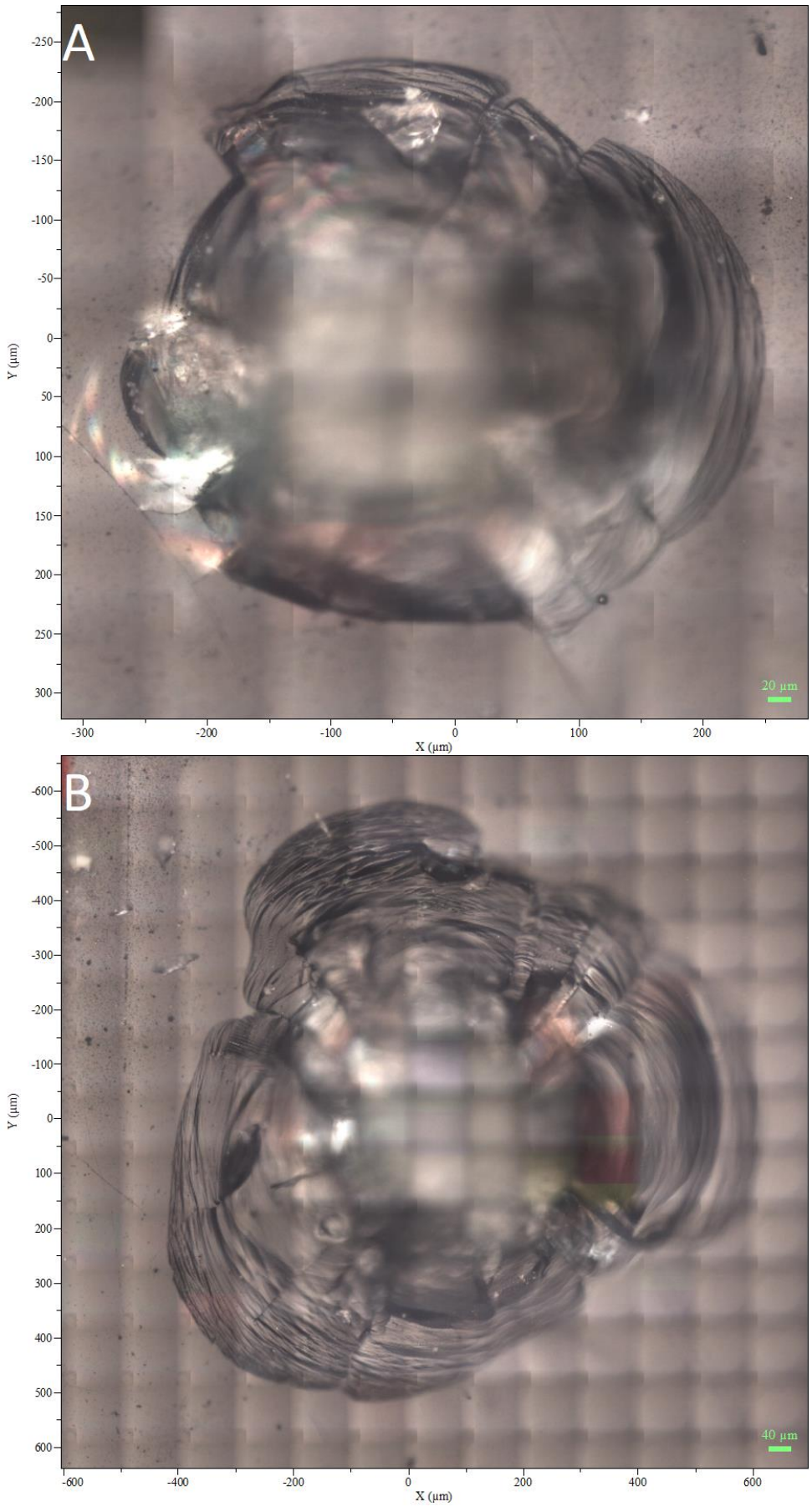


Figure 5.9: Optical montage images (x50 magnification) of the quartz targets (A) G051114#3 where V = 2.02 km s^{-1} and (B) G241014#1 where V = 3.32 km s^{-1}.

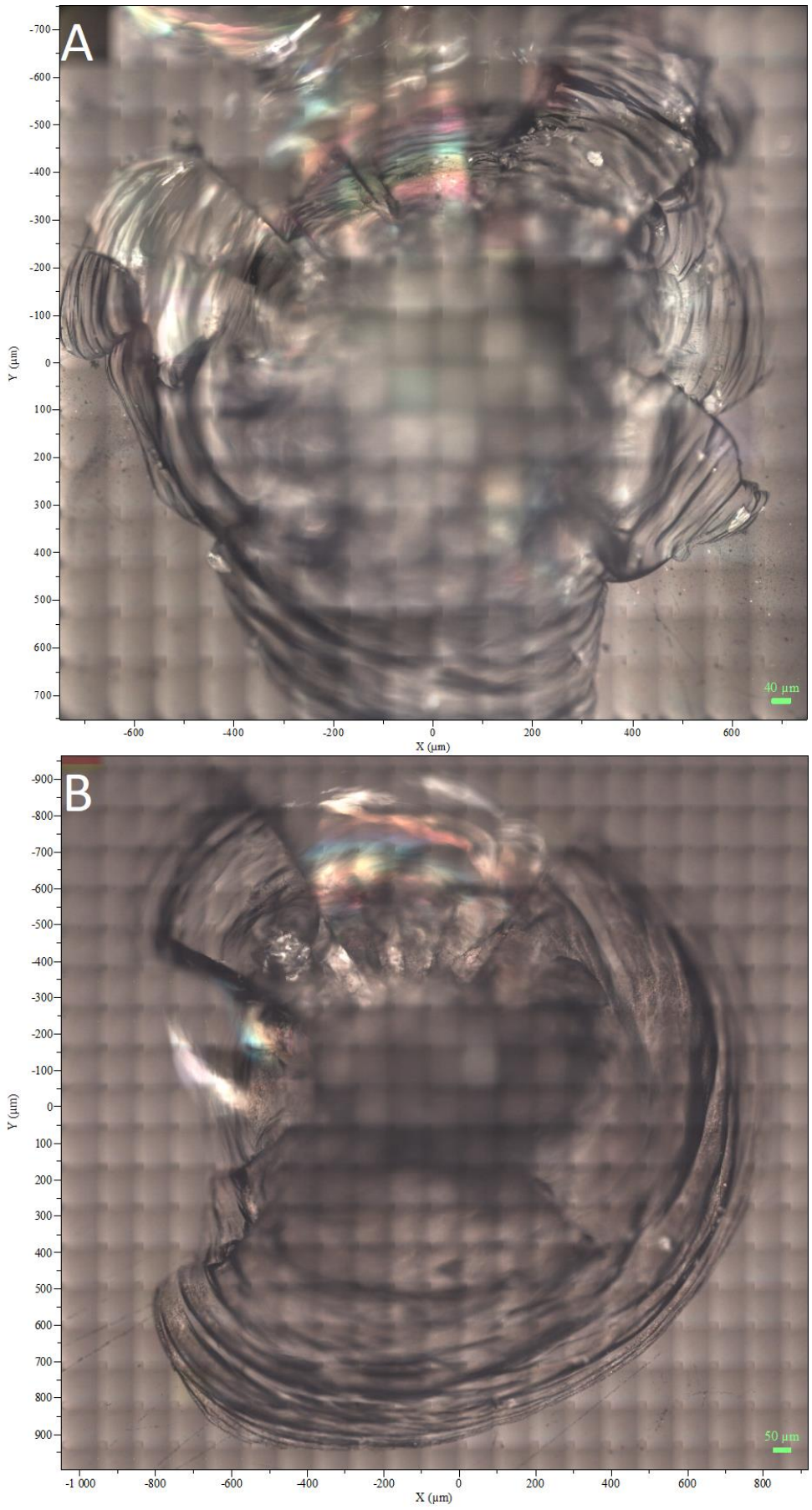


Figure 5.10: Optical montage images (x50 magnification) of the quartz targets (A) G270515#3 where V = 4.48 km s^{-1} and (B) G271114#2 where V = 5.27 km s^{-1}.

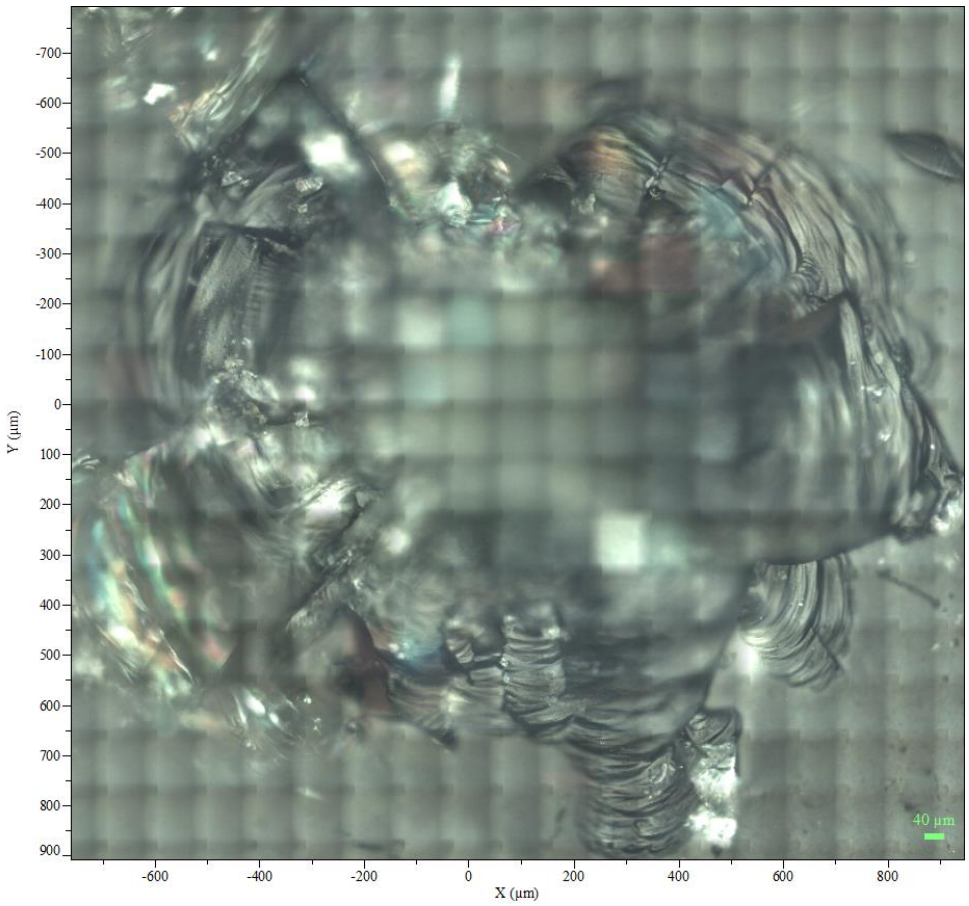


Figure 5.11: Optical montage images (x50 magnification) of the quartz target G100615#1 where V = 6.40 km s^{-1}.

5.3.1.1 Target: Quartz, V = 0.373 km s^{-1}, Shot Number S030615#2

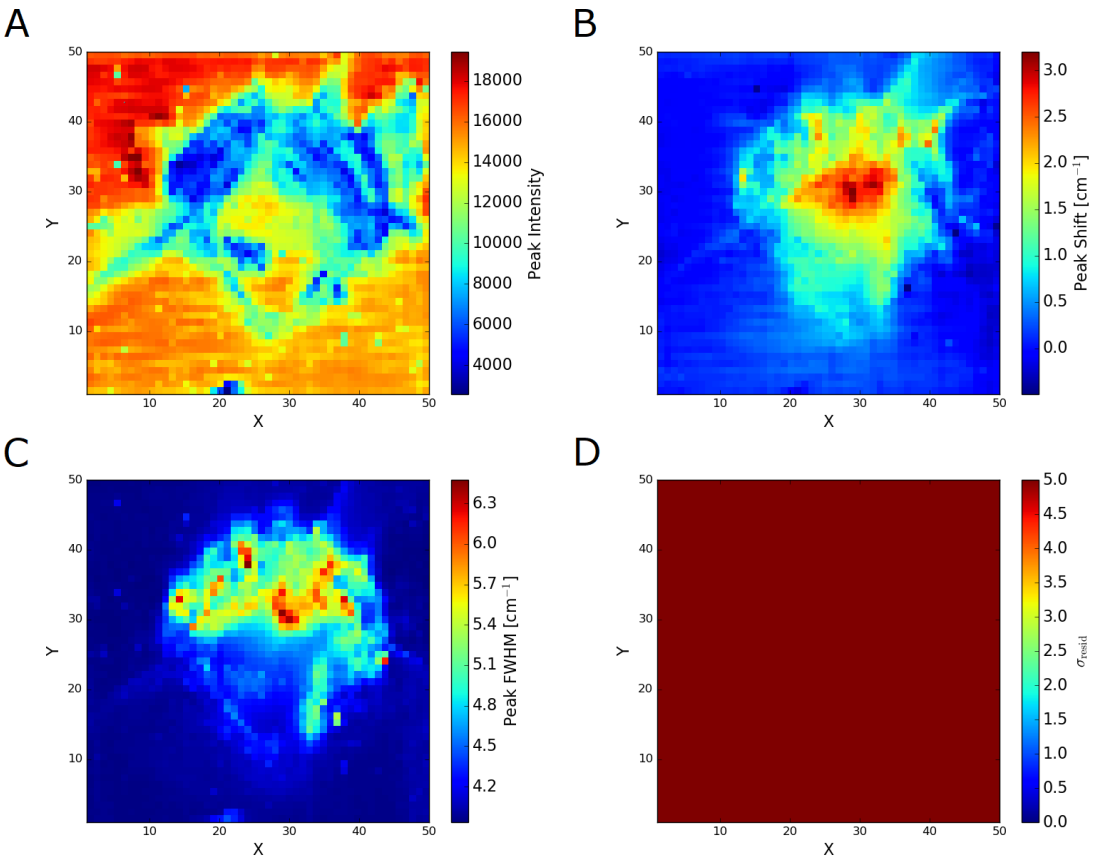


Figure 5.12: Raman map images for the quartz target S030615#2 where V = 0.373 km s^{-1}. (A) Intensity map. (B) Peak shift map. (C) FWHM map. (D) σ_{resid} map.

Figure 5.12.D shows high σ_{resid} values (average σ_{resid} of 46.9) for all data in the map for this shot, meaning there is a good fit to all spectra.

The optical image for this impact (Figure 5.7.A) shows more damage at the top of the crater. This is also shown in the intensity map (Figure 5.12.A), as evidenced by the lower intensity blue regions. This implies that those areas of the crater are deeper, as explained in Section 5.2.2.

Figure 5.12.B shows that outside the crater no peak shift has occurred, but inside the crater the peak shift increases to a maximum of +3.2 cm^{-1} at the centre of the crater. This is a positive shift which represents the peak moving further away from the laser line at 0 cm^{-1}.

The FWHM (Figure 5.12.C) also increases from its unshocked value (4.0 cm^{-1}) up to a maximum of 6.5 cm^{-1} in the centre of the crater, coincident with the highest peak shift. Interestingly, the FWHM does not seem to have been altered significantly at the shallower part of the crater (lower portion of the map), while the peak shift in this region has been altered.

5.3.1.2 Target: Quartz, V = 0.515 km s^{-1}, Shot Number S241117#1

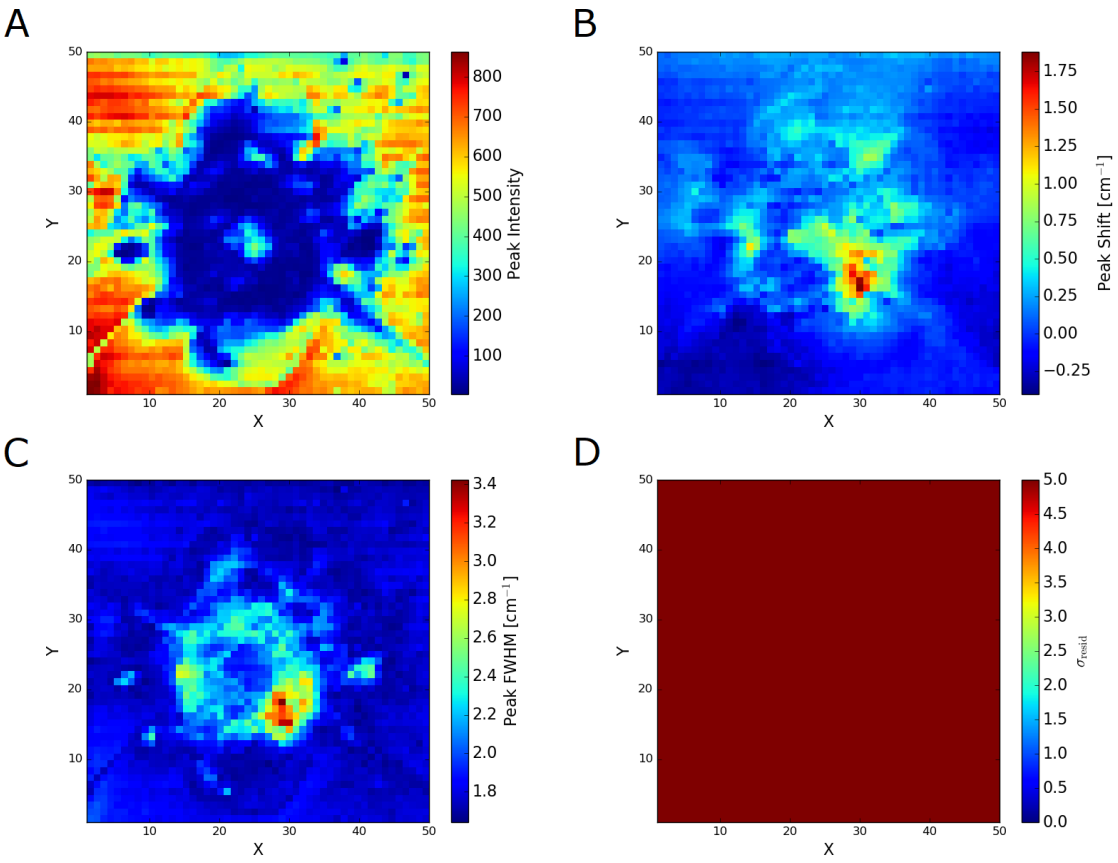


Figure 5.13: Raman map images for the quartz target S241117#1 where V = 0.515 km s^{-1}. (A) Intensity map. (B) Peak shift map. (C) FWHM map. (D) σ_{resid} map.

Figure 5.13.D shows high σ_{resid} values (average σ_{resid} of 206.8) for all data in the map for this shot, meaning there is a good fit to all spectra.

Figure 5.13.A, the intensity map, demonstrates a reasonable match to Figure 5.7.B, the optical image for this shot. The general outline of the crater as seen in the optical image can be identified in the intensity map as the edges of the blue area in the centre of the map. Part of the chaotic terrain in the centre of the crater can be seen in the middle of the blue area of the map.

The shift map Figure 5.13.B shows a positive shift within the crater, reaching a maximum of +1.9 cm^{-1} at (30,16). There is also an area of small negative shift in the bottom left of the map which reaches a maximum of -0.4 cm^{-1} at (12,11).

The FWHM map Figure 5.13.C shows a ring of peak-broadening along the crater walls with unaltered material at the centre of the crater. Within the ring the broadening reaches a maximum of 3.4 cm^{-1} up from the nominal value of 1.8 cm^{-1}.

5.3.1.3 Target: Quartz, V = 0.910 km s^{-1}, Shot Number S091014#1

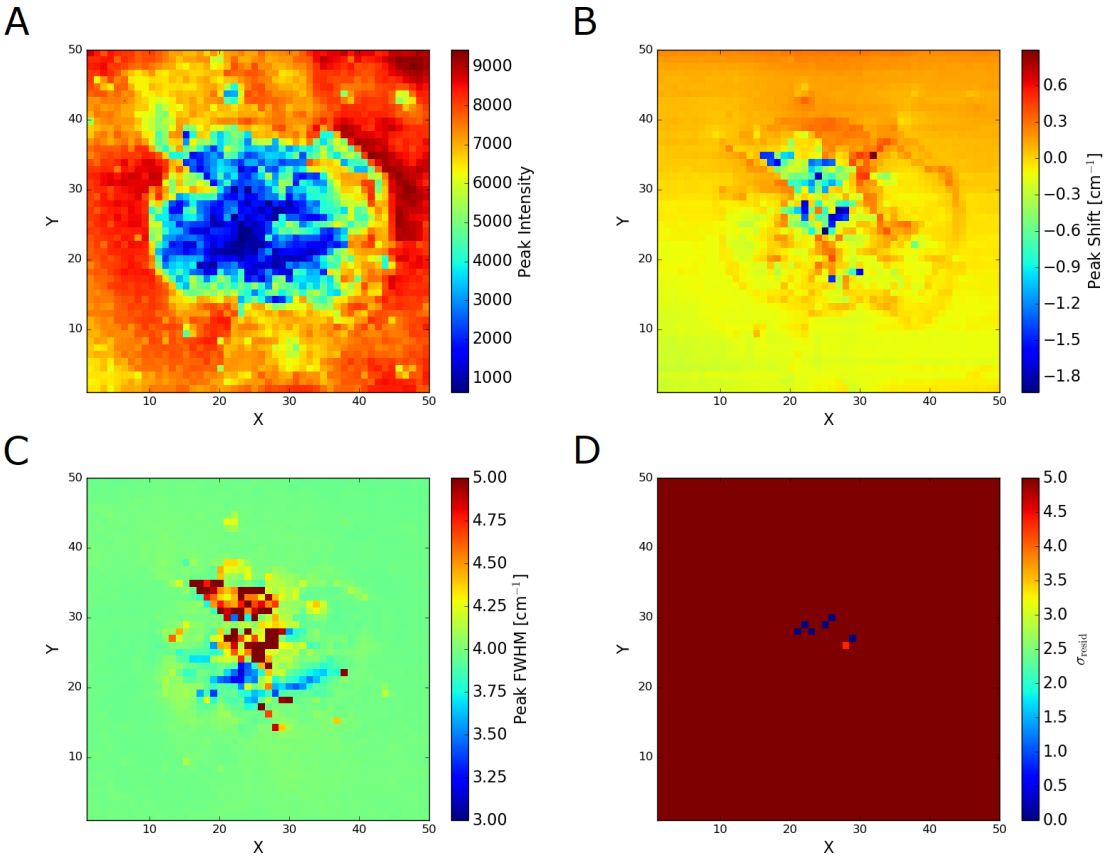


Figure 5.14: Raman map images for the quartz target S091014#1 where V = 0.910 km s^{-1}. (A) Intensity map. (B) Peak shift map. (C) FWHM map. (D) σ_{resid} map.

Figure 5.14.D shows generally high σ_{resid} values (average σ_{resid} of 20.5) with six pixels towards the centre that have failed to fit to the data (dark blue).

The intensity map for this shot (Figure 5.14.A) shows a good match to the optical image (Figure 5.8.A) with both images showing the crater to be generally circular. The intensity map shows a diagonal linear feature between (20,30) and (15,35) in the top left of the crater, which is also present in the optical image. The intensity map implies the crater has a deep region in its centre with steep walls on its top, bottom, and left sides due to the rapid change in colour in those regions.

The shift map (Figure 5.14.B) shows a ring of material around the edge of the crater has undergone a slight positive shift; this is likely the crater rim. Regions in the centre of the crater have suffered a negative shift of -1.9 cm^{-1}. Towards the top right of the crater, in the area previously noted as likely having a more sloping edge, is a region of small positive shift (maximum of +0.9 cm^{-1}).

In the map for the FWHM (Figure 5.14.C), the bottom on the crater shows a region with a decrease from the unshocked value (from 4.0 cm^{-1} to 3.0 cm^{-1}). The centre and "rim" of the crater shows an increase from the unshocked value (from 4 cm^{-1} to 5 cm^{-1}). The crater rim also has a slight increase up to 4.2 cm^{-1} from 4.0 cm^{-1}.

5.3.1.4 Target: Quartz, V = 1.35 km s^{-1}, Shot Number G151014#1

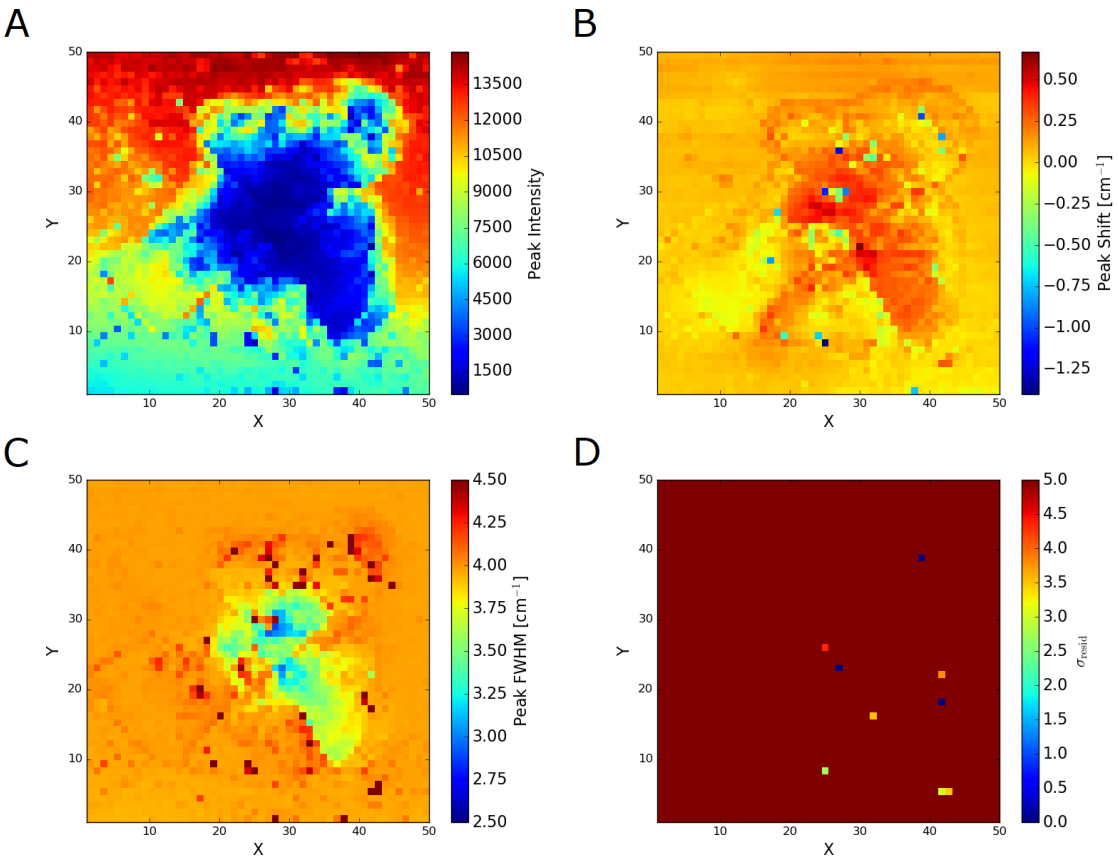


Figure 5.15: Raman map images for the quartz target G151014#1 where V = 1.35 km s^{-1}. (A) Intensity map. (B) Peak shift map. (C) FWHM map. (D) σ_{resid} map.

Figure 5.15.D generally shows a good fit, with high σ_{resid} values across the map (average σ_{resid} of 23.3). However there are a number of poorly fit pixels scattered throughout the map with values of less than 3 sigma.

Figure 5.15.A, the intensity map for this shot, demonstrates a good match with the optical image (Figure 5.8.B), with a clear crater in the centre of both images. The area on the bottom left of the optical image is surface material that has been forced upwards due to a fracture below the surface. This can also be seen in the intensity map due to the lower intensity in that region.

Ignoring the pixels with poor fit, the peak shift map (Figure 5.15.B) shows the large region in the centre of the crater having a positive shift of approximately +0.5 cm^{-1}, as well as a line of +0.2 to +0.3 cm^{-1} shift along the top rim of the crater. The uplifted region in the bottom left of the crater appears to have suffered a small negative shift of -0.1 cm^{-1}. However the measurement accuracy of the spectrometer is 0.1 cm^{-1} so these small shifts should be treated with caution.

Again ignoring the pixels with poor fit, the FWHM map (Figure 5.15.C) shows that inside the crater the FWHM has decreased from 4.0 cm^{-1} to a low of 2.5 cm^{-1} in some areas, while outside the crater it has increased slightly to 4.5 cm^{-1}. This is especially noticeable in the top right of the map in a region that both the optical image and the intensity map show to be a steep part of the crater wall.

5.3.1.5 Target: Quartz, V = 2.02 km s^{-1}, Shot Number G051114#3

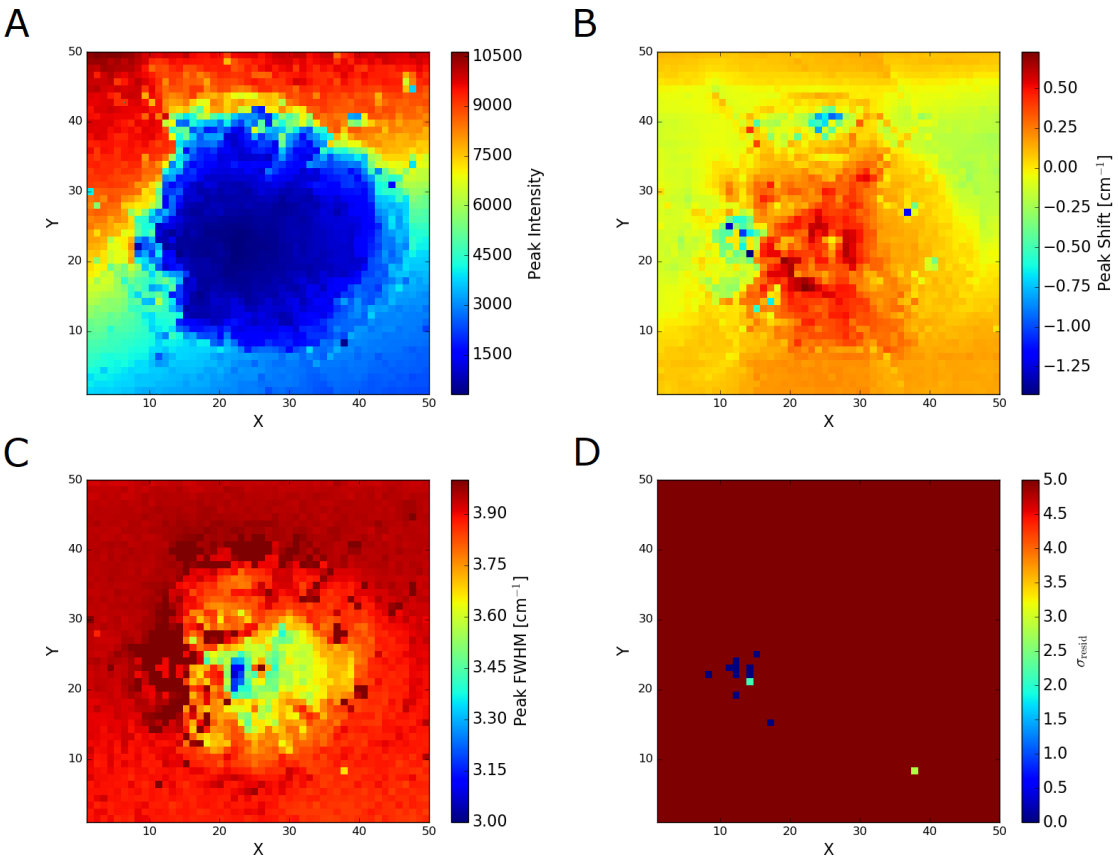


Figure 5.16: Raman map images for the quartz target G051114#3 where V = 2.02 km s^{-1}. (A) Intensity map. (B) Peak shift map. (C) FWHM map. (D) σ_{resid} map.

Figure 5.16.D shows good σ_{resid} values across the map (average σ_{resid} of 18.8). There are twelve bad pixels, mainly concentrated to the left of the map.

Figure 5.16.A exhibits a good match to the optical image (Figure 5.9.A) with both presenting a circular crater. There is a gradient across the intensity map image from high intensity in the top left corner to low intensity in the bottom right corner. This is likely due to the sample not being perfectly flat under the objective lens.

The peak shift map, Figure 5.16.B, demonstrates a positive shift within the crater, peaking at +0.7 cm^{-1}. There are slightly negatively shifted areas to the left and right of the crater, though these only have a value of -0.1 cm^{-1}, which is just within the measurement accuracy of the spectrometer. There are a few highly negatively shifted areas in the map (15,25) and (25,40), though (15,25) is within the area that failed to fit and should be treated with caution.

Figure 5.16.C shows the FWHM to be decreasing towards the centre of the crater down to 3.0 cm^{-1} (from 4.0 cm^{-1}). There is a small area showing no change in FWHM in the very centre of the crater at (25,25).

5.3.1.6 Target: Quartz, V = 3.32 km s^{-1}, Shot Number G241014#1

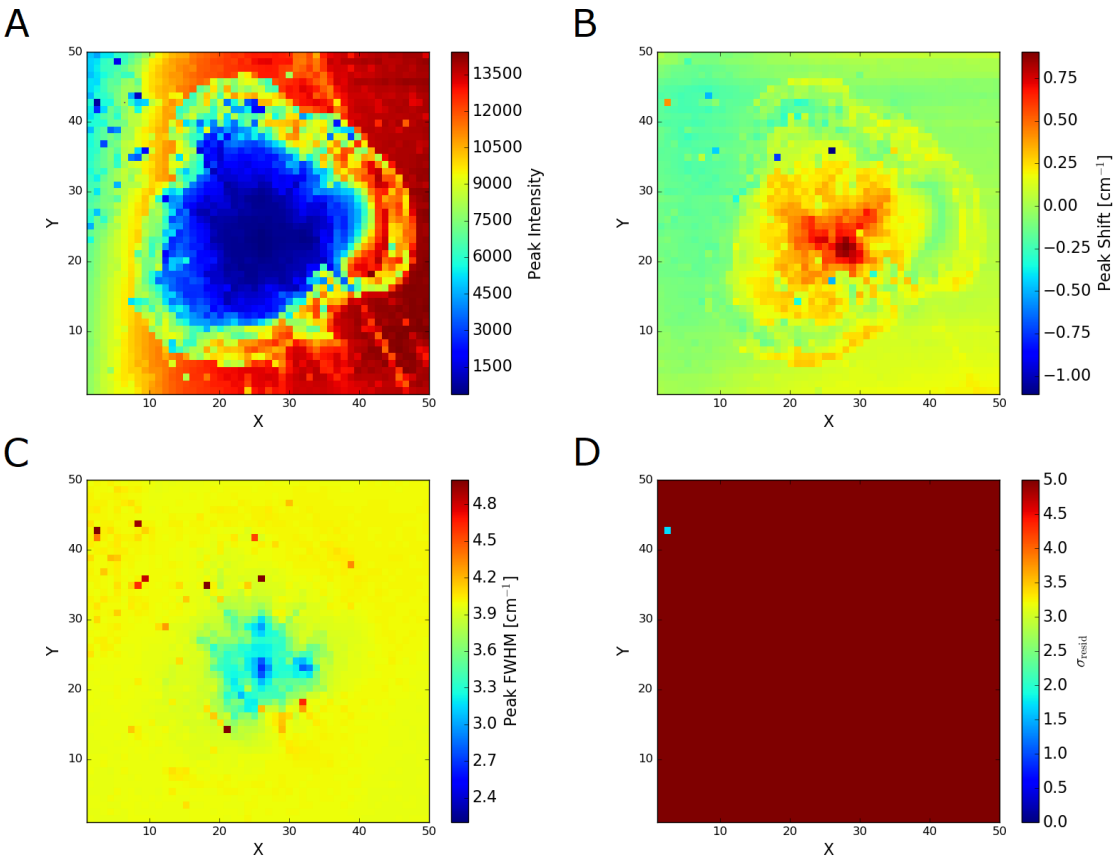


Figure 5.17: Raman map images for the quartz target G241014#1 where V = 3.32 km s^{-1}. (A) Intensity map. (B) Peak shift map. (C) FWHM map. (D) σ_{resid} map.

Figure 5.17.D shows good σ_{resid} values across the map (average σ_{resid} of 20.2) with only one pixel to be disregarded at (2,43).

The intensity map (Figure 5.17.A) demonstrates a good match to Figure 5.9.B, the optical image for this shot. Both show a generally circular crater and the intensity map clearly shows the location of the crater walls by the presence of the rapidly changing intensity just outside the central low intensity (blue) area.

The peak shift map (Figure 5.17.B) shows a ring of positively shifted material around the "rim" of the crater (averaging +0.2 cm^{-1}) while the central pit of the crater is more highly shifted with a max of +0.9 cm^{-1}. There are a few pixels of negative shift scattered across the map, the largest shift being -1.1 cm^{-1}.

Figure 5.17.C shows the FWHM decreasing towards the centre of the crater down from 3.9 cm^{-1} to 2.6 cm^{-1}. There are also scattered pixels showing FWHM increases (maximum of 5 cm^{-1}) the positions of which correspond to the negatively shifted pixels in Figure 5.17.B.

5.3.1.7 Target: Quartz, V = 4.48 km s^{-1}, Shot Number G270515#3

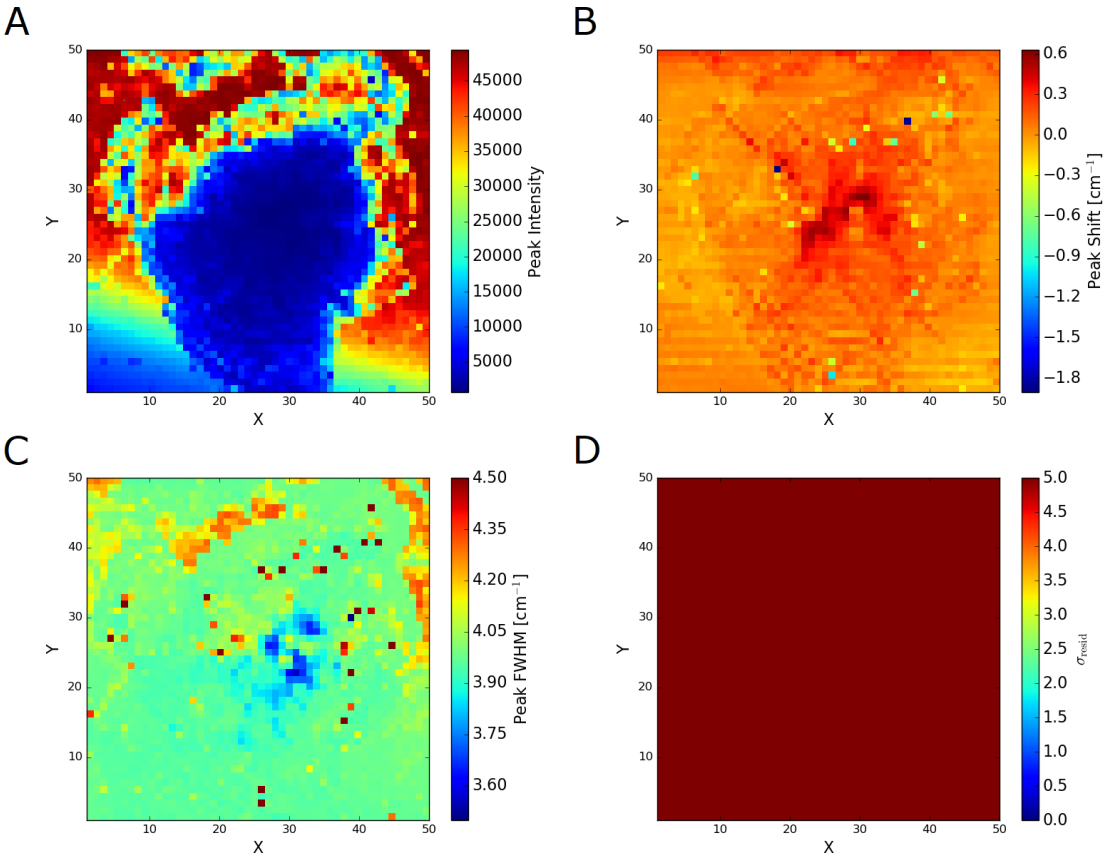


Figure 5.18: Raman map images for the quartz target G270515#3 where V = 4.48 km s^{-1}. (A) Intensity map. (B) Peak shift map. (C) FWHM map. (D) σ_{resid} map.

Figure 5.18.D exhibits good σ_{resid} values across the entire map (average σ_{resid} of 52.7). There are no areas or individual pixels that should be excluded.

The intensity map (Figure 5.18.A) demonstrates a good match to its optical counterpart (Figure 5.10.A). This particular crater was on the edge of the table of the target gemstone. This can be seen by the rapid change in intensity in the bottom left corner of the intensity map. It is also clear that the bottom edge of the crater itself is not on the table.

Figure 5.18.B, the peak shift map, shows a small positive shift within the crater of up to +0.6 cm^{-1}. There is also the occasional pixel displaying a significant negative shift up to -1.9 cm^{-1}. Although these data have good σ_{resid} values, the negatively shifted pixels seem randomly located and do not relate to any particular feature of the crater.

Figure 5.18.C shows the FWHM increasing for areas on the periphery of the crater while becoming smaller towards the centre of the crater. While these changes are small (increasing from 4.0 to 4.5 cm^{-1} and decreasing from 4.0 to 3.5 cm^{-1}), it is interesting to note that they do occur in localised areas that clearly match features which can be seen in Figure 5.18.A and Figure 5.10.A.

5.3.1.8 Target: Quartz, V = 5.27 km s^{-1}, Shot Number G271114#2

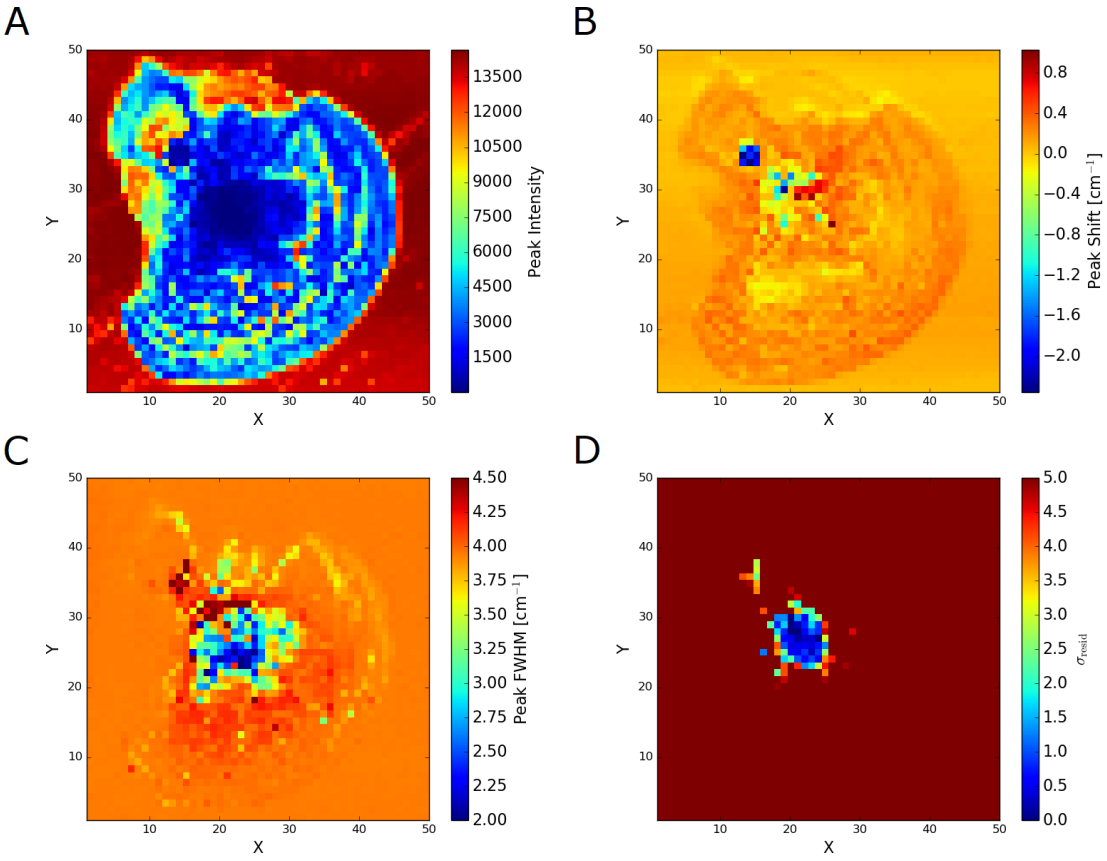


Figure 5.19: Raman map images for the quartz target G271114#2 where V = 5.27 km s^{-1}. (A) Intensity map. (B) Peak shift map. (C) FWHM map. (D) σ_{resid} map.

97.6% of the map (Figure 5.19.D) shows σ_{resid} values of higher than 5.0 (average σ_{resid} of 18.8). The exception to this is the low σ_{resid} values at the very centre of the crater as well as in a small region towards the top left of the crater at (14,35). SEM analysis shows that these areas of the crater still contain the molecular constituents of quartz (silicon and oxygen), but analysis of the Raman spectra shows that the intensity of the quartz peak has fallen below the noise implying that the quartz has lost its structure due to the impact, forming diaplectic glass. No firm conclusions will be drawn from these two regions due to their poor σ_{resid} values.

The intensity map (Figure 5.19.A) shows a clearly defined crater rim of the same shape as that in the optical image (Figure 5.10.B). The area at the top of the crater with slightly lower intensity than the surrounding unshocked material is an area where the subsurface has fractured and forced the surface material upwards; this is similar to the 1.35 km s^{-1} shot (G151014#1) described in Section 5.3.1.4.

Ignoring the areas of poor fit in the peak shift map (Figure 5.19.B) for this shot, there is a small positive increase in peak position of +0.4 cm^{-1} along the crater wall. The map shows negative shifts (up to -2.3 cm^{-1}) in the poorly fit areas, but no firm conclusions should be drawn from this.

The FWHM (Figure 5.19.C) shows a similar pattern to the peak shift map. Along the crater wall there is a small increase from 4.0 to 4.3 cm^{-1}, while the poorly fit regions vary across the entire scale for the map (from 2.0 to 4.5 cm^{-1}).

5.3.1.9 Target: Quartz, V = 6.40 km s^{-1}, Shot Number G100615#1

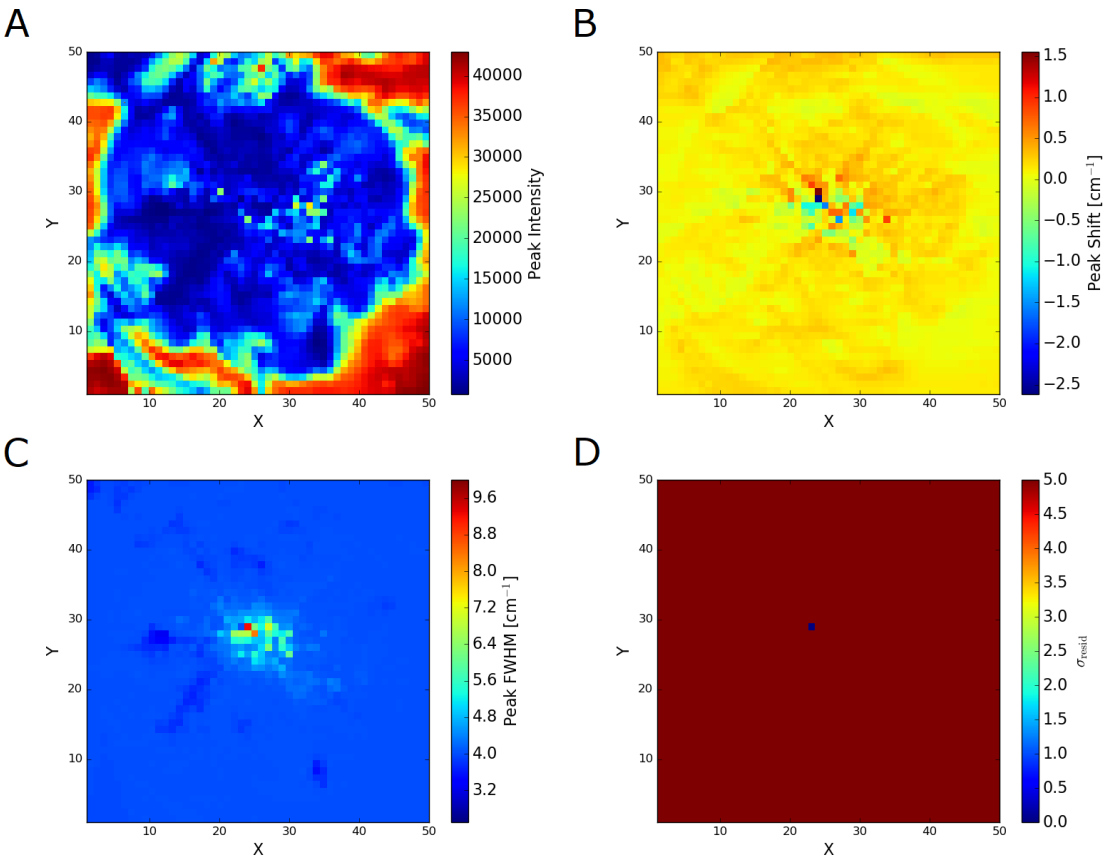


Figure 5.20: Raman map images for the quartz target G100615#1 where V = 6.40 km s^{-1}. (A) Intensity map. (B) Peak shift map. (C) FWHM map. (D) σ_{resid} map.

Figure 5.20.D exhibits good σ_{resid} values (average σ_{resid} of 53.2) on all but one pixel. This pixel will be disregarded for the analysis on the other maps.

The features in Figure 5.20.A correspond to the features in the optical image Figure 5.11. The crater is generally circular with jagged edges which can be seen in both images. The low intensity area in the top left of the intensity map is an area of material that has been pushed upwards by a subsurface fracture.

Figure 5.20.B shows the position of the peak changing within the crater. Along the crater walls the position increases by as much as +0.3 cm^{-1}, however, in the centre of the crater the shift ranges from -2.6 cm^{-1} to +1.5 cm^{-1} with no clearly defined areas.

The FWHM map (Figure 5.20.C) displays a clear trend. The peak has increased broadening towards the centre of the crater, increasing from 4.0 cm^{-1} to as high as 9.2 cm^{-1}. The highly broadened pixel in the centre of this map, which has a value of 10 cm^{-1} is actually a poorly fit pixel and has been disregarded.

5.3.1.10 Quartz Summary

For the quartz shot programme, nine shots are presented with impact speeds between 0.373 km s^{-1} and 6.40 km s^{-1} (peak pressures of 2.01 GPa and 105.28 GPa). The largest positive Raman shift is +3.2 cm^{-1} for the 0.373 km s^{-1} shot, while the largest negative shift of -2.6 cm^{-1} can be found in the 6.40 km s^{-1} shot. The greatest broadening of the FWHM is observed in the 6.40 km s^{-1} shot where it increases by 5.2 cm^{-1} from 4.0 cm^{-1} to 9.2 cm^{-1}, while the greatest narrowing of the FWHM can be seen in the 5.27 km s^{-1} shot where there is a decrease of 2.0 cm $^{-1}$ from 4.0 cm^{-1} to 2.0 cm^{-1}.

5.3.2 Olivine

As discussed in Section 4.2.1, olivine has a pair of distinctive peaks at approximately 823.0 cm^{-1} and 855.0 cm^{-1} which are attributed to the internal stretching vibrational modes of the SiO_4 ionic group [122]. It is the changes to these Raman peaks that were investigated here. The peak at 823.0 cm^{-1} will be referred to as peak 1 (P1), while the 855.0 cm^{-1} peak will be referred to as peak 2 (P2).

There are eight maps presented for each shot. These maps are split across two figures for each shot, the first of which contains: the P1 intensity, the P2 intensity, the P1 FWHM, the P2 FWHM. While the second contains: the P1 shift, the P2 shift, the separation between the P1 and P2 peaks, and finally the $\sigma_{resid.}$

Often, the P1 and P2 peaks in olivine do not shift in tandem, nor the same directions, for a particular shot. Because of this, one of the maps chosen to be displayed here is a peak separation map. This map displays the separation between the positions of P1 and P2 and helps to illustrate what is happening to the sample as a whole, instead of just to a single peak.

Figure 5.21, Figure 5.22, Figure 5.23, and Figure 5.24 show the optical images of the craters from the olivine shot programme. In each Figure the X and Y axes are in micrometres. Note, as for the quartz targets, that for impact velocities below approximately 1 km s^{-1} a "bruise" is formed on the surface rather than a crater. This is because the impact did not have sufficient energy to excavate any target material from the surface and has instead only distorted it.

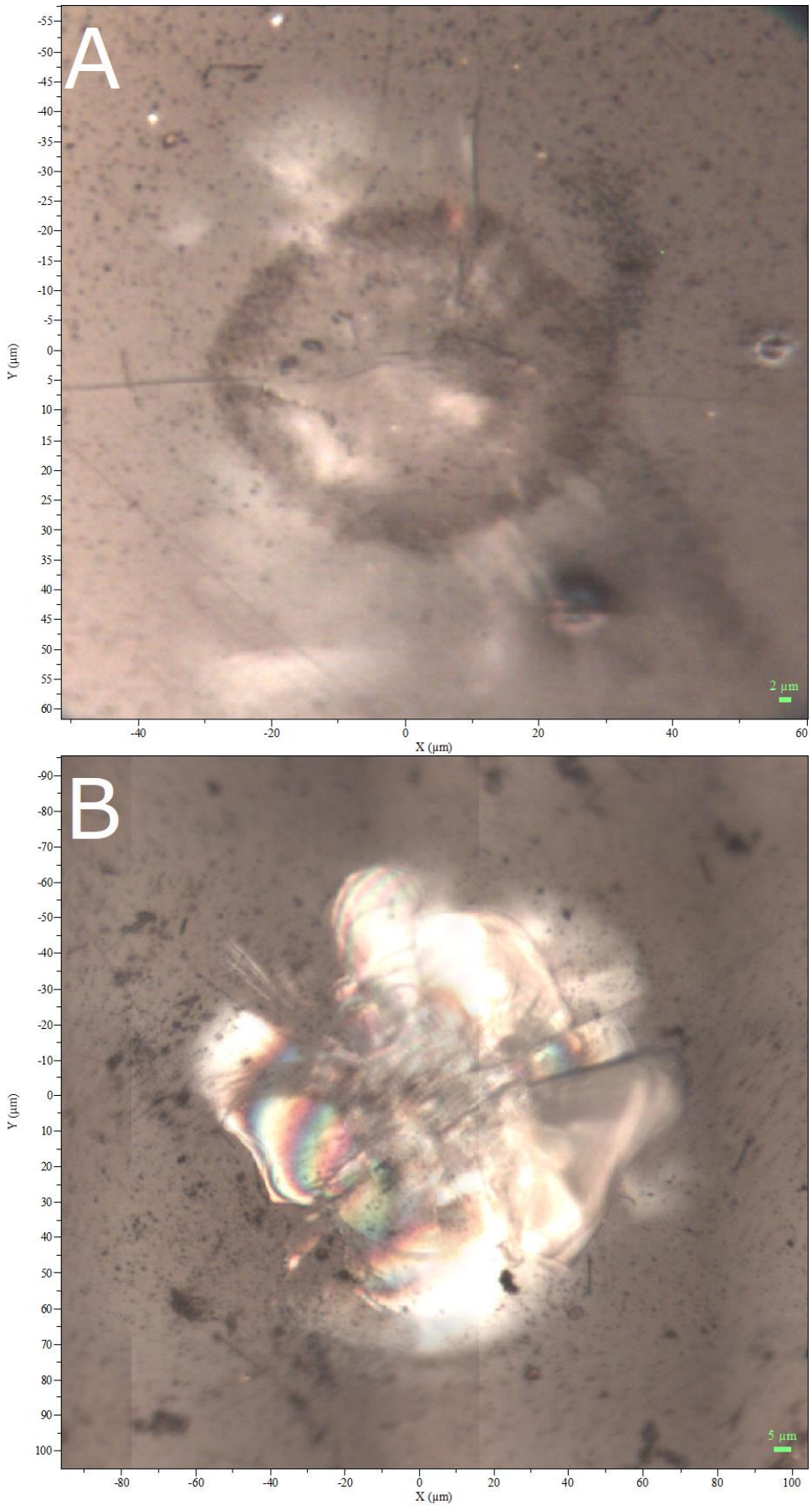


Figure 5.21: Optical montage images (x50 magnification) of the olivine targets (A) E240614#1 where V = 0.576 km s^{-1} and (B) E130614#1 where V = 0.602 km s^{-1}.

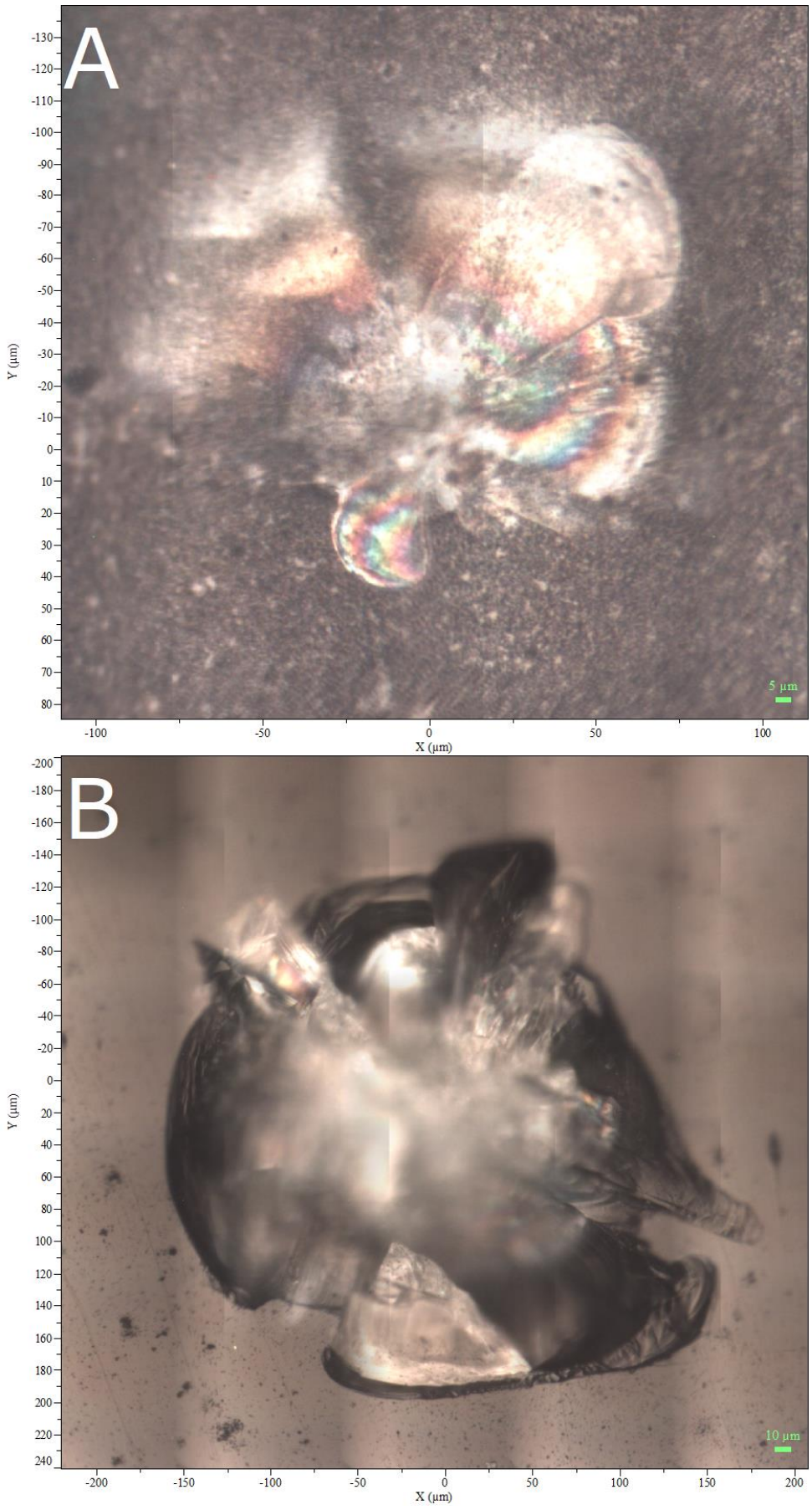


Figure 5.22: Optical montage images (x50 magnification) of the olivine targets (A) S260614#1 where V = 0.638 km s^{-1} and (B) G151014#1 where V = 1.35 km s^{-1}.

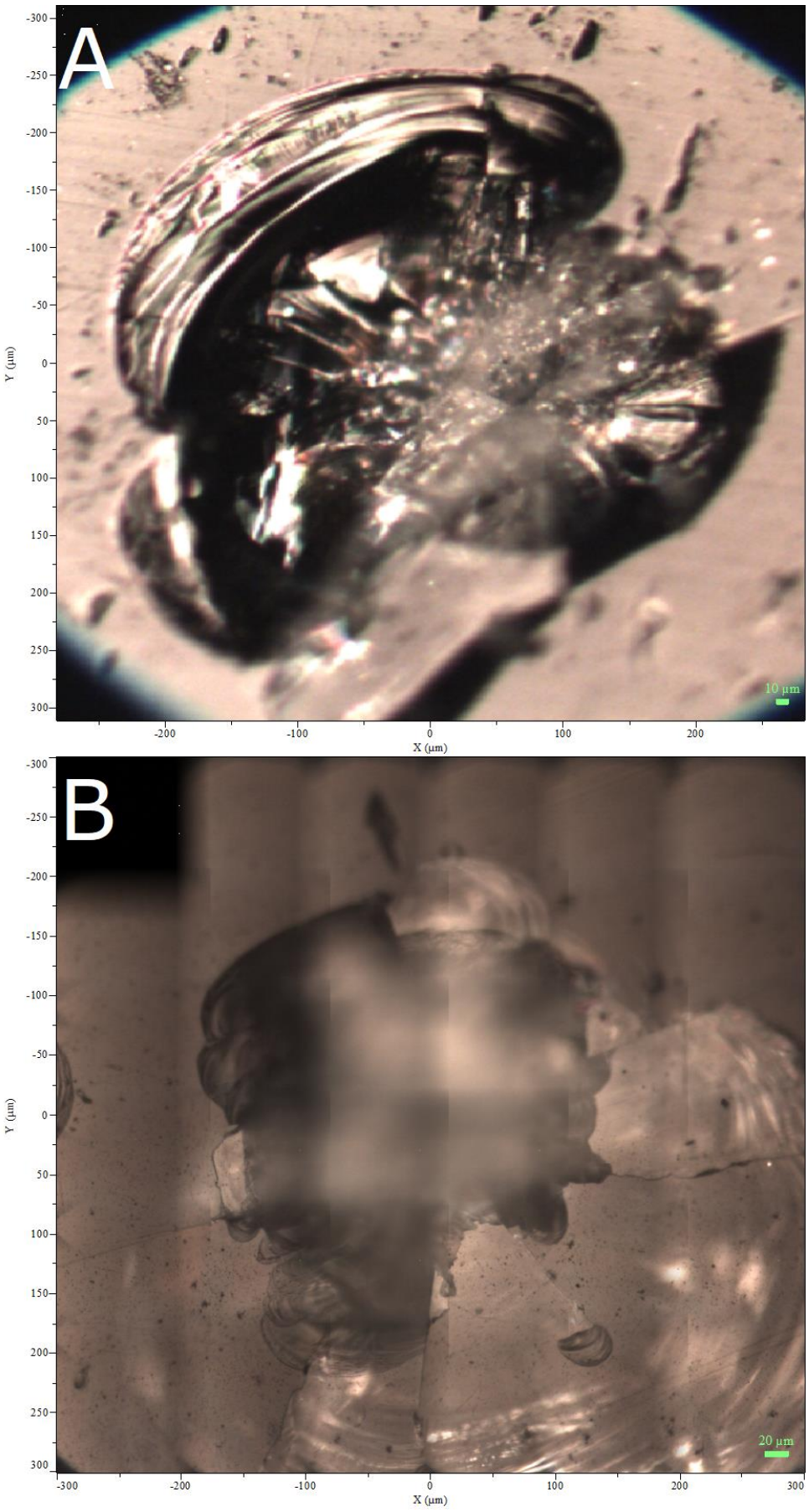


Figure 5.23: Optical montage images (x50 magnification) of the olivine targets (A) G150114#1 where V = 1.57 km s^{-1} and (B) G051114#3 where V = 2.02 km s^{-1}.

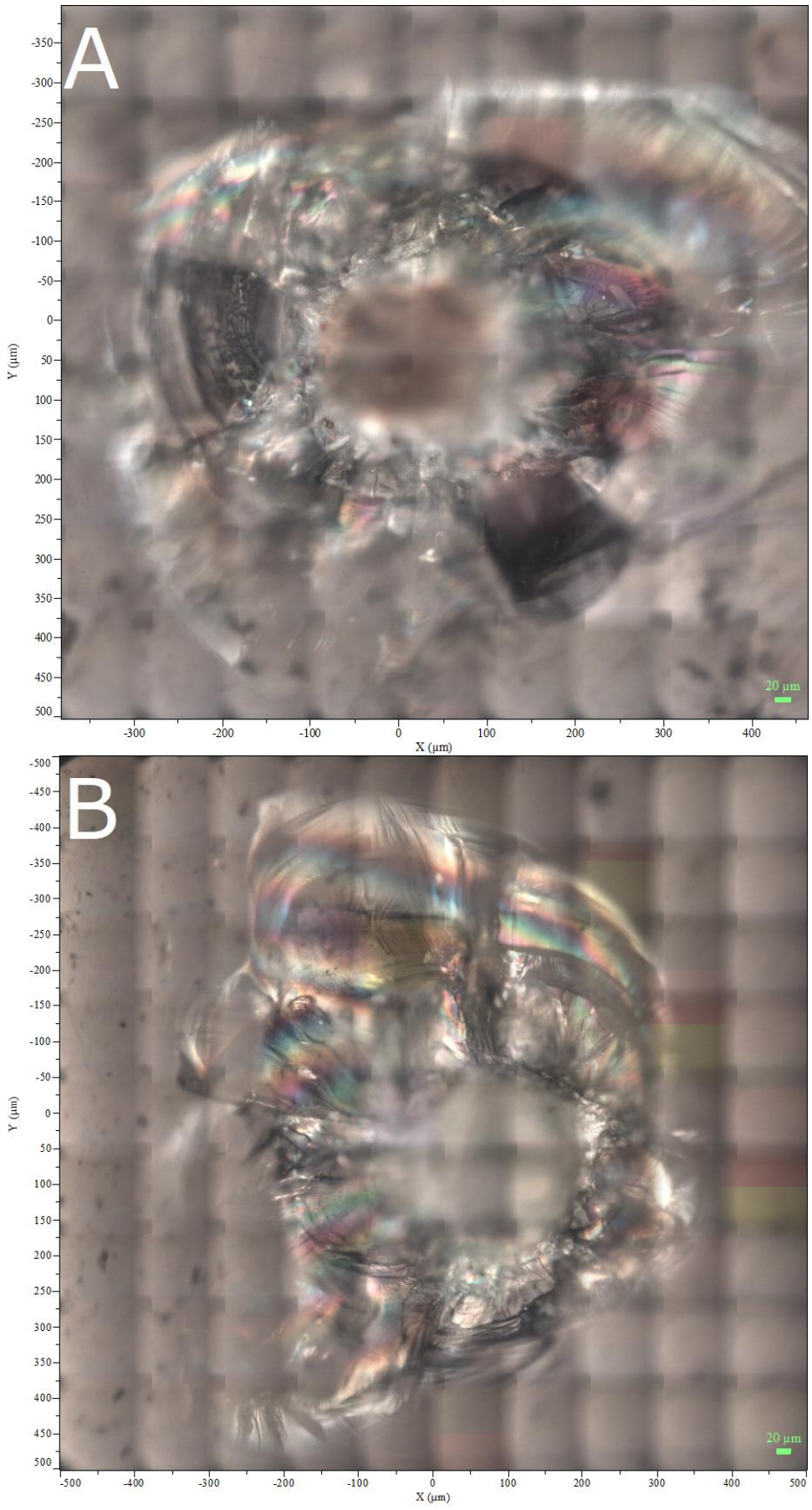


Figure 5.24: Optical montage images (x50 magnification) of the olivine targets (A) G150114#2 where V = 3.03 km s^{-1} and (B) G241014#1 where V = 3.32 km s^{-1}.

5.3.2.1 Target: Olivine, V = 0.576 km s^{-1}, Shot Number E240614#1

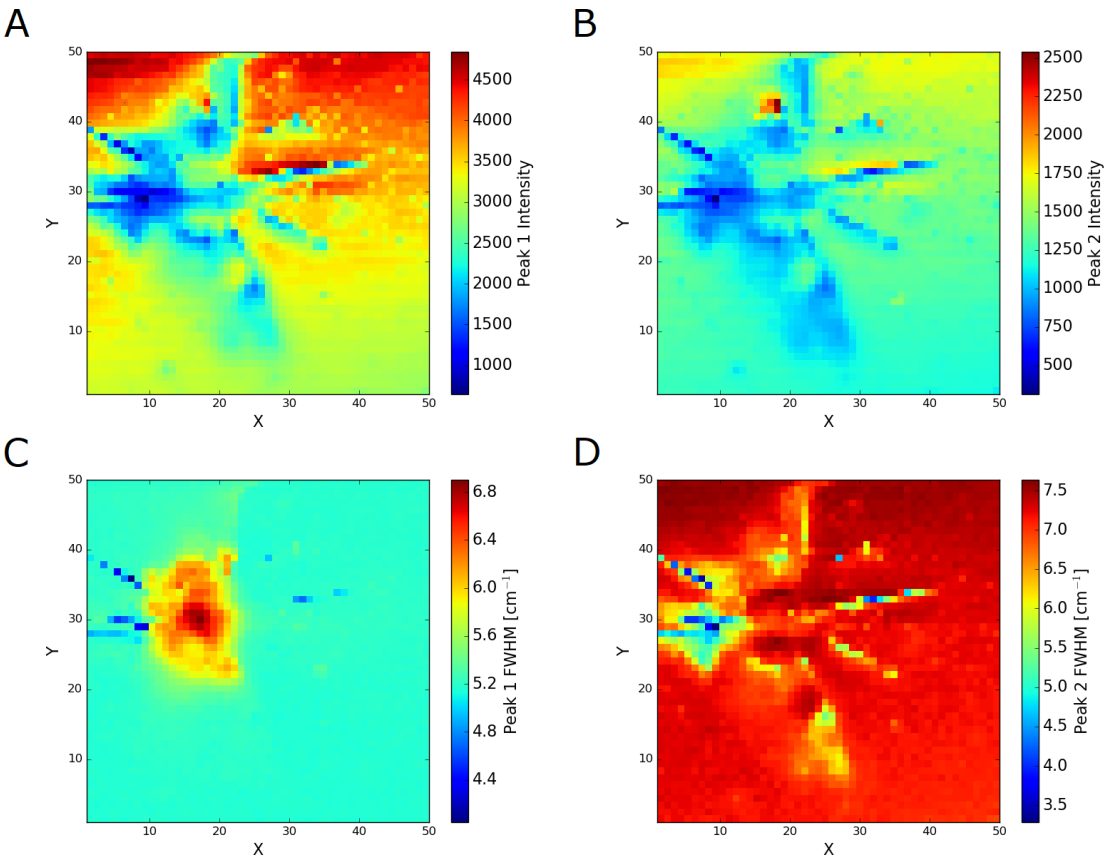


Figure 5.25: Raman map images for the olivine target E240614#1 where V = 0.576 km s^{-1}. (A) P1 Intensity map. (B) P2 intensity map. (C) P1 FWHM map. (D) P2 FWHM map.

Figure 5.26.H presents high σ_{resid} values across the entire map (average σ_{resid} of 32.1), giving confidence in the accuracy of the data presented.

Figure 5.25.A and Figure 5.25.B both show a good match to the optical image, Figure 5.21.A. There are three linear features in the intensity maps. The crack running through the "bruise" from left-to-right, as well as the crack running from the top of the image to the centre of the "bruise", can be seen in both the intensity maps and the optical image. However, the third linear feature running diagonally through the "bruise" from (0,40) to (35,20) is not present in the optical image. The optical image also seems to show a bulge in the centre of the "bruise" that can likewise be seen in the intensity maps at around (18,33).

The FWHM maps (Figure 5.25.C and Figure 5.25.D) each show different behaviour for the two peaks. The FWHM map for P1 only shows parts of the linear features that are present in the intensity maps, while the P2 FWHM map clearly shows the entirety of the features. The dominant feature in the P1 FWHM map is a region where the FWHM steadily increases from the baseline value of 5.2 cm^{-1} up to a maximum of 6.9 cm^{-1}. However, the P2 FWHM map has no such corresponding region and instead has regions where the FWHM decreases. These decreases (from 7 cm^{-1} to a minimum of 3.2 cm^{-1}) are primarily located around the line features to the left of the map with another such region towards the bottom of the map (with a minimum of 6 cm^{-1}).

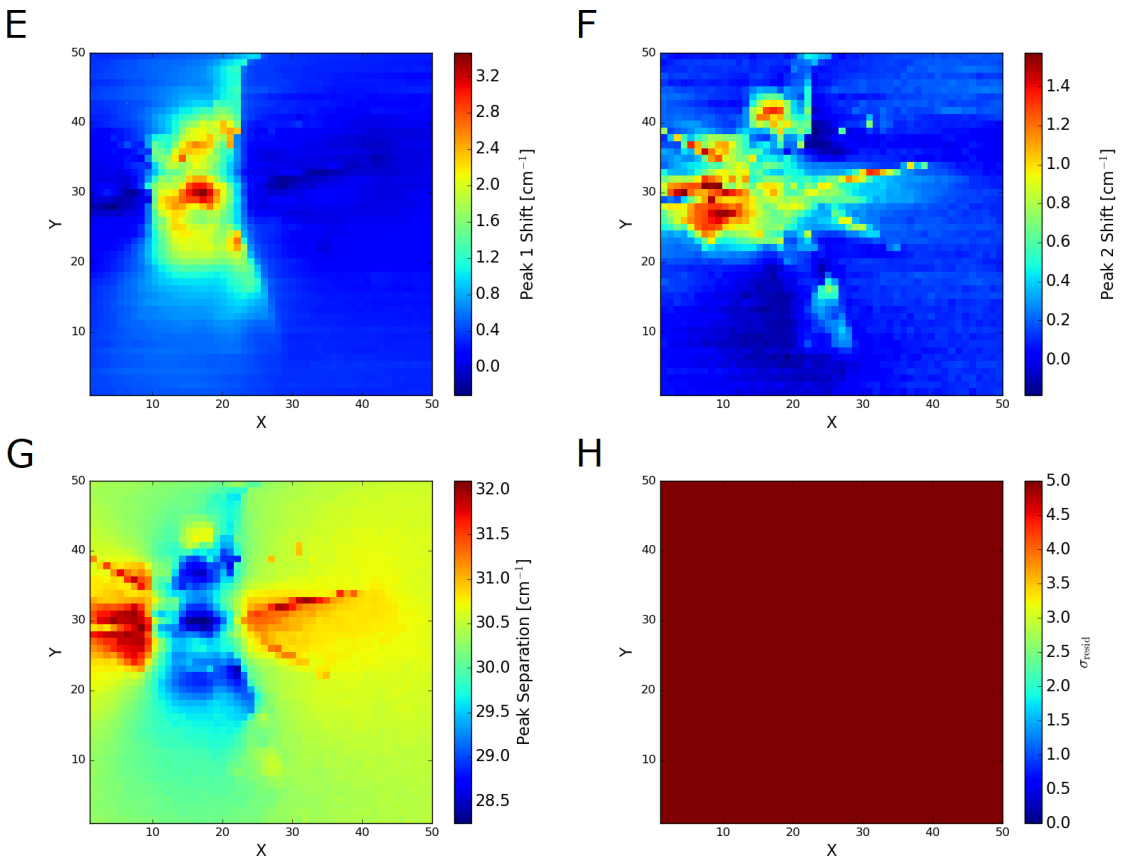


Figure 5.26: Raman map images for the olivine target E240614#1 where V = 0.576 km s^{-1}. (E) P1 shift map. (F) P2 shift map. (G) Peak separation map. (H) σ_{resid} map.

The shift maps for this shot, Figure 5.26.E and Figure 5.26.F, show very different features. The P1 map shows a similar structure to Figure 5.25.C. There is a small negative shift of -0.3 cm^{-1} along the left-to-right linear feature, whereas the main feature in this map is the large area of increasing shift up to +3.4 cm^{-1}. The P2 map has a more convoluted structure. All three lines from the intensity maps are clearly visible and present with positive shifts (up to +1.3 cm^{-1}), while the left of the map is dominated with a large area of positive shift (up to +1.6 cm^{-1}).

Figure 5.26.G is the peak separation map. This map shows the distance between the P1 and P2 peaks at each point of the map. For example, if both peaks shift in exactly the same way this map would be entirely flat. In the case of this shot, each peak has behaved very differently resulting in a strange "butterfly" effect. The blue region shows the distance between the peaks decreasing and approximately matches the shape of the positively shifted area in Figure 5.26.E. The reason for this match is that the same area in Figure 5.26.F has not shifted in the same manner allowing P1 to "catch up" to P2. The red regions to either side are due to Figure 5.26.E showing either negative or no shift in those areas while Figure 5.26.F shows positive shifts in the same areas resulting in the two peaks moving away from each other.

5.3.2.2 Target: Olivine, V = 0.602 km s^{-1}, Shot Number E130614#1

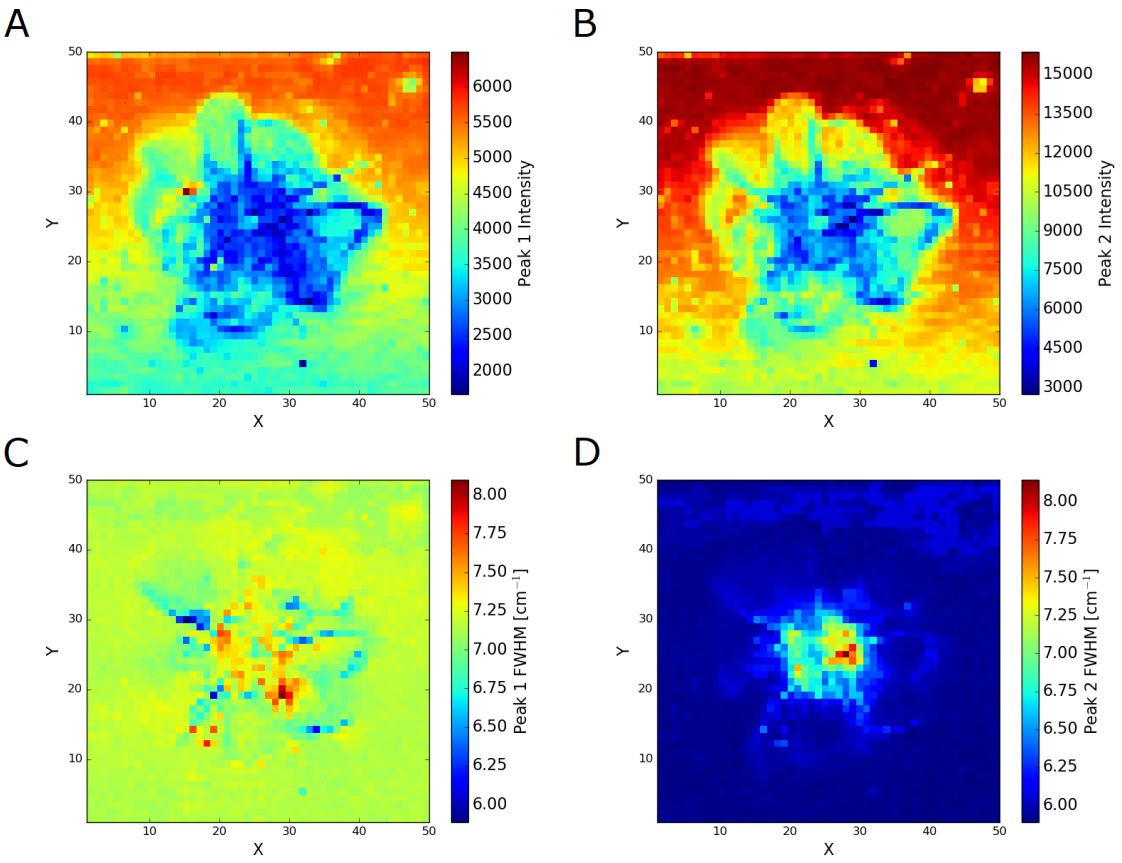


Figure 5.27: Raman map images for the olivine target E130614#1 where V = 0.602 km s^{-1}. (A) P1 Intensity map. (B) P2 intensity map. (C) P1 FWHM map. (D) P2 FWHM map.

Figure 5.28.H demonstrates high σ_{resid} values for all pixels in the map for this shot (average σ_{resid} of 20.3). There are no areas or individual pixels that should be excluded from the analysis.

The intensity maps for both P1 (Figure 5.27.A) and P2 (Figure 5.27.B) both represent a good match to their optical counterpart, Figure 5.21.B. Although the optical image suffers from over-exposure in some areas, the structure of the "bruise" can still be seen and corresponds to features in the intensity maps. The most distinct feature is on the right of the "bruise". In the optical image there is a distinct horizontal line that marks the top edge of a piece of uplifted material. This line is clearly present in both intensity maps as a blue line running from approximately (30,27) to (43,27). There is also a gradient across the intensity maps from high intensity at the top to low intensity at the bottom. This is likely due to the sample not being perfectly flat under the objective lens.

Figure 5.27.C, the FWHM map for P1, and Figure 5.27.C, the FWHM map for P2, show very different features to one another. The P2 map clearly shows the "bruise" to have an increased FWHM at its centre (from 6.0 cm^{-1} to 8.1 cm^{-1}). While the P1 map has a more chaotic structure with scattered regions of both increases (up to 8.1 cm^{-1}) and decreases (down to 5.9 cm^{-1}) to the FWHM compared to the unshocked material FWHM (7.1 cm^{-1}).

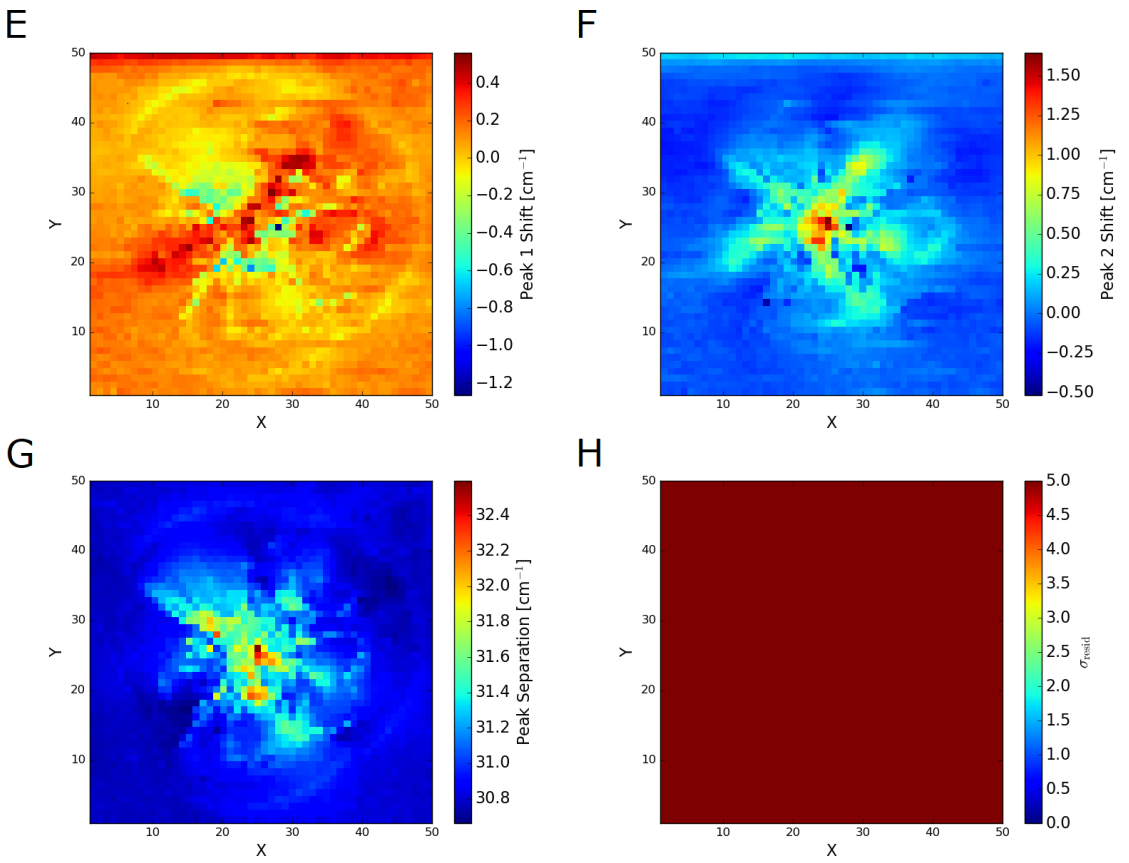


Figure 5.28: Raman map images for the olivine target E130614#1 where V = 0.602 km s^{-1}. (E) P1 shift map. (F) P2 shift map. (G) Peak separation map. (H) σ_{resid} map.

Figure 5.28.E and Figure 5.28.F are the P1 and P2 shift maps for this shot. The P1 shift map shows a ring of negatively shifted (-0.1 cm^{-1}) material around most of the "bruise". Interestingly, this does not match the boundaries of the "bruise" as seen in Figure 5.21.B, Figure 5.28.E or Figure 5.28.F. There is a band of positively shifted (by +0.3 to +0.5 cm^{-1}) material through the centre of the "bruise" with regions of negative shift above and below this band. The maximum negative shift is -1.3 cm^{-1} at (28,25) though this is only for a single pixel. There are, however, many -0.6 cm^{-1} pixels scattered over the negatively shifted regions.

The P2 shift map does not show a ring feature as seen in the P1 shift map, and also has a much clearer structure. Here the shift increases towards the centre of the "bruise" to a maximum of +1.6 cm^{-1} with some negatively shifted pixels scattered, seemingly randomly, across the "bruise". Another noteworthy feature is the same band of material that can be seen in Figure 5.28.E also positively shifted, albeit by a lesser amount (maximum of +0.8 cm^{-1}) than the centre of the "bruise".

The peak separation map Figure 5.28.G shows the P1 and P2 peaks to be moving apart inside the "bruise". This is because although most pixels have shifted in the same direction (if they have shifted at all), P2 has shifted by a greater amount than P1 resulting in an increase in the distance between the peaks.

5.3.2.3 Target: Olivine, V = 0.638 km s^{-1}, Shot Number S260914#1

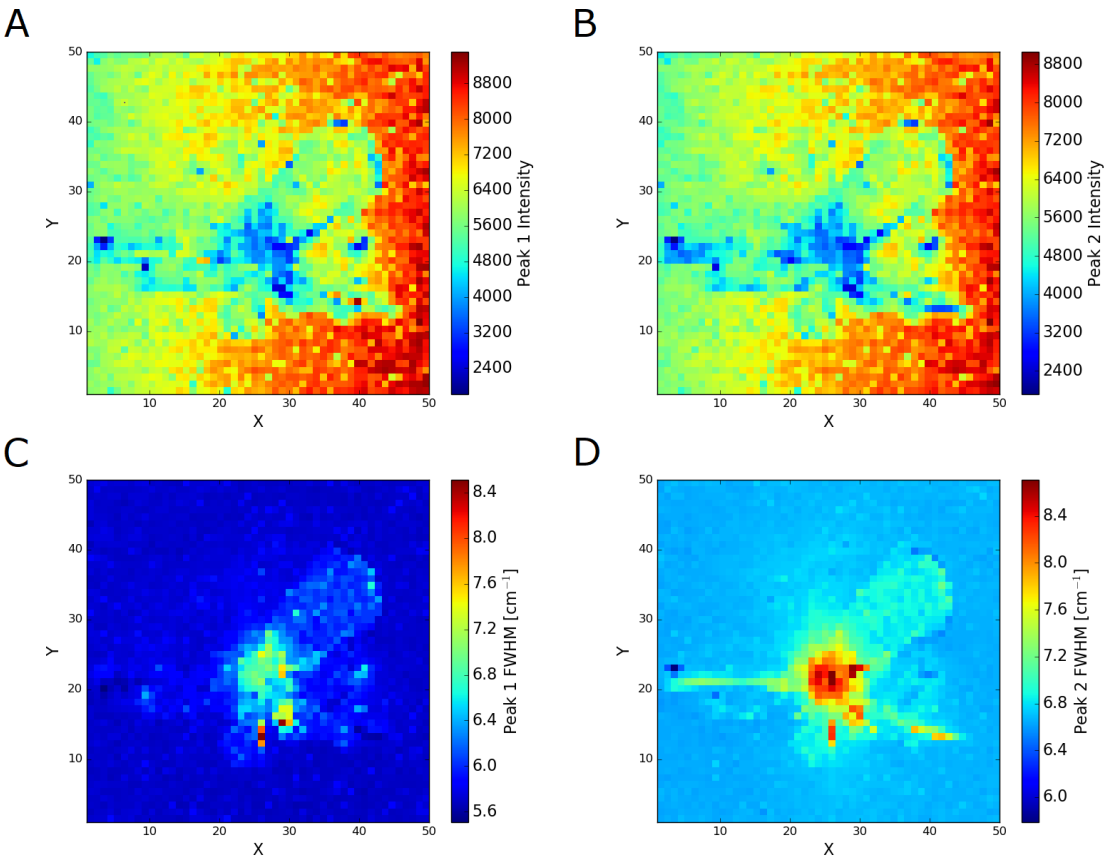


Figure 5.29: Raman map images for the olivine target S260614#1 where V = 0.638 km s^{-1}. (A) P1 Intensity map. (B) P2 intensity map. (C) P1 FWHM map. (D) P2 FWHM map.

Figure 5.30.H presents high σ_{resid} values across the entire map (average σ_{resid} of 26.8). There are no areas or individual pixels that should be excluded from analysis.

Figure 5.22.A is the optical image for this shot and is very similar to Figure 5.21.B in that a "bruise" has been formed rather than a crater. The "bruise" consists of loops of depressed material coming out from a central pit. These loops can be identified in the optical image as the areas with large amounts of glare.

The intensity maps Figure 5.29.A and Figure 5.29.B are well matched to Figure 5.22.A. In both maps the central pit of the "bruise" is represented as the blue area in the middle of the map while the loops of material can be seen in green. There is an area of low intensity centred around (3,22) in both maps which does not appear to be an area that has been affected by the impact, but is an area of debris on the surface of the target as seen in Figure 5.22.A.

Figure 5.29.C shows the P1 peak has broadened to a maximum of 8.5 cm^{-1} (up from 5.6 cm^{-1}) in the centre of the "bruise". There is also broadening (maximum of 6.7 cm^{-1}) in the loop to the top right of the "bruise". Figure 5.29.D shows similar behaviour for the FWHM of P2 to that described for the FWHM of P1. Here the centre has increased from 6.8 cm^{-1} to a maximum FWHM of 8.7 cm^{-1}, while the loop in the top right shows a maximum of 7.2 cm^{-1}.

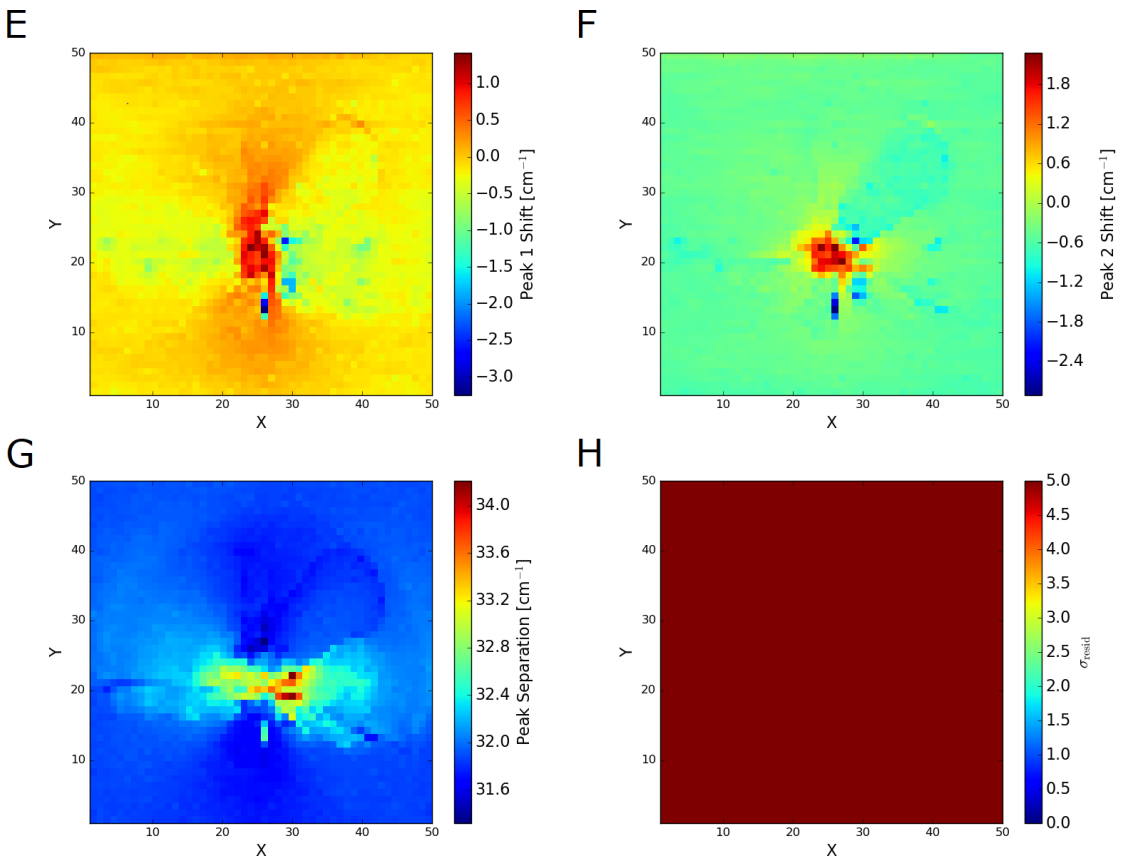


Figure 5.30: Raman map images for the olivine target S260914#1 where V = 0.638 km s^{-1}. (E) P1 shift map. (F) P2 shift map. (G) Peak separation map. (H) σ_{resid} map.

This loop is more pronounced in the P2 FWHM map than the P1 FWHM map, with the change appearing to be well defined for P2 and more scattered for P1. The size of the change, however, is smaller for P2 with an increase of 0.4 cm^{-1}; whereas P1 shows an increase of 1.1 cm^{-1}.

The isolated area of low intensity at (2,22) in Figure 5.29.A and Figure 5.29.B is also present in Figure 5.29.D. Here it represents an area of peak narrowing where the FWHM has been reduced to a minimum of 5.8 cm^{-1}.

Figure 5.30.E is the shift map for P1, and shows positive shift (to a maximum of +1.2 cm^{-1}) in the centre of the "bruise" and negative shifts (to a maximum of -2.5 cm^{-1}) in the loops. Three small areas contain the largest negative shifts in this map at (26,14), (30,17), and (29,23). These areas have a maximum shift of -3.4 cm^{-1} and correspond to the positions with the broadest peaks in Figure 5.29.C and Figure 5.29.D.

The P2 shift map (Figure 5.30.F) shows the same as the P1 shift map, but the central area with the increase is smaller in size, but the shift has a higher maximum of +2.2 cm^{-1}. The loops in this map have negative shifts, like the P1 shift map, but their maxima are -1.0 cm^{-1}. The small areas of large negative shift are still present in Figure 5.30.F, but they have a maximum of -2.9 cm^{-1}.

Figure 5.30.G, the peak separation map, shows a band feature with increasing separation closer to its centre. This is because although Figure 5.30.E and Figure 5.30.F both show the same trends, the values of the shifts are different and result in the peaks moving further apart.

5.3.2.4 Target: Olivine, V = 1.35 km s^{-1}, Shot Number G151014#1

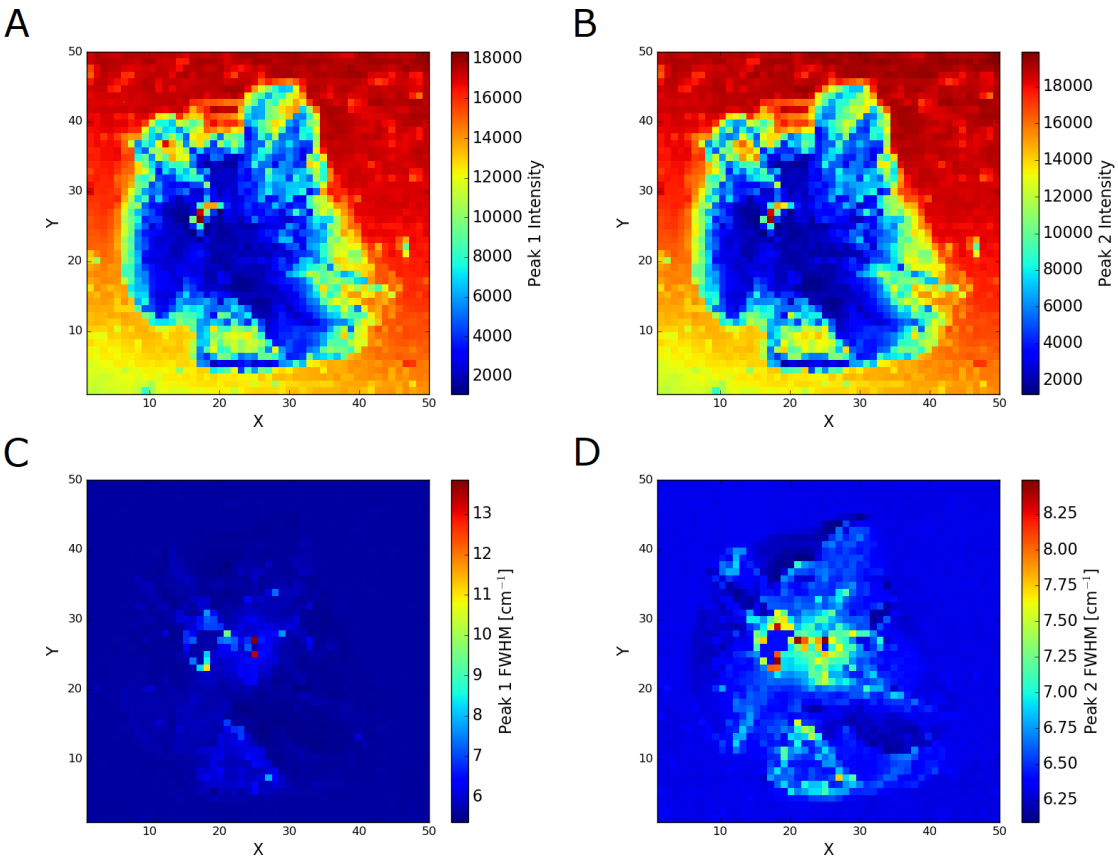


Figure 5.31: Raman map images for the olivine target G151014#1 where V = 1.35 km s^{-1}. (A) P1 Intensity map. (B) P2 intensity map. (C) P1 FWHM map. (D) P2 FWHM map.

Figure 5.32.H exhibits high σ_{resid} values across most of the map (average σ_{resid} of 26.0) with the exception of the area around (18,26), which has failed to fit. Examination of the spectra for the pixels in this area shows that this is not olivine. It appears to be a contaminant on the surface of the crater, likely some residue from the light gas gun. This area will be ignored.

Figure 5.31.A and Figure 5.31.B, the intensity maps, are consistent with Figure 5.22.B, the corresponding optical image. The central depression of the crater and the irregular shapes around the edge of the crater are present in all images. The region of increased intensity at the bottom of the crater in both of the intensity maps is not present in the optical image; this is the contaminant previously mentioned and should be ignored.

The FWHM maps Figure 5.31.C and Figure 5.31.D both show the region around (18,26) which is to be disregarded. Both maps also present widening of the FWHM in other areas on the crater. The P1 FWHM map shows an area centred on (25,25) where the FWHM has increased from 5.7 cm^{-1} to 13.8 cm^{-1} with other areas on this map having smaller increases up to a maximum of 10.5 cm^{-1} at (18,23). The P2 map shows the FWHM to be increasing on the walls of the crater, reaching a maximum of 8.5 cm^{-1} in the centre of the crater (up from 6.4 cm^{-1}).

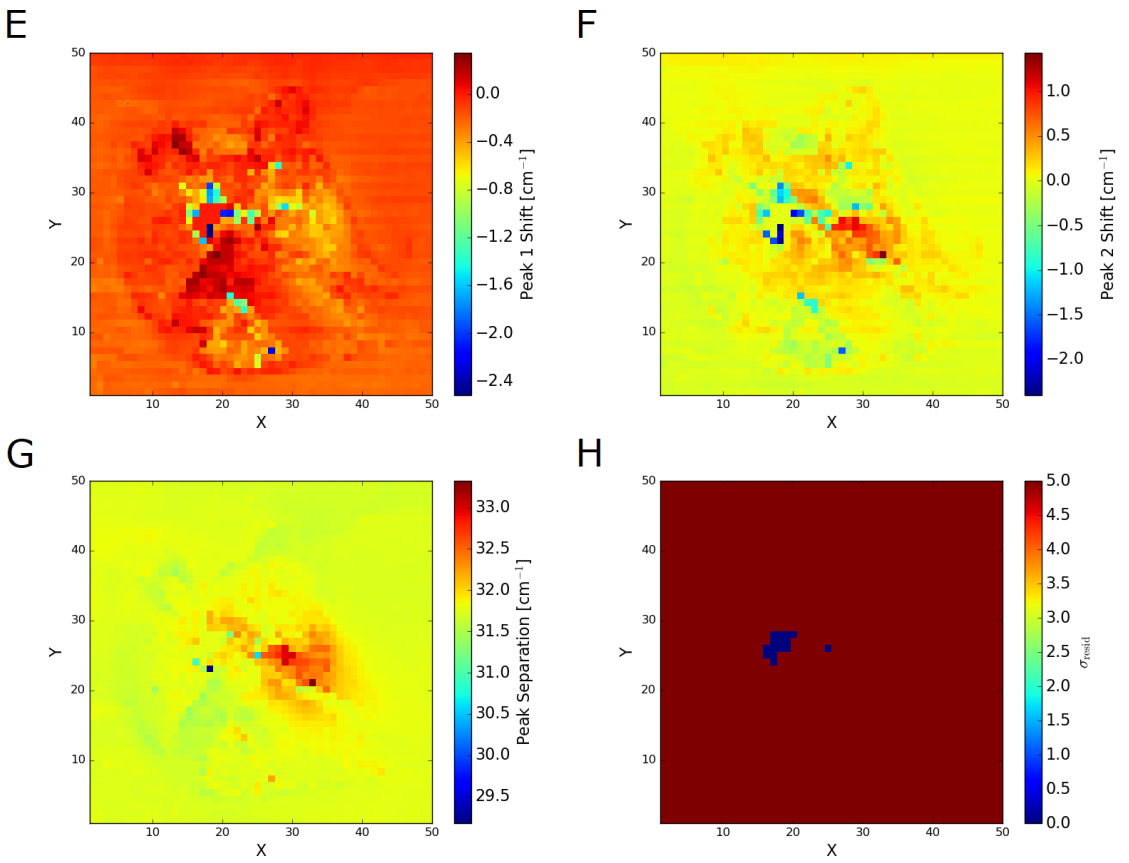


Figure 5.32: Raman map images for the olivine target G151014#1 where V = 1.35 km s^{-1}. (E) P1 shift map. (F) P2 shift map. (G) Peak separation map. (H) σ_{resid} map.

The P1 shift map (Figure 5.32.E) shows mostly negative shifts across the crater. To the right of the map is a large area corresponding to the wall of the crater, with an approximate -0.5 cm^{-1} shift. Below the contaminant is a diagonal band of material with a positive shift (having a maximum of +0.3 cm^{-1}). The P2 map (Figure 5.32.F) shows the walls of the crater to have a consistent +0.5 cm^{-1} shift and a region centered on (30,23) to have a maximum shift of +1.4 cm^{-1}. In both maps, the pixels immediately adjacent to the area at (18,26) show a negative shift of up to -2.5 cm^{-1} for P1 and -2.4 cm^{-1} for P2. This suggests that this would be a large area of highly negative shift for both peaks had it not been obscured by gun residue.

Figure 5.32.G is the peak separation map for this shot. Here we can see that the areas where the peaks have shifted negatively have shifted by similar amounts. However, when the peaks shifted in the positive direction, the P2 shift is more extreme than the P1 shift resulting in a separation of the peaks represented by the large area in the middle of this map.

5.3.2.5 Target: Olivine, V = 1.57 km s^{-1}, Shot Number G150114#1

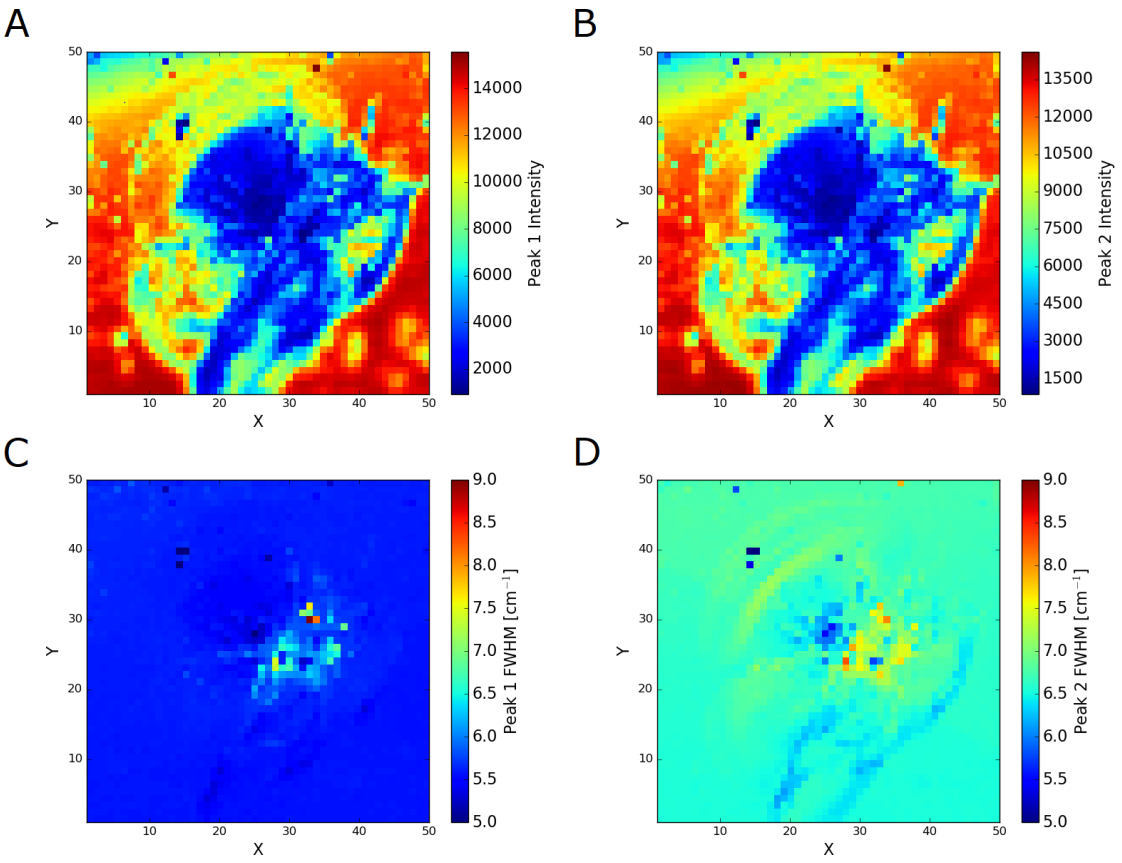


Figure 5.33: Raman map images for the olivine target G150114#1 where V = 1.57 km s^{-1}. (A) P1 Intensity map. (B) P2 intensity map. (C) P1 FWHM map. (D) P2 FWHM map.

Figure 5.34.H presents high σ_{resid} values for all but three pixels in the map (average σ_{resid} of 26.6). These pixels will be disregarded in the analysis.

Figure 5.23.A is the optical image for this shot. It shows a crater with three bulges around it that make up the majority of the crater 'rim'; one in the top left, one in the bottom left and one in the right of the image. This crater, and all three of these bulges, can be seen in both intensity map images Figure 5.33.A and Figure 5.33.B. It is even possible to see some of the ripples in the top left bulge on the intensity maps. There is a region on both intensity maps at (25,5) that is displayed in green representing a decrease in intensity. This region's position corresponds to material that is out of focus in the optical image, thus this is a region that is elevated from the surface of the target and not a depression that is shallower than the main crater.

The P1 FWHM map (Figure 5.33.C) shows a region of peak-broadening around (30,25), increasing from 5.6 cm^{-1} up to a maximum of 9.0 cm^{-1}. This feature is also present in the P2 FWHM map (Figure 5.33.D) but here the increase is smaller; from 6.6 cm^{-1} to 9.0 cm^{-1}. The P2 FWHM map also has a distinct area of peak narrowing at (25,28) corresponding to the deepest part of the crater. There is also narrowing of the P2 peak along the bottom edge of the crater and the uplifted material at the bottom of the map that is not present in P1 FWHM map.

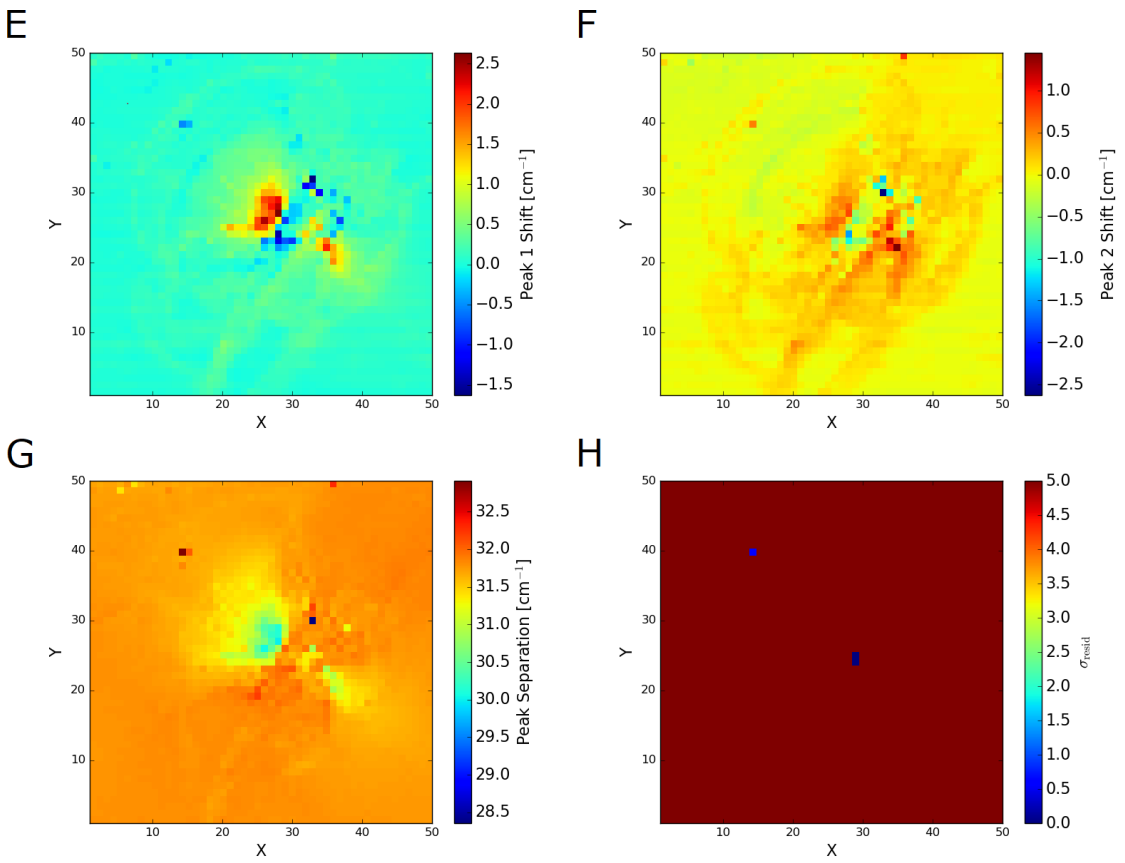


Figure 5.34: Raman map images for the olivine target G150114#1 where V = 1.57 km s^{-1}. (E) P1 shift map. (F) P2 shift map. (G) Peak separation map. (H) σ_{resid} map.

The P1 shift map (Figure 5.34.E) shows two distinct areas of positive shift and two areas of negative shift with the crater wall showing a shift of +0.5 cm^{-1}. The positive area at (25,28) has a maximum shift of +2.6 cm^{-1}, while the other at (35,22) has a maximum shift of +2.1 cm^{-1}. The negative areas have a maximum shift of -1.6 cm^{-1} and are connected by a band of material with smaller negative shifts.

The P2 shift map (Figure 5.34.F) shows the crater walls having a positive shift of +0.3 cm^{-1}. The area at (25,28) is less pronounced in the P2 with a maximum shift of +0.6 cm^{-1}, while (35,22) has the largest positive shift of +1.5 cm^{-1}. The negatively shifted band is also present, but is only really distinct at the areas at the ends of the band while the connecting material remains mostly unaffected. The area at (33,31) shows a maximum shift of -2.6 cm^{-1} while the area at (28,23) shows a maximum shift of -1.0 cm^{-1}.

Figure 5.34.G is the peak separation map. It has a 'butterfly' pattern similar to that in Figure 5.26.G. The area at (25,28) is the most prominent feature and is the result of the P2 having a lesser shift there than the P1 causing the peaks to come closer together. The band of material previously mentioned can also be seen and is the consequence of P2 having shifted more than P1, resulting in the peaks moving further apart.

5.3.2.6 Target: Olivine, V = 2.02 km s^{-1}, Shot Number G051114#3

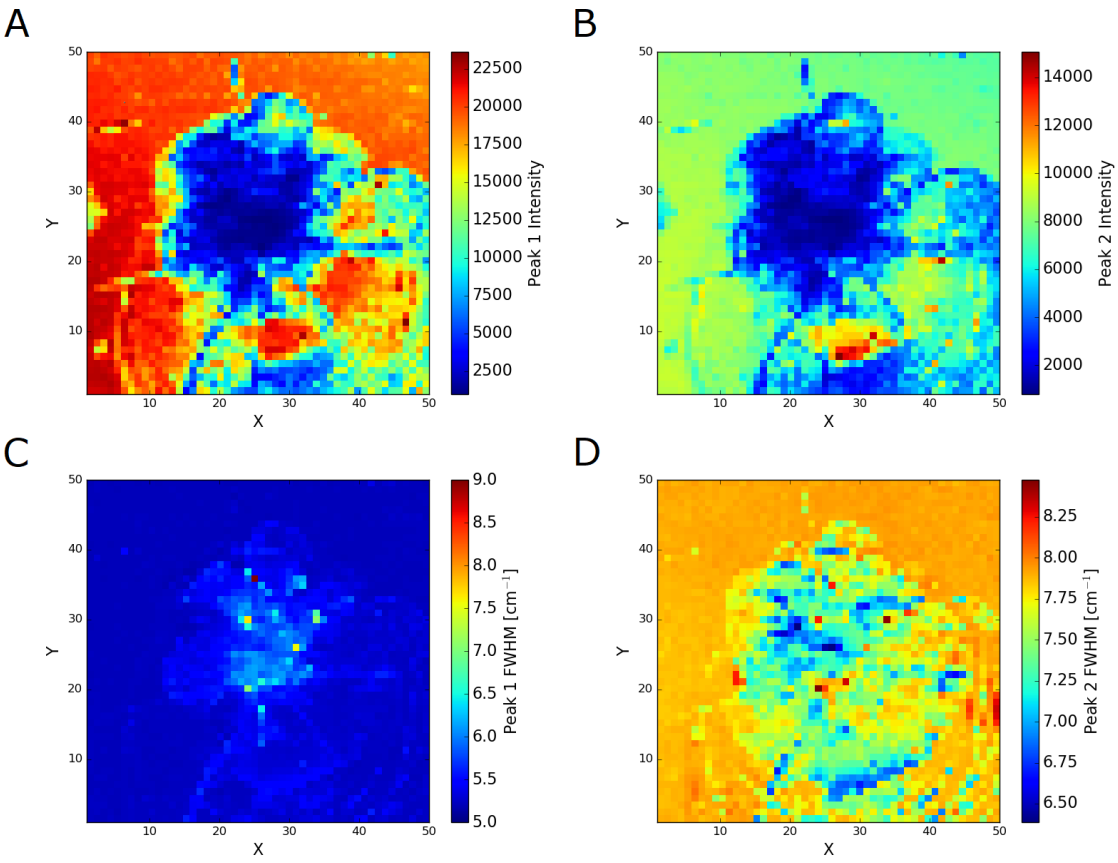


Figure 5.35: Raman map images for the olivine target G051114#3 where V = 2.02 km s^{-1}. (A) P1 Intensity map. (B) P2 intensity map. (C) P1 FWHM map. (D) P2 FWHM map.

Figure 5.36.H demonstrates high σ_{resid} values for all pixels in the map for this shot (average σ_{resid} of 27.1). There are no areas or individual pixels that should be excluded.

Figure 5.23.B is the optical image for this shot. It shows a crater with a large amount of rippled, uplifted material adjacent to it, in the bottom right of the image. The intensity maps Figure 5.35.A and Figure 5.35.B also show these features. The crater itself is represented by the large blue area in the centre, while the uplifted material can be seen as the chaotic feature dominating the bottom right of the maps.

Figure 5.35.C depicts the FWHM of P1 for this shot. It shows a slight broadening on the crater's walls and across the uplifted material (from 5.2 cm^{-1} to 5.7 cm^{-1}). Further broadening can be seen in the centre of the crater with small scattered areas (located at (10,21), (24,20), (24,30), (26,35) and (34,30)) showing the highest levels of increase. The biggest increase can be found at (26,35) where the FWHM has a value of 9.0 cm^{-1}. All of these locations are found at the boundary between the crater itself and the uplifted material.

Conversely, Figure 5.35.D shows mostly narrowing of P2 with the smallest value being 6.4 cm^{-1} (down from 7.8 cm^{-1}) which can be found in the centre of the crater. There are a few small areas where the FWHM of P2 increases (up to a maximum of 8.5 cm^{-1}); these can be found scattered across the map in positions corresponding to the largest increases in the FWHM of P1.

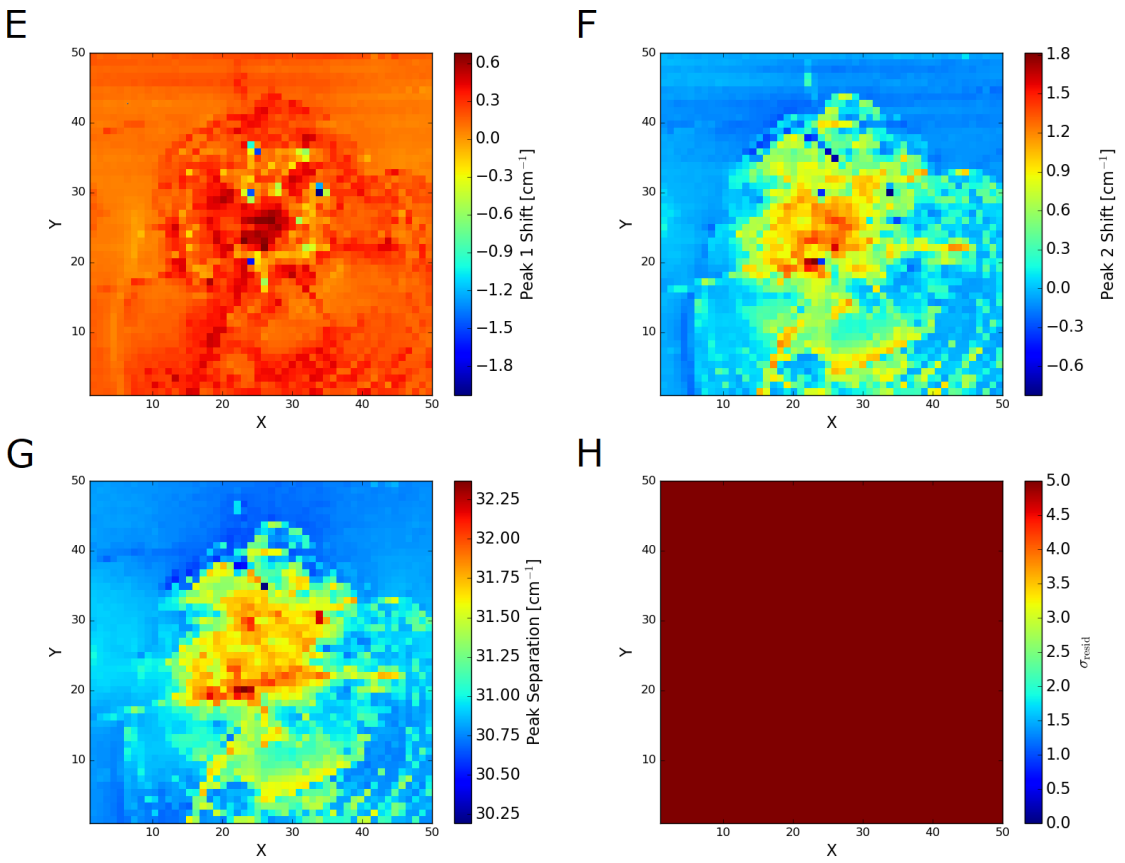


Figure 5.36: Raman map images for the olivine target G051114#3 where V = 2.02 km s^{-1}. (E) P1 shift map. (F) P2 shift map. (G) Peak separation map. (H) σ_{resid} map.

The P1 shift map (Figure 5.36.E) shows a positive shift in the uplifted material and on the crater walls, with the centre of the crater showing the largest shift of +0.7 cm^{-1}. There are scattered areas of negative shift up to -2.0 cm^{-1}, the locations of which match the locations of greatest broadening described above.

Figure 5.36.F, the shift map for P2, follows the same trend as Figure 5.36.E but with larger positive shifts and smaller negative shifts. Here the largest positive shift is +1.8 cm^{-1} at (23,20) and the largest negative shift is -0.8 cm^{-1} at (26,35). Also visible in this map are the 'ripples' in the uplifted material that can be seen in Figure 5.23.B.

The peak separation map (Figure 5.36.G) generally shows the P1 and P2 positions getting further apart. This is because when the shift is positive, P2 has shifted more than P1; and when the shift is negative P1 and shifted more than P2, resulting in the two peaks moving away from each other.

5.3.2.7 Target: Olivine, V = 3.03 km s^{-1}, Shot Number G150114#2

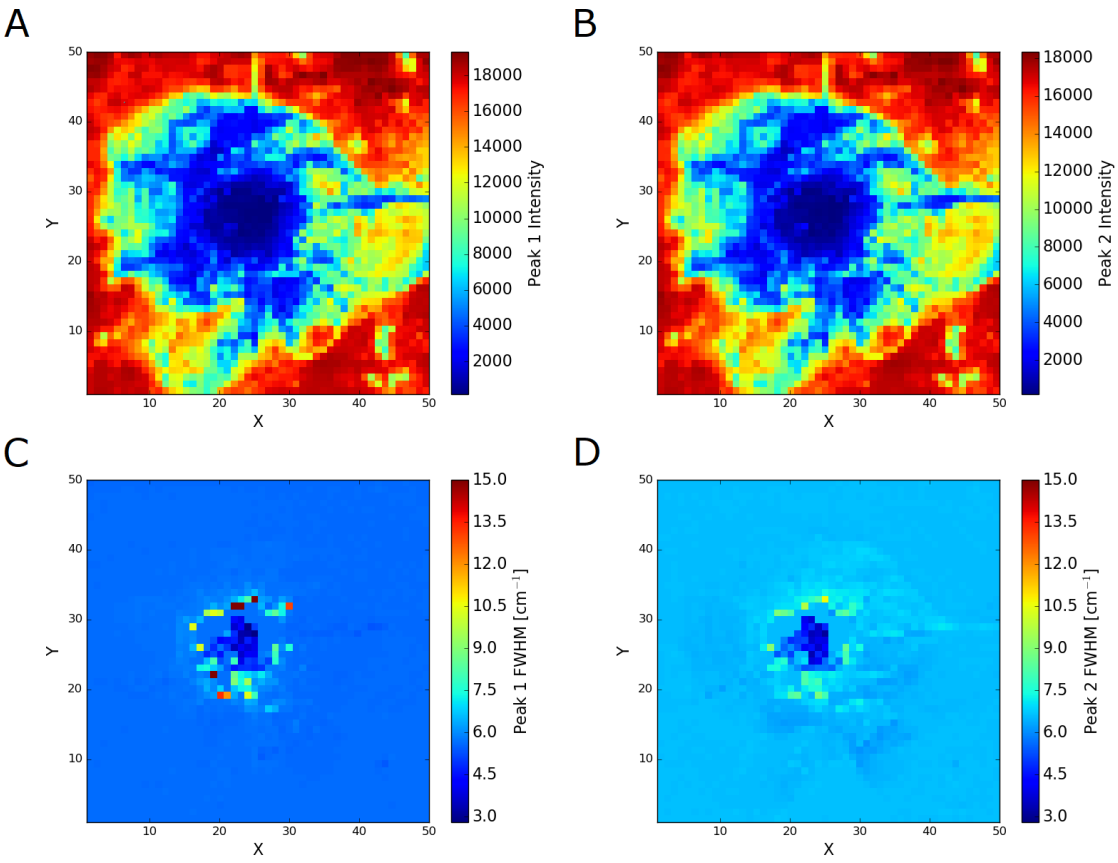


Figure 5.37: Raman map images for the olivine target G150114#2 where V = 3.03 km s^{-1}. (A) P1 Intensity map. (B) P2 intensity map. (C) P1 FWHM map. (D) P2 FWHM map.

Figure 5.38.H shows high σ_{resid} values (average σ_{resid} of 27.5) for most of the data except for the large blue areas in the centre of the map. These areas are where the fitting script has failed to fit the data resulting in σ_{resid} values of 0.0. Like the 5.25 km s^{-1} quartz shot, SEM analysis of this region shows that the elemental composition is still that of olivine, but the intensity of P1 and P2 has fallen below the noise in the spectra making it impossible to fit the peaks. This implies that the structure of the olivine in this area has broken down forming a melt of diaplectic glass. These areas should be ignored in the other maps of this shot.

Figure 5.37.A and Figure 5.37.B both demonstrate a good match to Figure 5.24.A, the optical image of the crater from this shot. The central pit surrounded by the crater walls is easily identifiable in all three images. Surface material around the rim of the crater that has broken away from the subsurface and been raised upwards by the impact can also be seen as the green/yellow areas around the main crater.

The P1 FWHM map Figure 5.37.C shows a ring of material around the outside centre of the crater where the peak has broadened from 5.6 cm^{-1} to a maximum of 15.0 cm^{-1}. Interestingly, inside this ring the peak appears to have narrowed to a minimum of 2.8 cm^{-1}. The same effect can be seen in Figure 5.37.D, the P2 FWHM map. Here the ring has a maximum of 10.6 cm^{-1} (from 6.6 cm^{-1}) while the centre has a minimum of 3.1 cm^{-1}.

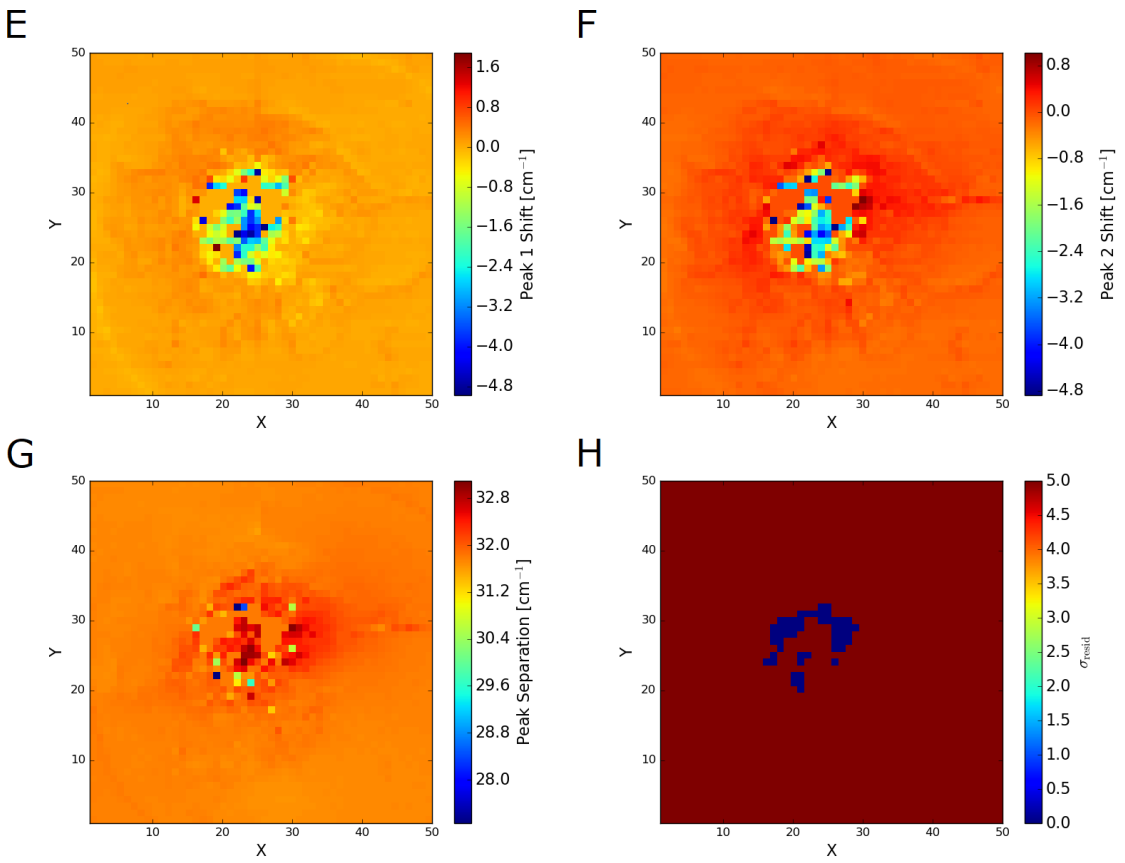


Figure 5.38: Raman map images for the olivine target G150114#2 where V = 3.03 km s^{-1}. (E) P1 shift map. (F) P2 shift map. (G) Peak separation map. (H) σ_{resid} map.

Figure 5.38.E and Figure 5.38.F are the peak shift maps for this shot. Both maps show a positive shift of +0.4 cm^{-1} on the crater walls except on the right side of the crater in the P1 map where it has remained unshifted. The peak position decreases in the centre of the crater with negative shifts of up to -5.0 cm^{-1} for P1 and -4.9 cm^{-1} for P2. The P2 map also has a small area at (30,28) which has shifted by +1.0 cm^{-1}.

The peak separation map Figure 5.38.G shows an increase in separation to the right of the crater. This is because the peak position of P1 has shifted positively in that area while P2 has remained unshifted in the same area.

5.3.2.8 Target: Olivine, V = 3.32 km s^{-1}, Shot Number G241014#1

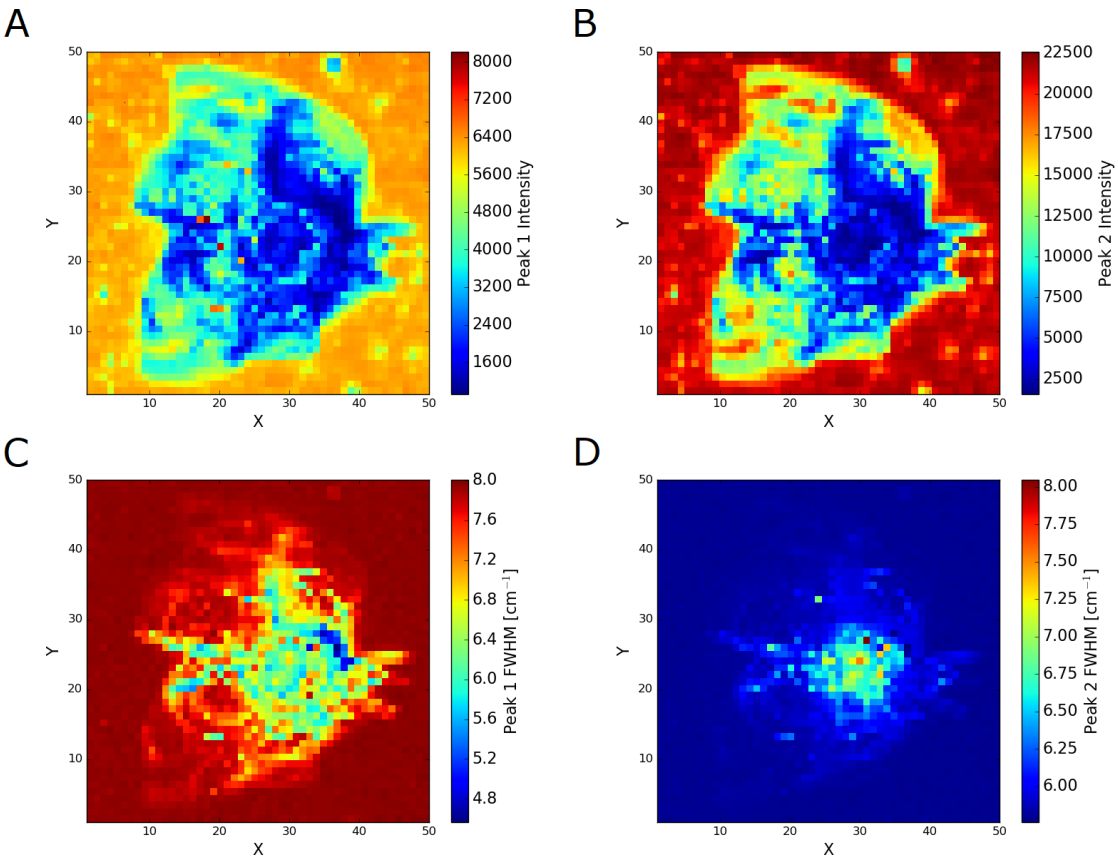


Figure 5.39: Raman map images for the olivine target G241014#1 where V = 3.32 km s^{-1}. (A) P1 Intensity map. (B) P2 intensity map. (C) P1 FWHM map. (D) P2 FWHM map.

Figure 5.40.H demonstrates high σ_{resid} values for all pixels in the map for this shot (average σ_{resid} of 21.7). There are no areas or individual pixels that should be excluded.

The optical image for this shot (Figure 5.24.B) shows a large amount of uplifted material around the crater, which is in agreement with the P1 and P2 intensity maps (Figure 5.39.A and Figure 5.39.B), where this material is represented by the large green areas surrounding the (blue) crater. The intensity maps also suggest that the darker material above the crater in the optical image is actually a depression in the surface due to the reduced intensity in that region.

There is a small area at (37,48) that shows a reduced intensity in both Figure 5.39.A and Figure 5.39.B. The optical image is out of focus in this area, but a dark patch can be made out suggesting that there is some material on the surface that is reducing the intensity of the Raman signal in that area.

Figure 5.39.C, the P1 FWHM map, shows a decrease in the centre of the crater compared to the unshocked material outside the crater. The minimum of 4.6 cm^{-1} (down from 8.0 cm^{-1}) can be found at (37,26). Figure 5.39.D shows the opposite to be true for P2, with an increase in FWHM towards the centre of the crater. The maximum FWHM is 8.0 cm^{-1} (up from 5.8 cm^{-1}) and can be found at (31,27).

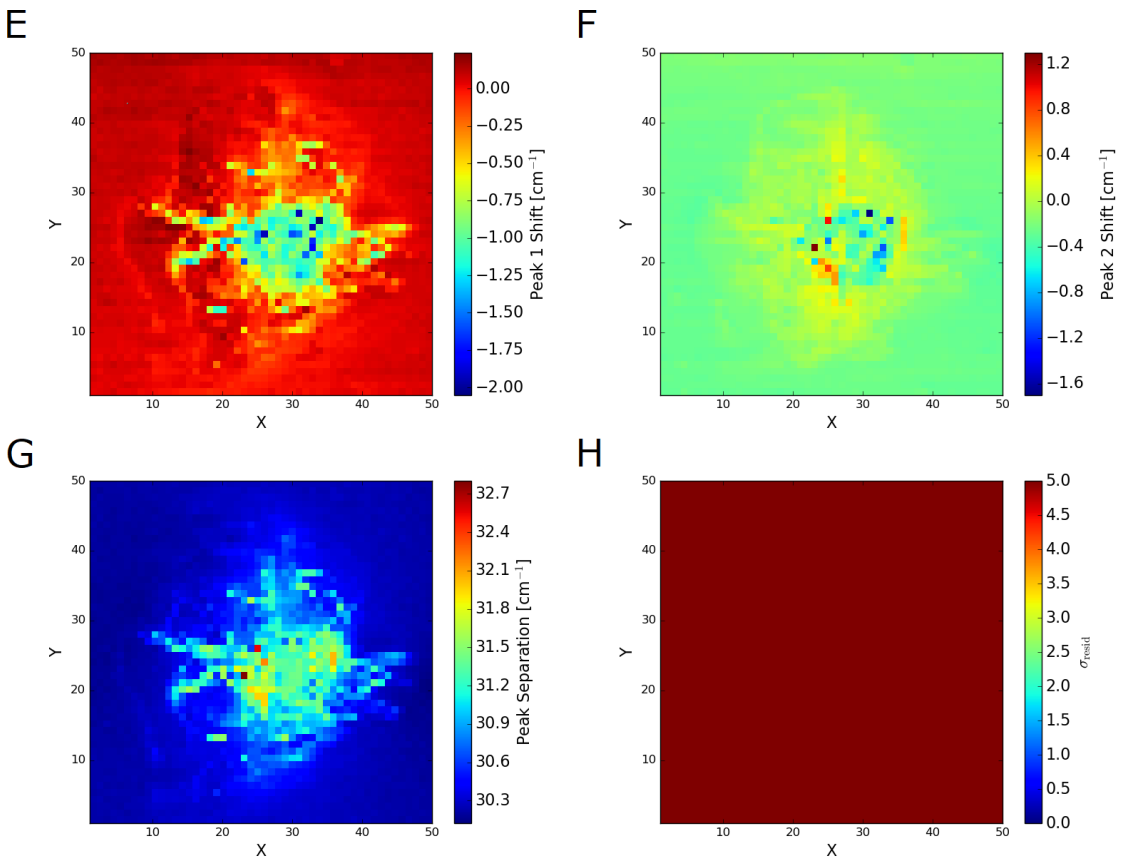


Figure 5.40: Raman map images for the olivine target G241014#1 where V = 3.32 km s^{-1}. (E) P1 shift map. (F) P2 shift map. (G) Peak separation map. (H) σ_{resid} map.

The P1 shift map (Figure 5.40.E) shows some positive shift along the crater walls to the left of the crater (maximum of +0.2 cm^{-1}) while the rest of the crater walls remain unshifted. Inside the crater the shift becomes negative, with the largest negative shift being -2.1 cm^{-1}.

The P2 shift map (Figure 5.40.F) shows a ring of positively shifted material (in yellow) along the crater walls (maximum of +0.4 cm^{-1}). On the very edges of the central part of the crater ((25,19), (36,24) and (25,26)) are areas of greater positive shift (maximum of +1.3 cm^{-1}), but the centre of the crater behaves similarly to P1 showing a negative shift with a maximum of -1.7 cm^{-1}.

Figure 5.40.G depicts the peak separation and shows an increase towards the centre of the crater. Although P1 and P2 have generally followed the same behaviour, P1 has shifted more negatively than P2.

5.3.2.9 Olivine Summary

For the olivine shot programme, eight shots are presented with impact speeds between 0.576 km s^{-1} and 3.32 km s^{-1} (8.76 GPa and 61.98 GPa). Above 4.00 km s^{-1} the olivine targets were catastrophically disrupted leaving no craters that could be mapped. The largest positive Raman shift is +3.4 cm^{-1} for P1 in the 0.576 km s^{-1} shot, while the largest negative shift of -5.0 cm^{-1} can be found in P1 in the 3.03 km s^{-1} shot. The greatest broadening of the FWHM is observed in P1 of the 3.03 km s^{-1} shot, where it increases by 9.4 cm^{-1} from 5.6 cm^{-1} to 15.0 cm^{-1}, while the greatest narrowing of the FWHM can be seen in P2 of the 0.576 km s^{-1} shot where there is a decrease of 3.8 cm^{-1} from 7.0 cm^{-1} to 3.2 cm^{-1}.

5.3.3 Labradorite

As discussed in Section 4.2.3, labradorite has a pair of distinctive peaks at approximately 480.0 cm^{-1} and 510.0 cm^{-1} which represents the symmetric stretching mode of the T-O-T linkage [177], where O is oxygen and T can be Si or Al; it is the changes to these Raman peaks that were investigated here. The peak at 480.0 cm^{-1} will be referred to as peak 1 (P1), while the 510.0 cm^{-1} peak will be referred to as peak 2 (P2).

There are eight maps presented for each shot. These maps are split across two figures for each shot, the first of which contains: the P1 intensity, the P2 intensity, the P1 FWHM, the P2 FWHM. While the second contains: the P1 shift, the P2 shift, the separation between the P1 and P2 peaks, and finally the $\sigma_{resid.}$

Often the P1 and P2 peaks in labradorite do not shift in tandem, nor the same directions, for a particular shot. Because of this, one of the maps chosen to be displayed here is a peak separation map. This map displays the separation between the positions of P1 and P2 and helps to illustrate what is happening to the sample as a whole instead of just to a single peak.

Figure 5.41, Figure 5.42, Figure 5.43, Figure 5.44, and Figure 5.45 show the optical images of the craters analysed for the labradorite shot programme. In each Figure the X and Y axes are in micrometres.

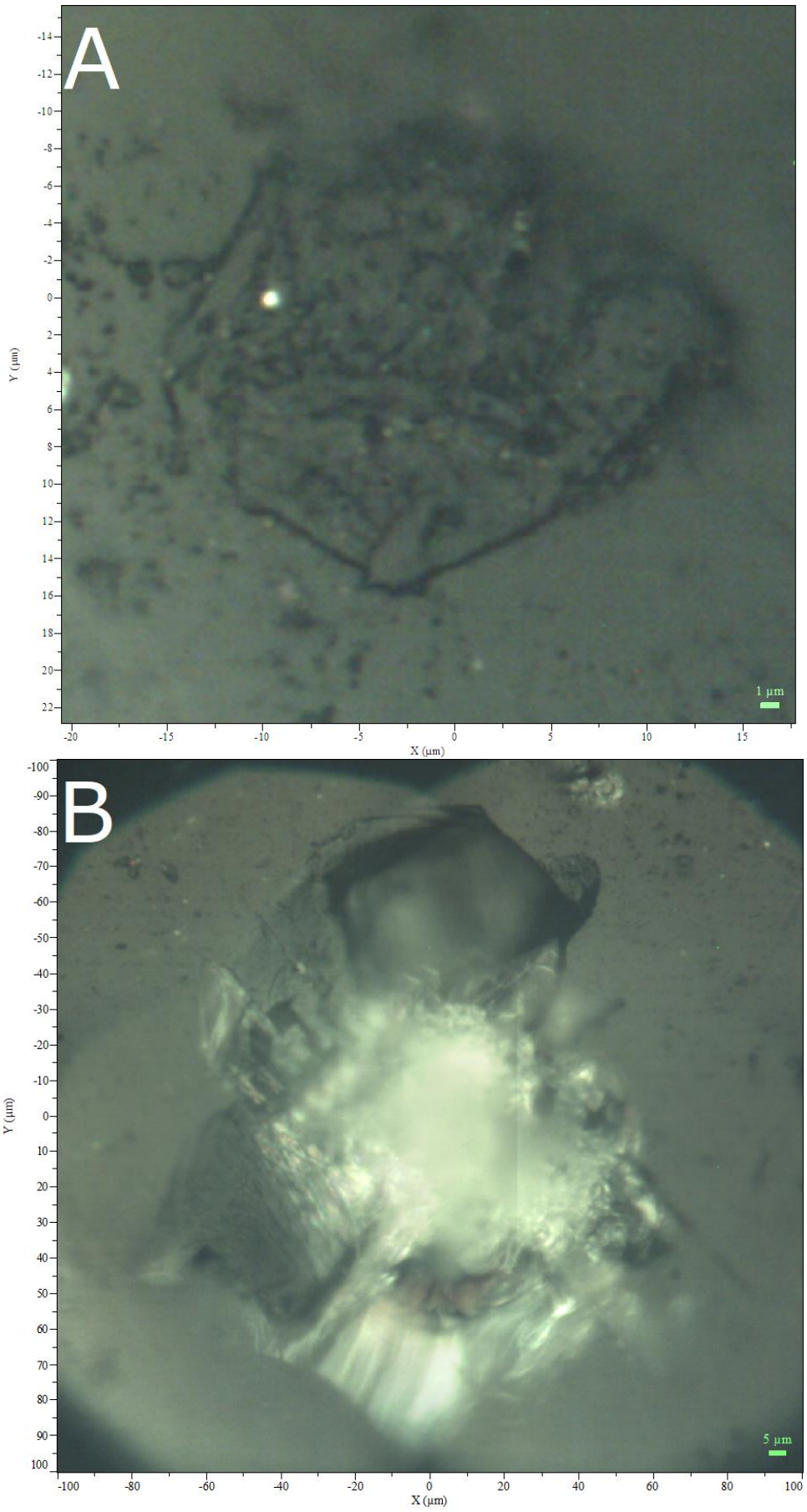


Figure 5.41: Optical montage images of the labradorite targets (A) S250915#1 where V = 0.291 km s^{-1} (x100) and (B) S160915#1 where V = 0.646 km s^{-1} (x50).

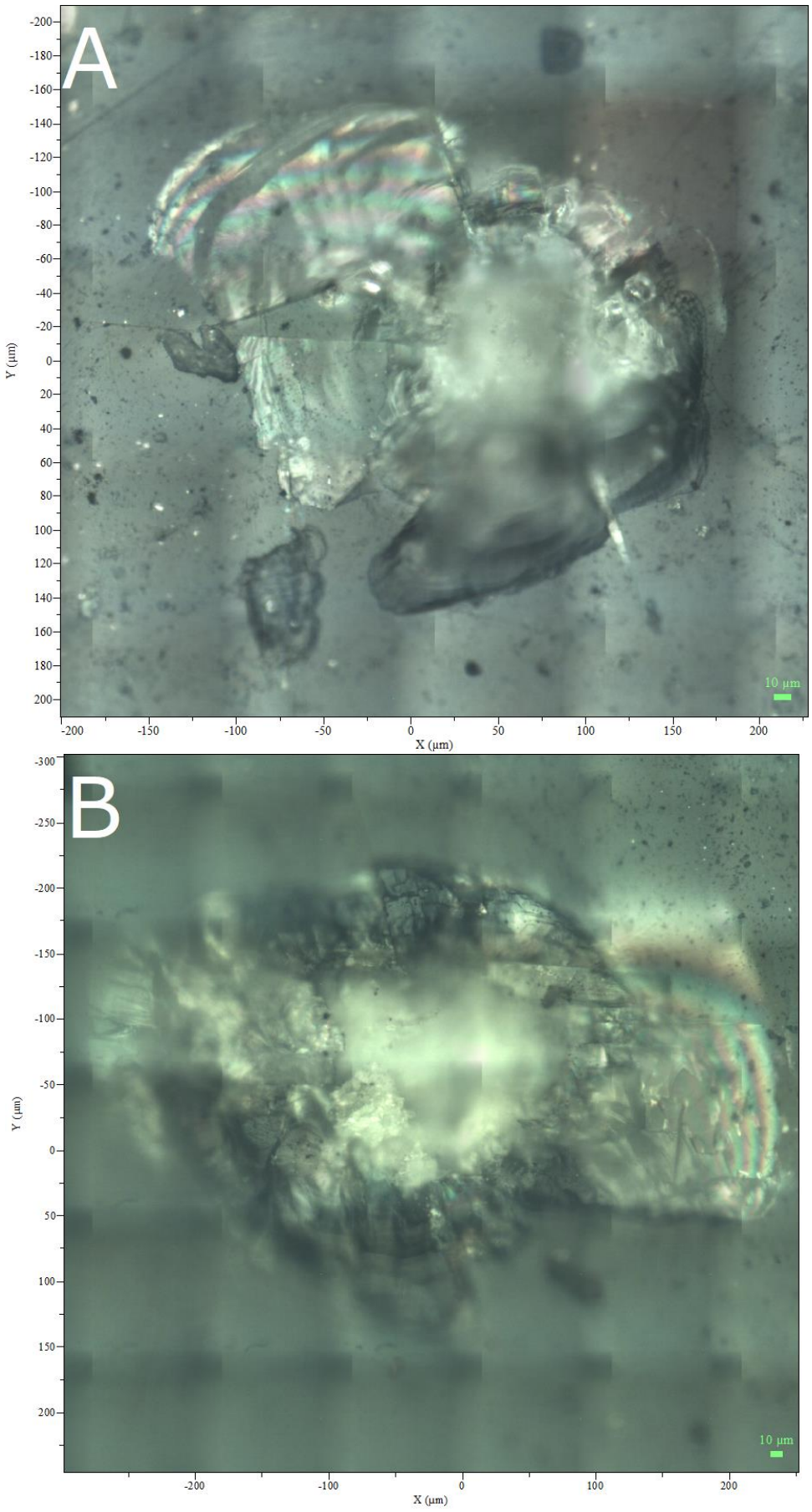


Figure 5.42: Optical montage images (x50 magnification) of the labradorite targets (A) S300715#1 where V = 0.997 km s^{-1} and (B) G181217#1 where V = 1.36 km s^{-1}.

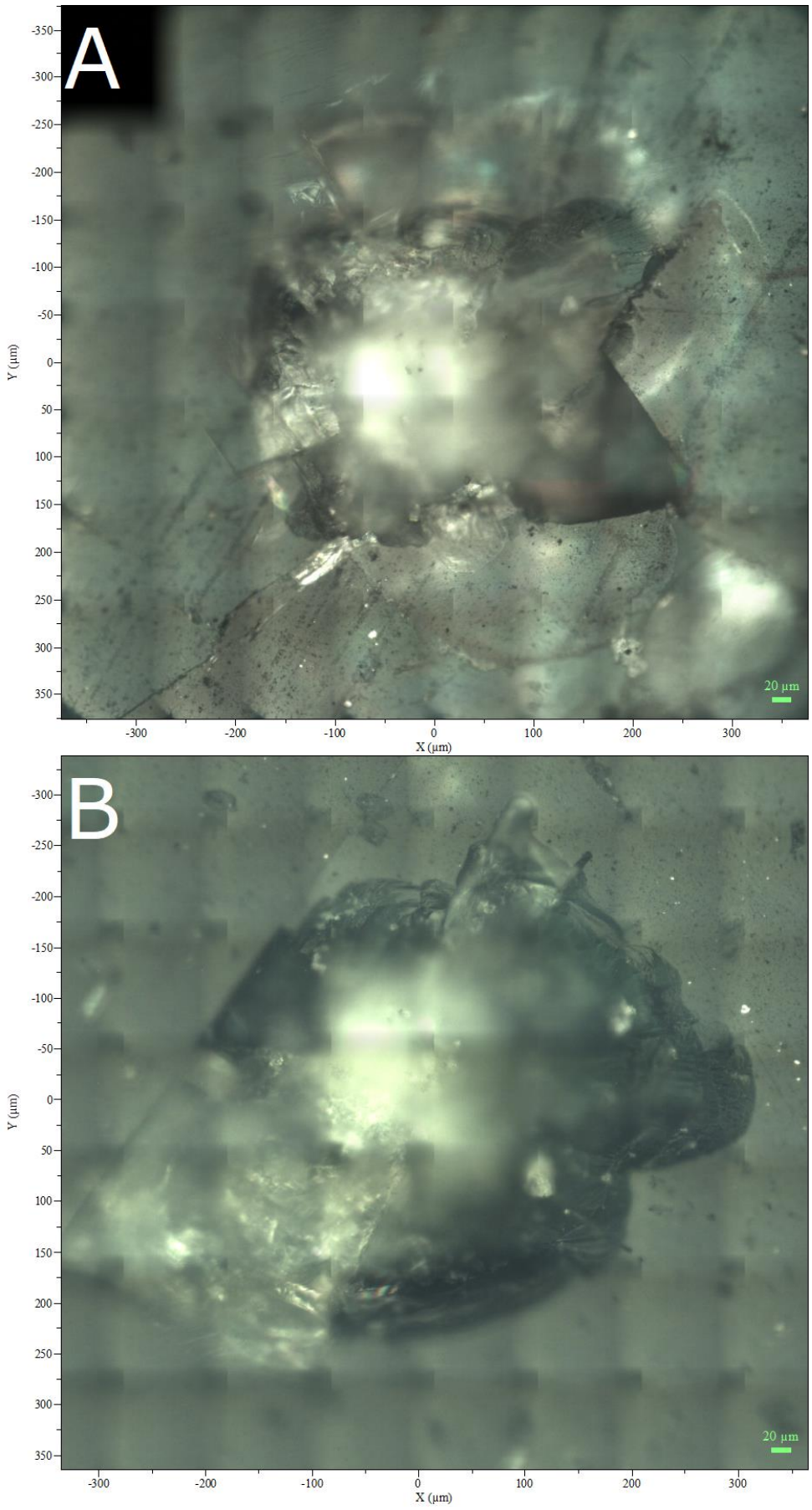


Figure 5.43: Optical montage images (x50 magnification) of the labradorite targets (A) G170615#2 where V = 1.81 km s^{-1} and (B) G050815#1 where V = 1.99 km s^{-1}.

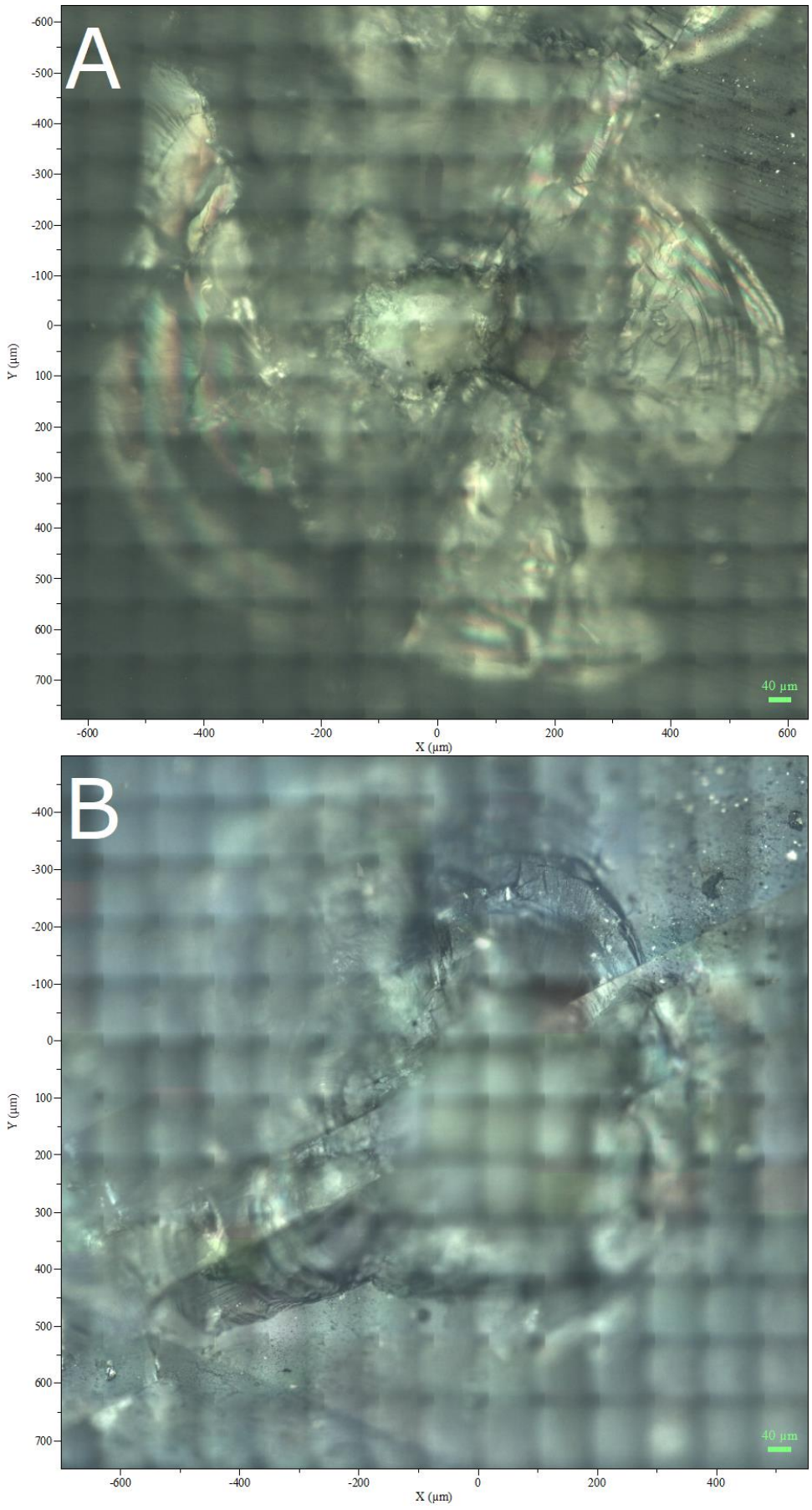


Figure 5.44: Optical montage images (x50 magnification) of the labradorite targets (A) G120815#1 where V = 2.72 km s^{-1} and (B) G100715#2 where V = 3.39 km s^{-1}.

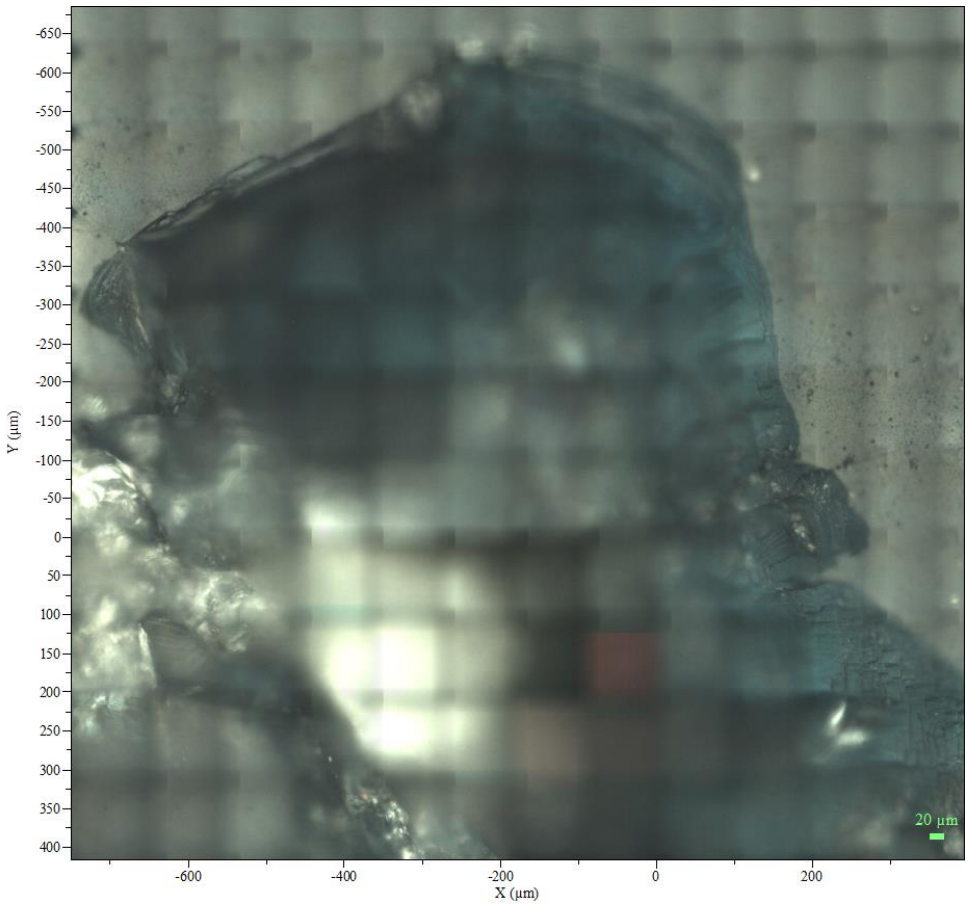


Figure 5.45: Optical montage images (x50 magnification) of the labradorite target G160915#2 where V = 5.06 km s^{-1}.

5.3.3.1 Target: Labradorite, V = 0.291 km s^{-1}, Shot Number S250915#1

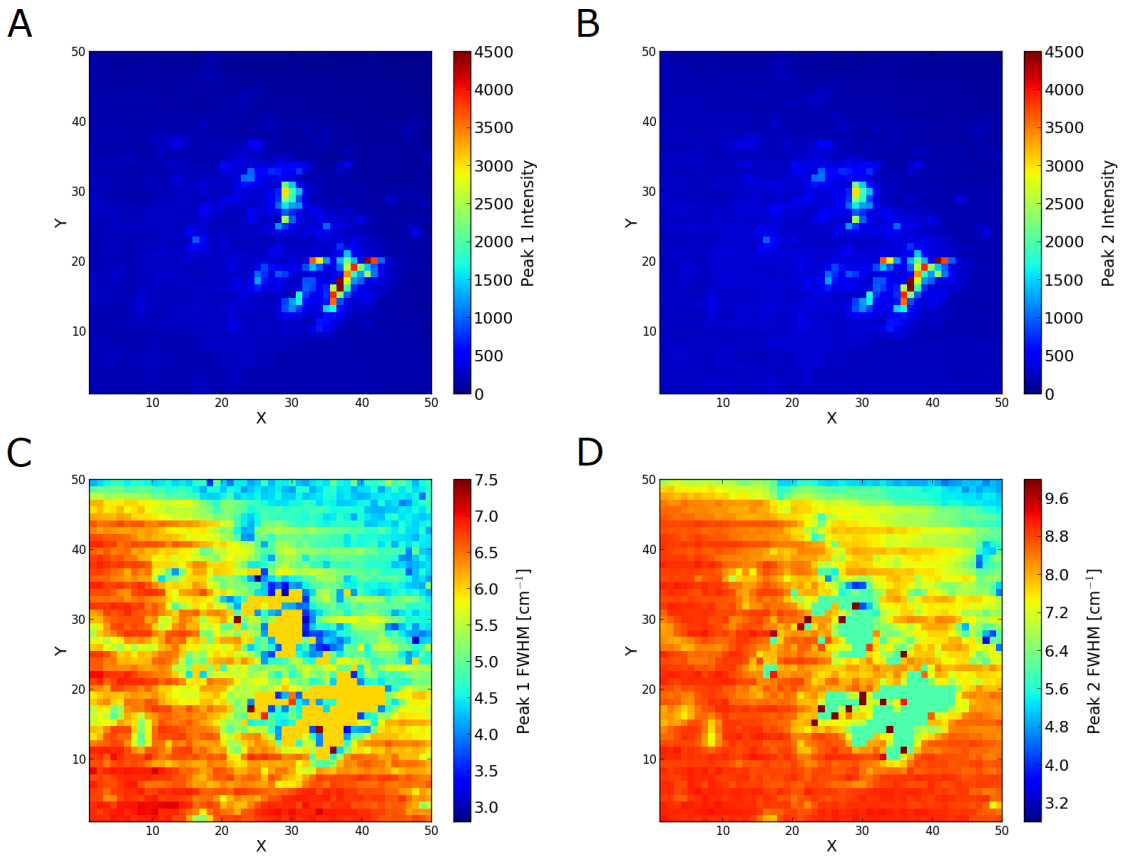


Figure 5.46: Raman map images for the labradorite target S250915#1 where V = 0.291 km s^{-1}. (A) P1 Intensity map. (B) P2 intensity map. (C) P1 FWHM map. (D) P2 FWHM.

Figure 5.47.H, the σ_{resid} map for this shot (average σ_{resid} of 83.5), shows several pixels that have σ_{resid} values less than 5.0. As explained in Section 5.2.1, any pixel will a σ_{resid} value of less than 3.0 will be disregarded in the analysis.

The intensity maps for this shot (Figure 5.46.A and Figure 5.46.B) lack detail concerning the shape of the crater due to a few high intensity pixels inflating the range of the scale. This makes it difficult to determine how accurately the intensity profile matches the optical image of the crater (Figure 5.41.A).

The P1 FWHM map (Figure 5.46.C) shows areas with a constant value of 6.0 cm^{-1} located at (29,28) and (38,17), the same location as the areas of high exaggerating in Figure 5.46.A and Figure 5.46.B. These areas are surrounded by pixels showing a reduced FWHM (as small as 3.2 cm^{-1}). The edges of the map show a broader FWHM (up to a maximum of 7.1 cm^{-1}), with the exception of the top right of the map where there peaks are narrower (down to a minimum of 3.8 cm^{-1}).

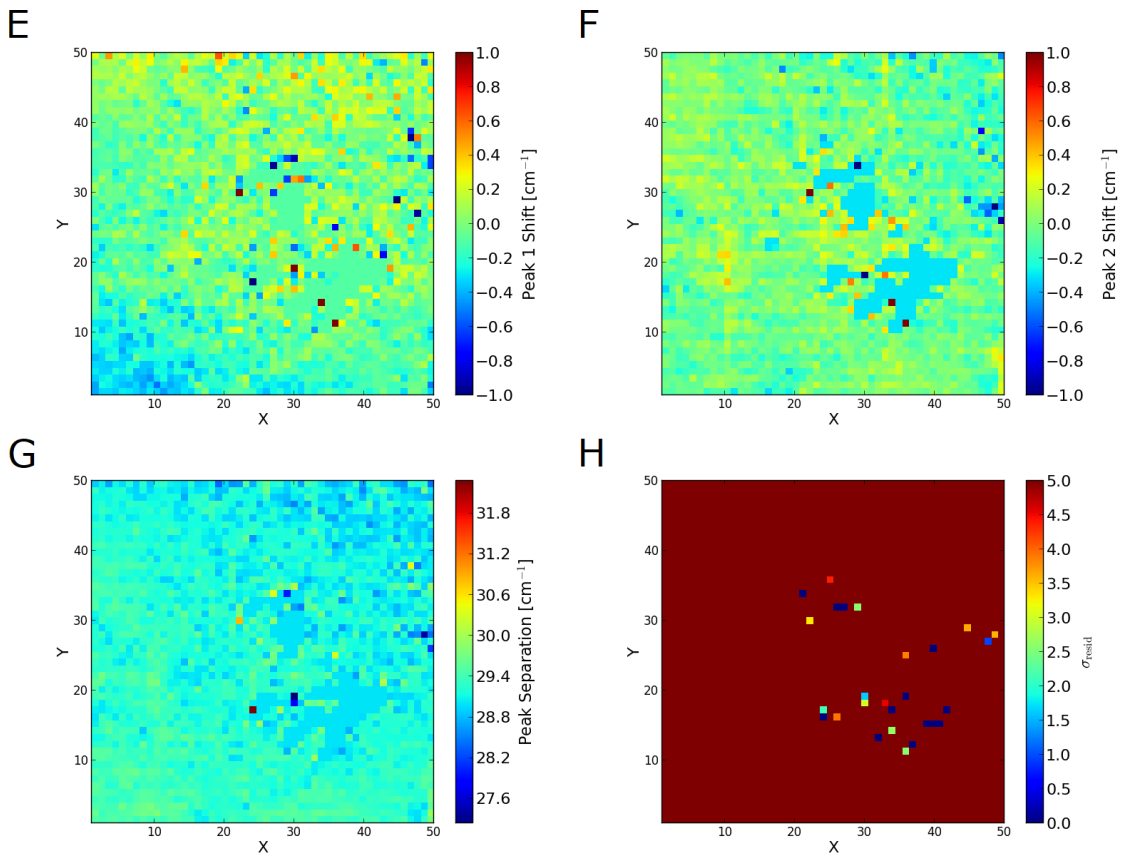


Figure 5.47: Raman map images for the labradorite target S250915#1 where V = 0.291 km s^{-1}. (E) P1 shift map. (F) P2 shift map. (G) Peak separation map. (H) σ_{resid} map.

The P2 FWHM map (Figure 5.46.D) shows the same structure as the P1 FWHM map but is much more defined. The areas located at (29,28) and (38,17) are still present (with a value of 6.1 cm^{-1}) and there are a number of pixels scattered near these areas showing broadened peaks with a value of 10.0 cm^{-1}. The positions of these pixels match those identified in Figure 5.47.D and should be disregarded. The surrounding material is more consistent in this map than the P1 FWHM map. The majority of the map shows the unaltered value of 8.9 cm^{-1} except for the top right of the map where the peaks are narrower decreasing to a minimum of 4.4 cm^{-1}.

The same constant areas seen in the FWHM maps can still be seen in Figure 5.47.E (the P1 shift map for this shot) and show as un-shifted material. The bottom left corner of the map shows an area of negative shift (maximum of -0.6 cm^{-1}). After disregarding the bad data points determined from Figure 5.47.D, the remainder of the map shows positive shifts (maximum of 1.0 cm^{-1}), but with no discernible structure.

The P2 shift map (Figure 5.47.F) is more defined than that of the P1 shift map. The areas seen in the FWHM maps are again present, but here they represent a negative shift of -0.3 cm^{-1}. Similar to Figure 5.47.E, the rest of the map shows positive shifts with little structure (maximum of 1.0 cm^{-1}).

The peak separation map (Figure 5.47.G) shows the peaks in the areas located at (29 28,) and (38,17) to have moved closer together due to the negative shift seen in Figure 5.47.F. The rest of the map shows very little change in peak separation apart from the top right corner where the peaks appear to have generally moved closer together.

5.3.3.2 Target: Labradorite, V = 0.646 km s^{-1}, Shot Number S160915#1

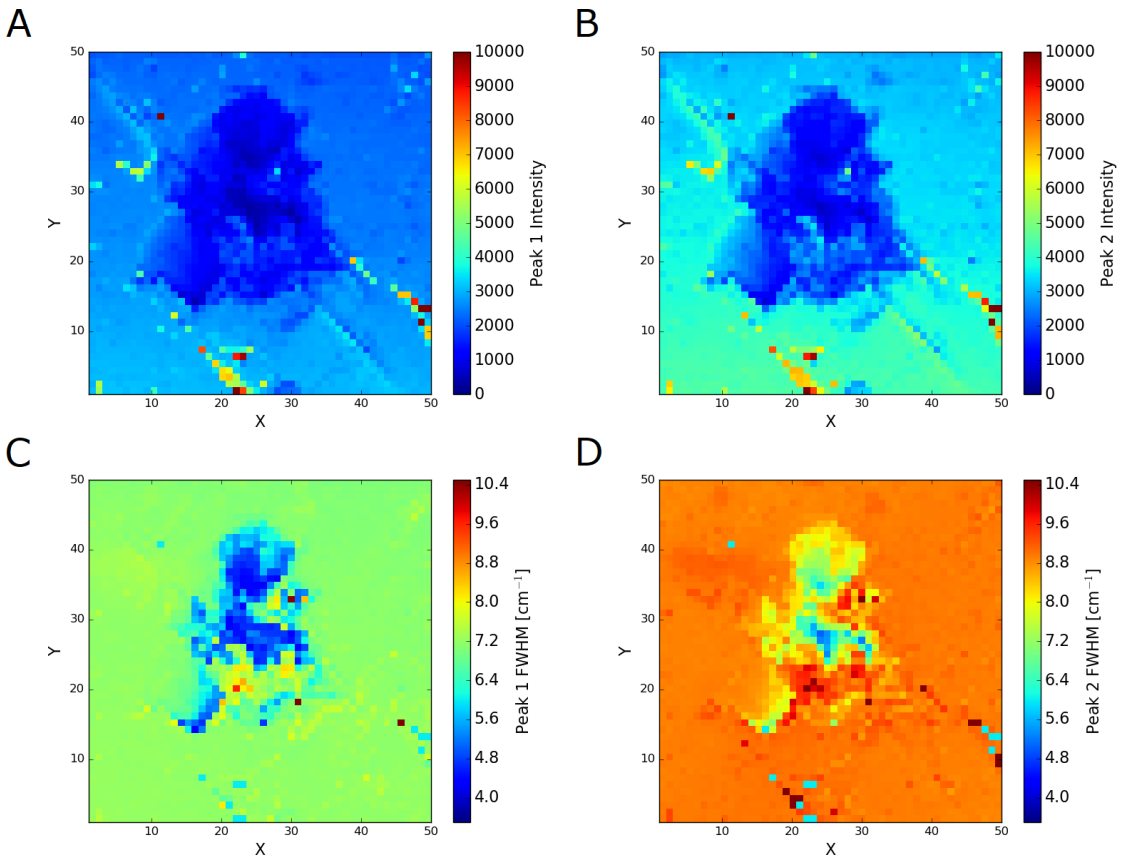


Figure 5.48: Raman map images for the labradorite target S160915#1 where V = 0.646 km s^{-1}. (A) P1 Intensity map. (B) P2 intensity map. (C) P1 FWHM map. (D) P2 FWHM map.

Figure 5.49.H shows σ_{resid} to have high values (average σ_{resid} of 12.0) in all but three pixels. Two of these pixels have values of less than 3.0 sigma and are located at (21,3), (30,33). They will be disregarded in the analysis for this shot.

The intensity maps (Figure 5.48.A and Figure 5.48.B) show a good match to Figure 5.41.B, the optical image for this shot. Both intensity maps show the shape of the crater as well as the cracks running diagonally through the crater.

The P1 FWHM map (Figure 5.48.C) shows the FWHM decreasing inside the crater (from 7.0 cm^{-1} to a minimum of 4.3 cm^{-1}), except for the area at (24,21) towards the bottom of the crater, where the FWHM shows an increase (from 7.0 cm^{-1} to a maximum of 9.6 cm^{-1}). The largest increase to the FWHM for P1 is 10.4 cm^{-1} and is located at (46,15). This position corresponds with one of the cracks present on the surface of the target.

The P2 FWHM map (Figure 5.48.D) shows the same features as the P1 FWHM map. Here the decrease inside the crater is from 8.8 cm^{-1} down to a minimum of 5.5 cm^{-1}, while the increase in the area at (24,21) is from 8.8 cm^{-1} up to a maximum of 10.5 cm^{-1}. This map also shows the cracks more clearly than Figure 5.48.C, specifically those that start at (23,0) and (50,9).

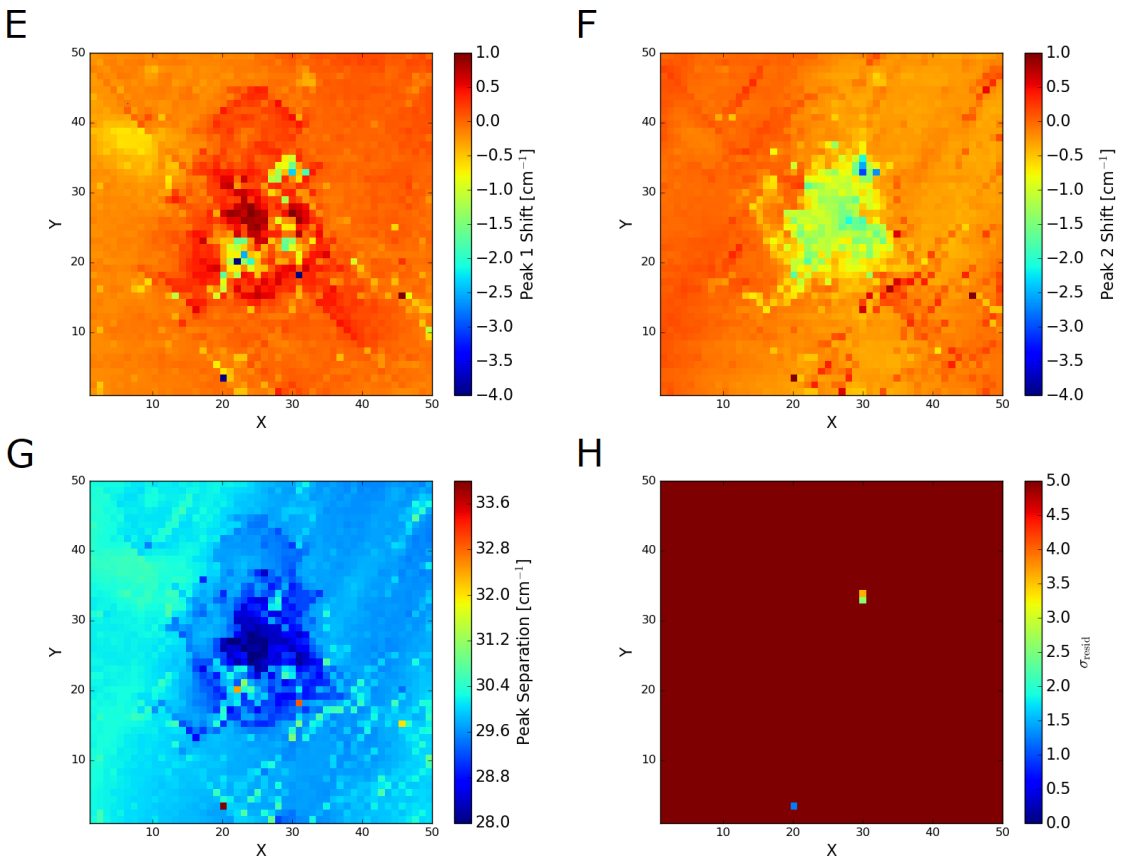


Figure 5.49: Raman map images for the labradorite target S160915#1 where V = 0.646 km s^{-1}. (E) P1 shift map. (F) P2 shift map. (G) Peak separation map. (H) σ_{resid} map.

Figure 5.49.E shows P1 shifting positively towards the centre of the crater up to a maximum shift of +1.0 cm^{-1}. There are two areas of negative shift; the first is located in the same place as the area of increasing FWHM from Figure 5.48.C and Figure 5.48.D, (24,21) with a maximum shift of -4.0 cm^{-1}. The second has a maximum shift of -2.3 cm^{-1} but located at (30,33) and therefore should be disregarded. Figure 5.49.F shows P2 shifting negatively towards the centre of the crater with a maximum shift of -2.7 cm^{-1} at (32,33). The largest negative shift of -3.1 cm^{-1} is located at (30,33) and therefore should be disregarded. The P2 map also shows an area of positive shift (maximum of +1.0 cm^{-1}) in the bottom right of the map corresponding to an area of uplifted material in the optical image (Figure 5.41.B).

The peak separation map (Figure 5.49.G) shows a large area in the centre of the map which indicated that the peaks have moved closer together. This is the result of the P1 shifting positively and the P2 shifting negatively in that area.

5.3.3.3 Target: Labradorite, V = 0.997 km s^{-1}, Shot Number S300715#1

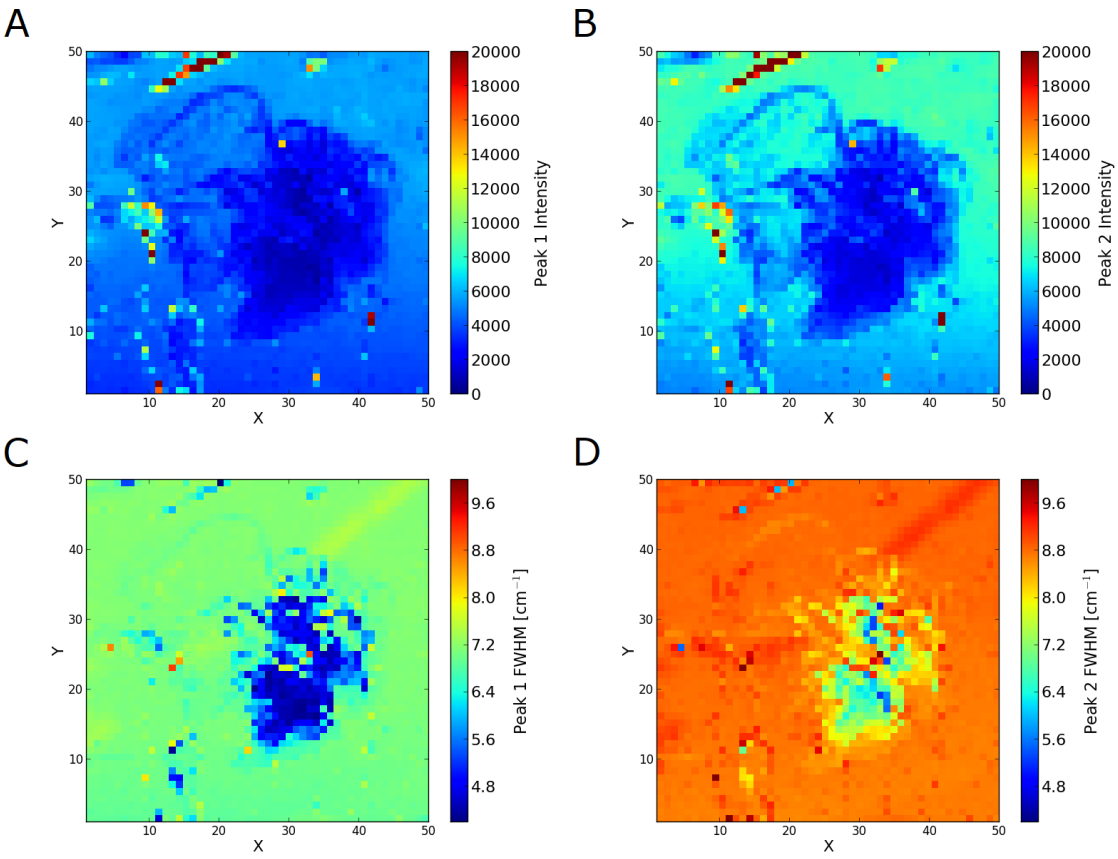


Figure 5.50: Raman map images for the labradorite target S300715#1 where V = 0.997 km s^{-1}. (A) P1 Intensity map. (B) P2 intensity map. (C) P1 FWHM map. (D) P2 FWHM map.

Figure 5.51.H shows high σ_{resid} values for the majority of the map (average σ_{resid} of 8.7) with four pixels with values of less than 3.0 sigma scattered randomly throughout the map. These will be disregarded during analysis.

Figure 5.42.A shows a good match to the intensity maps for this shot, Figure 5.50.A and Figure 5.50.B. Both intensity maps show the central crater, as well as the edges of the uplifted material to the top left of the crater. A faint crack can also be seen above the uplifted material in Figure 5.42.A that is also present in the intensity maps between (21,50) and (11,45).

Figure 5.50.C and Figure 5.50.D are the FWHM maps and show a large area depicting a decrease in FWHM. For P1 this decrease is from 7.0 cm^{-1} to a minimum of 4.2 cm^{-1}, while for P2 this decrease is from 8.7 cm^{-1} to a minimum of 5.1 cm^{-1}. The crack between (21,50) and (11,45) can also be seen in both maps as having a decrease in the FWHM, down to 3.5 cm^{-1} for P1 and 6.0 cm^{-1} for P2. Both maps show scattered pixels with increased FWHM with maxima of 9.1 cm^{-1} and 10.0 cm^{-1} for P1 and P2 respectively.

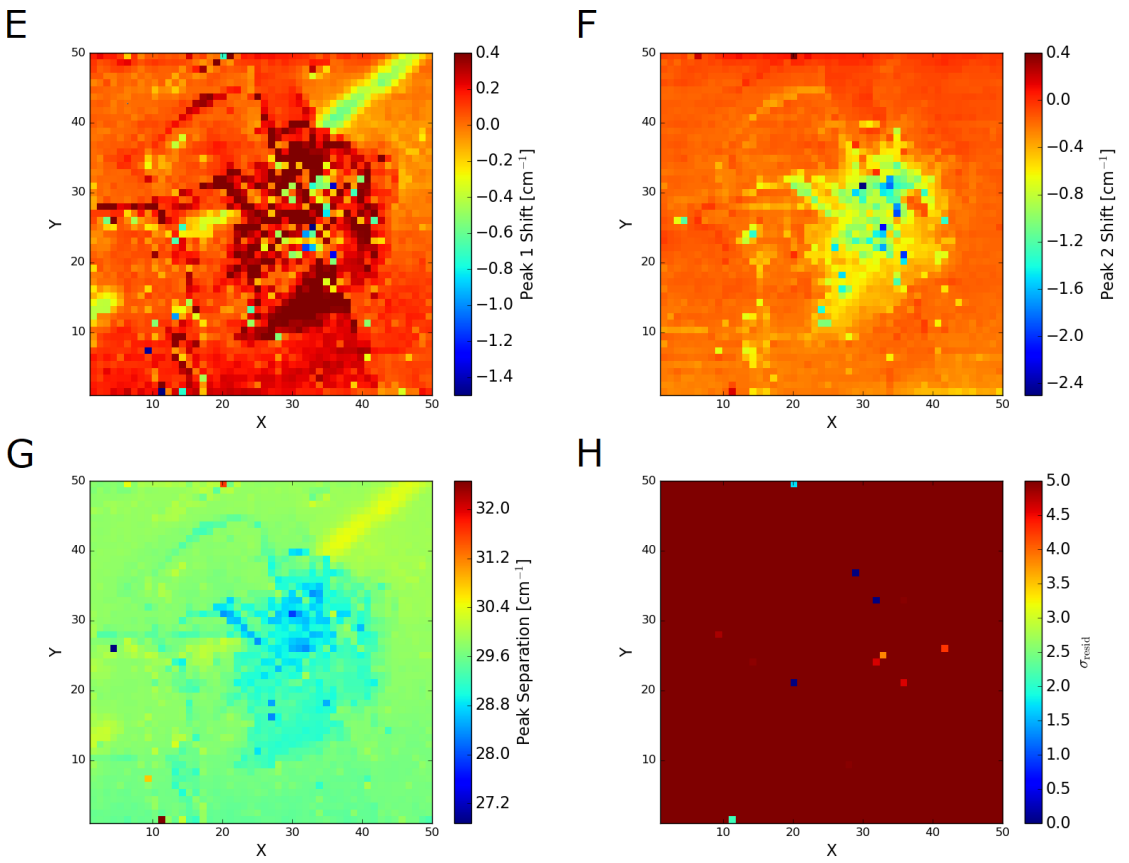


Figure 5.51: Raman map images for the labradorite target S300715#1 where V = 0.997 km s^{-1}. (E) P1 shift map. (F) P2 shift map. (G) Peak separation map. (H) σ_{resid} map.

The P1 shift map (Figure 5.51.E) shows that the peak position has generally shifted positively along the edge of the uplifted material and the crater walls, to a maximum of +0.4 cm^{-1}. Inside the crater there are areas showing a maximum negative shift of -1.5 cm^{-1}. However, the most distinct feature on this map is the diagonal line of negative shift (maximum shift of -0.6 cm^{-1}) originating in the top right of the image. Figure 5.42.A does not show any physical feature that could be the origin of this feature and the line is not present in either of the intensity maps, or the P2 shift map.

By contrast, Figure 5.51.F shows the crater to primarily consist of a large area of negative shift for P2 with a maximum of -2.5 cm^{-1}. Indeed, the only positive shift depicted in this map is a single pixel with a value of +0.2 cm^{-1} located at (20,50). Though this position corresponds to one of the disregarded pixels discussed earlier.

Figure 5.51.G, the peak separation map, shows that the peaks have become closer together inside the crater. This is because P1 has shifted positively, while P2 has shifted negatively in that region. The diagonal line originating in the top right of the image shows the distance between the peaks increasing; this is the result of P1 shifting negatively while P2 has remained unshifted.

5.3.3.4 Target: Labradorite, V = 1.36 km s^{-1}, Shot Number G181217#1

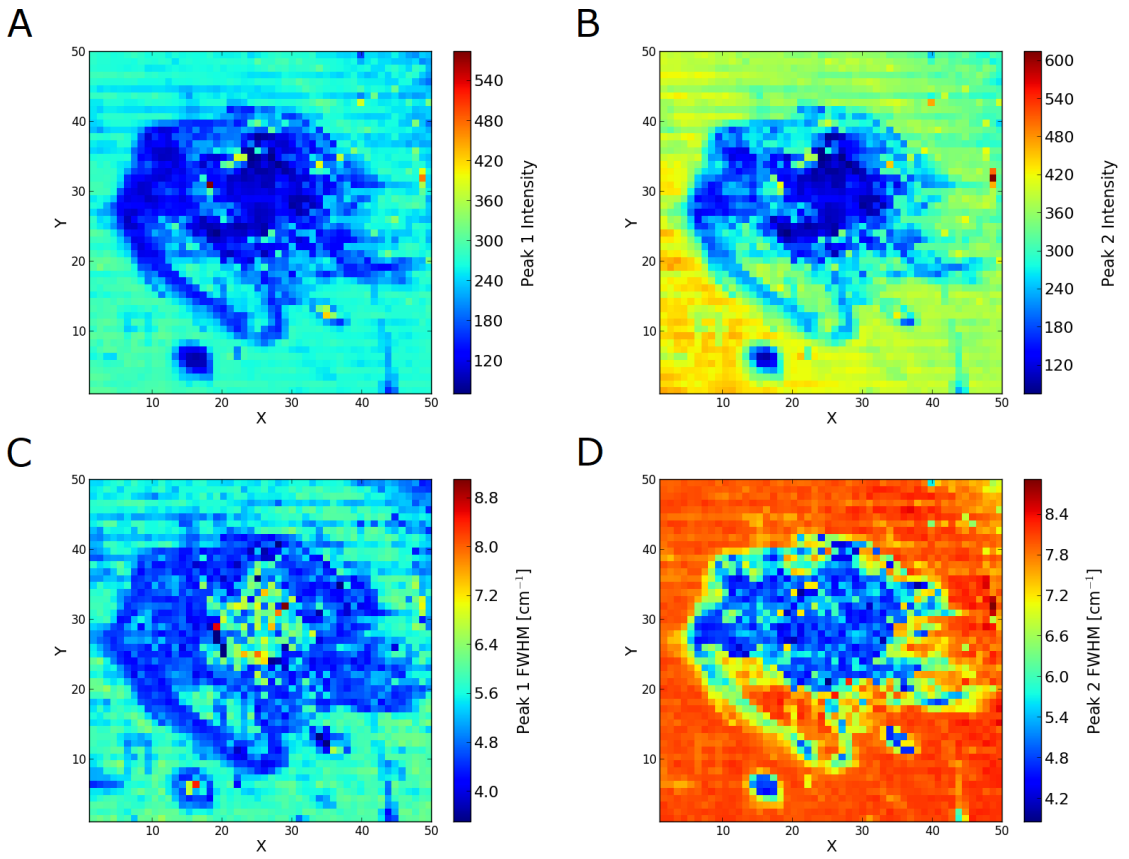


Figure 5.52: Raman map images for the labradorite target G181217#1 where V = 1.36 km s^{-1}. (A) P1 Intensity map. (B) P2 intensity map. (C) P1 FWHM map. (D) P2 FWHM

Figure 5.53.H shows high σ_{resid} values for the majority of the map (average σ_{resid} of 49.7) with only a few pixels having values of less than 3.0 sigma. These pixels will be disregarded during analysis of the other maps.

The intensity maps (Figure 5.52.A and Figure 5.52.B) both show a good agreement with the optical image Figure 5.42.B. The outline of the crater is clearly discernible in both maps and corresponds to that of the crater seen in the optical image.

Figure 5.52.C and Figure 5.52.D are the FWHM maps. Once again, the shape of the crater can be seen in these maps. The P1 map shows narrowing of the peaks along the crater walls (to a minimum of 3.5 cm^{-1}) and an area in the centre of the crater that shows broadening of the peaks (to a maximum of 9.1 cm^{-1}). The P2 map shows narrowing of the peaks inside the crater that increases towards the centre of the crater (to a minimum of 3.8 cm^{-1}).

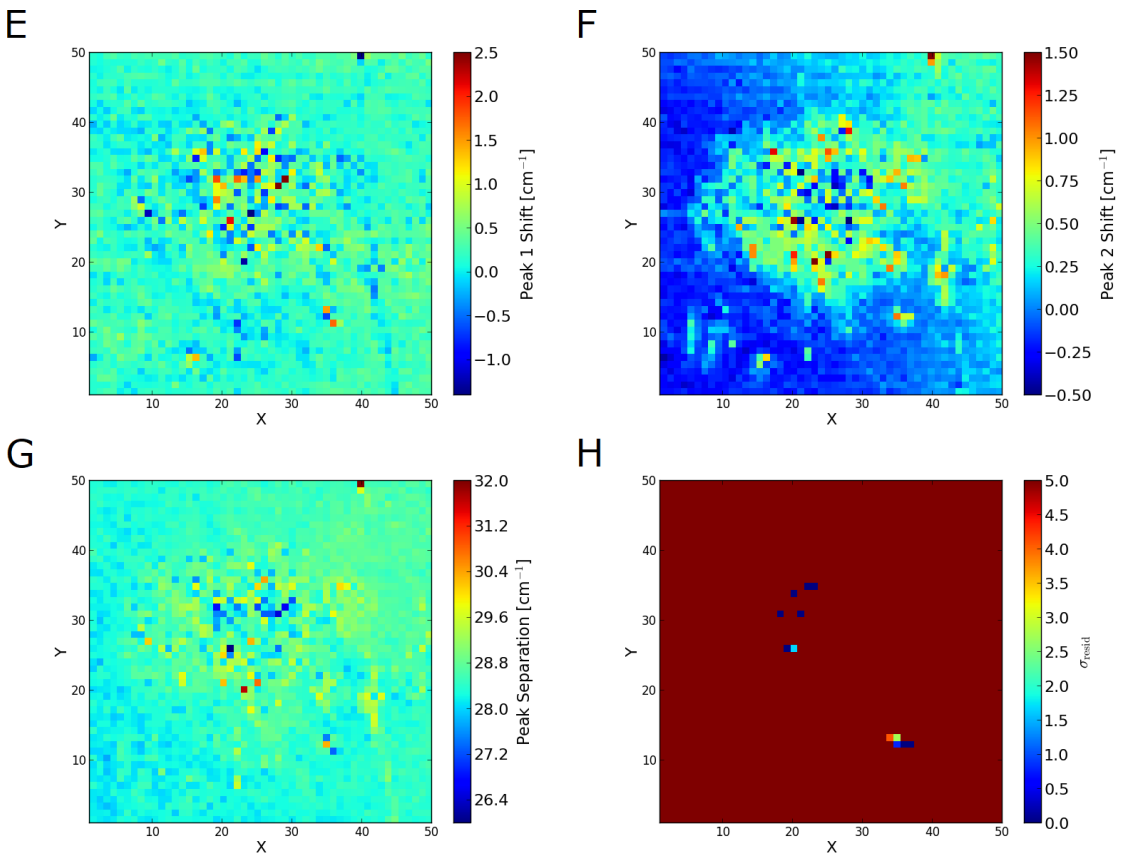


Figure 5.53: Raman map images for the labradorite target G181217#1 where V = 1.36 km s^{-1}. (E) P1 shift map. (F) P2 shift map. (G) Peak separation map. (H) σ_{resid} map.

The structure of the crater is not visible in the P1 shift map (Figure 5.53.E). The shifts are both positive and negative across the map but look to be more extreme towards the centre of the map where the largest shifts of +2.5 cm^{-1} and -1.5 cm^{-1} can be seen.

Some of the crater structure can be seen in the P2 shift map (Figure 5.53.F), but it is not as well defined as in any of the maps from Figure 5.52. Positive shifts can be seen in the top right of the map (maximum of +1.5 cm^{-1}) and along the crater walls (maximum of +1.5 cm^{-1}). Negative shifts can be seen at the centre of the crater with a maximum shift of -0.5 cm^{-1}.

Figure 5.53.G is the peak separation map. It shows a collection of dark blue pixels located around (25,31) that represent the peaks coming much closer together than in the rest of the map. This is due to there being a concentration of negatively shifted pixels for P2 combined with the presence of positively shifted pixels in the same region.

5.3.3.5 Target: Labradorite, V = 1.81 km s^{-1}, Shot Number G170615#2

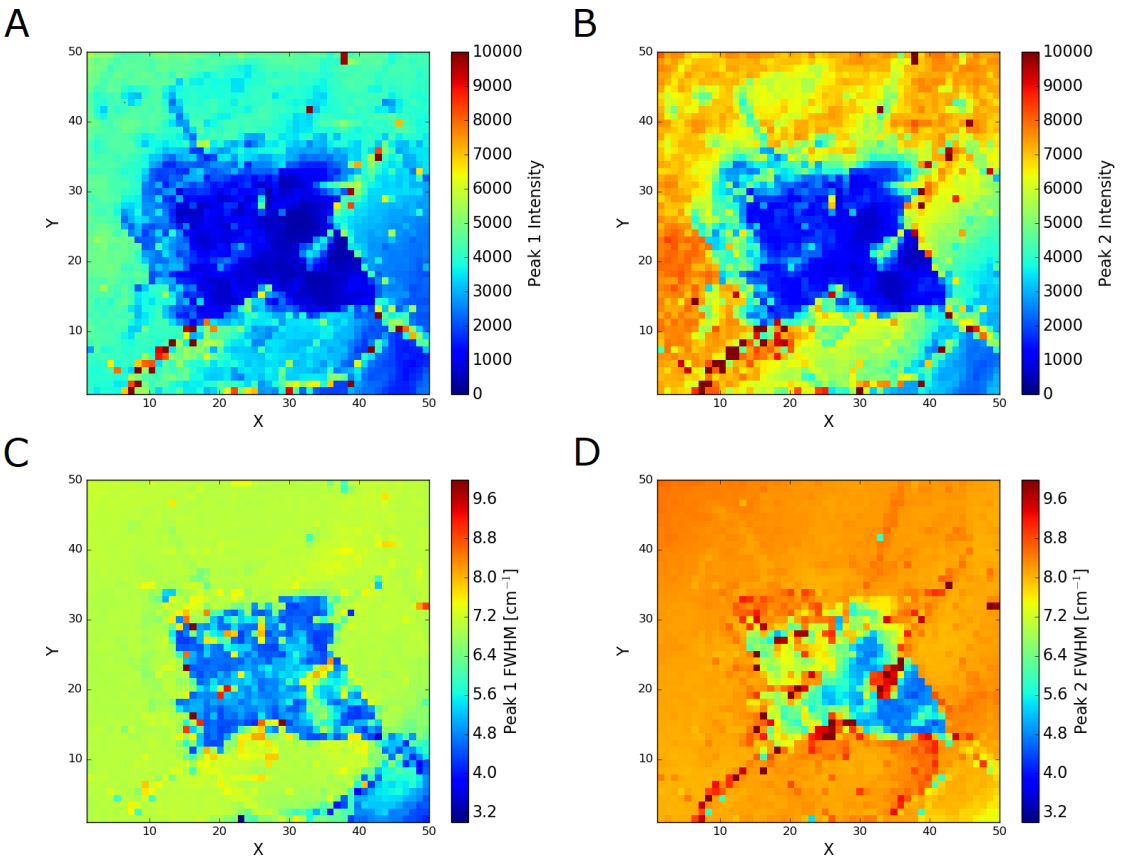


Figure 5.54: Raman map images for the labradorite target G170615#2 where V = 1.81 km s^{-1}. (A) P1 Intensity map. (B) P2 intensity map. (C) P1 FWHM map. (D) P2 FWHM map.

The σ_{resid} map (Figure 5.55.H) shows high values across most of the map (average σ_{resid} of 11.2). There are however a number of pixels that have a value of less than 5.0 sigma, mostly located along the 'rim' of the crater. Many of these pixels have values of less than 3.0 sigma and will be disregarded in the analysis (there are too many to list their exact positions here).

Figure 5.54.A and Figure 5.54.B are the intensity maps for this shot with both showing a good match to the optical image Figure 5.43.A. The shape of the crater is easily discernible as well as the cracks radiating outwards from the crater at (15,40), (12,7), (46,10), and (42,32). The bottom right corner of the maps shows a significant decrease in intensity. This is because this impact occurred near the edge of the table and this corner of the map is on the crown of the gemstone.

The FWHM maps, Figure 5.54.C and Figure 5.54.D, show the peaks to have narrowed inside the crater, while broadening along the cracks. For P1, the peak has narrowed from 7.0 cm^{-1} to a minimum of 4.4 cm^{-1} inside the crater while broadening to a maximum of 10.0 cm^{-1} outside the crater and 7.8 cm^{-1} along the cracks below the crater. For P2, the peak has narrowed from 8.2 cm^{-1} to a minimum of 4.5 cm^{-1} inside the crater, and broadened to a maximum of 10.0 cm^{-1} along the cracks and bottom rim of the crater.

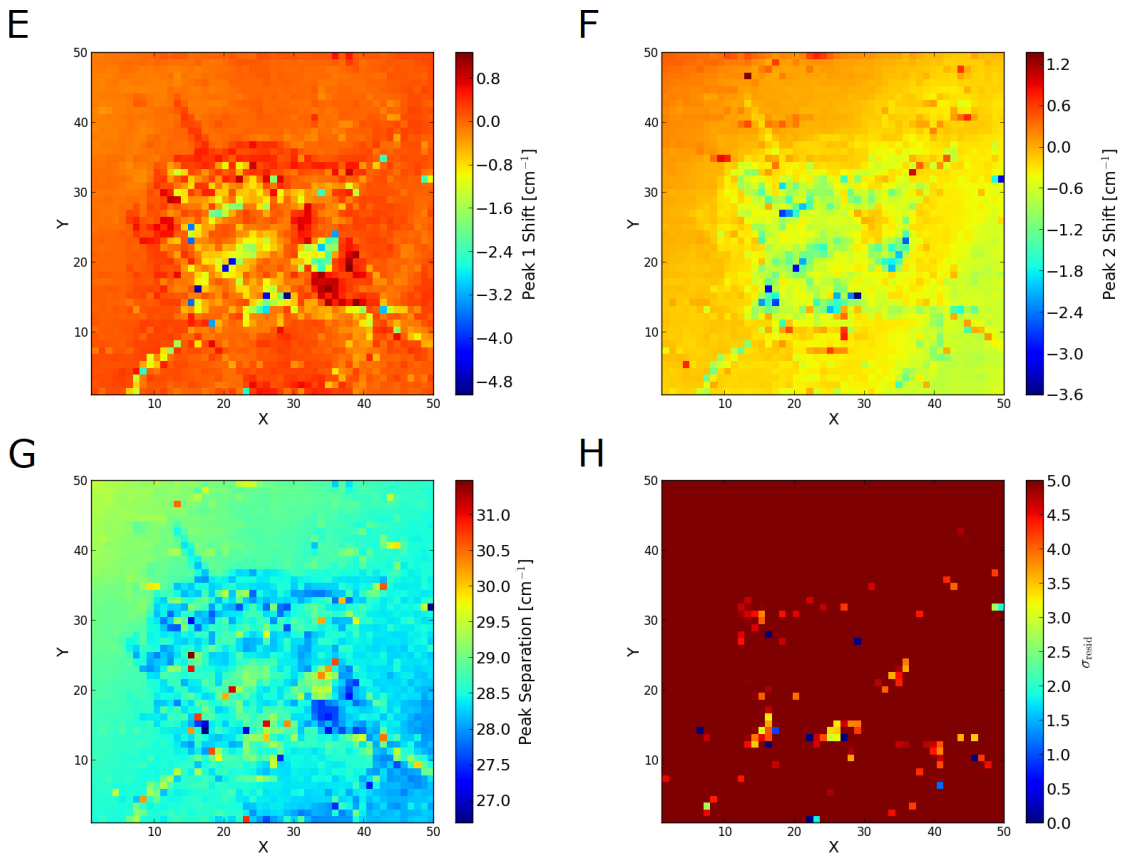


Figure 5.55: Raman map images for the labradorite target G170615#2 where V = 1.81 km s^{-1}. (E) P1 shift map. (F) P2 shift map. (G) Peak separation map. (H) σ_{resid} map.

The P1 shift map (Figure 5.55.E) shows negative shifts inside the crater and along the cracks, with the most extreme shifts matching the positions of the broadened P1 pixels from Figure 5.54.C and have a maximum of -5.0 cm^{-1}. There is one area of positive shift at (35,15) which shows a maximum shift of +1.3 cm^{-1}.

The P2 shift map (Figure 5.55.F) also shows negative shifts inside the crater and along the cracks. Again, the areas of most extreme shift match the positions of greatest broadening in the corresponding FWHM map (Figure 5.54.D) and have a maximum shift of -3.6 cm^{-1}. While there are no large areas of positive shift, there are some scattered pixels that show shifts of up to +1.4 cm^{-1}.

Figure 5.55.G is the peak separation map. It shows that the peaks have mostly become closer together in the crater with a few scattered pixels showing an increase in separation. These scattered pixels generally match the positions of the largest negative shifts in both shift maps as P1 has shifted more negatively that P2 in these areas.

5.3.3.6 Target: Labradorite, V = 1.99 km s^{-1}, Shot Number G050815#1

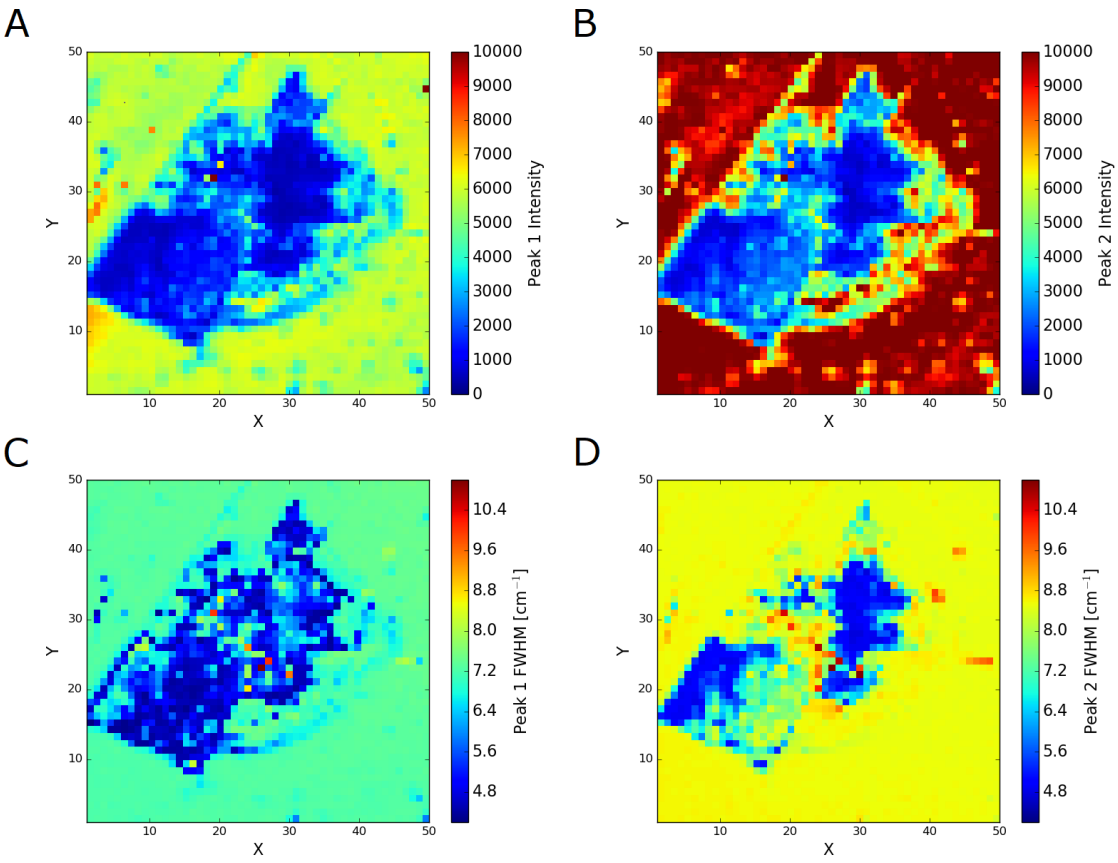


Figure 5.56: Raman map images for the labradorite target G050815#1 where V = 1.99 km s^{-1}. (A) P1 Intensity map. (B) P2 intensity map. (C) P1 FWHM map. (D) P2 FWHM map.

Figure 5.57.H shows σ_{resid} to have high values across the map (average σ_{resid} of 15.6) with the exception of a few scattered areas showing values of less than 3.0 sigma. These areas will be ignored for the analysis of this shot.

The intensity maps Figure 5.56.A and Figure 5.56.B both demonstrate a good match to the optical image Figure 5.43.B. The shape of the crater is clearly identifiable and the crack at the top of the crater is also present running from (25,50), along the top edge of the crater to (0,18). In both maps there is a band of lower intensity material centred at (23,26) that defines the boundary between the crater and a large region of uplifted material.

Figure 5.56.C is the FWHM map for P1. It clearly shows that P1 has narrowed from a FWHM of 7.3 cm^{-1} outside the crater, to a minimum of 4.2 cm^{-1} inside the crater. There are also a few scattered pixels inside the crater showing an increase in the FWHM up to a maximum of 11.0 cm^{-1}. The positions of these pixels lies within the band of lower intensity material described in the intensity maps.

Figure 5.56.D shows two regions of narrowing for the FWHM of P2 centred at (15,18) and (30,31). Here the FWHM has decreased from 8.6 cm^{-1} to a minimum of 4.8 cm^{-1}. These two regions are separated by a region where the FWHM has increased to a maximum of 11.0 cm^{-1}. The position of this region of increase matches the position of the band of lower intensity material described in the intensity maps.

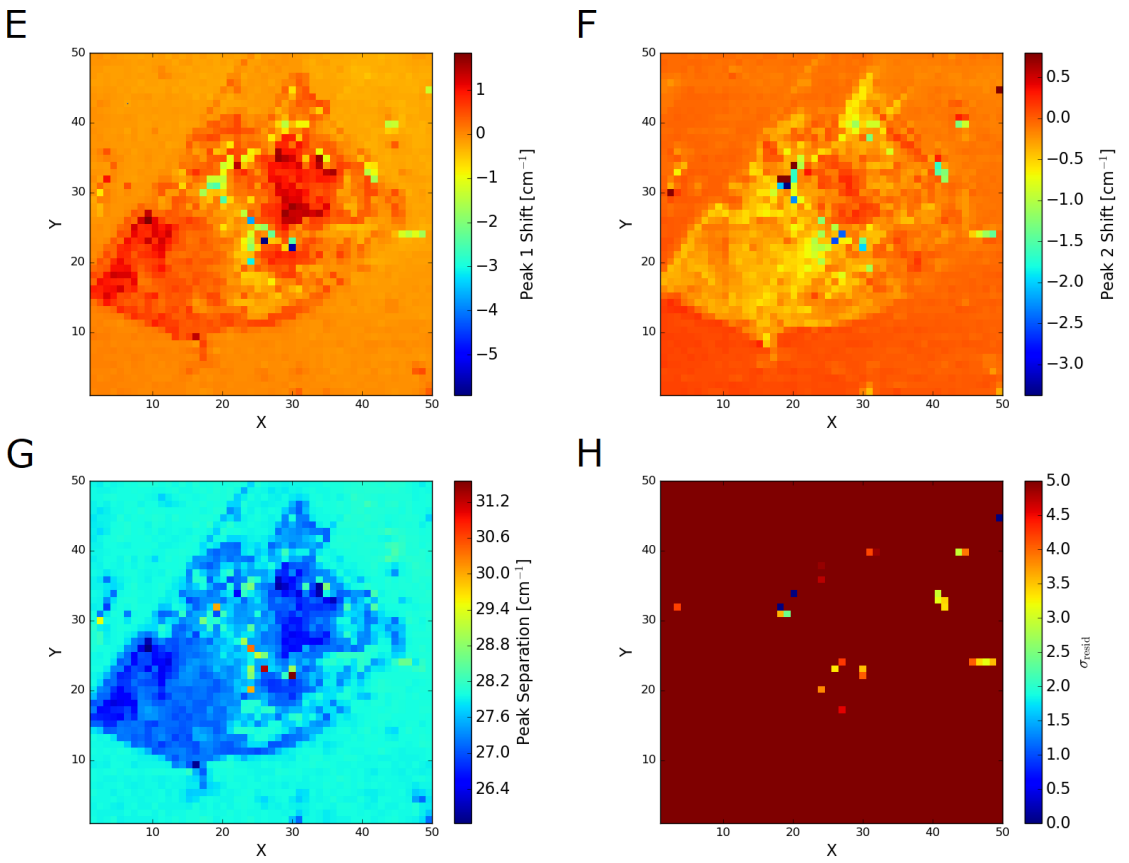


Figure 5.57: Raman map images for the labradorite target G050815#1 where V = 1.99 km s^{-1}. (E) P1 shift map. (F) P2 shift map. (G) Peak separation map. (H) σ_{resid} map.

The P1 and P2 shift maps (Figure 5.57.E and Figure 5.57.F) both show the band of material at the edge of the crater to have suffered a negative shift. For P1 this shift has a maximum of -5.9 cm^{-1} and for P2 this shift has a maximum of -3.4 cm^{-1}.

The inside of the crater, centred at (30,31), also shows a positive shift for P1 (maximum of +1.8 cm^{-1}) and P2 (maximum of +0.2 cm^{-1}). The region of uplifted material centred at (15,18) shows a positive shift for P1 (maximum of +1.8 cm^{-1}) and a negative shift for P2 (maximum of -0.5 cm^{-1}).

Figure 5.57.G represents the peak separation of P1 and P2 for this shot. It shows that the peaks have generally moved closer together inside the crater.

5.3.3.7 Target: Labradorite, V = 2.72 km s^{-1}, Shot Number G120815#1

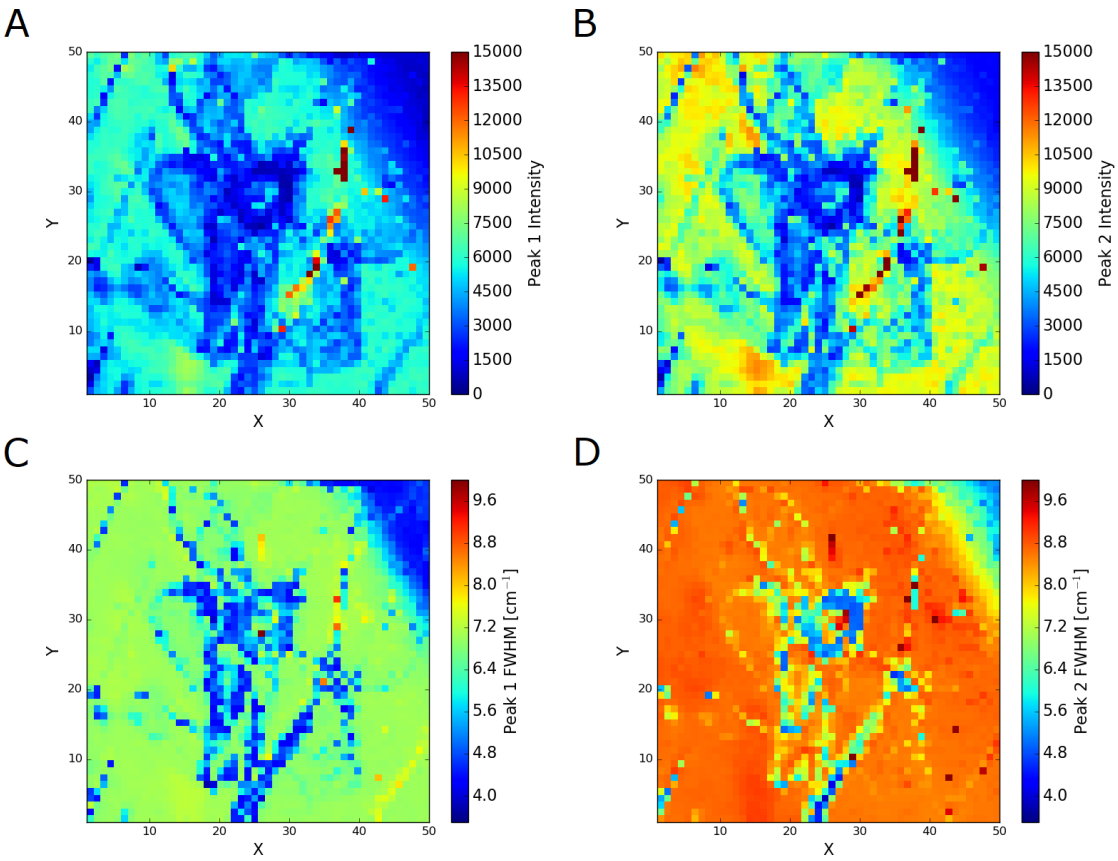


Figure 5.58: Raman map images for the labradorite target G120815#1 where V = 2.72 km s^{-1}. (A) P1 Intensity map. (B) P2 intensity map. (C) P1 FWHM map. (D) P2 FWHM map.

Figure 5.59.H shows high σ_{resid} values across the majority of the map (average σ_{resid} of 12.0) with eleven pixels with values lower than 3.0 sigma. These pixels appear to fall along 'cracks' that are visible in the intensity maps (Figure 5.58.A and Figure 5.58.B). They will be ignored during analysis.

The intensity maps do not appear to show a good match to the optical image (Figure 5.44.A). This is likely because the central crater is surrounded extensively by uplifted material as can be seen in the optical image. This uplifted material could be obscuring features like the rim of the crater that are normally visible due to being the same height as the rim. The intensity maps also present what appear to be cracks in the surface of the target though these are not identifiable in the optical image. The area in the top right of the image is part of the undamaged original surface of the target.

The P1 FWHM map (Figure 5.58.C) shows that the area in the middle of the map that aligns with the location of the centre of the crater has had its FWHM decrease from 6.2 cm^{-1} to a minimum of 4.4 cm^{-1}; while the uplifted material surrounding this area shows an increase to a maximum of 7.0 cm^{-1}.

The P2 FWHM map (Figure 5.58.D) shows the central part of the crater to have had a reduction in FWHM from 6.8 cm^{-1} down to a minimum of 4.9 cm^{-1} as well as a reduction in one of the cracks originating at (23,0) to a minimum of 3.8 cm^{-1}. The uplifted material dominates this map with an orange colour showing an increase in FWHM to 8.8 cm^{-1}.

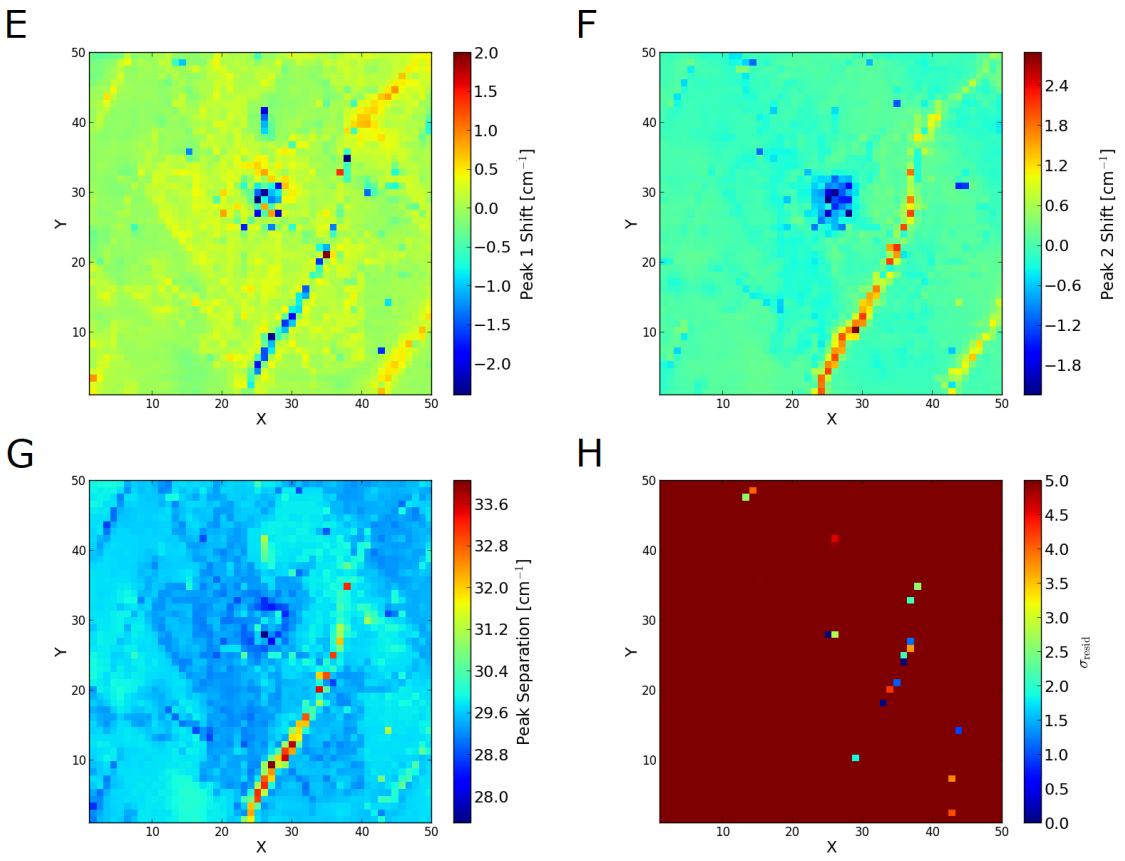


Figure 5.59: Raman map images for the labradorite target G120815#1 where V = 2.72 km s^{-1}. (E) P1 shift map. (F) P2 shift map. (G) Peak separation map. (H) σ_{resid} map.

Figure 5.59.E shows negative shifts in the central crater (to a maximum shift of −2.5 cm^{-1}) and along the crack originating at (23,0) (to a maximum shift of −2.5 cm^{-1}). Some areas of the uplifted material also show positive shifts, with the maximum being +0.8 cm^{-1}. The few pixels showing larger positive shifts correspond to pixels identified in Figure 5.59.H as having poor σ_{resid} values and should be disregarded.

Figure 5.59.F shows negative shifts in the centre of the crater (to a maximum shift of −2.2 cm^{-1}) and positive shifts along the crack originating at (23,0) (to a maximum shift of +2.2 cm^{-1}). The uplifted material has also shifted positively with an average shift of +0.1 cm^{-1}.

The peak separation map (Figure 5.59.G) shows the peaks to have generally maintained their separation throughout the map except along the crack feature where their separation has increased significantly (by approximately 3.0 cm^{-1}).

5.3.3.8 Target: Labradorite, V = 3.39 km s^{-1}, Shot Number G100715#2

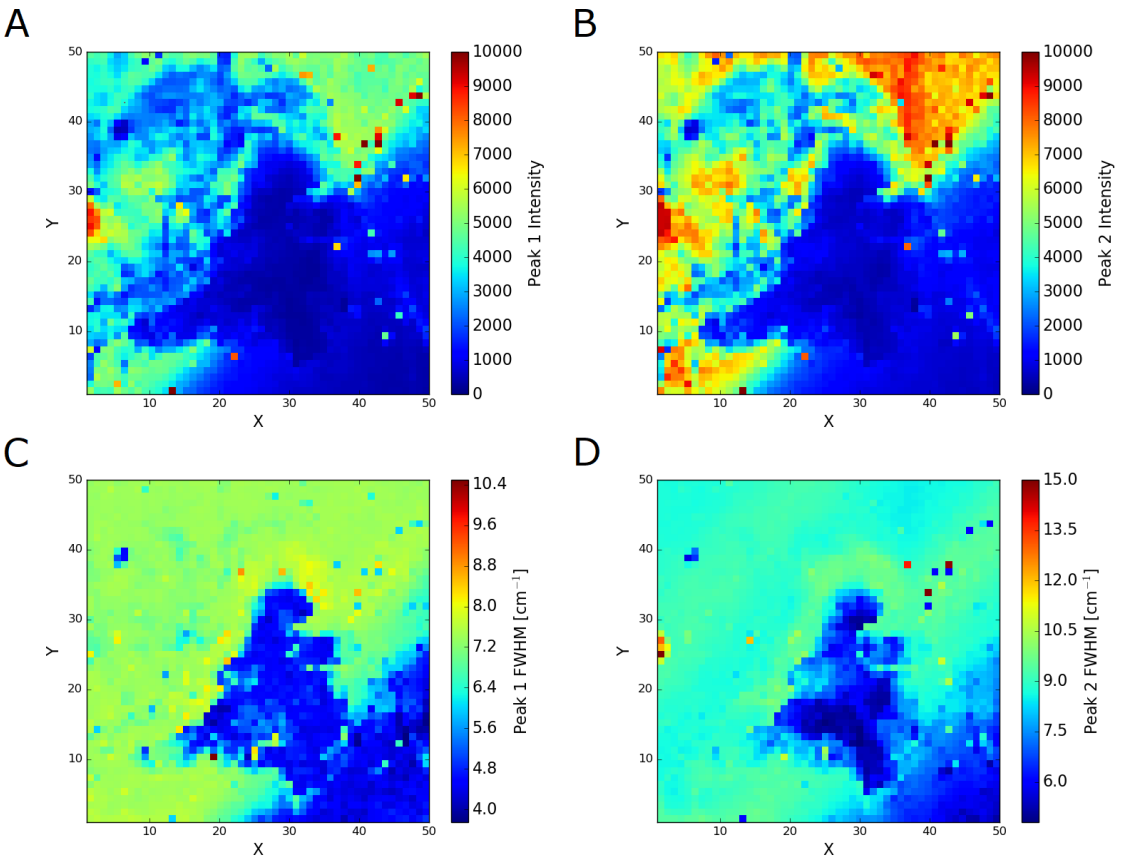


Figure 5.60: Raman map images for the labradorite target G100715#2 where V = 3.39 km s^{-1}. (A) P1 Intensity map. (B) P2 intensity map. (C) P1 FWHM map. (D) P2 FWHM map.

Figure 5.61.H shows σ_{resid} to have high values across the map (average σ_{resid} of 26.2) apart from some scattered pixels with values of less than 3.0 sigma. These pixels will be disregarded for the analysis of this shot.

The intensity maps Figure 5.60.A and Figure 5.60.B initially appear to be a poor match to the optical image Figure 5.44.B. The bottom right of the intensity maps shows a large area of low intensity making it impossible to discern the shape of the crater, which is clearly present in the optical image. This is because the material outside the crater in this corner of the map has risen above the surface of the crater and become out of focus, reducing its Raman intensity. This boundary is clearly present in the optical image as a crack that runs diagonally through the crater, and in the intensity maps as a line that runs from (13,0) to (50,41).

The FWHM maps (Figure 5.60.C and Figure 5.60.D) show narrowing of both P1 and P2 inside the crater and on the uplifted material in the bottom right of the map. For P1 the FWHM has reduced from 7.4 cm^{-1} to a minimum of 3.7 cm^{-1} while for P2 the FWHM has reduced from 8.8 cm^{-1} to a minimum of 4.8 cm^{-1} inside the crater and on the uplifted material.

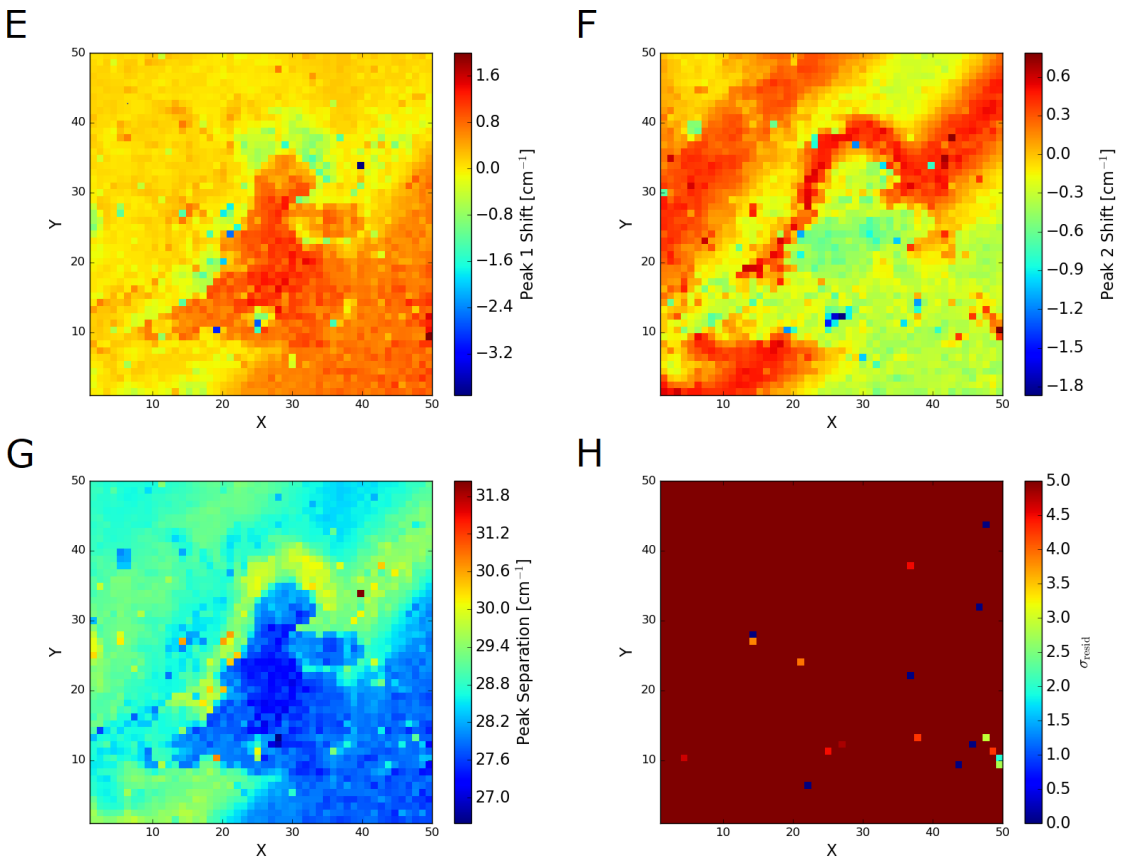


Figure 5.61: Raman map images for the labradorite target G100715#2 where V = 3.39 km s^{-1}. (E) P1 shift map. (F) P2 shift map. (G) Peak separation map. (H) σ_{resid} map.

Figure 5.61.E is the P1 shift map. It shows a maximum positive shift of +1.4 cm^{-1} for P1 inside the crater and on the uplifted material. There is a negative shift along the rim at the top of the crater with a maximum of – 1.0 cm^{-1}.

The P2 shift map (Figure 5.61.F) shows the inverse of the P1 shift map. There are negative shifts inside the crater and on the uplifted material as well as positive shifts along the rim at the top of the crater. The maximum negative shifts of – 1.9 cm^{-1} are located at (27,12), while the maximum positive shift is +0.8 cm^{-1}.

Figure 5.61.G is the peak separation map. It shows P1 and P2 coming closer together inside the crater and on the uplifted material while moving away from each other along the top 'rim' of the crater.

5.3.3.9 Target: Labradorite, V = 5.06 km s^{-1}, Shot Number G160915#2

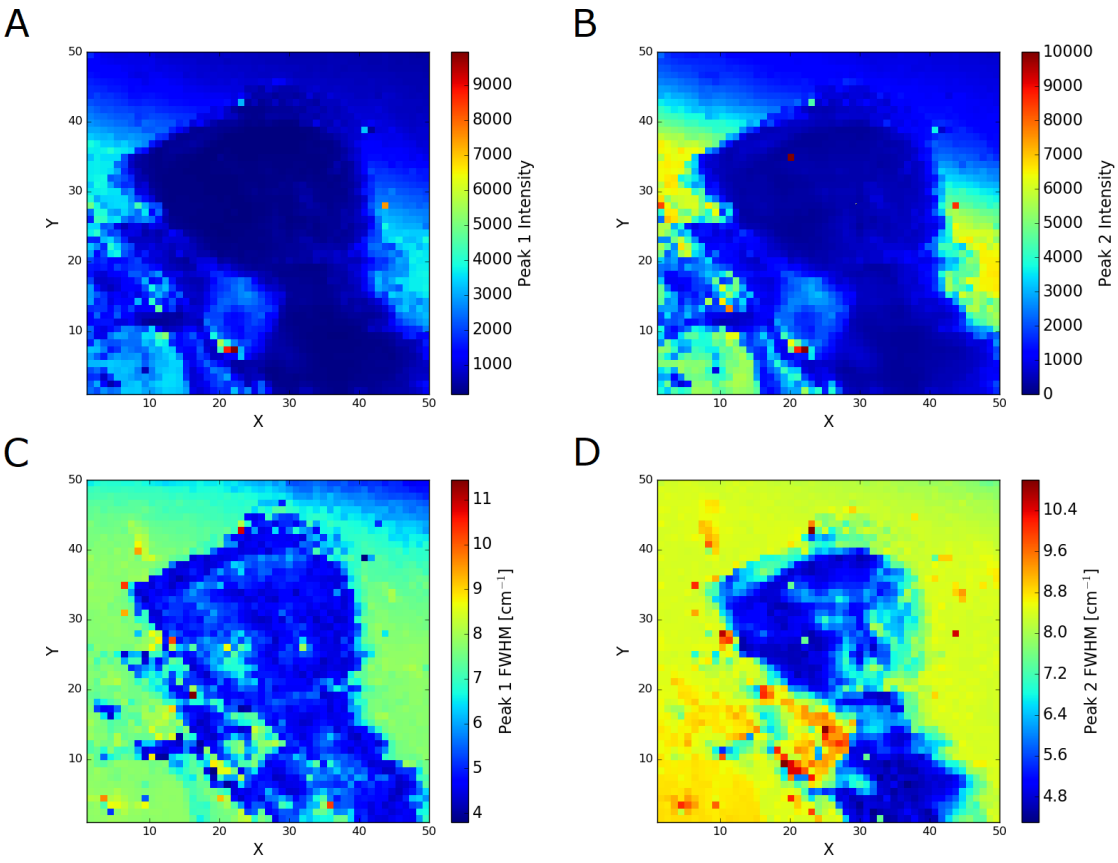


Figure 5.62: Raman map images for the labradorite target G160915#2 where V = 5.06 km s^{-1}. (A) P1 Intensity map. (B) P2 intensity map. (C) P1 FWHM map. (D) P2 FWHM map.

Figure 5.63.H shows high σ_{resid} values across most of the map (average σ_{resid} of 20.0). There are however a number of pixels that have a value of less than 5.0 sigma. Many of these are still above 3.0 sigma (particularly the area in the top left of the map), however, several pixels have values of less than 3.0 sigma, meaning they will be disregarded in the analysis (their exact positions are not listed here).

The P1 and P2 intensity maps (Figure 5.62.A and Figure 5.62.B) show a good match to the optical image for this shot (Figure 5.45). Both maps show the crater itself covering the majority of the map as the region with the lowest intensity, as well as the uplifted material centred at (5,15) also having a lower intensity than the surrounding area.

Figure 5.62.C, the P1 FWHM map, shows the peak narrows within the crater to a minimum of 3.8 cm^{-1}, down from the unshocked value of 6.3 cm^{-1}. The peak has broadened around the crater to 7.8 cm^{-1} with some scattered pixels (mainly located around the very edge of the crater) that show an increase in the FWHM to a maximum of 10.5 cm^{-1}.

Figure 5.62.D shows the same trend for the P2 FWHM with the peak narrowing inside the crater (to a minimum of 4.4 cm^{-1} down from 8.0 cm^{-1}) and broadening outside the crater (to 8.4 cm^{-1}) with the maximum increases located at the area around (25,15) at a value of 11.7 cm^{-1}.

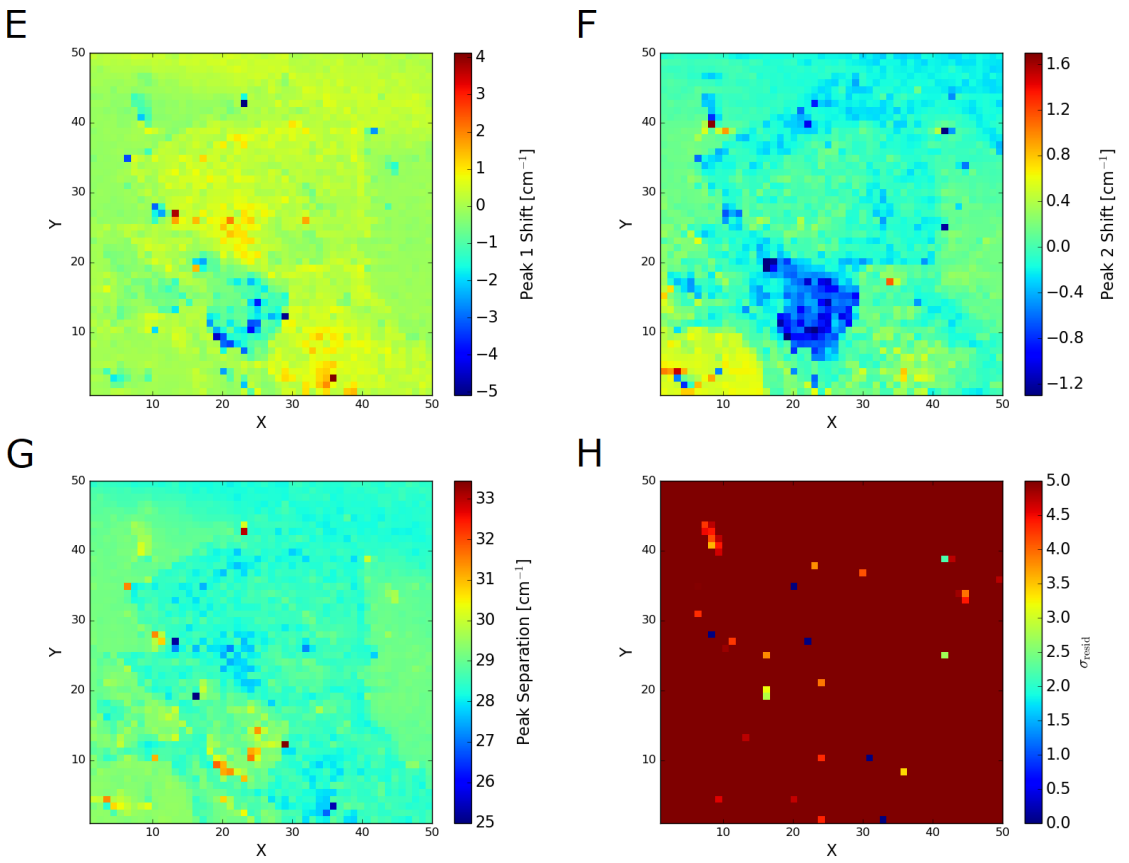


Figure 5.63: Raman map images for the labradorite target G160915#2 where V = 5.06 km s^{-1}. (E) P1 shift map. (F) P2 shift map. (G) Peak separation map. (H) σ_{resid} map.

The P1 shift map (Figure 5.63.E) shows the peak to have shifted positively inside the crater (to a maximum of +4.1 cm^{-1} at (36,3)) and an area of negative shift centred at (23,12) (with a maximum shift of -5.0 cm^{-1}). It is also possible to follow a line of positively shifted material (approximately +1.0 cm^{-1}) that follows the top and right sides of the crater.

Figure 5.63.F, the P2 shift map, again shows the area of negative shift at (23,12) but although it has a smaller shift (maximum of -1.3 cm^{-1}), it is more clearly pronounced. The same line along the sides of the crater as the one in Figure 5.63.E can also be seen in this map, but here the shift is negative (approximately -0.3 cm^{-1}). The bottom left of the map shows an area of positive shift averaging +0.6 cm^{-1} but peaking at an increase of +1.7 cm^{-1}. There is no detectable shift inside the crater.

Figure 5.63.G is the peak separation map for this shot. It shows the peaks moving closer together along the sides of the crater while moving further apart at the area located at (23,12) due to the much larger shift in P1 than in P2.

5.3.3.10 Labradorite Summary

For the labradorite shot programme, nine shots are presented with impact speeds between 0.291 km s^{-1} and 5.06 km s^{-1} (2.84 GPa and 86.98 GPa). The largest positive Raman shift is +4.1 cm^{-1} for P1 in the 5.06 km s^{-1} shot, while the largest negative shift of -5.9 cm^{-1} can be found in P1 in the 1.99 km s^{-1} shot. The greatest broadening of the FWHM is observed in P2 in the 3.39 km s^{-1} shot, where it increases by 6.2 cm^{-1} from 8.8 cm^{-1} to 15.0 cm^{-1}, while the greatest narrowing of the FWHM can be seen in P2 of the 3.39 km s^{-1} shot where there is a decrease of 4.5 cm^{-1} from 9.3 cm^{-1} to 4.8 cm^{-1}.

5.4 Summary

This chapter has described the experimental and analytical procedures used to obtain the data presented here. The methods of interpretation of those data have also been described. An attempt to summarise the interpretation of these maps is provided in Table 5.2 and below.

These data have only been presented and described in this chapter while the identification and examination of any trends is presented in Chapter 6.

Table 5.2: A summary of the data for each shot, including: velocity, peak shock pressure, peak shift, and changes in the FWHM of the peaks.

Shot ID	Mineral	Velocity (km s^{-1})	Peak Shock Pressure (GPa)	Max Positive Shift (cm^{-1})		Max Negative Shift (cm^{-1})		Peak Separation (cm^{-1})			Min FWHM (cm^{-1})		Max FWHM (cm^{-1})		Unshocked FWHM (cm^{-1})	
S030615#2	Quartz	0.373	2.01	+3.2		0.0		N/A	N/A	N/A	4.0		6.5		4.0	
S241117#1	Quartz	0.515	2.95	+1.9		-0.4		N/A	N/A	N/A	1.6		3.4		1.8	
S091014#1	Quartz	0.910	6.04	+0.9		-1.9		N/A	N/A	N/A	3.0		5.0		4.0	
G151014#1	Quartz	1.35	10.23	+0.5		-0.1		N/A	N/A	N/A	2.5		4.5		4.0	
G051114#3	Quartz	2.02	18.03	+0.7		-0.1		N/A	N/A	N/A	3.0		4.0		4.0	
G241014#1	Quartz	3.32	37.60	+0.9		-1.1		N/A	N/A	N/A	2.6		5.0		3.9	
G270515#3	Quartz	4.48	59.67	+0.6		-1.9		N/A	N/A	N/A	3.5		4.5		4.0	
G271114#2	Quartz	5.27	77.09	+0.4		-2.3		N/A	N/A	N/A	2.0		4.5		4.0	
G100615#1	Quartz	6.40	105.28	+1.5		-2.6		N/A	N/A	N/A	4.0		9.2		4.0	
				P1	P2	P1	P2	Min	Nominal	Max	P1	P2	P1	P2	P1	P2
E240614#1	Olivine	0.576	8.76	+3.4	+1.6	-0.3	-0.2	28.3	30.6	32.1	4.0	3.2	6.9	7.6	5.2	7.0
E130614#1	Olivine	0.602	9.18	+0.5	+1.6	-1.3	-0.5	30.6	31.9	32.6	5.9	5.9	8.1	8.1	7.1	6.0
S260914#1	Olivine	0.638	9.75	+1.2	+2.2	-3.4	-2.9	31.4	31.8	34.2	5.6	5.8	8.5	8.7	5.6	6.8
G151014#1	Olivine	1.35	21.85	+0.3	+1.4	-2.5	-2.4	29.2	31.6	33.3	5.7	6.0	13.8	8.5	5.7	6.4
G150114#1	Olivine	1.57	25.85	+2.6	+1.5	-1.6	-2.6	28.4	31.9	32.9	5.0	5.0	9.0	9.0	5.6	6.6
G051114#3	Olivine	2.02	34.41	+0.7	+1.8	-2.0	-0.8	30.2	31.6	32.3	5.0	6.4	9.0	8.5	5.2	7.8
G150114#2	Olivine	3.03	55.46	+0.4	+1.0	-5.0	-4.9	27.3	32.0	33.0	2.8	3.1	15.0	10.6	5.6	6.6
G241014#1	Olivine	3.32	61.98	+0.2	+1.3	-2.1	-1.7	30.1	31.6	32.8	4.6	5.8	8.0	8.0	8.0	5.8
S250915#1	Labradorite	0.291	2.84	+1.0	+1.0	-0.6	-0.3	27.2	29.2	32.3	3.2	4.4	7.1	8.9	6.9	8.9
S160915#1	Labradorite	0.646	6.70	+1.0	+1.0	-4.0	-2.7	28.0	30.0	34.0	4.3	5.5	10.4	10.5	7.0	8.8
S300715#1	Labradorite	0.997	10.92	+0.4	+0.2	-1.5	-2.5	26.9	30.0	32.5	4.2	5.1	9.1	10.0	7.0	8.7
G181217#1	Labradorite	1.36	15.71	+2.5	+1.5	-1.5	-0.5	26.0	28.6	32.0	3.5	3.8	9.1	8.9	6.0	8.0
G170615#2	Labradorite	1.81	22.22	+1.3	+1.4	-5.0	-3.6	26.7	29.1	31.5	4.4	4.5	10.0	10.0	7.0	8.2
G050815#1	Labradorite	1.99	25.00	+1.8	+0.2	-5.9	-3.4	25.8	27.9	31.6	4.2	4.8	11.0	11.0	7.3	8.6
G120815#1	Labradorite	2.72	37.25	+0.8	+2.2	-2.5	-2.2	27.4	29.7	34.0	4.4	3.8	7.0	8.8	6.2	6.8
G100715#2	Labradorite	3.39	49.88	+1.4	+0.8	-1.0	-1.9	26.6	28.9	32.0	3.7	4.8	10.5	15.0	7.4	8.8
G160915#1	Labradorite	5.06	86.98	+4.1	+1.7	-5.0	-1.3	25.0	28.7	33.4	3.8	4.4	10.5	11.7	6.3	8.0

Chapter 6 - Raman Spectrometry as a Shock Barometer II

6.1 Introduction

Chapter 5 presented maps produced from the Raman data generated from the impact experiments described in Section 5.2. Each map relates to one of three parameters for the peaks investigated: peak intensity, peak width, and peak position. This chapter will analyse those data in an attempt to determine if Raman spectrometry can be used as a shock barometer.

6.2 Peak Intensity

Section 1.1.1 describes how the intensity of a Raman peak is governed by the change in polarisability of the molecule. It is possible that a shock event, such as an impact, could cause a change in polarisability of a molecule by distorting/straining the molecule, thereby changing the intensity and frequency of the peak. If this change could be detected and characterised it could be used as a shock barometer. However, the intensity of a Raman peak is also dependent upon how well the laser is focused on the sample. All of the Raman intensity maps presented in Chapter 5 are of impact craters, and, as such, are not flat surfaces. This causes variation in the focus of the laser across the crater resulting in a variation in the intensity of the Raman peaks. If there were a change in the Raman intensity due to a change in polarisability, this would be masked by the changes due to the variation in the focus of the laser. Unfortunately, this means that the Raman intensity maps alone cannot be used as a shock barometer.

Although the Raman intensity maps cannot be used as a shock barometer, they have proven to display a good match to their optical counterparts. Section 5.2.2 explains how the change in intensity due to the change in focus can be used as a "depth gauge" for a crater. In essence, the changes in intensity in the maps can be interpreted as changes in the distance between the sample and the objective lens (as no calibration was possible). While this technique cannot give an actual distance measurement from the objective lens, it can provide insight as to the relative heights of two areas on the surface of the target, which can then be used to interpret the shape of the craters.

Good examples of this technique can be seen in Sections 5.3.1.8 (the 5.27 km s^{-1} shot onto quartz) and 5.3.2.6 (the 2.02 km s^{-1} shot onto olivine). As described in Section 5.3.1.8, the intensity map (Figure 5.19.A) depicts a good likeness to the optical image of the crater (Figure 5.10.B), with the outline of the crater being clearly visible and the intensity map even being able to distinguish material that has been uplifted due to subsurface cracking. Section 5.3.2.6 explains how the intensity maps (Figure 5.35.A and Figure 5.35.B) illustrate not only the shape of the crater, but also other features seen in the optical image (Figure 5.23.B), including rippled and uplifted material surrounding the central crater. As explained, while this interpretation does not provide exact measurements for the depth of the crater, it does provide a measure of relative height between pixels, which is sufficient to be able to resolve features seen in the optical images. Therefore, it is still worthwhile to analyse the Raman intensity maps for use as an additional diagnostic tool for interpreting the shapes of the craters.

6.3 Peak Width

As discussed in Section 1.1.1, the position of a Raman peak is determined by the frequency of the vibrational mode it represents. If all of the same vibrations in a sample were to generate the exact same frequency, it would be expected that the Raman peak would be extremely narrow, as only that specific frequency would be detected. In reality, a Raman peak usually has a measureable width (of order of a few cm^{-1}) due to variations in the exact frequency of a particular vibration within a sample. Because of this, the width, or the full-width half-maximum (FWHM), of a Raman peak can be used to interpret the variation in the vibration associated with that peak: a narrow Raman peak has less variation in the vibration than that of a broader Raman peak at the same position.

During a shock event, a shock front passes through the target and projectile materials causing compression which is immediately followed by release. This happens quickly and often the material does not have sufficient time to 'bounce back' to its original structure from before the shock event. This generates stresses in the material structure where the atoms have been either stretched apart, or compressed together relative to their original positions. Therefore, while the constituent elements of the vibrations have not changed, it is expected that a greater degree of variation in the length of the vibration would be produced resulting in a broader Raman peak [186].

Examples of this can be seen in some of the impact experiments presented in Chapter 5, such as Figure 5.12.C in Section 5.3.1.1 and Figure 5.29.C and Figure 5.29.D in Section 5.3.2.3. These examples show that the FWHM has been increased inside the crater compared to the unshocked region outside of the crater.

It is expected that a more energetic impact would cause a greater degree of peak-broadening than a less energetic impact, thereby allowing the change in the FWHM of the Raman peaks to be used as a shock barometer. Upon analysis of the FWHM maps in Chapter 5, it was discovered that this expectation is false.

For the lower speed impacts (generally below 1.0 km s^{-1}), peak-broadening is common; however, as the impact speed is increased, there comes a point (unique to each mineral) where it becomes more common to find regions where the impacts have resulted in the narrowing of the Raman peaks. This implies that the variation in the vibration frequency has been reduced. Examples of this can be seen in Sections 5.3.1.5 (Figure 5.16.C) and 5.3.3.5 (Figure 5.54.C and Figure 5.54.D), where the peaks become progressively narrower towards the centre of the craters. Interestingly, a ring feature has formed in some craters showing peak-broadening along the crater walls, but narrowing in the centre of the crater. This can be seen in the 0.515 km s^{-1} quartz shot in Section 5.3.1.2 (Figure 5.13.C) and the 3.03 km s^{-1} olivine shot in Section 5.3.2.7 (Figure 5.37.C and Figure 5.37.D).

An impact event causing the narrowing of Raman peaks is an unexpected result until it is remembered that in an impact event, not only is there a shock front propagating through the material, but there is also an increase in temperature. If the increase in temperature is great enough, it is possible to reach the annealing temperature of the target material. Annealing is a process used to reduce the internal stresses of a material by heating said material to its annealing temperature and allowing it to cool slowly. If the annealing temperature of the targets (Table 6.1) has been attainted during the impact, this could provide an explanation as to how the stresses in the material have (seemingly) been removed resulting in the narrower Raman peaks.

Impacts produce the greatest increase in temperature at the centre of the crater [42] which would account for the localised narrowing seen in the centre of many of the craters.

Table 6.1: The annealing temperatures of the minerals examined in this study.

Mineral	Annealing Temperature (°C)
Quartz	1150 [187]
Olivine	1250 [188]
Labradorite	900 [189]

One possible explanation for the ring features seen in Sections 5.3.1.2 and 5.3.2.7, is that the impact may have caused the temperature to reach the annealing point in the centre of the craters but not along the crater walls. This would result in peak narrowing at the centre of the crater with peak-broadening along the crater walls, thereby forming the ring feature. To test this theory, an experiment was conducted whereby an unshocked sample was examined using Raman spectroscopy before and after being annealed. The FWHM of the peaks from before and after annealing were then compared in order to determine if the width of a Raman peak can be used to detect the narrowing of the peaks due to the annealing process.

6.3.1 Annealing Test

To perform the annealing test, one of the quartz gemstones described in Section 4.2.4 was used. Before the sample was subjected to any heating, a 50 x 50 pixel Raman map was taken across the table of the gemstone. The FWHM map generated from these data can be seen in Figure 6.1. The map shows that the FWHM is consistent across the sample displaying a value of 3.99 cm^{-1} (± 0.05 cm^{-1}).

The sample was then placed in a furnace and heated to 1200 °C at a rate of 20 °C per minute (the annealing temperature of quartz is 1150 °C [187]) and held at temperature for three hours. After this time, the sample was allowed to cool to room temperature at a controlled rate of 10 °C per minute. Once the sample reached room temperature, a second Raman map was performed over its surface and the data processed as before. The FWHM map generated from this second Raman map can be seen in Figure 6.2.

Figure 6.1 shows an average FWHM of 3.99 cm^{-1} (± 0.05 cm^{-1}) for P1 of quartz before the annealing test, while Figure 6.2 shows an average FWHM of 3.35 cm^{-1} (± 0.25 cm^{-1}) for P1 of quartz after the annealing test. While the variation in peak width has increased, it is clear that there has been an overall reduction in peak width across the sample as a result of the annealing test. Therefore, if the temperature increase generated by the impact is large enough, it is possible that the peak narrowing seen in these impact experiments is the result of impact annealing.

In this test, the FWHM has narrowed by an average of 0.64 cm^{-1}. The largest FWHM reduction seen for quartz is 2.0 cm^{-1} in the target of the 5.27 km s^{-1} shot. Although the impacted targets have been seen to be able to produce a greater degree of peak narrowing than the annealing test shown here, the values are comparable to one another.

Unfortunately, this test could not be repeated for olivine and labradorite due to a lack of samples from the same batch as those used in the impact experiment.

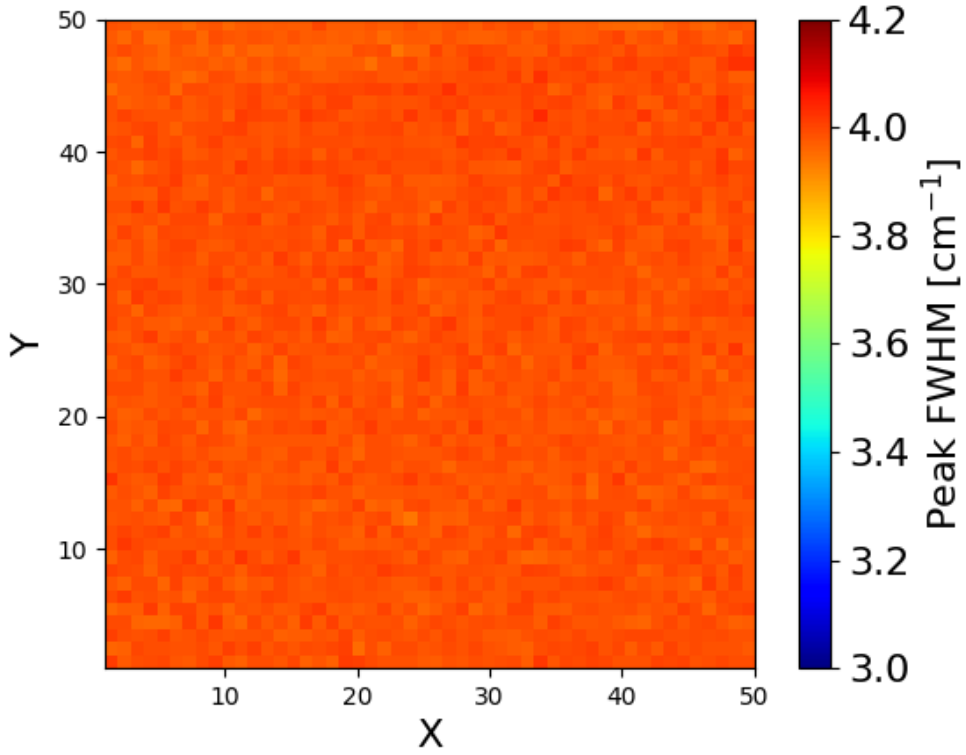


Figure 6.1: The FWHM map generated from the Raman map of the quartz gemstone before the annealing test.

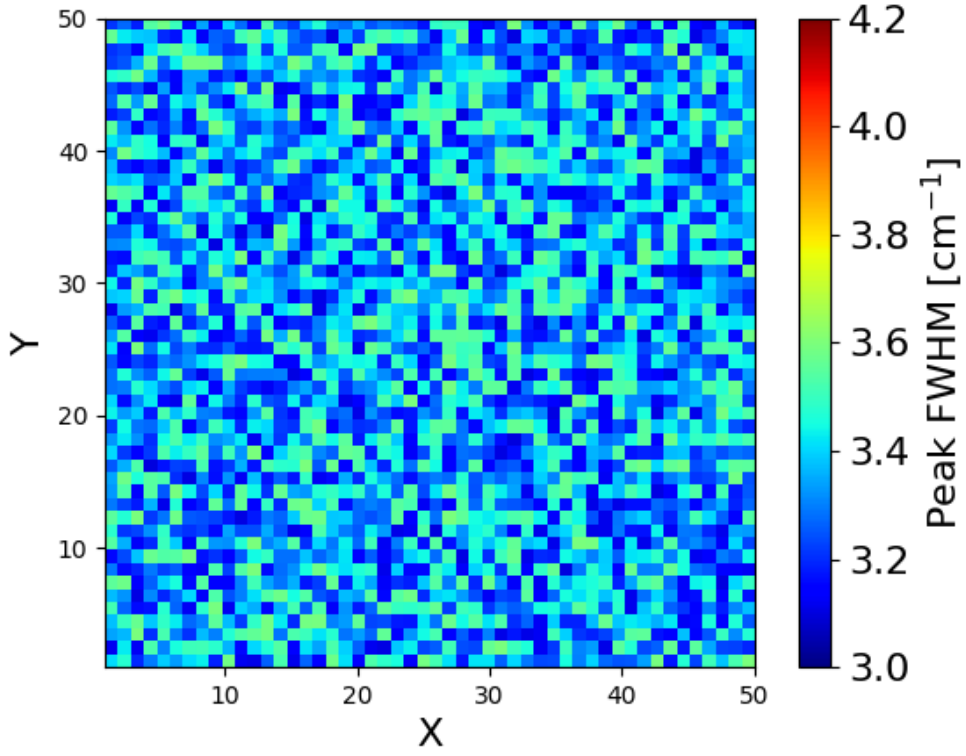


Figure 6.2: The FWHM map generated from the Raman map of the quartz gemstone after the annealing test.

6.3.2 Quartz

Note: As can be seen in Table 5.2, the quartz gemstones had a nominal FWHM value for P1 of 4.0 cm^{-1} ± 0.1 cm^{-1}, with the exception of the 0.515 km s^{-1} shot which had a nominal FWHM value of 1.8 cm^{-1}.

For the slowest shot of the quartz shot program (0.373 km s^{-1}, Section 5.3.1.1), the FWHM increases inside the crater by as much as 2.5 cm^{-1} with a clear pattern of increasing width towards the centre of the crater. This implies that the shock event has increased the degree of variation in the frequency of the vibration inside the crater, with the largest increase being at the point of greatest shock pressure, the centre of the crater.

The 0.515 km s^{-1} quartz shot (Section 5.3.1.2) displays one of the previously discussed ring features, which is comprised of material that displays an increase in the FWHM of the Raman peaks (by a maximum of 1.6 cm^{-1}). Inside the ring, there appears to be no change in the FWHM compared to the unshocked value. A possible explanation for this is that the temperature increase produced by the impact was sufficient to cause some degree of annealing in the centre of the crater, where the temperature increase is greatest, but not along the crater walls. This would have counteracted an increase in FWHM at the centre of the crater, but not along the crater walls where the peaks have broadened.

Figure 5.14.C in Section 5.3.1.3 presents the FWHM map for the 0.910 km s^{-1} quartz shot. It shows both increases (maximum of +1.0 cm^{-1}) and decreases (maximum of -1.0 cm^{-1}) in the FWHM inside the crater. Unlike the ring feature seen in the previous quartz shot, the area of decreased FWHM is shown to be at the bottom of the crater, while the area of increased FWHM is at the top of the crater. This arrangement is unexpected. One possible cause is that micro fractures have formed at the top of the crater generating greater disorder (and therefore peak-broadening), while the bottom of the crater has been annealed.

The remaining shots in the quartz shot program show only narrowing of the FWHM inside their craters (maximum decrease in FWHM of: 1.5 cm^{-1} for the 1.35 km s^{-1} shot, 1.0 cm^{-1} for the 2.02 km s^{-1} shot, 1.3 cm^{-1} for the 3.32 km s^{-1} shot, 0.5 cm^{-1} for the 4.48 km s^{-1} shot, and 2.0 cm^{-1} for the 5.27 km s^{-1} shot) with the exception of the 6.40 km s^{-1} shot in Section 5.3.1.9. For this shot, only broadening of the FWHM (by a maximum of 5.2 cm^{-1}) can be seen. This is likely because the impact created a temperature increase sufficient enough to cause vaporisation of the target material thereby removing material instead of annealing it, leaving only disordered material behind inside the crater.

6.3.3 Olivine

Two Raman peaks have been analysed for olivine, P1 and P2 (Section 4.2.1). The FWHM of these peaks do not behave in the same manner for each of the shots and, as such, the changes in the FWHM for the olivine shot program will be analysed separately for each peak.

6.3.3.1 Olivine P1

Note: As can be seen in Table 5.2, the olivine gemstones had a nominal FWHM value for P1 of 6.6 cm^{-1} ± 1.4 cm^{-1}.

For P1, the 0.576 km s^{-1} shot (Section 5.3.2.1) shows broadening of the FWHM increasing towards the centre of the crater (by a maximum of +1.7 cm^{-1}). Narrowing of the FWHM can also be observed along some of the surface cracks, reducing by as much as -1.2 cm^{-1}.

The 0.602 km s^{-1} shot (Section 5.3.2.2) again shows peak-broadening to be the dominant process inside the crater for P1 (by a maximum of 1.0 cm^{-1}), but in this case there are some localised areas of peak narrowing along the crater walls (by a maximum of 1.2 cm^{-1}). If the narrowing of peaks is due to an annealing effect, as has been previously speculated, it would seem odd to find a reduction in the FWHM at the crater walls where the temperature is lower than the centre of the crater where no such reduction has occurred.

Section 5.3.2.3 presents the 0.638 km s^{-1} olivine shot. The FWHM map for P1 (Figure 5.29.C) shows an increase in the FWHM inside the crater by as much as 2.9 cm^{-1}.

Figure 5.31.C, the P1 FWHM map for the 1.35 km s^{-1} olivine shot (Section 5.3.2.4), shows almost no change in the widths of the peaks inside the crater except for a small number of pixels which display a large amount of broadening (as much as 8.1 cm^{-1}). These extreme pixels have compressed most of the information in the map to the lower end of the scale making it difficult to interpret anything other than those pixels. Figure 6.3 presents Figure 5.31.C again but this time with the scale having the upper limit of 8.0 cm^{-1} in order to investigate those data compressed into the lower end of the scale in the original map.

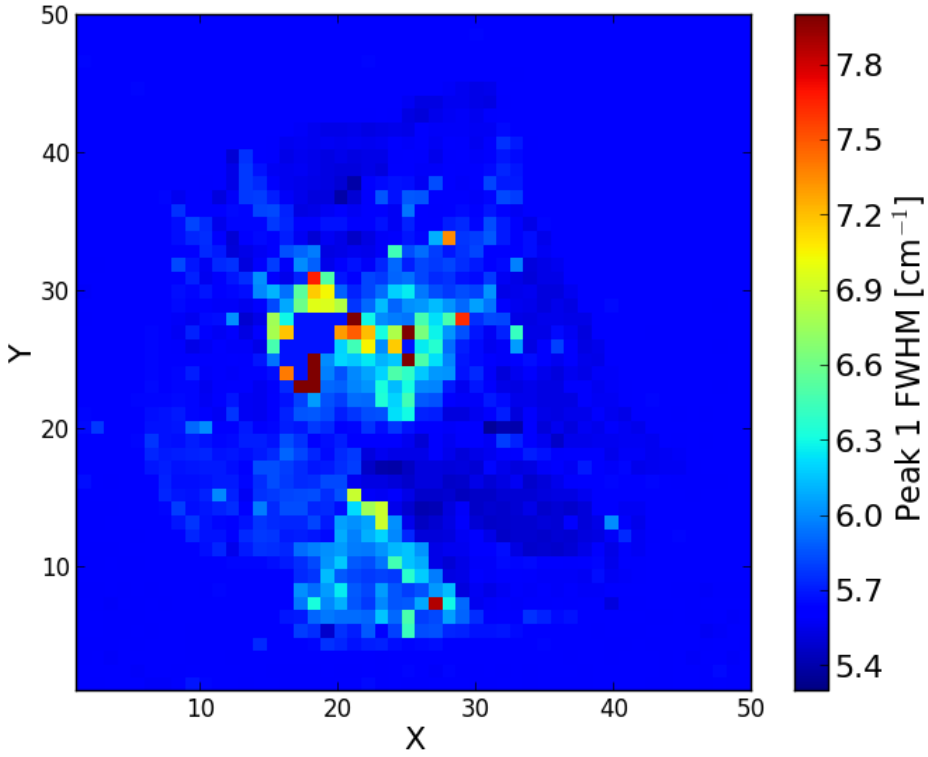


Figure 6.3: The P1 FWHM map from the olivine shot G151014#1 (1.35 km s^{-1}) re-displayed with an upper limit of 8.0 cm^{-1} and a lower limit of 5.3 cm^{-1}.

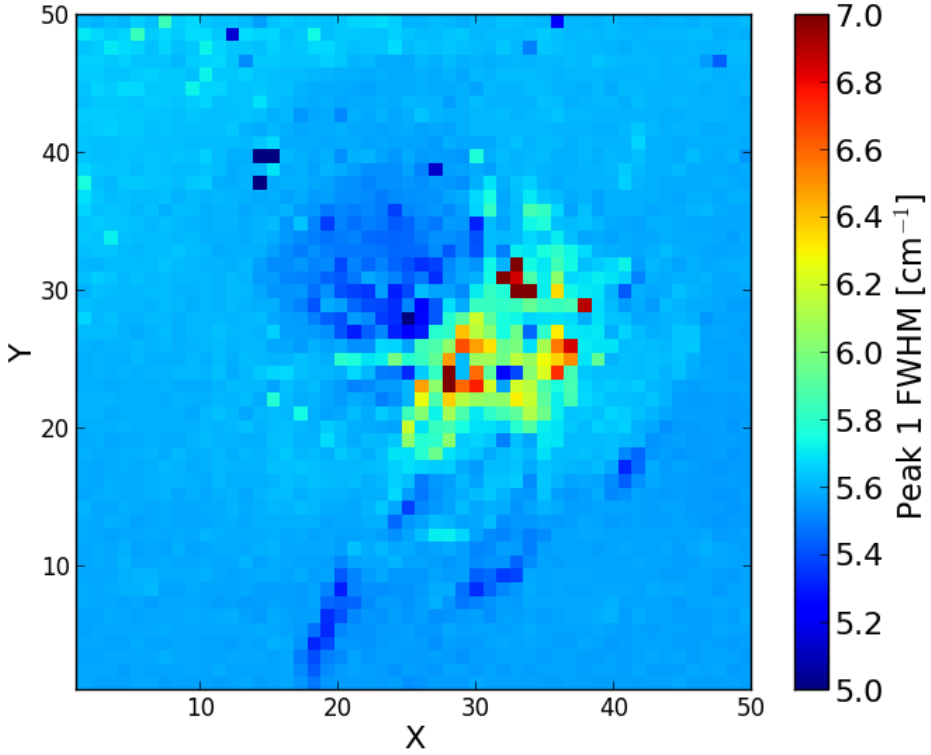


Figure 6.4: The P1 FWHM map from the olivine shot G150114#1 (1.57 km s^{-1}) re-displayed with an upper limit of 7.0 cm^{-1} and a lower limit of 5.0 cm^{-1}.

The previously identified pixels in Figure 5.31.C display as dark red in Figure 6.3 as their values are above the 8.0 cm^{-1} limit. The new map displays more detail and shows that there are a large number of pixels where the FWHM has increased by up to 2.0 cm^{-1} inside the crater that was previously unseen.

The P1 FWHM map (Figure 5.33.C) for the 1.57 km s^{-1} shot shows a region of peak-broadening inside the crater (with a maximum increase of 3.5 cm^{-1}) surrounded by what appears to be un-altered material. Once again, there are only a small number of pixels that have broadened by this large amount and, therefore, information has been compressed into the lower end of the scale. Figure 6.4 re-displays Figure 5.33.C with the upper limit of the scale having been limited to 7.0 cm^{-1}. Any pixels with a FWHM value larger than the limit of 7.0 cm^{-1} will be displayed as having a value of 7.0 cm^{-1} instead of their true values.

After this rescaling, the area of peak-broadening previously noted can still be seen, however, now areas of peak narrowing can be seen along cracks and at the centre of the crater. The pixels along the cracks show a maximum reduction of 0.3 cm^{-1}, while the area at the centre of the crater shows a maximum reduction of 0.6 cm^{-1}.

Figure 5.35.C is presented in a very similar manner as Figure 5.33.C, with an area of peak-broadening inside the crater (with a maximum increase of +3.8 cm^{-1}) that contains only a few pixels at the upper end of the scale. The result of applying the same rescaling technique to this image yields Figure 6.5, which shows the area of peak-broadening inside the crater in more detail, as well as previously unseen peak-broadening along cracks in the crater walls. From this image it can be seen that most of the pixels in the central area have increased their FWHM by between 0.5 cm^{-1} and

0.9 cm^{-1} with only a small number of pixels increasing up to the maximum increase of 3.8 cm^{-1}. The cracks show the peaks to have broadened by as much as 0.4 cm^{-1}. No peak narrowing is observed for this shot.

The 3.03 km s^{-1} olivine shot (Section 5.3.2.7) has previously been identified as one of the shots displaying the ring feature in its FWHM maps. Figure 5.37.C is the P1 FWHM map and shows a ring of pixels representing broadened peaks (a maximum increase of 9.4 cm^{-1}) surrounding the central area of pixels representing narrowed peaks (maximum decrease of 2.8 cm^{-1}). Due to the large alterations to the FWHM in both directions, the scale for this map covers a wide range, compressing most of the information to a small part of the scale. Figure 6.6 re-displays Figure 5.37.C with the scale limited to a range of 5.0 - 7.0 cm^{-1} in an effort to show detail closer to the unaltered FWHM value of 5.6 cm^{-1}. Figure 5.37.C shows the ring feature to be only a few pixels in thickness but analysis of Figure 6.6 shows it to be wider and more well defined than initially thought. It is also possible to see narrowing of the FWHM (maximum of 0.3 cm^{-1}) along a crack to the right of the crater that was not clearly visible in the original map. A possible explanation for the origin of this ring feature is discussed in Section 6.3.

The final olivine P1 FWHM map (Figure 5.39.C) shows only narrowing of the Raman peaks inside the crater with a maximum decrease of -3.4 cm^{-1} from the unaltered value.

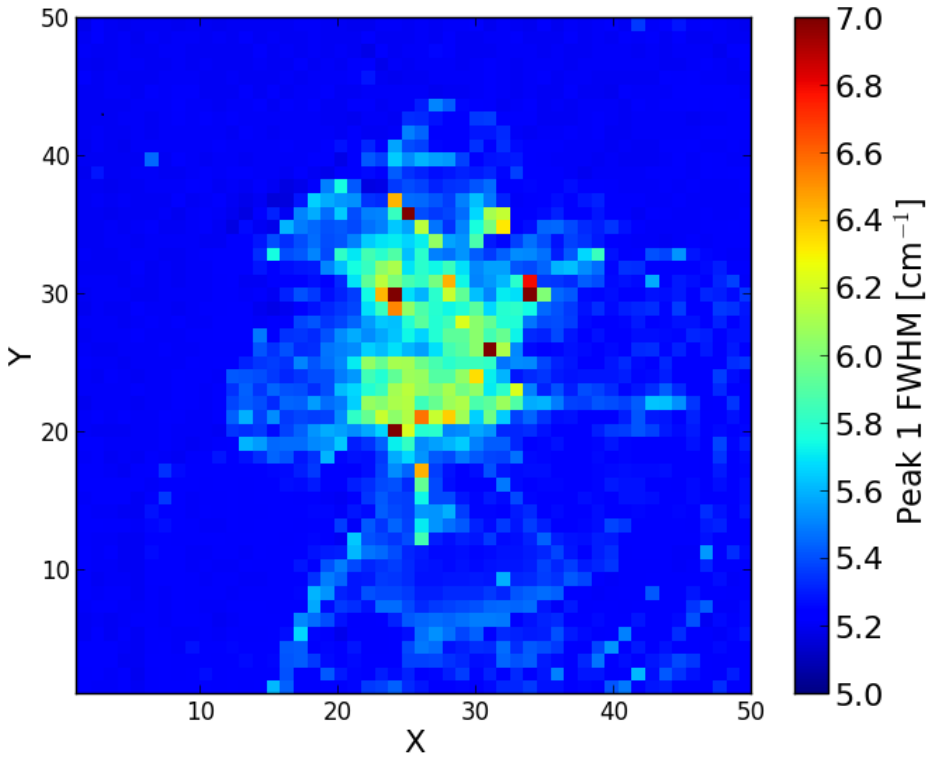


Figure 6.5: The P1 FWHM map from the olivine shot G051114#3 (2.02 km s^{-1}) re-displayed with an upper limit of 7.0 cm^{-1} and a lower limit of 5.0 cm^{-1}.

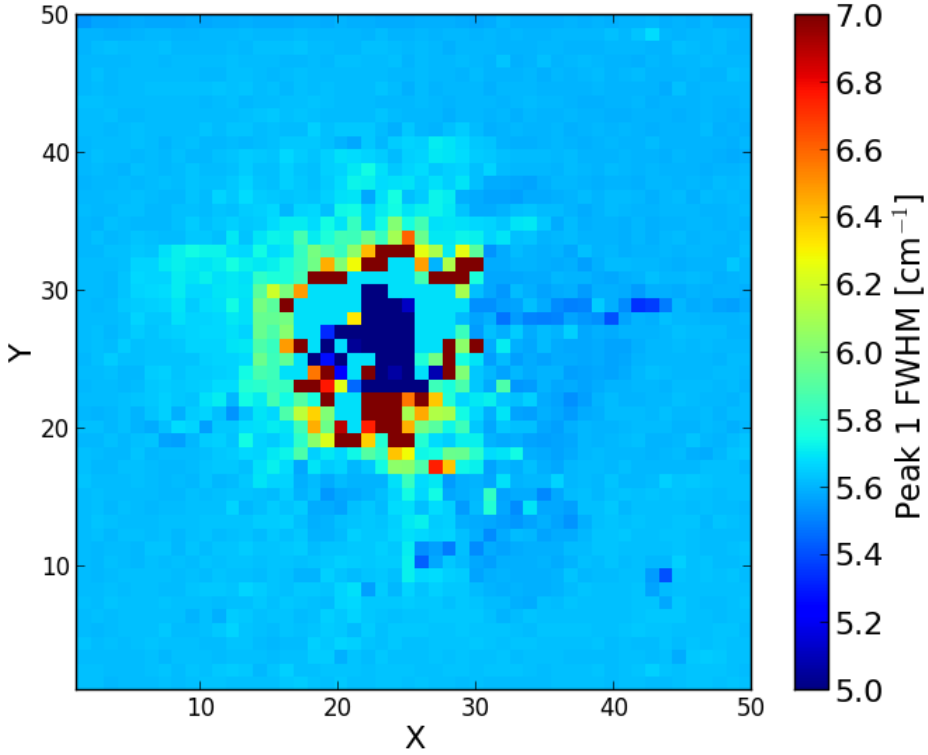


Figure 6.6: The P1 FWHM map from the olivine shot G150114#2 (3.03 km s^{-1}) re-displayed with an upper limit of 7.0 cm^{-1} and a lower limit of 5.0 cm^{-1}.

In general, the olivine shot program shows the P1 FWHM to increase inside the crater for impact speeds below 3.03 km s^{-1}. Some peak-narrowing is also seen for these shots but it is mostly confined to cracks surrounding the craters with the exception of the 1.57 km s^{-1} shot, which contained an area of peak narrowing inside the crater. The peak-narrowing seen at the cracks in the targets is possibly due to material stresses being relieved at those locations due to the cracks themselves. At 3.03 km s^{-1} the ring feature is observed, which shows both peak-broadening and peak narrowing inside the same crater. Peak narrowing is the only observable feature of the 3.32 km s^{-1} shot.

6.3.3.2 Olivine P2

Note: As can be seen in Table 5.2, the olivine gemstones had a nominal FWHM value for P2 of 6.8 cm^{-1} ± 1.0 cm^{-1}.

Figure 5.25.D, the P2 FWHM map for the 0.576 km s^{-1} shot, shows peak-broadening in the centre of the crater (a maximum increase of +0.6 cm^{-1}) and peak narrowing along the cracks radiating out from the crater (a maximum decrease of -3.8 cm^{-1}).

Section 5.3.2.2 presents the 0.602 km s^{-1} olivine shot and the P2 FWHM map associated with that shot (Figure 5.27). Figure 5.27 shows only increases in FWHM inside the crater, with a maximum increase of +2.1 cm^{-1}.

Similar to the 0.602 km s^{-1} olivine shot, the 0.638 km s^{-1} olivine shot (Section 5.3.2.3) shows broadening of the P2 FWHM inside the crater, with a maximum increase of +1.9 cm^{-1}. There is also a small concentration of pixels showing narrowing of the Raman peaks at (3,23), with a maximum decrease of -1.0 cm^{-1}. However, this location corresponds to a dark patch that can be seen to the left of the crater on the surface of

the target in Figure 5.22.A and is likely a contaminant. The observed peak narrowing may be due to the presence of this contaminant and, therefore, un-related to the impact event.

Figure 5.31.D is the P2 FWHM map for the 1.35 km s^{-1} olivine shot (Section 5.3.2.4). Ignoring the region of poor data, the map shows peak-broadening inside the crater and along the crater walls presenting a maximum increase in FWHM of 2.1 cm^{-1}.

Section 5.3.2.5 presents Figure 5.33.D, the P2 FWHM map for the 1.57 km s^{-1} olivine shot. This map shows peak narrowing in the centre of the crater (maximum reduction of -1.1 cm^{-1}) and along cracks at the bottom edge of the crater (maximum reduction of -0.4 cm^{-1}). There is also a localised area of peak-broadening to the right of the centre of the crater (maximum increase of +1.8 cm^{-1}). The map also contains a small number of pixels that occupy the extreme ends of the scale. In order to observe more detail contained at the central part of the scale, Figure 6.7 re-displays Figure 5.33.D with a scale of 6.0 – 7.5 cm^{-1}.

Figure 6.7, clearly shows a band of material at (20,35) where the FWHM increased by as much as +0.5 cm^{-1}, which was difficult to detect in the original version of the map. This band, and the area of peak-broadening, are located on opposite sides of the area of peak narrowing beginning to encompass it. It is possible that this could be the beginning of the formation of a ring feature.

The P2 FWHM map (Figure 5.35.D) presented in Section 5.3.2.6 shows the FWHM of the Raman peaks to have decreased inside the crater and on the uplifted material below the crater (maximum reduction of -1.4 cm^{-1}), with the exception of a handful of scattered pixels that show an increase in the width of the peaks (maximum increase of +0.7 cm^{-1}). The reason for the presence of these few pixels of increased peak width is unknown.

The 3.03 km s^{-1} olivine shot (Section 5.3.2.7) shows a ring feature in its FWHM maps. The P2 FWHM map (Figure 5.37.D) shows an area at the centre of the crater having undergone a reduction in the width of the Raman peaks (maximum decrease of -3.5 cm^{-1}) surrounded by a ring of material with increased peak widths (maximum increase of +4.0 cm^{-1}). The wide range of the scale obscures finer details located around the unaltered FWHM value of 6.6 cm^{-1} and, as such, the image has been re-scaled (Figure 6.8).

The re-scaled image (Figure 6.8) shows the ring of broadened material around the centre of the crater to be thicker than it was initially observed to be in Figure 5.37.D. Also, material with a reduction in FWHM (maximum of -0.5 cm^{-1}) can be seen at the bottom of the crater outside the ring. A possible explanation for the origin of this ring feature is discussed in Section 6.3.

Counter to P1, the P2 FWHM map for the 3.32 km s^{-1} olivine shot (Figure 5.39.D) shows peak-broadening inside the crater, increasing the width of the peaks by a maximum of +2.2 cm^{-1}.

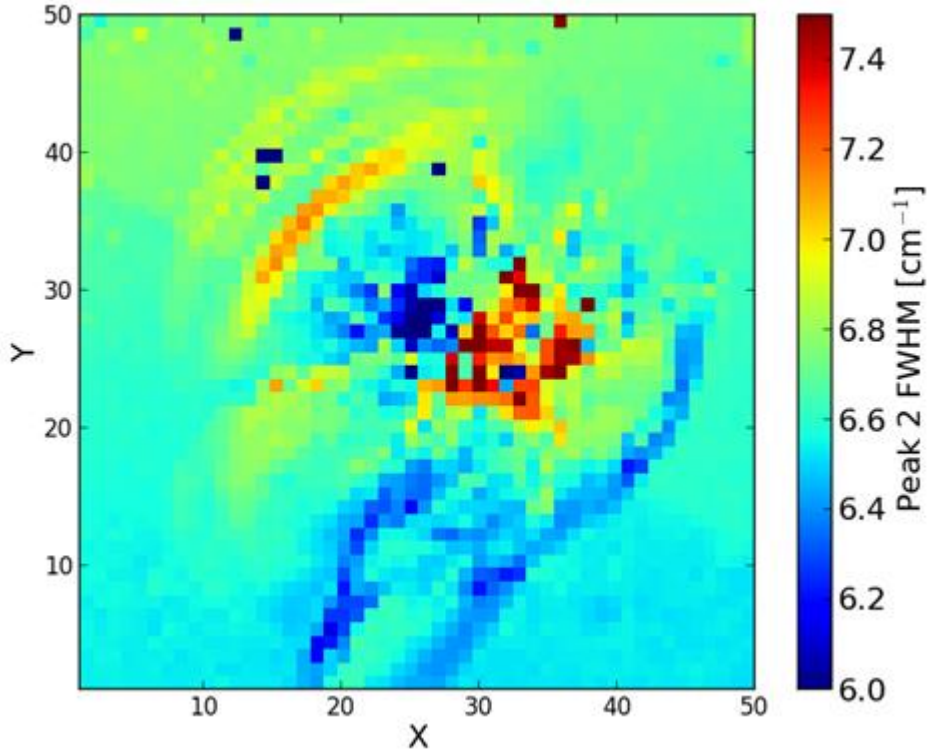


Figure 6.7: The P2 FWHM map from the olivine shot G150114#1 (1.57 km s^{-1}) re-displayed with an upper limit of 7.5 cm^{-1} and a lower limit of 6.0 cm^{-1}.

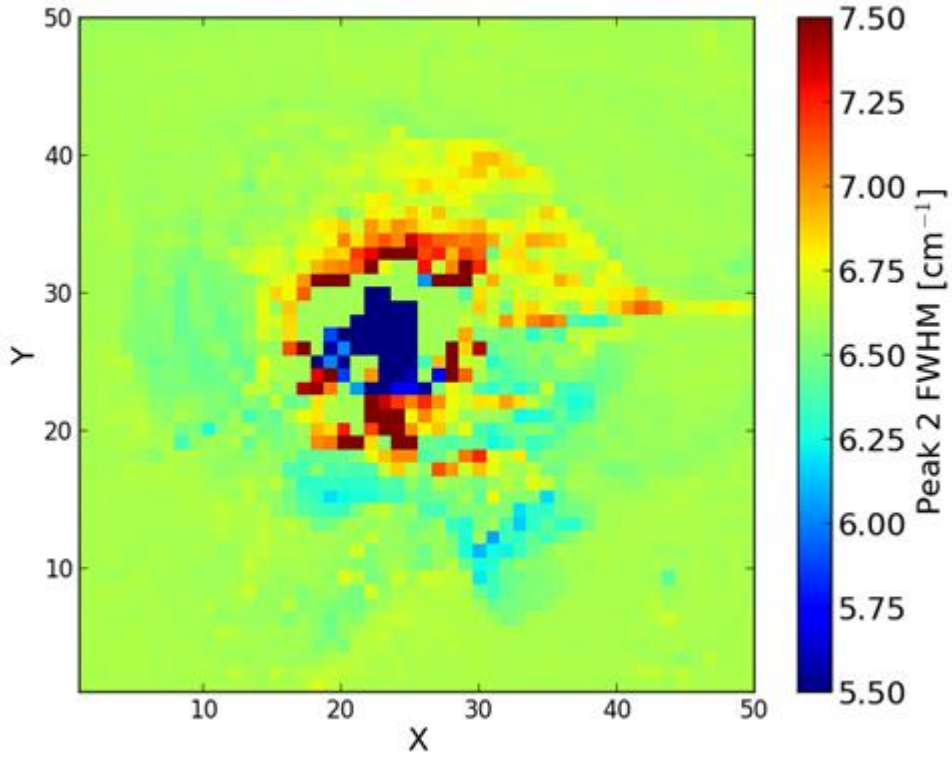


Figure 6.8: The P2 FWHM map from the olivine shot G150114#2 (3.03 km s^{-1}) re-displayed with an upper limit of 7.5 cm^{-1} and a lower limit of 5.5 cm^{-1}.

In general, the olivine shot program shows the P2 FWHM to increase inside the crater for impact speeds up to 1.35 km s^{-1}. Some narrowing can also be seen for these shots, but it is confined to cracks, or contaminants, on the surface of the targets. At 1.57 km s^{-1} the centre of the crater contains areas of both peak-broadening and peak narrowing. The rescaled image Figure 6.7 also shows a band of broadened material above the area of peak narrowing which could indicate the beginning of the formation of a ring feature. The 2.02 km s^{-1} shot shows peak narrowing inside the crater with scattered pixels of peak-broadening, while the 3.03 km s^{-1} shot shows a ring feature with peak narrowing in the centre surrounded by peak-broadening. Finally, the 3.32 km s^{-1} shot shows only peak-broadening for the P2 FWHM.

6.3.4 Labradorite

Two Raman peaks have been analysed for labradorite, P1 and P2 (Section 4.2.1). The FWHM of these peaks do not necessarily behave in the same manner for each of the shots and, as such, the changes in the FWHM for the labradorite shot program will be analysed separately for each peak.

6.3.4.1 Labradorite P1

Note: As can be seen in Table 5.2, the labradorite gemstones had a nominal FWHM value for P1 of 6.7 cm^{-1} ± 0.7 cm^{-1}.

For P1, Figure 5.25.C shows peak narrowing inside the crater including large areas presenting as a constant reduction in FWHM of -2.8 cm^{-1}. These areas are surrounded by pixels of further narrowing showing a maximum reduction in peak width of -3.7 cm^{-1} inside the crater. Outside the crater, in the top right of the map, an area of peak narrowing is observed showing a reduction in FWHM towards the corner of the map (maximum reduction in peak width of -3.8 cm^{-1}). The reason for this gradient feature in the top right of the map is unknown. There are no features in the optical image of the crater (Figure 5.41.A) or the intensity maps of the crater (Figure 5.25.A and Figure 5.25.B) that would explain its presence.

The 0.646 km s^{-1} labradorite shot shows peak narrowing to be the dominant feature inside the crater for P1 (Figure 5.48.C), with a maximum reduction of -2.7 cm^{-1} in peak width. This implies that the crater has undergone the annealing effect previously discussed. However, a small area located inside the crater at (24,21) shows peak-broadening (maximum increase of +2.6 cm^{-1}), the presence of which is in disagreement with the annealing effect theory. Inspecting the optical image of this crater, Figure 5.41.B shows the material inside the crater to be fractured. One possible explanation for the presence of the area of peak-broadening is that the material in that location was annealed, but the fractures in the sub-surface generated by the impact caused the material in that location to become detached from the crater revealing the shocked, but un-annealed, material below.

The P1 FWHM map (Figure 5.50.C) presented in Section 5.3.3.3 shows a large area of peak narrowing inside the crater giving a maximum reduction in FWHM of -2.8 cm^{-1}.

The P1 FWHM map for the 1.36 km s^{-1} labradorite shot (Figure 5.52.C) shows a ring feature unlike those previously discussed. Here the centre consists of pixels showing a mix of broadened, narrowed, and un-altered pixels, while the ring is comprised of pixels showing peak narrowing (maximum reduction of -3.5 cm^{-1}). The theory for the formation of the ring feature proposed in Section 6.3 does not explain this ring feature. However, it is possible that this is not a true ring feature and that the central

region was formed in the same way as that proposed for the broadened region of the 0.646 km s^{-1} labradorite shot. The annealed material in that area may have become detached from the crater due to the fracturing of the material surrounding it.

Figure 5.54.C shows narrowing of the P1 FWHM inside the crater for the 1.81 km s^{-1} shot with a maximum reduction of -2.6 cm^{-1}. The map also contains scattered pixels of peak-broadening (maximum increase of +3.0 cm^{-1}) that have extended the upper limit of the scale. Figure 6.9 shows a re-displayed version of Figure 5.54.C in an effort to discern any un-seen features around the nominal value for this shot of 7.0 cm^{-1}.

The re-scaled image (Figure 6.9) reveals some details of the FWHM for pixels located around the edges of the crater. To the top right of the crater at (37,40) an area of peak-broadening can be seen (maximum increase of +0.8 cm^{-1}). Matching this position to the optical image of this shot (Figure 5.43.A) shows that this is the location of uplifted material generated in the impact. To the left of the crater at (13,25), an area of peak narrowing with a maximum reduction of -0.4 cm^{-1} can be seen. The location (13,25) in this map corresponds to (-125,50) in the optical image (Figure 5.43.A) which is part of the crater wall. Another area of interest can be found below the crater at (20,5), showing peak-broadening (maximum increase of +0.6 cm^{-1}) along a crack on the surface of the target extending to the bottom of the map.

The 1.99 km s^{-1} labradorite shot shows a reduction in the P1 FWHM inside the crater by as much as -3.1 cm^{-1} (Figure 5.56.C). There are a few scattered pixels of broadening inside the crater, but they correspond to poorly fit pixels identified in Figure 5.57.D. Rescaling this image to reduce the effect of these high value pixels on the scale produces Figure 6.10.

The maps of Section 5.3.3.6 (excluding the σ_{resid} map Figure 5.57.D) contain a band of material through the centre of the crater. Comparing these maps to the optical image (Figure 5.43.B), it can be seen that the crater seen in the maps can be diagonally divided into two distinct regions: a deeper region towards the top right of the crater and an area of uplifted material towards the bottom left of the crater. The band of material separating these regions can be seen in Figure 6.10 as a band of pixels showing peak-broadening inside a crater of otherwise narrowed pixels. Figure 6.10 also shows the region to the right of the band to have suffered less narrowing than the region to the left of the band. One possible explanation for this discrepancy is that the material seen inside the crater would have been shocked to a greater degree than the uplifted material outside the crater.

Figure 5.58.C, the P1 FWHM map for the 2.72 km s^{-1} labradorite shot, covers an area including a central crater surrounded by an expanse of fractured material. Peak narrowing can be seen in the centre of the crater (maximum reduction of -1.8 cm^{-1}) as well as on some of the uplifted material. The map also contains a few pixels of broadened peaks, however, these match to poorly fit pixels identified in Figure 5.59.D. In order to better interpret the map, the scale has been adjusted to remove these poorly fit pixels and re-displayed as Figure 6.11. Figure 6.11 presents no new features but gives a more clearly defined view as to the extent of the narrowed pixels on the fractured material.

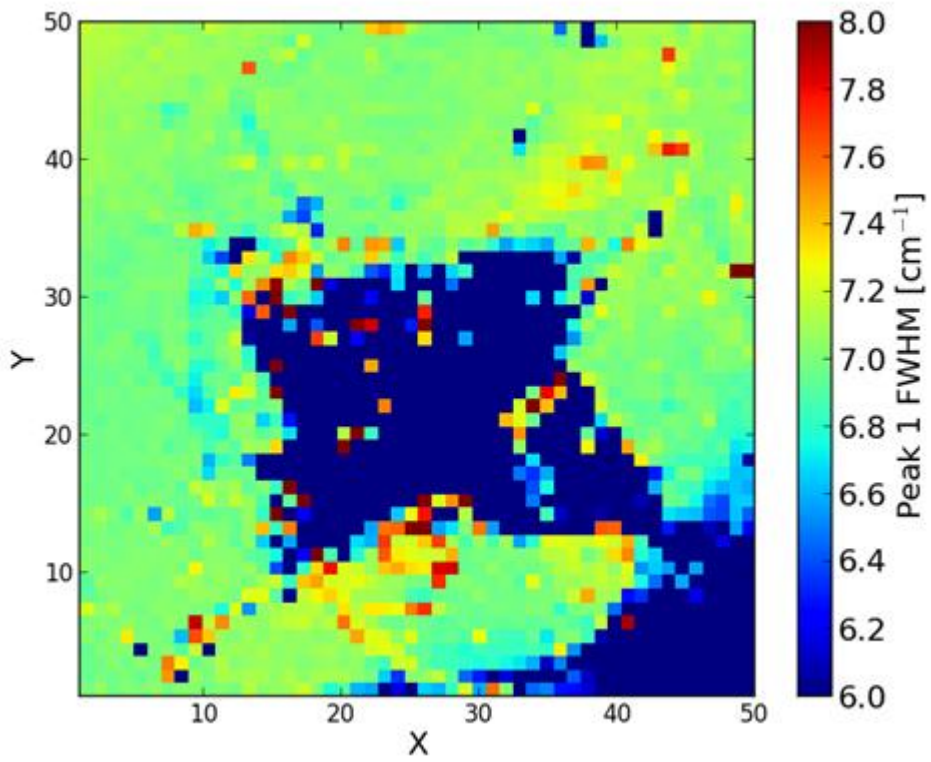


Figure 6.9: The P1 FWHM map from the labradorite shot G170615#2 (1.81 km s^{-1}) re-displayed with an upper limit of 8.0 cm^{-1} and a lower limit of 6.0 cm^{-1}.

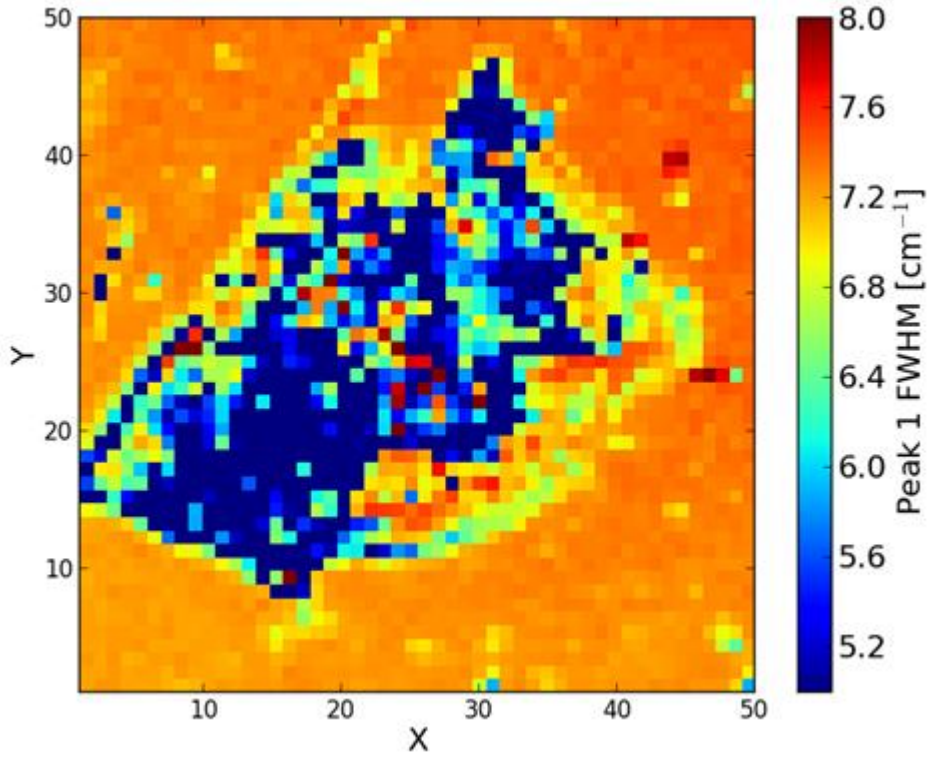


Figure 6.10: The P1 FWHM map from the labradorite shot G050815#1 (1.99 km s^{-1}) re-displayed with an upper limit of 8.0 cm^{-1} and a lower limit of 5.0 cm^{-1}.

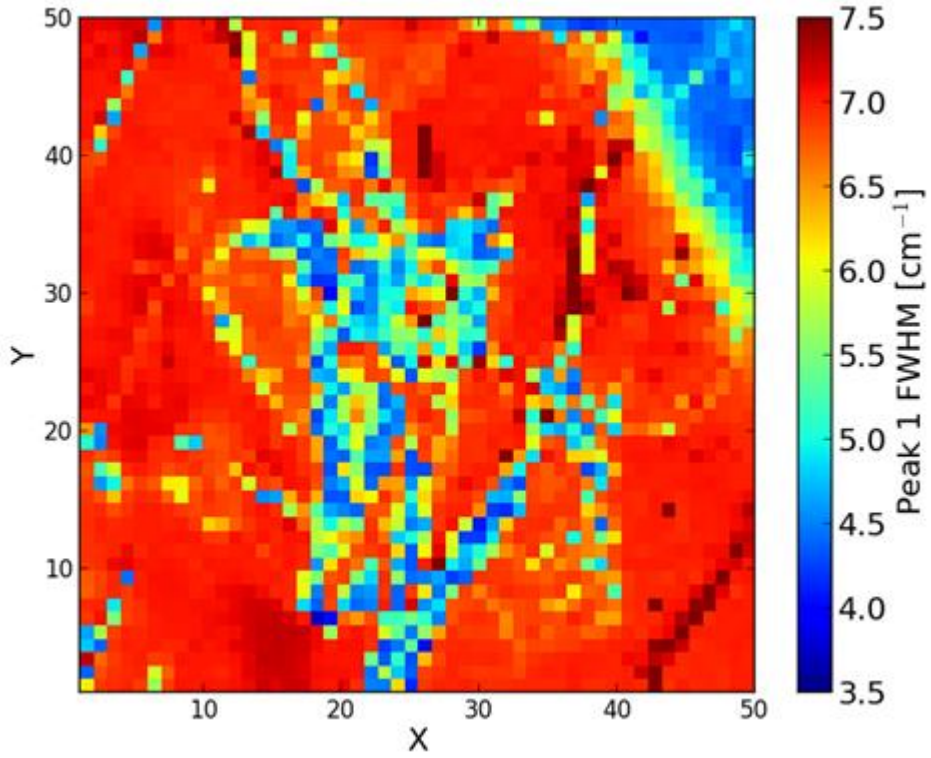


Figure 6.11: The P1 FWHM map from the labradorite shot G120815#1 (2.72 km s^{-1}) re-displayed with an upper limit of 7.5 cm^{-1} and a lower limit of 3.5 cm^{-1}.

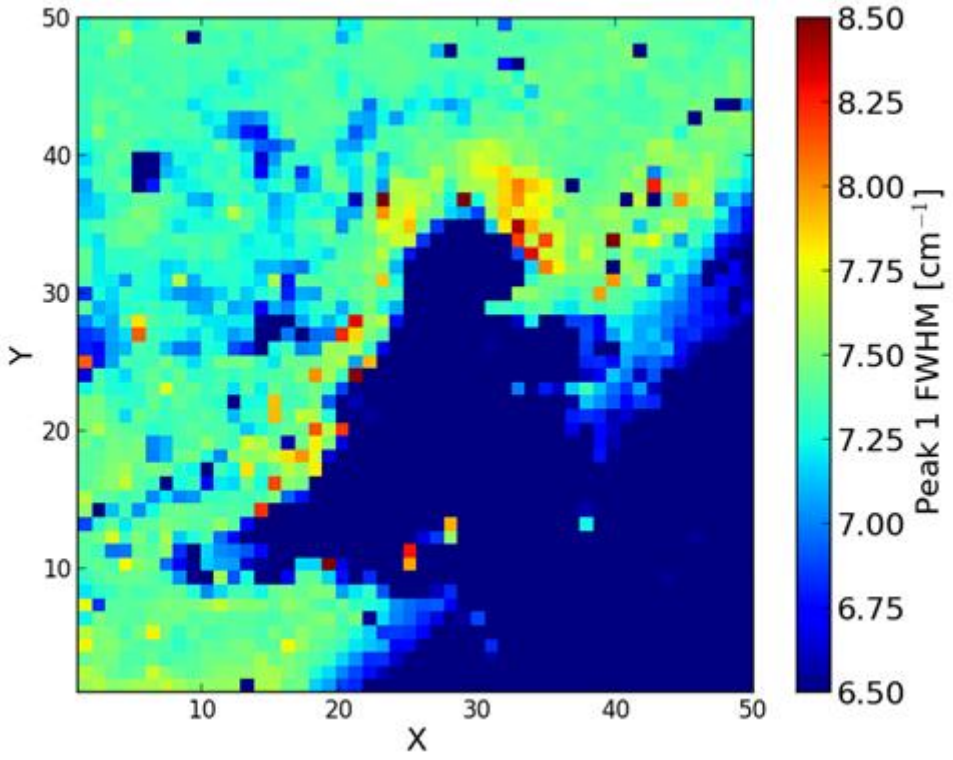


Figure 6.12: The P1 FWHM map from the labradorite shot G100715#2 (3.39 km s^{-1}) re-displayed with an upper limit of 8.5 cm^{-1} and a lower limit of 6.5 cm^{-1}.

The P1 FWHM map for the 3.39 km s^{-1} labradorite shot (Figure 5.60.C) shows a large area of narrowing inside the crater (maximum reduction of -3.7 cm^{-1}) surrounded by peak-broadening (maximum increase of +3.1 cm^{-1}). Due to the wide scale produced by a single high value pixel at (19,10), it is hard to determine if the broadened pixels are merely scattered around the outside of the crater or form part of a defined feature. Figure 6.12 is a re-scaled map of Figure 5.60.C with a lower limit of 6.5 cm^{-1} and an upper limit of 8.5 cm^{-1}. This new map shows that the area of peak narrowing is bordered by pixels of increased FWHM along a large portion of its boundary, possibly showing the beginnings/remnants of a ring feature.

Figure 5.62, the P1 FWHM map for the 5.06 km s^{-1} labradorite shot, is dominated by a large area of peak narrowing which represents the inside of the crater (maximum reduction of -2.5 cm^{-1}). There are a few pixels showing an increase in peak width on the edges of the crater, with a maximum increase of +4.2 cm^{-1}.

The labradorite shot program shows some degree of narrowing of the P1 FWHM in all of the shots. Several of the shots also show broadening of the P1 FWHM, either as scattered pixels (in the case of the 1.81 km s^{-1} shot), or as some form of more defined feature. The 0.646 km s^{-1} shot contains a small concentrated area of broadening, while the 1.99 km s^{-1} shot shows a band of broadened material between the crater and a region of uplifted material. The 3.39 km s^{-1} and the 5.06 km s^{-1} shots both clearly show narrowing inside the crater, but also show broadened pixels surrounded these regions. These broadened pixels do not form a clear feature, but could possibly be the result of a ring feature starting to form. Finally, the 1.36 km s^{-1} shot shows a ring feature different to those previously seen; an area of broadened pixels surrounded by narrowed pixels. As previously discussed, this could be due to the annealed material having been excavated due to sub-surface cracking generated during the impact.

6.3.4.2 Labradorite P2

Note: As can be seen in Table 5.2, the labradorite gemstones had a nominal FWHM value for P2 of 8.5 cm^{-1} ± 0.5 cm^{-1}, with the exception of the 2.72 km s^{-1} shot which had a nominal FWHM value of 6.8 cm^{-1}.

Figure 5.46.D is the P2 FWHM map for the 0.291 km s^{-1} labradorite shot (Section 5.3.3.1), which shows peak narrowing inside the crater, including large areas of constant FWHM representing the maximum reduction in peak width inside the crater (reduction of -2.8 cm^{-1}). Outside the crater, in the top right of the map, an area of peak narrowing is observed showing a reduction in FWHM towards the corner of the map (maximum reduction in peak width of -4.5 cm^{-1}). As stated in Section 6.3.4.1, the reason for this gradient feature is unknown.

The P2 FWHM map for the 0.646 km s^{-1} labradorite shot (Figure 5.48.D) shows a decrease in peak width inside the crater, with the maximum reduction of -3.8 cm^{-1} found at the centre of the crater. Two areas of peak-broadening can be seen below, and to the right of, the crater at (23,20) and (30,33). Both areas present a maximum increase in FWHM of +1.7 cm^{-1}. Comparing these locations to the optical image of the crater (Figure 5.41.B) shows them to be located on uplifted material rather than on the flat surfaces surrounding the crater. These areas are also present in the P1 FWHM map for this shot (Figure 5.48.C), albeit much less defined.

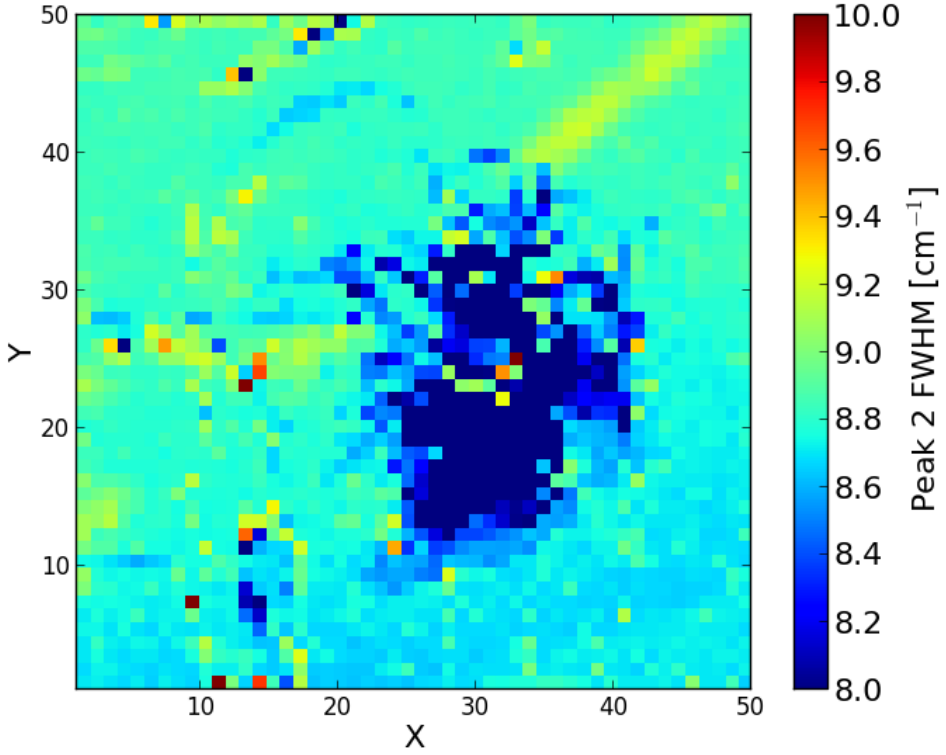


Figure 6.13: The P2 FWHM map from the labradorite shot S300715#1 (0.997 km s^{-1}) re-displayed with an upper limit of 10.0 cm^{-1} and a lower limit of 8.0 cm^{-1}.

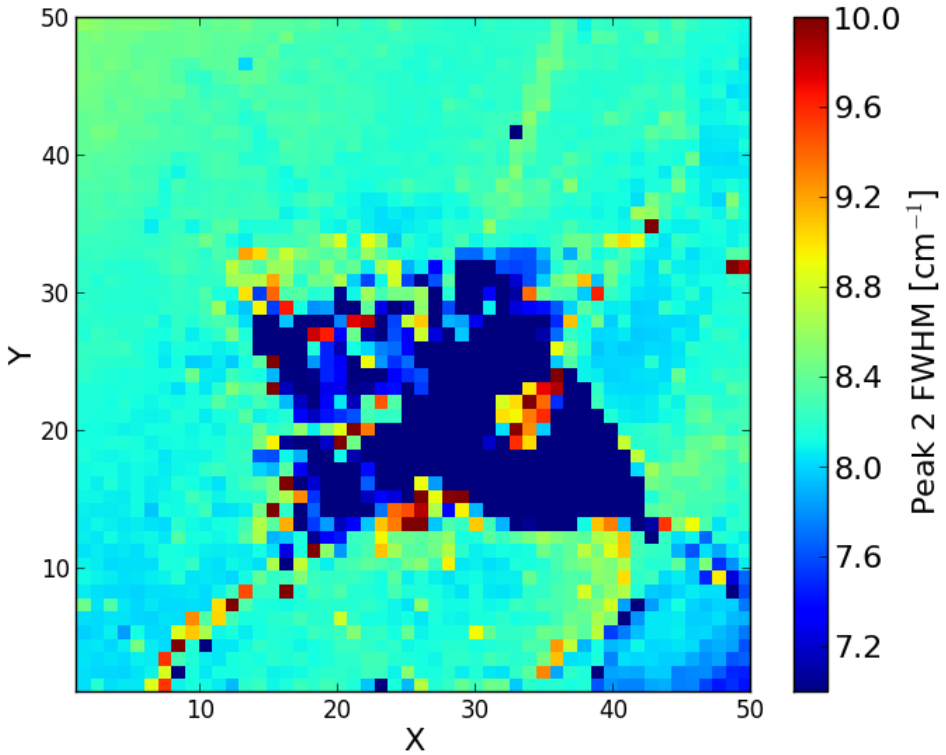


Figure 6.14: The P2 FWHM map from the labradorite shot G170615#2 (1.81 km s^{-1}) re-displayed with an upper limit of 10.0 cm^{-1} and a lower limit of 7.0 cm^{-1}.

The 0.997 km s^{-1} labradorite shot shows narrowing of P2 inside the crater (Figure 5.50.D) by a maximum of -3.6 cm^{-1}. The map contains some scattered pixels with large FWHM values which, when combined with the substantial narrowing inside the crater, has compressed information in the regions outside the crater into a smaller range of the scale. Figure 6.13 re-displays Figure 5.50.D with a modified scale in an attempt to discern more detail from these regions. Figure 6.13 reveals two previously unseen features: an area of peak narrowing below the crater (with maximum reduction of -0.2 cm^{-1}), and a band of peak-broadening showing a maximum increase of +0.4 cm^{-1} between (36,40) and (46,50). The origin of both of these features is unknown due to a lack of any corresponding feature in either the optical image of the intensity maps for this shot.

Section 5.3.3.4 presents Figure 5.52.D, the P2 FWHM map for the 1.36 km s^{-1} labradorite shot. Figure 5.52.D shows only peak narrowing inside the crater with a maximum reduction in FWHM of -4.2 cm^{-1}.

The P2 FWHM map for the 1.81 km s^{-1} labradorite shot (Figure 5.54.D) shows peak narrowing inside the crater with a maximum decrease in FWHM of -3.7 cm^{-1}. Peak-broadening can also be seen along cracks in the surface of the target, and along the bottom rim of the crater at (26,14), showing a maximum increase of +1.8 cm^{-1}. Re-scaling the image in an attempt to reveal features closer to the un-altered value of 8.2 cm^{-1} reveals material showing slight peak narrowing (-0.2 cm^{-1}), flanking the crack that runs from (8,0) through the crater to (46,40) (Figure 6.14).

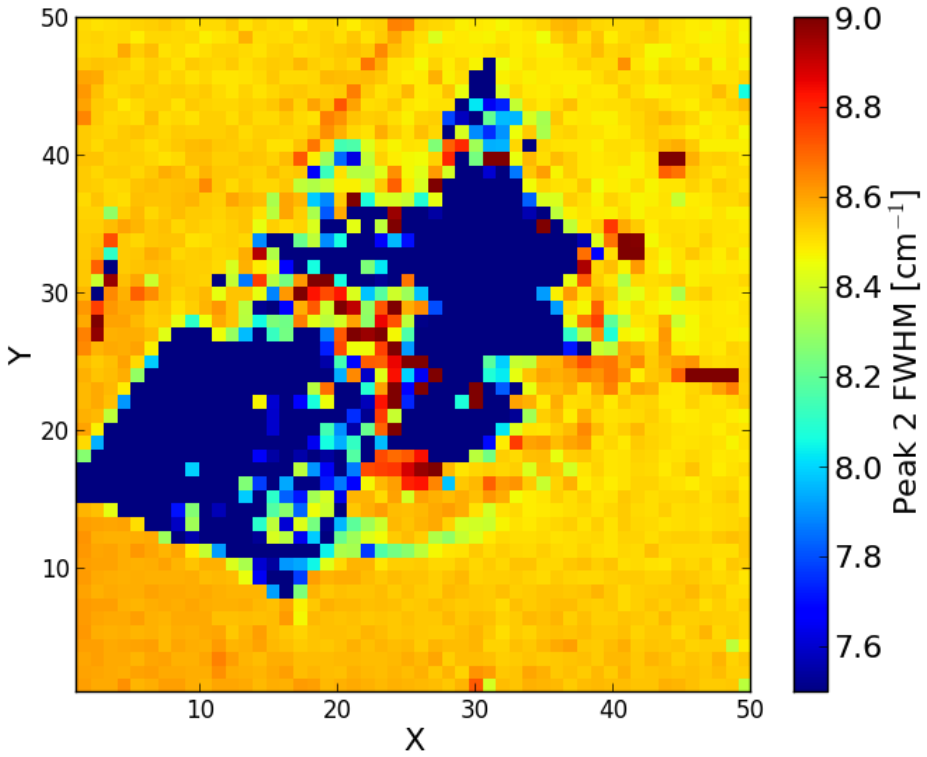


Figure 6.15: The P2 FWHM map from the labradorite shot G050815#1 (1.99 km s^{-1}) re-displayed with an upper limit of 9.0 cm^{-1} and a lower limit of 7.5 cm^{-1}.

The 1.99 km s^{-1} labradorite shot shows two distinct areas of peak-narrowing for P2, with a maximum reduction of -3.8 cm^{-1} (Figure 5.56.D). These two areas are separated by a band of material displaying broadening of the P2 FWHM, with a maximum increase of +2.4 cm^{-1}. Figure 6.15 shows a re-scaled version of Figure 5.56.D with a minimum FWHM value of 7.5 cm^{-1} and a maximum FWHM value of 9.0 cm^{-1}. This new image more clearly shows the band separating the crater and the uplifted material.

Figure 5.58.D is the P2 FWHM map for the 2.72 km s^{-1} labradorite shot (Section 5.3.3.7). It shows the same features as its P1 counterpart, Figure 5.58.C, with a reduction in the P2 FWHM in the centre of the crater (maximum of -1.9 cm^{-1}) and on some on the uplifted material surrounding the crater (maximum of -3.0 cm^{-1}). Similar to its P1 counterpart, there are some scattered pixels showing peak-broadening. However, these pixels match the locations of poorly fit pixels in the σ_{resid} map for this shot (Figure 5.59.D) and should be discounted. In order to remove their effect on the map, Figure 6.16 shows a re-displayed version of Figure 5.58.D with limits of 7.0 cm^{-1} and 9.0 cm^{-1}. This new map reveals no new features but does more clearly show the boundaries of the features already discussed here and in Section 5.3.3.7.

Section 5.3.3.8 presents Figure 5.60.D, the P2 FWHM map for the 3.39 km s^{-1} labradorite shot. This map is dominated by a large area of peak narrowing which represents the crater and uplifted material below the crater (maximum reduction of 4.0 cm^{-1}). Surrounding the crater are pixels showing slight broadening on the FWHM. Figure 6.17 shows a re-scaled version of Figure 5.60.D in an effort to more clearly display these broadened pixels. A diagonal band of material running from (20,50) to (30,0) is now visible, showing a maximum increase in FWHM of +0.5 cm^{-1}.

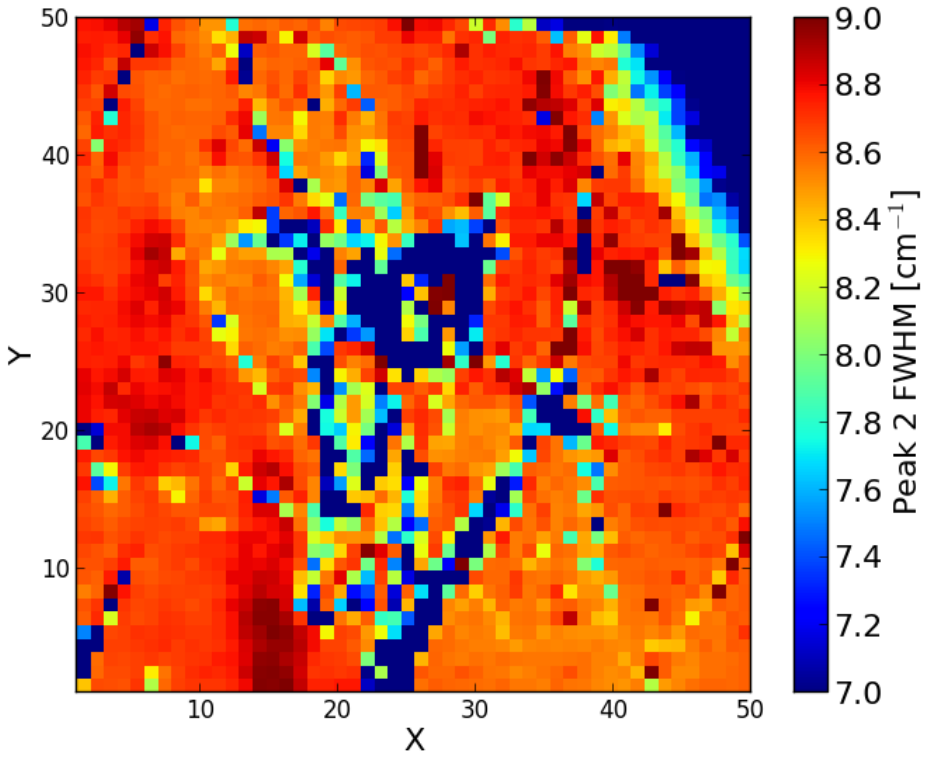


Figure 6.16: The P2 FWHM map from the labradorite shot G120815#1 (2.72 km s^{-1}) re-displayed with an upper limit of 9.0 cm^{-1} and a lower limit of 7.0 cm^{-1}.

Also visible in Figure 6.17 is material along the edge of the crater showing an increased peak width, with an average increase of about +1.0 cm^{-1} (a maximum increase of +6.2 cm^{-1} is seen, but this is outside the scale of Figure 6.17). This structure, combined with that seen for P1 in Figure 6.12 (Section 6.3.4.1), gives more credibility to the theory that this is a ring feature (as explained in Section 6.3).

The P2 FWHM map for the 5.06 km s^{-1} labradorite shot (Figure 5.62.D) shows peak narrowing inside the crater (maximum reduction of -3.6 cm^{-1}) and peak-broadening mainly below, and to the left, of the crater with some scattered areas elsewhere in the map (maximum increase of +3.7 cm^{-1}). The extent of the peak-broadening can be more easily seen in Figure 6.18, a re-scaled version of Figure 5.62.D with an upper limit of 9.5 cm^{-1} and a lower limit of 6.5 cm^{-1}. This new map shows that the area near (21,12) is a region of peak-broadening, whereas in the P1 FWHM map for this shot (Figure 5.62.C) it is an area of peak narrowing. The optical image Figure 5.45 identifies this region as an area of uplifted material.

As with P1, the labradorite shot program shows some degree of narrowing of the P2 FWHM inside the craters of every shot. Peak-broadening is also seen in several of the shots. The 0.646 km s^{-1} and 5.06 km s^{-1} shots show peak-broadening on regions of uplifted material outside the crater, while the 1.81 km s^{-1} shot shows peak-broadening along the cracks running through the crater. A band of peak-broadening can be seen separating two regions of peak narrowing inside the crater in the 1.99 km s^{-1} shot. A ring feature has formed as a result of the 3.39 km s^{-1} shot with peak-broadening along the edge of the area of peak narrowing that represents the crater itself.

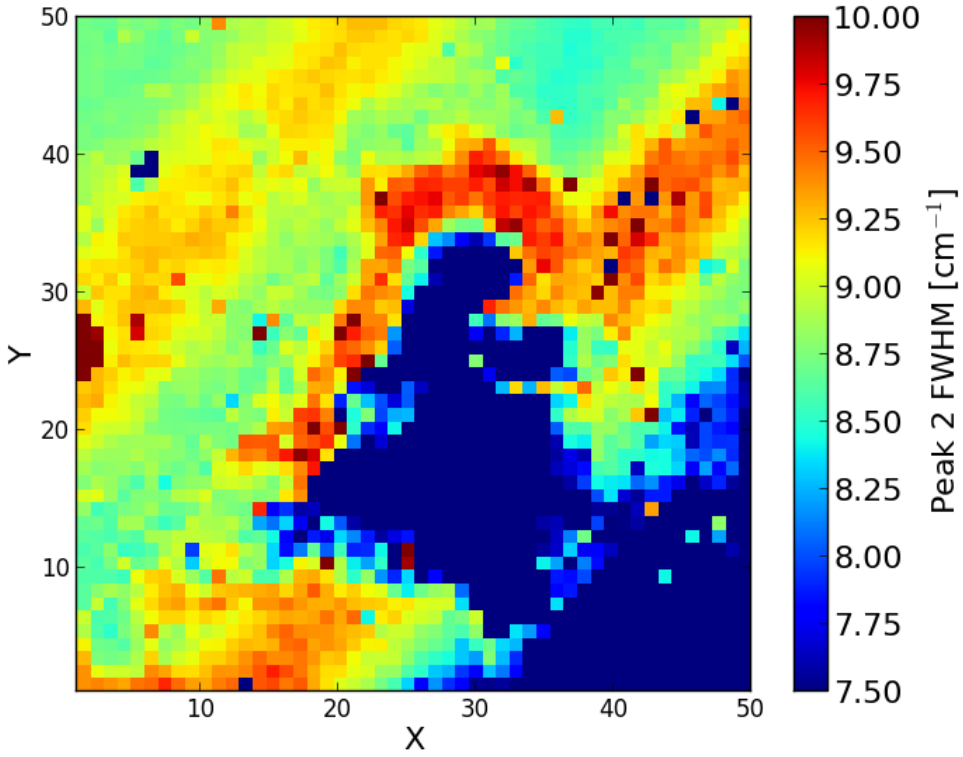


Figure 6.17: The P2 FWHM map from the labradorite shot G100715#1 (3.39 km s^{-1}) re-displayed with an upper limit of 10.0 cm^{-1} and a lower limit of 7.5 cm^{-1}.

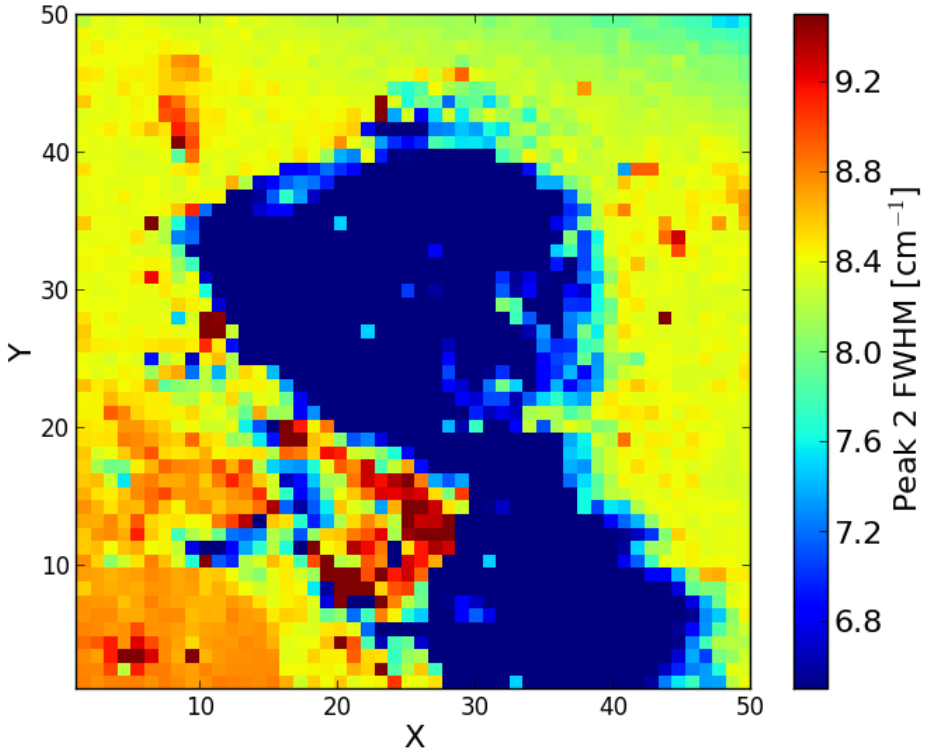


Figure 6.18: The P2 FWHM map from the labradorite shot G160915#1 (5.06 km s^{-1}) re-displayed with an upper limit of 9.5 cm^{-1} and a lower limit of 6.5 cm^{-1}.

6.4 Peak Position

Every shot presented in Chapter 5 showed shifts in the Raman peak positions by some degree. A change in the position of a Raman peak means a change has occurred in either the structure, or the effective mass of the bond that the peak represents (Equation 2.4). A change in either of those parameters will result in a change in the length of the bond. As both positive and negative shifts have been observed here, both increases and decreases in bond length have occurred.

Changes in the strength of the bond can be the result of alterations to the atomic structure of the sample. This can be due to pressure being applied to the sample which results in compression of the structure. Hydrostatic pressure tests apply such compressions and have shown changes in Raman peak position [129-133].

Changes to the effective mass of a bond occur if one (or more) of the atoms within the bond is replaced by an atom of a different element. This is common in mineral samples when the structure of the mineral allows for more than one element to occupy its ion sites (as has been previously explained for olivine in Section 4.2.1).

In order to begin to investigate the cause of the Raman shifts seen in these impact experiments, it must first be determined if these changes are due to elemental or structural alterations to the sample, or a combination of both.

6.4.1 Elemental Composition

To determine if the elemental composition of the samples has changed due to the impacts, quantitative energy dispersive X-ray (EDX) analysis was performed using a scanning electron microscope (SEM).

Each of the targets from the impact experiments described in Chapter 5 were placed in the SEM. The impact craters previously investigated using Raman spectroscopy in Chapter 5 were located and a total of ten EDX spectra were obtained for each crater, five from inside the crater and five from unshocked material outside the crater. These sets of five spectra were averaged before being processed quantitatively to determine the ratio of elements present for the shocked and unshocked material. Each ratio was calculated using the atomic abundance of each of the elements present (rather than the atomic weights) and the calibration for the abundances was made via comparison to a cobalt standard.

Table 6.2 shows the results of this experiment. For quartz the ratio of silicon to oxygen is shown; for olivine the ratio of magnesium to iron (known as the forsterite number $Fo_{\#}$) is shown; and for labradorite the ratio of calcium to sodium (see Section 4.2.3) is shown.

Table 6.2 shows very little change in the elemental ratios inside the crater for all of the shots. The largest change in ratio is 0.03, for the 0.997 km s^{-1} and 2.72 km s^{-1} labradorite shots, which is not a large enough change in ratio to show a detectable change in Raman peak position [122]. Therefore, if the shifts in Raman peak position are not due to changes in elemental composition, they must be due to changes in the crystal structure of the target minerals.

Table 6.2: The elemental ratios for each of the mineral targets before and after being shocked due to impact.

Mineral	Shot Velocity (km s^{-1})	Elemental Ratio		Change in Ratio
		Unshocked	Shocked	
Quartz	0.373	0.71	0.71	0.00
O/(O+Si)	0.515	0.71	0.71	0.00
	0.91	0.71	0.72	0.01
	1.35	0.71	0.71	0.00
	2.02	0.70	0.70	0.00
	3.32	0.71	0.72	0.01
	4.48	0.71	0.69	0.02
	5.27	0.71	0.69	0.02
	6.40	0.70	0.70	0.00
Olivine	**Shot Velocity**	**Unshocked**	**Shocked**	**Change**
Mg/(Mg+Fe)	0.576	0.91	0.89	0.02
	0.602	0.91	0.91	0.00
	0.638	0.90	0.90	0.00
	1.35	0.91	0.92	0.01
	1.57	0.91	0.92	0.01
	2.02	0.91	0.91	0.00
	3.03	0.91	0.89	0.02
	3.32	0.91	0.91	0.00
Labradorite	**Shot Velocity**	**Unshocked**	**Shocked**	**Change**
Ca/(Ca+Na)	0.291	0.51	0.52	0.01
	0.646	0.52	0.53	0.01
	0.997	0.55	0.52	0.03
	1.36	0.53	0.52	0.01
	1.81	0.52	0.52	0.00
	1.99	0.52	0.54	0.02
	2.72	0.52	0.55	0.03
	3.39	0.51	0.53	0.02
	5.06	0.52	0.52	0.00

6.4.2 Structural Changes

It has been determined that the shifts in Raman peak position observed here are due to changes in the crystal structure of the target minerals. Previous studies have shown that pressure being applied to a sample can cause shifts in Raman peak positions [129-135]. Many of these studies observe a sample while it is under pressure during a hydrostatic pressure test. In which, the sample is enclosed inside a pressure vessel with pressure being applied to the sample equally from all directions. The resulting compression of the sample's structure causes its Raman peaks to alter their positions as a function of the amount of pressure applied [129-133].

Raman studies of quartz undergoing hydrostatic pressure show that as the pressure is increased, the peak position of the P1 peak increases [129-131]. Figure 6.19 shows this trend can be approximated to be linear up to 4.0 GPa.

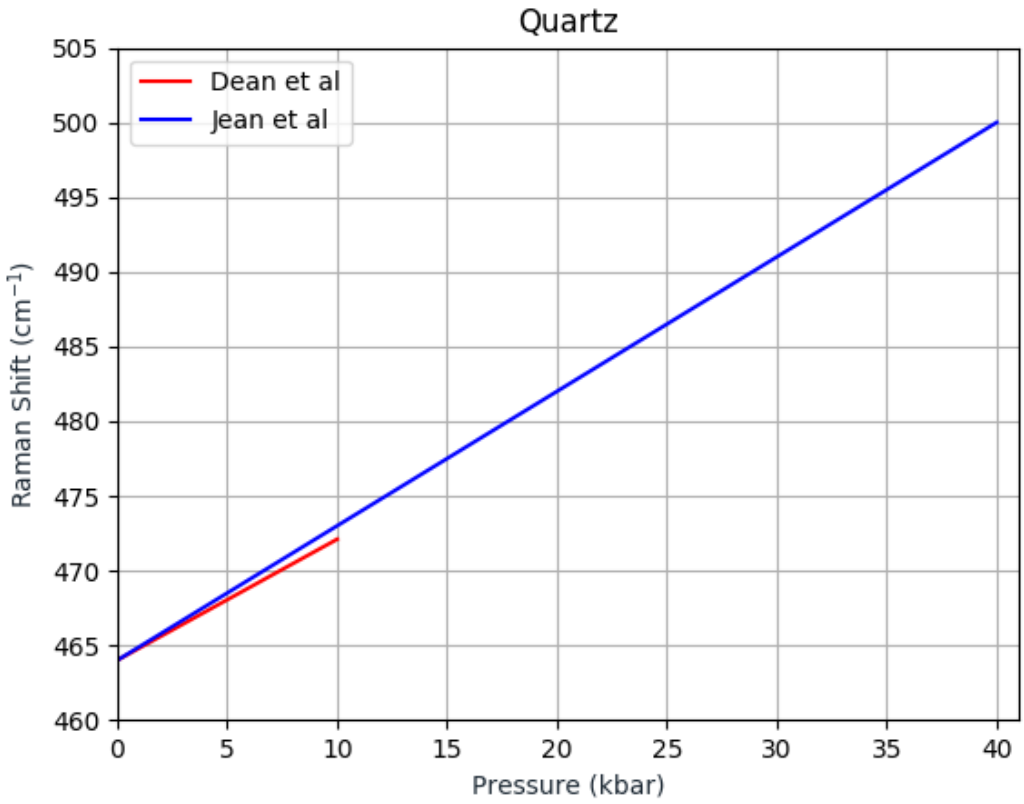


Figure 6.19: Quartz P1 peak position vs static pressure. Data recreated from Dean *et al* [129] and Jean *et al* [130].

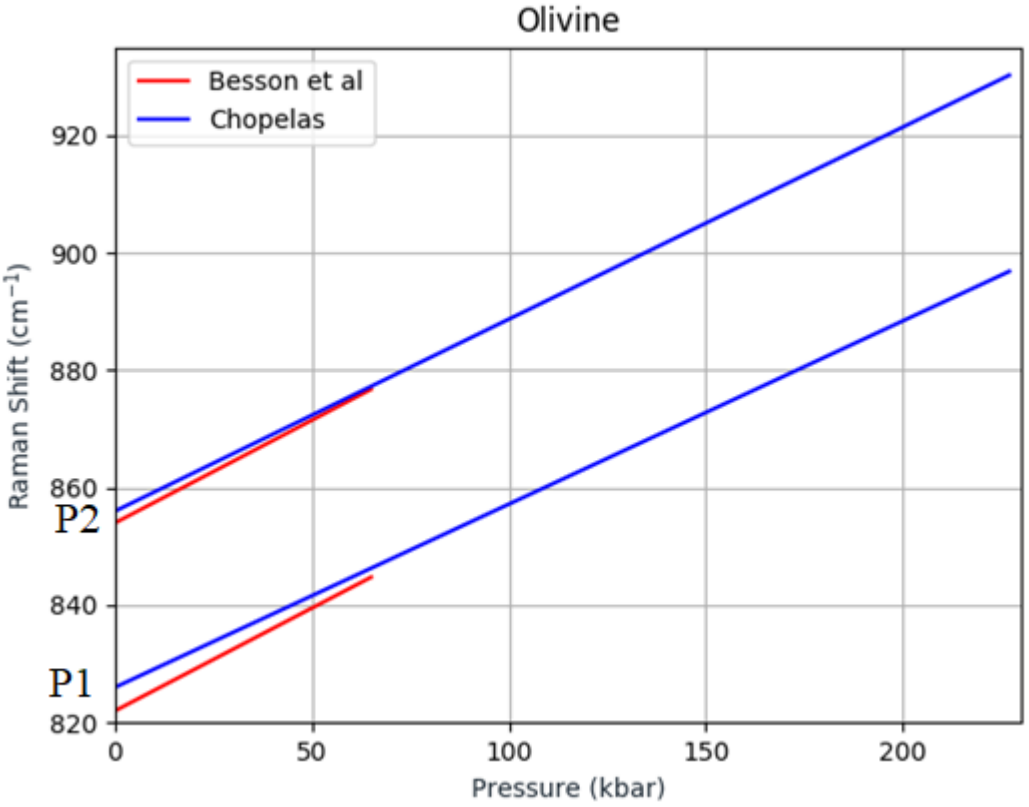


Figure 6.20: Olivine P1 and P2 peak position vs static pressure. Data recreated from Besson *et al* [132] and Chopelas [133].

Similar studies carried out on olivine for P1 and P2 show the same overall trend for both peaks [132, 133]; as the pressure is increased, the peak position of each of the peaks increases. Figure 6.20 shows this trend to be linear for P1 and P2 up to 22.7 GPa. Unfortunately, it seems as if similar studies for labradorite have not yet been conducted.

The equations used to reproduce the data in Figure 6.19 and Figure 6.20 are:

$$Quartz\ P1 - \text{Dean } et\ al\text{: } Raman\ Shift = (0.81 \times \text{Pressure}) + 464 \quad (6.1)$$

$$Quartz\ P1 - \text{Jean } et\ al\text{: } Raman\ Shift = (0.90 \times \text{Pressure}) + 464 \quad (6.2)$$

$$Olivine\ P1 - \text{Besson } et\ al\text{: } Raman\ Shift = (0.35 \times \text{Pressure}) + 822 \quad (6.3)$$

$$Olivine\ P1 - \text{Chopelas: } Raman\ Shift = (0.312 \times \text{Pressure}) + 826 \quad (6.4)$$

$$Olivine\ P2 - \text{Besson } et\ al\text{: } Raman\ Shift = (0.35 \times \text{Pressure}) + 854 \quad (6.5)$$

$$Olivine\ P2 - \text{Chopelas: } Raman\ Shift = (0.327 \times \text{Pressure}) + 856 \quad (6.6)$$

In each of these studies the Raman peaks return to their original positions once the pressure is relieved. This is not the case for the experiments performed here, as the Raman shifts have remained 'locked in' the sample after the pressure has been relieved. It is likely that the 'locked in' changes seen here are the result of the pressure having been applied to the target material by an impact event rather than a hydrostatic test. Section 2.1.3 explains that during an impact event, pressure is applied to the target in one direction in the form of a shock wave, before it is then released. This process happens very quickly and therefore does not always allow for the target material to revert back to its original state (this is how high pressure polymorphs are formed in impacts - Section 2.1.4). Therefore, if Raman spectroscopy can be used as a barometer to determine how much pressure a sample is under during hydrostatic tests, can it be used to do the same for the samples that have undergone shock pressure?

Another important point to consider is that all of these studies put a sample under pressure (or compression) and result in increases to the Raman peak positions. Therefore, it is reasonable to assume that tension would have the opposite effect and result in decreases to the Raman peak positions. This means that an area inside the crater consisting of material that has been exposed by other material breaking away is likely to present as negative Raman shift. This is because the material would have first stretched under tension before reaching its tensile limit and breaking/failing.

6.4.3 Quartz

The first quartz shot (0.373 km s^{-1}, Section 5.3.1.1) shows the peak position increasing in value up to a maximum of +3.2 cm^{-1} at the centre of the crater (Figure 5.12.B). As the greatest shock pressure will have occurred at the centre of the crater, it seems reasonable that the greatest change in peak position will also be seen in in the same location, with both the shock pressure and peak shift decreasing towards the edge of the crater.

The 0.515 km s^{-1} quartz shot (Section 5.3.1.2) shows the peak shift increasing inside the crater (Figure 5.13.B). Interestingly, the point of maximum shift is not at the centre where it is expected that the most pressure would be exerted, but at a point in the bottom right of the crater. The maximum shift seen at this position is +1.9 cm^{-1}. The areas outside the crater remain largely unchanged by the impact, with the exception being a region in the bottom left of the map where the peak position has shifted negatively by as much as -0.4 cm^{-1}.

Figure 5.14.B, the shift map for the 0.910 km s^{-1} quartz shot (Section 5.3.1.3), shows the crater rim to have undergone a slight positive shift (maximum of +0.6 cm^{-1}) while the inside of the crater has undergone negative shift by as much as -1.9 cm^{-1}. This is contrary to what is expected as the centre of the crater is the region that has experienced the greatest amount of (compressive) pressure and should, therefore, be the region of the crater that shows the greatest amount of positive Raman shift.

Examination of the optical images of the craters for this shot (Figure 5.8.A) and the slowest quartz shot (Figure 5.7.A) may offer some explanation as to why this is the case. The image of the 0.373 km s^{-1} shot shows the surface of the target to be cracked but still fully present, while the image of the 0.910 km s^{-1} shot shows that material has been excavated from the target in order to form a crater. It is likely that this excavated material is the material that would have been compressed (and therefore had a positive Raman shift) during the impact and the material remaining in the bottom of the crater would have undergone tension as it separated from the excavated material (and therefore shows a negative Raman shift).

Section 5.3.1.4 describes the 1.35 km s^{-1} quartz shot, including its shift map (Figure 5.15.B). Figure 5.15.B shows the inside the crater to be a region of positive shift with uplifted material located along the edges of the crater being regions of negative shift. The presence of some poorly fit pixels has increased the size of the scale obscuring detail in this map; therefore, a re-scaled version of this map can be seen in Figure 6.21 in order to allow for this detail to be seen.

Figure 6.21 shows that the regions of positive shift increase to a maximum shift of +0.5 cm^{-1} inside the crater while also showing that the rim at the top of the crater has also undergone positive shift (maximum of 0.2 cm^{-1}). Unlike the previous shot, this crater produces the expected result of an impact causing an increase in the Raman peak position despite the excavation of material.

The 2.02 km s^{-1} quartz shot shows the peak shift to increase inside the crater by a maximum of +0.7 cm^{-1} (Figure 5.16.B). A small number of pixels to the left of the crater showing a large negative shift have expanded the scale, obscuring detail in the centre of the crater. In an effort to overcome this, a re-scaled version of Figure 5.16.B can be seen in Figure 6.22.

Figure 6.22 shows a positive peak shift that increases from the edge of the crater and reaches a maximum shift of +0.7 cm^{-1} at (22,16). Interestingly, this point is not the centre of the crater where the greatest amount of shock pressure would have been exerted. The two regions of negative shift at (15,25) and (25,40) can be matched to areas of uplifted material seen in the optical image Figure 5.9.A. This material would have undergone tension as it separated from the material below it.

The peak shift map for the 3.32 km s^{-1} quartz shot (Figure 5.17.B) shows a positive peak shift inside the crater, increasing to a maximum shift of +0.9 cm^{-1} at the centre of the crater. The rim of the crater can also be seen as a ring of positively shifted

material averaging a shift of +0.2 cm^{-1}. There are also a few pixels of negative shift scattered across the map, the largest shift being -1.1 cm^{-1}. However, these pixels do not appear to correspond to any physical feature that can be seen in the optical images of the crater and therefore may simply be the result of some contaminant inside the crater. Generally speaking, this shot looks very similar to 0.373 km s^{-1}.

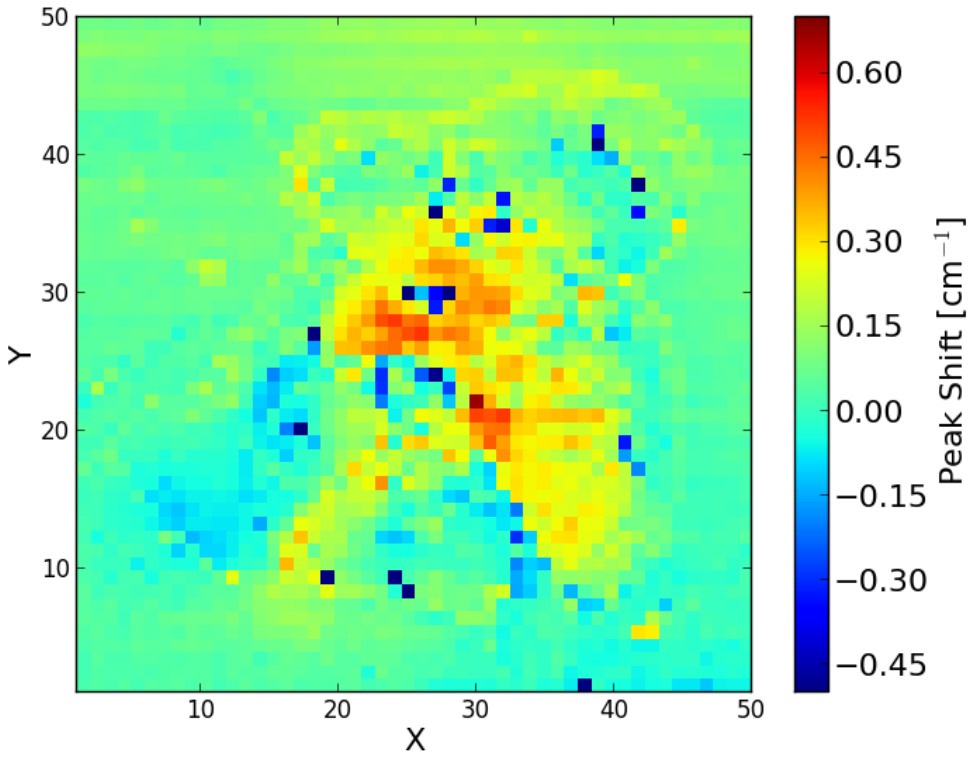


Figure 6.21: The shift map from the quartz shot G151014#1 (1.35 km s^{-1}) re-displayed with an upper limit of 0.7 cm^{-1} and a lower limit of -0.5 cm^{-1}.

Figure 5.18.B, the shift map for the 4.48 km s^{-1} quartz shot (Section 5.3.1.7), shows positive shift in the areas representing the inside of the crater (maximum shift of +0.6 cm^{-1}). However, there are a small number of pixels showing a relatively large negative shift (as much as -1.9 cm^{-1}) which is compressing the information for the inside of the crater into a small part of the scale. Figure 6.23 shows a re-scaled version of Figure 5.18.B showing only the positive shift in the map (0.0 to +0.6 cm^{-1}).

Similar to features seen in the 0.373 km s^{-1} and the 3.32 km s^{-1} shots, Figure 6.23 shows the peak shift increasing to the maximum observed shift (+0.6 cm^{-1}) at the centre of the crater where the largest amount of shock pressure would have been exerted.

Due to the poorly fit pixels identified in Figure 5.19.D, a large region of the shift map for the 5.27 km s^{-1} quartz shot (Figure 5.19.C) should be disregarded. This disregarded region corresponds with the centre of the crater, leaving only the crater walls and the outside of the crater to be examined. The poorly fit pixels have contributed to the scale of the shift map being expanded, thereby making it harder to see any features located on the crater walls. To remedy this, a re-scaled version of Figure 5.19.B has been produced in Figure 6.24 to show the shift map with a scale of between -0.1 cm^{-1} and 0.5 cm^{-1} and the poorly fit pixels replaced with white pixels.

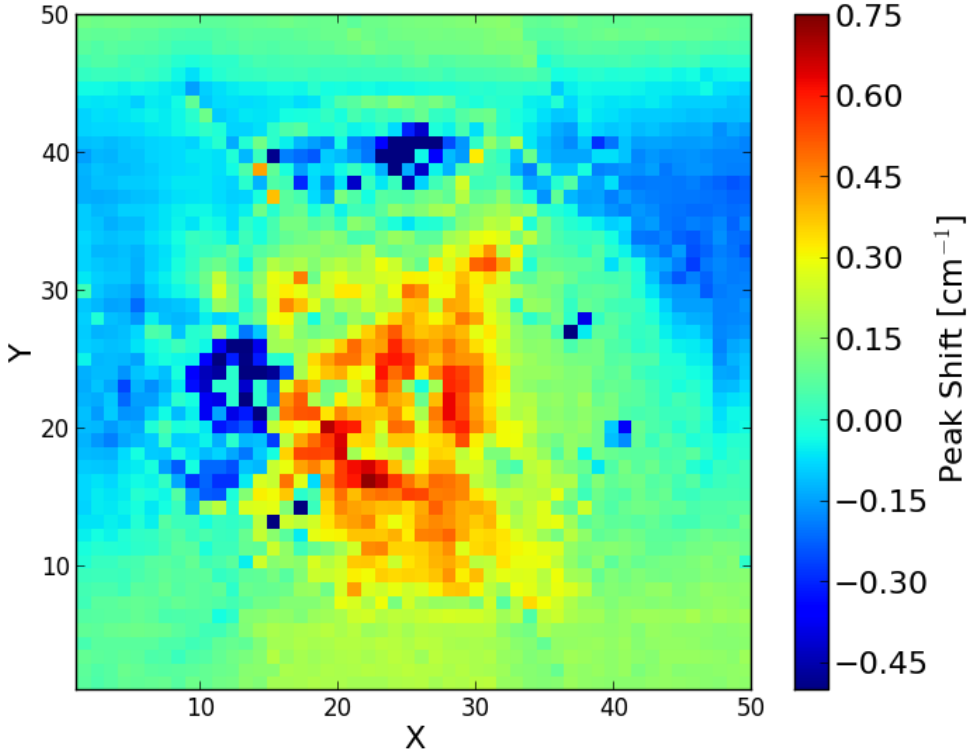


Figure 6.22: The shift map from the quartz shot G051114#3 (2.02 km s^{-1}) re-displayed with an upper limit of 0.75 cm^{-1} and a lower limit of -0.5 cm^{-1}.

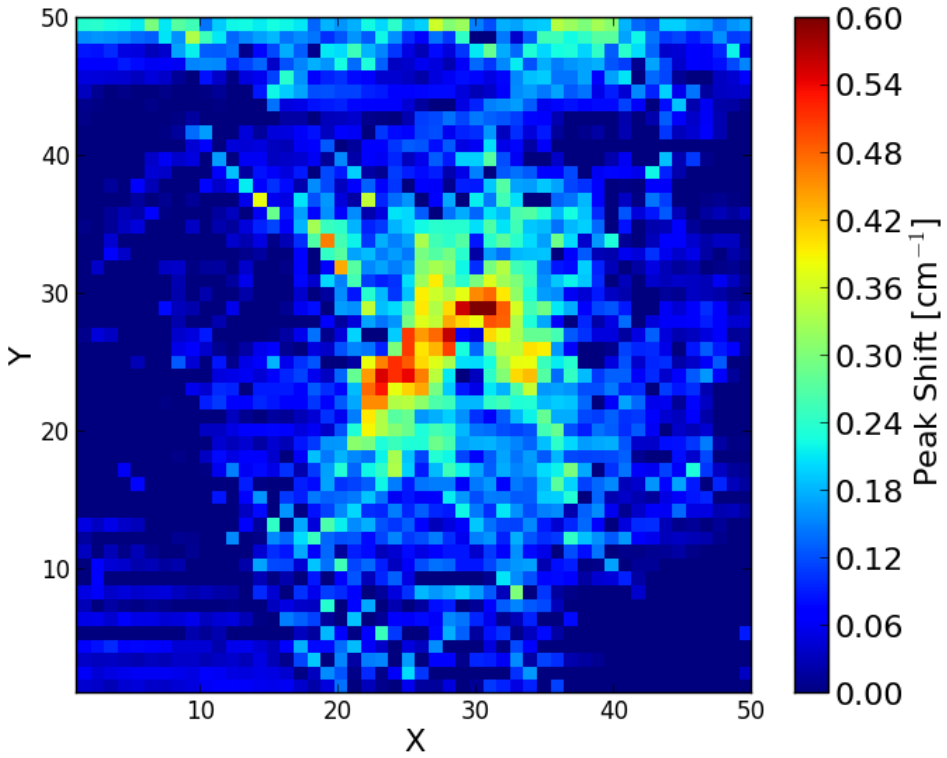


Figure 6.23: The shift map from the quartz shot G270515#3 (4.48 km s^{-1}) re-displayed with an upper limit of 0.60 cm^{-1} and a lower limit of 0.0 cm^{-1}.

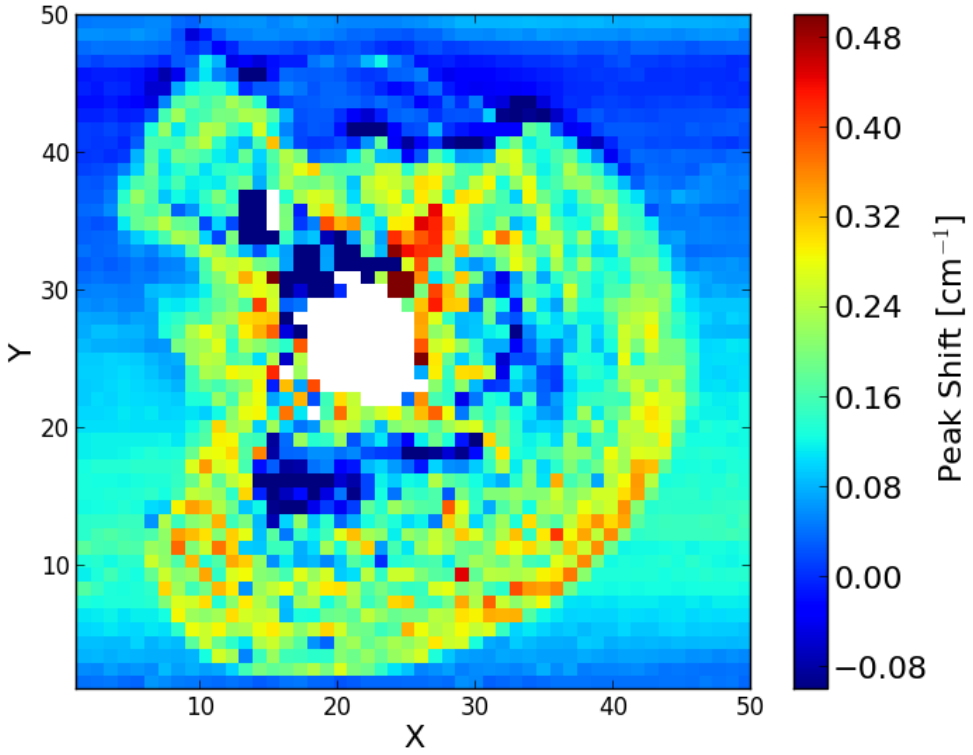


Figure 6.24: The shift map from the quartz shot G271114#2 (5.27 km s^{-1}) re-displayed with an upper limit of 0.50 cm^{-1} and a lower limit of -0.1 cm^{-1}. The poorly fit pixels have been replaced with white pixels.

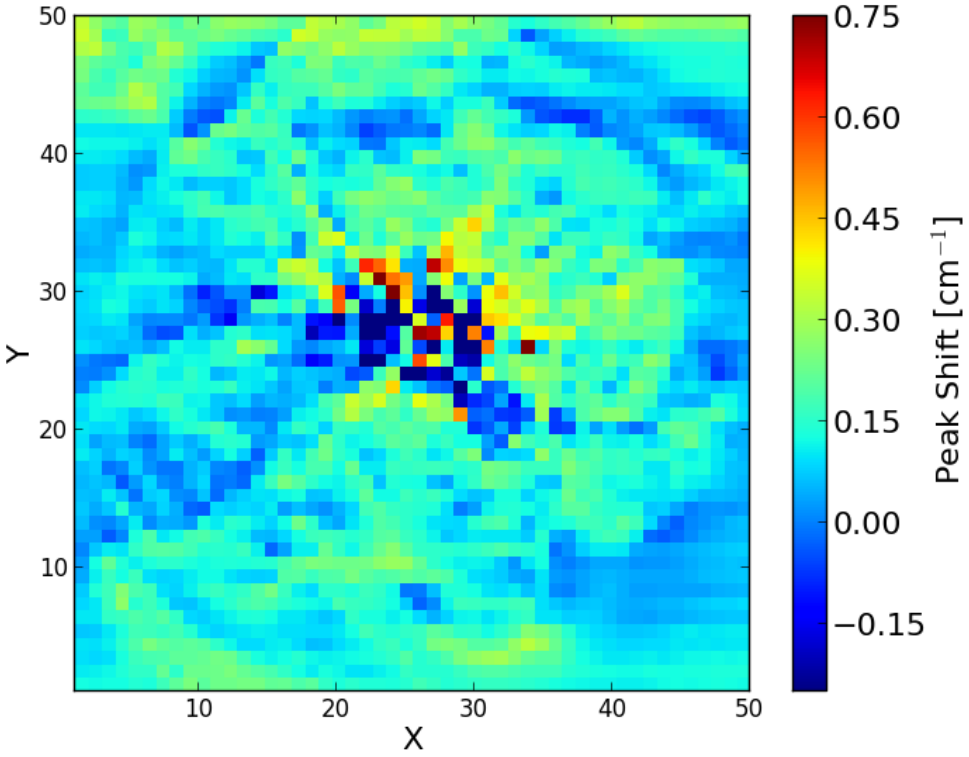


Figure 6.25: The shift map from the quartz shot G100615#1 (6.40 km s^{-1}) re-displayed with an upper limit of 0.75 cm^{-1} and a lower limit of -0.25 cm^{-1}.

Figure 6.24 shows positive shift (maximum of +0.3 cm^{-1}) on the edges of the crater walls gradually decreasing towards a negative shift near the centre of the crater (max negative shift of -0.2 cm^{-1} as measured from Figure 5.19.B). The negatively shifted region at (14,35), first identified in Section 5.3.1.8, shows a much larger negative shift well outside the scale of Figure 6.24 (maximum of -2.3 cm^{-1}). This region corresponds to a "lump" that can be seen in the optical image (Figure 5.10.B) at (-450,-400) and may be a piece of material that has come to rest in that part of the crater after the crater was formed, thereby explaining why it is so different from the material surrounding it.

Section 5.3.1.9 presents the 6.40 km s^{-1} quartz shot. The shift map for this shot, Figure 5.20.B, shows variations in peak position of between -2.6 cm^{-1} and +1.5 cm^{-1} in the centre of the crater. This large scale has resulted in a loss of detail on the crater walls in that figure; therefore a re-scaled version of that map is presented in Figure 6.25 in order to investigate any peak shift features present in the crater wall regions.

Figure 6.25 shows that there is some structure in the shift pattern seen on the crater walls for this shot. In general, the peak position on the crater walls can be seen to be increasing towards the centre of the crater (from 0.0 cm^{-1} up to +0.3 cm^{-1}) before devolving into the structureless shifts seen in the central region.

6.4.3.1 Summary

As described above, all of the quartz shots show both positive and negative Raman shifts with the exception of the slowest shot at 0.373 km s^{-1}. In this particular shot, a bruise-like feature was formed rather than a traditional crater. This results in no material having been excavated from the surface of the target meaning the target material has been compressed. In hydrostatic pressure tests, samples are put under compression and, as seen in Section 6.4.2, only positive Raman shifts are observed as a result of this compression.

In the other quartz shots, there are regions of both compression and tension. The regions of compression are formed during the impact and the regions of tension are the result of the excavation of material when the crater itself is formed. Knowing that compression results in positive Raman shifts, it follows that negative Raman shifts would be the result of tension in the crystal structure. If so, this could explain why both positive and negative shifts are seen alongside one another in the same impact feature.

With regards to the size of the shifts as the magnitude of the peak shock pressures (i.e. the impact speed) increases, there appears to be no trend. This is likely due to the fact that the material that would have encountered the peak shock pressure (at the interface between the target and the projectile) is no longer present in the crater either due to vaporisation or excavation. The observed shifts also cannot be compared to samples that have undergone equivalent hydrostatic pressure tests for this same reason, as there is no way to know how much pressure the material that is being observed has been subjected to. Therefore Raman peak shift cannot be used as a shock barometer for the quartz samples discussed here. It may be possible to do this for the low speed shots that do not excavate material but the dataset presented here only contains one such shot which is not enough to draw any conclusions from.

6.4.4 Olivine

Two Raman peaks have been analysed for olivine, P1 and P2 (Section 4.2.1). The peak shifts of P1 and P2 do not always behave in the same manner for each of shot. As such, the changes in the peak position for each peak are first analysed separately before being compared to one another. After this the changes in peak shift for the entire olivine shot programme will be discussed.

The 0.576 km s^{-1} olivine shot (Section 5.3.2.1) shows that for P1 the maximum positive peak shift is located at (16,30) with a shift of +3.4 cm^{-1} (Figure 5.26.E). Two other nodes of positive shift are located above and below this at (16,37) and (16,24). This shift pattern is similar to the of the 0.373 kms^{-1} quartz shot (Figure 5.12.B); and like that shot, this impact only generated a "bruise" on the surface of the target rather than the craters seen in the higher velocity impacts. The other feature seen in P1 shift map for the 0.576 km s^{-1} olivine shot is a line of negative shift across the map (maximum shift of -0.3 cm^{-1}). The location of this line corresponds to a crack seen in the optical image of the "bruise" (Figure 5.7.A).

For P2, Figure 5.26.E shows a large area of positive shift, with the largest shifts of +1.6 cm^{-1} located on the left of the crater rather than the centre where the largest amount of shock pressure would have occurred. Interestingly, the cracks seen in the surface of the target in Figure 5.21.A show positive shift in P2 whereas in the P1 shift map (and the olivine P1 shift maps of other shots discussed later) the cracks show a negative shift.

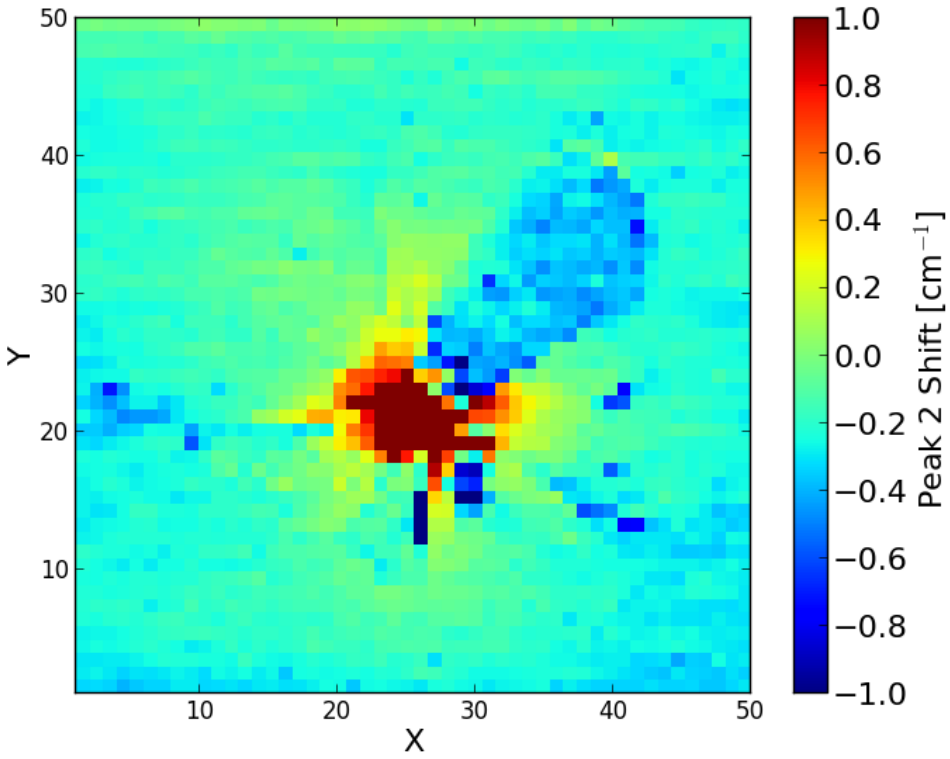


Figure 6.26: The P2 shift map from the olivine shot S260914#1 (0.638 km s^{-1}) re-displayed with an upper limit of 1.0 cm^{-1} and a lower limit of -1.0 cm^{-1}.

Figure 5.28.E, the P1 shift map for the 0.602 olivine shot, shows a ring of negatively shifted (approx. -0.1 cm^{-1}) material around the edge of the map. This ring encircles approximately 75% of the "bruise" seen in the optical image for this shot (Figure 5.21.B), but does not match any feature seen in that image. In the centre of the map, a band of positively shifted material is observed (max shift of +0.5 cm^{-1}) flanked by regions of negative shift above and below this band. The maximum negative shift seen in these regions is -1.3 cm^{-1}, however, this only occurs in a single pixel and the value of -0.6 cm^{-1} is much more common. Visually, this map presents itself as a kind of butterfly pattern, with the band of positively shifted material making up the body of the butterfly and the negatively shifted regions representing the wings.

Unlike the P1 shift map, the P2 shift map (Figure 5.28.F) does not show a butterfly pattern. Instead, a large feature mostly consisting of positive shift which increases in size towards its centre (maximum shift of +1.6 cm^{-1}) is seen. This feature also contains a small number of pixels displaying negative shift scattered around its central area (maximum shift of -0.5 cm^{-1}), the locations of which do not seem to match any physical feature seen in the optical image (Figure 5.21.B).

The 0.638 km s^{-1} olivine shot is presented in Section 5.3.2.3. Like the previous two olivine shots, this impact also produced a "bruise" on the surface of the target rather than a traditional crater (Figure 5.22.A). The P1 shift map for this shot is presented in Figure 5.30.E and shows another of the butterfly patterns observed above. The map shows an area of positively shifted material (maximum shift of +1.2 cm^{-1}) at (25,22) flanked by two loops of negatively shifted material (maximum shift of -2.5 cm^{-1}) to the left and right of this area.

The P2 shift map (Figure 5.30.F) shows that the locations of the largest positive shift (+2.2 cm^{-1}) and largest negative shift (-1.0 cm^{-1}) are the same in P1 and P2. It is difficult to determine if a butterfly pattern is also present in P2 due to the scale of the map covering such a large range. As such, a re-scaled version of the P2 shift map with the scale more closely centred on 0.0 cm^{-1} is presented in Figure 6.26 in an attempt to see if the same pattern as P1 is present in P2. Figure 6.26 does not show as clearly a defined butterfly pattern, as that in Figure 5.30.E for P1. While the body of the butterfly can be seen in both maps, the areas of the re-scaled map that should consist of the wings of the butterfly are comprised of regions of negative shift similar to the P1 map and areas where no shift has occurred.

Although not identical, the P1 and P2 shift maps show the same overall trends. The direction of the shifts are similar in both maps and it is only the magnitude of the shifts that vary between them.

The 1.35 km s^{-1} olivine shot is the first olivine shot where a traditional crater has formed rather than a "bruise". The P1 shift map for this shot (Figure 5.32.E) shows mostly negative shifts inside the crater. To the right of the map is a large region of yellow/orange (shift of -0.5 cm^{-1}) which is located on the crater walls. While at the bottom of the map is another large region of yellow/orange (shift of -0.5 cm^{-1}) but this is located on an area of uplifted material. Section 5.3.2.4 highlights the presence of a region located at (18,26) that has failed to fit and suggests a possible reason for this. Surrounding this un-fit region are pixels of greater negative shift then those seen on the crater walls (maximum shift of -2.5 cm^{-1}) suggesting that this region would be the centre of an area of negative shift inside the crater had it not been obscured. An area of positive shift is located inside the crater at (19,19) and has a maximum shift of +0.3 cm^{-1}.

In the P2 shift map for this shot (Figure 5.32.F) the pixels near the un-fit region behave the same way as they do in the P1 shift map, however, the maximum amount of shift is different (-2.4 cm^{-1} in P2 compared to -2.5 cm^{-1} in P1). The uplifted material mentioned in P1 also has a negative shift in P2, this is consistent with the hypothesis put forward in Section 6.4.3 which supposes that negative shift (i.e. tension in the bond) is present in areas where material, such as the uplifted material seen here, has broken away from the target below the surface. However, along the crater walls P1 and P2 do not behave in the same way. In P2 the crater walls show a consistent positive shift of +0.5 cm^{-1} where as in P1 these same areas show negative shifts of up to -0.3 cm^{-1} or, sometimes, no shift at all.

Figure 5.34.E presents the P1 shift map for the 1.57 km s^{-1} olivine shot. Here the structure of the crater seen in the optical image Figure 5.23.A (including the rim of the crater and the crater walls) can be seen as material showing a shift of +0.5 cm^{-1}. At the centre of the crater two areas of positive shift and two areas of negative shift can be seen. The areas of positive shift are located at (25,28) and (35,22) with maximum shifts of +2.6 cm^{-1} and +2.1 cm^{-1} respectively. The areas of negative shift are located at (28,23) and (33,31) with both having a maximum shift of -1.6 cm^{-1}.

Figure 5.34.F presents the P2 shift map for the 1.57 km s^{-1} olivine shot. All of the same features are seen in P2 as in P1 with the same directions to their shifts; however, the sizes of those shifts vary between the peaks. In P2, the areas of positive shift located at (25,28) and (35,22) show shifts of +0.6 cm^{-1} and +1.5 cm^{-1} respectively, while the areas of negative shift located at (28,23) and (33,31) show shifts of -1.0 cm^{-1} and -2.6 cm^{-1}, respectively. The rim and walls of the crater are seen to have a maximum shift of +0.3 cm^{-1} in P2.

The P1 shift map for the 2.02 km s^{-1} olivine shot (Figure 5.36.E) shows mostly positive shifts with some negative shift inside the crater. The positive shifts are located on the uplifted material seen around the crater in Figure 5.23.B and in the centre of the crater (maximum shift of +0.7 cm^{-1}). The pixels showing negative shift are located at the boundary of the crater before it gives way to uplifted material (maximum shift of -2.0 cm^{-1}).

Similar to the previous shot, the P2 shift map for this shot (Figure 5.36.F) shows the same features as its P1 counterpart. The positive shifts seen in the centre of the crater have a maximum shift of +1.8 cm^{-1} while those on the uplifted material have a maximum of +1.0 cm^{-1}. The pixels showing negative shift are once again located at the boundary of the crater, but have a smaller maximum shift of -0.8 cm^{-1}.

Figure 5.58.E, the P1 shift map for the 3.03 km s^{-1} olivine shot, shows negative shift at the centre of the crater (by a maximum of -5.0 cm^{-1}) and positive shift on the crater walls and uplifted material around the crater (maximum shift of +0.4 cm^{-1}).

Once again, P2 shows the same behaviour as P1 except that the values of the shifts are different for each peak. It is difficult to see the crater walls in Figure 5.58.F; therefore, a re-scaled version of the map that focuses on the positive shift is shown in Figure 6.27, which shows the clearly defined structure of the crater walls with the shift becoming increasingly positive (maximum shift of +0.5 cm) towards the negative region at the centre of the crater. In P2, the maximum negative shift seen at the centre of the crater is -4.9 cm^{-1} while the maximum positive shift seen is located at (30,28) with a value of +1.0 cm^{-1}.

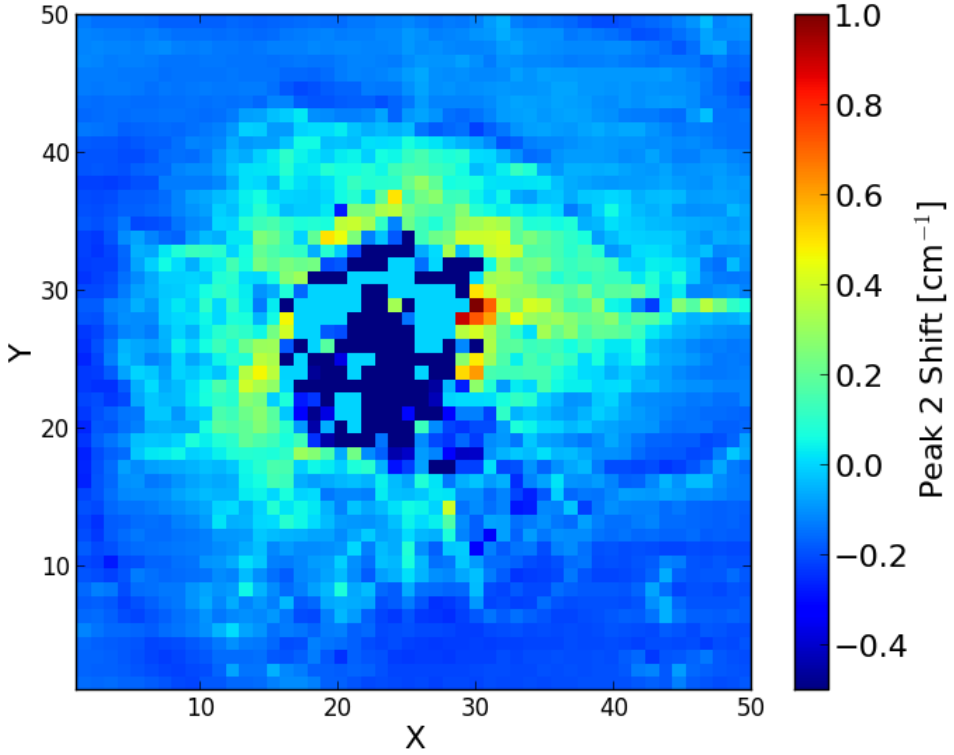


Figure 6.27: The P2 shift map from the olivine shot G150114#2 (3.03 km s^{-1}) re-displayed with an upper limit of 1.0 cm^{-1} and a lower limit of -0.5 cm^{-1}.

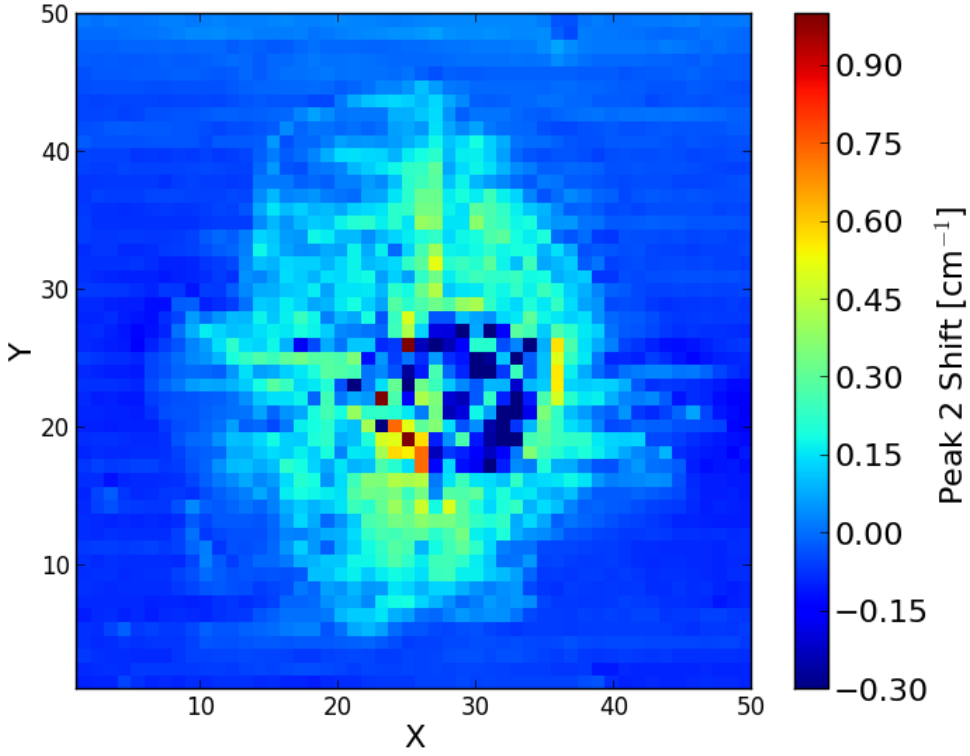


Figure 6.28: The P2 shift map from the olivine shot G241014#1 (3.32 km s^{-1}) re-displayed with an upper limit of 1.0 cm^{-1} and a lower limit of -0.3 cm^{-1}.

Section 5.3.2.8 discusses the 3.32 km s^{-1} olivine shot, including Figure 5.40.E the P1 shift map for this shot. Inside the crater, P1 becomes increasingly negative towards the centre to a maximum shift of – 2.1 cm^{-1}. Outside the crater, positive shift can be seen on the uplifted material with a maximum shift of +0.2 cm^{-1}.

Figure 5.40.F, the P2 shift map for this shot, shows a central area of negative shift similar to that seen in Figure 5.40.E for P1 but with a smaller maximum shift of -1.7 cm^{-1}. On the very edges of this central area in the P2 shift map at (25,19), (36,24), and (25,26) are areas of positive shift with a maximum shift of +1.3 cm^{-1}. Looking at Figure 6.28, a re-scaled version of Figure 5.40.F created in an effort to better investigate the smaller shifts seen on the crater walls, it can be seen the crater walls show a slight positive shift which increases in size (maximum shift of +0.4 cm^{-1}) towards the areas of negative shift.

6.4.4.1 Summary

Section 6.4.3.1 explains that the majority of the quartz shots displayed both positive and negative Raman shifts. The exception to this was the slowest shot at 0.373 km s^{-1} where only a bruise was formed on the surface rather than a traditional crater, where only positive Raman shift was seen. For olivine, all shots, including the lower speed impacts, show both positive and negative Raman shifts for P1 and P2.

The three slowest shots into olivine (0.576, 0.602 and 0.638 km s^{-1}) all produced a bruise on the surface rather than a crater. This is similar to the 0.373 km s^{-1} shot onto quartz, however, the shot onto quartz did not show negative Raman shift. The negative shifts in P1 seen in the 0.576 km s^{-1} olivine shot are located along a line running through the main feature of the shift map (Figure 5.26.E) which corresponds to a crack in the surface of the target. While the P2 negative shift is also located in an area that corresponds to the same crack, it is localised to a small number of pixels on the left of the map (Figure 5.26.F). This material would have undergone tension before eventually breaking and forming the aforementioned crack in the surface. For both the 0.602 and the 0.638 km s^{-1} shots, the P1 and P2 shifts are positive in the centre of the crater, but the surrounding areas contain negative shifts. This could be because the surface surrounding the positively shifted area has stretched (and thus has undergone tension) to accommodate the compression of the material in the centre of the crater. These three examples give further evidence to support the theory that negative shift is the result of tension in the crystal structure of the target.

Much like quartz, there appears to be no trend between the observed peak shifts and the magnitude of the peak shock pressures for either P1 or P2. For the higher speed shots (1.35 kms^{-1} and above), this is likely once again due to the fact that the material that would have encountered the peak shock pressure has been removed due to the formation of a crater. For this reason, it is also not possible to compare the samples to an equivalent hydrostatic pressure test.

It is difficult to determine if there is a trend present for lower speed shots as all three have very similar impact velocities and, therefore, only have a small difference of 0.99 GPa in peak shock pressure between them. The P1 peak shift magnitude appears to be very inconsistent in both the positive and negative directions across these shots, while P2 presents as much more stable in terms of the magnitudes of the positive and negative Raman shifts with only small localised areas altering the maximum recorded values. In order to determine if there is a trend present here, more low speed shots

need to be conducted over a broader range of velocities (for example, between 0.3 and 1.0 km s^{-1}).

Hydrostatic pressure tests shows the peaks would increase by approximately +4.0 cm^{-1} at these pressures [132, 133]. However, we see a maximum shift of only +2.2 cm^{-1} in the experiments conducted here. This is likely due to the fast-acting nature of a shock event and the shift being 'locked in' to the structure instead of the constant pressure applied to a sample in a hydrostatic pressure test as discussed in Section 6.4.2.

A final observation with regards to the peak shifts seen in the olivine shot program, is that for the high speed shots P1 and P2 tend to shift in the same direction for a particular pixel in the shift maps, albeit by varying amounts. However, for the low speed shots, P1 and P2 show variation in both magnitude and direction of the shift for a particular pixel. As explained in Section 4.2, P1 and P2 in the Raman spectrum of olivine are attributed to the internal stretching vibrational modes of the SiO_4 ionic group [122]. Due to the tetrahedral construction of this bond (Figure 4.2), P1 and P2 are not in the same orientation. As such, when this structure is subjected to a shock, P1 and P2 will be stretched/compressed differently to one another based on the angle that the shock wave is propagating through the structure. Therefore, it is entirely possible that P1 and P2 can shift in different directions after being subjected to the same shock event.

For the higher speed shots, it is probably the case that the destruction of target material is the dominant process in determining if a particular point will be under tension or compression, resulting in both P1 and P2 shifting in the same direction. Whereas for the lower speed shots, the impact process is much more subtle and the shock wave generated by the impact propagating through the region surrounding the impact site is the dominant process for determining the direction of the shift for a P1 and P2, which is much heavily influenced by the angle that the shock wave propagates through the SiO_4 structure.

6.4.5 Labradorite

Two Raman peaks have been analysed for labradorite, P1 and P2 (Section 4.2.1). The peak shifts of P1 and P2 do not always behave in the same manner for each of shot. As such, the changes in the peak position for each peak are first analysed separately before being compared to one another. After this, the changes in peak shift for the entire labradorite shot programme will be discussed.

Despite being the slowest shot across all of the shot programmes discussed here, the 0.291 km s^{-1} labradorite shot (Section 5.3.3.1) did not generate a "bruise" on the surface like the low speed shots onto other minerals. Instead, a shallow area of cracked material that appears to contain no overall structure was generated (Figure 5.41.A).

The P1 shift map for this shot (Figure 5.47.E) does not appear to show the location of any of the cracks seen in Figure 5.41.A and instead shows a random pattern of positive and negative shifts (maximums of +1.0 cm^{-1} and -1.0 cm^{-1}). The P2 shift map (Figure 5.47.B) is similar to the P1 shift map except that there are areas centred on (29,28) and (38,17) show a constant negative shift of -0.3 cm^{-1}. The cause of these negatively shifted areas is unknown as their locations do not match any feature seen in the optical image of the impact.

The P1 shift map for the 0.646 km s^{-1} labradorite shot (Figure 5.49.E) shows positive shift in the centre of the crater (maximum shift of +1.0 cm^{-1}) surrounded by concentrated areas of negative shift (maximum of -4.0 cm^{-1}). Beyond these areas of negative shift, the crater walls show positive shift up to a maximum of +0.3 cm^{-1}.

The P2 shift map (Figure 5.49.F) shows only negative shift inside the crater, increasing to a maximum shift of -2.7 cm^{-1} at (32,33). The small area of extreme negative shift at (30,33) has been disregarded since they are poorly fit pixels. Outside the crater in the bottom right corner of the map is an area of positive shift (maximum shift of +1.0 cm^{-1}) corresponding to an area of uplifted material in the optical image (Figure 5.41.B).

The 0.997 km s^{-1} labradorite shot is presented in Section 5.3.3.3 and the P1 shift map for this shot is shown in Figure 5.51.E. In this map, positive shift (maximum shift of +0.4 cm^{-1}) can be seen on the crater walls and along the edges of the uplifted material seen in the optical image Figure 5.43.A. At the centre of the crater there is a mix of both positive and negative shifts (maximums of +0.4 cm^{-1} and -1.5 cm^{-1}). However, the most interesting feature of this map is the diagonal line comprising of negatively shifted material originating in the top right corner of the map and running through the crater. There is nothing in the optical image, or either of the intensity maps for this shot, that would explain the presence of this feature and, therefore, its origin is currently unknown.

Figure 5.51.F, the P2 shift map for this shot, shows only negative shifts inside the crater (maximum of -2.5 cm^{-1}) and along the edges of the uplifted material (maximum shift of -0.4 cm^{-1}).

Section 5.3.3.4 presents P1 and P2 shift maps (Figure 5.53.E and Figure 5.53.F respectively) for the 1.36 km s^{-1} labradorite shot. Figure 5.53.E presents no real pattern to the shift for this peak and simply shows a mix of positive and negative shift (maximum shifts of +2.5 cm^{-1} and –1.5 cm^{-1}) towards the centre of the map at the location where the crater is situated. Figure 5.53.F clearly shows the location of the crater. Here the crater walls are presented as having shifted positively by +0.5 cm^{-1} with scattered pixels reaching as much as +1.5 cm^{-1}, while the centre of the crater shows negative shifts reaching a maximum of -0.5 cm^{-1}. Uplifted material to the right of the crater also shows a positive shift of +0.5 cm^{-1}.

The P1 shift map for the 1.81 km s^{-1} labradorite shot (Figure 5.55.E) shows negative shifts at the bottom of the crater (maximum shift of -5.0 cm^{-1}) and along the cracks seen coming from the crater in the optical image Figure 5.43.A (maximum shift of -2.6 cm^{-1}). Positive shift can be seen on the uplifted material around the crater (+0.4 cm^{-1}) and an area with the greatest positive shift is located on the crater walls at (35,15), showing a maximum shift of +1.3 cm^{-1}.

Figure 5.55.F, the P2 shift map, also shows negative shift inside the crater and along the cracks (maximum of -3.6 cm^{-1}). There are no concentrated areas of positive shift in this map, but there are scattered pixels showing (real) shifts of up to +1.4 cm^{-1}.

The crater produced in the 1.99 km s^{-1} labradorite impact generated a large area of uplifted material to the left of the crater (Figure 5.43.B). In the P1 shift map (Figure 5.57.E), both the crater and the uplifted material are seen as positively shifted material by a maximum of +1.8 cm^{-1}; while in the P2 shift map (Figure 5.57.F) the centre of the crater has shifted by a maximum of +0.2 cm^{-1} and the uplifted material has shifted by a maximum of -0.5 cm^{-1}. In both maps there is a band of negatively

shifted material that separates the crater from the uplifted region. In P1, this material has a maximum negative shift of -5.9 cm^{-1} while in P2 this material has a maximum negative shift of -3.4 cm^{-1}. The pixels with the largest positive shifts in the P2 shift map are badly fit pixels and should be ignored.

The 2.72 km s^{-1} labradorite shot is presented in Section 5.3.3.7 and the optical image for the crater generated in this impact can be found in Figure 5.44.A. This image shows a crater surrounded by an expansive region of uplifted material. The P1 shift map (Figure 5.59.E) shows the maximum negative shift of -2.5 cm^{-1} in the crater and also at points along the crack showing negative shift originating from (23,0). Positive shift can be seen in some regions of the uplifted material with the largest positive shift of +0.8 cm^{-1} being located at (40,45) in the top right of the map.

The P2 shift map (Figure 5.59.F) also shows the maximum negative shift (-2.2 cm^{-1}) to be located inside the central crater. However, the crack that was negatively shifted in the P1 shift map presents as positively shifted material in the P2 shift map with a maximum shift of +2.2 cm^{-1} (the pixel with the largest positive shift of +2.9 cm^{-1} is actually a badly fit pixel). The uplifted material around the crater shows a mix of positive and negative shifts that are difficult to resolve due to the scale associated with the map.

The broad scales of both the P1 and P2 shift maps are the result of the large negative shifts seen in the central crater and the large positive shifts produced by a small number of badly fit pixels in both maps. This makes it difficult to perform a detailed examination of the shifts seen in the uplifted material. As such, both maps have been re-scaled to exclude these more extreme shifts. The re-scaled version of the P1 shift map can be seen in Figure 6.29, while the re-scaled version of the P2 shift map can be seen in Figure 6.30.

Figure 6.29 shows the previously mentioned largest positive shift of +0.8 cm^{-1} at (45,40) as well as a large expanse of material depicted in green/yellow that also represents a positive shift. Ignoring the previously discussed cracks, Figure 6.30 shows the uplifted material to be comprised of a mix of positively and negatively shifted material with average shifts of between +0.3 cm^{-1} and -0.6 cm^{-1} with scattered pixels showing negative shifts of as much as -1.4 cm^{-1}.

Section 5.3.3.8 presents the 3.39 km s^{-1} labradorite shot. The P1 shift map for this shot (Figure 5.61.E) shows positive shift inside the crater and on the uplifted material below the crater (maximum shift of +1.4 cm^{-1}). At the top and also the right of the crater along the 'rim', negatively shifted material (maximum shift of -1.0 cm^{-1}) can be seen. The P2 shift map (Figure 5.61.F) is the complete inverse of its P1 counterpart. Here, the inside of the crater shows negative shift (maximum shift of -1.9 cm^{-1}) while the 'rim' material is positively shifted (maximum shift of +0.8 cm^{-1}).

Figure 5.63.E, the P1 shift map for the 5.06 km s^{-1} labradorite shot, has the broadest scale of any shift map in the entire shot programme, therefore, gaining specific detail from this map is difficult and a series of re-scaled images have been produced. The largest positive shift seen for P1 is +4.0 cm^{-1} and is located inside the crater at (36,3) followed by a pixel showing a shift of +3.7 cm^{-1} located at (13,27), also inside the crater. After these two pixels, the remaining positively shifted pixels are all between 0.0 cm^{-1} and +2.0 cm^{-1}. Therefore, the first re-scaled image is of the P1 shift map between 0.0 cm^{-1} and +2.0 cm^{-1} (Figure 6.31).

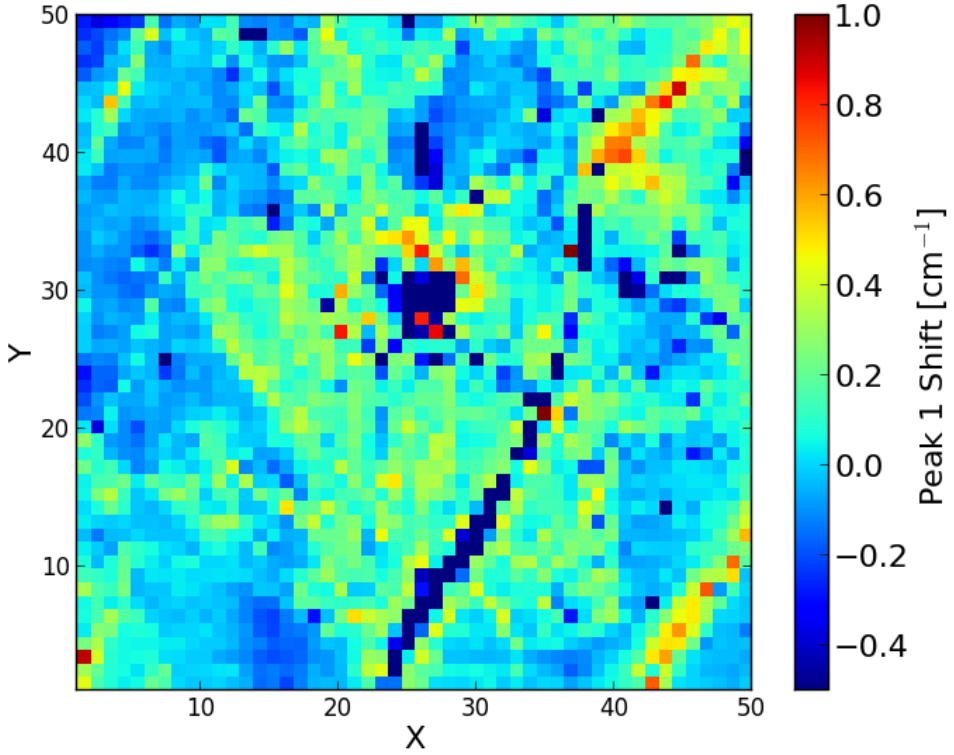


Figure 6.29: The P1 shift map from the labradorite shot G120815#1 (2.72 km s^{-1}) re-displayed with an upper limit of 1.0 cm^{-1} and a lower limit of -0.5 cm^{-1}.

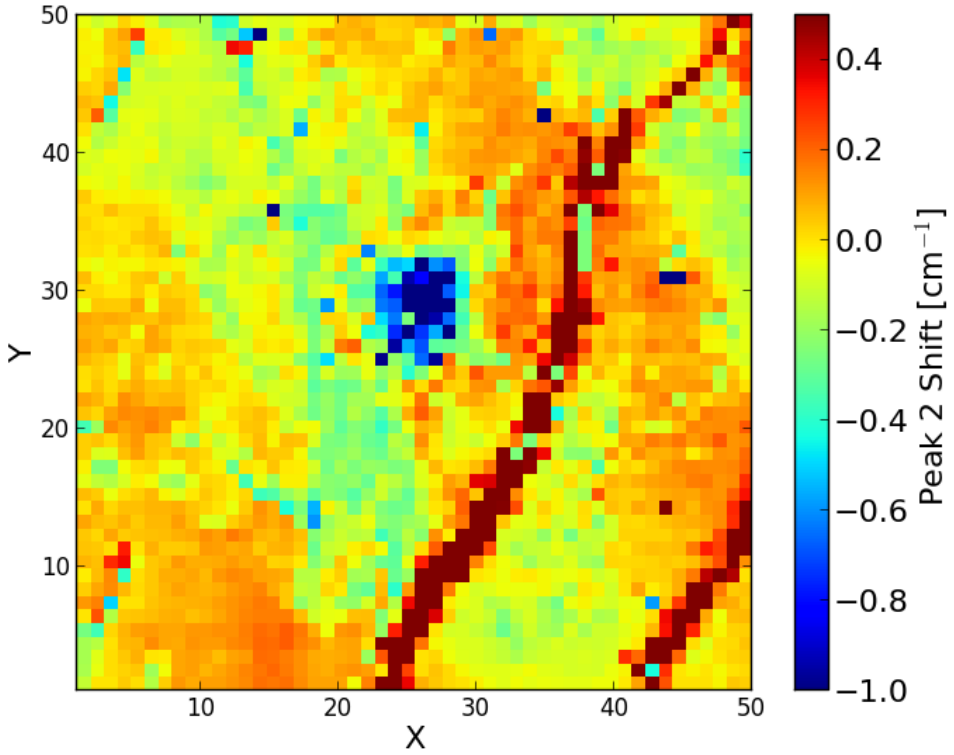


Figure 6.30: The P2 shift map from the labradorite shot G120815#1 (2.72 km s^{-1}) re-displayed with an upper limit of 0.5 cm^{-1} and a lower limit of -1.0 cm^{-1}.

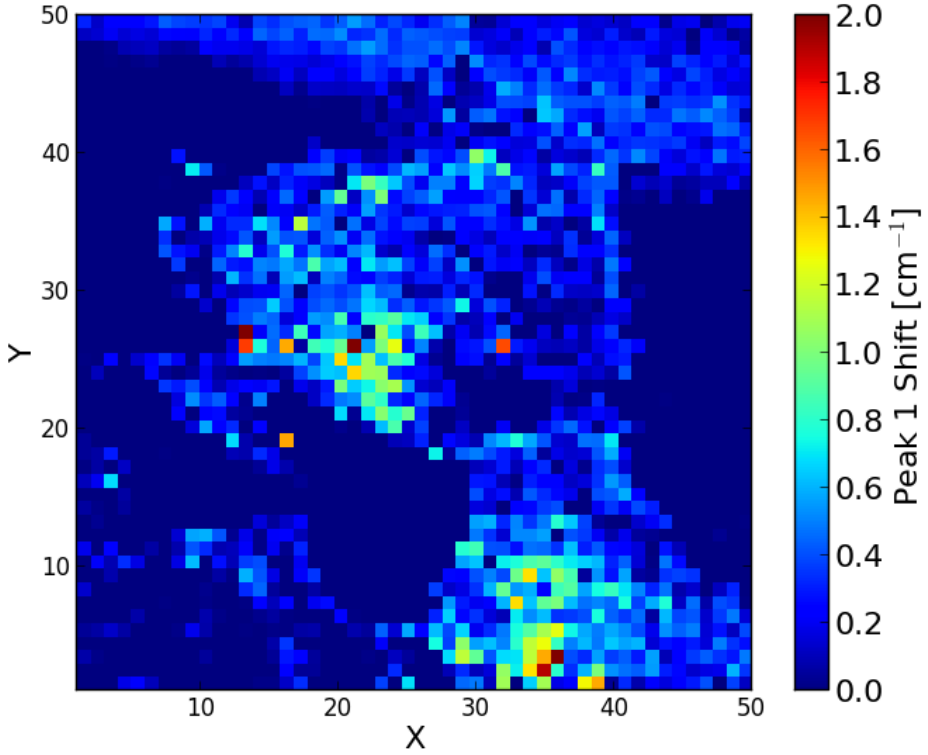


Figure 6.31: The P1 shift map from the labradorite shot G160915#2 (5.06 km s^{-1}) re-displayed with an upper limit of 2.0 cm^{-1} and a lower limit of 0.0 cm^{-1}.

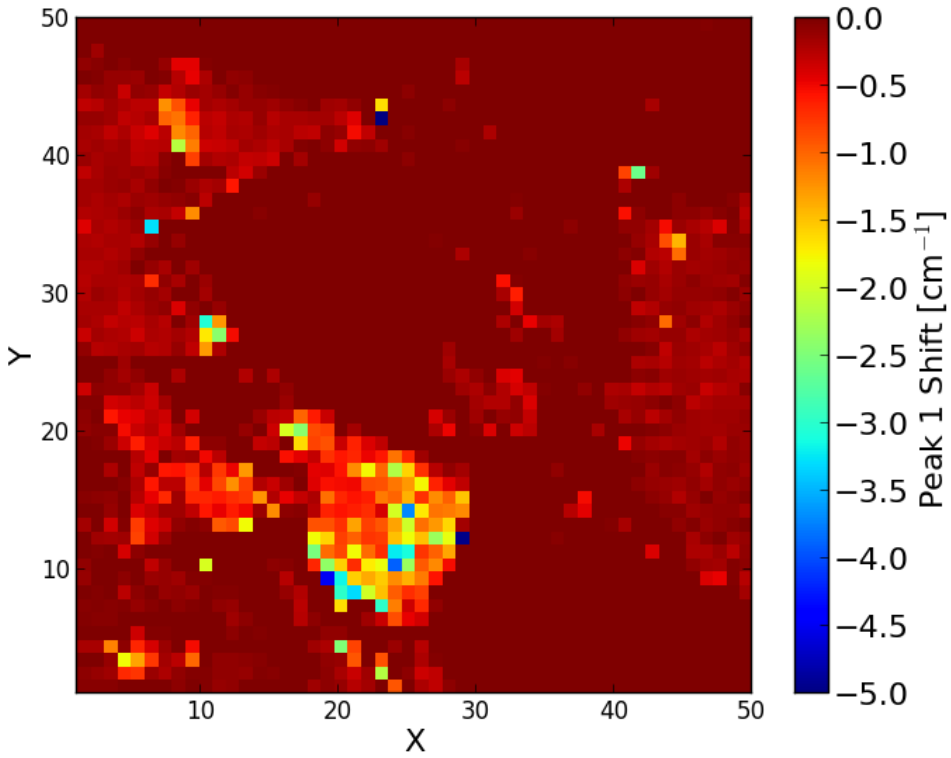


Figure 6.32: The P1 shift map from the labradorite shot G160915#2 (5.06 km s^{-1}) re-displayed with an upper limit of 0.0 cm^{-1} and a lower limit of -5.0 cm^{-1}.

Figure 6.31 shows the positive shift for P1 in the 5.06 km s^{-1} labradorite shot. Any pixels representing negative shift are depicted as dark blue and will be ignored for the time being. This map clearly shows the outline of the crater as seen in Figure 5.45 and that the inside of the crater is largely made up of positively shifted material between 0.0 cm^{-1} and +2.0 cm^{-1} with the largest shifts being the two pixels located at (36,3) and (13,27) mentioned above. There is also a region of positive shift above the crater, though there does not appear to be any feature such as uplifted material in the optical image (Figure 5.45) to explain this.

As well as the positive shifts, the P1 shift map Figure 5.63.E also shows a region of negative shift centred at (23,12), with a maximum shift of -5.0 cm^{-1}. In the optical image Figure 5.45, this area is overexposed, but it appears to be at a shallower depth to the rest of the crater. This may mean it has undergone a different process to the rest of the crater, thereby explaining why it has behaved differently. Figure 6.32 is a re-scaled version of Figure 5.63.E showing only negative shifts. Any pixels representing positive shift are depicted as dark red and are discussed above. Figure 6.32 clearly shows the negative region centred at (23,12) as well as other areas of lesser negative shift around the periphery of the crater.

For P2, no detectable shift can be seen inside the crater apart from the area of negative shift at (23,12), which is still present (Figure 5.63.F). Although this area has a smaller maximum shift (-1.3 cm^{-1} as opposed to -5.0 cm^{-1}), the shift across the region is more consistent. The 'rim' of the crater can also be seen as negative shift in this map showing the outline of the crater. An area of positive shift is located at the bottom left corner of the map. The cause of this shift is unknown, as there does not appear to be any feature in that area in the optical image (Figure 5.45). It is possible that there is uplifted material at this location; but it is difficult to know for certain.

6.4.5.1 Summary

Similar to the results of the olivine shots discussed in Section 6.4.4, both peaks in the labradorite shot programme show positive and negative shifts across all of the shot speeds. As previously postulated, this means there is both tension and compression present for both peaks. Interestingly, the labradorite P1 and P2 sometimes shift in different directions for the same pixel in a given map. Unlike olivine, where the P1 and P2 shift tended to shift in the same direction at higher speeds, for labradorite, the P1 and P2 shifts tended to act independently of each other at all speeds. As explained in Section 4.2, P1 and P2 in the Raman spectrum of labradorite are associated with the symmetric stretching mode of the T-O-T linkage, ([177, 178] these bonds are not in the same orientation (Figure 4.8). As such, when this structure is subjected to a shock, P1 and P2 will be stretched/compressed differently to one another based on the angle that the shock wave is propagating through the structure. Therefore, it is entirely possible that P1 and P2 can shift in different directions after being subjected to the same shock event.

The cracks formed in in the labradorite shots followed the same trends as the olivine shots discussed in Section 6.4.4. With the exception of the P2 shift for the 2.72 km s^{-1} shot, the trend along a crack line in the surface of the labradorite shows negative shift for both peaks. In the case of the P2 shift for the 2.72 km s^{-1} shot, this may not actually be a crack.

The labradorite gemstones appear to be more prone to cracking than the quartz and olivine gemstones making it more likely for material to become detached from the

target. This interrupts the patterns seen in the labradorite craters as there are sometimes localised regions showing different features to the rest of the crater, complicating the interpretation of the Raman maps.

Line features, such as the ones seen in 2.27 km s^{-1} shot, when seen in other shots have corresponded to the locations of cracks in the target material. For this particular shot, an actual crack cannot be observed in the optical image, instead the optical images shows a mass of broken material. Previously, it had been assumed this feature was also a crack. However, the analysis of the P2 shift for this shot does not support this assumption, as the shift was positive instead of negative. The positive shift would suggest the material underwent compression instead of the tension normally observed in a crack. Upon reviewing the optical image after analysing the P2 shift data, it would appear this feature is unique to this shot.

With regards to the size of the shifts as the magnitude of the peak shock pressures (i.e. the impact speed) increases, there appears to be no trend. This is likely due to the fact that the material that would have encountered the peak shock pressure (at the interface between the target and the projectile) is no longer present in the crater either due to vaporisation and/or excavation. Therefore, Raman peak shift cannot be used as a shock barometer for the labradorite samples discussed here.

Unfortunately, Raman studies on labradorite undergoing hydrostatic pressure tests have not yet been conducted meaning the shifts observed in this study cannot be compared to an equivalent static pressure shift.

6.5 Summary

This chapter has investigated whether Raman peak intensity, peak width, and peak position can be used as a shock barometer for the mineral samples examined in this study.

As discussed in Section 6.2, the peak intensity of the Raman spectra cannot be used to determine the degree of shock the samples have undergone. This is because for these experiments there are two separate processes that affect the intensity of the Raman peaks. The first is the polarisability of the target material that may or may not have been altered by the impacts. The second is the focus of the incident laser which is not consistent across the sample due to the formation of the craters which are not flat. There is no way to de-convolve these two processes from each other for these data and, as such, measuring the peak intensity cannot be used as a shock barometer.

However, it was discovered that change in peak intensities due to the change in focus across the sample could be used to gain information about the relative heights of areas in the Raman maps. While this does not give quantitative information (without calibration) about the relative heights within a map, it can be used in conjunction with optical images taken of the same areas in order to better interpret those optical images.

With regards to the analysis of the widths of the peaks, each of the peaks investigated showed peak broadening and peak narrowing at some point in their shock programs. As described in Section 6.3, it is theorised that the narrowing of the peaks is a result of the target material having undergone some form of annealing. If this is the case, then it is expected that peak narrowing would only occur once the increase in

temperature generated by the impact is sufficient to reach the target's annealing temperature. As such, for impacts that do not impart sufficient energy to increase the temperature to this point, only peak broadening would be seen due to the disorder introduced to the target from the impact shock wave. However, if the temperature increase is too great, then the melting (or perhaps even the vaporisation) temperature of the target material will be reached and the material will no longer be annealed but instead be susceptible to the disorder introduced by the impact shock wave.

The quartz shot program illustrates the full range of this process. The slowest quartz shot shows only peak broadening but as the speed is increased various degrees of peak narrowing (or annealing) are observed. Firstly, so-called ring features are seen before giving way to the entire crater showing peak narrowing. Finally, the fastest shot shows no peak narrowing within the crater, instead the impact has generated too much heat in the target causing melting/vaporisation.

The same process is seen for olivine. For P1 and P2, the slower shots are dominated by peak broadening inside the crater before giving way to peak narrowing as the speed increases. At the fastest impact velocity of 3.32 km s^{-1} the two peaks diverge in their behaviour. P1 continues to show an increased amount of peak narrowing, while P2 appears to have gone past this part of the process and has reverted to peak broadening once again.

For labradorite, peak narrowing is the dominant feature for both P1 and P2 in all of the shots. Peak broadening is observed in both peaks, but this is generally restricted to areas of uplifted material or showing surface cracking rather than inside the crater itself.

Whether changes in peak width can be used to quantify the amount of shock a sample has been subjected to, is indeterminate. However, it can be used to determine if some area of the target has been heated to between its annealing and melting temperatures as a result of the impact. This is based upon the presence of peak narrowing inside the crater being a result of annealing, but turning to peak broadening at temperatures above the melting point. While not particularly revealing on its own, when combined with other analysis techniques, this method may be able to provide further insight.

Chapter 4 explored how the Raman peaks of these minerals reacted under a range of temperature conditions. These experiments did not heat the minerals sufficiently to reach their annealing temperatures and, as such, at this time we are unable to determine if the amount of peak narrowing corresponds to a particular temperature above the annealing temperature. This could be an area of further study to investigate in the future.

The final part of the Raman spectrum to be investigated as a shock barometer was peak position. It is important to recognise that the position of any given Raman peak is based on both the structure and the effective mass of the bond that the peak represents and a change to either of these will result in a change to the Raman peak position. In order to change the effective mass of a bond, one or more of the elemental constituents of said bond would need to be changed. Section 6.4.1 has shown that for all of the shots performed in this study the elemental composition has not been detectably altered and therefore it must be a change in the structure of the bonds that is generating any observed Raman peak shift.

These changes in bond structure are the result of the shock waves generated during the impact propagating through the target and causing distortions in the molecular

structure of the material. Section 2.1.3 explains that that process happens very quickly (a few nanoseconds for the impacts shown here) and therefore does not always allow for the target material to revert back to its original state once the shock wave has passed. It follows that the extent of the distortion may be a measure of the magnitude of the shock wave that caused that distortion. The experimental program performed here shows us that this is not the case for higher speed shots where material has been excavated in order to form a crater. This is because the material that has been subjected to the calculated peak shock pressure has been removed from the target during the crater formation process meaning that the material being observed is material that has been subjected to an unknown, lesser degree of shock.

There is some potential for Raman peak position as a shock barometer for the lower speed impacts where material has not been excavated; however, there are only a small number of such shots performed in this study spread across multiple minerals which is not enough to draw any significant conclusions. As such, further work would need to be undertaken to perform an extensive shot program shots where all of the target material is retained for each of the minerals investigated.

Chapter 7 - Conclusions and Future Work

7.1 Conclusions

The overall aim of this study was to determine if Raman spectroscopy can be used for determining the degree of shock a mineral sample on the Martian surface has been subjected to. This was done by accomplishing the following goals:

1 Creating and utilising a controlled method for producing shock events in mineral samples at a wide range of shock pressures, which will have a minimum effect on the quality of the Raman spectra produced by the sample.

2 Determining if the environment in which the Raman spectra will be gathered (i.e. the Martian surface) has a significant effect on the Raman spectra produced by the samples.

3 Determining if Raman spectroscopy can be used to detect changes in shocked mineral samples, and if the extent of those changes can be used to determine the degree of shock experienced by the sample as a shock barometer.

To achieve goal 1, the University of Kent's light gas gun (LGG) was used to generate shock events by performing impact experiments. In its standard configuration, the LGG has a minimum velocity of 1.2 km s^{-1}, which equates to a peak shock pressure of approximately 10.0 GPa (depending on the target and projectile materials). In order to investigate shock velocities below this value, modification to the LGG was needed to lower its minimum speed. This was accomplished by converting the normal two-stage operation of the LGG to a single stage system (Section 3.3). This was first achieved by using a weaker 50 micron thick burst disk (down from 0.5 mm) to separate the evacuated target chamber from the pressurised pump tube and then simply increasing the pressure in the pump tube until said burst disk failed (at 86 bar ± 2 bar). Unfortunately, this method provided little control over the impact velocity of the projectile, or the timing of firing process itself.

This method was further built upon by the implementation of the electronic burst disk (Section 3.4). The electronic burst disk (EBD) also works by converting the LGG to single stage operation, but in this case, the 100 micron thick burst disk is designed to be able to withstand 190 bar ± 5 bar before failing. In order to fire the LGG at pressures lower than this, an electrical current is passed through the burst disk in order to melt (or fuse) it, thereby removing the barrier withholding the gas. This has allowed the minimum velocity of the LGG to be lowered from 1.2 km s^{-1} to as low as 0.1 km s^{-1}. This method has the advantage that it will not fire until an electrical current is applied across the burst disk, allowing the firing pressure (and thus the impact speed) to be exactly selected. However, the EBD is not without disadvantages. The complexity of the system results in reliability issues, which appeared to be the result of the hand-made nature of the prototype parts. Upon developing a method of mass production for improved consistency of these parts, the fusing reliability of the system greatly improved but blockages which prevent gas from expanding into the launch tube are still common. The system is now at the stage where an extensive, separate, testing program using 80 micron thick foil instead of 100 micron thick foil is required.

In order to maintain the quality of the Raman spectrum of the shocked mineral sample, it was decided that the target would consist of the mineral which ensured that there would always be Raman spectra of that mineral to analyse instead of relying on locating residue of that mineral inside a crater on another material.

The projectile was a buckshot of 50 micron diameter molybdenum spheres. Molybdenum was chosen as it does not have a Raman spectrum of its own and therefore, the only complication its presence could add to the interpretation of the Raman spectra would be to obscure areas of the crater rather then add other peaks and features to the spectra that may be misinterpreted. A buckshot of small spheres was chosen in lieu of a single projectile in order to eliminate the possibility of the single projectile breaking up during acceleration and, consequently, generating an impact that was not consistent with the rest of the shot program. In addition, the smallest single projectiles that the LGG is capable of firing are spheres of 0.1 mm diameter, which would have been too large for the gemstone targets to withstand at the higher velocities seen in the impact experiments. Using a buckshot approach avoided this potential point of failure and almost guaranteed that comparable impacts would occur during each of the shots.

To accomplish goal 2, experiments were conducted to simulate the temperature environment of the Martian surface (Chapter 4). Each of the minerals (quartz, olivine, and labradorite) was subjected to temperatures between -150 °C and 550 °C with Raman spectra being gathered every 10 °C. This was achieved using a "Linkam" temperature stage.

The Stokes/anti-Stokes method was then applied to each spectrum to calculate the temperature of the sample at the sampling point. These temperatures were then compared to the measured temperatures of the Linkam stage. This comparison showed that the calculated Stokes temperature (which should be a direct measure of the sample itself rather than the heating/cooling stage) was consistently lower than the stage temperature. While this may seem reasonable when heating the sample above room temperature due to inefficiencies in heat transfer between the stage and the sample, this was also occurring for temperatures well below room temperature, implying that the sample was colder than the stage that was cooling it. Therefore, calibration of the experiment was needed to determine the cause of this 'cooling effect'.

A calibration test was designed to determine two things: the exact temperature of a sample on the stage and how long was needed for a sample to reach thermal equilibrium with the stage. This was achieved by using a PT100 platinum resistance thermometer (PRT) as the sample on the stage and measuring the resistance across the PTR during a temperature experiment. This calibration test determined two things: first, that the one hour the mineral samples were being held at temperature before Raman data was gathered was more than sufficient for the sample and the stage to be in thermal equilibrium; second, and more importantly, that the temperature reported by the stage was inaccurate. Using the temperature values from the calibration experiment, a correction formula was calculated for the temperature reported by the Linkam stage. Knowing that the stage temperature was now accurate, the Stokes/anti-Stokes temperatures were re-analysed and shown to still be incorrect. The reason for this was that the ratio between the Stokes and anti-stokes intensities of the measured peaks needed to be corrected for using the instrument response function (IRF) of the Raman spectrometer's CCD, which is used to account for the variation in sensitivity of the CCD to different wavelengths. The IRF of the University of Kent's

Raman spectrometer is not currently known and, as such, an alternative correction was devised.

Using the stage temperature as a reference point, a correction factor was calculated for each Stokes/anti-Stokes ratio which would allow the calculated Stokes temperature to coincide with the stage temperature. While this is not a perfect means of calibration, as it is only valid for the particular peaks observed in this experiment, it was the best option available in the absence of the IRF.

Throughout this calibration process, the peak positions of the selected peaks for each mineral were also measured at each temperature. These data showed that for each of the peaks, the peak position decreased as the temperature was increased. This occurred at different rates for each of the peaks, showing that it is important to calibrate this effect in order to remove it when gathering Raman data in an environment with a variable temperature, such as the Martian surface. These data also showed that calibration is especially vital for samples where peak positions can be used to infer their composition, such as olivine. It was shown in Section 4.4.1.1 that it is possible to misinterpret the forsterite number of an olivine sample if the changes in peak shift due to sample temperature were not first taken into account.

Using the temperature calibration experiments described, a further experiment was conducted with the aim of determining if the size of the grains for the selected minerals affects the Raman spectrum produced due to the amount of heating generated by the laser. During the experiment, grains of various sizes for each of the minerals were placed on a thin film to minimise the amount of heat lost through conduction. Raman spectra were then gathered from various points across the grains before being averaged. The Stokes/anti-Stokes method, along with the relevant calibration from the previous experiments, was then applied to these spectra to determine the effect that grain size has on the temperature of the sample during acquisition, thereby giving a value as to how much "laser heating" occurs in the sample. This laser heating can then be accounted for using the peak position vs. temperature calibration also performed earlier.

This sample size experiment failed to produce any meaningful results. Two main reasons are attributed to this failure. First, the lack of knowledge of the instrument response function causes inaccuracies to the calculated Stokes temperature. Second, the method for measuring the surface area of the grains is crude at best. Ideally, the grains tested would be spherical in shape with diameters in the scale of nanometres rather than the 10s-100s of micrometres seen here. However, this would require a way to manipulate these very small grains to place them in isolation on the support films.

With regards to goal 3, an isolated crater on each of the impacted mineral samples was analysed using the Raman spectrometer. 2500 spectra were gathered across each crater in the form of a 50 by 50 pixel map, with the selected peaks of each spectrum being compared to baseline spectra taken before each shot. Specifically, the intensity, full-width-half-maximum (FWHM), and position of the peaks were analysed to determine the presence of any modification due to the impact. It was hoped that any such changes would be quantifiable and could therefore be used as a shock barometer.

It was found that peak intensity could not be used as a shock barometer for any of the minerals (Section 6.2). This is because for these experiments there are two separate

processes that affect the intensity of the Raman peaks. The first is the polarisability of the target material that may, or may not, have been altered by the impacts. The second is the focus of the incident laser which is not consistent across the sample due to the formation of the craters which are not flat. There is no way to de-convolve these two processes from each other and, as such, measuring the peak intensity cannot be used as a shock barometer.

However, a secondary use for the peak intensity maps presented itself. Due to the change in laser focus caused by the topographical changes to the surface of the target during the impacts, the intensity is heavily dependent on the distance between the objective lens and the target's surface at each point on the map. As a result of this, the peak intensity could be used to gain information about the relative heights of each point in the Raman maps. While this technique cannot be used to give quantitative information about the relative heights within a map (due to the possible presence of material that has undergone a change in polarisability due to the impact), it can be used to better interpret optical images taken of the same crater.

Analysis of the FWHM of the peaks showed an unexpected result. The FWHM of a Raman peak is an indication of the variation in bond length of bond that represent that peak are. In other words, if all of the bonds were precisely the same length the peak would be extremely narrow, while an increasing amount of variation in the length of the bonds is represented as an increasing broadening of the peak. Therefore, the FWHM is a measure of how ordered the molecular structure of the sample is.

As the experiments presented here involved passing a shockwave through the target material, it is expected that a greater degree of disorder would have been introduced into the molecular structure. While this is certainly the case for some of the data gathered, a large proportion (and in some instances, entire craters) show peak narrowing implying that the target material has become more ordered as a result of the impact.

Section 6.3 discusses a possible cause for the narrowing of the peaks. During an impact, not only does a shockwave propagate through the target and projectile materials, but heat is also generated. It is believed that this increase in temperature has been sufficient to cause the target materials to reach their annealing temperatures, thereby allowing a process which relieves stresses in the structure of materials to occur which then presents itself as a narrowing of the Raman peaks.

This means that there are potentially two processes with influence over the FWHM of the Raman peaks are occurring at the same time: broadening due to the shockwave, and narrowing as a result of annealing. Currently, there is no way to de-convolve these two effects as it is not possible to know exactly how much pressure a particular point of material inside the crater has been subjected to. Therefore, the FWHM of Raman peaks cannot be used as an exact shock barometer. However, the data showed that this annealing effect did not occur for smaller impacts where the heat generated was insufficient to reach the annealing temperature; and would also cease to occur in larger impacts when the heated material was either excavated or melted/vaporised (and was therefore no longer present to be analysed). As such, the presence of peak narrowing can be used to give an approximation to the temperatures reached by the sample during the impact - hot enough to reach the annealing temperature of the material but cool enough so as not to reach the melting/vaporisation temperature. While not particularly revealing on its own, when combined with other analysis techniques, this method may be able to provide further insight.

It may be possible to use the FWHM as a shock barometer for impacts small enough where the annealing effect does not occur, but an extensive low-speed shot program would first need to be performed to generate suitable targets for analysis.

Finally, the peak position as a shock barometer was considered. Previous studies have shown that increases in static pressure result in increases in Raman peak positions [129-133]. Using this as a basis, it was expected that the increase in pressure, generated by the shockwave passing through the minerals, would cause shifts in Raman peak position. Analysis of the Raman data proved that this was the case.

However, as the position of a Raman peak is dependent on the length of the bond that it represents, Equation 2.4 shows us that a change in either the structure or the effective mass of that bond will change its length. As such, it was first shown that the shifts seen in this study are the result of a change in the structure of the bond and not a change in the elemental constituents that make up said bond.

Section 6.4.1 describes an experiment whereby the ratio of the relevant elements for each mineral was compared for shocked and unshocked material. These results showed that the largest change in elemental ratio was 3%, which is insufficient to account for the shifts observed in the Raman data gathered here and, importantly, showed that no impact devolatilisation of elements present in the quartz, olivine, or labradorite targets. Therefore, the shifts in peak position presented in this study are the result of changes to the structure of the material due to the impact.

Analysis of the Raman data showed that both positive and negative shifts are present within the dataset. There does not appear to be a relationship between the size of the peak shift and the degree of shock pressure experienced by the target. It is believed that the crater formation process is to blame for lack of correlation. As during the crater formation process material is excavated from the target surface and, as such, is not present during analysis with the Raman spectrometer. In fact, the material being analysed is material that was already below the surface of the target before the impact and would have been subjected to a lesser (unknown) degree of shock than the calculated peak shock pressure. A small number of the impacts performed in the shot program did not form fully fledged crater but instead created 'bruises' on the target, merely pushing material down below the surface without removing it. It is shots of this nature, where all of the impacted material is still present, that may be able to show a correlation between peak shift and shock pressure that would form the basis of a shock barometer. However, there were not enough of these shots performed in this study from which to draw any conclusions and as such, a further low speed shot program would need to be undertaken in order to test this.

To complicate matters further, both pressure and temperature effects are involved during an impact event. The temperature experiments in Chapter 4 showed that the Raman peaks returned to their original position after the sample returned to room temperature. However, impact events occur over a very short space of time and it is possible that the peak shifts generated by the increase in temperature are being 'locked in' to the target in the same way as the shifts generated by the shock pressures. This further convolutes an already complicated dataset.

7.2 Future work

During the experimentation and analysis performed throughout this study, a number of areas of potential improvement have been identified that would allow for further progress towards meeting the above goals:

1. Determine the instrument response function (IRF) of the Raman spectrometer at the University of Kent to allow for accurate calculation of the Stokes/anti-Stokes temperatures.

2. Repeat the temperature versus peak position experiment in Chapter 4 with an increased temperature range of up to 1200 °C. This temperature is sufficient to include the annealing temperatures of all of the minerals investigated and would therefore provide an overlap with the annealing observed in the pressure experiments presented in Chapter 5 and Chapter 6, The FWHM of these new data should also be investigated for temperatures above the annealing temperature for each mineral, as a possible calibration for the impact annealing effect.

3. The grain size experiment should be repeated, using the techniques and processes developed in Chapter 4 as a basis, with smaller grains. Specifically, of the nanometre scale or smaller. Performing such an experiment, in conjunction with knowledge of the IRF suggested earlier, would hopefully produce meaningful data that would be able to provide insight into the effects of grain size on the Raman spectrum of the minerals.

4. Further development of the electronic burst disk (EBD) system. Specifically, with a calibration shot program that would allow opportunities to continue to develop best practices for the manufacture and assembly of EBD components, as well as calibrate the pressure versus velocity data for multiple common projectiles.

5. As seen above, the excavation of material complicated the Raman analysis of the craters due to the loss of the information contained within the removed material. In the case of a crater, material that is side-by-side may not have been subjected to the same degree of shock. This could be overcome by continuing the impact experiments presented in this study in two ways:

    a. Performing an extensive low speed shot program with the intention of creating impacts where the target is 'bruised' by the impact but no material is excavated. These data would allow for further investigation into the viability of peak position and FWHM as shock barometers for low speed impacts, with the insights gained potentially giving perspective to the high velocity impacts already seen here.

    b. Performing new high speed shots in the same manner as this study, but with the addition of an ejecta capture system to allow for the analysis of the excavated material. This only partially overcomes the problem as the original location of the ejecta would still be unknown and some material may still be lost due to vaporisation.

6. Perform static pressure Raman tests on labradorite to allow low speed labradorite shots to be directly compared to a static pressure counterpart.

7. After the above work has been completed, it will then be possible to compare these new data to Raman spectra gathered from meteorite samples (as well as spectra gathered by the upcoming *Rosalind Franklin* and *Mars 2020* rover mission) containing the same minerals investigated here. This will provide a method for interpreting the shock history of those samples as a means of understanding their origins.

Bibliography

1. Bogard DD, Johnson P. Martian Gases in an Antarctic Meteorite? *Science*. 1983; 221(4611): 651-4.

2. Klein HP, Horowitz NH, Levin GV, Oyama VI, Lederberg J, Rich A, et al. The Viking Biological Investigation: Preliminary Results. *Science*. 1976; 194(4260): 99-105.

3. Wänke H, Brückner J, Dreibus G, Rieder R, Ryabchikov I. Chemical Composition of Rocks and Soils at the Pathfinder Site. *Space Science Reviews*. 2001; 96(1): 317-30.

4. Malin MC, Carr MH, Danielson GE, Davies ME, Hartmann WK, Ingersoll AP, et al. Early Views of the Martian Surface from the Mars Orbiter Camera of Mars Global Surveyor. *Science*. 1998; 279(5357): 1681-5.

5. Balme M, Mangold N, Baratoux D, Costard F, Gosselin M, Masson P, et al. Orientation and Distribution of Recent Gullies in the Southern Hemisphere of Mars: Observations from High Resolution Stereo Camera/Mars Express (HRSC/MEX) and Mars Orbiter Camera/Mars Global Surveyor (MOC/MGS) Data. *J Geophys Res*. 2006; 111.

6. Feldman WC, Prettyman TH, Maurice S, Plaut JJ, Bish DL, Vaniman DT, et al. Global Distribution of Near-Surface Hydrogen on Mars. *J Geophys Res*. 2004; 109.

7. Orosei R, Lauro SE, Pettinelli E, Cicchetti A, Coradini M, Cosciotti B, et al. Radar Evidence of Subglacial Liquid Water on Mars. *Science*. 2018; 361(6401): 490-3.

8. PIA19106: Components of Beagle 2 Flight System on Mars. NASA's Jet Propulsion Laboratory [cited 2019 Jun 10]. Available from: https://photojournal.jpl.nasa.gov/catalog/PIA19106.

9. Bridges JC, Clemmet J., Croon M., Sims MR, Pullan D., Muller J.-P., et al. Identification of the Beagle 2 Lander on Mars. *Royal Society Open Science*. 2017; 4(10): 170785.

10. Crisp JA, Adler M, Matijevic JR, Squyres SW, Arvidson RE, Kass DM. Mars Exploration Rover Mission. *J Geophys Res*. 2003; 108.

11. Kirk RL, Howington-Kraus E, Rosiek MR, Anderson JA, Archinal BA, Becker KJ, et al. Ultrahigh Resolution Topographic Mapping of Mars with MRO HiRISE Stereo Images: Meter-Scale Slopes of Candidate Phoenix Landing Sites. *J Geophys Res*. 2008; 113.

12. Golombek M, Grant J, Kipp D, Vasavada A, Kirk R, Fergason R, et al. Selection of the Mars Science Laboratory Landing Site. *Space Science Reviews*. 2012; 170(1): 641-737.

13. Taylor J, Lee DK, Shambayati S. Chapter 6: Mars reconnaissance orbiter. In: Deep Space Communications. Taylor J, editor. p. 193-250; 2016.

14. Smith PH, Tamppari LK, Arvidson RE, Bass D, Blaney D, Boynton WV, et al. H_2O at the Phoenix Landing Site. *Science*. 2009; 325(5936): 58-61.

15. Prakash R, Burkhart P, Chen A, Comeaux KA, Guernsey C, Kipp DM, et al. Mars Science Laboratory Entry, Descent, and Landing System Overview. *2008 IEEE Aerospace Conference.* 2008:1-18.

16. Jakosky BM, Grebowsky JM, Luhmann JG, Brain DA. Initial Results from the MAVEN Mission to Mars. *Geophys Res Lett*. 2015; 42(21): 8791-802.

17. Jakosky BM, Grebowsky JM, Luhmann JG, Connerney J, Eparvier F, Ergun R, et al. MAVEN Observations of the Response of Mars to an Interplanetary Coronal Mass Ejection. *Science*. 2015; 350(6261).

18. NASA'a InSight Detects First Likely 'Quake' on Mars. NASA's Jet Propulsion Laboratory [cited 2019 Jun 10]. Available from: https://www.jpl.nasa.gov/news/news.php?feature=7383.

19. Korablev O, Vandaele AC, Montmessin F, Fedorova AA, Trokhimovskiy A, Forget F, et al. No Detection of Methane on Mars from Early ExoMars Trace Gas Orbiter Observations. *Nature*. 2019; 568(7753): 517-20.

20. Heymann D. Raman Spectra of Carbon in the Canyon Diablo Iron Meteorite. *18th lunar and planetary science conference;* 1987.

21. McMillan PF, Wolf GH, Lambert P. A Raman Spectroscopic Study of Shocked Single Crystalline Quartz. *Physics and Chemistry of Minerals*. 1992; 19(2): 71-9.

22. Burchell MJ, Cole MJ, McDonnell JAM, Zarnecki JC. Hypervelocity impact studies using the 2 MV Van de Graaff accelerator and two-stage light gas gun of the University of Kent at Canterbury. - *Measurement Science and Technology.* 1999(-1):- 41.

23. Durand-Manterola H, Cordero G. Assessments of the Energy, Mass and Size of the Chicxulub Impactor. *arXiv*. 2014; 1403.6391.

24. Schulte P, Alegret L, Arenillas I, Arz JA, Barton PJ, Bown PR, et al. The Chicxulub Asteroid Impact and Mass Extinction at the Cretaceous-Paleogene Boundary. *Science*. 2010; 327(5970): 1214-8.

25. Souness C, Hubbard B, Milliken RE, Quincey D. An Inventory and Population-Scale Analysis of Martian Glacier-Like Forms. *Icarus*. 2012; 217.

26. Cameron AGW, Benz W. The Origin of the Moon and the Single Impact Hypothesis IV. *Icarus*. 1991; 92(2): 204-16.

27. Lugmair GW, Shukolyukov A. Early Solar System Timescales According to 53Mn-53Cr Systematics. *Geochimica et Cosmochimica Acta*. 1998; 62(16): 2863-86.

28. Wiechert U, Halliday AN, Lee D-, Snyder GA, Taylor LA, Rumble D. Oxygen Isotopes and the Moon-Forming Giant Impact. *Science*. 2001; 294(5541): 345-8.

29. Zhang J, Dauphas N, Davis AM, Leya I, Fedkin A. The Proto-Earth as a Significant Source of Lunar Material. *Nature Geoscience*. 2012; 5: 251.

30. Menicucci A, Drolshagen G, Kuitunen J, Butenko Y, Mooney C. In-Flight and Post-Flight Impact Data Analysis from DEBIE2 (Debris in-Orbit Evaluator) on Board of ISS. *6th European Conference on Space Debris*. 2013: 723.

31. Theall J, Liou JC, Matney M, Kessler D. The Space Debris Environment for the ISS Orbit. *Proceedings of the Third European Conference on Space Debris*. 2001: 429.

32. Popova OP, Jenniskens P, Emel'yanenko V, Kartashova A, Biryukov E, Khaibrakhmanov S, et al. Chelyabinsk Airburst, Damage Assessment, Meteorite Recovery, and Characterization. *Science*. 2013; 342(6162): 1069-73.

33. Brown PG, Assink JD, Astiz L, Blaauw R, Boslough MB, Borovicka J, et al. A 500-Kiloton Airburst Over Chelyabinsk and an Enhanced Hazard from Small Impactors. *Nature*. 2013; 503: 238.

34. Johnson D, Tyldesley J, Lowe T, Withers PJ, Grady MM. Analysis of a Prehistoric Egyptian Iron Bead with Implications for the use and Perception of Meteorite Iron in Ancient Egypt. *Meteorit Planet Sci*. 2013; 48(6): 997-1006.

35. Comelli D, D'orazio M, Folco L, El-Halwagy M, Frizzi T, Alberti R, et al. The Meteoritic Origin of Tutankhamun's Iron Dagger Blade. *Meteorit Planet Sci*. 2016; 51(7): 1301-9.

36. ANSMET, the Antarctic Search for Meteorites. Case Western Reserve University [cited 2018 Jul 22]. Available from: http://caslabs.case.edu/ansmet/.

37. Expedition to Uncover the 'Lost' Meteorites of Antarctica. British Antarctic Survey [cited 2018 Jul 22]. Available from: https://www.bas.ac.uk/media-post/expedition-to-uncover-the-lost-meteorites-of-antarctica/.

38. Bland PA, Spurný P, Bevan AWR, Howard KT, Towner MC, Benedix GK, et al. The Australian Desert Fireball Network: A New Era for Planetary Science. *Aust J Earth Sci*. 2012; 59(2): 177-87.

39. Meteors & Meteorite. NASA's Jet Propulsion Laboratory [cited 2018 Jul 22]. Available from: https://solarsystem.nasa.gov/small-bodies/meteors-and-meteorites/in-depth/.

40. Simms MJ. Where are all the Terrestrial Meteorites? *74th annual meeting of the meteoritical society;* London, U.K. 2011. p. A214.

41. American Meteor Society - Meteor FAQS. The American Meteor Society, Ltd [cited 2018 Jul 22]. Available from: https://www.amsmeteors.org/meteor-showers/meteor-faq/.

42. Melosh HJ. Impact Cratering: A Geologic Process. New York: Oxford University Press (Oxford Monographs on Geology and Geophysics, No.11); 1989.

43. French BM. Traces of Catastrophe: A Handbook of Shock-Metamorphic Effects in Terrestrial Meteorite Impact Structures. Lunar and Planetary Institute, Houston: LPI Contribution No.954; 1998.

44. Osinski GR, Elisabetta P. Impact Cratering Processes and Products. Malaysia: Wiley-Blackwell; 2013.

45. Burchell MJ. Chapter 8 - shocked rocks: Impacts from the laboratory to the solar system. In: EMU Notes in Mineralogy, Vol 15, Planetary Mineralogy. Lee MR, Leroux H, editors. p. 227-51. European Mineralogical Union and the Mineralogical Society of Great Britain & Ireland; 2015. London, UK.

46. Coes L. A New Dense Crystalline Silica. *Science*. 1953; 118(3057): 131-2.

47. Chao ECT, Shoemaker EM, Madsen BM. First Natural Occurrence of Coesite. *Science*. 1960; 132(3421): 220-2.

48. Osinski GR. Impact Metamorphism of CaCO3-Bearing Sandstones at the Haughton Structure, Canada. *Meteoritics & Planetary Science*. 2007; 42(11): 1945-60.

49. Stishov SM, Popova SV. A New Modification of Silica. *Geochemistry*. 1961; 10: 923-6.

50. De Carli PS, Milton DJ. Stishovite: Synthesis by Shock Wave. *Science*. 1965; 147(3654): 144-5.

51. Masaitis VL. Popigai Crater: Origin and Distribution of Diamond-Bearing Impactites. *Meteoritics & Planetary Science*. 1998; 33(2): 349-59.

52. Hough RM, Gilmour I, Pillinger CT, Arden JW, Gilkess KWR, Yuan J, et al. Diamond and Silicon Carbide in Impact Melt Rock from the Ries Impact Crater. *Nature*. 1995; 378: 41.

53. Gilmour I, French BM, Franchi IA, Abbott JI, Hough RM, Newton J, et al. Geochemistry of Carbonaceous Impactites from the Gardnos Impact Structure, Norway. *Geochimica et Cosmochimica Acta*. 2003; 67(20): 3889-903.

54. Michel-Levy MC, Lautie A. Microanalysis by Raman Spectroscopy of Carbon in the Tieschitz Chondrite. *Nature*. 1981; 292: 321-2.

55. Wopenka B, S, ford SA. Laser Raman Microprobe Study of Mineral Phases in Meteorites. *47th annual meeting of the meteoritical society;* 1984. p. 160.

56. Perry CH, Agrawal DK, Anastassakis E, Lowndes RP, Rastogi A, Tornberg NE. Infrared and Raman Spectra of Lunar Samples from Apollo 11, 12 and 14. *The moon*. 1972; 4(3): 315-36.

57. Price MC, Wozniakiewicz PJ, Bridges JC, Hicks LJ, Burchell MJ. Raman Analyses of Stardust Terminal Grain in Track 170. *European planetary science congress 2012;* 2012. p. EPS2012-333.

58. Price MC, Bridges JC, Hicks LJ, Wozniakiewicz PJ. Raman Spectroscopy of Stardust Tracks 170, 176, 177 and 178: Comparison to Chondrules from QUE 99177. *77th annual meeting of the meteoritical society;* 2014. p. 5247.

59. Noguchi T, Bridges JC, Hicks LJ, Gurman SJ, Kimura M, Hashimoto T, et al. Mineralogy of Four Itokawa Particles Collected from the First Touchdown Site. *Earth, Planets and Space*. 2014; 66(1): 124.

60. Smekal A. Zur Quantentheorie Der Dispersion. *Naturwissenschaften*. 1923; 11(43): 873-5.

61. Raman CV, Krishnan KS. A New Type of Secondary Radiation. *Nature*. 1928; 121: 501.

62. *Tuschel D.* Raman Thermometry. Spectroscopy. 2016; 31(12).

63. Smith E, Dent G. Modern Raman Spectroscopy: A Practical Approach. England: Wiley; 2005.

64. Raman Scattering and Flourescence. Horiba [cited 2018 Jul 22]. Available from: http://www.horiba.com/fileadmin/uploads/Scientific/Documents/Raman/Fluorescence01.pdf.

65. Schrader B, Hoffmann A, Keller S. Near-infrared Fourier transform Raman spectroscopy: Facing absorption and background. *Spectrochimica Acta Part A: Molecular Spectroscopy.* 1991;47(9):1135-48.

66. Thorley FC, Baldwin KJ, Lee DC, Batchelder DN. Dependence of the Raman Spectra of Drug Substances upon Laser Excitation Wavelength. *J Raman Spectrosc*. 2006; 37(1): 335-41.

67. Salahioglu F. Application of Raman Spectroscopy to the Differentiation of Lipsticks for Forensic Purposes [dissertation]. University of Kent; 2012.

68. Macdonald AM, Wyeth P. On the use of Photobleaching to Reduce Fluorescence Background in Raman Spectroscopy to Improve the Reliability of Pigment Identification on Painted Textiles. *J Raman Spectrosc*. 2006; 37(8): 830-5.

69. de Faria D,L.A., de Souza M,A. Raman Spectra of Human Skin and Nail Excited in the Visible Region. *J Raman Spectrosc*. 1999; 30: 169-71.

70. Buzzini P, Massonnet G, Sermier FM. The Micro Raman Analysis of Paint Evidence in Criminalistics: Case Studies. *J Raman Spectrosc*. 2006; 37(9): 922-31.

71. Teixeira AMR, Freire PTC, Moreno AJD, Sasaki JM, Ayala AP, Mendes Filho J, et al. High-pressure Raman study of l-alanine crystal. *Solid State Communications.* 2000;116(7):405-9.

72. Schuster KC, Reese I, Urlaub E, Gapes JR, Lendl B. Multidimensional Information on the Chemical Composition of Single Bacterial Cells by Confocal Raman Microspectroscopy. *Anal Chem*. 2000; 72(22): 5529-34.

73. Alexander TA, Pellegrino PM, Gillespie JB. Near-Infrared Surface-Enhanced-Raman-Scattering-Mediated Detection of Single Optically Trapped Bacterial Spores. *Appl Spectrosc*. 2003; 57(11): 1340-5.

74. Wold JP, Marquardt BJ, Dable BK, Robb D, Hatlen B. Rapid Quantification of Carotenoids and Fat in Atlantic Salmon (Salmo Salar L.) by Raman Spectroscopy and Chemometrics. *Appl Spectrosc*. 2004; 58(4): 395-403.

75. Arcangeli C, Cannistraro S. In-Situ Raman Microspectroscopic Identification and Localization of Carotenoids: Approach to Monitoring of UV-B Irradiation Stress on Antarctic Fungus. *Biopolymers*. 2000; 57(3): 179-86.

76. Manfait M, Lamaze P, Lamfarraj H, Pluot M, Sockalingum G. Diagnosis and Prognosis of Tissue Pathologies by Raman Microspectroscopy: An Application to Human Thyroid Tumors. *Proc SPIE Int Soc Opt Eng*. 2000; 3918.

77. Frank CJ, McCreery RL, Redd DCB. Raman Spectroscopy of Normal and Diseased Human Breast Tissues. *Anal Chem*. 1995; 67(5): 777-83.

78. Deisingh AK. Pharmaceutical Counterfeiting. *Analyst*. 2005; 130(3): 271-9.

79. Eliasson C, Matousek P. Noninvasive Authentication of Pharmaceutical Products through Packaging using Spatially Offset Raman Spectroscopy. *Anal Chem*. 2007; 79(4): 1696-701.

80. Wesełucha-Birczyńska A, Nakamoto K. Study of the Interaction of the Antimalarial Drug Cinchonine with Nucleic Acids by Raman Spectroscopy. *J Raman Spectrosc*. 1996; 27(12): 915-9.

81. Butler CA, Cooney RP, Denny WA. Resonance Raman Study of the Binding of the Anticancer Drug Amsacrine to DNA. *Appl Spectrosc*. 1994; 48(7): 822-6.

82. Glice MM, Leś A, Bajdor K. IR, Raman and theoretical ab initio RHF study of aminoglutethimide — an anticancer drug. *Journal of Molecular Structure.* 1998;450(1):141-53.

83. Centeno SA, Shamir J. Surface enhanced Raman scattering (SERS) and FTIR characterization of the sepia melanin pigment used in works of art. *Journal of Molecular Structure.* 2008;873(1):149-59.

84. Edwards HGM. Analytical Raman spectroscopic discrimination between yellow pigments of the Renaissance. *Spectrochimica Acta Part A: Molecular and Biomolecular Spectroscopy.* 2011;80(1):14-20.

85. Clark RJH. Pigment identification by spectroscopic means: an arts/science interface. *Comptes Rendus Chimie.* 2002;5(1):7-20.

86. Chen K, Leona M, Vo-Dinh K, Yan F, Wabuyele MB, Vo-Dinh T. Application of Surface-Enhanced Raman Scattering (SERS) for the Identification of Anthraquinone Dyes used in Works of Art. *J Raman Spectrosc*. 2006; 37(4): 520-7.

87. Jurasekova Z, del Puerto E, Bruno G, García-Ramos JV, Sanchez-Cortes S, Domingo C. Extractionless Non-Hydrolysis Surface-Enhanced Raman Spectroscopic Detection of Historical Mordant Dyes on Textile Fibers. *J Raman Spectrosc*. 2010; 41(11): 1455-61.

88. Edwards HGM, Brooke CJ, Tait JKF. Fourier Transform Raman Spectroscopic Study of Pigments from English Mediaeval Wall Paintings. *J Raman Spectrosc*. 1997; 28(2): 95-8.

89. Bioletti S, Leahy R, Fields J, Meehan B, Blau W. The Examination of the Book of Kells using Micro-Raman Spectroscopy. *J Raman Spectrosc*. 2009; 40(8): 1043-9.

90. Edwards HGM, Gwyer ER, Tait JKF. Fourier Transform Raman Analysis of Paint Fragments from Biodeteriorated Renaissance Frescoes. *J Raman Spectrosc*. 1997; 28(9): 677-84.

91. Clark RJH. Applications of Raman Spectroscopy to the Identification and Conservation of Pigments on Art Objects. ; 2006.

92. Rull Perez F, Edwards HGM, Rivas A, Drummond L. Fourier Transform Raman Spectroscopic Characterization of Pigments in the Mediaeval Frescoes at Convento De La Peregrina, Sahagun, Léon, Spain. Part 1 — Preliminary Study. *J Raman Spectrosc*. 1999; 30(4): 301-5.

93. Burgio L, Clark RJH. Comparative Pigment Analysis of Six Modern Egyptian Papyri and an Authentic One of the 13th Century BC by Raman Microscopy and Other Techniques. *J Raman Spectrosc*. 2000; 31(5): 395-401.

94. West MJ, Went MJ. The spectroscopic detection of drugs of abuse in fingerprints after development with powders and recovery with adhesive lifters. *Spectrochimica Acta Part A: Molecular and Biomolecular Spectroscopy.* 2009;71(5):1984-8.

95. West MJ, Went MJ. The spectroscopic detection of exogenous material in fingerprints after development with powders and recovery with adhesive lifters. *Forensic Science International.* 2008;174(1):1-5.

96. West MJ, Went MJ. The spectroscopic detection of drugs of abuse on textile fibres after recovery with adhesive lifters. *Forensic Science International.* 2009;189(1):100-3.

97. López-López M, Ferrando JL, García-Ruiz C. Comparative Analysis of Smokeless Gunpowders by Fourier Transform Infrared and Raman Spectroscopy. *Analytica Chimica Acta.* 2012;717:92-9.

98. Hatab NA, Eres G, Hatzinger PB, Gu B. Detection and Analysis of Cyclotrimethylenetrinitramine (RDX) in Environmental Samples by Surface-Enhanced Raman Spectroscopy. *J Raman Spectrosc*. 2010; 41(10): 1131-6.

99. Xu Z, Meng X. Detection of 3-nitro-1,2,4-triazol-3-one (NTO) by Surface-Enhanced Raman Spectroscopy. *Vibrational Spectroscopy.* 2012;63:390-5.

100. Ali EMA, Edwards HGM, Hargreaves MD, Scowen IJ. In-Situ Detection of Drugs-of-Abuse on Clothing using Confocal Raman Microscopy. *Analytica Chimica Acta.* 2008;615(1):63-72.

101. Day JS, Edwards HGM, Dobrowski SA, Voice AM. The detection of drugs of abuse in fingerprints using Raman spectroscopy II: cyanoacrylate-fumed fingerprints. *Spectrochimica Acta Part A: Molecular and Biomolecular Spectroscopy.* 2004;60(8):1725-30.

102. De Gelder J, Vandenabeele P, Govaert F, Moens L. Forensic Analysis of Automotive Paints by Raman Spectroscopy. *J Raman Spectrosc*. 2005; 36(11): 1059-67.

103. Zięba-Palus J, Wąs-Gubała J. An investigation into the use of micro-Raman spectroscopy for the analysis of car paints and single textile fibres. *Journal of Molecular Structure.* 2011;993(1):127-33.

104. Zięba-Palus J, Michalska A, Wesełucha-Birczyńska A. Characterisation of paint samples by infrared and Raman spectroscopy for criminalistic purposes. *Journal of Molecular Structure.* 2011;993(1):134-41.

105. Claybourn M, Ansell M. Using Raman Spectroscopy to solve crime: inks, questioned documents and fraud. *Science & Justice.* 2000;40(4):261-71.

106. Wang XF, Yu J, Zhang AL, Zhou DW, Xie MX. Nondestructive identification for red ink entries of seals by Raman and Fourier transform infrared spectrometry. *Spectrochimica Acta Part A: Molecular and Biomolecular Spectroscopy.* 2012;97:986-94.

107. Roy D, Chhowalla M, Wang H, Sano N, Alexandrou I, Clyne TW, et al. Characterisation of carbon nano-onions using Raman spectroscopy. *Chemical Physics Letters.* 2003;373(1):52-6.

108. Jorio A, Santos AP, Ribeiro HB, Fantini C, Souza M, Vieira JPM, et al. Quantifying Carbon-Nanotube Species with Resonance Raman Scattering. *Phys Rev B*. 2005; 72(7): 075207.

109. Gu B, Tio J, Wang W, Ku YK, Dai S. Raman Spectroscopic Detection for Perchlorate at Low Concentrations. *Appl Spectrosc*. 2004; 58: 741-4.

110. Ianoul A, Coleman T, Asher SA. UV Resonance Raman Spectroscopic Detection of Nitrate and Nitrite in Wastewater Treatment Processes. *Anal Chem*. 2002; 74(6): 1458-61.

111. Ruan C, Luo W, Wang W, Gu B. Surface-enhanced Raman spectroscopy for uranium detection and analysis in environmental samples. *Analytica Chimica Acta.* 2007;605(1):80-6.

112. Cerdeira F, Fjeldly TA, Cardona M. Effect of Free Carriers on Zone-Center Vibrational Modes in Heavily Doped P-Type Si. II. Optical Modes. *Phys Rev B*. 1973; 8(10): 4734-45.

113. Jimenez-Sandoval S. Micro-Raman Spectroscopy: A Powerful Technique for Materials Research. *Microelectronics Journal.* 2000;31(6):419-27.

114. Zhu J, Xu F, Schofer SJ, Mirkin CA. The First Raman Spectrum of an Organic Monolayer on a High-Temperature Superconductor: Direct Spectroscopic Evidence for a Chemical Interaction between an Amine and $YBa_2Cu_3O_{7-\Delta}$. *J Am Chem Soc*. 1997; 119(1): 235-6.

115. El-Harrad I, Ridah A, Carabatos-Nédelec C, Becker P, Handerek J, Ujma Z, et al. Raman Scattering Investigation with Temperature of Phase Transitions in (Pb1-xBax)ZrO3 Ceramics at Critical Compositions X=0.175 and 0.35. *J Raman Spectrosc*. 1998; 29(2): 123-9.

116. Potgieter-Vermaak SS, Potgieter JH, Van Grieken R. The Application of Raman Spectrometry to Investigate and Characterize Cement, Part I: A Review. *Cement and Concrete Research.* 2006;36(4):656-62.

117. Garton A, Batchelder DN, Cheng C. Raman Microscopy of Polymer Blends. *Appl Spectrosc*. 1993; 47(7): 922-7.

118. Jackson KDO, Loadman MJR, Jones CH, Ellis G. Fourier Transform Raman Spectroscopy of Elastomers: An Overview. *Spectrochimica Acta Part A: Molecular Spectroscopy.* 1990;46(2):217-26.

119. Tashiro K, Sasaki S, Ueno Y, Yoshioka A, Kobayashi M. Crystallization Behavior of Polymers as Viewed from the Molecular Level. *Korea Polymer Journal*. 2000; 8(3): 103-15.

120. Cornell SW, Koenig JL. The Raman Spectra of Polybutadiene Rubbers. *Macromolecules*. 1969; 2(5): 540-5.

121. Raman Spectroscopy for Geological Materials Analysis. Horiba [cited 2018 Jul 22]. Available from: http://www.horiba.com/fileadmin/uploads/Scientific/Documents/Raman/RA23-Raman_spectroscopy_for_geological_materials_analysis.pdf.

122. Kuebler KE, Jolliff BL, Wang A, Haskin LA. Extracting olivine (Fo–Fa) compositions from Raman spectral peak positions. *Geochimica et Cosmochimica Acta.* 2006;70(24):6201-22.

123. Vandenabeele P, Edwards HGM, Jehlicka J. The Role of Mobile Instrumentation in Novel Applications of Raman Spectroscopy: Archaeometry, Geosciences, and Forensics. *Chem Soc Rev*. 2014; 43(8): 2628-49.

124. Deneckere A, Leeflang M, Bloem M, Chavannes-Mazel CA, Vekemans B, Vincze L, et al. The use of Mobile Raman Spectroscopy to Compare Three Full-Page Miniatures from the Breviary of Arnold of Egmond. *Spectrochimica acta.Part A, Molecular and biomolecular spectroscopy*. 2011; 83(1): 194-9.

125. Rull F, Martinez-Frias J, Sansano A, Medina J, Edwards HGM. Comparative Micro-Raman Study of the Nakhla and Vaca Muerta Meteorites. *J Raman Spectrosc*. 2004; 35(6): 497-503.

126. Wang A, Kuebler KE, Jolliff B, Haskin LA. Mineralogy of a Martian Meteorite as Determined by Raman Spectroscopy. *J Raman Spectrosc*. 2004; 35(6): 504-14.

127. Frosch T, Tarcea N, Schmitt M, Thiele H, Langenhorst F, Popp J. UV Raman Imaging A Promising Tool for Astrobiology: Comparative Raman Studies with Different Excitation Wavelengths on SNC Martian Meteorites. *Anal Chem*. 2007; 79(3): 1101-8.

128. Fritz J, Greshake A, Stöffler D. Micro-Raman Spectroscopy of Plagioclase and Maskelynite in Martian Meteorites: Evidence of Progressive Shock Metamorphism. *Antarctic Meteorite Research*. 2005; 18: 96.

129. Dean KJ, Sherman WF, Wilkinson GR. Temperature and pressure dependence of the Raman active modes of vibration of α-quartz. *Spectrochimica Acta Part A: Molecular Spectroscopy.* 1982;38(10):1105-8.

130. Asell JF, Nicol M. Raman Spectrum of A Quartz at High Pressures. *J Chem Phys*. 1968; 49(12): 5395-9.

131. Jayaraman A, Wood DL, Maines RG. High-Pressure Raman Study of the Vibrational Modes in AlPO4 and SiO2 (Alpha-Quartz). *Phys.Rev.B*. 1987; 35(16): 8316-21.

132. Besson JM, Pinceaux JP, Anastopoulos C, Velde B. Raman Spectra of Olivine Up to 65 Kilobars. *J Geophys Res*. 1982; 87: 10773-5.

133. Chopelas A. Thermal Properties of Forsterite at Mantle Pressures Derived from Vibrational Spectroscopy. *Physics and Chemistry of Minerals*. 1990; 17: 149-56.

134. Foster NF, Wozniakiewicz PJ, Price MC, Kearsley AT, Burchell MJ. Identification by Raman spectroscopy of Mg–Fe content of olivine samples after impact at 6kms−1 onto aluminium foil and aerogel: In the laboratory and in Wild-2 cometary samples. *Geochimica et Cosmochimica Acta.* 2013;121:1-14.

135. Harriss KH, Burchell MJ. A Study of the Observed Shift in the Peak Position of Olivine Raman Spectra as a Result of Shock Induced by Hypervelocity Impacts. *Meteorit Planet Sci*. 2016; 51(7): 1289-300.

136. Edwards HGM, Hutchinson I, Ingley R. The ExoMars Raman Spectrometer and the Identification of Biogeological Spectroscopic Signatures using a Flight-Like Prototype. *Analytical and Bioanalytical Chemistry*. 2012; 404(6): 1723-31.

137. Vago J, Witasse O, Svedhem H, Baglioni P, Haldemann A, Gianfiglio G, et al. ESA ExoMars Program: The Next Step in Exploring Mars. *Solar System Research*. 2015; 49(7): 518-28.

138. What Types of Laser (Rayleigh) Filtering are used? Horiba [cited 2018 Jul 22]. Available from: http://www.horiba.com/scientific/products/raman-spectroscopy/raman-academy/raman-faqs/what-types-of-laser-rayleigh-filtering-are-used/.

139. Linkam THMS600. Linkam [cited 2018 Jul 22]. Available from: http://www.linkam.co.uk/thms600-features.

140. Two-Stage Gas Guns. Physics Application Inc. [cited 2018 Jul 22]. Available from: http://www.physicsapp.com/two-stage_gas_guns.html.

141. Kearsley AT, Burchell MJ, Hörz F, Cole MJ, Schwandt CS. Laboratory Simulation of Impacts on Aluminum Foils of the Stardust Spacecraft: Calibration of Dust Particle Size from Comet Wild-2. *Meteoritics & Planetary Science*. 2006; 41(2): 167-80.

142. Brownlee D, Tsou P, Aléon J, Alexander CMO, Araki T, Bajt S, et al. Comet 81P/Wild 2 Under a Microscope. *Science*. 2006; 314(5806): 1711-6.

143. Hörz F, Bastien R, Borg J, Bradley JP, Bridges JC, Brownlee DE, et al. Impact Features on Stardust: Implications for Comet 81P/Wild 2 Dust. *Science*. 2006; 314(5806): 1716-9.

144. Price MC, Kearsley AT, Burchell MJ, Hörz F, Borg J, Bridges JC, et al. Comet 81P/Wild 2: The Size Distribution of Finer (Sub-10 μm) Dust Collected by the Stardust Spacecraft. *Meteoritics & Planetary Science*. 2010; 45(9): 1409-28.

145. Burchell MJ, Fairey SAJ, Wozniakiewicz P, Brownlee DE, Hörz F, Kearsley AT, et al. Characteristics of Cometary Dust Tracks in Stardust Aerogel and Laboratory Calibrations. *Meteoritics & Planetary Science*. 2008; 43(1): 23-40.

146. Price MC, Kearsley AT, Burchell MJ, Howard LE, Hillier JK, Starkey NA, et al. Stardust Interstellar Dust Calibration: Hydrocode Modeling of Impacts on Al-1100 Foil at Velocities Up to 300 km/s and Validation with Experimental Data. *Meteoritics & Planetary Science*. 2012; 47(4): 684-95.

147. Burchell MJ, Mann J, Bunch AW, Brandão PFB. Survivability of Bacteria in Hypervelocity Impact. *Icarus.* 2001;154(2):545-7.

148. Price MC, Solscheid C, Burchell MJ, Josse L, Adamek N, Cole MJ. Survival of yeast spores in hypervelocity impact events up to velocities of 7.4km/s. *Icarus.* 2013;222(1):263-72.

149. Burchell MJ, Harriss KH, Price MC, Yolland L. Survival of Fossilised Diatoms and Forams in Hypervelocity Impacts with Peak Shock Pressures in the 1–19GPa Range. *Icarus.* 2017;290:81-8.

150. Price MC, Burchell MJ, Cole MJ. The Influence of Target Temperature on Crater Morphometry: Experiments and Hydrocode Modelling. *42nd lunar and planetary science conference;* The Woodlands, Texas. 2011. p. 2328.

151. McDermott KH, Burchell MJ. Impact Melting Experiments in a Hot Basalt Target. *Bridging the gap III: Impact cratering in nature, experiments, and modeling;* University of Freiburg, Germany. 2015. p. 1007.

152. Morris AJW, Price MC, Cole MJ, Kearsley AT, Burchell MJ. Cratering Efficiency in Rocks as a Function of Rock Temperature. *42nd lunar and planetary science conference;* The Woodlands, Texas. 2011. p. 1943.

153. Morris AJW, Burchell MJ. Hypervelocity Impacts in the Laboratory on Hot Rock Targets. *Procedia Engineering.* 2017;204:300-7.

154. Shrine NRG, Burchell MJ, Grey IDS. Velocity Scaling of Impact Craters in Water Ice over the Range 1 to 7.3 km s−1. *Icarus.* 2002;155(2):475-85.

155. Grey IDS, Burchell MJ, Shrine NRG. Scaling of Hypervelocity Impact Craters in Ice with Impact Angle. *J Geophys Res*. 2002; 107: 6,1; 6-8.

156. Grey IDS, Burchell MJ. Hypervelocity Impact Cratering on Water Ice Targets at Temperatures Ranging from 100 K to 253 K. *J Geophys Res*. 2003; 108.

157. Harriss KH, Burchell MJ. Hypervelocity Impacts into Ice-Topped Layered Targets: Investigating the Effects of Ice Crust Thickness and Subsurface Density on Crater Morphology. *Meteorit Planet Sci*. 2017; 52(7): 1505-22.

158. Burchell MJ, Morris AJW, Price MC, Cole MJ. Is the Large Crater on the Asteroid (2867) Steins really an Impact Crater? *The Astrophysical Journal Letters*. 2013; 774(1): L11.

159. Pasini DLS, Price MC, Burchell MJ, Cole MJ. Survival of the Tardigrade Hypsibius Dujardini during Hypervelocity Impact Events Up to 3.23 km/S. *European planetary science congress;* Cascais, Portugal. 2014. p. EPSC2014-67.

160. Milner DJ, Burchell MJ, Creighton JA, Parnell J. Oceanic Hypervelocity Impact Events: A Viable Mechanism for Successful Panspermia? *International Journal of Astrobiology*. 2006; 5(3): 261-7.

161. Baldwin EC, Milner DJ, Burchell MJ, Crawford IA. Laboratory Impacts into Dry and Wet Sandstone with and without an Overlying Water Layer: Implications for Scaling Laws and Projectile Survivability. *Meteoritics & Planetary Science*. 2007; 42(11): 1905-14.

162. Price MC, Ramkissoon NK, McMahon S, Miljković K, Parnell J, Wozniakiewicz PJ, et al. Limits on Methane Release and Generation Via Hypervelocity Impact of Martian Analogue Materials. *International Journal of Astrobiology*. 2014; 13(2): 132-40.

163. Burchell MJ, Galloway JA, Bunch AW, Brandão PFB. Survivability of Bacteria Ejected from Icy Surfaces After Hypervelocity Impact. *Origins of life and evolution of the biosphere*. 2003; 33(1): 53-74.

164. Moritoh T, Kawai N, Nakamura KG, Kondo K. Optimization of a Compact Two-Stage Light-Gas Gun Aiming at a Velocity of 9 km/S. *Rev Sci Instrum*. 2001; 72(11): 4270-2.

165. Doolan CJ. A two-stage light gas gun for the study of high speed impact in propellants. Salisbury: Department of Defense; 2001. Report No.: 1092.

166. Ramkissoon NK. The Role of Impact Driven Chemistry on the Lithosphere of Mars [dissertation]. University of Kent; 2016.

167. Pavlenko AV, Balabin SI, Kozelkov OE, Kazakov DN. A One-Stage Light-Gas Gun for Studying Dynamic Properties of Structural Materials in a Range Up to 40 GPa. *Instruments and Experimental Techniques*. 2013; 56(4): 482-4.

168. Jones AH, Isbell WM, Maiden CJ. Measurement of the Very-High-Pressure Properties of Materials using a Light-Gas Gun. *J Appl Phys*. 1966; 37(9): 3493-9.

169. Hibbert R, Cole MJ. Light Gas Gun Operation Manual. Training Manual. University of Kent: 2017.

170. What is the Temperature on Mars? space.com [cited 2018 Jul 22]. Available from: https://www.space.com/16907-what-is-the-temperature-of-mars.html.

171. Koeppen WC, Hamilton VE. Global Distribution, Composition, and Abundance of Olivine on the Surface of Mars from Thermal Infrared Data. *J Geophys Res*. 2008; 113.

172. Smith MR, Bandfield JL. Geology of Quartz and Hydrated Silica-Bearing Deposits Near Antoniadi Crater, Mars. *Journal of Geophysical Research (Planets)*. 2012; 117: 6007.

173. Milam KA, McSween Jr. HY, Moersch J, Christensen PR. Distribution and Variation of Plagioclase Compositions on Mars. *J Geophys Res*. 2010; 115.

174. Etchepare J, Merian M, Smetankine L. Vibrational Normal Modes of SiO2. I. A and B Quartz. *J Chem Phys*. 1974; 60.

175. Lopes R, Gregg T. Volcanic Worlds: Exploring the Solar System's Volcanoes. First ed. Springer-Verlag Berlin Heidelberg; 2004.

176. Greenwood NN, Earnshaw A. Chapter 9 - silicon. In: Chemistry of the Elements (Second Edition). Greenwood NN, Earnshaw A, editors. Second ed. p. 328-66. Butterworth-Heinemann; 1997. Oxford.

177. Freeman JJ, Wang A, Kuebler KE, Jolliff BL, Haskin LA. Characterization of Natural Feldspars by Raman Spectroscopy for Future Planetary Exploration. *canmin*. 2008; 46(6): 1477-500.

178. Loewenstein W. The Distribution of Aluminum in the Tetrahedra of Silicates and Aluminates. *ammin*. 1954; 39(1-2): 92-6.

179. Gem Cutting Acronyms and their Meanings. International Gem Society [cited 2018 Jul 22]. Available from: https://www.gemsociety.org/article/gem-cutting-acronyms-and-their-meanings/.

180. Tsuchiyama A, Takahashi E. Melting Kinetics of a Plagioclase Feldspar. *Contributions to Mineralogy and Petrology*. 1983; 84(4): 345-54.

181. Robbins SJ, Hynek BM. A New Global Database of Mars Impact Craters ≥1 km: 1. Database Creation, Properties, and Parameters. *J Geophys Res*. 2012; 117.

182. Melosh HJ. The Contact and Compression Stage of Impact Cratering. *Impact Cratering.* 2012.

183. Overview of Silica Polymorphs. The Quartz Page [cited 2018 Jul 22]. Available from: http://www.quartzpage.de/gen_mod.html#.

184. Helffrich GR, Wood BJ. The Earth's Mantle. *Nature*. 2001; 412(6846): 501-7.

185. Jaret SJ, Woerner WR, Phillips BL, Ehm L, Nekvasil H, Wright SP, et al. Maskelynite Formation Via Solid-State Transformation: Evidence of Infrared and X-Ray Anisotropy. *J Geophys Res Planets*. 2015; 120(3): 570-87.

186. Liermann H, Downs RT, Yang H. Site Disorder Revealed through Raman Spectra from Oriented Single Crystals: A Case Study on Karooite (MgTi2O5). *ammin*. 2006; 91(5-6): 790-3.

187. Fused Quartz Proper Usage Guidelines. The L. W. Wallace Co. [cited 2018 Jul 22]. Available from: https://technicalglass.com/usage_guide.html.

188. Kohlstedt DL, Nichols HPK, Hornack P. The Effect of Pressure on the Rate of Dislocation Recovery in Olivine. *J Geophys Res*. 1980; 85: 3122-30.

189. Ostertag R. Annealing Behaviour of Diaplectic Plagioclase Glass. *Lunar and planetary science xiii;* 1982. p. 607-8.

Appendix A – Stokes Temperature Tables

This appendix contains the data tables for the calculated Stokes temperatures at various stages of the analysis of the temperature experiment described in Section 4.4.

Table A.1: The Linkam stage temperature and the calculated Stokes temperatures for quartz P1, olivine P1, olivine P2, labradorite P1 and Labradorite P2 using Equation 4.3.

Linkam Stage Temp (°C)	Quartz P1 Stokes Temp (°C)	Olivine P1 Stokes Temp (°C)	Olivine P2 Stokes Temp (°C)	Labradorite P1 Stokes Temp (°C)	Labradorite P2 Stokes Temp (°C)
-150.0	-71.4	No Data	No Data	-72.4	-60.4
-140.0	-72.3	No Data	No Data	-67.0	-54.8
-130.0	-62.8	No Data	No Data	-56.3	-47.7
-120.0	-58.2	No Data	No Data	-59.8	-44.2
-110.0	-54.6	No Data	No Data	-45.1	-39.0
-100.0	-49.9	No Data	No Data	-41.6	-30.9
-90.0	-42.7	No Data	No Data	-33.7	-26.7
-80.0	-36.5	No Data	No Data	-33.3	-21.6
-70.0	-30.4	No Data	No Data	-24.5	-15.2
-60.0	-22.1	No Data	No Data	-26.9	-10.6
-50.0	-13.3	-27.0	-26.4	-10.9	-1.4
-40.0	-6.2	-18.7	-17.8	-10.3	0.3
-30.0	1.2	-10.6	-8.4	-0.3	13.4
-20.0	8.5	1.2	2.4	2.3	18.8
-10.0	17.7	8.1	9.0	5.2	22.4
0.0	26.4	22.4	23.2	20.9	34.7
10.0	34.9	31.4	33.0	26.8	43.0
20.0	44.2	44.3	46.8	28.5	47.1
30.0 (cold)	50.7	51.7	52.9	42.5	60.4
40.0 (cold)	61.5	59.1	60.8	53.1	65.8
30.0 (hot)	49.0	64.4	58.8	14.7	57.3
40.0 (hot)	56.4	71.3	72.1	28.0	66.0
50.0	64.0	81.7	81.9	31.9	69.7
60.0	69.9	96.3	92.5	40.5	79.7
70.0	76.6	105.1	103.6	41.7	85.7
80.0	82.5	111.8	114.0	54.2	95.8
90.0	89.5	129.5	126.3	60.5	102.7
100.0	94.8	138.0	138.3	68.5	114.2
110.0	102.4	148.7	147.6	73.7	119.9
120.0	109.3	160.0	157.5	85.3	127.4
130.0	116.0	170.1	168.3	90.6	136.5
140.0	122.6	177.3	176.6	95.9	147.1
150.0	130.6	190.2	187.0	271.4	266.5
160.0	138.4	198.7	198.9	204.6	232.1
170.0	143.8	209.2	212.2	141.8	192.5
180.0	152.2	217.2	217.7	131.9	188.4
190.0	157.6	229.0	227.5	117.0	179.5
200.0	165.1	234.7	239.3	114.5	188.5
210.0	173.3	247.3	249.3	135.8	196.2

220.0	178.9	253.9	257.6	145.5	201.7
230.0	189.7	270.3	267.2	159.0	217.5
240.0	193.0	282.4	282.7	171.7	227.1
250.0	199.3	283.7	293.1	194.0	242.5
260.0	210.6	292.6	301.9	191.2	246.3
270.0	216.7	314.9	318.9	198.1	260.4
280.0	220.9	327.6	329.8	211.9	263.3
290.0	229.3	340.2	340.7	217.6	272.7
300.0	235.9	345.6	354.2	230.6	282.0
310.0	242.5	360.0	363.0	228.6	293.5
320.0	250.6	374.1	378.6	240.2	304.3
330.0	259.9	390.4	392.5	246.9	311.3
340.0	265.9	389.2	398.1	258.8	320.1
350.0	273.5	414.7	415.5	265.5	328.6
360.0	281.6	422.7	426.3	280.6	334.8
370.0	289.5	435.6	443.7	298.4	348.8
380.0	301.6	448.3	457.1	294.7	351.0
390.0	301.4	451.1	458.6	307.4	359.1
400.0	309.3	477.2	476.1	327.1	375.9
410.0	319.5	495.7	495.2	323.0	380.9
420.0	327.8	493.8	507.7	335.7	387.8
430.0	339.7	513.5	515.3	357.5	406.2
440.0	344.4	520.3	527.1	356.4	407.5
450.0	354.0	542.4	542.8	365.8	422.6
460.0	363.2	543.7	554.1	378.9	419.5
470.0	371.2	555.9	566.5	364.0	431.1
480.0	374.9	564.7	573.7	383.1	433.5
490.0	382.4	581.1	588.9	384.6	449.8
500.0	392.5	589.5	596.4	388.3	450.6
510.0	398.7	603.0	611.4	395.8	455.8
520.0	405.9	614.1	621.0	408.7	457.9
530.0	420.4	628.1	637.7	392.5	458.4
540.0	429.2	648.5	647.1	408.8	472.7
550.0	434.3	665.8	670.1	400.1	470.4

Table A.2: The corrected Linkam stage temperature (Equation 4.5) and the calculated Stokes temperatures for quartz P1, olivine P1, olivine P2, labradorite P1 and Labradorite P2 using Equation 4.3.

Corrected Linkam Stage Temp (°C)	Quartz P1 Stokes Temp (°C)	Olivine P1 Stokes Temp (°C)	Olivine P2 Stokes Temp (°C)	Labradorite P1 Stokes Temp (°C)	Labradorite P2 Stokes Temp (°C)
-140.1	-71.4	No Data	No Data	-72.4	-60.4
-130.6	-72.3	No Data	No Data	-67.0	-54.8
-121.1	-62.8	No Data	No Data	-56.3	-47.7
-111.6	-58.2	No Data	No Data	-59.8	-44.2
-102.2	-54.6	No Data	No Data	-45.1	-39.0
-92.7	-49.9	No Data	No Data	-41.6	-30.9
-83.2	-42.7	No Data	No Data	-33.7	-26.7
-73.7	-36.5	No Data	No Data	-33.3	-21.6
-64.3	-30.4	No Data	No Data	-24.5	-15.2
-54.8	-22.1	No Data	No Data	-26.9	-10.6
-45.3	-13.3	-27.0	-26.4	-10.9	-1.4
-35.8	-6.2	-18.7	-17.8	-10.3	0.3
-26.4	1.2	-10.6	-8.4	-0.3	13.4
-16.9	8.5	1.2	2.4	2.3	18.8
-7.4	17.7	8.1	9.0	5.2	22.4
2.0	26.4	22.4	23.2	20.9	34.7
11.5	34.9	31.4	33.0	26.8	43.0
21.0	44.2	44.3	46.8	28.5	47.1
30.5(cold)	50.7	51.7	52.9	42.5	60.4
39.9(cold)	61.5	59.1	60.8	53.1	65.8
30.5(hot)	49.0	64.4	58.8	14.7	57.3
39.9(hot)	56.4	71.3	72.1	28.0	66.0
49.4	64.0	81.7	81.9	31.9	69.7
58.9	69.9	96.3	92.5	40.5	79.7
68.4	76.6	105.1	103.6	41.7	85.7
77.8	82.5	111.8	114.0	54.2	95.8
87.3	89.5	129.5	126.3	60.5	102.7
96.8	94.8	138.0	138.3	68.5	114.2
106.3	102.4	148.7	147.6	73.7	119.9
115.7	109.3	160.0	157.5	85.3	127.4
125.2	116.0	170.1	168.3	90.6	136.5
134.7	122.6	177.3	176.6	95.9	147.1
144.2	130.6	190.2	187.0	271.4	266.5
153.6	138.4	198.7	198.9	204.6	232.1
163.1	143.8	209.2	212.2	141.8	192.5
172.6	152.2	217.2	217.7	131.9	188.4
182.1	157.6	229.0	227.5	117.0	179.5
191.5	165.1	234.7	239.3	114.5	188.5
201.0	173.3	247.3	249.3	135.8	196.2

210.5	178.9	253.9	257.6	145.5	201.7
220.0	189.7	270.3	267.2	159.0	217.5
229.4	193.0	282.4	282.7	171.7	227.1
238.9	199.3	283.7	293.1	194.0	242.5
248.4	210.6	292.6	301.9	191.2	246.3
257.8	216.7	314.9	318.9	198.1	260.4
267.3	220.9	327.6	329.8	211.9	263.3
276.8	229.3	340.2	340.7	217.6	272.7
286.3	235.9	345.6	354.2	230.6	282.0
295.7	242.5	360.0	363.0	228.6	293.5
305.2	250.6	374.1	378.6	240.2	304.3
314.7	259.9	390.4	392.5	246.9	311.3
324.2	265.9	389.2	398.1	258.8	320.1
333.6	273.5	414.7	415.5	265.5	328.6
343.1	281.6	422.7	426.3	280.6	334.8
352.6	289.5	435.6	443.7	298.4	348.8
362.1	301.6	448.3	457.1	294.7	351.0
371.5	301.4	451.1	458.6	307.4	359.1
381.0	309.3	477.2	476.1	327.1	375.9
390.5	319.5	495.7	495.2	323.0	380.9
400.0	327.8	493.8	507.7	335.7	387.8
409.4	339.7	513.5	515.3	357.5	406.2
418.9	344.4	520.3	527.1	356.4	407.5
428.4	354.0	542.4	542.8	365.8	422.6
437.9	363.2	543.7	554.1	378.9	419.5
447.3	371.2	555.9	566.5	364.0	431.1
456.8	374.9	564.7	573.7	383.1	433.5
466.3	382.4	581.1	588.9	384.6	449.8
475.7	392.5	589.5	596.4	388.3	450.6
485.2	398.7	603.0	611.4	395.8	455.8
494.7	405.9	614.1	621.0	408.7	457.9
504.2	420.4	628.1	637.7	392.5	458.4
513.6	429.2	648.5	647.1	408.8	472.7
523.1	434.3	665.8	670.1	400.1	470.4

Table A.3: The corrected Linkam stage temperature (Equation 4.5) and the corrected Stokes temperatures calculated using Equation 4.3 and Equations 4.6 – 4.10.

Corrected Linkam Stage Temp (°C)	Quartz P1 Corrected Stokes Temp (°C)	Olivine P1 Corrected Stokes Temp (°C)	Olivine P2 Corrected Stokes Temp (°C)	Labradorite P1 Corrected Stokes Temp (°C)	Labradorite P2 Corrected Stokes Temp (°C)
-140.1	-141.8	No Data	No Data	-104.6	-147.2
-130.6	-144.8	No Data	No Data	-95.9	-128.4
-121.1	-120.0	No Data	No Data	-80.0	-111.4
-111.6	-110.7	No Data	No Data	-85.1	-104.4
-102.2	-104.0	No Data	No Data	-64.5	-94.7
-92.7	-95.7	No Data	No Data	-59.7	-81.3
-83.2	-83.9	No Data	No Data	-49.3	-74.7
-73.7	-74.5	No Data	No Data	-48.9	-67.3
-64.3	-65.4	No Data	No Data	-37.6	-58.1
-54.8	-53.7	No Data	No Data	-40.6	-51.7
-45.3	-41.5	-56.3	-53.8	-20.5	-39.5
-35.8	-32.2	-46.5	-43.9	-19.7	-37.3
-26.4	-22.4	-37.5	-33.6	-7.3	-20.5
-16.9	-13.0	-24.8	-22.2	-4.1	-13.9
-7.4	-1.1	-17.7	-15.4	-0.6	-9.5
2.0	9.9	-3.2	-1.2	18.7	5.4
11.5	20.6	5.7	8.3	25.8	15.3
21.0	32.3	18.2	21.6	27.9	20.1
30.5	40.4	25.2	27.4	45.0	35.7
39.9	53.8	32.2	34.8	57.8	41.9
30.5	38.3	37.2	32.9	11.1	32.1
39.9	47.4	43.7	45.3	27.3	42.2
49.4	56.9	53.3	54.3	32.1	46.5
58.9	64.2	66.7	64.1	42.5	58.0
68.4	72.5	74.7	74.1	43.9	64.9
77.8	79.8	80.8	83.4	59.1	76.5
87.3	88.6	96.6	94.4	66.8	84.3
96.8	95.2	104.2	105.1	76.5	97.4
106.3	104.6	113.7	113.3	82.8	103.9
115.7	113.2	123.6	122.1	96.9	112.3
125.2	121.6	132.5	131.5	103.4	122.7
134.7	129.9	138.8	138.7	109.9	134.7
144.2	139.8	150.0	147.7	No Data	No Data
153.6	149.6	157.4	158.0	No Data	No Data
163.1	156.4	166.4	169.5	No Data	No Data
172.6	167.0	173.3	174.2	No Data	No Data
182.1	173.8	183.4	182.5	No Data	No Data
191.5	183.2	188.2	192.5	132.7	181.5

201.0	193.8	198.9	201.0	158.9	190.2
210.5	200.9	204.5	207.9	171.0	196.5
220.0	214.7	218.3	216.0	187.9	214.4
229.4	218.9	228.5	229.0	203.8	225.3
238.9	227.0	229.5	237.6	231.9	242.9
248.4	241.6	237.0	244.9	228.4	247.2
257.8	249.5	255.4	259.0	237.1	263.3
267.3	254.9	265.9	267.9	254.8	266.5
276.8	265.9	276.3	276.8	262.1	277.3
286.3	274.5	280.7	287.8	278.9	288.0
295.7	283.2	292.5	295.0	276.3	301.2
305.2	293.9	303.9	307.6	291.3	313.7
314.7	306.2	317.1	318.7	300.1	321.7
324.2	314.2	316.1	323.2	315.7	331.8
333.6	324.4	336.5	337.1	324.5	341.7
343.1	335.2	342.9	345.7	344.4	348.9
352.6	345.8	353.2	359.5	368.2	365.1
362.1	362.2	363.2	370.0	363.2	367.8
371.5	362.0	365.5	371.2	380.3	377.1
381.0	372.7	385.9	384.9	406.9	396.8
390.5	386.7	400.4	399.7	401.3	402.6
400.0	398.1	398.9	409.4	418.6	410.7
409.4	414.6	414.2	415.3	448.6	432.4
418.9	421.2	419.5	424.4	447.2	433.9
428.4	434.5	436.5	436.4	460.2	451.8
437.9	447.5	437.4	445.0	478.6	448.1
447.3	458.8	446.8	454.4	457.6	461.9
456.8	464.1	453.5	459.9	484.5	464.8
466.3	474.7	466.0	471.4	486.6	484.1
475.7	489.2	472.3	477.0	491.8	485.1
485.2	498.1	482.5	488.3	502.3	491.4
494.7	508.5	490.8	495.4	520.7	493.8
504.2	529.6	501.3	507.9	497.7	494.4
513.6	542.5	516.5	514.8	520.8	511.5
523.1	550.0	529.3	531.8	508.5	508.8